Fabricating and Processing Carbon Nanomaterials using Vortex Fluidic Technology

By

Thaar Muqhim D. Alharbi

Thesis
Submitted to Flinders University for the degree of

Doctor of Philosophy

College of Science and Engineering

November 2020

Contents

LIST OF FIGURES

LIST OF ABBREVIATIONS

AFM	Atomic force microscopy
CNT	Carbon nanotube
DWCNT	Double walled carbon nanotube
FT-IR	Fourier transform infrared spectroscopy
FWHM	Full width of half maximum
HRTEM	High resolution transmission electron microscopy
HRSEM	High resolution scanning electron microscopy
ID	Inner diameter
IONP	Iron oxide nanoparticle
MW	Molecular weight
MWCNT	Multiwalled carbon nanotube
MFM	Magnetic force microscopy
NMP	N-methyl pyrrolidone
NMR	Nuclear magnetic resonance spectroscopy
Nd:YAG	Neodymium-doped yttrium aluminum garnet
NIR	Near infrared
OD	Outer diameter
1D	One dimensional
PL	Photoluminescence
SAED	Selected area electron diffraction
SWCNT	Single walled carbon nanotube
SEM	Scanning electron microscopy
SANS	Small angle neutron scattering
TEM	Transmission electron microscopy
TGA	Thermo-gravimetric analysis
2D	Two dimensional
UV-Vis	Ultraviolet visible spectroscopy

QD	Quantum dot
VFD	Vortex fluidic device
XPS	X-ray photoelectron spectroscopy
XRD	X-ray powder diffraction
GO	Graphene oxide
GOS	Graphene oxide scrolls
rGO	Reduced graphene oxide
VACNTs	Vertically aligned carbon nanotubes
CVD	Chemical vapour deposition
0D	Zero dimensional
3D	Three dimensional
FIB-SEM	Focused ion beam field emission scanning electron microscopy
PVDF	Polyvinylidene difluoride
HAADF	High-angle annular dark-field
STEM	Scanning Transmission Electron Microscope
NP	Nanoparticles
M_S	Saturation magnetization
C_{60}	Fullerene C_{60}
CD	Charge/discharge
CV	Cyclic voltammetry
IPA	Isopropyl alcohol
I_D/I_G	Ratio of the intensity of D- Raman peak and G- Raman peak
BF	Bright field
MOF	Metal organic framework
BSA	Bovine serum albumin
PSF	Polysulfone

SUMMARY

The availability of carbon nanomaterials with controllable size, shape and morphology has attracted considerable attention due to their explicit chemical and physical properties, such as excellent thermal and optical properties, high mechanical strength and electrical conductivity. Various methods have been developed to date for the ‘top down’ and ‘bottom up’ fabrication of carbon nanomaterials with specific control of their size, shape, morphology and surface property, featuring in a diverse range of applications. While there has been spectacular progress in fabricating nanomaterials with such properties, there are several limitations and challenges to overcome. These include the need for high molecular weight reagents, long and tedious processing conditions, the use of chemical stabilisers, the inherent high cost of the associated complex processing, and low yields. These limitations and challenges can be overcome using thin film microfluidics which has emerged in the last few years with remarkable outcomes, as highlighted by the development of simple one step methods of controlling the fabrication of zero dimensional (0D), one dimensional (1D) and two dimensional (2D) nanomaterials. Collectively, these are also important in developing environmentally sustainable processes, which are also economically feasible. Thin film microfluidics have potential advantages in chemical processing which relates to the large surface-to-volume ratio in the thin films, reduced reaction times, precise control over residence time and temperature, improved safety, and more importantly the ability to address scalability at the inception of the science.

The focus of this dissertation is creating a paradigm shift in nanoscience by using a thin film microfluidics platform, the vortex fluidic device (VFD), to control the fabrication of nanocarbon materials. The VFD has proved its capabilities in diverse areas, which includes but not limited to controlling the length of single and multiwalled carbon nanotubes, overcoming the high tensile strength of SWCNTs to form highly magnetic coiled rings, controlling the crystallisation of 0D fullerenes and fabricating composites of nanomaterial. These composite materials have proven potential in supercapacitors, with other potential applications under consideration. Within all the processing capabilities, the key advantage of the VFD is the ability to control the fabrication of nanomaterials without the need for toxic and harsh chemicals, as simple one step methods devoid of chemical stabilisers and surfactants and most importantly while simultaneously scalability of the processing.

DECLARATION

I certify that this thesis does not incorporate without acknowledgment any material previously submitted for a degree or diploma in any university; and that to the best of my knowledge and belief it does not contain any material previously published or written by another person except where due reference is made in the text.

Signed Thaar Alharbi

Date November 2020

ACKNOWLEDGEMENTS

First and foremost, I would like to express my gratitude to Allah (God) almighty for blessing me with the determination, health and wisdom to complete this thesis. Allah will not thank a person who does not thank people. Thus, this thesis would not have been possible without the help, patient, support and guidance of numerous people. I would like to express my gratitude attitude to all of them.

First, I would like to express my deepest thanks and appreciations to my principal supervisor, Professor Colin L. Raston. Your guidance and support throughout my candidature has been shown me the way I wish to lead a research group. Colin showed confidence in me and gave me opportunities, advice, encouragement and motivation. He has taught me that the key to a successful career is passion and hard work and for that I am sincerely grateful. Thanks for being a great mentor.

I would also like to thank my co-supervisor, Professor Warren Lawrance for his guidance, encouragement and positive attitude. A significant part of this research would not have been possible without our keen collaborators from a number of local and international universities, most importantly Prof. Rob Lamb (The University of Melbourne), Prof. Qin Li (Griffith University) and Dr. Mahmoud Moussa (The University of Adelaide).

I owe my deepest gratitude to my supervisors, Prof. Tomonobu Nakayam and Dr Yoshitaka Shingaya from the National Institute of Material Sciences (NIMS) in Japan for their time and guidance, particularly during my fellowship visit. I feel privileged to have had the opportunity to work at NIMS and gain invaluable experience at one of the world's most accomplished research institutes. I would also like to thank his group for their support.

I would like to say thank you to all the members of the Raston group, for creating an upward and harmonious environment in which I have been enjoying every day. All the members have been very friendly and supportive throughout the PhD. Special thanks go to Dr. Kasturi Vimalanathan for shearing her knowledge and expertise with me during this journey.

I would like to sincerely thank Taibah University and Ministry of Education in Saudi Arabia, for their financial support for my PhD. I would like to thank the staff from the School of Chemical and Physical Sciences, Australia Microscopy & Microanalysis Research Facility (AMMRF) and the Australian National Fabrication Facility (ANFF) for accessing microscopic facilities. I would like to thank Dr. Ashley Slattery From Adelaide Microscopy at the University of Adelaide for his kind help.

Last but not least, I would like to extend special thanks to my family, especially my parents, brothers and sisters for their love and encouragement. Most of all, I am very much indebted to my loving wife

"Amal Alharbi" who accompanied me from throughout my PhD study until the finishing. I really appreciate her lasting love and patience have encouraged me to get over every barrier in the process of my PhD. Without her support and tremendous encouragement, I certainly could not have reached this far.

.

DETAILS OF PUBLICATIONS

Journal articles

1. **Alharbi, T. M.**; Vimalanathan, K.; Lawrance, W. D.; Raston, C. L., Controlled slicing of single walled carbon nanotubes under continuous flow. *Carbon* **2018**, 140, 428-432.
2. **Alharbi, T. M.**; Harvey, D.; Alsulami, I. K.; Dehbari, N.; Duan, X.; Lamb, R. N.; Lawrance, W. D.; Raston, C. L., Shear stress mediated scrolling of graphene oxide. *Carbon* **2018**, 137, 419-424.
3. **Alharbi, T. M.**; Andersson, G. G., Ordering in Surfactant Foam Films Transferred onto Hydrophilic and Hydrophobic Substrates. *J. Phys. Chem. C* **2017,** *121*, 25967-25977.
4. **Alharbi, T. M.**; Vimalanathan, K.; Alsulami, I.; Raston, C. L., Vertically Aligned Laser Sliced MWCNTs. *Nanoscale* **2019**, 11, 21394–21403.
5. **Alharbi, T. M.**; Shingaya, Y.; Vimalanathan, K.; Nakayama, T.; Raston, C. L., High Yielding Fabrication of Magnetically Responsive Coiled Single Walled Carbon Nanotube Under Flow. *ACS Appl. Nano Mater.* **2019**, 2, 8, 5282-5289.
6. **Alharbi, T. M.**; Alghamdi, A. R.; Vimalanathan, K.; Raston, C. L., Continuous flow photolytic reduction of graphene oxide. *Chem. Commun.* **2019**, 55, 11438-11441.
7. **Alharbi, T. M.**; Al-Antaki, A. H. M.; Moussa, M.; Hutchison, W.; Raston, C. L., Three-step-in-one synthesis of supercapacitor MWCNT superparamagnetic magnetite composite material under flow. *Nanoscale Adv.* **2019**, 1, 3761-3770.
8. Alsulam, I. K.; **Alharbi, T. M.**; Moussa, M.; Raston, C. L. J. A. O., High-Yield Continuous-Flow Synthesis of Spheroidal C_{60}@ Graphene Composites as Supercapacitors. *ACS Omega* **2019**, 4, 19279-19286.
9. Alsulami, I.; **Alharbi, T. M.**; Harvey, D.; Gibson, C. T.; Raston, C. L., Controlling the growth of fullerene C60 cones under continuous flow. *Chem. Commun.* **2018**, 54, 7896-7899.
10. Luo, X.; Al-Antaki, A. H.; **Alharbi, T. M.**; Hutchison, W. D.; Zou, Y.-c.; Zou, J.; Sheehan, A.; Zhang, W.; Raston, C. L., Laser-Ablated Vortex Fluidic-Mediated Synthesis of Superparamagnetic Magnetite Nanoparticles in Water Under Flow. *ACS Omega* **2018,** *3*, 11172-11178.
11. Al-Antaki, A. H. M.; Luo, X.; **Alharbi, T. M.**; Harvey, D. P.; Pye, S.; Zou, J.; Lawrance, W.; Raston, C. L., Inverted vortex fluidic exfoliation and scrolling of hexagonal-boron nitride. *RSC Adv.* **2019,** *9*, 22074-22079.
12. Vimalanathan, K.; Suarez-Martinez, I.; Peiris, C.; Antonio, J.; de Tomas, C.; Zou, Y.-C.; Zou, J.; Duan, X.; Lamb, R.; Harvey, D., **Alharbi T. M.**; Gibson C. T.; Marks N. A.; Darwish

N.; Raston C. L. Vortex fluidic mediated transformation of graphite into highly conducting graphene scrolls. *Nanoscale Adv.* **2019**, 1, 2495-2501.

13. Al-Antaki, A. H. M.; **Alharbi, T. M.**; Kellici, S.; Power, N. P.; Lawrance, W.; Raston, C. L., Vortex Fluidic Mediated Synthesis of TiO2 Nanoparticle/MXene Composites. *ChemNanoMat* **2020**, 6, 657.

Awards

1. **Alharbi, T. M.** Best Higher Degree by Research Student Publication, **2018,** Flinders University.

Patents

1. **Alharbi, T. M.** and Raston C. L, Provisional Patent*, Reduced graphene oxide and preparation method thereof*, **2019.**
2. **Alharbi, T. M.** and Raston C. L. *et al.,* PCT, *Carbon nanomaterials Processing and involving graphene oxide scrolls and fused SWCNT rings*, **2018.**
3. **Alharbi, T. M.** and Raston C. L. *et al.,* PCT*, Controlled slicing of carbon nanotubes under high shear continuous flow*, **2017.**
4. Raston C. L. and ***Alharbi, T. M.*** *et al., Devices and Methods for Thin Film Chemical Processing, US Patent App. 16/763,523,* ***2020.***

Conferences

1. **Alharbi, T. M;** Vimalanathan K.; Lawrence W.; and Raston C. L, **2016** ‘Controlling the lateral slicing of SWCNTs under shear stress ’, NanoCentre Conference 2016, Adelaide, Australia.
2. **Alharbi, T. M;** Lawrance W. D; and Raston C. L, **2017** ‘ Controlling the lateral slicing of Single Walled Carbon Nanotubes (SWCNTs) under shear stress’**,** 8th International Conference on Advanced Materials and Nanotechnology, Queenstown, New Zeland.
3. **Alharbi, T. M;** Lawrance W. D; and Raston C. L, **2018** ‘ Controlling the lateral slicing of Single Walled Carbon Nanotubes (SWCNTs) under shear stress’, Workshop on Emerging Nanoscience and Nanotechnology, National Institute for Materials Science (NIMS), Tsukuba, Japan.
4. **Alharbi, T. M;** Lawrance W. D; and Raston C. L, **2018** ‘Shear stress mediated scrolling of graphene oxide’, First Australian Eu Graphene Flagship workshop, The University of Adelaide, Adelaide, Australia.
5. **Alharbi, T. M;** Lawrance W. D; and Raston C. L, **2018** ‘Shear stress mediated scrolling of graphene oxide’, NanoCentre Conference 2018, Adelaide, Australia.
6. **Alharbi, T. M;** Al-Antaki A. H.; Moussa M.; Hutchison W. D.; and Raston C. L, **2018,** ‘Shear stress and laser mediated decoration of multi-walled carbon nanotubes with magnetite nanoparticles under continuous flow’ 2nd CSE HDR Conference, Adelaide, Australia.
7. **Alharbi, T. M;** and Raston C. L, **2018** ‘Continuous flow photolytic reduction of graphene Oxide’, NanoCentre Conference 2019, Adelaide, Australia.
8. **Alharbi, T. M;** and Raston C. L, **2018,** ‘Fabricating and Processing of Carbon nanomaterials using Vortex Fluidic Technology’ 3rd CSE HDR Conference, Adelaide, Australia.

Chapter One

General Introduction

1.1. Thesis Overview

In this dissertation, the objective was to explore facile and green approaches for fabricating, sorting, and controlling the self-assembly, of carbon nanomaterials including composites with other nanomaterials, and using these hybrid materials in applications, for example supercapacitors. The new approach for processing carbon nanomaterials focused on using the dynamic thin film within the vortex fluidic device (VFD). Fabricating nanomaterials using the VFD has overcome some limitations of traditional batch processing methods including uniformity of the product and scalability, as well as developing processes that are environmentally sustainable and economically feasible. The structure of the thesis is set out below, with Chapter 1 providing an introduction to the associated fields of science, followed by Chapters 2 to 9 as the basis for separate papers published or papers submitted for publication, then Chapter 10 as the place for discussion for overall conclusions and future work.

Chapter 1 provides a succinct history on carbon nanomaterials including fullerene C_{60}, carbon nanotubes, graphene and carbon nanorings, which are all relevant to the research herein. Discussion is also provided on the structure, synthesis and properties of these carbon nanomaterials.

Chapter 2 reports on controlling the length of sliced single walled carbon nanotubes (SWCNTs) using a VFD while simultaneously irradiated with a Nd:YAG pulsed laser operating at 1064 nm. This study established the ability to slice SWCNTs, with laser pulse energies of 250, 400 and 600 mJ affording 700, 300 and 80 nm length distributions of SWCNTs respectively. The processing is scalable as continuous flow processes, and avoids the need for using any other reagents. Of particular note, is that the processing does not introduce defects into the side walls of the SWCNTs.

Chapter 3 focuses on controlling the slicing of MWCNTs into specific lengths using the VFD while irradiated with a Nd:YAG pulsed laser operating at 1064 nm. Three different length distributions were achieved, centred at 75 ± 2.1 nm, 300 ± 1.8 nm and 550 ± 1.4 nm. In addition, the short MWCNTs were found to vertically self-assemble on a silicon substrate, as a simple dipping and rinsing method.

Chapter 4 presents the fabrication of coiled SWCNT rings in high yield (80%) using the VFD with the processing in the absence of any toxic chemicals and surfactants. The magnetic interactions of these rings were investigated using magnetic force microscopy (MFM), and the results show that the magnetic interaction is strongly dependent on the thickness of the rings.

Chapter 5 reports on the ability to fabricate graphene oxide scrolls (GOS) in a high yield using a vortex fluidic device (VFD) while the solution of GO is irradiated with a pulsed laser operating at 1064 nm and 250 mJ. In also applying the principles of green chemistry metrics, the processing is in the absence of any other reagents.

Chapter 6 reports on studies directed at understanding the fluid flow in the VFD, establishing the ability to scroll and unscroll GO, depending on the rotational speed of the rapidly rotating tube in the VFD and the nature of the liquid. In addition, the ability to manipulate the structure of sell-assembled C_{60} in the VFD, depending on these parameters and more, was mapped out to determine the properties of liquids in the device, and more.

Chapter 7 provides a new strategy for generating reduced graphene oxide (rGO) from GO dispersed in water using VFD simultaneously irradiated with a UV light ($\lambda = 254$ nm, 20 W). The processing is scalable and in the absence of harsh reducing agents. The product (rGO) has a resistance of 2.2×10^5 Ω and a remarkably high conductivity of 2×10^4 S/cm, making the material comparable (if not better) to that formed using waste generating chemical based processing.

Chapter 8 reports on the synthesis of graphene spheres confining fullerene C_{60} at room temperature in the absence of surfactants and other auxiliary substances using the VFD. The diameters of the composite spheres (C_{60}@graphene) can be controlled with size distributions ranging from 1.5 to 3.5 µm. The composite material (C_{60}@graphene) used as an active electrode for supercapacitor and shows a high areal capacitance of 103.4 mF cm^{-2} at a scan rate of 5 mV s^{-1}.

Chapter 9 reports a successful three step in one synthesis of composite material of MWCNT and superparamagnetic magnetite nanoparticles (Fe_3O_4@MWCNT) using a pulsed laser operating at 1064 nm with the VFD. This involves generating the magnetite nanoparticles *in situ*, slicing the MWCNTs, and their decoration with magnetite NPs. These composite materials were used in a supercapacitor, showing high gravimetric and areal capacitances of 834 F g^{-1} and 1317.7 mF cm^{-2} at a scan rate of 10 mV s^{-1}, respectively, and are thus a promising material for use in the next generation of energy storage devices.

Chapter 10 provides discussion on conclusions derived from the results along with highlighting the significance of the research. It also includes future directions of the research, supported by some feasibility studies.

1.2. Nanocarbon Materials

Carbon is inimitable and a vital element on earth because it has a unique ability to form robust covalent bonds with other carbon atoms in varied hybridization states (sp, sp^2, sp^3).[1-3] It can also participate in covalent bonding with various non-metallic elements resulting in a wide range of structures, ranging from small molecules to long chains. Covalent bonding between carbon atoms allows the element to be tailored to form different morphologies, as the so-called allotropes of carbons, and some of these are in the nanometre range. Different types of nanocarbon include activated carbon, carbon nanotubes, fullerenes (C_{60}, C_{70}, etc.) as molecular carbon, graphene, graphene scrolls, nano-diamonds, and more. These carbon nanomaterials can exhibit remarkable properties including high electrical and thermal conductivity, high structural stability, high mechanical strength, high surface area and outstanding photoluminescent properties. These properties makes carbon nanomaterials useful for a diversity of applications, including in drug delivery, solar voltaic cells, thin-film transistors, photovoltaics, energy storage, supercapacitors, biosensors, photothermal therapy, heat dissipation, and more.[4]

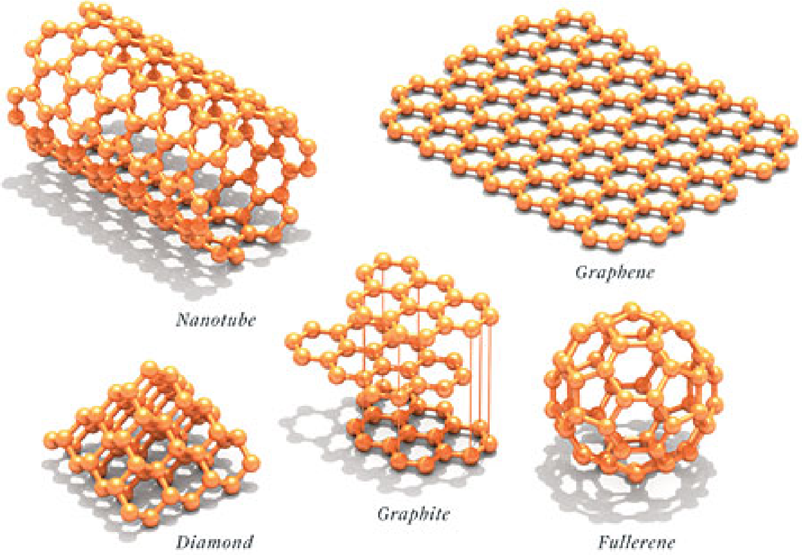

Figure 1. 1 Structural illustration of allotropes of carbon nanomaterials with sp^2 and sp^3 hybridisation. This figure has been copied from reference 5.

Among the different nanocarbon allotropes (Figure 1. 1), 0D fullerenes, 1D carbon nanotubes, and 2D graphene can be considered as members of the same group since they are comprised of sp^2 carbon atoms, except where there are otherwise dangling bonds, for example at the edges of graphene sheets. All these nanocarbon allotropes have hexagonal networks of carbon atoms, except for the fullerenes which can also take on five membered rings, and also defects in other material. They have significant difference in their physical and chemical properties because of their different shapes and sizes.[1] The next section covers details on the fabrication, properties, and applications of three popular nanocarbon allotropes, notably fullerenes, CNTs, and graphene, along with analogous background for carbon nanorings which also feature in the proposed research.

1.2.1. Fullerenes

Fullerenes are the OD form of graphitic carbon and are formed in different shapes and various forms, as summarised in Figure 1. 2. The size of the fullerene is based on the number of carbon atoms, within the range of 30 to 3000 carbon atoms. A number of fullerenes have been discovered, imcluding C_{20}, C_{24}, C_{28}, C_{32}, C_{36}, C_{50}, C_{60}, C_{70}, C_{76}, C_{78}, C_{80}, C_{82}, and C_{84}. Among all those the most stable and indeed most studied fullerene is C_{60}, being 1.01 nm in diameter, as the link between molecules and nanomaterials.[1, 6] Fullerenes were discovered in 1985 by Harry Kroto, Robert Curl and Richard Smalley, and was recognised by their award of 1995 Nobel Prize in Chemistry. The geometric shapes of fullerenes resemble the shape of Buckminster Fuller's geodesic dome and hence they are also named "Buckminsterfullerenes".[7, 8]

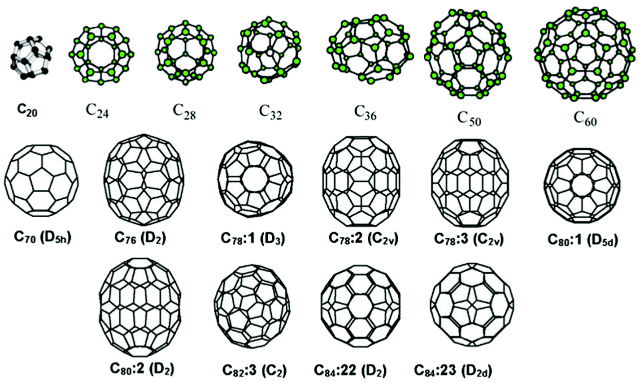

Figure 1. 2 The structure of some of the different fullerenes which have been established. This figure has been copied from reference 8.

1.2.2. Structure

The extraordinary chemical and physical properties of fullerenes relate to their different shapes, sizes, and arrangement of carbon atoms, which gives rise to unique electronic structures. All fullerenes have an even number of carbon atoms organised over the surface of a closed hollow cage. Each carbon atom is bonded on the vertex of a polyhedron, covalently to other three carbon of atoms, which results in formation of two single bonds along with one double bond, and hence is sp^2 hybridisation.

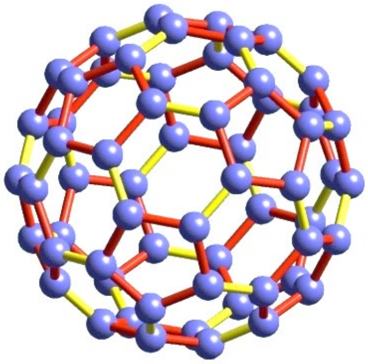

Figure 1. 3 Structure of fullerene C60. This figure has been copied from reference 9.

The most abundant fullerene C_{60} consists of 20 hexagonal and 12 pentagonal rings, Figure 1.3 and has conjugated double bonds. C-C bonds between hexagonal and pentagonal rings behave like single bonds whereas those between two hexagonal rings behave like double bonds. The single bond character between pentagonal and hexagonal rings is associated with poor electron delocalisation. As a result, the fullerene acts like an electron-deficient alkene and reacts rapidly with electron-rich species. The C_{60} molecule has a van der Waals diameter of 1.01 nm, and nucleus to nucleus diameter of around 0.71 nm.[9] In the solid phase, C_{60} exists in two different forms, as aggregates or as a continuous crystalline structure, the most stable form taking on an *fcc* (face-centred cubic) lattice.[1]

1.2.3. Synthesis.

The first synthesis of fullerenes featured a laser vaporisation technique.[9] The one disadvantage of this method is the low yield of fullerenes. Another technique involves two carbon electrodes kept in an inert atmosphere, with a large DC current applied between them. This results in a build-up of a carbon plasma arc between the electrodes which eventually cools down resulting in a fluffy condensate residue (soot), Figure 1. 4, from which fullerene can be isolated by solvent extraction.[10] Another method to prepare fullerenes is the catalytic CVD (chemical vapour deposition) method using a carbon sources.[11] Laser irradiation of polyaromatic hydrocarbons is another useful method to prepare large quantities of fullerenes.[9] Fullerenes

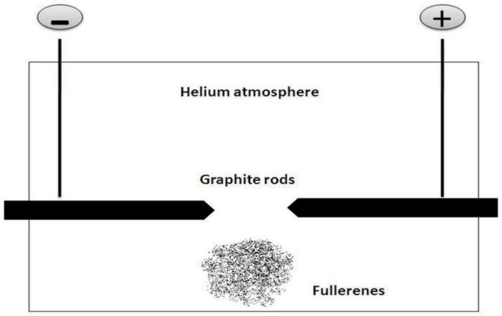

Figure 1. 4 Scheme for fullerene synthesis involving graphite heating using the electric arc discharge method. This figure has been copied from reference 9.

can be readily characterised using a number of techniques, notably FTIR, UV-visible, NMR and Raman spectroscopy, and mass spectroscopy.

1.2.4. Properties

Pristine fullerene molecules are insoluble in water and have limited soluble in most organic solvents.[12] Fullerene C_{60} has moderate solubility in aromatic solvents, for example toluene (2.8 mg/mL), and carbon disulfide (8.0 mg/mL). The spheroidal cage-like structure is remarkable stable in the absence of oxygen and other oxidising agents, to temperatures above 1000 °C. At high pressures C_{60} polymerises with other fullerene molecules through covalent bond formation.[1, 12] As previously discussed, the presence of single bond characteristics between pentagon and hexagon rings (5:6) and the double bond character between two hexagon rings (6:6) results in a poor electron delocalisation. Hence, fullerenes act like an electron-deficient alkene and react rapidly with nucleophiles. Most reactants attack the two hexagonal ring intersections which have higher electron densities.[13] Fullerenes have been widely used in biopharmaceuticals as antioxidants due to their high reactivity with free radicals, which is a result of the availability of a large number of conjugated double bonds as well as low lying Lowest Unoccupied Molecular Orbitals (LUMO).

Fullerene C_{60} molecules is one of the most efficient radical scavengers, able to trap 34 methyl radicals onto it surface.[14] Fullerenes in general can also be used as antimicrobial, and antiviral agents.[15-17] They find application in drug delivery, in chemically modified forms which become biocompatible, with controlled release of the drug at the targeted site. Hydrophobic fullerenes can be made water-soluble by reacting them with hydrophilic species.[18, 19] Fullerene $C_{59}NH_5$ is formed by the nitrogen doping C_{60}, and is effective for hydrogen uptake and storage.[12] Its energy level arrangement is exceptional, with a small difference between singlet and triplet excited states (0.15 eV), accounting for abnormally fast intersystem crossing with efficiency of around 96%. This property in manifested in its wide used in photochemical transfer reactions as a dopant.[20, 21] Functional fullerenes find application in polymer solar cells, as in for example fullerene PCBM molecule (1-(3-methoxycarbonyl) propyl-1-phenyl[6,6]C61).[22, 23]

1.2.2. Carbon Nanotubes

Carbon nanotubes (CNTs) are the one-dimensional form of graphitic carbon. CNTs were first discovered in 1991 by Iijima.[24] They have remarkable properties, and still attract much attention from the scientific community.

1.2.3. Structure

CNTs has a hollow cylindrical structure that can thought of as rolled up sheets of graphite which can be in different ways, Figure 1. 5. The most used CNTs are single-walled carbon nanotubes (SWCNTs) and multi-walled carbon nanotubes MWCNTs. As the name suggests, SWCNTs can be designed by the rolling of a graphene layer into a unified cylinder. However, MWCNTs consists of multiple layers of graphite rolled in on themselves to form a tube shape with different diameters. The diameter of SWCNTs is around few nanometres (~1-3 nm), but the diameter of MWCNTs ranges from few nanometres to several tens of nanometres (typically 4-11 nm) with lengths in general in the micrometre range. The properties of MWCNTs are very different from SWCNTs due to the interplay of the concentric tubes in MWCNTs. Like fullerenes, these also have trigonal sp^2 hybridised carbon atoms

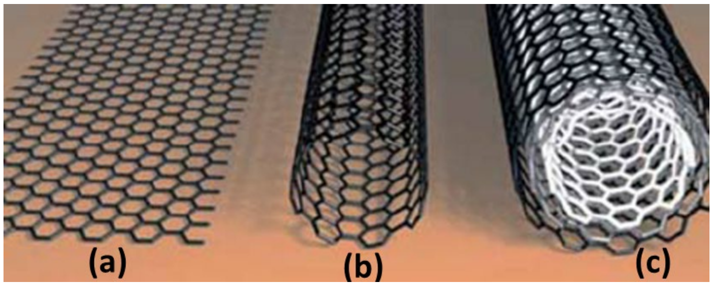

Figure 1. 5 Structure of (a) a graphene sheet, (b) SWCNT and (c) a three shell MWCNT. This figure has been copied from reference 12.

(each surrounded by three carbon atoms),[25] but now with all carbon atoms in hexagonal rings, with an overall seamless honeycomb lattice, Figure 1. 6.

As discussed before, a CNT can be obtained by rolling a graphene sheets, and this is with minimal distortion and can occur un many ways. The direction of folding of graphene decides the structure and properties of carbon nanotubes. The basic structure of CNTs can be divided into three types.

1. Zig-Zag
2. Arm Chair
3. Chiral

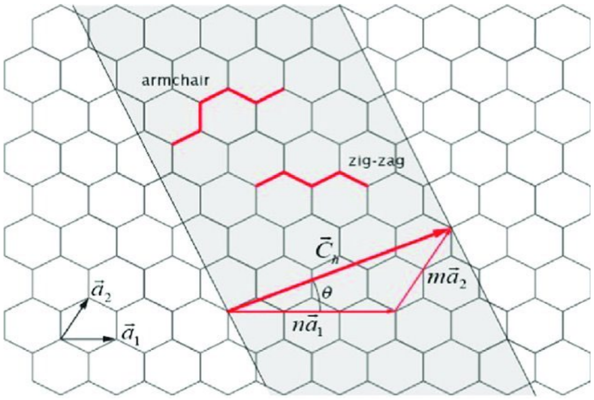

Figure 1. 6 Schematic diagram of the chiral vector and the chiral angle in a SWCNT. This figure has been copied from reference 26.

This categorisation is done in terms of chiral vector (C_h) and the chiral angle (θ) shown in (Fig. 1). The Chiral vector (C_h) can be expressed by equation (1)

$$\overrightarrow{C_h} = n\overrightarrow{a_1} + m\overrightarrow{a_2} \tag{1}$$

Where a_1 and a_2 are the base vectors. (n, m) is the integer pair and called the and indices of translation. This integer pair decides the structure around the circumferences.

Chiral angle (θ) can be expressed as in equation (2)

$$\theta = \arccos\frac{2n+m}{2\sqrt{(m^2+n^2+mn)}} \tag{2}$$

If θ = 0º the structure of SWCNTs is zigzag if θ = 30º, the structure of SWCNTs is armchair, and for chiral SWCNTs, θ should be in between 0º to 30º. The diameter of a CNT resulting from a chiral vector (n, m) is given by (3)

$$d = \mathrm{a}\sqrt{n^2 + m^2 + nm} \tag{3}$$

where *d* is the diameter and *a* = 2.49 A is the lattice constant of the honeycomb lattice. The diameter of three CNTs in Figure 1. 7 are almost the same, but they show very different electrical properties.[26]

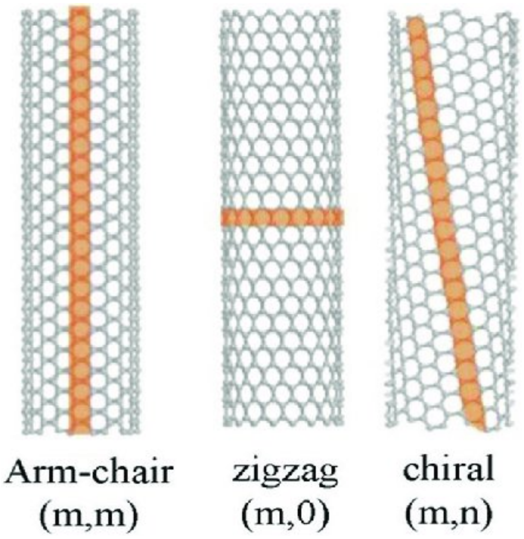

Figure 1. 7 Different types of arrangement of atoms in carbon nanotubes: Armchair (Left), zigzag (Middle) and Chiral (Right). This figure has been copied from reference 26.

1.2.4. Synthesis

CNTs were first synthesised by Iijima in 1991 using the arc discharge deposition method.[26-28] Other methods include laser ablation and chemical vapour deposition (CVD). In the early days of development of CNTs, high-temperature arc discharge and laser ablation were the most popular to prepare the material (Figure 1. 8). Smalley *et al.* developed a unique method in 1995 using traditional laser ablation method to heat graphitic carbon, in replacing the arc discharge method.[29] However, the disadvantage of these techniques is the high costs and complexity of the processing. Currently, low-temperature methods are more popular, as in chemical vapour deposition (CVD) for temperatures < 800ºC. An advantage of this method over high-temperature techniques is the high control on the orientation, length,

Figure 1. 8 Different methods used to prepare CNTs. This figure has been copied from reference 28.

diameter and purity of CNTs.[30, 31] Carbon monoxide, methanol, ethanol, and hydrocarbons are the most popular source of carbon for generating CNTs. In 2004, Hata *et al.* modified the CVD method, dramatically extending the lifetime of the catalyst, and producing SWCNTs millimetres in length.[32] More recently, the outer diameter of CNTs was found to depend on the size of the catalyst particle. In 2006, Yamada *et al.* reported on the selective formation of double walled CNTs, which are generated by simply changing the size of the catalyst particle.[33] After preparing CNTs, another major challenge is their purification. Depending on the method used for preparing CNTs, they can have different impurities, with the main impurities being carbonaceous materials such as amorphous carbon, metal catalyst and the smaller fullerenes. [34]

A number of techniques are available for characterising CNTs, including photoluminescence spectroscopy, IR and Raman and UV spectroscopy, scanning tunnelling microscopy, transmission electronic microscopy, scanning electronic microscopy, thermal analysis (TGA/DTG), X-ray photoelectron spectroscopy, and neutron and X-ray diffraction.[34]

1.2.5. Properties

The exceptional electronic, mechanical and thermal properties of CNTs' have attracted much interest both for fundamental understanding of their structure, and applications. Results from many theoretical and experimental studies show that the CNTs have a high Young's modulus along with high tensile strength, electrical and thermal conductivity. The geometric differences in CNTs such as chirality, different diameters and the degree of crystallinity significantly affect their electronic properties. SWNTs can be semi-metallic or metallic in nature with resistivities ranging from 0.000035 to 0.00012 ohm-cm, but this depends on their chiralities. Thio *et al.* established that the current densities of metallic CNTs are ca 6×10^{6} A cm^{-2}.[35] Overall, the unique electronic properties of CNTs results in their use in transistors, as an emitter, in sensors, in vacuum microelectronics, and for X-ray generation. CNTs are considered exceptionally strong materials, having high Young's modulus, from ca 271 to 951 GPa. The tensile strength is also very high, in the range of 11–63 GPa. CNTs have excellent thermal properties. SWCNTs with a diameter of 1.6 nm exhibit thermal conductivity of 3500 W/mK, and the thermal conductivity of MWCNTs at room temperature is > 3000 W/mK. Other properties of CNTs include high catalytic activity in oxygen reduction reaction, with their both chemical and physical properties manifested in their incorporation in polymers as high-performance fillers.[36]

1.2.3. Methods for cutting CNTs

The size of as-synthesized carbon nanotubes is usually a few tens of micrometres. The as-synthesized CNTs are highly hydrophobic and hence this limits their processability. For example, due to their high Young's modulus, SWCNTs are used to increase the mechanical performance of polymers, but because of their hydrophobic characteristics, dispersing SWCNTs in polymer is challenging. This can be addressed by reducing the length of SWCNT, ideally to specific lengths to suit a particular application.[37] In another example, short length nanotubes have better performance in transistors compared to the long length nanotubes.[38] CNTs with lengths < 299 nm can drastically improve their biocompatibility and the cellular

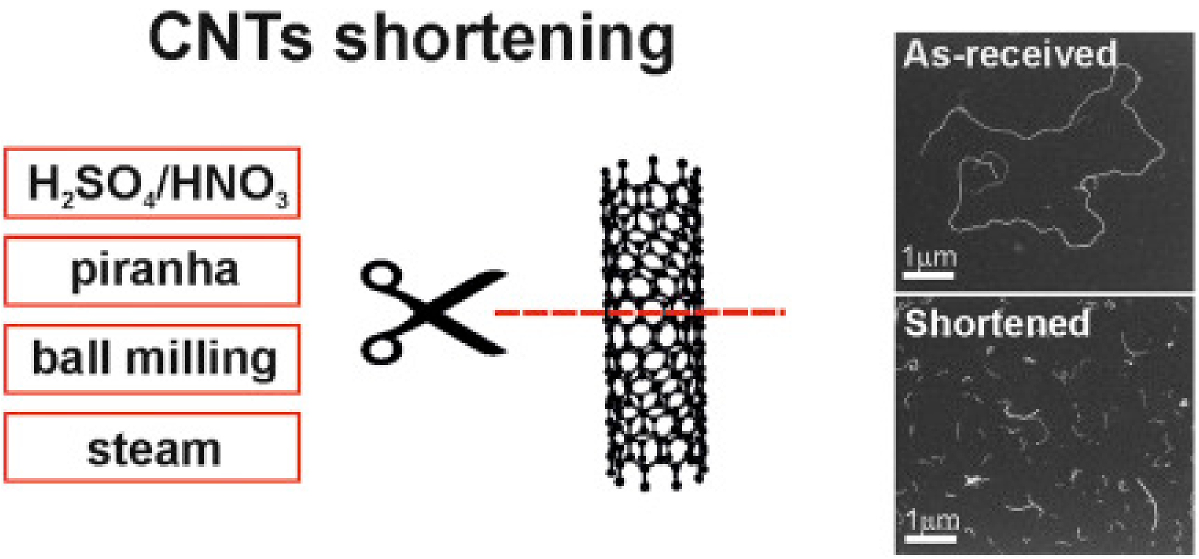

Figure 1. 9 Cutting of carbon nanotubes using chemical and physical strategies. This figure has been copied from reference 44.

uptake.[39, 40] Importantly, short CNTs are less persistent in the body and are effortlessly biodegradable compared to their longer counterparts. Researchers have established that short CNTs are cleared faster from the lungs than their long counterparts.[41, 42] The thermal and electrical conductivity of short CNTs is higher compared to longer CNTs.[43] Many articles have appeared dedicated to shortening of CNTs, with two methods standing out:-

1. Chemical methods
2. Physical methods

Reactions occurring at sidewall defects (shortening) and highly reactive ends (cutting) are used as the design strategy to chemically shorten CNTs, but which further leads to formation of functionalized and/or open-ended nanotubes. Acid etching, ozonolysis, fluorination and steam treatment are some of the chemical strategies used to shorted CNTs. Physical methods include using different energy sources including electrons, ɣ-rays and sonication. Mechanical cutting is also part of physical methods. Each strategy leads to gaining access to samples which possess different functional groups, structural defects and impurities and not surprisingly the yield and utility of the ensuing material is different in each case. Thus, in focusing on a particular application, there are optional strategies to generate the optimal CNTs. Shortening can be done on a large scale and the cutting methods for the same are categorized into three types namely mechanical, liquid-phase oxidative and solid-state reaction cutting (Figure 1. 9).[44]

1.2.3.1. Liquid-phase oxidative cutting

One or more oxidants like HNO_3, H_2O_2 or a mixture of H_2O_2 and HCl, a mixture of H_2SO_4, HNO_3, $KMnO_4$ and NaOH, and $KMnO_4$, are typically used in the liquid-phase oxidative cutting method. It provides the benefit of simultaneous elimination of both amorphous carbon and metal catalyst which is not possible in gas phase oxidation. The one disadvantage of this method is that it results significant defects on the surface of CNTs (including cutting and opening CNTs).[45] Smalley *et al.* published a two-step process which utilized the liquid phase oxidative technique for cutting single-walled carbon nanotubes (SWNTs) (Figure 1. 10). The two-step process involves the rupturing of C-C bonds in the matrix followed by etching at damaged sites to produce short nanotubes. Fluorination is used to introduce C-C bond breakage points, and piranha solutions have been used for the etching step. The CNTs produced using these method have an average length of approx.100 nm (Figure 1. 10).[46]

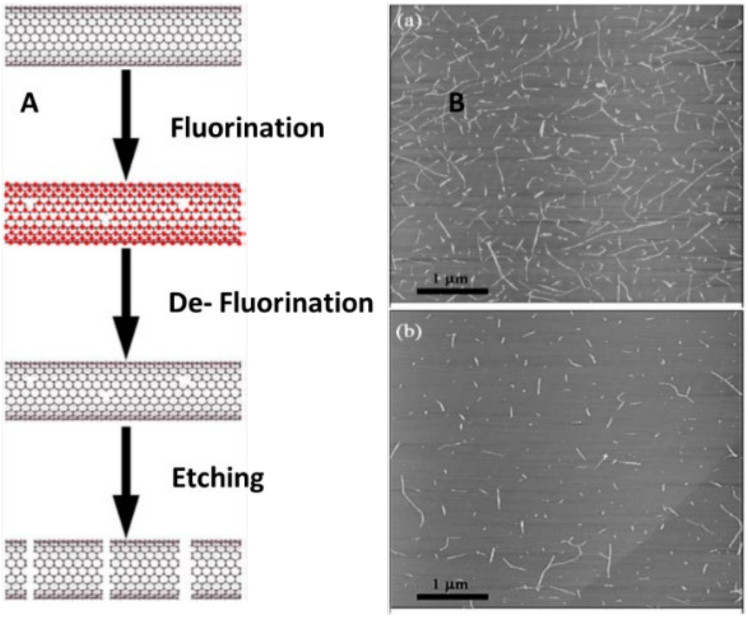

Figure 1. 10 (A) Liquid phase oxidative cutting scheme; (B) AFM image for defluorinated nanotubes, (a) before and (b) after treating with Caro's acid (H_2SO_5). This figure has been copied from reference 45.

1.2.3.2. Solid-state cutting

Solid state cutting of CNTs typically result in lengths ranging up to few micrometres. An exception is the work by Wang *et al.* for the cutting of MWCNT to less than 200 nm in length which is associated with disentanglement of the starting material. This involved depositing NiO particles on the surface of the CNTs which react with each other, resulting in a narrow length distribution as well as being highly dispersed. Another advantage of this method is that the loss of material during the process is considerably less compared to gaseous or liquid-state reaction. Figure 1. 11 shows the TEM images for CNTs at each stage of the solid-state reaction procedure.[47]

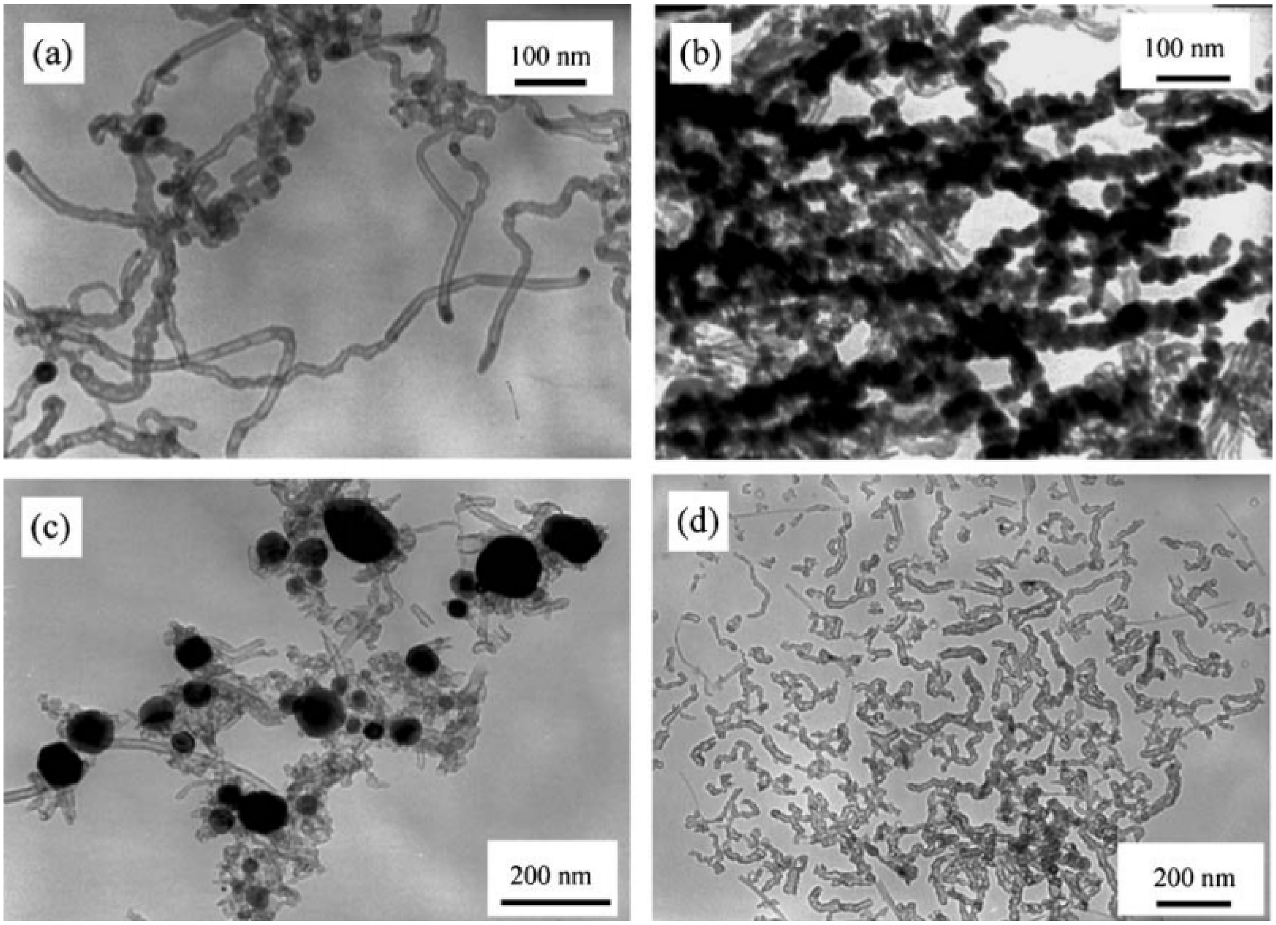

Figure 1. 11 TEM images of MWCNTs at different stages of processing. (a) Original material. (b) Material after Ni deposition. (c) NiO mediated cutting of MWCNTs. (d) Processed MWCNTs after removal of Ni particles. This figure has been copied from reference 47.

1.2.3.3. Mechanical cutting

Mechanical cutting is the combination of more than one process, which includes grinding, ball-milling and sonicating. A number of examples in the literature use cyclodextrin as a solid solvent for efficient cutting of SWCNT, with the original work reported by Chen *et al.* This method has the advantage over oxidative cutting in that it does not damage the small diameter nanotubes.[48] N. Pierard *et al.* used ball milling to produce short MWCNTs. The overall procedure involved decomposition of acetylene on different types of supported metal catalysts, and then the cleavage of the resulting MWCNTs arising from collisions between an agate ball and the nanotube powder contained in an agate mortar. The average length of the CNTs produced by this method is approx. 0.8 µm.[49]

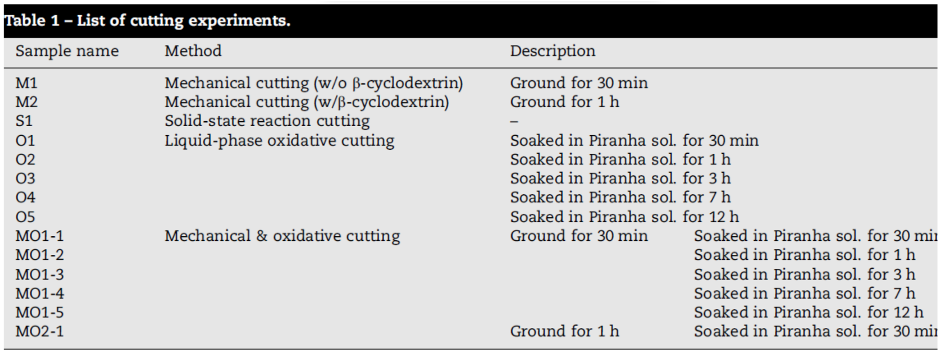

Table 1 – List of cutting experiments.

Sample name	Method	Description	
M1	Mechanical cutting (w/o β-cyclodextrin)	Ground for 30 min	
M2	Mechanical cutting (w/β-cyclodextrin)	Ground for 1 h	
S1	Solid-state reaction cutting	–	
O1	Liquid-phase oxidative cutting	Soaked in Piranha sol. for 30 min	
O2		Soaked in Piranha sol. for 1 h	
O3		Soaked in Piranha sol. for 3 h	
O4		Soaked in Piranha sol. for 7 h	
O5		Soaked in Piranha sol. for 12 h	
MO1-1	Mechanical & oxidative cutting	Ground for 30 min	Soaked in Piranha sol. for 30 mi
MO1-2			Soaked in Piranha sol. for 1 h
MO1-3			Soaked in Piranha sol. for 3 h
MO1-4			Soaked in Piranha sol. for 7 h
MO1-5			Soaked in Piranha sol. for 12 h
MO2-1		Ground for 1 h	Soaked in Piranha sol. for 30 mi

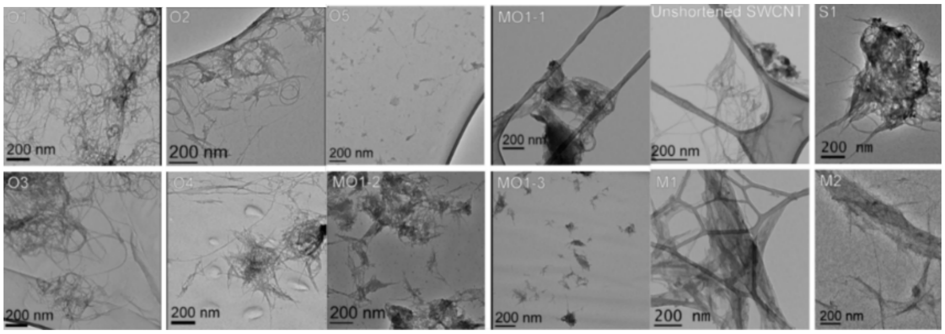

Figure 1. 12 TEM images of different methods of cutting CNTs. This figure has been copied from reference 50.

Pfefferle and co-worker reported a new approach which combines the above methods, resulting in 50 to 200 nm long SWCNTs. This involved liquid- phase oxidation (Piranha solution) and ball milling, Table 1, with the mechanical grinding introducing sidewall defects in the SWCNTs. These can be removed by soda lime, with then sonication in ethanol being effective in removing other defects on the surface of the shortened nanotubes. TEM images of the various stages of the process are given in Figure 1. 12.[50]

1.2.4. Carbon nanorings

The last few years has scene developments in overcoming the high tensile strength of CNTs, with the now the ability to exquisitely manipulate their size and morphology, notably into nanorings [51, 52], nanorods [53, 54], nanosphere [55, 56] and more. Carbon nanorings can be formed from both SWCNTs and MWCNTs, and they are termed single-walled carbon nanorings (SWCNRs) and multi-walled carbon nanorings (MWCNRs), respectively. The nanorings are considered crucially important carbon structure as promising materials for device technologies. Nanoring CNTs are also termed as toroidal CNTs. [51]

Carbon nanorings exhibit different properties compared to the straight CNTs. This is due to the difference in the geometry as carbon nanorings have a circular geometry. Recently, a number of research groups have reported the fabrication of carbon nanorings using a post-treatment processes. This is done by bending CNTs into rings using chemical treatment. The disadvantage of this method is that it can results in change is some of the crucial characteristics of nanotubes. To overcome these problems, the carbon nanorings are fabricated directly on the substrate. Fabrication of carbon nanoring is possible using a number of methods, including laser-growth, ultrasonic, chemical reactions, and chemical vapour deposition (CVD). CVD is more advantageous over the other methods in being a single-step process. Two step processes involve first the synthesis of the CNTs followed by acid treatment to form rings. Liu *et al.* first prepared toroidal CNTs in 1997. The diameter of these carbon nanorings range from 300 nm to 500 nm and can be 5–15 nm wide. SEM and TEM studies revealed that SWNT ropes with 10 to 100 nanotubes were the foundation base for the carbon nanorings' fabrication. Martel *et al.* used an ultrasound-aided acid technique to synthesise carbon nanorings with typical diameters a few hundred nanometres [10, 11]. Figure 1. 13 shows different kinds of carbon nanorings.[51]

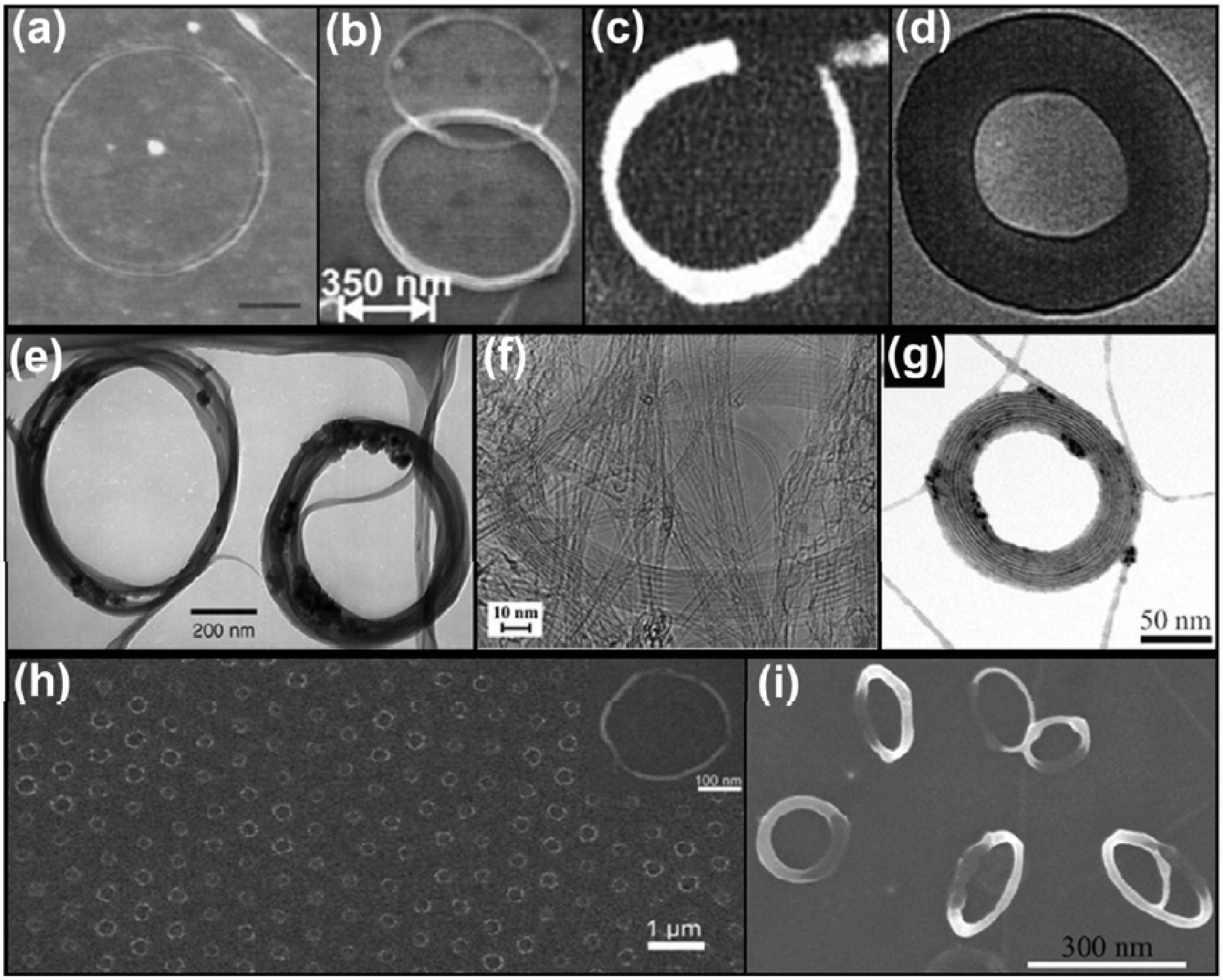

Figure 1. 13 SEM and TEM images of different types of toroidal CNTs. This figure has been copied from reference 51.

Carbon nanorings have high mechanical strength, conductivity and a paramagnetic moment.[58] They have potential for use in ultrasensitive force sensors, which benefits from their reversible elasticity, with the same property also having potential in flexible and stretchable nanodevices. The magnetic properties of carbon nanorings have resulted in their use in electromagnetic oscillators, and given their variable electronic properties, they can also be used alongside nanoscale devices to build integrated circuits. Specifically, the tube-like structure of the carbon nanorings helps in trapping ions, atoms and molecules, and has potential as material for storing hydrogen.[58]

1.2.5. Graphene

Graphene is the building block of natural graphite and is a remarkable material. Indeed, it is the strongest known material in the nature world. Both fullerenes and CNTs can be considered as being derived from the 2D graphene sheet. Graphene itself, with its unique properties came to attention of the scientific community in 2004 with the report published by Geim and Novoselov. They used a micromechanical exfoliation method to prepare single graphene sheets directly from graphite.[59]

1.2.5.1. Structure

Graphene consists of sp^2 hybridised carbon atoms arranged in a hexagonal honeycomb lattice, which relate in structure to the O-dimensional fullerenes and 1D-dimensional nanotubes, and can stack into the three-dimensional graphite structure Figure 1. 14.[60]

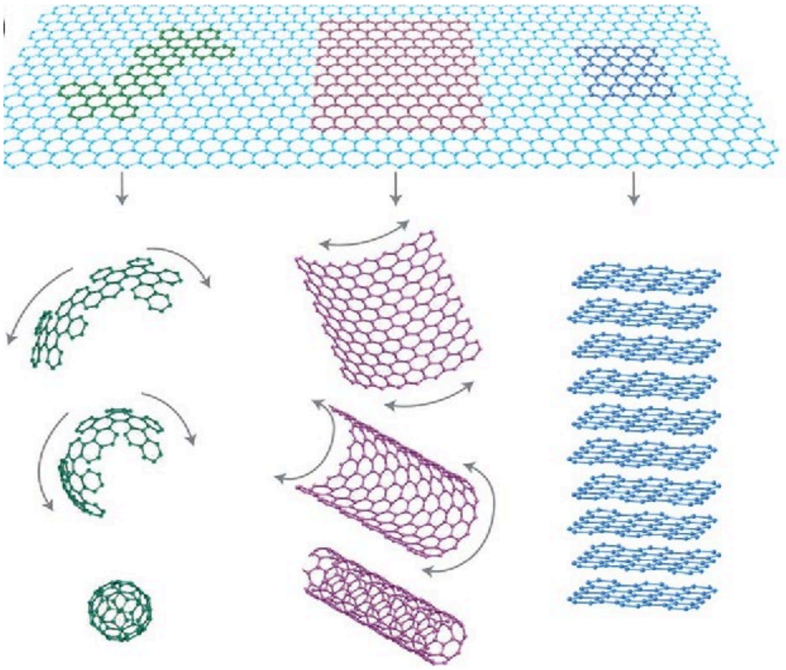

Figure 1. 14 Transformation of graphene into fullerene, SWCNT, and graphite. This figure has been copied from reference 60.

1.2.5.2. Synthesis

There are two primary methods used for the synthesise graphene. These are (Figure 1. 15):

1. top-down
2. bottom-up

The top-down exfoliation methods include mechanical (scotch tape), chemical (solution-based exfoliation or graphite oxide exfoliation/reduction), or electrochemical exfoliation (oxidation or reduction). The purpose of these methods is to overcome the strong van der Waals forces between the graphene layers. Another process which comes under the same category is the formation of graphene nanoribbons, arising from opening or unzipping carbon nanotubes using chemical or thermal processes. Alternatively, as the name suggests, the bottom-up method involves degradation of small molecules to form graphene. This can be achieved by means of chemical (organic synthesis), thermal (SIC decomposition) or catalytic (CVD) processess.[3]

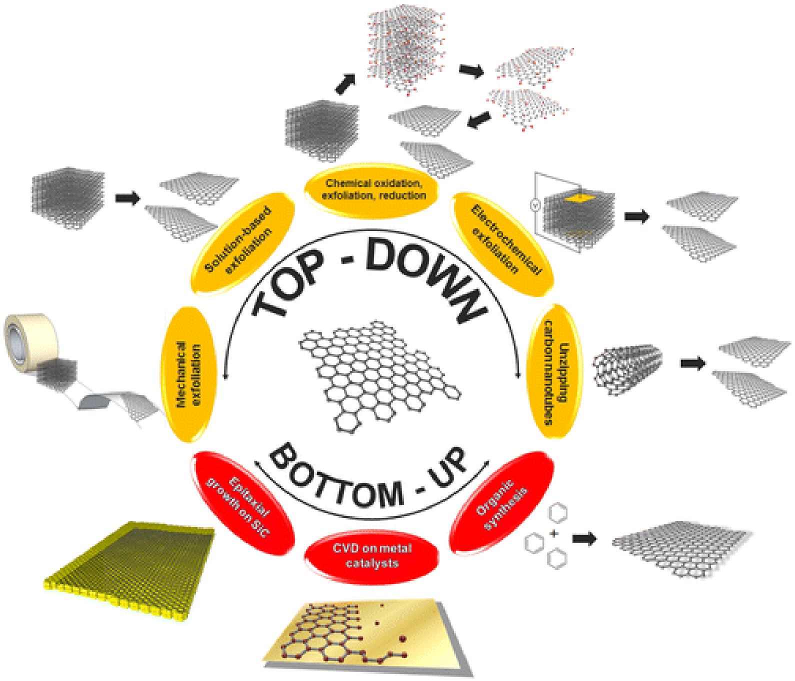

Figure 1. 15 Different methods for the 'top down' and 'bottom up' fabrication of graphene and graphene based materials. This figure has been copied from reference 3.

1.2.5.3. Properties

Graphene has been extensively studied, in exploring its exceptional mechanical, electronic and thermal properties, having high tensile strength, high Young's modulus, high surface area and high thermal conductivity. In 2008, J. Hone *et al.* measured the elastic properties and intrinsic strength of a monolayer of graphene, revealing 126 GPa and 1100 GPa tensile strength and Young's modulus respectively, thereby establishing it as the hardest material measured thus far, and highlighting its potential in applications for ultra-strong materials and composites thereof.[61] H.L. Stormer determined the electrical conductivity of graphene as 1 × 10^8 S/m and charge mobility as 2 × 10^5 $cm^2/(V\ s)$, and these high values highlight the potential of graphene for use in different electronic devices.[62] M. D. Stroller *et al.* determined the specific surface area of mono graphene as 2629 m^2/g, which is exceptionally high, leading to it being considered as a material of choice in energy storage.[63]

1.2.6. Graphene Oxide and Reduced Graphene Oxide

Graphene oxide (GO) is the oxidised form of graphene with a subsequent reduction step to then afford single layered graphene sheets, referred to as reduced graphene oxide (rGO), Figure 1. 16. Schafhacutl reported the first synthesis of graphene oxide in 1840 involving intercalation of the graphite sheets. Other popular techniques used for the production of graphite oxide include the Brodie, Hofmann, Staudenmaier, and Hummers methods, Figure 1. 17. All these methods involve the chemical treatment of graphite powder with strong acids such as hydrochloric acid, sulfuric acid and nitric acid. This is followed by the formation of graphene layers in graphite being intercalated by alkali metals which results in the breakdown of graphitic layers into smaller pieces.[64] The one crucial characteristic of all these methods for preparing GO is that it involves chemical processing which generates a waste stream, and thus the production of graphene as such is not sustainable. Nevertheless, the hydrophilic GO is readily processible in water, in which it forms stable aqueous colloids.[65]

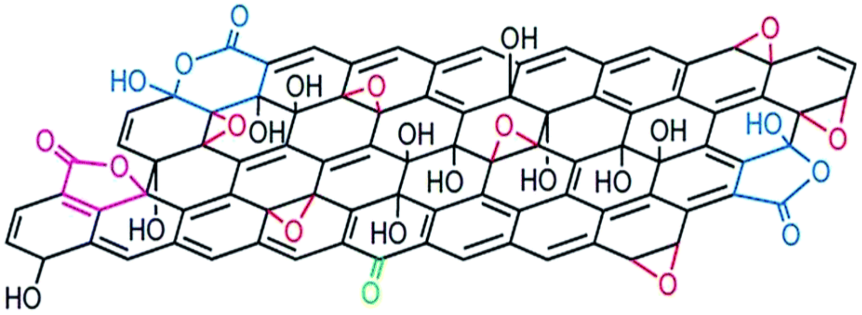

Figure 1. 16 The proposed structure of graphene oxide (GO). This figure has been copies from reference 64.

Graphene oxide is less aromatic compared to graphene, which impinges on its electrical properties, with GO acting as a semiconductor, distinctly different to graphene starting material which is a perfect conductor of electricity. One strategy to improve the conductivity of GO is to restore its aromaticity, as would be expected by reducing GO to the so called reduced graphene oxide, rGG. Indeed, such reduction is possible using thermal or chemical processing. The latter is the most extensively applied method to gain access to rGO, as shown in Figure 1. 18.[66] The first step of this process involves ultrasonication of GO in water, in generating a homogeneous colloidal dispersion of the material in water, which is followed by adding strong reducing agents like $NaBH_4$, and this leads to the formation of a waste stream. This reduced graphene oxide, is structurally graphene like, but the materials is not pristine, in having structural defects, with residual oxygen incorporated along with other heteroatoms. Also noteworthy is that the reduced graphene oxide is colloidally unstable in water, affording a black precipitate. This is because the newly formed graphite domains in each graphene results in increased hydrophobic behaviour with a consequentially tendency to π -stack.[67]

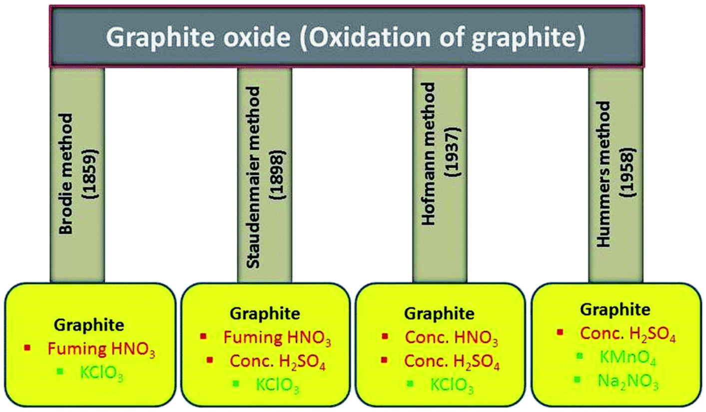

Figure 1. 18 Methods developed to prepare graphite oxide (GO), which feature the use of strong acids and powerful oxidising agents. This figure has been copied from reference 64.

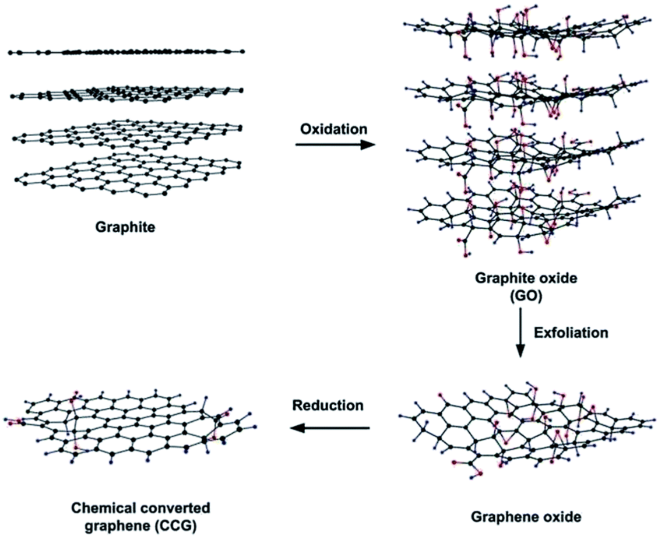

Figure 1. 17 CCG (chemically converted graphene) prepared by the reduction of graphene oxide. This figure has been copied from reference 64.

1.3. Dynamic Thin Films

Given the remarkable properties of the abovementioned carbon nanomaterials, developing novel techniques for fabricating them using both ‘top down’ and ‘bottom up’ methods with control over their formation while minimising the generation of waste is an important scientific endeavour. While traditional methods have made significant advances in gaining access to various nanocarbon materials, there are a number of challenges which warrant consideration, specifically in terms of the cost of the processing, the yields and the waste streams produced as a result of using toxic and harsh chemicals and other reagents, and this includes surfactants that result in contamination of the product.

This thesis focuses on studies into overcoming some of these challenges, using a continuous flow thin-film microfluidic platform for developing novel methods to fabricate nanocarbon of various forms and dimensionalities, along with studying their properties for potential applications.

Continuous flow thin film platforms that have been widely used to date include:

1, The Spinning Disc Processor (SDP)

2. The Rotating Tube Processor (RTP)

3. The Vortex Fluidic Device (VFD)

These platforms have shown versatility in many fields, beyond preparing nanomaterials, which harness the tuneable shear stress generated as a result of the varying the rotational speed of the disc (SDP) or tube (RTP or VFD). Compared to conventional methods, these continuous flow microfluidic devices have shown advantageous for accelerating chemical reactions[68] with enhancement of reaction selectivity,[69] fabricating drug formulation,[70] controlling the crystallisation of nanoparticles[71] and fabricating composite materials.[72] Such control is related to the intense shear produced inside the thin films, which in the case of the SDP arises from the viscous drag as the liquid accelerates centrifugally from the centre of the rapidly rotating disc. In the rotating tube processor (RTP), the shear stress is associated with the liquid whirling along the tube which also creates viscous drag. The design of the vortex fluidic device (VFD) is very similar to the horizontally aligned rotating tube processor (RTP), although the fluid dynamics and associated shear stress is inherently complex and poorly understood, as discussed below. Nevertheless, in terms of utility and applications, it has been shown to be more versatile than both the SDP and RTP.[73] There is also a tube in a tube reactor which has high shear stress associated with the liquid being forced under high pressure between two surfaces moving relative to each other.[74]

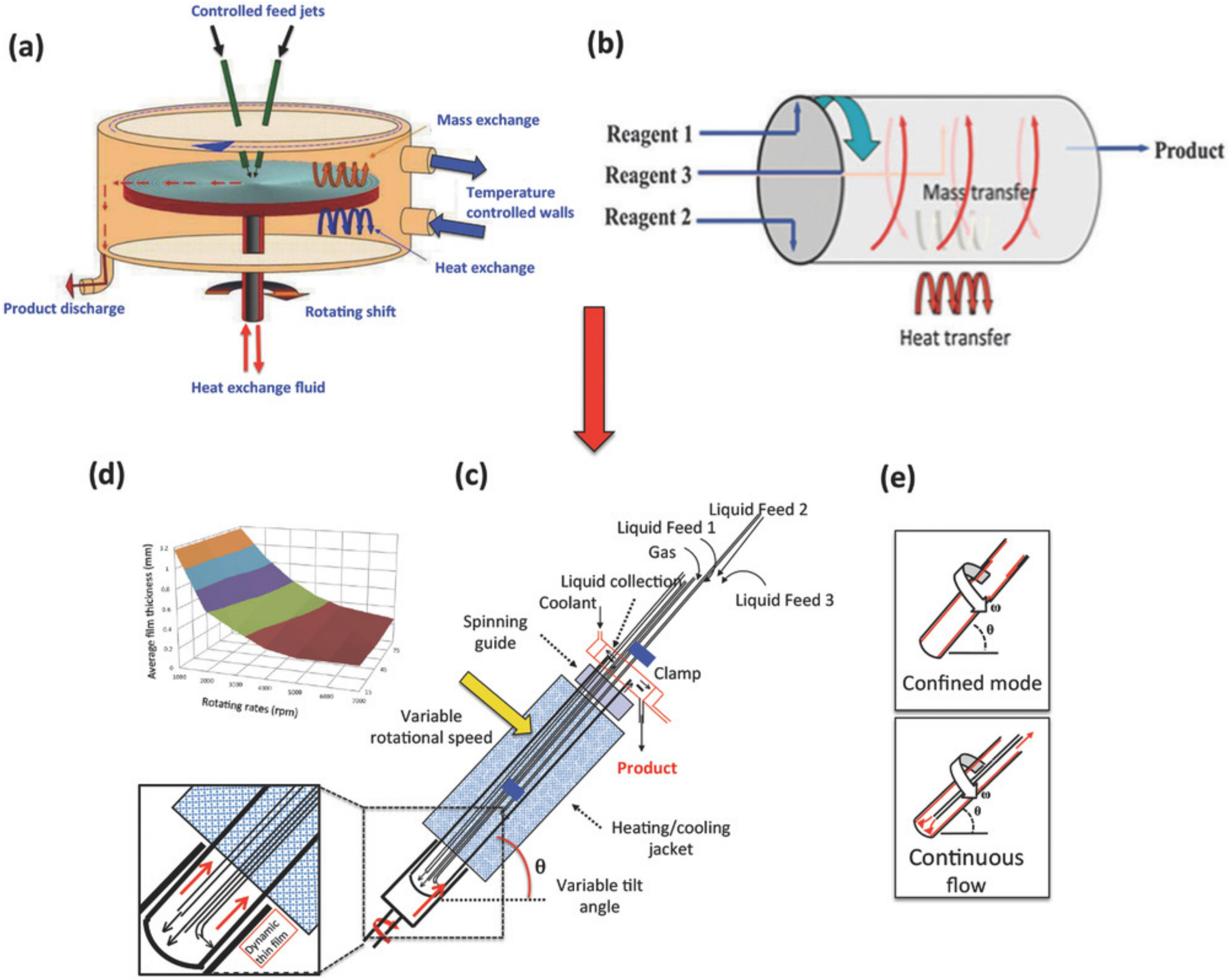

Figure 1. 19 (a) Spinning disc processor (SDP), (b) rotating tube processor (RTP), (c) the vortex fluidic device (VFD), (d) the average film thickness (mm) versus tilt angle (θ) in the VFD, and (e) representation of the confined mode and continuous flow modes of operation of the VFD. This figure has been copies from reference 73.

1.3.1. Vortex Fluidic Device

C. L. Raston invented and designed the vortex fluidic device (VFD) with the first publication in 2012.[75] It is a novel approach in microfluidics, with a diversity of applications, including in organic synthesise, probing the structure of self-organised systems and preparing nanomaterials. The VFD has a borosilicate glass or quartz tube with a diameter of 20 mm, internal diameter 17.5 mm. The tube has one end open and can rotate at speeds ranging from 2000 to 10000 rpm which generates a thin film of liquid along the tube, depending on the volume present. The tube in the VFD is inclined at a tilt angle, θ, which can be readily changed from 0° to 90°, Figure 1. 19c. The addition of the reactants and the collection of the product in the reaction differ according to the mode of processing. Processing in VFD has two modes of operation, specified as the continuous flow mode and the confined flow mode, Figure 1. 19d. Continuous flow (CF) has solutions delivered to the inside of the tube through jet feeds, to the base or at strategic positions along the tube, with the flow rate of the liquids varied along with the rotational speed and inclination angle. The confined mode is where a finite volume of liquid is added to a tube, which is spun across the rotational landscape with the tilt angle varied. Both of these modes generate dynamic thin films with the thickness ≥ 200 µm.[69, 74] The uniformity and thickness of the dynamic thin films depends upon the flow rate, inclination angle of the tube, residence time and the rotational speed of the tube, with the film extending to the upper lip where the liquid is forced out of the tube. In the confined mode, the height of the film depends on the amount of liquid, rotational speed and tilt angle. Both modes of operation of the VFD have shear stress, ie. induced mechanical energy, but the nature of the fluid flow is inherently complex, involving eddies from Faraday waves with associated pressure fluctuations, with a contribution from Stewartson and Ekman layers and viscous drag due to the whirling of the liquid along the tube.[74, 76]

As previously mentioned, The VFD has distinct advantages over the SDP and RTP in terms of operating features and applications. For the SDP and RTP, the amount of liquid needed for maintaining consistent shear intensity in the liquids flowing over the surfaces of rotating tubes, coupled with finite residence times and high cost of construction, can limit the scope of their applications. The design of the VFD lends itself to applying fields around the tube, such that molecules are treated close to the same as they move along the tube. The thickness of the film and its large surface area are clearly important here. As an example, photoredox reactions can greatly benefit from VFD processing, dramatically improving the conversion, up to 96%, with the ability to shroud the rotating tube with LED light sources.[77]

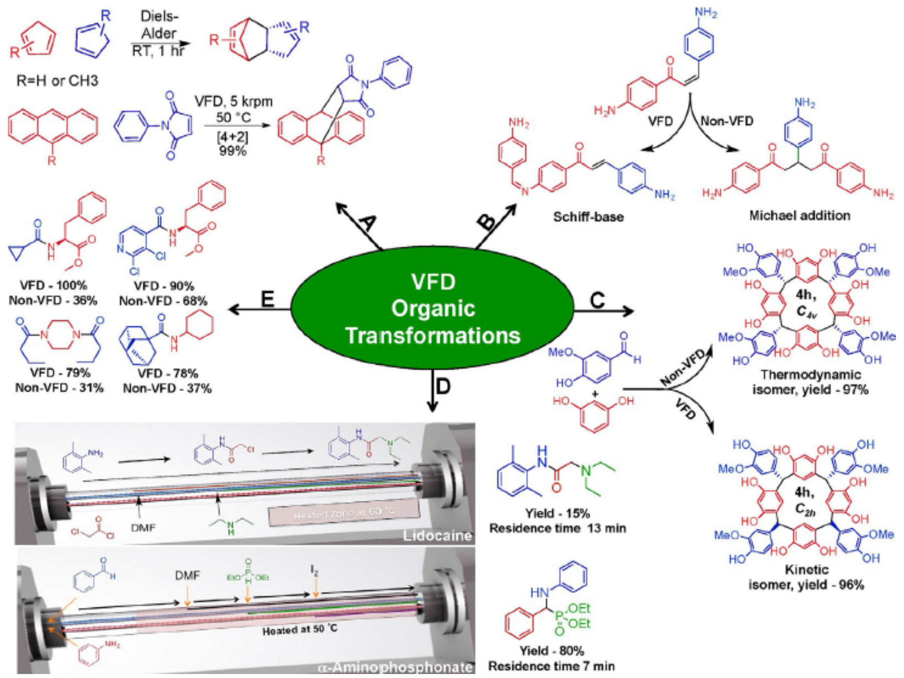

Figure 1. 20 Examples of VFD-mediated organic synthesis greatly benefiting their outcome in terms of selectivity, yield, and the ability to make complex molecules in minutes for a single pass of liquid along the tube using strategically placed jet feeds. This figure has been copies from reference 74.

An importantly characteristic of dynamic thin film in the VFD is the high mass and heat transfer. However, reactions in the RTP can have relatively poor mixing and reduced heat transfer specifically at larger scales. The use of the relatively inexpensive VFD technique overcome these issues, as established for [4+2] Diels–Alder reactions, with no reaction for classical batch processing (non-VFD control), Figure 20A. Another example is shown in Figure 1. 20B, which focuses on the synthesis of 2,4,6-triarylpyridines. Here the Michael addition product is formed instead of the Schiff-base product. This chemoselectivity contrasts with the outcome in a round bottom flask (traditional batch processing), in which uneven heating prevails, and the opposite result occurs. Similarly, the results in Figure 1. 20C, highlight the difference in the outcome of reactions using a VFD compared to conventional heating, with all the products in the VFD mediated synthesis chromatographically isolated, having >95% purity.[74]

1.3.2. Processing of carbon-based materials using the VFD

1.3.2.1. Carbon nanotubes

1.3.2.1.1. Lateral 'slicing' of single, double and multi-walled carbon nanotubes

In 2016, K. Vimalanathan *et al.*[78] reported a novel method for the lateral slicing of carbon nanotubes CNTs (single, double and multi-walled, respectively SWCNTs, DWCNTs and MWCNTs)) within the dynamic thin film in the VFD. This involves simultaneously irradiating the liquid in the rapidly glass tube with a pulsed laser, in particular a Nd:YAG crystal laser operating at 1064 nm, Figure 1. 21. The VFD was operated at an inclination angle of 45°, which is now recognised as the optimal angle for processing in general using the VFD, and 7500 rpm rotational speed, Figure 1. 21D. The advantages of this method of slicing CNTs over the conventional methods is that the resulting short tubes are devoid of surface defects, as well as avoiding the use of toxic reagents and harsh chemicals. Controlled slicing of SWCNTs, DWCNTs and MWCNTs was established with length distributions centred at *ca* 190, 160 nm and 171 nm, respectively, as determined using AFM, and supported by small-angle neutron scattering solution data.[78] In addition, time-dependent studies showed that with the increase in the irradiation time, more slicing and narrow length distribution was evident for SWCNTs compared to DWCNTs and MWCNTs. The slicing of the CNTs using the VFD was for both modes of operation of the device, namely continuous flow and confined mode, with the latter better able control the length of SWCNTs compared to the DWCNTs and MWCNTs.

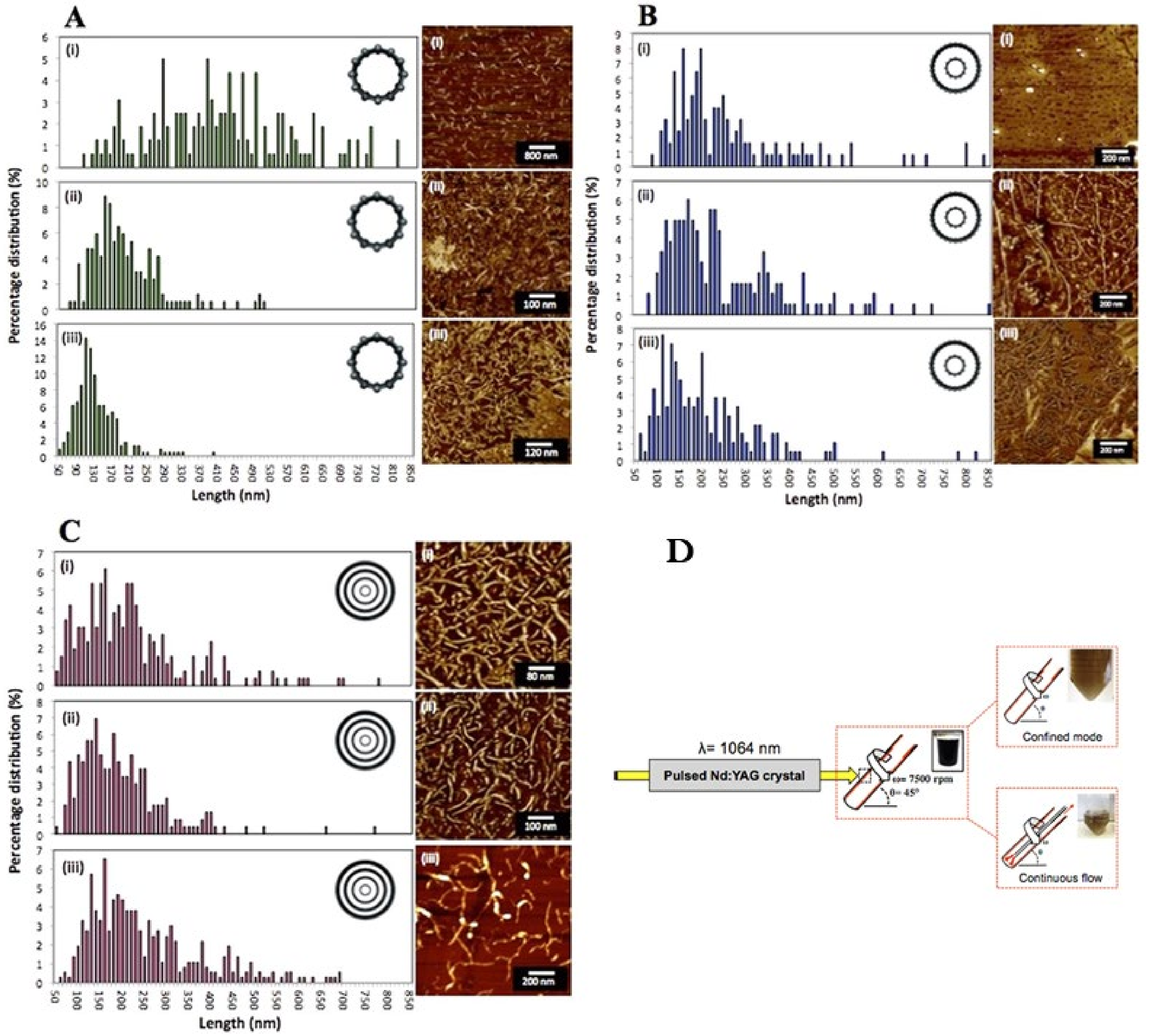

Figure 1. 21 AFM height images of laterally sliced CNTs for reaction times of (1) ten minutes, (ii) thirty-minutes and (iii) one hour, for (A) SWCNTs, (B), DWCNTs, and (C), and MWCNTs. (D) Experimental setup for lateral slicing CNTs. This figure has been copies from reference 78.

1.3.2.1.2. Fabricating of carbon nanorings toroid structure

Raston and co-worker [79] have developed a novel VFD mediated approach to prepare single-wall carbon nanorings of various morphologies with control over their diameter, as characterised using AFM and TEM. They were fabricated using an immiscible solvent system of toluene and water, with an optimal rotational speed of 7500 rpm, and a tilt angle of 45°. The nanorings comprised of coiled SWCNTs with diameters ranging from 300 to 700 nm, for a 20 mm dimeter glass tube (ID 17.5 mm), Figure 1. 22, and 100 to 200 nm for a 10 mm OD glass tube (ID 8.5 mm). This is the first report on gaining insight into the effects of varying the diameter of the tube.[79] The results clearly show that SWCNTs are bent from the shear stress in the VFD, and this is important in considering the effect of the pulsed laser for sling SWCNTs, and also DWCNTs and MWCNTs, as discussed above. The vibrational energy from absorption of the NIR radiation results in C-C bond cleavage associated with shear stress induced bending of the SWCNTs.

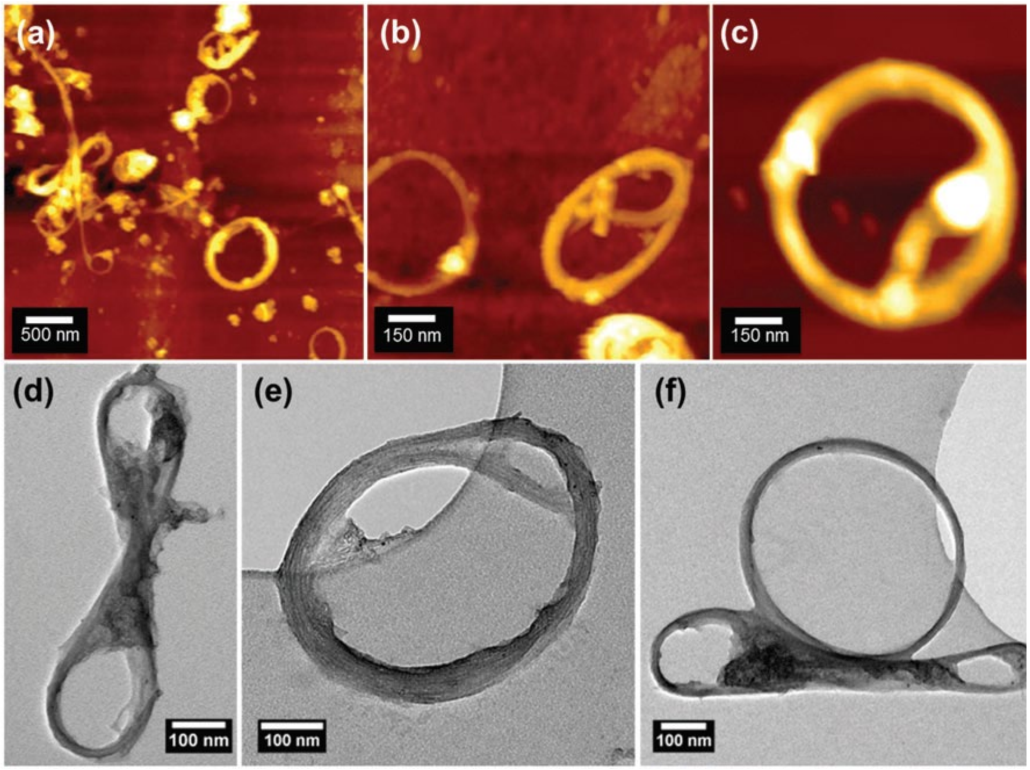

Figure 1. 22 (a-c) AFM images of carbon nanorings made up of coiled SWCNTs, and (d-f) and TEM images of the different carbon nanoring structures, with all the rings formed in a 20 mm OD glass tube. This figure has been copied from reference 79.

1.3.2.1.3. Synthesis of luminescent carbon nanodots

X. Luo *et al.* [80] reported a simple, environmentally friendly novel continuous flow method to prepare water-soluble carbon nanodots (CDs) using the VFD. The flow rate was set at 0.45 mL min^{-1}. This involved delivering a dispersion of MWCNTs in 30% H_2O_2 created in a magnetically stirred syringe, to the VFD tube which was simultaneously irradiated with a Q-switch Nd:YAG laser operating at 1064 nm. The resulting carbon nanodots CDs which arise form controlled oxidation of the carbon material were characterised using a diversity of techniques, including SEM, TEM, AFM, Rama, IR, UV-visible, fluorescence, and X-ray photoelectron spectroscopy. The as-prepared CDs are quasi-spherical with an average diameter of 6 nm (ranging from 3 to 13 nm), with the data consistent with the proposed structure shown in Figure 1. 23, comprising a number of layers of graphene sheets.

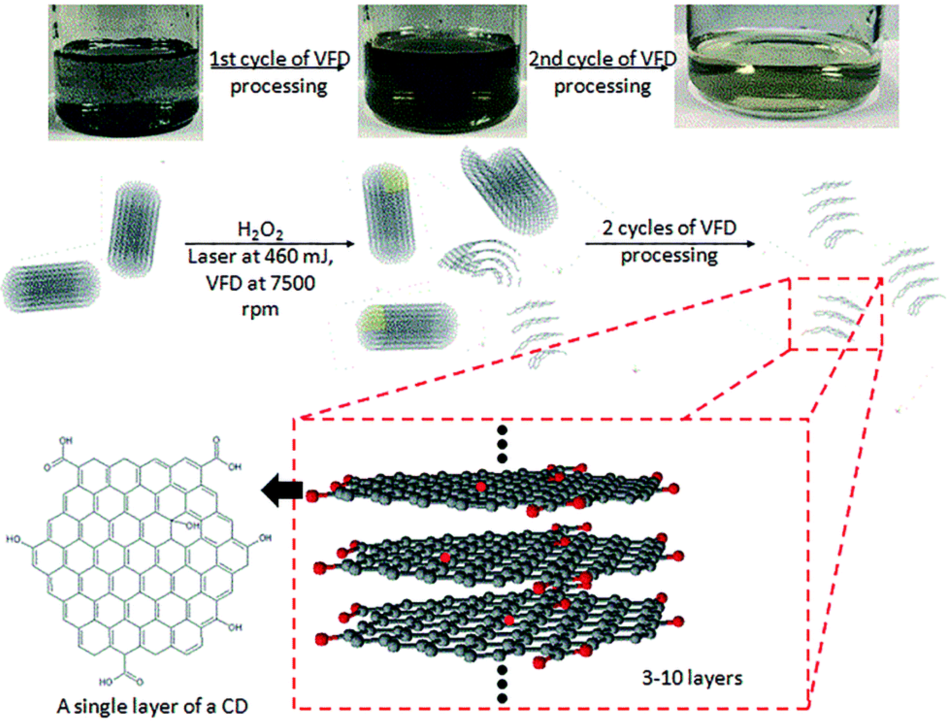

Figure 1. 23 Schematic representation of NIR laser-VFD mediated fabrication of carbon dots (CDs) from multiwall carbon nanotubes. CDs fabricated under optimized conditions (two cycles continuous flow, 0.1 mg mL^{-1}, flow rate of 0.45 mL min^{-1}, 7500 rpm, 450 mJ, at 45° tilt angle). This figure has been copies from reference 80.

1.3.2.2. Fullerene C_{60}

1.3.2.2.1. VFD mediated self-assembly of C_{60} into nanotubules

There are a variety of methods reported on controlling the crystallisation of C_{60} molecules, in forming a diversity of different structures. Most of the methods developed thus far use surfactants and toxic solvents. K. Vimalanathan *et al.* developed a method to fabricate hollow tubules of self-assembled fullerene C_{60}[81] using the VFD, without the use of any surfactants, where the fullerene dissolved in toluene and water were delivered in separate jet feeds, under continuous flow conditions, with water effectively the anti-solvent (ratio of toluene and water 1:1). Optimisation of the process for such control of nucleation and growth of nano-structures of C_{60} involved systematically varying the processing parameters of the device, initially rotational speed and inclination angle of the glass tube, before translating the processing into continuous flow. The hollow nanotubules, Figure 1. 24, are approximate 0.4 to 3 μm in length with an inner diameter of about 100 to 400 nm, which were formed using an inclination angle 45° and a rotational speed of 7000 rpm.

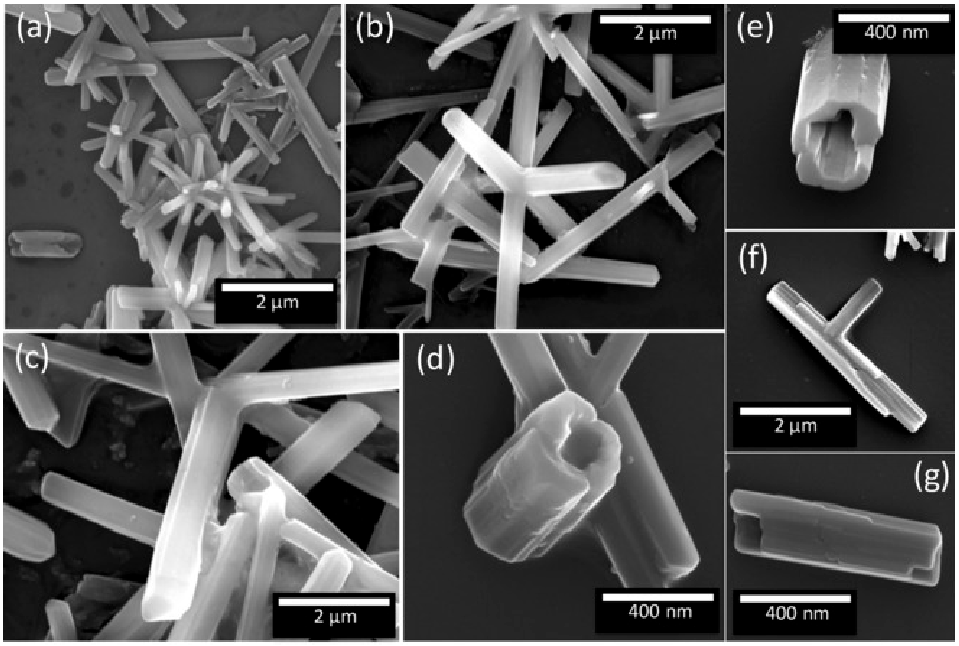

Figure 1. 24 SEM images of C_{60} nanotubules fabricated in the VFD at 7000 rpm, using a mixture of toluene and water in a 1:1 ratio. This figure has been copies from reference 81.

1.3.2.2.2. VFD mediated self-assembly of C_{60} into cones

Self-assembled cone-shaped fullerenes have been synthesised under continuous flow processing in the VFD, Figure 26. Here, as received C_{60} was dissolved in *o*-xylene over 24 hours, followed by filtration and then mixing with dimethyl formamide (DMF) as an anti-solvent during the VFD processing.[82] Separate syringe pumps were used to deliver a 1:1 mixture of *o*-xylene solution of the fullerene and DMF to the hemispherical base of the rapidly rotating tube through jet feeds 1 and 2, Figure 26a. The resulting cones are uniform in shape, as determined using SEM, without the necessity to coat them with Pt to impart conduction, as highlighted for the cones in Figure 1. 25c-g. The diameter of the cones ranged from 0.5 to 2.5 µm, and their thickness ranged from 120 nm to 310 nm. They were also characterized using XRD, Raman, TGA and DSC. Interestingly, other ratios of the solvents were not as effective as the 1: 1 ratio.[82]

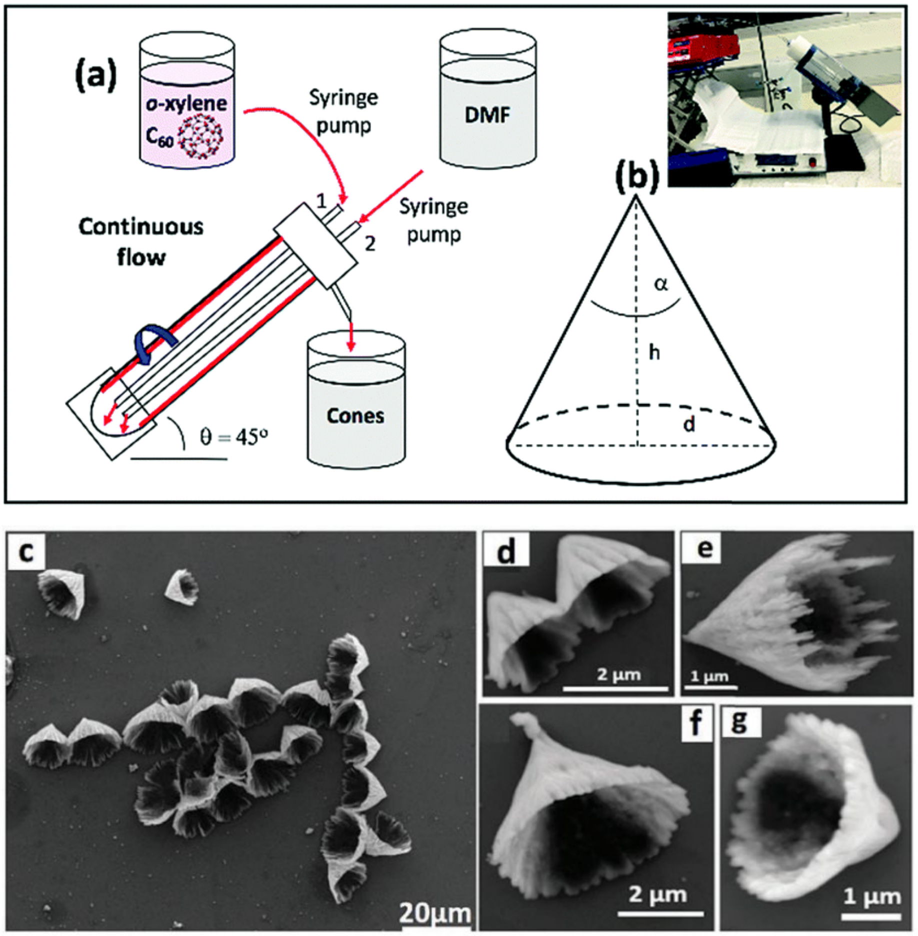

Figure 1. 25 (a) Schematic representation of self-assembly of C_{60} using the VFD; (c)–(g) SEM images of the cones fabricated under continuous flow mode at 4000 rpm, flow rate, 0.5 mL min^{-1} and C_{60} concentration 0.5 mg mL^{-1}. This figure has been copied from reference 82.

1.3.2.3. Exfoliation of 2D materials

1.3.2.3.1. Exfoliation of 2D Carbon Nanomaterial

The Raston research group reported on the ability of the VFD to exfoliate 2D graphite and isostructural 2D hexagonal boron nitride in N-methyl-pyrrolidone (NMP), as the solvent of choice at the time.[75] Indeed, this work, published in 2012, was the first report on VFD processing, which featured a 10 mm dimeter glass tube, with now most of the processing in a 20 mm OD tube. The processing was in the confined mode of operation, and was optimal for a tilt angle of 45º, with the tube rotating at 7000 and 8000 rpm for graphite and BN respectively. Exfoliation of graphene using the spinning disc processors (SDP) was also investigated, but this led to small amounts of graphene scrolls, and required recycling.[83] A difficulty here was the need for large volumes of solvent for any optimisation of the process. The same would also apply to the use of the RTP.

Shearing and the consequential exfoliation in the VFD was thought to involve displacement of graphene or *h*-BN sheets relative to each other, Figure 1. 26b, and/or slippage at the interface of graphite flakes with the surface of the tube.

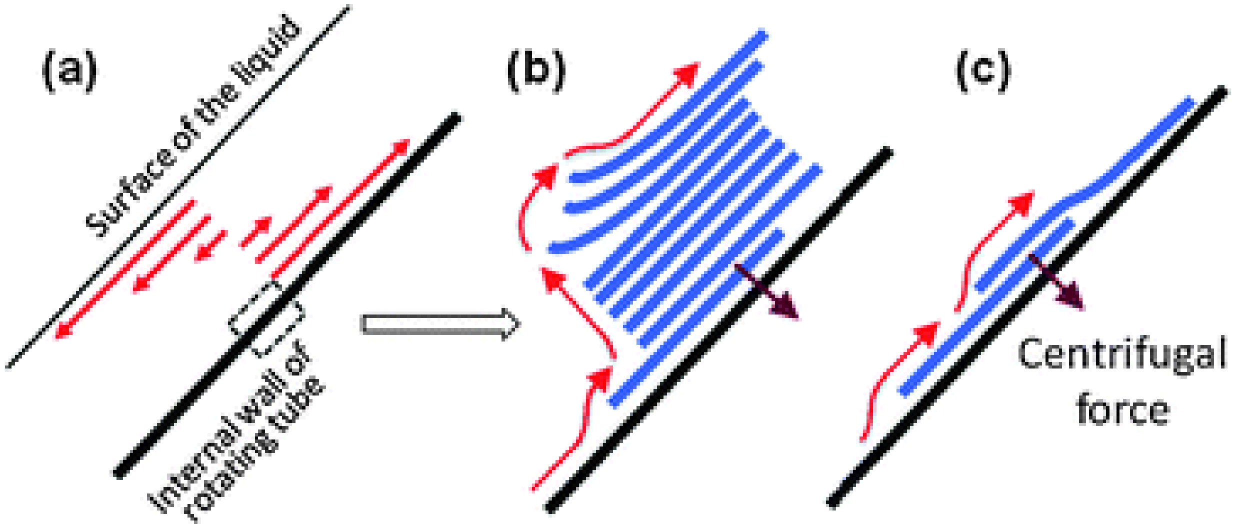

Figure 1. 26 Illustration of (a) the microfluidic flow velocity indicted by red arrows for a section of the rotating tube, and (b) the exfoliation process on the upper surface of a graphite flake, and (c) slippage on the inner surface of the tube. This figure has been copies from reference 75.

1.3.2.3.2. Exfoliation of Phosphorene Nanosheets

A practical, simple, and fast "top-down" VFD mediated method has been developed to produce solution-processable few-layer phosphorene nanosheets under confined mode of operation of the VFD.[84] NIR radiation from a pulsed laser also featured in the exfoliation process, with the ensuing sheets of phosphorene extremely thin (4.3 ± 0.4 nm), and having high crystallinity Figure 1. 27. These nanosheets have been incorporated into perovskite solar cells as the effective electron transporting material, resulting in an increase in average power conversion efficiency (PCE) from 14.32% to 16.53%. DFT studies are consistent with the PCE improvements arising from the high carrier mobility and suitable band energy alignment of the phosphorene [84].

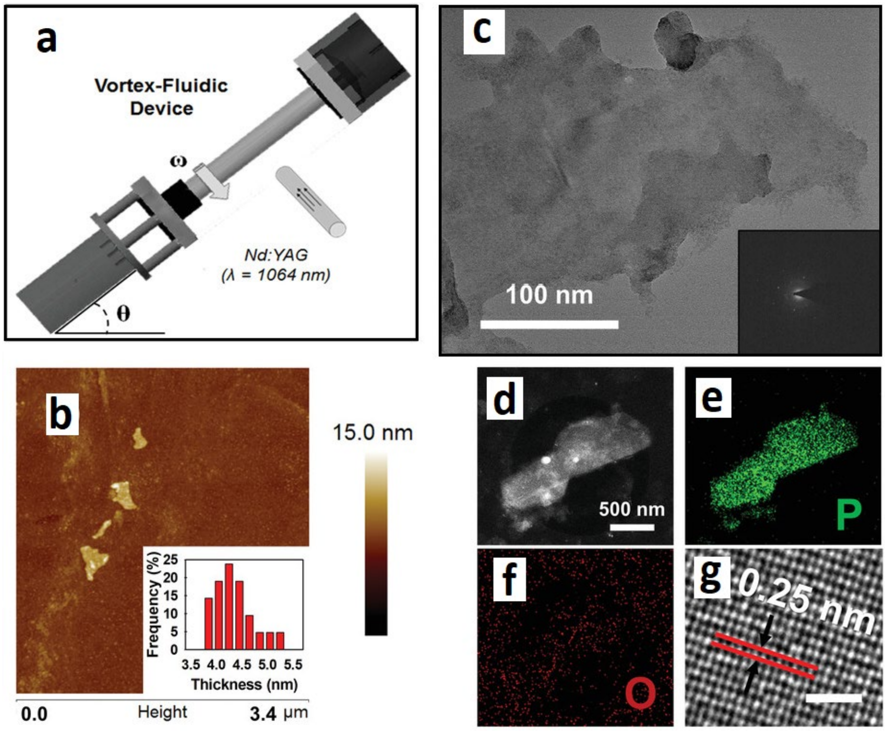

Figure 1. 27 (a) Schematic for production phosphorene using the VFD at 6000 rpm, operating under the confined mode of operation, with a Nd:YAG pulsed laser operating at 280 mJ and 1064 nm. (b) AFM image of few-layer phosphorene nanosheets. Inset shows the histogram of heights. (c) TEM image of phosphorene nanosheet. Inset shows the SAED pattern. (d-f) High-angle annular dark-field (HAADF STEM) image with its EDX elemental mapping. (g) High-resolution TEM image of phosphorene. Scale bar: 1 nm. This figure has been copied from reference 84.

1.3.2.3.3. Plasma assisted VFD manipulation of graphene oxide and oxidation methylene blue

The Raston group has developed a VFD where a plasma is generated over the dynamic thin liquid film, Figure 1.28[85] The species in the plasma are drawn into the thin film as a high mass transfer process, at the plasma-liquid interface, and depending on the choice of gas, nanomaterials can be modified, as established for graphene oxide. The same device has other applications, including breaking down of dyes, as a proof of concept environmental remediation process.

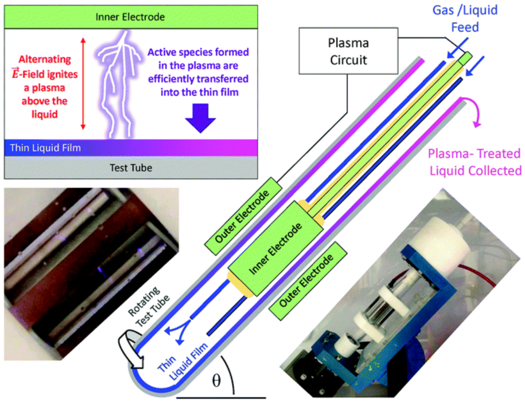

Figure 1. 28 A modified VFD for generating a plasma over the surface of the thin film in the device, (insets) a schematic representation of the plasma generation above the liquid film, a photo of the device and the micro discharges observed during the plasma-processing. This figure has been copies from reference 85.

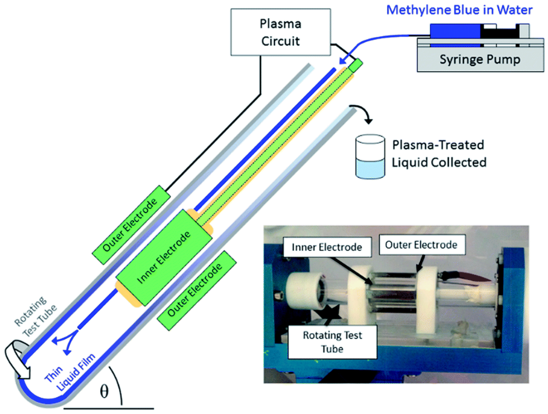

Figure 1. 29 Schematic for oxidation of methylene blue using non-thermal plasma thin film processing within a continuous flow VFD. An inset photograph of the device highlights the key features of the process. This figure has been copied from reference 86.

Jones *et al.* have also developed another continuous flow non-thermal plasma VFD, which under continuous flow results in oxidations of methylene blue (Figure 1.29).[86] Furthermore, the thin film of liquid can be adjusted by varying the rotational of The VFD. Overall, reducing the film thickness enhances the oxidation of the precursor. This feature within VFD processing allows flux-driven chemical processing, such as photo-catalysis, photo-redox and electrochemistry. Such a technique will improve green chemistry metrics by reducing the environmental and economic impact of chemical processing through more efficient energy usage.[86]

1.3.2.4. Scrolling of 2D materials

1.3.2.4.1. Scrolling of graphene from graphite

2D Graphene has high stiffness, but nevertheless it can be rolled up into 3D graphene scrolls, with the ability to modify the diameter of these scrolls by varying the method used to fabricate them. In this way graphene scrolls have potential in a number of applications, including in hydrogen storage and supercapacitors. All methods reported thus far for generating scrolls come with some limitations, especially their formation in low yields, for example in using a SDP.[83] This was overcome in a method developed by Vimalanathan *et al.* which involves the formation of graphene scroll directly from graphite flakes using the VFD.[87] Here the combination of interfacial tension from the immiscible solvent of toluene and water and shear stress generated within the dynamic thin films facilitated the shearing and bending of the graphene sheets, affording the scrolls. These were characterised using AFM, SEM, TEM and HRTEM and Raman spectroscopy, Figure 1. 30(b-d). Optimal processing for generating scrolls directly from graphite is for a concentration at 0.5 mg.mL^{-1} with the ratio of graphite in toluene and water at 1:1, with the scrolls having san average lattice spacing of 0.367 nm.[87]

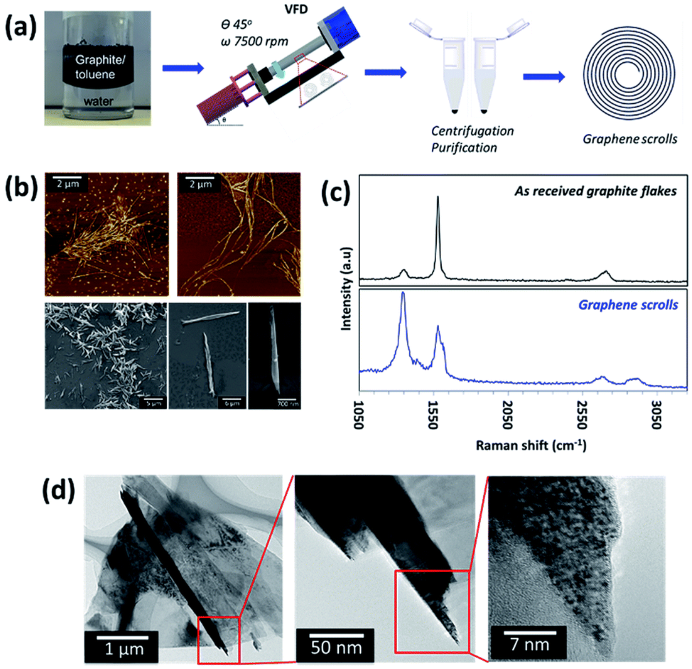

Figure 1. 30 (a) Schematic of the fabrication of graphene scrolls from graphite dispersed in toluene and water (1:1) with a starting concentration of 0.5 mg mL^{-1}, using the confined mode of operation of the VFD, with the tube rotating at 7500 rpm. (b) AFM and SEM images of the graphene scrolls. (c) Raman spectra of as received graphite flakes and the graphene scrolls (d) TEM and HRTEM characterization of an individual graphene scroll. This figure has been copied from reference 87.

1.3.2.4.2. Scrolling hexagonal boron nitride (*h*-BN)

Hexagonal boron nitride (*h*-BN) is readily exfoliated or exfoliated with scrolling in water using the VFD operating under continuous flow conditions[88] as an environmentally friendly method, using a benign solvent, with the processing devoid of harsh chemicals and surfactants. Exfoliation versus scrolling is simply achieved by small changes in the operating parameters of the VFD, including concentration and flow rate, and this highlights the complexity of the fluid flow in the device.[88] Scrolls are generated at 6000 rpm, with a concentration of *h*-BN in water at 0.1 mg.mL^{-1}, and a flow rate of 0.75 mL.min^{-1}, whereas exfoliation is optimal at the same speed, but with a concentration of 0.3 mg/mL dispersed in water and a flow rate of 0.75 mL.min^{-1}, Figure 1.31. Interestingly, a key difference of this processing relative to all other processing in the VFD is that the tilt angle of the tube was -45º;[88] all other applications of VFD have an optimal tilt angle of +45º. This was found necessary to overcome the build-up of material in the tube at +45º, and the new tilt angle reduced the residence time of liquid in the tube from 6 min at +45º to 2 minutes at -45º. The formation of the scrolls versus exfoliation comes from AFM, SEM, TEM and HRTEM, and Raman spectroscopy.[88]

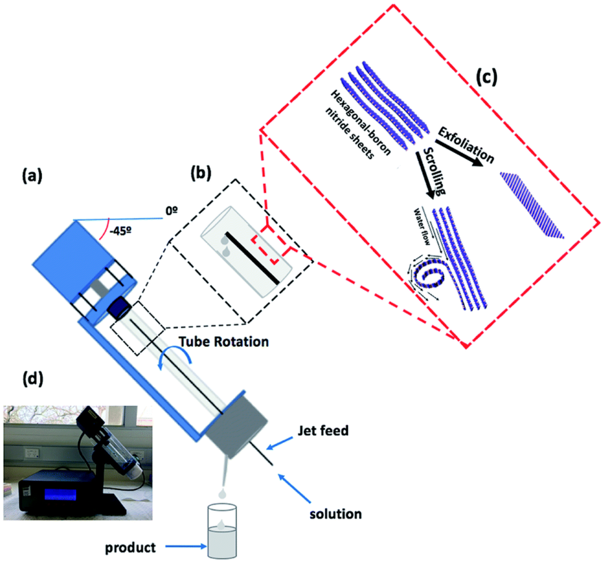

Figure 1. 31 (a) Diagram of the VFD set up for selectively exfoliating or scrolling hexagonal boron nitride. (b) Zoomed in section showing transport of the liquid inside the rapidly rotating tube. (c) The different manipulation of the hexagonal-boron nitride during VFD processing. This figure has been copied from reference 88.

1.3.2.5. Synthesis of metal oxide nanoparticles

1.3.2.5.1. Synthesis of superparamagnetic magnetite nanoparticles

A number of methods have been developed for preparing superparamagnetic magnetite, Fe_3O_4, nanoparticles including in the VFD under continuous flow conditions, as an adaption of the device for metal vapour synthesis, which avoids the use of any chemicals.[89] Here a Nd:YAG pulsed laser irradiates a pure iron target in the VFD tube, generating a plume of metal. This reacts with oxygen forming particles of magnetite which are drawn in the liquid, affording spherical or hexagonal shaped nanoparticles, as individual single crystals approximately 15 nm in diameter (Figure 1.32).[89]

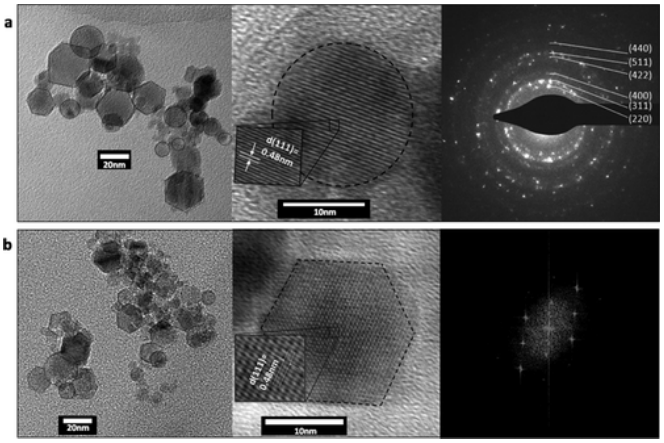

Figure 1. 32 TEM, HRTEM, and SAED for generating magnetite NPs involving laser irradiation (1064 nm, 360 mJ) of an iron rod placed inside the VFD tube with the device operated under continuous flow mode, rotational speed 7500 rpm and flow rate 0.1 mL.min^{-1}. (a) Magnetite nanoparticles which exited the VFD, and (b) magnetite nanoparticles which were retained inside the tube during processing. This figure has been copied from reference 89.

1.3.2.5.2. Synthesis of copper oxide nanoparticles

In the same way, dicopper oxide (Cu_2O) nanoparticles are generated as a NIR pulsed laser ablation of copper metal inside the rapidly rotating VFD tube.[90] Both continuous flow and confined flow modes of operation of the VFD are effective in generating Cu_2O nanoparticles in high yield. Solutions of these particles transform to copper oxide (CuO) in water at 50 °C over 10 h, Figure 1.33a-c. The use of water as a solvent is also noteworthy, in avoiding potentially waste generating reagents, which feature in the conventional synthesis of the material.[90] The two different materials, varying in oxidation of the metal, can be readily distinguished using X-ray diffraction, with the size of the nanoparticles determined using the Scherrer equation, Figure 1.33d and e.[90]

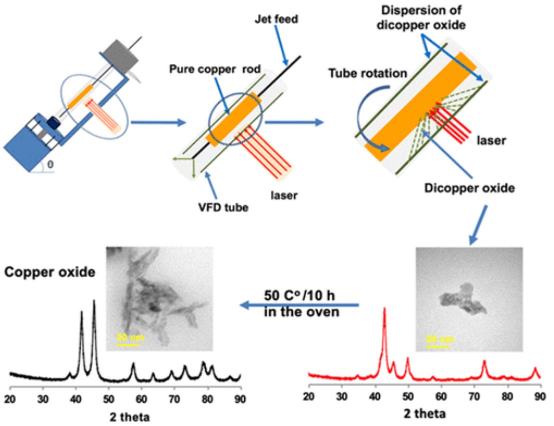

Figure 1. 33 (a) Diagram of VFD processing for generating Cu_2O nanoparticles. (b and c) Zoomed-in of the tube where Cu_2O is formed after the irradiation of the copper rod. (d and e) X-ray diffraction patterns for Cu_2O and CuO. This figure has been copied from reference 90.

1.3.2.6. Synthesis of composite materials in the VFD

1.3.2.6.1. h-BN@magnetite

Following the success of generating magnetite nanoparticles in the VFD, the same processing was investigated, now with the thin film of water containing *h*-BN (0.1 mg.mL^{-1}), in developing a one step process for gaining access to a composite materials.[91] The optimum tilt angle was +45° and the optimal rotational speed was 7500 rpm, with the material characterised using AFM, SEM, TEM and HRTEM, and Raman spectroscopy, Figure 1. 34. The product has superparamagnetic magnetite nanoparticles dispersed randomly on the surface of h-BN, with the composite material, *h*-BN@magnetite, having high

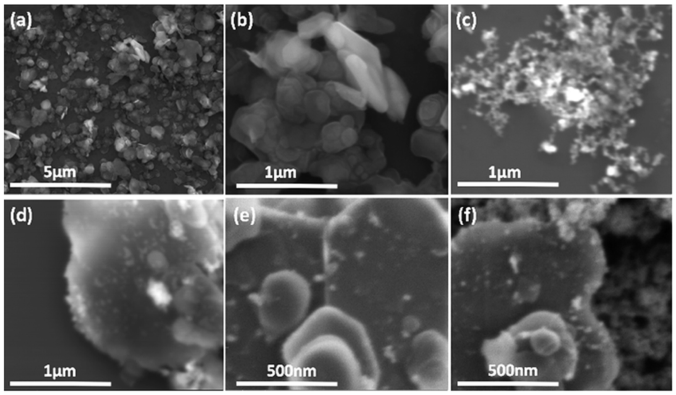

Figure 1. 34 SEM images of (a-b) As received *h*-BN. (c) Magnetite NPs formed in the absence of *h*-BN. (d–f) Phosphate binding h-BN@magnetite hybrid material, fabricated in the VFD under 7500 rpm and *h*-BN dispersed in water (0.1 mg.mL^{-1}), with a pulsed laser operating at 1064 nm and 360 mJ. This figure has been copied from reference 91.

porosity and high surface area.[91] It is effective in removing phosphate from waste water, with the material able to be readily recycled.

1.3.2.6.2. Decorating nanoparticles on carbon nanomaterials

The VFD is effective in decorating platinum nanoparticles on carbon nano-onions,[92] with the processing in water and the ability to control the density of nanoparticles, depending on the operating parameters of the device, using hydrogen as the reducing agent, Figure 1. 35. The Pt NP decorated carbon nano-onions composites have excellent electrocatalytic activity. In a similar way, Pt nanoparticles were successfully decorated on carbon nano-onion using environmentally friendly ascorbic acid as the reducing agent. Formation of the two types of deductions of platinum (hydrogen versus ascorbic acid) rely on the shear stress in the VFD.[92]

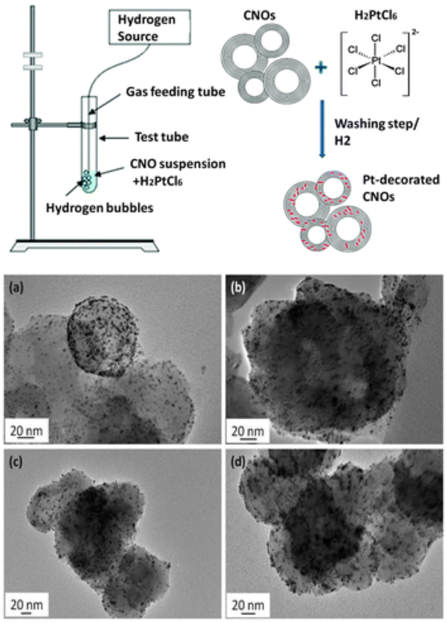

Figure 1. 35 Scheme representing the process for decoration carbon nanoonions (CNOs) with Pt nanoparticles. (a-d) TEM images of Pt/CNOs decorated at various temperatures. This figure has been copied from reference 92.

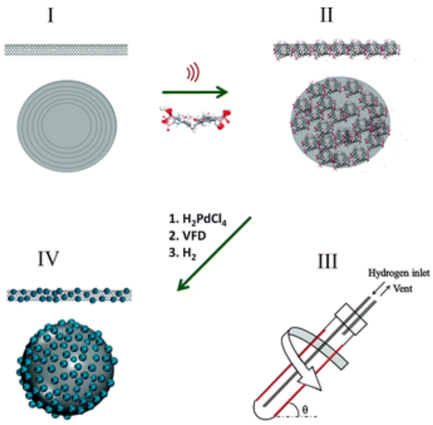

Figure 1. 36 Diagrammatic decoration of (I) Carbon nanomaterials (CNMs) including carbon nanotubes and carbon nano onion with palladium nanoparticles. (II) Calixarene functionalized CNMs using a different speed of the VFD (III), in affording (IV). This figure has been copied from reference 93.

SWCNTs can also be decorated with palladium nanoparticles using the VFD,[93] Figure 1. 36, in forming a composite material which effectively combines the electrical properties of the SWCNTs with a hydrogen absorption ability of Pd, for use in sensor applications. The first step of the processing is binding Pd^{2+} to *p*-phosphonated calixarenes on the surface of the SWCNTs, with reduction taking place in the VFD affording Pd nanoparticles 1–5 nm in diameter. The composite material is effective in sensing hydrogen gas in the range of 0.1–10%.[93]

1.3.2.6.3. Synthesis of hybrid carbon nanomaterials involving microorganisms

Microencapsulation of bacteria is of interest in providing a protective layer while retaining their function, except for replication which can clog the matrix.[94] The VFD has shown promise in this regard,[94] with the ability to encapsulate *R. Opacus* and *S. Aureus* bacteria with graphene oxide while keeping the cells alive and biologically active, Figure 1. 37. This used a 10 mm OD dimeter tube and a 1:1 mixture of 0.1 mg/mL graphene oxide and 0.5 mL of bacterial solution, using the confined mode for rotational speeds of 5000 and 8000 rpm for 1 minute after mixing both solutions of GO and bacteria.[94] The ability to wrap bacteria with different morphologies "spherical and rod shaped" relates to the nature of the fluid flow in the VFD, and part of this thesis is focused at understanding this.

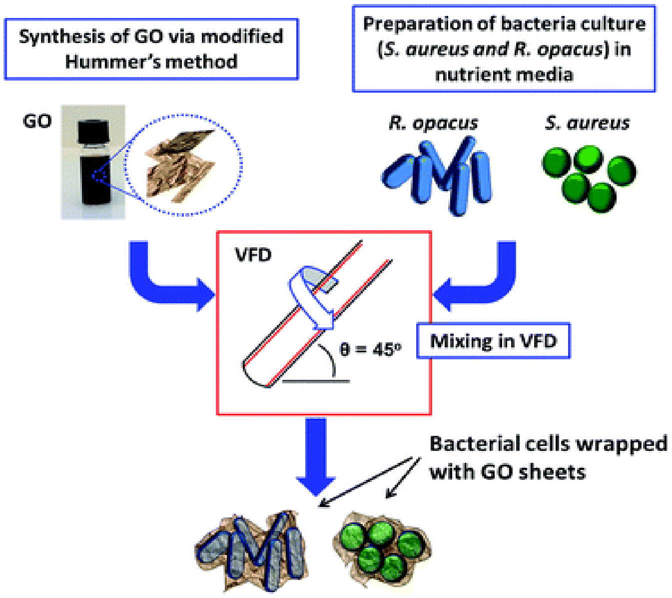

Figure 1. 37 Diagram of the preparation of graphene oxide wrapped bacteria using a 10 mm VFD tube, operating at 5000and 8000 rpm. This figure has been copied from reference 94.

1.3.2.6.4. Graphene encapsulation of algal cells

The VFD was also effective in in exfoliating graphene as multilayered material and then partial wrapping of algal cells.[95] The exfoliation of graphite flakes was in water using the confine mode of the VFD, for a 10 mm OD tube. The cross-section area of the graphite flakes was 7-10 µm and the inclination angle of the tube was optimal at 45° with the rotational speed optimal at 7000 rpm for 30 minutes of processing. The wrapping step involved addition 1 mL of a suspension of wild type *Chlorella Vulgaris* and the mixture recycled through the VFD under continuous flow conditions, also using a 10 mm OD glass tube, Figure 1. 38.[95]

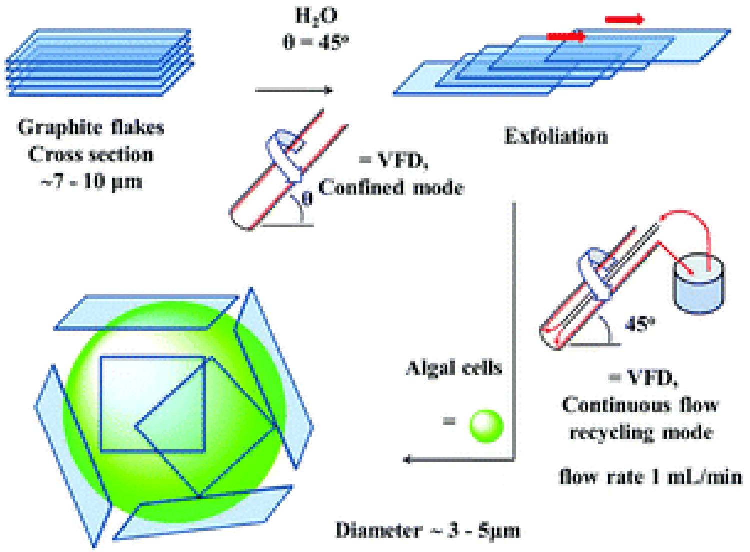

Figure 1. 38 Illustration of the VFD mediated hybridization procedure for exfoliating multi-layered graphene and wrapping algal cells using a 10 mm OD glass tube. This figure has been copied from reference 95.

1.4. Research Aims and Objectives

The main focus of this thesis centres around the ability to fabricate and manipulate carbon materials under continuous flow, without altering their explicit properties, which can be benefit for wide range of applications.

Conventional batch processing methods have dominated the field of fabricating material science. Carbon nanomaterials have been extensively studied, due to their seemingly limitless and extraordinary properties that can be utilized in a diversity of fields. Many successful methods have been reported, in significantly advancing the field. However, there are still some challenges and limitations which need to be addressed in the area of fabricating nanomaterials, such as scalability, the quality of the material, economic sustainability and the environmental impact issues.

Fulfilling the demand for the availability of different carbon nanomaterials, having precisely controlled nanoscale length with scalability incorporated into the processing, is important for future uptake by industry for which there are a myriad of applications.

Another effective strategy over traditional batch processing is therefore required, and this led to the development of innovative processing platforms which can address the above limitations while controlling the length scales. Thus, employing the use of controllable mechanoenergy generated in the VFD microfluidic platform, has potential for developing novel methods to gain access to various nanocarbon material, and indeed new materials, with uniformity of structure, as well as properties, at the same time incorporating sustainability/green chemistry metrics.

These challenges have been addressed in the research undertaken and described in this thesis under the specific aims: The thesis is presented with the chapters ordered relative to the development of the VFD processing, initially for manipulate carbon nanotubes, followed by processing of 2D materials, then the fabrication of novel composite materials.

1. Control the length of sliced SWCNTs in a scalable way using the VFD, without introducing defects into the side walls of the SWCNTs, and avoiding the use of hazardous chemicals or surfactant.
2. Develop a novel method to vertically self-assemble aligned sliced MWCNTs on a silicon substrate, after the availability of the tubes with a short length scale and narrow size distribution.
3. Fabricate coiled SWCNT rings as a high yield process in the VFD, in the absence of surfactant or any other reagents, and investigate their magnetic properties.
4. Fabricate graphene oxide scrolls in aqueous solution as a high yield process in the VFD, incorporating principles of green chemistry metrics in avoiding the use of other reagents.
5. Understand the fluid flow in the VFD, by establishing the ability to scroll and unscroll GO sheets, depending on the rotational speed of the VFD and the nature of the liquid, along with the ability to manipulate the structure of sell-assembled C_{60}.
6. Develop a new strategy for generating reduced graphene oxide (rGO) from GO dispersed in water, using VFD processing, such that it is scalable and avoids the use of harsh reducing agents.
7. Fabricate composite materials of MWCNTs decorated with metal nanoparticles in the VFD, to overcome the otherwise use of long processing times and harsh chemicals, and appraise these composite materials for applications in energy storage.
8. Develop simple methods to synthesis composite spherical materials of graphene and fullerenes C_{60} at room temperature in the VFD, without using harsh chemicals or surfactants, and appraise them as material in supercapacitors.

Results of each aim are reported in published articles, which form the basis of the following chapters.

1.5. References

1. Georgakilas, V.; Perman, J. A.; Tucek, J.; Zboril, R., Broad family of carbon nanoallotropes: classification, chemistry, and applications of fullerenes, carbon dots, nanotubes, graphene, nanodiamonds, and combined superstructures. *Chem. Rev.,* **2015,** *115*, 4744-4822.
2. Li, Z.; Liu, Z.; Sun, H.; Gao, C., Superstructured assembly of nanocarbons: fullerenes, nanotubes, and graphene. *Chem. Rev.,* **2015,** *115*, 7046-7117.
3. Ambrosi, A.; Chua, C. K.; Bonanni, A.; Pumera, M., Electrochemistry of graphene and related materials. *Chem. Rev.,* **2014,** *114*, 7150-7188.
4. Al-Jumaili, A.; Alancherry, S.; Bazaka, K.; Jacob, M. V., Review on the antimicrobial properties of carbon nanostructures. *Materials,* **2017,** *10*, 1066.
5. Sinitskii, A.; Tour, J., Graphene electronics, unzipped. *IEEE Spectrum,* **2010,** *47*, 28-33.
6. Dresselhaus, M. S.; Dresselhaus, G.; Eklund, P. C., Science of fullerenes and carbon nanotubes: *their properties and applications.* Elsevier, Orlando, Florida, 1996.
7. Kroto, H. W.; Heath, J. R.; O'Brien, S. C.; Curl, R. F.; Smalley, R. E., C60: Buckminsterfullerene. *Nature,* **1985,** *318*, 162-163.
8. Yan, Q.-L.; Gozin, M.; Zhao, F.-Q.; Cohen, A.; Pang, S.-P., Highly energetic compositions based on functionalized carbon nanomaterials. *Nanoscale,* **2016,** *8*, 4799-4851.
9. Nimibofa, A.; Newton, E. A.; Cyprain, A. Y.; Donbebe, W., Fullerenes: Synthesis and Applications. *J. Mater. Sci. Res.,* **2018,** *7*, 22.
10. Geckeler, K. E.; Samal, S., Syntheses and properties of macromolecular fullerenes, a review. *Polym.Int.,* **1999,** *48*, 743-757.
11. Chuvilin, A.; Kaiser, U.; Bichoutskaia, E.; Besley, N. A.; Khlobystov, A. N., Direct transformation of graphene to fullerene. *Nature Chem.,* **2010,** *2*, 450.
12. Yang, Z.; Ren, J.; Zhang, Z.; Chen, X.; Guan, G.; Qiu, L.; Zhang, Y.; Peng, H., Recent advancement of nanostructured carbon for energy applications. *Chem. Rev.,* **2015,** *115*, 5159-5223.
13. Chen, L.; Chen, W.; Huang, H.; Zhang, H. L.; Yuhara, J.; Wee, A. T. S., Tunable arrays of C60 molecular chains. *Adv. Mater.,* **2008,** *20*, 484-488.
14. Fowler, P.; Ceulemans, A., Electron deficiency of the fullerenes. *J. Phys. Chem.,* **1995,** *99*, 508-510.
15. Friedman, S. H.; DeCamp, D. L.; Sijbesma, R. P.; Srdanov, G.; Wudl, F.; Kenyon, G. L., Inhibition of the HIV-1 protease by fullerene derivatives: model building studies and experimental verification. *J. Am. Chem. Soc.,* **1993,** *115*, 6506-6509.
16. Krusic, P. J.; Wasserman, E.; Keizer, P. N.; Morton, J. R.; Preston, K. F., Radical reactions of C_{60}. *Science,* **1991,** *254*, 1183-1185.
17. Gharbi, N.; Pressac, M.; Hadchouel, M.; Szwarc, H.; Wilson, S. R.; Moussa, F., [60] Fullerene is a powerful antioxidant in vivo with no acute or subacute toxicity. *Nano Lett.,* **2005,** *5*, 2578-2585.
18. Foley, S.; Crowley, C.; Smaihi, M.; Bonfils, C.; Erlanger, B. F.; Seta, P.; Larroque, C., Cellular localisation of a water-soluble fullerene derivative. *Biochem. Biophys. Res. Commun.,* **2002,** *294*, 116-119.
19. Isobe, H.; Nakanishi, W.; Tomita, N.; Jinno, S.; Okayama, H.; Nakamura, E., Gene delivery by aminofullerenes: structural requirements for efficient transfection. *Chem.–Asian J.*, **2006,** *1*, 167-175.
20. Sugunan, S. K.; Greenwald, C.; Paige, M. F.; Steer, R. P., Efficiency of Noncoherent Photon Upconversion by Triplet–Triplet Annihilation: The C60 Plus Anthanthrene System and the Importance of Tuning the Triplet Energies. *J. Phys. Chem. A,* **2013,** *117*, 5419-5427.

21. Kim, Y.; Cook, S.; Tuladhar, S. M.; Choulis, S. A.; Nelson, J.; Durrant, J. R.; Bradley, D. D.; Giles, M.; McCulloch, I.; Ha, C.-S.; Ree, M., A strong regioregularity effect in self-organizing conjugated polymer films and high-efficiency polythiophene: fullerene solar cells. *Nat. Mater.,* **2006**, 5, 197.
22. Dou, L.; You, J.; Hong, Z.; Xu, Z.; Li, G.; Street, R. A.; Yang, Y., 25th anniversary article: a decade of organic/polymeric photovoltaic research. *Adv. Mater.,* **2013,** *25*, 6642-6671.
23. Günes, S.; Neugebauer, H.; Sariciftci, N. S., Conjugated polymer-based organic solar cells. C*hem. Rev.,* **2007,** *107*, 1324-1338.
24. Iijima, S., Helical microtubules of graphitic carbon. *Nature* **1991,** *354*, 56-58.
25. Nessim, G. D., Properties, synthesis, and growth mechanisms of carbon nanotubes with special focus on thermal chemical vapor deposition. *Nanoscale,* **2010,** *2*, 1306-1323.
26. Boumia, L.; Zidour, M.; Benzair, A.; Tounsi, A.; Nanostructures, A Timoshenko beam model for vibration analysis of chiral single-walled carbon nanotubes. *Phys. E: Low-Dimens. Syst. Nanostruct.,* **2014,** *59*, 186-191.
27. De Volder, M. F. L.; Tawfick S. H.; Baughman R. H.; Hart, A. J.; Carbon Nanotubes: Present and Future Commercial Applications, *Science*, 2013, 339, 535.
28. Prasek, J.; Drbohlavova, J.; Chomoucka, J.; Hubalek, J.; Jasek, O.; Adam, V.; Kizek, R., Methods for carbon nanotubes synthesis. *J. Mater. Chem.,* **2011,** *21*, 15872-15884.
29. Guo, T.; Nikolaev, P.; Thess, A.; Colbert, D. T.; Smalley, R. E., Fullerene Nanotubes in Electric-Fields. *Chem. Phys.Lett.,* **1995,** *243*, 49-54.
30. Fan, S.; Chapline, M. G.; Franklin, N. R.; Tombler, T. W.; Cassell, A. M.; Dai, H., Self-oriented regular arrays of carbon nanotubes and their field emission properties. *Scienec,* **1999,** *283*, 512-514.
31. Reina, A.; Hofmann, M.; Zhu, D.; Kong, J., Growth mechanism of long and horizontally aligned carbon nanotubes by chemical vapor deposition. *J. Phys. Chem. C,* **2007,** *111*, 7292-7297.
32. Hata, K.; Futaba, D. N.; Mizuno, K.; Namai, T.; Yumura, M.; Iijima, S., Water-assisted highly efficient synthesis of impurity-free single-walled carbon nanotubes. *Scienec,* **2004,** *306*, 1362-1364.
33. Yamada, T.; Namai, T.; Hata, K.; Futaba, D. N.; Mizuno, K.; Fan, J.; Yudasaka, M.; Yumura, M.; Iijima, S., Size-selective growth of double-walled carbon nanotube forests from engineered iron catalysts. *Nat. Nanotechnol.,* **2006,** *1*, 131-136.
34. Aqel, A.; El-Nour, K. M. A.; Ammar, R. A.; Al-Warthan, A., Carbon nanotubes, science and technology part (I) structure, synthesis and characterisation. *Arabian J. Chem.,* **2012,** *5*, 1-23.
35. Ebbesen, T.; Lezec, H.; Hiura, H.; Bennett, J.; Ghaemi, H.; Thio, T., Electrical conductivity of individual carbon nanotubes. *Nature,* **1996,** *382*, 54.
36. Ibrahim, K. S., Carbon nanotubes-properties and applications: a review. *Carbon Lett.,* **2013,** *14* (3), 131-144.
37. Wang, S.; Liang, R.; Wang, B.; Zhang, C., Dispersion and thermal conductivity of carbon nanotube composites. *Carbon,* **2009,** *47*, 53-57.
38. Seidel, R.; Graham, A.; Kretz, J.; Rajasekharan, B.; Duesberg, G.; Liebau, M.; Unger, E.; Kreupl, F.; Hoenlein, W., Sub-20 nm short channel carbon nanotube transistors. *Nano Lett.,* **2005,** *5*, 147-150.
39. Smart, S.; Cassady, A.; Lu, G.; Martin, D., The biocompatibility of carbon nanotubes. *Carbon,* **2006,** *44*, 1034-1047.
40. Kolosnjaj-Tabi, J.; Hartman, K. B.; Boudjemaa, S.; Ananta, J. S.; Morgant, G.; Szwarc, H.; Wilson, L. J.; Moussa, F., In vivo behavior of large doses of ultrashort and full-length single-walled carbon nanotubes after oral and intraperitoneal administration to Swiss mice. *ACS Nano,* **2010,** *4*, 1481-1492.

41. Muller, J.; Huaux, F.; Moreau, N.; Misson, P.; Heilier, J.-F.; Delos, M.; Arras, M.; Fonseca, A.; Nagy, J. B.; Lison, D., Respiratory toxicity of multi-wall carbon nanotubes. *Toxicol. Appl. Pharmacol.,* **2005,** *207*, 221-231.
42. Modugno, G.; Ksar, F.; Battigelli, A.; Russier, J.; Lonchambon, P.; da Silva, E. E.; Ménard-Moyon, C.; Soula, B.; Galibert, A.-M.; Pinault, M.; Flahaut, E.; Mayne-L'Hermite, M.; Bianco, A., A comparative study on the enzymatic biodegradability of covalently functionalized double- and multi-walled carbon nanotubes. *Carbon,* **2016,** *100*, 367-374.
43. Fonseca, A.; Reijerkerk, S.; Potreck, J.; Nijmeijer, K.; Mekhalif, Z.; Delhalle, J., Very short functionalized carbon nanotubes for membrane applications. *Desalination,* **2010,** *250*, 1150-1154.
44. Kierkowicz, M.; Pach, E.; Santidrián, A.; Sandoval, S.; Gonçalves, G.; Tobías-Rossell, E.; Kalbáč, M.; Ballesteros, B.; Tobias, G., Comparative study of shortening and cutting strategies of single-walled and multi-walled carbon nanotubes assessed by scanning electron microscopy. *Carbon,* **2018,** *139*, 922-932.
45. Hou, P.-X.; Liu, C.; Cheng, H.-M., Purification of carbon nanotubes. *Carbon,* **2008,** *46*, 2003-2025.
46. Ziegler, K. J.; Gu, Z.; Peng, H.; Flor, E. L.; Hauge, R. H.; Smalley, R. E., Controlled oxidative cutting of single-walled carbon nanotubes. *J. Am. Chem. Soc.,* **2005,** *127*, 1541-1547.
47. Wang, X. X.; Wang, J. N.; Su, L. F.; Niu, J. J., Cutting of multi-walled carbon nanotubes by solid-state reaction. *J. Mater. Chem.,* **2006,** *16*, 4231-4234.
48. Chen, J.; Dyer, M. J.; Yu, M.-F. J., Cyclodextrin-mediated soft cutting of single-walled carbon nanotubes. *J. Am. Chem. Soc.,* **2001,** *123*, 6201-6202.
49. Pierard, N.; Fonseca, A.; Konya, Z.; Willems, I.; Van Tendeloo, G.; Nagy, J. B., Production of short carbon nanotubes with open tips by ball milling. *Chem. Phys. Lett.,* **2001,** *335*, 1-8.
50. Ren, F.; Kanaan, S. A.; Khalkhal, F.; Loebick, C. Z.; Haller, G. L.; Pfefferle, L. D., Controlled cutting of single-walled carbon nanotubes and low temperature annealing. *Carbon,* **2013,** *63*, 61-70.
51. Wang, W.; Laird, E. D.; Gogotsi, Y.; Li, C. Y., Bending single-walled carbon nanotubes into nanorings using a Pickering emulsion-based process. *Carbon,* **2012,** *50*, 1769-1775.
52. Sun, J.; Liu, H.; Chen, X.; Evans, D. G.; Yang, W.; Duan, X., Carbon nanorings and their enhanced lithium storage properties. *Adv. Mater.,* **2013,** *25*, 1125-1130.
53. Ye, X. R.; Lin, Y.; Wang, C.; Wai, C. M., Supercritical fluid fabrication of metal nanowires and nanorods templated by multiwalled carbon nanotubes. *Adv. Mater.,* **2003,** *15*, 316-319.
54. Shang, P.; Zhang, J.; Tang, W.; Xu, Q.; Guo, S., 2D Thin nanoflakes assembled on mesoporous carbon nanorods for enhancing electrocatalysis and for improving asymmetric supercapacitors. *Adv. Funct. Mater.,* **2016,** *26*, 7766-7774.
55. Zhang, P.; Qiao, Z.-A.; Dai, S., Recent advances in carbon nanospheres: synthetic routes and applications. *Chem. Commun.,* **2015,** *51*, 9246-9256.
56. Shao, Y.; Zhou, L.; Bao, C.; Ma, J., A facile approach to the fabrication of rattle-type magnetic carbon nanospheres for removal of methylene blue in water. *Carbon,* **2015,** *89*, 378-391.
57. Liu, L.; Zhao, J., Toroidal and coiled carbon nanotubes. *in Syntheses and Applications of Carbon Nanotubes and Their Composites; Suzuki, S., Ed.; InTech: Rijeka, Croatia,* **2013**, 257-281.
58. Liu, L.; Liu, F.; Zhao, J., Curved carbon nanotubes: From unique geometries to novel properties and peculiar applications. *Nano Res.,* **2014,** *7*, 626-657.
59. Novoselov, K. S.; Geim, A. K.; Morozov, S. V.; Jiang, D.; Zhang, Y.; Dubonos, S. V.; Grigorieva, I. V.; Firsov, A. A., Electric field effect in atomically thin carbon films. *Science,* **2004,** *306*, 666-669.
60. Geim, A. K.; Novoselov, K. S., The rise of graphene. *Nat. Mater.,* **2007,** *6*, 183-191.

61. Lee, C.; Wei, X.; Kysar, J. W.; Hone, J., Measurement of the elastic properties and intrinsic strength of monolayer graphene. *Science,* **2008,** *321*, 385-388.

62. Bolotin, K. I.; Sikes, K. J.; Jiang, Z.; Klima, M.; Fudenberg, G.; Hone, J.; Kim, P.; Stormer, H. L., Ultrahigh electron mobility in suspended graphene. *Solid State Commun.,* **2008,** *146*, 351-355.

63. Stoller, M. D.; Park, S.; Zhu, Y.; An, J.; Ruoff, R. S., Graphene-based ultracapacitors. *Nano Lett.,* **2008,** *8*, 3498-3502.

64. Singh, R. K.; Kumar, R.; Singh, D. P., Graphene oxide: strategies for synthesis, reduction and frontier applications. *RSC Adv.,* **2016,** *6*, 64993-65011.

65. Gao, W.; Alemany, L. B.; Ci, L.; Ajayan, P. M., New insights into the structure and reduction of graphite oxide. *Nat.Chem.,* **2009,** *1*, 403-408.

66. Stankovich, S.; Dikin, D. A.; Piner, R. D.; Kohlhaas, K. A.; Kleinhammes, A.; Jia, Y.; Wu, Y.; Nguyen, S. T.; Ruoff, R. S., Synthesis of graphene-based nanosheets via chemical reduction of exfoliated graphite oxide. *Carbon,* **2007,** *45*, 1558-1565.

67. Bai, H.; Li, C.; Shi, G., Functional composite materials based on chemically converted graphene. *Adv. Mater.,* **2011,** *23*, 1089-1115.

68. Britton, J.; Meneghini, L. M.; Raston, C. L.; Weiss, G. A., Accelerating enzymatic catalysis using vortex fluidics. *Angew. Chem., Int. Ed.,* **2016,** *55*, 11387–11391.

69. Yasmin, L.; Chen, X.; Stubbs, K. A.; Raston, C. L., Optimising a vortex fluidic device for controlling chemical reactivity and selectivity. *Sci. Rep.,* **2013,** *3*, 2282.

70. Dev, S.; Iyer, K. S.; Raston, C. L., Nanosized drug formulations under microfluidic continuous flow. *Lab Chip,* **2011,** *11*, 3214-3217.

71. Chin, S. F.; Iyer, K. S.; Raston, C. L.; Saunders, M., Size selective synthesis of superparamagnetic nanoparticles in thin fluids under continuous flow conditions. *Adv. Funct. Mater.,* **2008,** *18*, 922-927.

72. Fang, J.; Evans, C. W.; Willis, G. J.; Sherwood, D.; Guo, Y.; Lu, G.; Raston, C. L.; Iyer, K. S., Sequential microfluidic flow synthesis of CePO 4 nanorods decorated with emission tunable quantum dots. *Lab Chip,* **2010,** *10*, 2579-2582.

73. Vimalanathan, K.; Raston, C. L., Dynamic Thin Films in Controlling the Fabrication of Nanocarbon and Its Composites. *Adv. Mater. Technol.,* **2017,** 2, 1600298.

74. Britton, J.; Stubbs, K. A.; Weiss, G. A.; Raston, C. L., Vortex Fluidic Chemical Transformations. *Chem.- Eur. J.,* **2017,** 23, 13270–13278.

75. Chen, X.; Dobson, J. F.; Raston, C. L., Vortex fluidic exfoliation of graphite and boron nitride. *Chem. Commun.,* **2012,** *48*, 3703-3705.

76. Alharbi, T. M.; Harvey, D.; Alsulami, I. K.; Dehbari, N.; Duan, X.; Lamb, R. N.; Lawrance, W. D.; Raston, C. L., Shear stress mediated scrolling of graphene oxide. *Carbon,* **2018**, 137, 419-424.

77. Gandy, M. N.; Raston, C. L.; Stubbs, K. A., Photoredox catalysis under shear using thin film vortex microfluidics. *Chem. Commun.,* **2015,** *51*, 11041-11044.

78. Vimalanathan, K.; Gascooke, J. R.; Suarez-Martinez, I.; Marks, N. A.; Kumari, H.; Garvey, C. J.; Atwood, J. L.; Lawrance, W. D.; Raston, C. L., Fluid dynamic lateral slicing of high tensile strength carbon nanotubes. *Sci. Rep.,* **2016,** *6*, 22865.

79. Vimalanathan, K.; Chen, X.; Raston, C. L., Shear induced fabrication of intertwined single walled carbon nanotube rings. *Chem. Commun.,* **2014,** *50*, 11295-11298.

80. Luo, X.; Al-Antaki, A. H. M.; Vimalanathan, K.; Moffatt, J.; Zheng, K.; Zou, Y.-C.; Zou, J.; Duan, X.; Lamb, R.; Wang, S., Laser irradiated vortex fluidic mediated synthesis of luminescent carbon nanodots under continuous flow. R*eact. Chem. Eng.,* **2018,** 3, 164-170.

81. Vimalanathan, K.; Shrestha, R. G.; Zhang, Z.; Zou, J.; Nakayama, T.; Raston, C. L., Surfactant-free Fabrication of Fullerene C60 Nanotubules Under Shear. *Angew. Chem. Int. Ed.,* **2017,** *56*, 8398-8401.
82. Alsulami, I.; Alharbi, T.; Harvey, D.; Gibson, C. T.; Raston, C. L., Controlling the growth of fullerene C60 cones under continuous flow. *Chem. Commun.,* **2018,** 54, 7896-7899.
83. Chen, X.; Boulos, R. A.; Dobson, J. F.; Raston, C. L., Shear induced formation of carbon and boron nitride nano-scrolls. *Nanoscale* **2013,** *5*, 498-502.
84. Batmunkh, M.; Vimalanathan, K.; Wu, C.; Bati, A. S.; Yu, L.; Tawfik, S. A.; Ford, M. J.; Macdonald, T. J.; Raston, C. L.; Priya, S.; Gibson, C. T.; Shapter, J, G., Efficient Production of Phosphorene Nanosheets via Shear Stress Mediated Exfoliation for Low-Temperature Perovskite Solar Cells. *Small Methods,* **2019,** *3*, 1800521.
85. Jones, D. B.; Chen, X.; Sibley, A.; Quinton, J. S.; Shearer, C. J.; Gibson, C. T.; Raston, C. L., Plasma enhanced vortex fluidic device manipulation of graphene oxide. *Chem. Commun.,* **2016,** *52*, 10755-10758.
86. Jones, D. B.; Raston, C. L., Improving oxidation efficiency through plasma coupled thin film processing. *RSC Adv.,* **2017,** *7*, 47111-47115.
87. Vimalanathan, K.; Suarez-Martinez, I.; Peiris, C.; Antonio, J.; de Tomas, C.; Zou, Y.-C.; Zou, J.; Duan, X.; Lamb, R.; Harvey, D.; Alharbi, T. M.; Gibson, C. T.; Marks, N. A.; Darwish, D.; Raston, C. L., Vortex fluidic mediated transformation of graphite into highly conducting graphene scrolls. *Nanoscale Adv.,* **2019,** 1, 2495-2501.
88. Al-Antaki, A. H. M.; Luo, X.; Alharbi, T. M.; Harvey, D. P.; Pye, S.; Zou, J.; Lawrance, W.; Raston, C. L., Inverted vortex fluidic exfoliation and scrolling of hexagonal-boron nitride. *RSC Adv.* **2019,** *9*, 22074-22079.
89. Luo, X.; Al-Antaki, A. H.; Alharbi, T. M.; Hutchison, W. D.; Zou, Y.-c.; Zou, J.; Sheehan, A.; Zhang, W.; Raston, C. L., Laser-Ablated Vortex Fluidic-Mediated Synthesis of Superparamagnetic Magnetite Nanoparticles in Water Under Flow. *ACS Omega,* **2018,** *3*, 11172-11178.
90. Al-Antaki, A. H. M.; Luo, X.; Duan, X.; Lamb, R. N.; Hutchison, W. D.; Lawrance, W.; Raston, C. L., Continuous Flow Copper Laser Ablation Synthesis of Copper (I and II) Oxide Nanoparticles in Water. *ACS Omega,* **2019,** *4*, 13577-13584.
91. Al-antaki, A. H. M.; Luo, X.; Duan, A.; Lamb, R. N.; Eroglu, E.; Hutchison, W.; Zou, Y.-C.; Zou, J.; Raston, C. L., Continuous flow synthesis of phosphate binding h-BN@ magnetite hybrid material. *RSC Adv.* **2018,** *8*, 40829-40835.
92. Lu, H.; Eggers, P. K.; Gibson, C. T.; Duan, X.; Lamb, R. N.; Raston, C. L.; Chua, H. T., Facile synthesis of electrochemically active Pt nanoparticle decorated carbon nano onions. *New J. Chem.,* **2015,** *39*, 915-920.
93. Goh, Y. A.; Chen, X.; Yasin, F. M.; Eggers, P. K.; Boulos, R. A.; Wang, X.; Chua, H. T.; Raston, C. L., Shear flow assisted decoration of carbon nano-onions with platinum nanoparticles. *Chem. Commun.,* **2013,** *49*, 5171-5173.
94. Wahid, M. H.; Eroglu, E.; LaVars S. M.; Newton K.; Gibson, C. T.; Stroeher U. H.; Chen, X.; Boulos, R. A.; Raston, C. L.; Harmer, S.-L. , Microencapsulation of bacterial strains in graphene oxide nano-sheets using vortex fluidics. *RSC Adv.,* **2015,** *5*, 37424-37430.
95. Wahid, M. H.; Eroglu, E.; Chen, X.; Smith, S. M.; Raston, C. L., Functional multi-layer graphene–algae hybrid material formed using vortex fluidics. *Green Chem.,* **2013,** *15*, 650-655.

Chapter Two

Controlled Slicing of Single Walled Carbon Nanotubes Under Continuous Flow

Thaar M. D. Alharbi[1, 2], Kasturi Vimalanathan[1], Warren D. Lawrance[3], Colin L Raston[1]*

[1] Flinders Institute for NanoScale Science and Technology, College of Science and Engineering, Flinders University, Adelaide SA 5001, Australia email: colin.raston@flinders.edu.au
[2] Physics Department, Faculty of Science, Taibah University, Almadinah Almunawarrah, Saudi Arabia
[3] College of Science and Engineering, Flinders University, Adelaide SA 5001, Australia

This study was published in ***Carbon***, Year **2018**, 140, 428-43210. The first page of the publication and SI are attached.

Author contributions: TA performed all the VFD and most characterization experiments and data analysis, and wrote all the primary content. **KV** helped with revised the manuscript before submitting, and also addressing the reviewers' comments. **WL** helped on some VFD experiments. **CR** supervised and coordinated the project and helped on the research directions and plan, and the final revision of the manuscript. All of the co-authors assisted with the revision of the manuscript before and during the publication process.

2.1. Abstract

Single walled carbon nanotubes (SWCNTs) are sliced with control over their length distribution within a laser irradiated dynamic thin film in a vortex fluidic device (VFD) operating under continuous flow conditions. Length control depends on the laser pulse energy, the flow rate of the liquid entering the device, the speed of the rapidly rotating tube and its tilt angle, choice of solvent and concentration of the as received SWCNTs. The induced mechanoenergy in the thin film while being simultaneously irradiated with a Nd:YAG pulsed laser operating at 1064 nm wavelength results in the slicing, with laser pulse energies of 250, 400 and 600 mJ affording 700, 300 and 80 nm length distributions of SWCNTs respectively. The processing avoids the need for using any other reagents, is scalable under continuous flow conditions, and does not introduce defects into the side walls of the SWCNTs.

Keywords; Single walled carbon nanotubes, length distribution, vortex fluidic device, thin film microfluidics, scalability.

Graphical Abstract

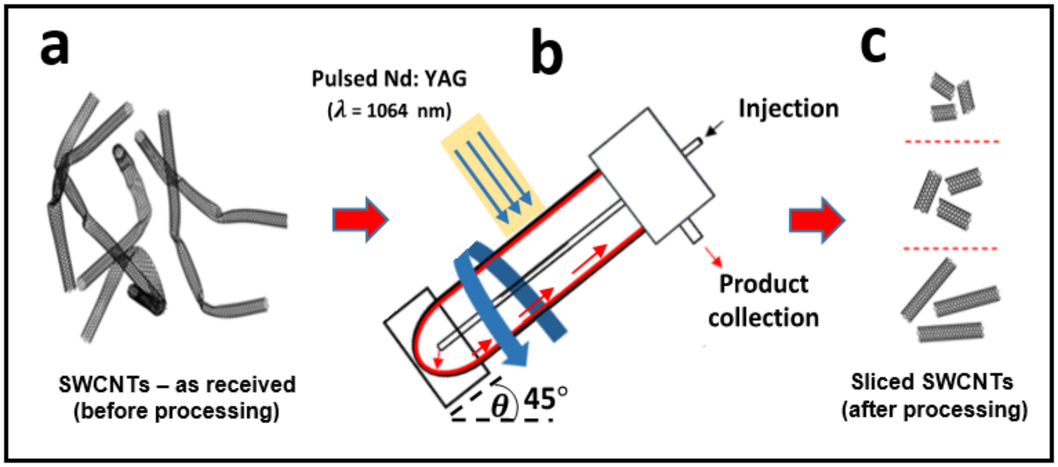

2.2. Introduction

Single-walled carbon nanotubes (SWCNTs) show remarkable physical, chemical, electrical, and mechanical properties with applications in a number of fields [1-3]. Many techniques have been used to produce CNTs, including chemical vapour deposition (CVD), arc-discharge and laser ablation [4-6]. As prepared SWCNTs typically have lengths greater than a few micrometers, and have a high degree of aggregation and bundling because of the high aspect ratio and favorable van der Waals interactions. In addition, they have various levels of side wall defects, leading them to not be atomically straight. These properties pose a number of challenges in developing many of the applications of SWCNTs. They are additional to the challenges in controlling the chirality of SWCNTs and in gaining access to high purity samples with all the SWCNTs having the same arrangement of carbon atoms, with them being all semi-conducting or conducting [7-8]. There have been advances in preparing pure long SWCNTs of the same chirality [9-11].

The availability of SWCNTs with a narrow length distribution and devoid of defects, other than at the ends of the tubes, would facilitate uptake of SWCNTs by industry for a number of applications where a specific length is required. This includes electronic devices, [2, 12] solar cell technology [13-14] and biomedical sciences[15]. Moreover, controlling the length of SWCNTS is important for facilitating the separation of different chirality SWCNTs, which then leads into other applications [7-8]. Several methods have been reported for shortening SWCNTs using different physical, electrical or chemical strategies [16-22]. Shortening SWCNTs usually requires high-energy sonication in toxic reagents, with long processing times, little control of the length, broad length distributions, and induced defects along the length of the tubes. In recent studies we developed the ability to slice SWCNTs, and indeed double walled and multi-walled CNTs, in a colloidal suspension of the material under high shear [23]. This involved the use of a vortex fluidic device (VFD), Figure 2. 1, as a thin film microfluidic platform, which can operate under the so-called confined or continuous flow modes [24-25]. The VFD is a versatile microfluidic platform with a number of applications in addition to slicing of CNTs, including protein folding [26], enhancing enzymatic reactions [27], protein immobilization [28], the fabrication of C_{60} tubules using water as an 'anti-solvent' [29], exfoliation of graphite and boron nitride [30], growth of palladium nano-particles on carbon nano-onions [31], the synthesis of carbon dots [32], decorating carbon nano-onion with Pt nanoparticles [33], transforming graphene oxide sheets into scrolls [34], probing the structure of self organized systems, and controlling chemical reactivity and selectivity [35]. The dynamic thin film in a VFD has Stewartson/Ekman layers, with the liquid accelerating up the tube and exiting at the top, with gravitational force affecting them [25].

The continuous flow mode of operation of the VFD has the attractive feature of addressing scalability of a process at the inception of the research. Here jet feeds deliver reagents into an inclined rapidly rotating 20 mm OD glass tube. We have reported optimized conditions for slicing SWCNTs, DWCNTs and MWCNTs down to lengths of 170 nm, 157 nm and 160 nm, respectively. [23] These involve the use of a mixture of water and N-methylpyrolidine (NMP) as the solvent. In the absence of the laser and using a water/toluene a solvent mixture, the SWCNTs role up into compact toroids comprised of a number of tubes, which establishes that under high shear the SWCNTs are bent [36]. This is important in understanding the mechanism of slicing using the pulsed laser, in that bending coupled with induced vibrational energy imparted by a pulsed laser leads to bond cleavage and slicing through the tubes, as supported by theoretical studies [23].

We hypothesized that the length of the sliced SWCNTs can be controlled by varying the energy of the pulsed laser and the shear stress determined by the rotational speed, and the process optimised by varying other operational parameters of the VFD. Indeed, in systematically exploring the parameter space of the device, we have established that the length can be controlled, achieving length distributions *ca*. 80, 300 and 700 nm, with a significant reduction in the level of defects along the tubes relative to the as received SWCNTs.

2.3. Experimental section

2.3.1. Chemicals and materials

SWCNTs were purchased from Carbon Solution with an as-received purity > 90%, and were used as received. SWCNTs with diameters of 1–3 nm, and lengths of 2–5 µm. N-methylpyrolidine (NMP) and *N,N*-Dimethylformamide (DMF) were purchased from Sigma-Aldrich and were used as received.

2.3.2. Sample preparation

SWCNTs were dispersed in mixture of NMP and water at a 1:1 ratio, at an overall concentration of 0.08 mg/mL. The solution was then ultrasonicated for 30 minutes to afford a black stable dispersion.

2.3.3. Instrumentation

Samples were irradiated in the VFD tube using the 1064 nm wavelength fundamental output of a Q-switched Nd:YAG laser (Spectra Physics GCR170) operating at a pulse repetition rate of 10 Hz. The laser pulse beam diameter is 8 mm and pulse duration is 5 ns. The laser was directed to the middle of the VFD tube. The sliced SWCNTs were characterized by atomic force microscopy (AFM) using a Nanoscope 8.10 in tapping mode, transmission electron microscopy (TEM) using a TECNAI 20 operating at 120 and 200 kV, and Raman spectroscopy using XploRA™ Horiba Scientific, recorded at an excitation wavelength of 532 nm (≤ 5mW) at room temperature.

2.4. Results and Discussion

Varying the power of the laser irradiating the SWCNTs dispersed in a 1:1 solution of NMP and water in the VFD was effective in controlling the length of the sliced SWCNTs. These results build on earlier studies focused on slicing SWCNTs, DWCNTs and MWCNTs in a VFD for a specific power setting of the laser without such control [23]. In the present study we have systematically studied the effect of varying the laser power, and other operating parameters of the VFD, in mapping out the parameter space of the device for controlling the length of the sliced SWCNTs. Initially, the rotational speed was varied from

4k to 9k rpm with the laser power set at 250 mJ. Thereafter the laser power was varied, with experiments primarily performed at 250 mJ, 400 mJ and 600 mJ, followed by varying the flow rate from 0.1 to 2 mL/min at concentrations of SWCNTs of 0.08, 0.016 and 0.2 mg/mL. In addition to using a 1:1 mixture of NMP and water (as established for the above feasibility studies) [23], DMF was also explored as an alternative solvent and gave similar results (Supplementary Information Figure S1).

A schematic of the process of slicing SWCNTs using the VFD is shown in Figure 2. 1 The choice of rotational speed, flow rate, tilt angle and concentration of the SWCNTs, as well as the laser power, are critical for controlling the length of the sliced material. The optimised parameters for controlling the length were found to be a rotational speed of 8.5k rpm, flow rate of 0.45 mL/min, tilt angle 45° and 0.08 mg/mL concentration, for a 1:1 mixture of NMP and water. Changing the laser power (260, 400 and 600 mJ) gave control over the lengths of the SWCNTs. There was no evidence for slicing SWCNTs in the absence of the pulsed laser using the aforementioned parameters. As an additional control experiment, 250 mJ laser irradiation of a solution without using the VFD showed uncontrolled fragmentation of the SWCNTs (Supplementary Information Figure S6). Thus the high heat and mass transfer in the presence of high shear in the VFD is important for heat dissipation into the liquid to ensure controlled slicing of the SWCNTs.

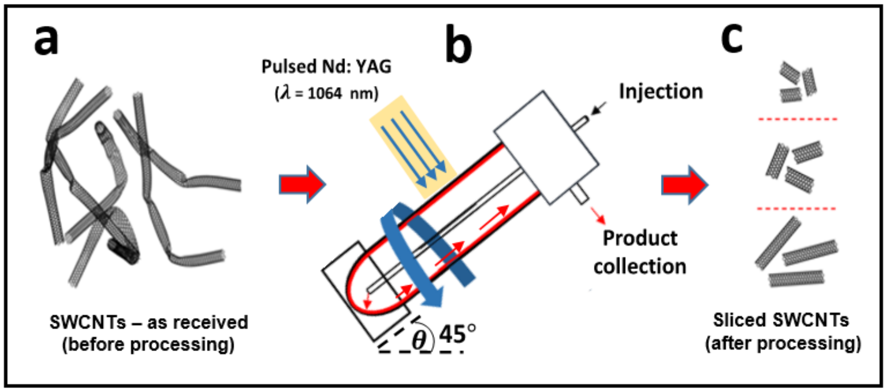

Figure 2. 1 Schematic illustration of the experimental procedure for controlling the length of SWCNTs. (a) SWCNTs before processing in the VFD which are intertwined with defects associated with being bent. (b)

Experimental set up for the vortex fluidic device (VFD) and laser Nd:YAG processing operating at 1064 nm. (c) Sliced SWCNTs of different lengths, depending on the operating parameters of the VFD, laser power, concentration and choice of solvent.

AFM images of the as received SWCNTs, Figure 2. 2, show that they are bundled and intertwined, and making an estimation of their length is challenging. Nevertheless, they appear to be longer than 1 µm, in accordance with the length of 2-5 µm specified by the supplier.

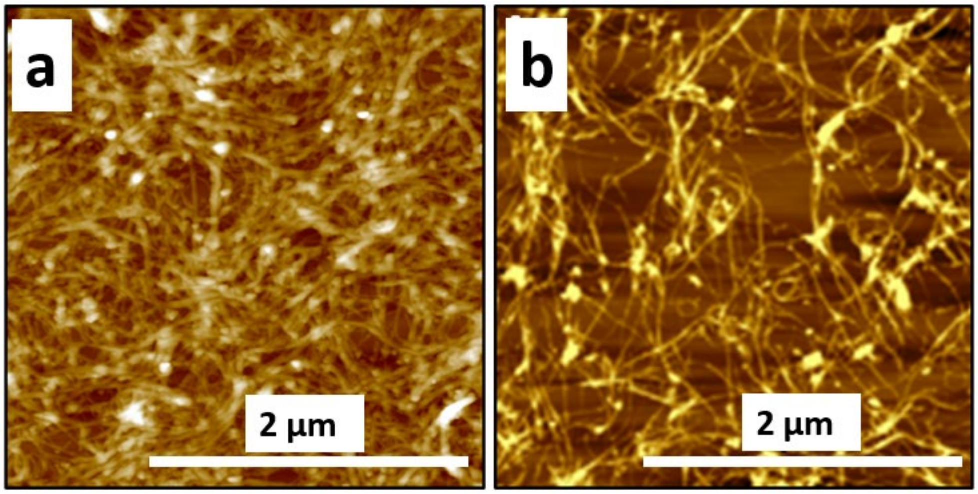

Figure 2. 2 AFM images of as received SWCNTs.

AFM and TEM were used in the current work to study the changes in the length of SWCNTs. Length distributions for sliced SWCNTs were determined by counting more than 350 individual tubes. Figure 2. 3 shows AFM images for sliced SWCNTs with different lengths, along with the corresponding length distributions. Figure 2. 3a shows images for low laser power, 250 mJ, with the length distribution centred around 700 nm and somewhat broad, Figure 2. 3d. Increasing the laser power to 400 mJ resulted in a reduction in the length of the SWCNTs, with the length centred at 300 nm, and a narrowing of the distribution (Figure 2. 3b, e). Shorter SWCNTs were obtained for higher laser power, 600 mJ, with a narrow size distribution centred at 80 nm, Figure 2. 3c,f This demonstrates that we are able to effectively control the length distributions of SWCNTs by varying the laser power, with all the other parameters set as discussed above.

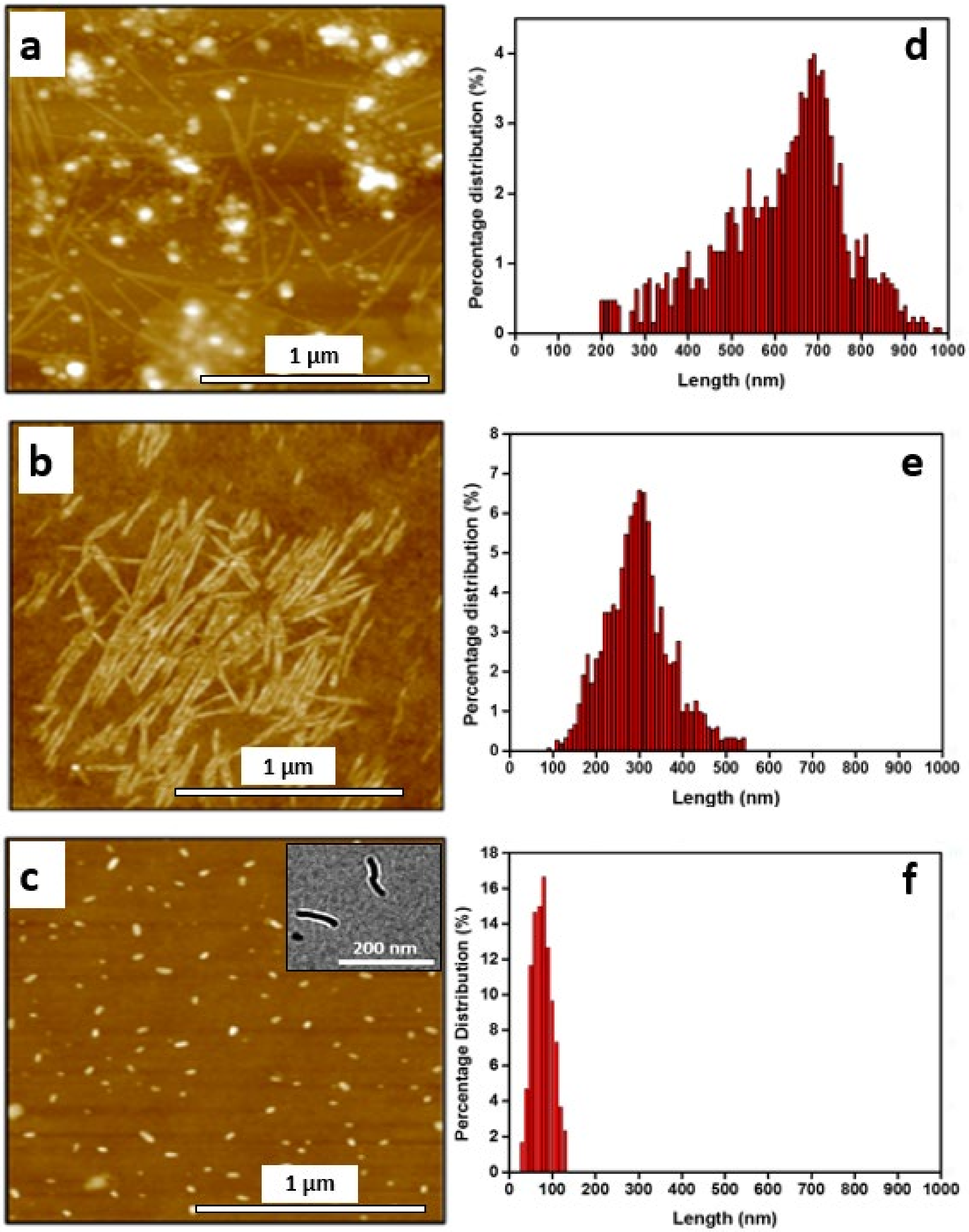

Figure 2. 3 AFM images of sliced SWCNTs with the associated length distribution plots, formed in the VFD at 8.5k rpm rotational speed, under continuous flow mode, with the concentration of the as received SWCNTs at 0.08

mg/mL (NMP/water at a 1:1 ratio), tilt angle 45°, for a flow rate of 0.45 mL/min, while irradiated with a pulsed laser operating at 1064 nm, and (a) 250 mJ, (b) 400 mJ and (c) 600 mJ; inset TEM image for the short SWCNTs. Note: The length distribution for each sample was obtained from measuring the length of > 1000 nanotubes.

The broadening of the length distribution as the targeted length of the sliced SWCNT increases is consistent with the mechanism of slicing whereby bending of the SWCNT and higher vibrational energy induced by laser irradiation results in bond cleavage at such a strained part of the SWCNT [16]. As the targeted length increases there will always be sliced SWCNTs that are too short for further slicing, and the tailing of the length more towards shorter SWCNTs, which is accentuated for the 600 mJ laser irradiation, is expected; there is no 'handle' on such SWCNTs to apply shear stress for further slicing. SWCNTs in solution longer than ca 700 nm in targeting this length can be further sliced, but there will be a situation where the resulting length after slicing off ca 700 nm is < 700 nm, and this is consistent with greater tailing of the length distribution towards shorter lengths, in contrast to the tailing towards longer lengths.

An important characteristic of the sliced SWCNTs is that they are relatively straight, Figure 2. 3, especially for the longer SWCNTs, compared to the as-received materials, Figure 2. 2, which are bundled and intertwined. This suggests that the defects present in the processed SWCNTs are minimal. Raman spectroscopy, which is widely used for evaluating the defects in carbon materials in general by measuring the ratio between the intensity of the D and G bands [37], was used to confirm this. Raman spectra were recorded using a 532 nm excitation laser, for the as received SWCNTs and the different length distributions of sliced SWCNTs (Figure 2. 4) The peaks observed were G and D bands, at 1597 and 1354 cm^{-1}, respectively. The G band exhibits two main features, G^+ and G^-, which arise from the curvature of the nanotube wall and are used to determine the diameter of the nanotubes, distinguish between semiconducting and metallic nanotubes and assign chirality of the nanotubes (*n,m*) [38].The average ratio intensity of the D and G bands for the as received SWCNTs was 0.54. After processing (lateral slicing) to *ca*. 80, 300 and 700 nm, the intensity of the D/G ratios were 0.25, 0.32 and 0.16, respectively. This reduction in the D/G ratio on processing in the VFD is consistent with a decrease in defects present on the walls of the sliced material. Pulsed laser irradiation of CNT is effective in decreasing defects and thus increasing their purity, with the surface temperature dramatically increasing with laser power [39-40]. Thus a reduction in side wall defects in the sliced SWCNTs in the present study is not surprising with the high energy input in the near infrared from the pulsed laser during the processing. Clearly defects will be present at the ends of the sliced SWCNTs, but the essentially straight SWCNTs have minimal side wall defects. Other strategies for reducing the length of SWCNTs, including the use of Piranha solutions [21], impact on the walls of the SWCNT.

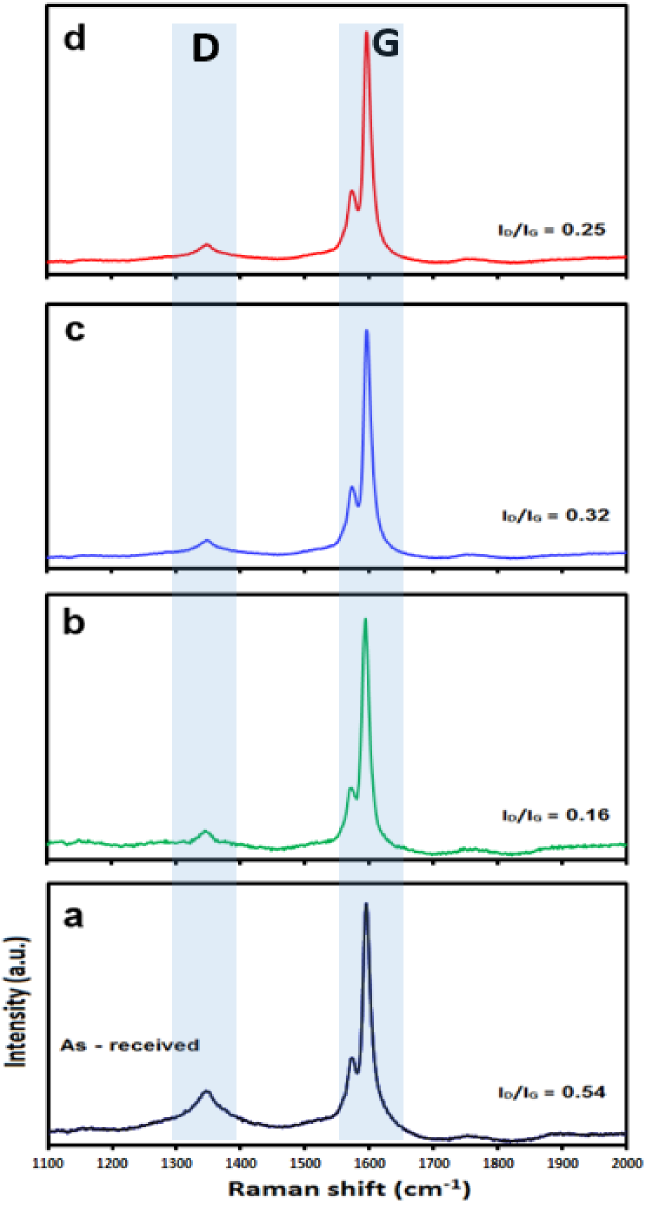

Figure 2. 4 Raman spectra for (a) as received SWCNTs and sliced SWCNTs with length distributions at 700 nm (b), 300 nm, (c) and 80 nm, (d).

2.5. Conclusions

We have established a process for the 'top down' fabrication of short length SWCNTs with controllable different length distributions, importantly in the absence of surfactants and harsh chemicals. The lengths can be controlled by varying the power of a pulsed laser (operating at 1064 nm wavelength) irradiating suspensions of long inter-twinned SWCNTs in a mixture of NMP and water (or DMF), as a dynamic thin film in a vortex fluidic device. The process is under continuous flow such that scalability can be readily addressed by using a number of VFD microfluidic platforms in parallel. We have successfully prepared 50 mg of sliced SWCNTs in one run over 21 hours for all lengths. In addition, the laterally sliced SWCNTs have a significantly reduced level of side wall defects, as established using Raman spectroscopy, and borne out in the AFM images, which show essentially straight sliced SWCNTs. The ability to control the length and reduce defects is important in developing the many applications of SWCNTs where length is important. For example, short lengths are required for use in drug delivery (the optimal length is *ca*. 100 nm [41-43]) while longer SWCNTs with reduced defects are required for electronic devices [44-45]. Clearly, the longer the targeted length of SWCNTs the greater the length distribution of the sliced material, tailing more towards shorter lengths as expected mechanistically. We have varied the operating parameters of the VFD to establish the fabrication of three different length distributions of SWCNTs. Other lengths can now be targeted, especially within the limits studied (80 – 700 nm), depending on the applications of the SWCNTs.

2.6. Acknowledgements

T. M. D. A would like to thank Taibah University (Ministry of Education, Saudi Arabia) for funding his scholarship. The authors also thank Australian Research Council, The Government of South Australia, and AMMRF for support of this work.

Author contributions

T.M.D.A, K.V., W.D.L. and C.L.R. designed the experiments and wrote the paper, T.M.D.A. performed the slicing experiments and carried out AFM, TEM, Raman and analysed the data.

2.7. References

1. Liu, L.; Yang, C.; Zhao, K.; Li, J.; Wu, H.-C., Ultrashort single-walled carbon nanotubes in a lipid bilayer as a new nanopore sensor. *Nature Commun.,* **2013,** *4*, 2989.
2. Javey, A.; Guo, J.; Paulsson, M.; Wang, Q.; Mann, D.; Lundstrom, M.; Dai, H., High-field quasiballistic transport in short carbon nanotubes. *Phys. Rev. Lett.,* **2004,** *92*, 106804.
3. Di, J.; Zhang, X.; Yong, Z.; Zhang, Y.; Li, D.; Li, R.; Li, Q., Carbon-Nanotube Fibers for Wearable Devices and Smart Textiles. *Adv. Mater.,* **2016,** *28* (47), 10529-10538.
4. Ebbesen, T.; Ajayan, P., Large-scale synthesis of carbon nanotubes. *Nature,* **1992,** *358*, 220-222.
5. Nikolaev, P. Catalytic growth of single-walled nanotubes by laser vaporization. Masters Thesis Rice University, 1996.
6. Endo, M.; Takeuchi, K.; Igarashi, S.; Kobori, K.; Shiraishi, M.; Kroto, H. W., *J. Phys. Chem. Solids,* **1993,** *54*, 1841-1848.
7. Liu, J.; Wang, C.; Tu, X.; Liu, B.; Chen, L.; Zheng, M.; Zhou, C., Chirality-controlled synthesis of single-wall carbon nanotubes using vapour-phase epitaxy. *Nature Commun.,* **2012,** *3*, 1199.
8. Casey, J. P.; Bachilo, S. M.; Moran, C. H.; Weisman, R. B., Chirality-resolved length analysis of single-walled carbon nanotube samples through shear-aligned photoluminescence anisotropy. *ACS Nano,* **2008,** *2*, 1738-1746
9. He, M.; Magnin, Y.; Amara, H.; Jiang, H.; Cui, H.; Fossard, F.; Castan, A.; Kauppinen, E.; Loiseau, A.; Bichara, C., Linking growth mode to lengths of single-walled carbon nanotubes. *Carbon,* **2017,** *113*, 231-236.
10. Hedman, D.; Larsson, J. A., Length dependent stability of single-walled carbon nanotubes and how it affects their growth. *Carbon,* **2017,** *116*, 443-447.
11. Liu, B.; Wu, F.; Gui, H.; Zheng, M.; Zhou, C., Chirality-controlled synthesis and applications of single-wall carbon nanotubes. *ACS Nano,* **2017,** *11*, 31-53.
12. Treacy, M. J.; Ebbesen, T. W.; Gibson, J. M., Exceptionally high Young's modulus observed for individual carbon nanotubes. *Nature,* **1996,** *381*, 678
13. Kalita, G.; Adhikari, S.; Aryal, H. R.; Umeno, M.; Afre, R.; Soga, T.; Sharon, M., Cutting carbon nanotubes for solar cell application. *Appl. Phys. Lett.,* **2008,** *92*, 123508.
14. Dang, X.; Yi, H.; Ham, M.-H.; Qi, J.; Yun, D. S.; Ladewski, R.; Strano, M. S.; Hammond, P. T.; Belcher, A. M., Virus-templated self-assembled single-walled carbon nanotubes for highly efficient electron collection in photovoltaic devices. *Nature Nanotech.,* **2011,** *6*, 377-384
15. Liu, L.; Yang, C.; Zhao, K.; Li, J.; Wu, H.-C., Ultrashort single-walled carbon nanotubes in a lipid bilayer as a new nanopore sensor. *Nature Commun.,* **2013,** *4,* 2989.
16. Deng, J.; Wang, C.; Guan, G.; Wu, H.; Sun, H.; Qiu, L.; Chen, P.; Pan, Z.; Sun, H.; Zhang, B., The Deformations of Carbon Nanotubes under Cutting. *ACS Nano,* **2017,** *11*, 8464-8470.
17. Li, L.; Yang, Z.; Gao, H.; Zhang, H.; Ren, J.; Sun, X.; Chen, T.; Kia, H. G.; Peng, H., Vertically aligned and penetrated carbon nanotube/polymer composite film and promising electronic applications. *Adv. Mater.,* **2011,** *23*, 3730-3735.
18. Rauwald, U.; Shaver, J.; Klosterman, D. A.; Chen, Z.; Silvera-Batista, C.; Schmidt, H. K.; Hauge, R. H.; Smalley, R. E.; Ziegler, K. J., Electron-induced cutting of single-walled carbon nanotubes. *Carbon,* **2009,** *47*, 178-185.
19. Weydemeyer, E. J.; Sawdon, A. J.; Peng, C.-A., Controlled cutting and hydroxyl functionalization of carbon nanotubes through autoclaving and sonication in hydrogen peroxide. *Chem. Commun.,* **2015,** *51*, 5939-5942.
20. Guan, G.; Deng, J.; Ren, J.; Pan, Z.; Zhuang, W.; He, S.; Wang, B.; Che, R.; Peng, H., Tailorable coaxial carbon nanocables with high storage capabilities. *J. Mater. Chem. A,* **2017,** *5*, 22125-22130.

21. Ren, F.; Kanaan, S. A.; Khalkhal, F.; Loebick, C. Z.; Haller, G. L.; Pfefferle, L. D., Controlled cutting of single-walled carbon nanotubes and low temperature annealing. *Carbon,* **2013,** *63*, 61-70.
22. Cabana, L.; Ke, X.; Kepić, D.; Oro-Solé, J.; Tobías-Rossell, E.; Van Tendeloo, G.; Tobias, G., The role of steam treatment on the structure, purity and length distribution of multi-walled carbon nanotubes. *Carbon,* **2015,** *93*, 1059-1067.
23. Vimalanathan, K.; Gascooke, J. R.; Suarez-Martinez, I.; Marks, N. A.; Kumari, H.; Garvey, C. J.; Atwood, J. L.; Lawrance, W. D.; Raston, C. L., Fluid dynamic lateral slicing of high tensile strength carbon nanotubes. *Sci. Rep.,* **2016,** *6*, 22865.
24. Yasmin, L.; Chen, X.; Stubbs, K. A.; Raston, C. L., Optimising a vortex fluidic device for controlling chemical reactivity and selectivity. *Sci. Rep.,* **2013,** *3*, 2282.
25. Britton, J.; Stubbs, K. A.; Weiss, G. A.; Raston, C. L., Vortex Fluidic Chemical Transformations. *Chem. - Eur. J.,* **2017**, 23, 13270–13278.
26. Yuan, T. Z.; Ormonde, C. F. G.; Kudlacek, S. T.; Kunche, S.; Smith, J. N.; Brown, W. A.; Pugliese, K. M.; Olsen, T. J.; Iftikhar, M.; Raston, C. L., Shear-Stress-Mediated Refolding of Proteins from Aggregates and Inclusion Bodies. *ChemBioChem,* **2015,** *16*, 393-396
27. Britton, J.; Meneghini, L. M.; Raston, C. L.; Weiss, G. A., Accelerating Enzymatic Catalysis Using Vortex Fluidics. *Angew. Chem.,* **2016,** *128*, 11559-11563.
28. Britton, J.; Raston, C. L.; Weiss, G. A., Rapid protein immobilization for thin film continuous flow biocatalysis. *Chem. Commun.,* **2016,** *52*, 10159-10162.
29. Vimalanathan, K.; Shrestha, R. G.; Zhang, Z.; Zou, J.; Nakayama, T.; Raston, C. L., Surfactant-free Fabrication of Fullerene C60 Nanotubules Under Shear. *Angew. Chem. Int. Ed.,* **2017**, 56, 8398-8401.
30. Chen, X.; Dobson, J. F.; Raston, C. L., Vortex fluidic exfoliation of graphite and boron nitride. *Chem.Commun.,* **2012,** *48*, 3703-3705.
31. Yasin, F. M.; Boulos, R. A.; Hong, B. Y.; Cornejo, A.; Iyer, K. S.; Gao, L.; Chua, H. T.; Raston, C. L., Microfluidic size selective growth of palladium nano-particles on carbon nano-onions. *Chem. Commun.,* **2012,** *48*, 10102-10104.
32. Luo, X.; Al-Antaki, A. H. M.; Vimalanathan, K.; Moffatt, J.; Zheng, K.; Zou, Y.-C.; Zou, J.; Duan, X.; Lamb, R.; Wang, S., Laser irradiated vortex fluidic mediated synthesis of luminescent carbon nanodots under continuous flow. *React. Chem. Eng.,* **2018**, 3, 164-170.
33. Goh, Y. A.; Chen, X.; Yasin, F. M.; Eggers, P. K.; Boulos, R. A.; Wang, X.; Chua, H. T.; Raston, C. L., Shear flow assisted decoration of carbon nano-onions with platinum nanoparticles. *Chem. Commun.,* **2013,** *49* , 5171-5173.
34. Alharbi, T. M.; Harvey, D.; Alsulami, I. K.; Dehbari, N.; Duan, X.; Lamb, R. N.; Lawrance, W. D.; Raston, C. L., Shear stress mediated scrolling of graphene oxide. *Carbon,* **2018**, 137, 419-424.
35. Yasmin, L.; Chen, X.; Stubbs, K. A.; Raston, C. L., Optimising a vortex fluidic device for controlling chemical reactivity and selectivity. *Sci. Rep.,* **2013,** *3*, 2282.
36. Vimalanathan, K.; Chen, X.; Raston, C. L., Shear induced fabrication of intertwined single walled carbon nanotube rings. *Chem. Commun.,* **2014,** *50*, 11295-11298.
37. Dresselhaus, M. S.; Dresselhaus, G.; Saito, R.; Jorio, A., Raman spectroscopy of carbon nanotubes. *Phys. Rep.,* **2005,** *409*, 47-99.
38. Telg, H.; Duque, J. G.; Staiger, M.; Tu, X.; Hennrich, F.; Kappes, M. M.; Zheng, M.; Maultzsch, J.; Thomsen, C.; Doorn, S. K., Chiral index dependence of the G+ and G–Raman modes in semiconducting carbon nanotubes. *ACS Nano,* **2011,** *6*, 904-911.
39. Souza, N.; Zeiger, M.; Presser, V.; Mücklich, F., In situ tracking of defect healing and purification of single-wall carbon nanotubes with laser radiation by time-resolved Raman spectroscopy. *RSC Adv.,* **2015,** *5*, 62149-62159.

40. Nakamiya, T.; Mitsugi, F.; Semba, K.; Kozai, R.; Ikegami, T.; Iwasaki, Y.; Sonoda, Y.; Tsuda, R., Pulsed Nd: YAG laser heating and treatment on multi-walled carbon nanotubes film. *Thin Solid Films* **2010,** *518*, 6604-6608.
41. Sahoo, A. K.; Kanchi, S.; Mandal, T.; Dasgupta, C.; Maiti, P. K., Translocation of Bioactive Molecules through Carbon Nanotubes Embedded in Lipid Membrane. *ACS Appl. Mater. Interfaces,* **2018**, *10*, 6168-6179.
42. Boyer, P. D.; Ganesh, S.; Qin, Z.; Holt, B. D.; Buehler, M. J.; Islam, M. F.; Dahl, K. N., Delivering single-walled carbon nanotubes to the nucleus using engineered nuclear protein domains. *ACS Appl. Mater. Interfaces,* **2016,** *8*, 3524-3534.
43. Farrera, C.; Torres Andón, F.; Feliu, N., Carbon Nanotubes as Optical Sensors in Biomedicine. *ACS Nano,* **2017,** *11*, 10637-10643.
44. Hennrich, F.; Li, W.; Fischer, R.; Lebedkin, S.; Krupke, R.; Kappes, M. M., Length-sorted, large-diameter, polyfluorene-wrapped semiconducting single-walled carbon nanotubes for high-density, short-channel transistors. *ACS Nano,* **2016,** *10*, 1888-1895.
45. Cao, Q.; Han, S.-j., Single-walled carbon nanotubes for high-performance electronics. *Nanoscale,* **2013,** *5* (19), 8852-8863.

Carbon 140 (2018) 428–432

Contents lists available at ScienceDirect

Carbon

journal homepage: www.elsevier.com/locate/carbon

Controlled slicing of single walled carbon nanotubes under continuous flow

Thaar M.D. Alharbi [a, b], Kasturi Vimalanathan [a], Warren D. Lawrance [c], Colin L. Raston [a, *]

[a] *Institute for NanoScale Science and Technology, College of Science and Engineering, Flinders University, Adelaide, SA, 5001, Australia*
[b] *Physics Department, Faculty of Science, Taibah University, Almadinah Almunawarrah, Saudi Arabia*
[c] *College of Science and Engineering, Flinders University, Adelaide, SA, 5001, Australia*

ARTICLE INFO

Article history:
Received 1 May 2018
Received in revised form
1 August 2018
Accepted 30 August 2018
Available online 31 August 2018

Keywords:
Single walled carbon nanotubes
Length distribution
Vortex fluidic device
Thin film microfluidics
Scalability

ABSTRACT

Single walled carbon nanotubes (SWCNTs) are sliced with control over their length distribution within a laser irradiated dynamic thin film in a vortex fluidic device (VFD) operating under continuous flow conditions. Length control depends on the laser pulse energy, the flow rate of the liquid entering the device, the speed of the rapidly rotating tube and its tilt angle, choice of solvent and concentration of the as received SWCNTs. The induced mechanoenergy in the thin film while being simultaneously irradiated with a Nd:YAG pulsed laser operating at 1064 nm wavelength results in the slicing, with laser pulse energies of 250, 400 and 600 mJ affording 700, 300 and 80 nm length distributions of SWCNTs respectively. The processing avoids the need for using any other reagents, is scalable under continuous flow conditions, and does not introduce defects into the side walls of the SWCNTs.

1. Introduction

Single-walled carbon nanotubes (SWCNTs) show remarkable physical, chemical, electrical, and mechanical properties with applications in a number of fields [1–3]. Many techniques have been used to produce CNTs, including chemical vapour deposition (CVD), arc-discharge and laser ablation [4–6]. As prepared SWCNTs typically have lengths greater than a few micrometers, and have a high degree of aggregation and bundling because of the high aspect ratio and favorable van der Waals interactions. In addition, they have various levels of side wall defects, leading them to not be atomically straight. These properties pose a number of challenges in developing many of the applications of SWCNTs. They are additional to the challenges in controlling the chirality of SWCNTs and in gaining access to high purity samples with all the SWCNTs having the same arrangement of carbon atoms, with them being all semi-conducting or conducting [7,8]. There have been advances in preparing pure long SWCNTs of the same chirality [9–11].

The availability of SWCNTs with a narrow length distribution and devoid of defects, other than at the ends of the tubes, would facilitate uptake of SWCNTs by industry for a number of applications where a specific length is required. This includes electronic devices [2,12], solar cell technology [13,14] and biomedical sciences [15]. Moreover, controlling the length of SWCNTS is important for facilitating the separation of different chirality SWCNTs, which then leads into other applications [7,8]. Several methods have been reported for shortening SWCNTs using different physical, electrical or chemical strategies [16–22]. Shortening SWCNTs usually requires high-energy sonication in toxic reagents, with long processing times, little control of the length, broad length distributions, and induced defects along the length of the tubes. In recent studies we developed the ability to slice SWCNTs, and indeed double walled and multi-walled CNTs, in a colloidal suspension of the material under high shear [23]. This involved the use of a vortex fluidic device (VFD), Fig. 1, as a thin film microfluidic platform, which can operate under the so-called confined or continuous flow modes [24,25]. The VFD is a versatile microfluidic platform with a number of applications in addition to slicing of CNTs, including protein folding [26], enhancing enzymatic reactions [27], protein immobilization [28], the fabrication of C_{60} tubules using water as an 'anti-solvent' [29], exfoliation of graphite and boron nitride [30], growth of palladium nano-particles on carbon nano-onions [31], the synthesis of carbon dots [32], decorating carbon nano-onion with Pt nanoparticles [33], transforming graphene oxide sheets into scrolls [34], probing the structure of self

---

* Corresponding author.
E-mail address: colin.raston@flinders.edu.au (C.L. Raston).

https://doi.org/10.1016/j.carbon.2018.08.066

Supplementary Information for

Controlled slicing of single walled carbon nanotubes under continuous flow

Thaar M. D. Alharbi[1, 2], Kasturi Vimalanathan[1], Warren D. Lawrance [3], Colin L Raston[1*]

[1] Flinders Centre for NanoScale Science & Technology, School of Chemical & Physical Sciences, Flinders University, Adelaide SA 5001, Australia email: colin.raston@flinders.edu.au

[2] Physics Department, Faculty of Science, Taibah University, Almadinah Almunawarrah, Saudi Arabia

[3]School of Chemical & Physical Sciences, Flinders University, Adelaide SA 5001, Australia

---

[*]Corresponding author:

Tel: +61 8 82017958 E-mail address: colin.raston@flinders.edu.au (Colin Raston)

Chapter Three

Vertically Aligned Laser Sliced MWCNTs

Thaar M. D. Alharbi, [†, §] Kasturi Vimalanathan, [†] Ibrahim K. Alsulami [†] and Colin L. Raston [†, *]

[†] Flinders Institute for Nanoscale Science and Technology, College of Science and Engineering, Flinders University, Adelaide SA 5001, Australia
[§] Physics Department, Faculty of Science, Taibah University, Almadinah Almunawarrah 42353, Saudi Arabia

This study was published in ***RSC Nanoscale***, Year **2019**, 11, 21394-21403. The first page of the publication and SI are attached.

Author contributions: **TA** performed all the VFD and most characterization experiments and data analysis, and wrote all the primary content. **KV** helped with the revised the manuscript before submitting and also in addressing the reviewers' comments. **IA** helped on some VFD experiments. **CR** supervised and coordinated the project and helped on the research directions and plan, and the final revision of the manuscript. All of the co-authors assisted with the revision of the manuscript before and during the publication process.

3.1. Abstract

Applications of multi-walled carbon nanotubes (MWCNTs) can benefit with the availability of specific lengths of the material while keeping the outer walls pristine, for example, for applications requiring vertically alignment tubes. To this end, a simple and effective continuous flow ‘top down’ process to control the length of sliced MWCNTs has been developed using a vortex fluidic device (VFD) coupled with a 1064 nm pulse laser, with the process in the absence of chemicals and any auxiliary substances. Three different length distributions of the sliced MWCNTs, centered at 75±2.1 nm, 300±1.8 nm and 550±1.4 nm, have been generated with the length depending on the VFD operating parameters and laser energy, with the processing resulting in a decrease in side wall defects of the material. We also show the ability to vertically self assemble short MWCNTs on a silicon substrate with control of the surface density coverage using a simple dipping and rinsing method.

Keywords; Multi-walled carbon nanotubes, Vortex fluidic device, Length distribution, Scalability, Thin film microfluidics, Vertical alignment.

Graphical Abstract

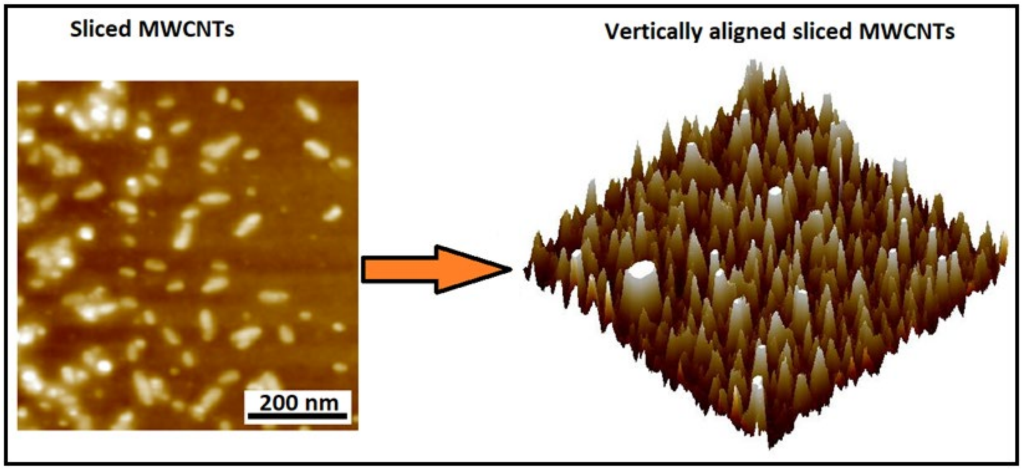

3.2. Introduction

Carbon nanotubes (CNTs) have attracted interest in a variety of fields because of their unique electronic, chemical, and mechanical properties, in particular for nanodevice based applications [1-3]. However, for most of these applications, it is pivotal to have selective and ordered control over the surface density and orientation of the nanotubes, either vertically or horizontally to gain optimum efficiencies [4-6]. In particular, vertically aligned carbon nanotubes (VACNTs) have gained much interest and has shown great potential in a number of applications, for example in photoelectric conversion [7, 8], energy storage [8, 9], nanoprobes in scanning probe microscopy [10, 11], electrochemical and bioelectrochemical sensing [4, 12, 13], and membrane separations [14, 15].

The two main methods that are typically used to fabricate VACNTs are direct growth on substrates [16, 17] and the immobilization of shortened CNTs on substrates via chemical assembly [18, 19]. Yu et al. [20] first reported the fabrication of VACNTs on silicon surfaces using a chemical attachment method. This involved reacting a hydroxylated surface with carboxylic acid functionalized SWCNTs, forming an ester linkage. Other studies reported by Ellis and colleagues [21, 22] featured an assembly method, involving reaction of chemically modified nanotubes bearing carboxyl (–COOH) and hydroxyl (–OH) groups, with covalent surface attachment through ester or amide linkages. Chemical vapour deposition (CVD) features in the direct growth of vertically aligned carbon nanotube arrays [16, 17], also VACNTs were prepared using nanowire arrays as template [23]. However, both of these methods are complex and/or require the need for toxic chemicals and other auxiliary substances, with limited economic and environmental sustainability metrics. While the vertical assembly of CNTs on surfaces has been extensively studied, a key challenge is gaining access to short length CNT below ≤ 200 nm in order to gain control of the alignment while maintaining a high density of coverage [4]. A diverse number of methods have been developed for controlling the length of CNTs, as top down fabrication processes, using mechanical, physical, electrical or chemical strategies. However again these methods are tedious, damaging to the material post processing and require the use of toxic chemicals [24-33].

We have reported in a previous study a more benign approach towards slicing single, double and multiwalled CNTs using the vortex fluidic device (VFD) coupled with a pulsed Nd:YAG laser [34]. The VFD, Figure 3. 1, is a microfluidic platform with a diversity of applications beyond slicing of CNTs, including protein folding [35], enhancing enzymatic reactions [36], protein immobilization [37], anti-solvent induced fabricating of C_{60} tubules in water [38], fabricating fullerene C_{60} cones [39], exfoliating boron nitride and graphite [40], fabricating coiled Single-Walled CNTs under Flow [41], coating carbon nano-onions with palladium nano-particles [42], preparing carbon dots [43], reduction and scrolling graphene oxide sheets [44, 45], probing the structural integrity of self-organized systems, and controlling chemical reactivity and selectivity [46]. Complex fluid dynamics prevail in the liquid thin film in the VFD, Figure 3. 1a, in addition to the Stewartson/Ekman layers and pressure induced Faraday waves, with the liquid forced up the tube against gravity in the rapidly rotating tube tilted at 45°, exiting at the top [47].

We recently reported the ability to control the lengths of SWCNTs in the VFD using a similar method while varying a number of operational conditions [48]. Slicing MWCNTs is more challenging given the large number of C-C bonds that needs to be cleaved in completely slicing through the tubes. Herein, we have further developed a method to control the length of MWCNTs using the VFD o while irradiated with a pulsed laser (Nd:YAG) operating at 1064 nm, using the more convenient solvent DMF (N,N-dimethylformamide) which is thermally stable . The sliced MWCNTs afforded had length distributions centered around 75±2.1 nm, 300±1.8 nm and 550±1.4 nm for the laser energy of 600 mJ, 250 mJ and 50 mJ, respectively, Figure 3. 2 We then show the ability to vertically align the short nanotubes using a simple dipping and rinsing method, with control over the density of coverage on a silicon substrate. All the processing (slicing and self assembly) circumvents the need for using other reagents, with the slicing under continuous flow conditions and is scalable.

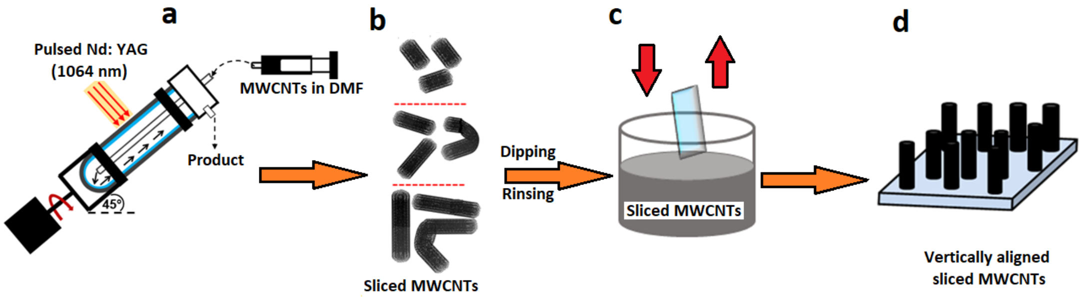

Figure 3. 1 Experimental set up for slicing MWCNTs. (a) The vortex fluidic device (VFD) simultaneously irradiated with a pulsed Nd: YAG laser operating at 1064 nm. A syringe pump is used to inject a DMF suspension of MWCNTs into the rapidly rotating glass tube in the VFD. (b) Sliced MWCNTs with different length distributions. (c) Process for self-assembly of the shortest MWCNTs on a silicon wafer, as depicted (d).

3.3. Experimental section

3.3.1. Materials and chemicals

MWCNTs, prepared using the chemical vapour deposition prepared method, were purchased from Sigma-Aldrich, purity of ≥ 98%, and were used as received. MWCNTs with outside diameter (O.D.) × inside diameter (I.D.) × length equivalent dimensions 10 nm ± 1 nm × 4.5 nm ± 0.5 nm, and 3 to 6 µm respectively. N,N-dimethylformamide (DMF) was purchased from Sigma-Aldrich and used as received.

3.3.2. VFD processing and sample preparation

MWCNTs were dispersed in DMF (0.08 mg/mL) and the mixture ultrasonicated for 15 minutes prior to VFD/laser processing. The experimental setup was adapted from previously published work for VFD mediated slicing of CNTs [34, 48]. Continuous flow mode of operation of the device, flow rate of 0.45 mL min^{-1}. MWCNTS dispersed in DMF solution was delivered through a stainless steel jet feed to the bottom of the rapidly rotating borosilicate glass tube (O.D. 20 mm, I.D. 17.5 mm). The tilt angle (θ) of the device was 45°. For slicing of the MWCNTs, samples were irradiated in the VFD tube at a wavelength of 1064 nm using a Q-switched Nd:YAG laser (Spectra Physics GCR170) operating at a pulse repetition rate of 10 Hz[46]. The diameter of the laser pulse beam was 8 mm and the pulse duration was 5 ns. The laser was directed to the center of the glass tube with respect to both its diameter and length.

3.3.3. Vertical alignment of sliced MWCNTs

p-Type Si (100) wafer substrates, cross section 1 × 1 cm^2 and 0.525 mm thick, with a low resistivity, <0.005 Ω.cm, which were purchased from Virginia Semiconductor, Inc. USA. Each wafer was first ultrasonicated in methanol for 30 min then acetone also for 30 min, to remove organic contaminants and then dried under nitrogen gas prior to use. Each silicon wafer surface was dipped into the solution of sliced MWCNTs in DMF for various periods of time. The samples were transferred onto a glass petri dish and then dried overnight at 40ºC prior to AFM and HRTEM characterization.

3.3.4. Characterisation

Sliced MWCNTs and as received MWCNTs were drop cast on silicon wafers for Raman spectroscopy measurements and atomic force microscopy (AFM) to measure the length distributions of the material. AFM images were recored using a Nanoscope 8.10 in tapping mode and Raman spectra were recorded at room temperature using a XploRA™ Horiba Scientific spectrometer, excitation wavelength 532 nm (≤ 5mW) at room temperature. A Bruker Advanced D8 diffractometer (capillary stage) was used for collecting X-ray powder diffraction (XRD) data, Co Kα radiation (λ= 1.7889 Å, 35 kW/28 mA, 2θ = 10 – 90°). Thermogravimetric analysis (TGA) was recorded on a Perkin Elmer STA8000 with a heating rate of 10 °C /min under a flow of air. Field-emission scanning electron microscopy, focused ion beam-scanning electron microscopy (FIB-SEM) (Helios Nova lab 600, FEI), for analysing VAMWCNTs using FE-SEM, the sample was tilted at 45°.Focused ion beam field-emission scanning electron microscopy (FIB-SEM) (Helios Nova lab 600, FEI) was used to analyse the sample as well as to carry out cross-sectional investigation. In situ Pt deposition was carried out only during cross-section preparation in FIB-SEM as a standard methodology as widely reported in literature [49]. Pt coating was deposited (in-situ) on the sample for FIB cutting, with the Pt coating preserving the surface morphology during the process [49]. High-resolution (HR)-TEM and TEM were performed using a Philips CM200 TEM.

3.4. Results and Discussion

The experimental design for the MWCNT slicing process is presented in Figure 3. 1 At high rotational speeds, the VFD has a dynamic thin film down to *ca* 200 μm in thickness, allowing for exposure to field effects in such a way that the material within the thin film is uniformly processed. This is applicable to laser irradiation, in controlling the length distribution of CNTs [48] and others fields such as plasmas [50, 51] and LEDs [52]. Previous studies on slicing MWCNTs (and also DWCNTs) used a fixed energy setting of the laser using a mixture of water and NMP as the solvent [34]. With the realisation that NMP can decompose to intractable material [53], as a potential contaminant of the sliced material, we explored other possible solvents and found that DMF alone is a suitable solvent, which simplifies the processing and work up of the samples. We chose three laser energies, 600 mJ, 250 mJ and 50 mJ, of a pulsed Q-switch laser (Nd:YAG) irradiating at 1064 nm on pristine MWCNT dispersed in DMF in a VFD under continuous flow mode of operation. We then systematically explored the VFD operating parameters, namely rotational speed of the VFD and concentration of the MWCNTs, to determine the optimal conditions for specific length distributions for each energy setting. The rotational speed was varied between 4k and 9k rpm for each of the selected laser energies, with the tilt angle set at 45°, followed by changing the concentration of MWCNTs, from 0.08, 0.16 and 0.2 mg/mL (see Supplementary Information), flow rate 0.45 mL/min. The choice of 45° tilt angle was based on this angle being optimal for a diversity of applications of the device, with then an established optimal rotational speed of 8.5k rpm, flow rate 0.45 mL/min, and concentration of MWCNTs in DMF at 0.08 mg/mL, for the three different energy settings of the laser. These optimised conditions are in agreement with the conditions for slicing MWCNTs in a 1:1 mixture of water and NMP using 260 mJ laser energies [34]. In the absence of using a laser, there was no evidence for slicing MWCNTs (see Supplementary Information Figure S5 (a, b)). Furthermore, under batch processing (no VFD) while the sample was laser irradiated at 250mJ the MWCNTs were fragmented into irregular particles (Supplementary Information Figure S5(c, d)).

High shear in the thin films in the VFD, in the absence of pulsed NIR laser irradiation, is effective in rolling up SWCNTs into compact toroidal structures establishing the high shear stress provides sufficient energy for the bending of the CNTs [54]. In the presence of NIR the induced high vibrational energy in the tubes results in bond rupture at a point, then spontaneous slicing [34, 48]. This method is also effective in slicing MWCNTs, despite now breaking a much higher number of C-C bonds associated with the concentric rings of tubes in the material. Indeed, after systematically evaluating the operating parameter space of the VFD (Supplementary Information Figure S1-S5), we show the ability to control the length distribution of sliced MWCNTs, for length distributions centred at *ca* 75±2.1, 300±1.8 and 550±1.4 nm, with a decrease in side wall defects along the tubes compared to as received MWCNTs. We anticipate that other lengths can now be achieved, depending on the target application, by varying the processing parameters in different ways.

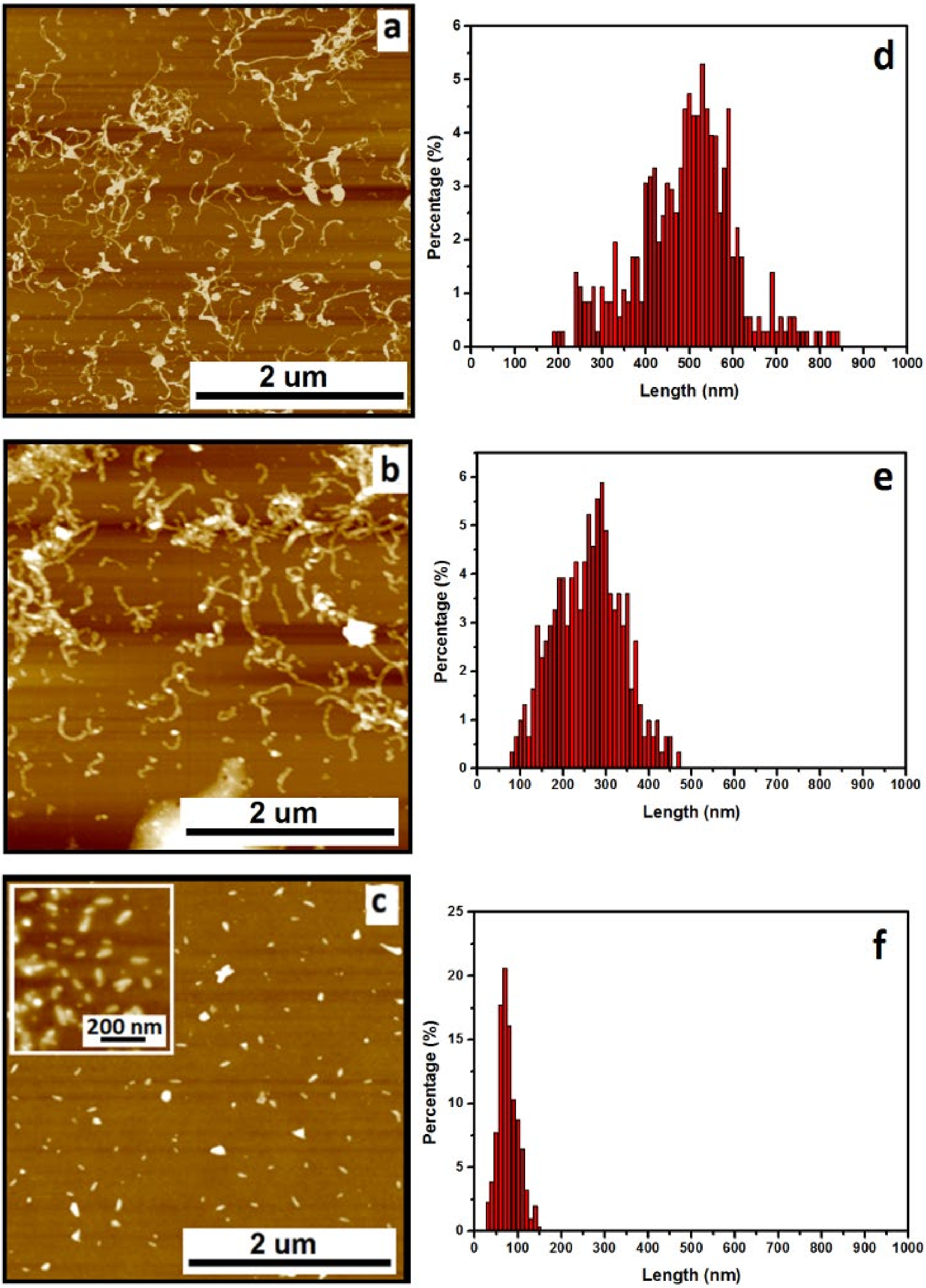

Figure 3. 2 AFM images of sliced MWCNTs, for material generated in the VFD operating at 8.5k rpm, under continuous flow mode, concentration of as received MWCNTs 0.08 mg/mL (DMF), tilt angle 45°, flow rate 0.45 mL/min, with a 1064 nm pulsed laser, and (a) 50 mJ, (b) 250 mJ and (c) 600 mJ; insert AFM image with large

magnification for short MWCNTs, with length distributions for MWCNTs in (d),(e) and (f) respectively. The length distribution for each sample are based on > 500 nanotubes.

Atomic force microscopy (AFM) was the primary characterisation technique for determining the length of the sliced MWCNTs, Figure 3. 2 There is an inverse relationship between the energy of the laser and length distribution. The high laser energy will provide a higher number of break points along the MWCNTs as they are bent under shear. Figure 3. 2a shows AFM images of the sliced MWCNTs with low laser energy, 50 mJ, which gave a broader distribution relative to the use of high laser energy, now centred at 550±1.4 nm. For an increase in laser energy to 250 mJ, there was a reduction in the length of the MWCNTs and narrowing of the length distribution, centred at 300±1.8 nm, Figure 3. 2b Shorter sliced MWCNTs were obtained using the higher laser energy, 600 mJ, with a dramatic narrowing of the length distribution to 80 nm, Figure 3. 2c The different histograms in Figure 3. 2 d-f establish the ability to control the slicing of the MWCNTs with the length distributions for each laser energy setting for each sample of sliced MWCNTs based on counting > 500 individual tubes.

Figure 3. 3 presents TEM and HRTEM images of the as received MWCNTs (before VFD processing) and after slicing to different lengths. As received MWCNTs are curved and entangled, Figure 3. 3a, and thus measuring their lengths is inherently difficult, but we note that according to the commercial supplier, the length of the MWCNTS is between 3 to 6 μm. After VFD processing incorporating a pulsed laser, TEM images established a decrease in the average length of the MWCNTs for increasing laser energy, with these results in agreement with the above AFM measurements. The structural integrity of the MWCNTs before and after processing was investigated using HRTEM, Figure 3. 3 This establishes that the tubular structure of the sliced MWCNTs has been preserved, with the interlayer spacing before and after slicing at 0.34 nm.

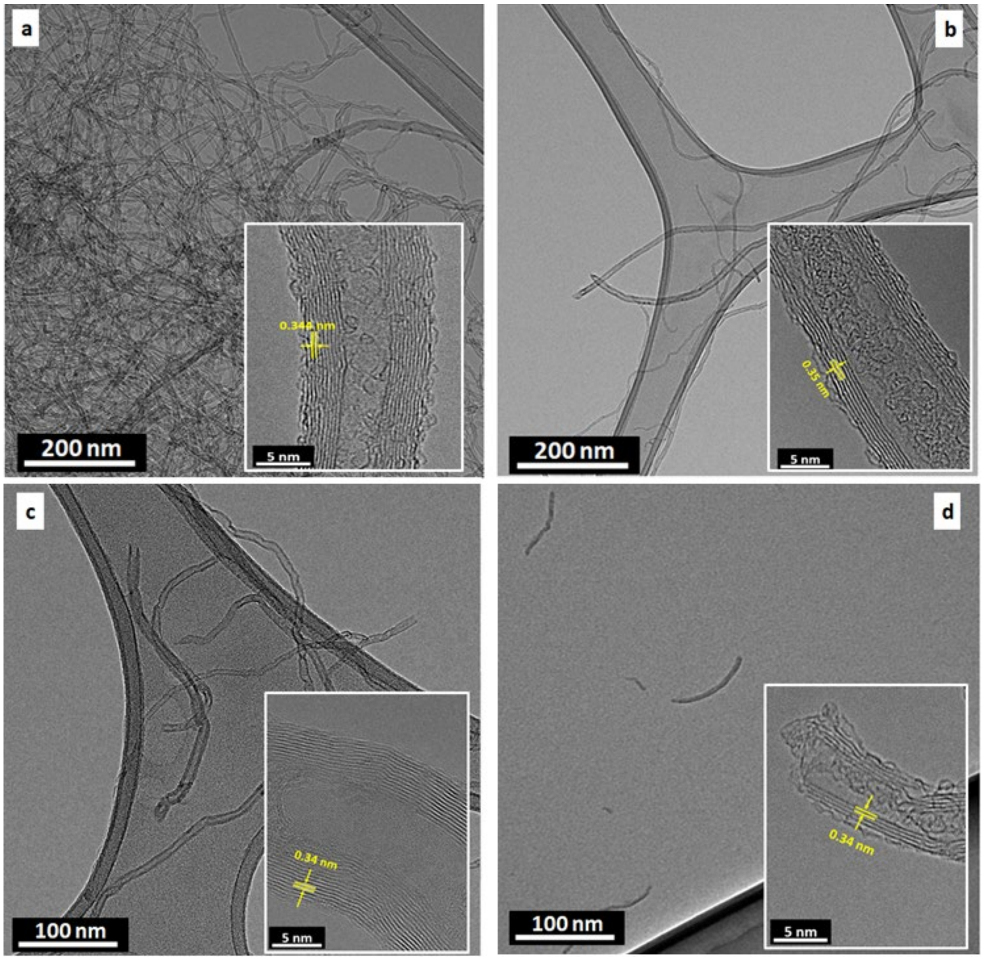

Figure 3. 3 TEM and HRTEM images (inset) of (a) as received MWCNTs and sliced MWCNTs, generated in the VFD, 8.5k rpm, continuous flow mode of operation, concentration of as received MWCNTs 0.08 mg/mL (DMF), tilt angle 45°, flow rate 0.45 mL/min, using a 1064 nm pulsed laser, operating at (b) 50 mJ, (c) 250 mJ and (d) 600 mJ.

Raman spectra were recorded with an excitation wavelength of 532 nm, for investigating the nature of the sliced MWCNTs and the level of defects present, noting that the ratio of the intensity between the D band (I_D) and G band (I_G) is used to determine the level of defects. The G band relates to planar vibrations, while the D band is a measure of the level of defects [55]. Figure 3. 4 presents Raman spectra of the three different length distributions of the sliced MWCNTs along with the as-received material. The G and D bands are observed at 1597 and 1354 cm-1, respectively, as expected for MWCNTs. The average of the D/G intensity ratios for the pristine

MWCNTs was 1.10, and after slicing, a decrease in the D/G intensity ratios was observed relative to the as received material. The higher the laser energy used, the shorter the length of the MWCNT afforded and the lower the amount of side wall defects. The induced vibrational energy of Nd:YAG laser processing where there is a dramatic increase in surface temperature and localised heating [56, 57] is clearly effective in removing surface defects of the CNT.

Thus, we have established that in contrast to chemical based approaches for ‘cutting’ CNT which introduces side wall defects [32], the ability to effectively slice MWCNTs with control in their length is with a reduction in surface defects. Defects are expected to be present at the ends of the MWCNTs, arising from the dangling bonds generated by the slicing process.

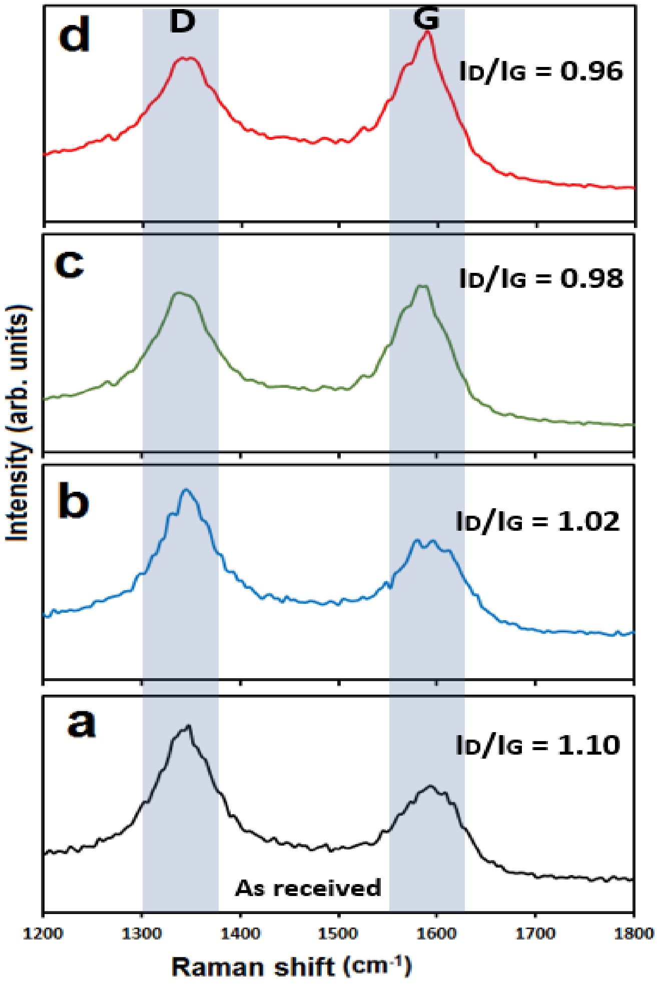

Figure 3. 4 Raman spectra of (a) as received MWCNTs and sliced MWCNTs formed in DMF in a VFD at 8.5k rpm, continuous flow 0.45 mL/min, 45° tilt angle, 1064 nm pulsed laser operating at (b) 50 mJ, (c) 250 mJ and (d) 600 mJ.

The longer the sliced MWCNTs, the greater the length distribution. This provides information on the mechanism of slicing, where under shear stress in the VFD, bond cleavage at a hair-pin bend in a tube leads to a cascade of bond cleavage across it. The stiffer MWCNTs relative to SWCNTs presumably requires higher energy to start bond cleavage on the outer concentric ring, then for successive bond cleavage across all of the concentric carbon nanotubes. Furthermore, the wider length distribution observed for longer MWCNT is consistent with the bond SWCNT cleavage mechanism also being applicable to MWCNTs. As the MWCNT length decreases, there will be a point at which there is no ‘handle’ for further slicing to occur. During this process, a certain length will have insufficient bending to start the slicing, either side of the centre of the length distribution.

The diameter of the sliced MWCNTs is unchanged after slicing at all three lengths (different laser energy) (see Supplementary Information Figure S6). Given the above reduction in defects in the sliced tubes, and that the shorter the tubes, the less likelihood there are of defects being present along the tube that would restrict dethreading. This is an important consideration noting that concentric carbon nanotubes have superlubricity [58]. However, under these conditions studied there was no evidence for dethreading, with no significant change in the average diameter of the sliced MWCNTs relative to the as received material.

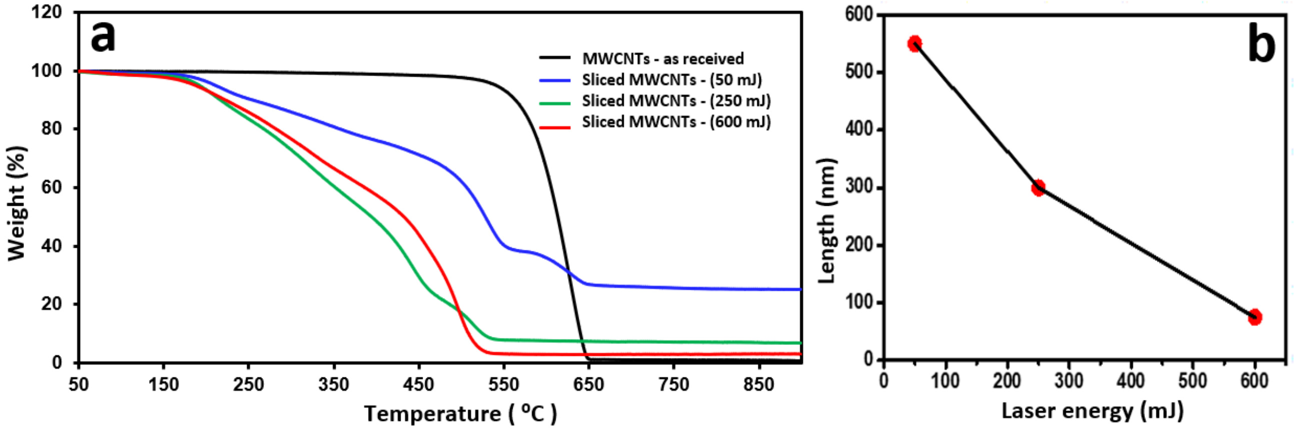

Figure 3. 5 (a) TGA curves (in air) for as received MWCNTs (black line) and sliced MWCNTs generated in the VFD, 8.5k rpm, continuous flow 0.45 mL/min, 45° tilt angle, 1064 nm pulsed laser operating at, 50 mJ (blue line), 250 mJ (green line) and 600 mJ (red line). (b) Centre of length distribution of sliced MWCNTs as a function of the laser energy.

Thermogravimetric analysis (TGA) was carried out under air, Figure 3. 5a For the as as-received MWCNT there is a large weight loss above 600 °C, which corresponds to decomposition of the MWCNTs [59]. The behaviour of the sliced MWCNTs are distinctly different to the as received material. This can be ascribed to the loss of solvent drawn into the internal cavity of the MWCNTs as they were sliced. Prior to slicing, not all the internal space of the MWCNTs is accessible to the solvent, as the end of the as received MWCNTs are sealed [60, 61]. As they are sliced the exposed void is thermodynamically expected to take up DMF, which will then be driven out for increasing temperatures. Accordingly, the weight loss in this regime for the longer sliced MWCNTs (50 mJ energy, 550±1.4 nm in length) is midway in behaviour relative to the shorter MWCNTs and as received MWCNTs, although there is little different between the tubes sliced at 250 mJ (300±1.8 nm in length) and 600 mJ (75±2.1 nm in length). Longer sliced MWCNTs, are likely to contain more internal defects which could limit the solvent uptake per unit length of the tubes. Further increase in temperature results in another weight loss (~ 45%) between 300 and 450 °C. This could be due to the thermal elimination of the hydroxyl (OH) groups, formed during the slicing of MWCNTs. Loss in mass over 450 °C for all the sliced MWCNTs, can be attributed to loss of dangling bonds formed at the point of slicing MWCNTs during processing. The higher residue in the TGA for the longer sliced MWCNTs generated at 50 mJ relative to as received and shorter sliced MWCNTs possibly relates to metal oxide nanoparticles generated from the laser inadvertently hitting the stainless steel jet feed, being drawn into the core of the tubes which are exposed once sliced [62, 63]. This type of in situ uptake of metal oxide particles has been noted when preparing composite material based on sliced MWCNTs and Fe_3O_4 nanoparticles [64].

Figure 3. 5b shows the length distribution of sliced MWCNTs as a function of the laser energy. At low laser energy, 50 mJ, the MWCNTs are sliced to a length centred at ~ 550±1.4 nm. Increasing the laser energy to 250 mJ results in shorter length sliced MWCNTs centred at ~300±1.8 nm. At higher laser energy, 600 mJ, shorter sliced MWCNTs are generated, centred at ~75±2.1 nm. These findings establish that increasing the laser energy, resulting in increaing induced vibrational energy from the Nd:YAG laser, results in shorter MWCNTs [56, 57].

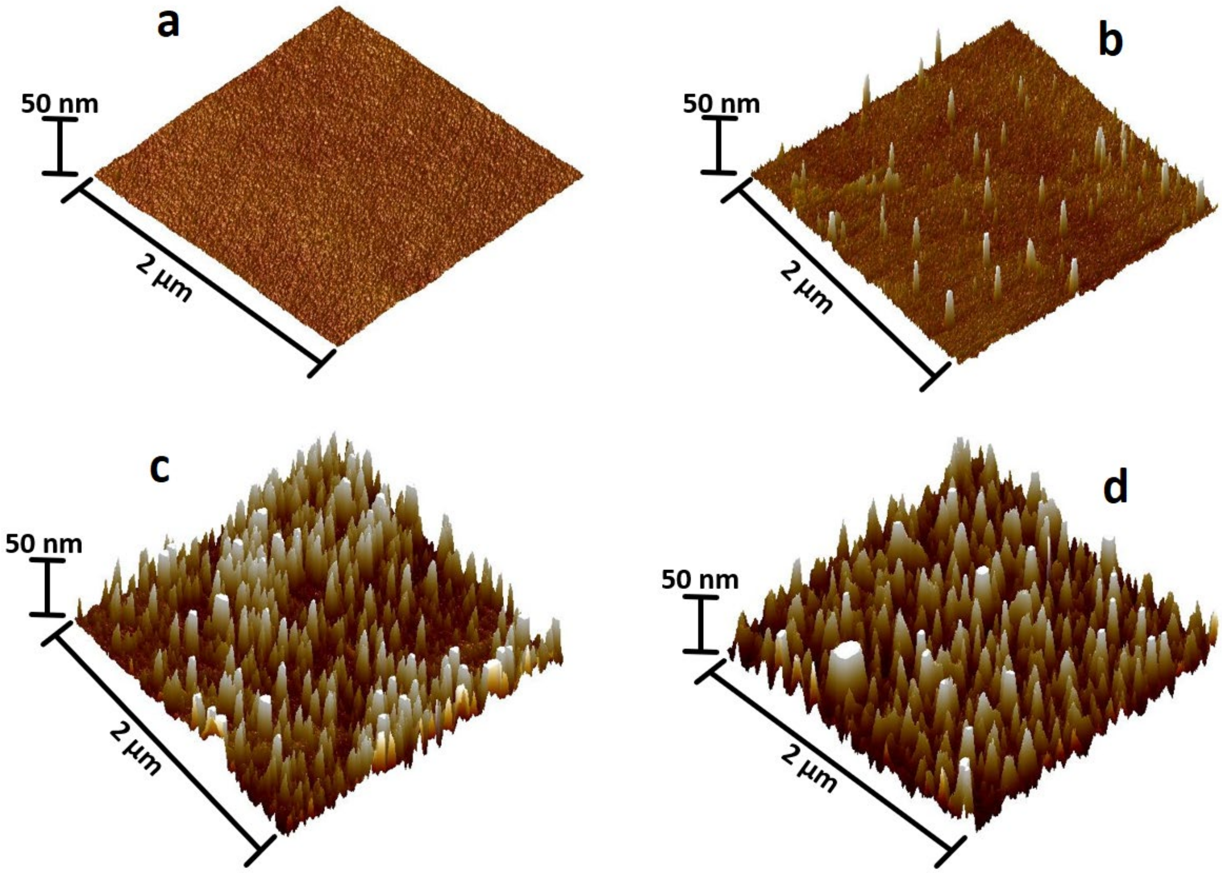

Figure 3. 6 3D AFM images of (a) a clean silicon wafer substrate (before dipping), after dipping for (b) 30 min, (c) 60 min, and (d) 120 min in a DMF solution of sliced MWCNTs (75±2.1 nm in length) in a VFD operating at 8.5k rpm, under continuous flow 0.45 mL/min, 45° tilt angle, 1064 nm pulsed laser operating at 600 mJ.

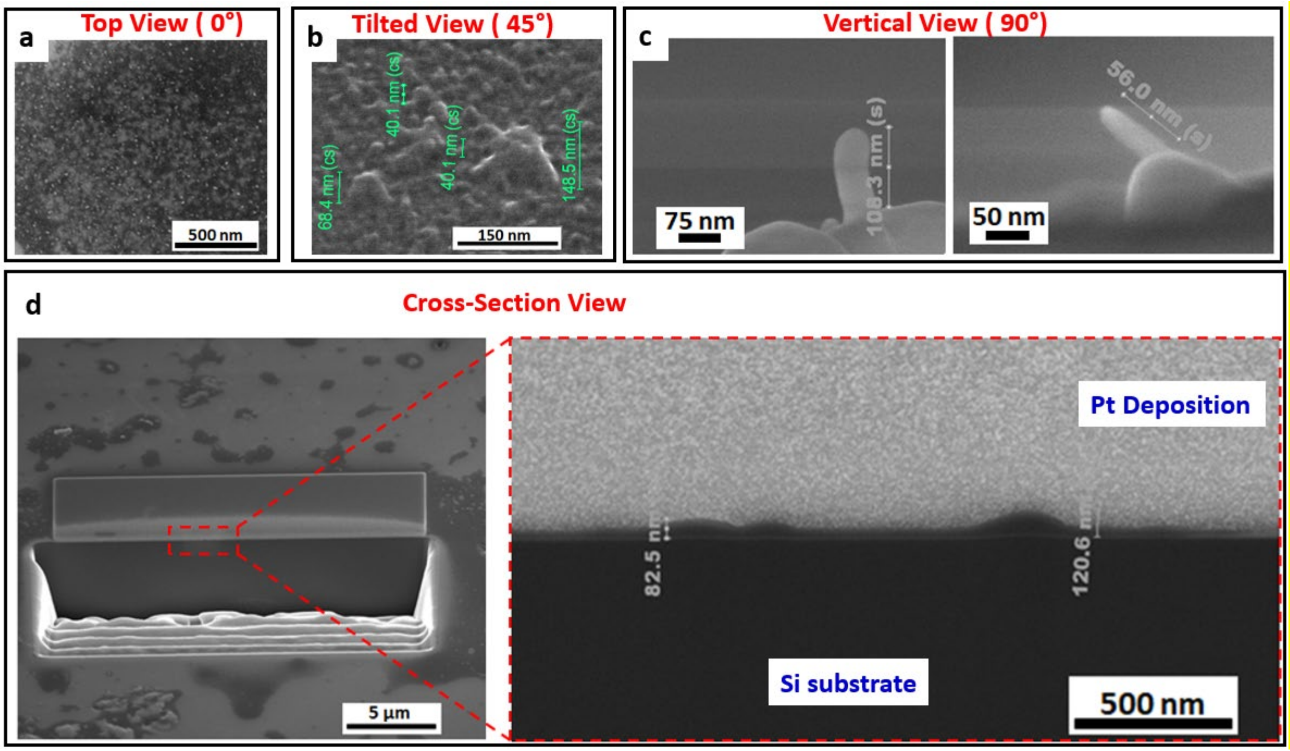

Figure 3. 7 HRSEM images of (a) Top view 0°, (b) tilted view 45°, (c) vertical view 90° and (d) cross-section view of vertically aligned sliced MWCNTs on silicon wafer substrate treated for 120 min in a DMF solution of sliced MWCNTs (75±2.1 nm in length) in the VFD operating at 8.5k rpm, under continuous flow 0.45 mL/min, using a 1064 nm pulsed laser operating at at 600 mJ.

We then attempted to vertically self-assemble the sliced MWCNTs on a silicon substrate using a simple dipping and rinsing method, Figure 3. 1 This involved dipping a silicon wafer in a DMF solution of short MWCNTs for different reaction times, specifically 30, 60, and 120 mins. AFM images were recorded before and after the immersing process. Figure 3. 6a shows silicon wafer before dipping in the solution, which appears clean and flat, devoid of any morphology. After the substrate was dipped into the solution of short MWCNTs, the attachment of the sliced MWCNTs was evident after 30 mins (Figure 3. 6(b)), with the level of coverage increasing as the immersion time increase to 60 mins (Figure 3. 6(c)) then 120 mins (Figure 3. 6(d)), with the sliced MWCNTs also vertically aligned.

Two factors were important for controlling the vertical alignment and density of the MWCNTs on the surface; (a) the immersion time and (b) the length of the MWCNTs. The shorter length MWCNT (75±2.1

nm) and 120 min immersion time gave the highest density of vertically aligned tubes on the surface, at 88 tubes per 2μm^2, Figure 3. 6d After the slicing process, dangling bonds, such as -COOH and –OH, are expected to be present at the ends of the tubes can form a strong interaction with the surface of the silicon substrate allowing for the vertical self assembly process. The other two lengths of sliced MWCNTs (300 and 550 nm) show sliced MWCNTs lying down horizontally on the surface (Figure S7 in Supplementary Information). The reason for them lying down presumably arises from the higher contact area as such as the length of the tube increases, relative to the contact area when they are standing up. Thus, there appears to be a limit on the ability to align CNTs on surfaces for increasing lengths.

Further characterisation of the morphology of these vertically aligned MWCNTs used high-resolution SEM (HRSEM). HRSEM images of vertically aligned MWCNTs for longest immersion time (120 min) at a different magnification are shown in Figure 3. 7 Note that the angle of the substrate was imaged at different angle with respect to the electron beam. Figure 3. 7 shows the VAMWCNTs from different views a) top view (0°), b) tilted view (45°), c) vertical view (90°) and (d) cross-section view, and show that the sliced MWCNTs are perpendicular to the substrate and that their average length is approximately 80 nm. The latter is in agreement with the specified diameter of the commercially supplied MWCNTs, and with the AFM data.

3.5. Conclusions

We have established a simple and effective top down method for slicing MWCNTs with control over the length distribution. This is under continuous flow conditions within the dynamic thin film of a vortex fluidic device while the liquid is irradiated *in situ* using a 1064 nm pulsed laser. The VFD is not only effective for dis-entangling MWCNTs under shear stress but simultaneously slicing them, with the length inversely proportional to the energy of the laser, as established in generating three length distribution centred at ca 75±2.1, 300±1.8 and 550±1.4 nm. The non-linearity of laser energy and the length of the

MWCNTs is possibly a consequence of different localised heating around the MWCNTs which will change the localised viscosities. This will affect the shear stress experienced by the MWCNTs for their ultimate slicing. The isolated yield of the sliced MWCNTs is high (90 %), using a continuous flow process, such that scalability can be addressed using parallel arrays of the VFD microfluidic platform. We explore scaling up using a single VFD, in preparing 13 mg of sliced MWCNTs in one run over 6 hours of the material for 180 mL of the solution passing through the VFD. In addition, Raman spectroscopy and HR-TEM established the structural integrity of the sliced MWCNTs, albeit with a decrease in side wall defects. Importantly the slicing is in a single solvent, DMF, which is stable under the processing, and the short MWCNTs can be readily vertically aligned on a silicon substrate using the simple dipping and rinsing method, with the density of coverage depending on the processing time. The length of MWCNTs is critical for a number of applications, including field emission devices and solar cells [4, 59]. The ability now to control their length using VFD and laser mediated processing has potential for fabricating MWCNTs which best suit the targeted application.

ASSOCIATED CONTENT

Supporting Information. Additional information on controlling experiments and optimizing conditions for slicing and vertically aligned MWCNT. This material is available free of charge via the Internet at http://pubs.acs.org.

AUTHOR INFORMATION

Corresponding Author

* E-mail address: colin.raston@flinders.edu.au (Colin Raston)

Author Contributions

The manuscript was written through contributions of all authors. All authors have given approval to the final version of the manuscript.

Notes

The authors declare no competing financial interest.

3.6. Acknowledgements

T. M. D. A would like to thank Taibah University (Ministry of Education, Saudi Arabia) for funding his scholarship. The authors also thank Australian Research Council, The Government of South Australia, and AMMRF for support of this work. T. M. D. A thanks Dr. Animesh Basak and Dr. Ashley slattery from Adelaide microscopy for their help.

3.7. References

1. Liu, L.; Yang, C.; Zhao, K.; Li, J.; Wu, H.-C., Ultrashort single-walled carbon nanotubes in a lipid bilayer as a new nanopore sensor. *Nat. Commun.,* **2013,** *4*, 2989.
2. Di, J.; Zhang, X.; Yong, Z.; Zhang, Y.; Li, D.; Li, R.; Li, Q., Carbon-Nanotube Fibers for Wearable Devices and Smart Textiles. *Adv. Mater.,* **2016,** *28*, 10529-10538.
3. Javey, A.; Guo, J.; Paulsson, M.; Wang, Q.; Mann, D.; Lundstrom, M.; Dai, H., High-field quasiballistic transport in short carbon nanotubes. *Phys. Rev. Lett.,* **2004,** *92*, 106804.
4. Diao, P.; Liu, Z., Vertically Aligned Single-Walled Carbon Nanotubes by Chemical Assembly–Methodology, Properties, and Applications. *Adv. Mater.,* **2010,** *22*, 1430-1449.
5. Ma, Y.; Wang, B.; Wu, Y.; Huang, Y.; Chen, Y., The production of horizontally aligned single-walled carbon nanotubes. *Carbon,* **2011,** *49*, 4098-4110.
6. Seah, C.-M.; Chai, S.-P.; Mohamed, A. R., Synthesis of aligned carbon nanotubes. *Carbon,* **2011,** *49*, 4613-4635.
7. Yin, Z.; Wang, H.; Jian, M.; Li, Y.; Xia, K.; Zhang, M.; Wang, C.; Wang, Q.; Ma, M.; Zheng, Q.-s., Extremely black vertically aligned carbon nanotube arrays for solar steam generation. *ACS Appl. Mater. Interfaces,* **2017,** *9*, 28596-28603.
8. Du, F.; Dai, Q.; Dai, L.; Zhang, Q.; Reitz, T.; Elston, L., Vertically-Aligned Carbon Nanotubes for Electrochemical Energy Conversion and Storage. In *Nanomate. Sustainable Energy*, Springer, **2016**; pp 253-270.
9. Wang, G.; Yao, J.; Liu, H.; Dou, S.; Ahn, J.-H. J. M.; International, M., Growth and lithium storage properties of vertically aligned carbon nanotubes. *Met. Mater. Int.,* **2006,** *12*, 413-416.
10. Wong, S. S.; Woolley, A. T.; Joselevich, E.; Cheung, C. L.; Lieber, C. M., Covalently-functionalized single-walled carbon nanotube probe tips for chemical force microscopy. *J. Am. Chem. Soc.,* **1998,** *120*, 8557-8558.
11. Druzhinina, T. S.; Hoeppener, S.; Schubert, U. S., Microwave-assisted fabrication of carbon nanotube AFM tips. *Nano Lett.,* **2010,** *10*, 4009-4012.

12. Zhou, S.; Feng, X.; Shi, H.; Chen, J.; Zhang, F.; Song, W., Direct growth of vertically aligned arrays of Cu (OH) 2 nanotubes for the electrochemical sensing of glucose. *Sens. Actuators, B,* **2013,** *177*, 445-452.
13. Kim, S. N.; Rusling, J. F.; Papadimitrakopoulos, F., Carbon nanotubes for electronic and electrochemical detection of biomolecules. *Adv. Mater.,* **2007,** *19*, 3214-3228.
14. Hinds, B. J.; Chopra, N.; Rantell, T.; Andrews, R.; Gavalas, V.; Bachas, L. G., Aligned multiwalled carbon nanotube membranes. *Scienec,* **2004,** *303*, 62-65.
15. Holt, J. K.; Park, H. G.; Wang, Y.; Stadermann, M.; Artyukhin, A. B.; Grigoropoulos, C. P.; Noy, A.; Bakajin, O., Fast mass transport through sub-2-nanometer carbon nanotubes. *Scienec,* **2006,** *312*, 1034-1037.
16. In, J. B.; Grigoropoulos, C. P.; Chernov, A. A.; Noy, A., Growth kinetics of vertically aligned carbon nanotube arrays in clean oxygen-free conditions. *ACS Nano,* **2011,** *5*, 9602-9610.
17. Gao, Z.; Zhang, X.; Zhang, K.; Yuen, M. M., Growth of vertically aligned carbon nanotube arrays on al substrates through controlled diffusion of catalyst. *J. Phys. Chem. C*, **2015,** *119*, 15636-15642.
18. Zuaznabar-Gardona, J. C.; Cao, R.; Suarez, M., Vertical self-assembly of modified multiwalled carbon nanotubes on gold surfaces induced by chitosan and Tween. *Chem. Commun.,* **2012,** *48*, 1910-1912.
19. Huang, X.-J.; Ryu, S.-W.; Im, H.-S.; Choi, Y.-K., Wet chemical needlelike assemblies of single-walled carbon nanotubes on a silicon surface. *Langmuir* **2007,** *23*, 991-994.
20. Yu, J.; Shapter, J. G.; Quinton, J. S.; Johnston, M. R.; Beattie, D. A., Direct attachment of well-aligned single-walled carbon nanotube architectures to silicon (100) surfaces: a simple approach for device assembly. *Phys. Chem. Chem. Phys*., **2007,** *9*, 510-520.
21. Poh, Z.; Flavel, B. S.; Shearer, C. J.; Shapter, J. G.; Ellis, A. V., Fabrication and electrochemical behavior of vertically-aligned carbon nanotube electrodes covalently attached to p-type silicon via a thioester linkage. *Mater. Lett.,* **2009,** *63*, 757-760.
22. Macdonald, T.; Gibson, C. T.; Constantopoulos, K.; Shapter, J. G.; Ellis, A. V., Functionalization of vertically aligned carbon nanotubes with polystyrene via surface initiated reversible addition fragmentation chain transfer polymerization. *Appl. Surf. Sci.,* **2012,** *258*, 2836-2843.
23. Zheng, K.; Shao, R.; Wang, J.; Liao, Z.; Marks, N.; Chen, P.; Lu, W.; Han, X.; Zou, J., Fabrication of individual carbon nanotubes and their arrays in a transmission electron microscope. *Carbon,* **2016,** *100*, 435-440.
24. Wang, Y.; Zhang, J.; Zang, J.; Ge, E.; Huang, H., Etching and cutting of multi-walled carbon nanotubes in molten nitrate. *Corros. Sci.,* **2011,** *53*, 3764-3770.
25. Rubio, N.; Fabbro, C.; Herrero, M. A.; de la Hoz, A.; Meneghetti, M.; Fierro, J. L.; Prato, M.; Vázquez, E., Ball-Milling Modification of Single-Walled Carbon Nanotubes: Purification, Cutting, and Functionalization. *Small,* **2011,** *7*, 665-674.
26. Lustig, S. R.; Boyes, E. D.; French, R. H.; Gierke, T. D.; Harmer, M. A.; Hietpas, P. B.; Jagota, A.; McLean, R. S.; Mitchell, G. P.; Onoa, G. B., Lithographically cut single-walled carbon nanotubes: controlling length distribution and introducing end-group functionality. *Nano Lett.,* **2003,** *3*, 1007-1012.
27. Jeong, S.-H.; Lee, O.-J.; Lee, K.-H.; Oh, S. H.; Park, C.-G., Preparation of aligned carbon nanotubes with prescribed dimensions: template synthesis and sonication cutting approach. *Chem. Mater.,* **2002,** *14*, 1859-1862.
28. Banhart, F.; Li, J.; Terrones, M., Cutting Single-Walled Carbon Nanotubes with an Electron Beam: Evidence for Atom Migration Inside Nanotubes. *Small,* **2005,** *1*, 953-956.

29. Rauwald, U.; Shaver, J.; Klosterman, D. A.; Chen, Z.; Silvera-Batista, C.; Schmidt, H. K.; Hauge, R. H.; Smalley, R. E.; Ziegler, K. J., Electron-induced cutting of single-walled carbon nanotubes. *Carbon,* **2009,** *47*, 178-185.
30. Lee, J.; Jeong, T.; Heo, J.; Park, S.-H.; Lee, D.; Park, J.-B.; Han, H.; Kwon, Y.; Kovalev, I.; Yoon, S. M., Short carbon nanotubes produced by cryogenic crushing. *Carbon,* **2006,** *44*, 2984-2989.
31. Wang, X. X.; Wang, J. N.; Su, L. F.; Niu, J. J., Cutting of multi-walled carbon nanotubes by solid-state reaction. *Mater. Chem.,* **2006,** *16*, 4231-4234.
32. Ren, F.; Kanaan, S. A.; Khalkhal, F.; Loebick, C. Z.; Haller, G. L.; Pfefferle, L. D., Controlled cutting of single-walled carbon nanotubes and low temperature annealing. *Carbon,* **2013,** *63*, 61-70.
33. Gu, Z.; Peng, H.; Hauge, R.; Smalley, R.; Margrave, J., Cutting single-wall carbon nanotubes through fluorination. *Nano lett.,* **2002,** *2*, 1009-1013.
34. Vimalanathan, K.; Gascooke, J. R.; Suarez-Martinez, I.; Marks, N. A.; Kumari, H.; Garvey, C. J.; Atwood, J. L.; Lawrance, W. D.; Raston, C. L., Fluid dynamic lateral slicing of high tensile strength carbon nanotubes. *Sci. Rep.,* **2016,** *6*, 22865.
35. Yuan, T. Z.; Ormonde, C. F. G.; Kudlacek, S. T.; Kunche, S.; Smith, J. N.; Brown, W. A.; Pugliese, K. M.; Olsen, T. J.; Iftikhar, M.; Raston, C. L., Shear-Stress-Mediated Refolding of Proteins from Aggregates and Inclusion Bodies. *ChemBioChem* **2015,** *16*, 393-396
36. Britton, J.; Meneghini, L. M.; Raston, C. L.; Weiss, G. A., Accelerating Enzymatic Catalysis Using Vortex Fluidics. *Angew. Chem.* **2016,** *128*, 11559-11563.
37. Britton, J.; Raston, C. L.; Weiss, G. A., Rapid protein immobilization for thin film continuous flow biocatalysis. *Chem. Commun.,* **2016,** *52*, 10159-10162.
38. Vimalanathan, K.; Shrestha, R. G.; Zhang, Z.; Zou, J.; Nakayama, T.; Raston, C. L., Surfactant-free Fabrication of Fullerene C60 Nanotubules Under Shear. *Angew. Chem. Int. Ed.,* **2017**. 56, 8398–8401.
39. Alsulami, I.; Alharbi, T.; Harvey, D.; Gibson, C. T.; Raston, C. L., Controlling the growth of fullerene C60 cones under continuous flow. *Chemical Communications* **2018**, *54,* 7896-7899.
40. Chen, X.; Dobson, J. F.; Raston, C. L., Vortex fluidic exfoliation of graphite and boron nitride. *Chem. Commun.,* **2012,** *48*, 3703-3705.
41. Alharbi, T. M.; Shingaya, Y.; Vimalanathan, K.; Nakayama, T.; Raston, C. L., High Yielding Fabrication of Magnetically Responsive Coiled Single Walled Carbon Nanotube Under Flow. *ACS Appl. Nano Mater.,* **2019**, 2, 5282-5289.
42. Yasin, F. M.; Boulos, R. A.; Hong, B. Y.; Cornejo, A.; Iyer, K. S.; Gao, L.; Chua, H. T.; Raston, C. L., Microfluidic size selective growth of palladium nano-particles on carbon nano-onions. *Chem. Commun.,* **2012,** *48*, 10102-10104.
43. Luo, X.; Al-Antaki, A. H. M.; Vimalanathan, K.; Moffatt, J.; Zheng, K.; Zou, Y.-C.; Zou, J.; Duan, X.; Lamb, R.; Wang, S., Laser irradiated vortex fluidic mediated synthesis of luminescent carbon nanodots under continuous flow. *React. Chem. Eng.,* **2018**, 3, 164-170.
44. Alharbi, T. M.; Harvey, D.; Alsulami, I. K.; Dehbari, N.; Duan, X.; Lamb, R. N.; Lawrance, W. D.; Raston, C. L., Shear stress mediated scrolling of graphene oxide. *Carbon,* **2018,** 137, 419-424.
45. Alharbi, T.; Alghamdi, A. R.; Vimalanathan, K.; Raston, C. L., Continuous flow photolytic reduction of graphene oxide. *Chem, Commun.,* **2019**, 55, 11438-11441.
46. Yasmin, L.; Chen, X.; Stubbs, K. A.; Raston, C. L., Optimising a vortex fluidic device for controlling chemical reactivity and selectivity. *Sci. Rep.,* **2013,** *3, 2282.*
47. Britton, J.; Stubbs, K. A.; Weiss, G. A.; Raston, C. L., Vortex Fluidic Chemical Transformations. *Chem.- Eur. J.* **2017**, 23, 13270-13278.

48. Alharbi, T. M.; Vimalanathan, K.; Lawrance, W. D.; Raston, C. L., Controlled slicing of single walled carbon nanotubes under continuous flow. *Carbon,* **2018**, 2018, 140, 428-432.
49. Kurdi, A.; Basak, A., Deformation of electrodeposited gradient Co/Sn multilayered coatings under micro-pillar compression. *Eng. Fract. Mech.,* **2018,** *204*, 138-146.
50. Jones, D. B.; Chen, X.; Sibley, A.; Quinton, J. S.; Shearer, C. J.; Gibson, C. T.; Raston, C. L., Plasma enhanced vortex fluidic device manipulation of graphene oxide. *Chem. Commun.,* **2016,** *52*, 10755-10758.
51. Jones, D. B.; Raston, C. L., Improving oxidation efficiency through plasma coupled thin film processing. *RSC Adv.,* **2017,** *7*, 47111-47115.
52. Ho, L. A.; Raston, C. L.; Stubbs, K. A., Angled Vortex Fluidic Mediated Multicomponent Photocatalytic and Transition Metal-Catalyzed Reactions. *Chem.– Eur.J.,* **2018**, 24, 8869-8874.
53. Liaw, D. J.; Liaw, B. Y., Synthesis and characterization of new soluble polyamides containing ether and pendant cyclododecylidene groups. *Polym. Adv. Technol.,* **1998,** *9*, 740-745.
54. Vimalanathan, K.; Chen, X.; Raston, C. L., Shear induced fabrication of intertwined single walled carbon nanotube rings. *Chem. Commun.,* **2014,** *50*, 11295-11298.
55. Dresselhaus, M. S.; Dresselhaus, G.; Saito, R.; Jorio, A., Raman spectroscopy of carbon nanotubes. *Phy. Rep.,* **2005,** *409*, 47-99.
56. Nakamiya, T.; Mitsugi, F.; Semba, K.; Kozai, R.; Ikegami, T.; Iwasaki, Y.; Sonoda, Y.; Tsuda, R., Pulsed Nd: YAG laser heating and treatment on multi-walled carbon nanotubes film. *Thin Solid Films* **2010,** *518*, 6604-6608.
57. Souza, N.; Zeiger, M.; Presser, V.; Mücklich, F., In situ tracking of defect healing and purification of single-wall carbon nanotubes with laser radiation by time-resolved Raman spectroscopy. *RSC Adv.,* **2015,** *5*, 62149-62159.
58. Zhang, R.; Ning, Z.; Zhang, Y.; Zheng, Q.; Chen, Q.; Xie, H.; Zhang, Q.; Qian, W.; Wei, F., Superlubricity in centimetres-long double-walled carbon nanotubes under ambient conditions. *Nat. Nanotechnol.,* **2013,** *8*, 912.
59. Vijaya Kumar Saroja A. P.; Muruganathan, M.; Mizuta, H.; Sundara, R., Enhanced Sodium Ion Storage in Interlayer Expanded Multiwall Carbon Nanotubes. *Nano lett.,* **2018**, 18, 5688-5636.
60. Li, C.; Chou, T.-W., A structural mechanics approach for the analysis of carbon nanotubes. *Int. J. Solids Struct.,* **2003,** *40*, 2487-2499.
61. Basiuk, E. V.; Monroy-Peláez, M.; Puente-Lee, I.; Basiuk, V. A., Direct solvent-free amination of closed-cap carbon nanotubes: a link to fullerene chemistry. *Nano Lett.,* **2004,** *4*, 863-866.
62. Kierkowicz, M.; Pach, E.; Santidrián, A.; Sandoval, S.; Gonçalves, G.; Tobías-Rossell, E.; Kalbáč, M.; Ballesteros, B.; Tobias, G. J. C., Comparative study of shortening and cutting strategies of single-walled and multi-walled carbon nanotubes assessed by scanning electron microscopy. *Carbon,* **2018,** *139*, 922-932.
63. Kierkowicz, M.; Pach, E.; Santidrián, A.; Tobías-Rossell, E.; Kalbáč, M.; Ballesteros, B.; Tobias, G., Effect of Steam-Treatment Time on the Length and Structure of Single-Walled and Double-Walled Carbon Nanotubes. *ChemNanoMat,* **2016,** *2* (2), 108-116.
64. Alharbi, T.; Al-Antaki, A. H. M.; Moussa, M.; Hutchison, W.; Raston, C. L., Three-step-in-one synthesis of supercapacitor MWCNT superparamagnetic magnetite composite material under flow. *Nanoscale Adv.,* **2019**, 1, 3761-3770.

Nanoscale

PAPER

View Article Online
View Journal

Check for updates

Cite this: DOI: 10.1039/c9nr08715j

Vertically aligned laser sliced MWCNTs†

Thaar M. D. Alharbi,[a,b] Kasturi Vimalanathan,[a] Ibrahim K. Alsulami[a] and Colin L. Raston *[a]

Applications of multi-walled carbon nanotubes (MWCNTs) benefit from the availability of specific lengths of the material while keeping the outer walls pristine, for example, for applications requiring vertically aligned tubes. To this end, a simple and effective continuous flow 'top down' process to control the length of sliced MWCNTs has been developed using a vortex fluidic device (VFD) coupled with a 1064 nm pulse laser, with the process in the absence of chemicals and any auxiliary substances. Three different length distributions of the sliced MWCNTs, centered at 75 ± 2.1 nm, 300 ± 1.8 nm and 550 ± 1.4 nm, have been generated with the length depending on the VFD operating parameters and laser energy, with the processing resulting in a decrease in side wall defects of the material. We also show the ability to vertically self assemble short MWCNTs on a silicon substrate with control of the surface density coverage using a simple dipping and rinsing method.

Received 10th October 2019,
Accepted 21st October 2019

DOI: 10.1039/c9nr08715j

rsc.li/nanoscale

1. Introduction

Carbon nanotubes (CNTs) have attracted interest in a variety of fields because of their unique electronic, chemical, and mechanical properties, in particular for nanodevice based applications.[1–3] However, for most of these applications, it is pivotal to have selective and ordered control over the surface density and orientation of the nanotubes, either vertically or horizontally to gain optimum efficiencies.[4–6] In particular, vertically aligned carbon nanotubes (VACNTs) have gained much interest and have shown great potential in a number of applications, for example in photoelectric conversion,[7,8] energy storage,[8,9] nanoprobes in scanning probe microscopy,[10,11] electrochemical and bioelectrochemical sensing,[4,12,13] and membrane separations.[14,15]

The two main methods that are typically used to fabricate VACNTs are direct growth on substrates[16,17] and the immobilization of shortened CNTs on substrates *via* chemical assembly.[18,19] Yu *et al.*[20] first reported the fabrication of VACNTs on silicon surfaces using a chemical attachment method. This involved reacting a hydroxylated surface with carboxylic acid functionalized SWCNTs, forming an ester linkage. Other studies reported by Ellis and colleagues[21,22] featured an assembly method, involving reaction of chemically modified nanotubes bearing carboxyl (–COOH) and hydroxyl (–OH) groups, with covalent surface attachment through ester or amide linkages. Chemical vapour deposition (CVD) features in the direct growth of VACNT arrays,[16,17] and VACNTs have been prepared using nanowire arrays as template.[23] However, these methods are complex and/or require the need for toxic chemicals and other auxiliary substances, with limited economic and environmental sustainability metrics. While the vertical assembly of CNTs on surfaces has been extensively studied, a key challenge is gaining access to short length CNT below ≤200 nm in order to gain control of the alignment while maintaining a high density of coverage.[4] A diverse number of methods have been developed for controlling the length of CNTs, as top down fabrication processes, using mechanical, physical, electrical or chemical strategies. However again these methods are tedious, damaging to the material post processing and require the use of toxic chemicals.[24–33]

We have reported in a previous study a more benign approach towards slicing single, double and multiwalled CNTs using the vortex fluidic device (VFD) coupled with a pulsed Nd:YAG laser.[34] The VFD, Fig. 1, is a microfluidic platform with a diversity of applications beyond slicing of CNTs, including protein folding,[35] enhancing enzymatic reactions,[36] protein immobilization,[37] anti-solvent induced fabricating of C_{60} tubules in water,[38] fabricating fullerene C_{60} cones,[39] exfoliating boron nitride and graphite,[40] fabricating coiled

---

[a] *Flinders Institute for Nanoscale Science and Technology, College of Science and Engineering, Flinders University, Adelaide, SA 5001, Australia. E-mail: colin.raston@flinders.edu.au*

[b] *Physics Department, Faculty of Science, Taibah University, Almadinah Almunawarrah 42353, Saudi Arabia*

† Electronic supplementary information (ESI) available: Additional information on controlling experiments and optimizing conditions for slicing and vertically aligned MWCNT. See DOI: 10.1039/c9nr08715j

Electronic Supplementary Material (ESI) for Nanoscale.

Supporting Information

Vertically Aligned Laser Sliced MWCNTs

Thaar M. D. Alharbi,[†, §] Kasturi Vimalanathan,[†] Ibrahim K. Alsulami[†] and Colin L. Raston[†, *]

[†] *Flinders Institute for NanoScale Science and Technology, College of Science and Engineering, Flinders University, Adelaide SA 5001, Australia*

[§] *Physics Department, Faculty of Science, Taibah University, Almadinah Almunawarrah 42353, Saudi Arabia*

Chapter Four

High Yielding Fabrication of Magnetically Responsive Coiled Single Walled Carbon Nanotube Under Flow

Thaar M. D. Alharbi, [†, §] Yoshitaka Shingaya, [‡] Kasturi Vimalanathan, [†] Tomonobu Nakayama [‡, *] and Colin L. Raston [†, *]

[†] Flinders Institute for Nanoscale Science and Technology, College of Science and Engineering, Flinders University, Adelaide SA 5001, Australia

[§] Physics Department, Faculty of Science, Taibah University, Almadinah Almunawarrah 42353, Saudi Arabia

[‡] International Center for Materials Nanoarchitectonics (WPI-MANA), National Institute for Materials Science (NIMS), Tsukuba, Ibaraki 305-0044, Japan

This study was published in ***ACS Appl. Nano Mater,*** Year **2019**, 2, 8, 5282-5289. The first page of the publication and SI are attached.

Author contributions: **TA** performed all the VFD and most characterization experiments and data analysis, and wrote all the primary content. **YS** helped with some MFM measurements. **KV** helped with the revised manuscript before submitting and also with addressing the reviewers' comments. **TN** and **CR** supervised and coordinated the project and helped on the research directions and plan, and the final revision of the manuscript. All of the co-authors assisted with the revision of the manuscript before and during the publication process.

4.1. Abstract

The curvature in coiled single walled carbon nanotubes (SWCNTs) rings impacts on their properties relative to straight CNTs, but the availability of such rings is limited. This has been addressed in developing a continuous flow method for fabricating coiled SWCNTs rings in high yield (80%) using a vortex fluidic device (VFD), in the absence of any toxic chemicals and surfactants. The VFD thin film microfluidic platform has a rapidly rotating angled glass tube with the processed liquid driven up and out of the tube. Magnetic force microscopy (MFM) established that the magnetic interaction of the resulting rings is strongly dependent on the thickness of the coiled SWCNT rings.

Keywords: Coiled single walled carbon nanotubes • Magnetic interactions • Vortex fluidic device • Magnetic force microscopy • Scalability • Phase shift.

Graphical Abstract

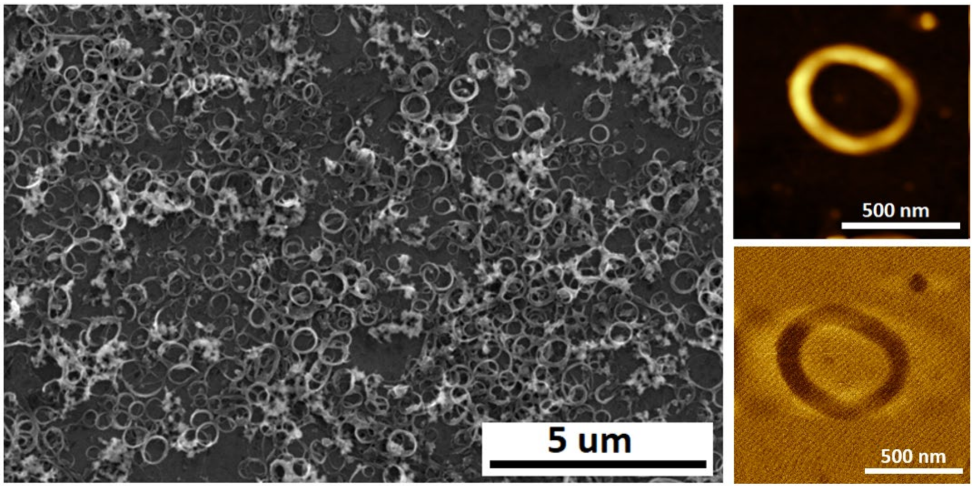

4.2. Introduction

Carbon nanomaterials have gained significant interest from the scientific community due to their unique physical and chemical properties.[1, 2] Single walled carbon nanotube (SWCNT) rings in particular, comprised of individual or bundled (coiled) SWCNTs have been a recent area of interest due to their unique morphology. Its high curvature and associated disorder results in novel mechanical, electronical and magnetic properties compared to pristine straight SWCNTs[3-5]. Coiled SWNCT rings have potential in diverse applications, for example, in small electromagnetic devices and flexible electronics. The many theoretical and experimental studies based on coiled SWCNT rings include investigating the persistent of current flow through the walls of the rings, studying their magnetic response and investigating the surface modes based on the engendered field distribution and electromagnetic energy confinement [6, 7]. In addition, due to the available charge free space in their interior cavity[8], coiled SWCNTs offer the ability to encapsulate cells[9] and metal chains such as Fe, Au and Cu[10].

Several strategies have been used to fabricate coiled SWCNT rings, including chemical vapor deposition (CVD),[11, 12] laser ablation,[13, 14] and synthesis from preformed SWCNTs involving ultrasonication,[15-17] organic reactions[18, 19] and a templated approach to bend SWCNTs.[15, 20, 21] However, these techniques suffer from various limitations, among them being difficulties in scaling the process, the use of harsh and toxic chemicals, long processing times and high-temperature processing. We have previously reported the synthesis of toroidal structures of SWCNTs of various morphologies using a microfluidic platform, the vortex fluidic device (VFD) in the confined mode (small aliquot processing)[22]. The method involved the use of a binary solvent system of toluene and water to afford rings of different morphologies that were and stable devoid of surfactants. It is noteworthy that scaling up using this confined mode approach is deemed problematic for large scale applications. Since our earlier work, we have now further developed the use of the VFD for fabricating coiled SWCNT rings with scalability incorporated into the process, operating under continuous flow processing and systematically studied the magnetic responses of the rings using magnetic force microscopy (MFM).

The VFD is a relatively new and versatile thin film microfluidic platform with a number of applications in addition to forming SWCNT rings,[22] including slicing and controlling the lengths of CNTs while irradiating with a pulsed laser,[23, 24] protein folding,[25] enhancing enzymatic reactions,[26] protein immobilization,[27] fabricating of C_{60} nanotubules using water as an 'anti-solvent',[28] exfoliation of graphite and boron nitride,[29] transforming graphene oxide sheets into scrolls,[30] the synthesis of carbon dots,[31] decorating carbon nano-onions with Pt nanoparticles,[32] probing the structure of self-organized systems, and controlling chemical reactivity and selectivity.[33] The thin film of liquid in the VFD has complex fluid dynamics, beyond the expected Stewartson/Ekman layers, which includes Faraday pressure waves, with the liquid moving up the tube against gravity at the ubiquitous optimised 45° tilt angle of the rapidly rotating tube in the device, and exiting at the top. [34]

Magnetic force microscopy (MFM) is a powerful characterisation technique, originally developed as a derivative of the atomic force microscopy (AFM). MFM has the ability for imaging and detecting magnetic interactions between a magnetised tip and nanomaterials deposited on a substrate under both ambient and buffer conditions. [35, 36] Essentially, MFM can distinguish the magnetic and nonmagnetic materials at the micro- and nano-scale dimensions.[37] It is used extensively in studying and localizing magnetic domains on a substrate such as magnetic bubble domains,[38] magnetic vortices in nanodisks[39] or skyrmions in helimagnets.[40-42]

Herein, we have developed a method to fabricate coiled (or toroidal) SWCNT rings in 80 % yield, under a continuous flow mode of operation, under ambient conditions, in the absence of any reagents or surfactants in the VFD. The rings were predominantly of torus morphologies with an average diameter of *ca* 300 nm and a wall thicknesses varying between 3-70 nm. We then employed the use of MFM to examine the magnetic response of these rings relative to geometric parameters. Our method involved firstly optimising the experimental conditions for the continuous flow process. This included systematically varying the operating parameter space of the VFD, including rotational speed, tilt angle, choice of solvent and concentration of the starting material. MFM was then used to characterize the magnetic response by analysing the phase shifts. A negative phase shift observed is due to the attractive interaction between the magnetic tip and the sample indicating a magnetic response from the sample. For the purpose of ensuring that no variations were observed due to a tip effect, all measurements were conducted using the same tip. We establish that there was no magnetic response when the rings exceed a minimum diameter cross section and when there is close interaction between different/a number of rings. Moreover, other minor morphologies that were also generated during the continuous flow processing, including figures of '8' and the crossed lattice shapes, showed no detectable magnetic response.

4.3. Results and discussion

4.3.1. Fabrication and mechanism of formation of SWCNT rings

As illustrated in Scheme 4. 1, SWCNT were dispersed in a mixture of toluene and water with a volume ratio of 1:1 and subjected to varying of the operating parameters of the VFD (rotational speed and tilt angle of the VFD, flow rate under continuous flow, and concentration of the dispersion) to achieve the highest yield of coiled rings. We determined that the optimized rotational speeds for the formation of the rings was at 8k rpm with speeds below and above this affording low yields of rings with aggregation of the SWCNT strands observed. The optimised angle and flow rate were at a 45^{o} tilt and at 0.45 mL/min respectively. A control experiment was carried out to study the effect of cavitational energy (bath sonication for 15 minutes) on the formation of the rings, but no rings were observed (Figure S1). The mechanism of formation of these coiled SWCNT rings is based on the formation of an emulsion of water and toluene pre-processing in the VFD.[22] Upon processing in the VFD, the bending of the carbon nanotubes would favour intertwining of the hydrophobic SWCNTs in the toluene phase, at the van der Waals limit, to form compact rings with different morphologies from the shear stress generated at high rotational speeds in the VFD.[23, 43]

The processed SWCNT rings were characterized using SEM, AFM, TEM and MFM. SEM image (Figure 4. 1A) shows a high conversion of coiled rings from the processing. The advantage of processing under continuous flow was the ability to generate coils with a yield of 80 %, albeit along with a small number of other morphologies, such as figure of ‘8’ and cross lattice structures, relative to those generated using the confined mode of operation of the VFD (Figure S2). Transmission electron microscopy (TEM) and high resolution TEM (HRTEM) were used to further determine the detailed structure of coiled SWCNT rings. TEM and HRTEM images show the rings are comprised of bundles of SWNT (Figure 1B- E). These rings have an average diameter of *ca* 300 nm (Figure 4. 1F) and a wall thickness (cross section) ranging from 3 to 70 nm, with an average thickness *ca* 40 nm (Figure 4. 1G).

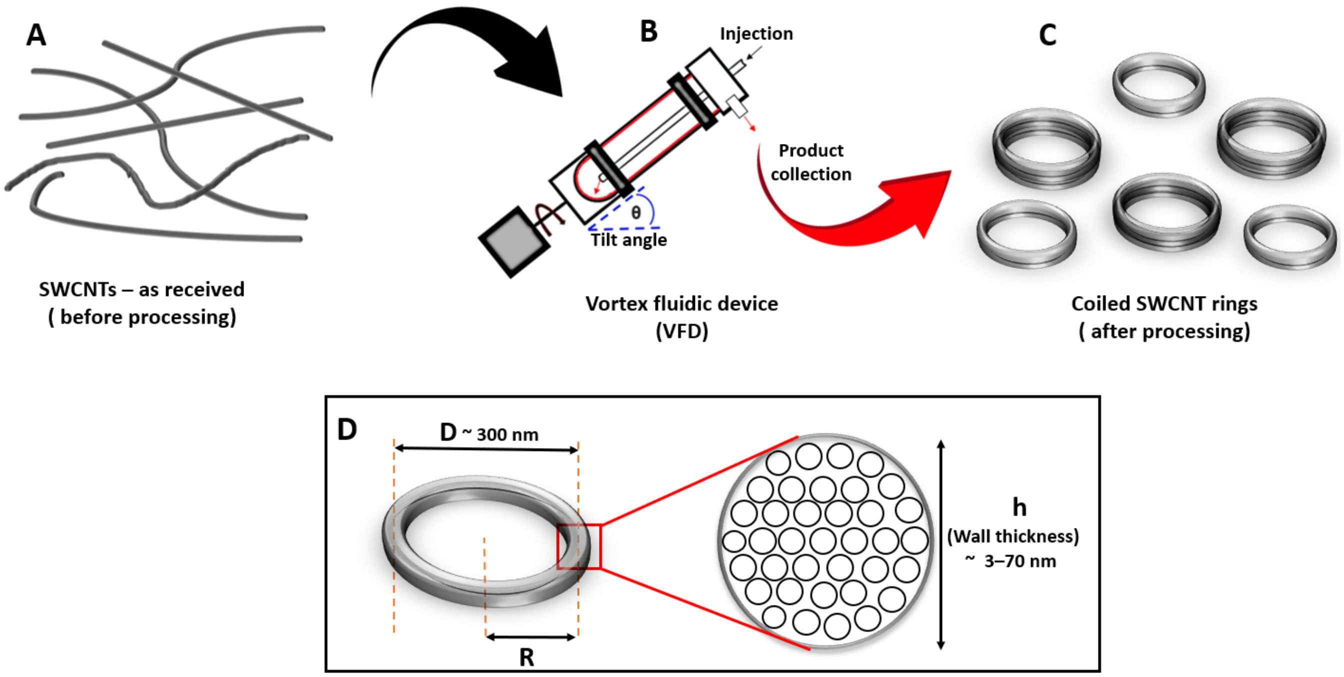

Scheme 4. 1 Schematic of the experimental process for fabricating coiled SWCNT rings. (A) Entangled SWCNTs before processing in the VFD. (B) Experimental set up of the VFD under continuous flow mode of operation. (C) Coiled SWCNT rings afforded post processing, and (D) the defining parameters of the coiled rings.

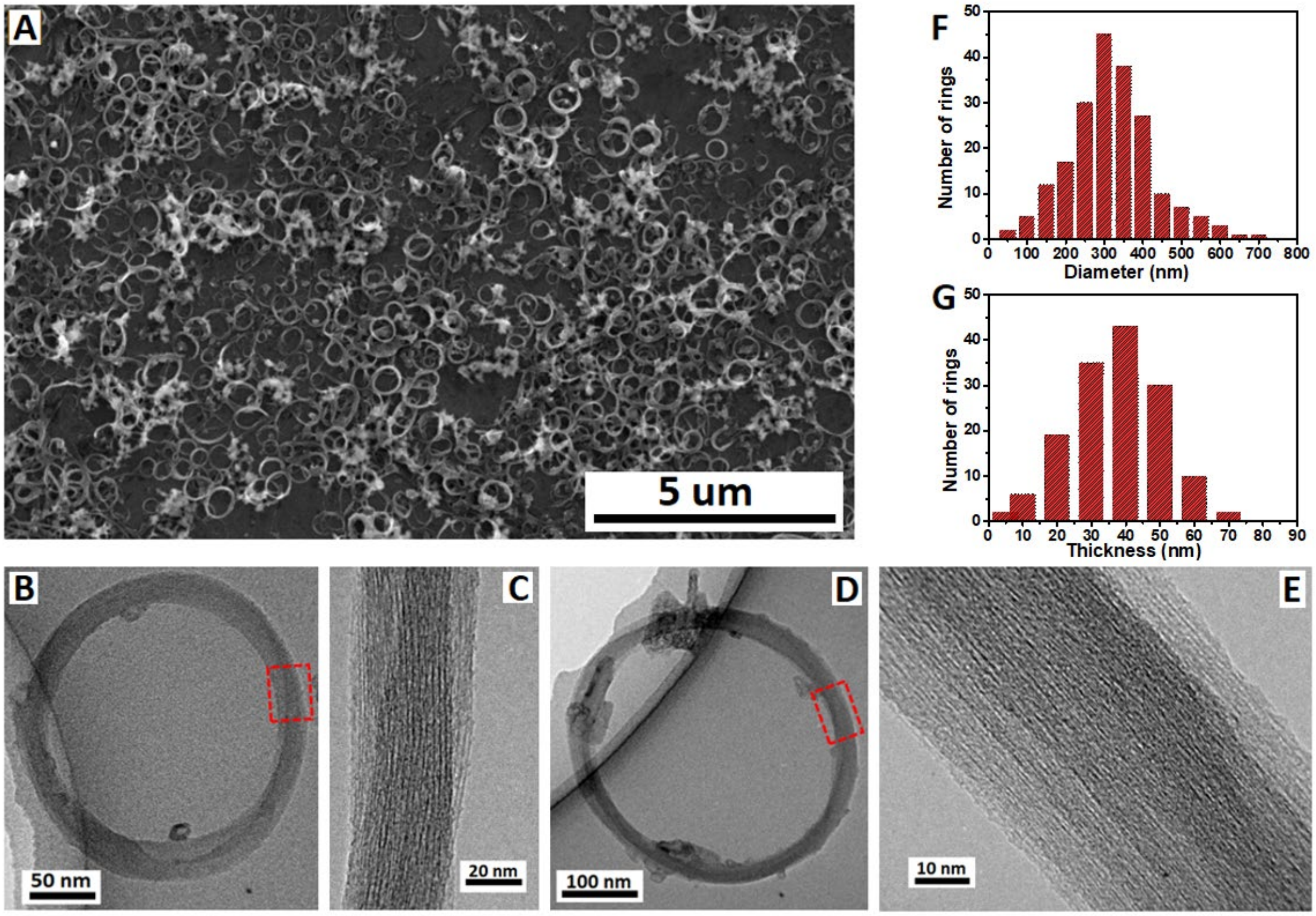

Figure 4. 1 (A) SEM image of coiled SWCNT rings, formed in the VFD at 8k rpm rotational speed, under continuous flow mode, with the concentration of the as received SWCNTs at 0.16 mg/mL (toluene/water at a 1:1 ratio), tilt angle 45°, flow rate 0.45 mL/min. (B, D) TEM images, and (C, E) HRTEM of the coiled SWCNT rings in (B, D). (F, G) Histograms showing the diameter and thickness distributions of the rings, respectively.

4.3.2. Magnetic properties of coiled SWCNT rings

MFM was used to characterize the magnetic responses of the SWCNT rings by analysing the phase shifts. The larger the negative phase shift, the stronger the attractive interaction between the magnetised tip and the SWCNT rings. In MFM, the magnetic contrast also depends on the lift height between the magnetized tip and the sample. The lift height mode is a two-scan technique for separating the long-range magnetic force from the short-range mechanical forces. In the first scan, the sample topography is determined, with the second scan involving increasing the distance (raising) of the magnetized tip from the surface of the sample to measure the magnetic force. At a certain lift height, the magnetic response can be separated from the topographical response, and as a result, the phase image is only due to the magnetic interactions between the magnetized tip and the sample.[35, 44-48]

We first measured the magnetic response of the coiled SWCNTs rings with a wall thickness of 50 nm, 35 nm and 20 nm. We then varied the lift heights (0 nm, 10 nm, 30 nm and 50 nm) to further confirm that the rings were indeed magnetic. Figure 4. 2 shows the MFM topography image and phase image obtained simultaneously for a coiled ring with a wall thickness of *ca* 50 nm. A strong negative phase shift was observed which decreased with increasing the lift height (0.6° for a lift height of 0 nm to 0.1° for a lift height of 50 nm).

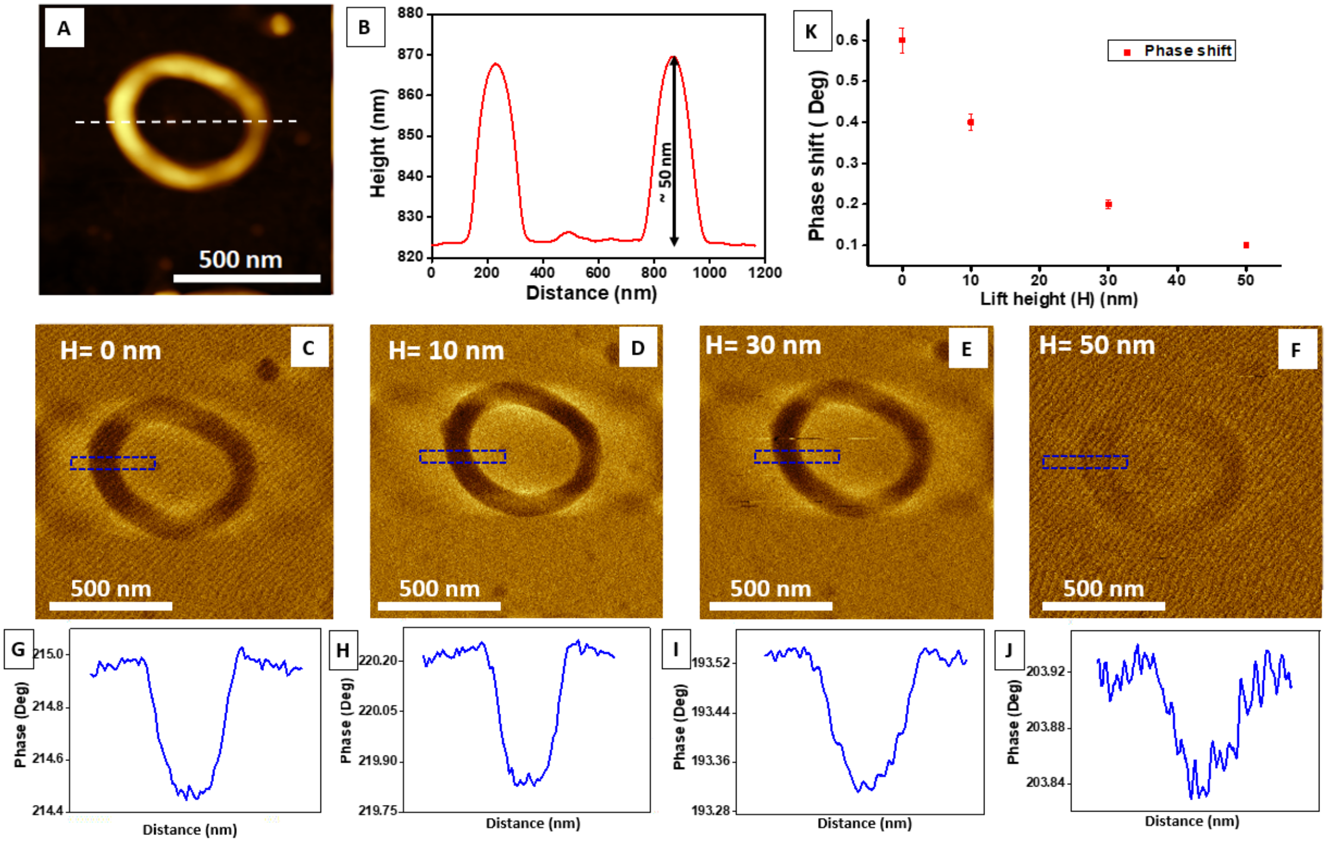

Figure 4. 2 MFM image of a coiled SWCNT ring with a wall thickness of *ca* 50nm: (A) MFM topography image, (B) the associated height profile of the ring showing the wall thickness *ca* 50 nm. (C-F) MFM phase images of at various lift heights: (C) 0, (D) 10, (E) 30, (F) 50 nm with their corresponding phase shifts respectively (G-J). (K) Plot of phase shift versus lift height.

SWCNT rings with smaller wall thicknesses (35 nm and 20 nm) (Figure 4. 3 and Figure 4. 4) had a much weaker negative phase shift compared to the ring with a 50 nm wall thickness (Figure 4. 2). At a lift height of 30 nm, the negative phase shift decreased from 0.20° to 0.10° for rings with a wall thickness of 50 nm and 35 nm respectively. The ring with a wall thickness of 20 nm showed a similar phase shift relative to a ring with a wall thickness of 35 nm, for the same lift height of 30 nm. This shows that rings with a larger wall thickness have a much stronger attractive interaction with the MFM tip compared to rings with a thinner wall. It is noteworthy that a ring with a much smaller wall thickness, *ca* ~ 7 ±1 nm (Figure S6), showed no noticeable phase shifts. Thus, there is a minimum wall thickness where the negative phase shift starts decreasing, and below this the nanorings are devoid or have no detectable magnetic behaviour.

The magnetic response of the SWCNT rings are dependent on a combination of a number of factors; (a) the electronic structure of the SWCNTs present and their chiralities, (b) the effects of curvature and (c) the arrangement of pentagons and heptagons due to the bending of the SWCNTs to form rings[3, 49, 50]. We provide some reasoning towards the observed magnetic response found in the present study. Firstly, the as received SWCNT are composed of both semiconducting and metallic chiralities with the chirality and orientation within the walls of the rings being random. The rings with larger wall thickness could potentially be made of a mixture of both armchair and zigzag nanotubes, with the former exhibiting a diamagnetic response and the latter having a slightly paramagnetic response, enough for the observed magnetic behavior. For thinner rings, there is a probability of the walls being made up of just the diamagnetic armchair SWCNTs, and thus with no magnetic response. Secondly, the rings are made of bundled SWCNTs that are bent and coiled in multiple turns to form rings. The multiple turns would allow for inter-tube tunneling whereby electrons can tunnel between individual SWCNTs within a coil, facilitated by the rings being tightly packed. The fewer the turns within each ring, the less likely that it is as tightly packed, potentially inhibiting inter-tube tunneling, with no detectable magnetic response [51, 52].

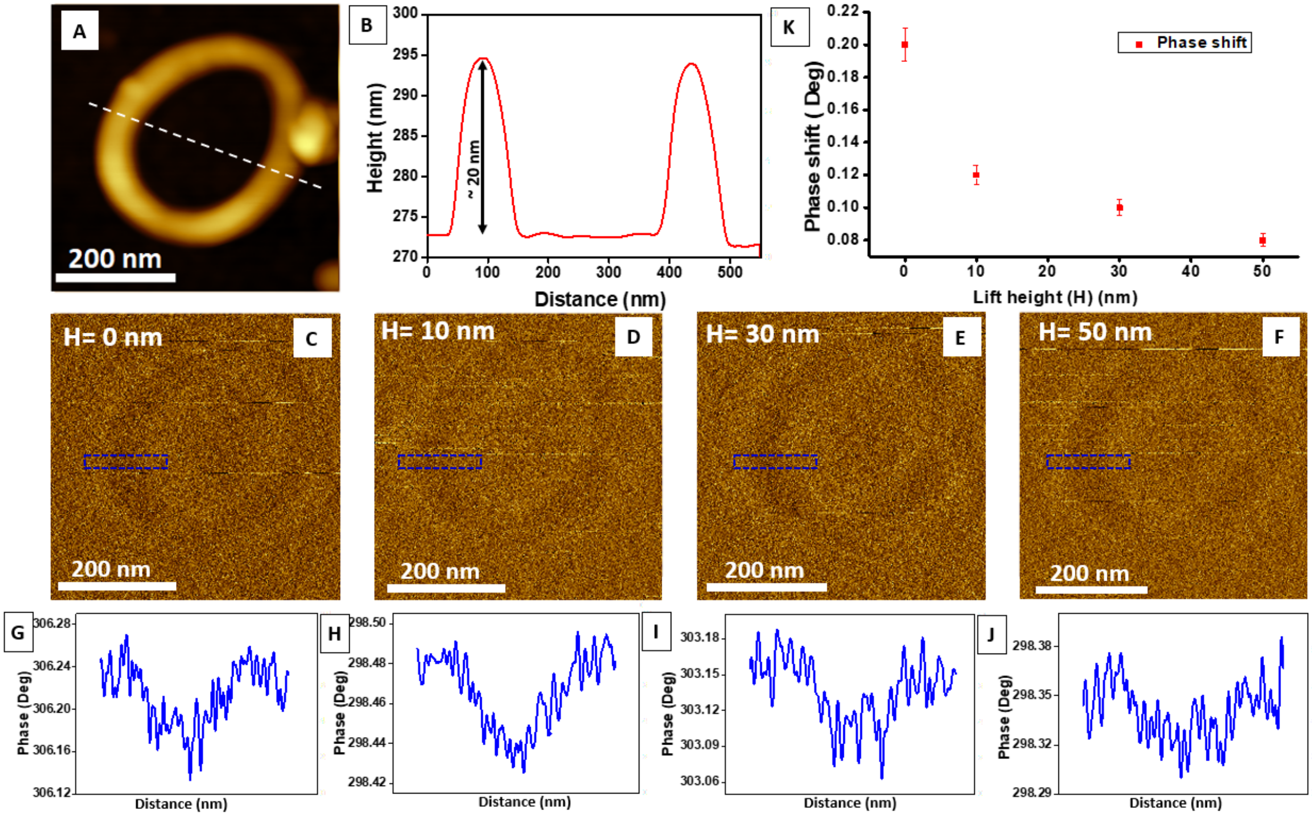

Figure 4. 3 MFM image of coiled SWCNT ring, for MFM imaging, after collecting the product, one drop of the solution was drop-casted onto silicon wafer and spin coated at 3k rpm for 30 seconds, then left to dry for 24 hours: (A) Topography, (B) height profile of the ring shows the wall thickness ca 20 nm. (C-F) MFM phase images at various lift heights: (C) 0, (D) 10, (E) 30, (F) 50 nm with their corresponding phase shift, respectively (G-J). (K) The plot of phase shift vs lift height obtained in the MFM measurement on a SWCNT ring.

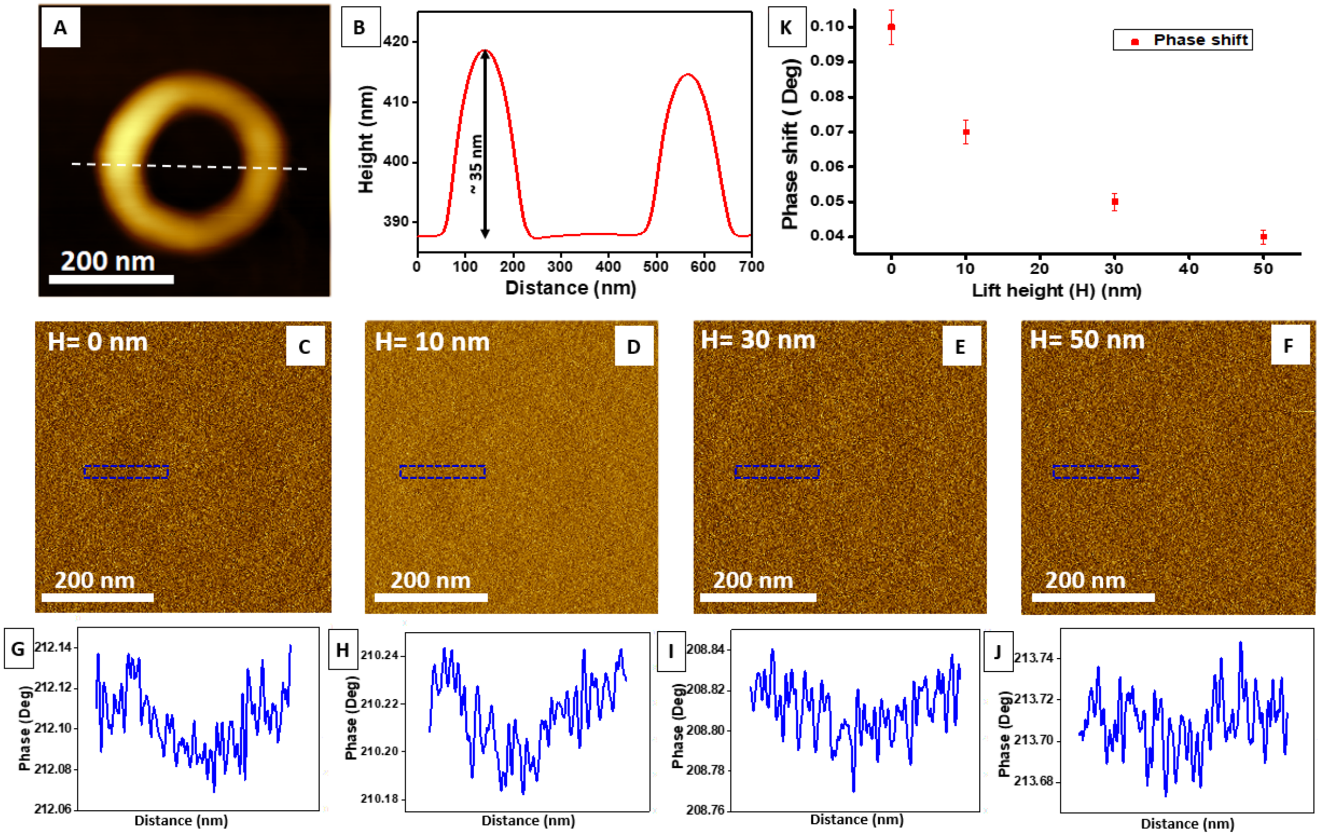

Figure 4. 4 MFM image of coiled SWCNT ring, for MFM imaging, after collecting the product, one drop of the solution was drop-casted onto a silicon wafer and spin coated at 3k rpm for 30 seconds, then left to dry for 24 hours: (A) Topography, (B) height profile establishing a wall thickness ca 35 nm. (C-F) MFM phase images at different lift heights: (C) 0, (D) 10, (E) 30, (F) 50 nm with their corresponding phase shift respectively (G-J). (K) Plot of phase shift versus lift height for MFM measurement on a coiled SWCNT ring.

We then investigated the magnetic response when rings with varying wall thicknesses were arranged in close contact to each other (Figure 4. 5A, B) and when a coiled ring is twisted into a figure of ‘8’ morphology (Figure 4. 5C). At a lift height of 10 nm, and other lift heights between 0-50 nm (Figure S7), no apparent phase shift was observed, and thus there was no detectable magnetic response. Any disturbance of the magnetic field from the MFM tip on the magnetic states is minimal. When the rings are in close contact with each other, there is potential for inter-tube shorting between the nanostructures and an associated higher resistance. Thus, no detectable magnetic response was observed. [51, 52].

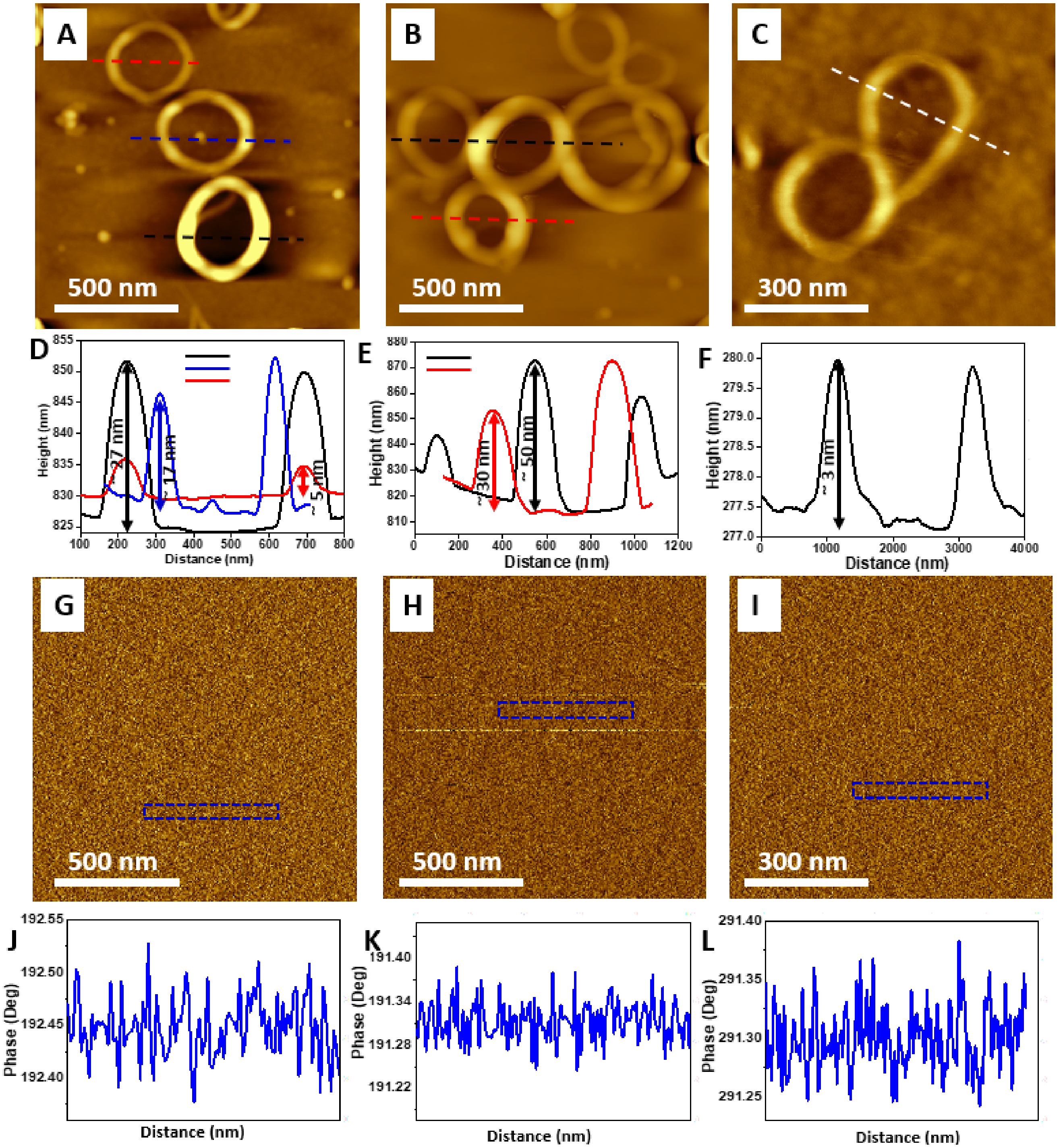

Figure 4. 5 (A-B) MFM topography image of coiled SWCNT ring patterns with variable thicknesses (~5-27 nm) (height profile of the ring shows the wall thickness ca 35 nm, with their corresponding phase images in (D and E) and the associated phase profiles (G and H) respectively, MFM topography image of a SWCNT ring with a figure of "8" morphology (C), (F, I and L) with its corresponding height profile, phase image and profile respectively.

4.4. Conclusions

We have demonstrated a simple method to fabricate coiled SWCNT rings in high yield (80%) under continuous flow conditions in the vortex fluidic device (VFD), with the processing devoid of using surfactants and toxic chemicals. The continuous flow processing in the VFD lends itself for scaling up the fabrication of the rings, avoiding batch-to-batch processing variances. The coiled rings have an average diameter of *ca* 300 nm and a wall thickness ranging between 3 to 70 nm. Magnetic force microscopy established that there is a stronger magnetic interaction for the thicker coiled rings, presumably arising from more efficient packing within the rings with more efficient tunneling of electrons. We envisage the practical use of the coiled rings in a diverse range of applications, especially with the potential to scale up the fabrication process under continuous flow conditions.

4.5. Experimental section

4.5.1. Materials and chemicals

The SWCNTs used in this study were purchased from Carbon Solution, Inc, with an as received purity > 90%, and were used as received. Toluene was purchased from Sigma Aldrich and used as received.

4.5.2. Preparation of coiled SWCNT rings

This involved a modified method previously reported for preparing them under confined mode of operation of the VFD. In brief, SWCNTs were dispersed in a mixture of toluene and water at 1:1 volume ratio at concentration of 0.16 mg mL^{-1}. The dispersion of SWCNTs was bath sonicated for 15 min forming a milky white mixture. For fabricating coiled SWCNT rings, initially in the confined mode of operation VFD, 1 mL of the milky mixture was placed in the 20 mm OD (17.5 mm ID) quartz or glass tube at a rotational speed of 8k rpm for a reaction time of 30 min. Further steps were then taken to optimize the experimental conditions for the formation of coiled rings under continuous flow. For this purpose, the rotational speed of the VFD was varied, using a flow rate of the mixture of water and toluene at 0.45 mL min^{-1}, which is the optimised flow rate for processing carbon materials in the VFD in general.[32-33] The experimental conditions for the formation of the coiled SWCNT was then optimized at 8k rpm. For rotational speeds < 7k rpm at a 45° tilt angle, aggregation of the SWCNT strands were observed with the formation of a small number of rings (Figure S3). At speeds above 8.5k rpm, very large bundles of SWCNTs were obtained (Figure S4). At 8k rpm, a significant amount of SWCNT formed ring structures compared to all other rotational speeds, and accordingly this speed was considered optimal. For characterisation, after collecting the product, one drop of solution was drop-cast onto a silicon wafer and spin coated, then left to dry for 24 hours.

4.5.3. Characterization

Magnetic force microscopy (MFM) was carried out with a commercial AFM instrument SII AFM (Hitachi High Technology), equipped with a scanner (20×20 μm2) under ambient conditions. Si cantilevers coated with a magnet film with the normal resonance frequency of 137 kHz and spring constant of 17 N/m (Type: SI-MF20) were used for MFM images. During the MFM measurements, the lift height was 10 nm if there was no specific clarification. High resolution transmission electron microscopy (HRTEM) (JEOL JEM-2100F) operated at 200 kV. Scanning electron microscopy (SEM) performed using a FEI Quanta 450 High Resolution Field Emission SEM, with a voltage of 5 kV, and working distance of 10 mm.

ASSOCIATED CONTENT

Supporting Information. Additional information on control experiments and optimizing conditions for fabricating coiled SWCNT rings. This material is available free of charge via the Internet at http://pubs.acs.org.

AUTHOR INFORMATION

Corresponding Author

* E-mail address: colin.raston@flinders.edu.au (Colin Raston)

* E-mail address: NAKAYAMA.Tomonobu@nims.go.jp (Tomonobu Nakayama)

Author Contributions

The manuscript was written through contributions of all authors. All authors have given approval to the final version of the manuscript.

Notes

The authors declare no competing financial interest.

4.6. Acknowledgements

T. M. D. A would like to thank Taibah University (Ministry of Education, Saudi Arabia) for funding his scholarship. The authors also thank Australian Research Council, The Government of South Australia, and AMMRF for support of this work.

4.7. References

1. Schnorr, J. M.; Swager, T. M., Emerging applications of carbon nanotubes. *Chem. Mater.,* **2011,** *23*, 646-657.
2. Hu, L.; Hecht, D. S.; Gruner, G., Carbon nanotube thin films: fabrication, properties, and applications. *Chem. Rev.,* **2010,** *110*, 5790-5844.
3. Liu, L.; Liu, F.; Zhao, J., Curved carbon nanotubes: From unique geometries to novel properties and peculiar applications. *Nano Res.,* **2014,** *7*, 626-657.
4. Liu, L.; Guo, G.; Jayanthi, C.; Wu, S., Colossal paramagnetic moments in metallic carbon nanotori. *Phys. Rev. lett.,* **2002,** *88*, 217206.
5. Kowsar, M.; Sabzyan, H., Nano-sized local magnetic field induced by circular motion of ions and molecules in a nanotorus under gigahertz rotating electric fields. *Mol. Phys.,* **2018**, 110-121.
6. Garapati, K. V.; Bagherian, M.; Passian, A.; Kouchekian, S. J. J. o. P. C., Plasmon dispersion in a multilayer solid torus in terms of three-term vector recurrence relations and matrix continued fractions. *J. Phys. Commun.,* **2018,** *2*, 015031.
7. Garapati, K. V.; Salhi, M.; Kouchekian, S.; Siopsis, G.; Passian, A. J. P. R. B., Poloidal and toroidal plasmons and fields of multilayer nanorings. *Phys. Rev. B,* **2017,** *95*, 165422.
8. Yazgan, E.; Taşci, E.; Malcioğlu, O. B.; Erkoç, Ş., Electronic properties of carbon nanotoroidal structures. *J. Mol. Struct.,* **2004,** *681*, 231-234.
9. Sharma, V.; Szymusiak, M.; Shen, H.; Nitsche, L. C.; Liu, Y. J. L., Formation of polymeric toroidal-spiral particles. *Langmuir,* **2011,** *28*, 729-735.
10. Lusk, M. T.; Hamm, N., Ab initio study of toroidal carbon nanotubes with encapsulated atomic metal loops. *Phys. Rev. B,* **2007,** *76*, 125422.
11. Song, L.; Ci, L.; Sun, L.; Jin, C.; Liu, L.; Ma, W.; Liu, D.; Zhao, X.; Luo, S.; Zhang, Z., Large-Scale Synthesis of Rings of Bundled Single-Walled Carbon Nanotubes by Floating Chemical Vapor Deposition. *Adv. Mater.,* **2006,** *18*, 1817-1821.
12. Zheng, M.; Ke, C., Mechanical deformation of carbon nanotube nano-rings on flat substrate. *J. Appl. Phys.,* **2011,** *109*, 074304.
13. Thess, A.; Lee, R.; Nikolaev, P.; Dai, H.; Petit, P.; Robert, J.; Xu, C.; Lee, Y. H.; Kim, S. G.; Rinzler, A. G., Crystalline ropes of metallic carbon nanotubes. *Science,* **1996,** *273*, 483-487.
14. Martel, R.; Shea, H. R.; Avouris, P., Rings of single-walled carbon nanotubes. *Nature,* **1999,** *398*, 299.
15. Wang, W.; Laird, E. D.; Gogotsi, Y.; Li, C. Y., Bending single-walled carbon nanotubes into nanorings using a Pickering emulsion-based process. *Carbon,* **2012,** *50*, 1769-1775.
16. Martel, R.; Shea, H. R.; Avouris, P., Ring formation in single-wall carbon nanotubes. *J. Phys. Chem. B,* **1999,** *103*, 7551-7556.
17. Komatsu, N., Ultrasonic isolation of toroidal aggregates of single-walled carbon nano tubes. *Carbon,* **2006,** *44*, 2091-2093.
18. Sano, M.; Kamino, A.; Okamura, J.; Shinkai, S., Ring closure of carbon nanotubes. *Science,* **2001,** *293*, 1299-1301.
19. Geng, J.; Ko, Y. K.; Youn, S. C.; Kim, Y.-H.; Kim, S. A.; Jung, D.-H.; Jung, H.-T., Synthesis of SWNT rings by noncovalent hybridization of porphyrins and single-walled carbon nanotubes. *The J. Phys. Chem. C,* **2008,** *112*, 12264-12271.
20. Tsukruk, V. V.; Ko, H.; Peleshanko, S., Nanotube surface arrays: weaving, bending, and assembling on patterned silicon. *Phys. Rev. lett.,* **2004,** *92*, 065502.
21. Wang, Y.; Maspoch, D.; Zou, S.; Schatz, G. C.; Smalley, R. E.; Mirkin, C. A., Controlling the shape, orientation, and linkage of carbon nanotube features with nano affinity templates. *Proc. Natl. Acad. Sci.,* **2006,** *103*, 2026-2031.
22. Vimalanathan, K.; Chen, X.; Raston, C. L., Shear induced fabrication of intertwined single walled carbon nanotube rings. *Chem. Commun.,* **2014,** *50*, 11295-11298.

23. Vimalanathan, K.; Gascooke, J. R.; Suarez-Martinez, I.; Marks, N. A.; Kumari, H.; Garvey, C. J.; Atwood, J. L.; Lawrance, W. D.; Raston, C. L., Fluid dynamic lateral slicing of high tensile strength carbon nanotubes. *Sci. Rep.,* **2016,** *6*, 22865.
24. Alharbi, T. M.; Vimalanathan, K.; Lawrance, W. D.; Raston, C. L., Controlled slicing of single walled carbon nanotubes under continuous flow. *Carbon,* **2018**. *140*, 428-432.
25. Yuan, T. Z.; Ormonde, C. F.; Kudlacek, S. T.; Kunche, S.; Smith, J. N.; Brown, W. A.; Pugliese, K. M.; Olsen, T. J.; Iftikhar, M.; Raston, C. L., Shear-Stress-Mediated Refolding of Proteins from Aggregates and Inclusion Bodies. *ChemBioChem,* **2015,** *16*, 393-396.
26. Britton, J.; Meneghini, L. M.; Raston, C. L.; Weiss, G. A., Accelerating enzymatic catalysis using vortex fluidics. *Angew. Chem.,* **2016,** *128*, 11559-11563.
27. Britton, J.; Raston, C. L.; Weiss, G. A., Rapid protein immobilization for thin film continuous flow biocatalysis. *Chem. Commun.,* **2016,** *52*, 10159-10162.
28. Vimalanathan, K.; Shrestha, R. G.; Zhang, Z.; Zou, J.; Nakayama, T.; Raston, C. L., Surfactant-free Fabrication of Fullerene C60 Nanotubules Under Shear. *Angew. Chem. Int. Ed.,* **2017,** *56*, 8398-8401.
29. Chen, X.; Dobson, J. F.; Raston, C. L., Vortex fluidic exfoliation of graphite and boron nitride. *Chem. Commun.,* **2012,** *48*, 3703-3705.
30. Alharbi, T. M.; Harvey, D.; Alsulami, I. K.; Dehbari, N.; Duan, X.; Lamb, R. N.; Lawrance, W. D.; Raston, C. L., Shear stress mediated scrolling of graphene oxide. *Carbon,* **2018**, *137*, 419-424.
31. Luo, X.; Al-Antaki, A. H. M.; Vimalanathan, K.; Moffatt, J.; Zheng, K.; Zou, Y.-C.; Zou, J.; Duan, X.; Lamb, R.; Wang, S., Laser irradiated vortex fluidic mediated synthesis of luminescent carbon nanodots under continuous flow. *React. Chem. Eng.,* **2018**, *3*, 164-170.
32. Goh, Y. A.; Chen, X.; Yasin, F. M.; Eggers, P. K.; Boulos, R. A.; Wang, X.; Chua, H. T.; Raston, C. L., Shear flow assisted decoration of carbon nano-onions with platinum nanoparticles. *Chem. Commun.,* **2013,** *49*, 5171-5173.
33. Yasmin, L.; Chen, X.; Stubbs, K. A.; Raston, C. L., Optimising a vortex fluidic device for controlling chemical reactivity and selectivity. *Sci. Rep.,* **2013,** *3,* 2282.
34. Britton, J.; Stubbs, K. A.; Weiss, G. A.; Raston, C. L., Vortex Fluidic Chemical Transformations. *Chem.- Eur. J.,* **2017**, *23*, 13270-13278.
35. Li, H.; Qi, X.; Wu, J.; Zeng, Z.; Wei, J.; Zhang, H., Investigation of MoS2 and graphene nanosheets by magnetic force microscopy. *ACS Nano,* **2013,** *7*, 2842-2849.
36. Tran, V. T.; Zhou, H.; Lee, S.; Hong, S. C.; Kim, J.; Jeong, S.-Y.; Lee, J. J. A. a. m.; interfaces, Magnetic-Assembly Mechanism of Superparamagneto-Plasmonic Nanoparticles on a Charged Surface. *ACS Appl. Mater. Interfaces.,* **2015,** *7*, 8650-8658.
37. Yang, S.; Wang, C.; Sahin, H.; Chen, H.; Li, Y.; Li, S.-S.; Suslu, A.; Peeters, F. M.; Liu, Q.; Li, J. J. N. l., Tuning the optical, magnetic, and electrical properties of ReSe2 by nanoscale strain engineering. *Nano Lett.,* **2015,** *15*, 1660-1666.
38. Wadas, A.; Wiesendanger, R.; Novotny, P., Bubble domains in garnet films studied by magnetic force microscopy. *J. Appl. Phys.,* **1995,** *78*, 6324-6326.
39. Shinjo, T.; Okuno, T.; Hassdorf, R.; Shigeto, K.; Ono, T., Magnetic vortex core observation in circular dots of permalloy. *Science,* **2000,** *289*, 930-932.
40. Milde, P.; Köhler, D.; Seidel, J.; Eng, L.; Bauer, A.; Chacon, A.; Kindervater, J.; Mühlbauer, S.; Pfleiderer, C.; Buhrandt, S., Unwinding of a skyrmion lattice by magnetic monopoles. *Science,* **2013,** *340*, 1076-1080.
41. Kézsmárki, I.; Bordács, S.; Milde, P.; Neuber, E.; Eng, L.; White, J.; Rønnow, H. M.; Dewhurst, C.; Mochizuki, M.; Yanai, K., Néel-type skyrmion lattice with confined orientation in the polar magnetic semiconductor GaV 4 S 8. *Nat. Mater.,* **2015,** *14*, 1116.
42. Zhang, S.; Bauer, A.; Burn, D.; Milde, P.; Neuber, E.; Eng, L.; Berger, H.; Pfleiderer, C.; Van Der Laan, G.; Hesjedal, T., Multidomain skyrmion lattice state in Cu_2OSeO_3. *Nano lett.,* **2016,** *16*, 3285-3291.

43. Chen, X.; Boulos, R. A.; Dobson, J. F.; Raston, C. L., Shear induced formation of carbon and boron nitride nano-scrolls. *Nanoscale,* **2013,** *5*, 498-502.
44. Li, Q.; Song, J.; Saura-Múzquiz, M.; Besenbacher, F.; Christensen, M.; Dong, M., Magnetic properties of strontium hexaferrite nanostructures measured with magnetic force microscopy. *Sci. Rep.,* **2016,** *6*, 25985.
45. Tao, L.; Meng, F.; Zhao, S.; Song, Y.; Yu, J.; Wang, X.; Liu, Z.; Wang, Y.; Li, B.; Wang, Y., Experimental and theoretical evidence for the ferromagnetic edge in WSe 2 nanosheets. *Nanoscale,* **2017,** *9*, 4898-4906.
46. Passian, A.; Siopsis, G., Quantum state atomic force microscopy. *Phys. Rev. A,* **2017,** *95*, 043812.
47. Passian, A.; Siopsis, G., Strong quantum squeezing near the pull-in instability of a nonlinear beam. *Phys. Rev. A,* **2016,** *94*, 023812.
48. Tetard, L.; Passian, A.; Farahi, R. H.; Thundat, T.; Davison, B. H., Opto-nanomechanical spectroscopic material characterization. *Nature Nanotech.,* **2015,** *10*, 870-877.
49. Zhang, Z.; Yuan, J.; Qiu, M.; Peng, J.; Xiao, F., Persistent currents in carbon nanotori: Effects of structure deformations and chirality. *J. Appl. Phys.,* **2006,** *99*, 104311.
50. Liu, C.; Xu, N., Magnetic response of chiral carbon nanotori: The dependence of torus radius. *Phys. B,* **2008,** *403*, 2884-2887.
51. Lin, M.; Chuu, D., Persistent currents in toroidal carbon nanotubes. *Phys. Rev. B* **1998,** *57*, 6731.
52. Liu, C.; Chen, H.; Ding, Magnetic response of carbon nanotori: the importance of curvature and disorder. *J. Phys.: Condens. Matter,* **2008,** *20*, 015206.

ACS APPLIED NANO MATERIALS
Article
Cite This: ACS Appl. Nano Mater. 2019, 2, 5282−5289
www.acsanm.org

High Yielding Fabrication of Magnetically Responsive Coiled Single-Walled Carbon Nanotube under Flow

Thaar M. D. Alharbi,[†,§] Yoshitaka Shingaya,[‡] Kasturi Vimalanathan,[†] Tomonobu Nakayama,[*,‡] and Colin L. Raston[*,†]

[†]Flinders Institute for Nanoscale Science and Technology, College of Science and Engineering, Flinders University, Adelaide, SA 5001, Australia

[§]Physics Department, Faculty of Science, Taibah University, Almadinah Almunawarrah 42353, Saudi Arabia

[‡]International Center for Materials Nanoarchitectonics (WPI-MANA), National Institute for Materials Science (NIMS), Tsukuba, Ibaraki 305-0044, Japan

Supporting Information

ABSTRACT: The curvature in coiled single-walled carbon nanotubes (SWCNTs) rings impacts on their properties relative to straight CNTs, but the availability of such rings is limited. This has been addressed in developing a continuous flow method for fabricating coiled SWCNTs rings in high yield (80%) using a vortex fluidic device (VFD), in the absence of any toxic chemicals and surfactants. The VFD thin film microfluidic platform has a rapidly rotating angled glass tube with the processed liquid driven up and out of the tube. Magnetic force microscopy (MFM) established that the magnetic interaction of the resulting rings is strongly dependent on the thickness of the coiled SWCNT rings.

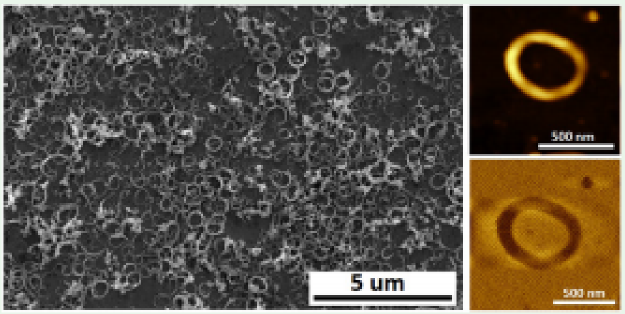

KEYWORDS: *coiled single-walled carbon nanotubes, magnetic interactions, vortex fluidic device, magnetic force microscopy, scalability, phase shift*

INTRODUCTION

Carbon nanomaterials have gained significant interest from the scientific community due to their unique physical and chemical properties.[1,2] Single-walled carbon nanotube (SWCNT) rings in particular, composed of individual or bundled (coiled) SWCNTs, have been a recent area of interest due to their unique morphology. Its high curvature and associated disorder results in novel mechanical, electronic, and magnetic properties compared to pristine straight SWCNTs.[3−5] Coiled SWNCT rings have potential in diverse applications, for example, in small electromagnetic devices and flexible electronics. The many theoretical and experimental studies based on coiled SWCNT rings include investigating the persistent of current flow through the walls of the rings, studying their magnetic response, and investigating the surface modes based on the engendered field distribution and electromagnetic energy confinement.[6,7] In addition, because of the available charge free space in their interior cavity,[8] coiled SWCNTs offer the ability to encapsulate cells[9] and metal chains such as Fe, Au, and Cu.[10]

Several strategies have been used to fabricate coiled SWCNT rings, including chemical vapor deposition (CVD),[11,12] laser ablation,[13,14] and synthesis from preformed SWCNTs involving ultrasonication,[15−17] organic reactions,[18,19] and a templated approach to bend SWCNTs.[15,20,21] However, these techniques suffer from various limitations, among them being difficulties in scaling the process, the use of harsh and toxic chemicals, long processing times, and high-temperature processing. We have previously reported the synthesis of toroidal structures of SWCNTs of various morphologies using a microfluidic platform, the vortex fluidic device (VFD) in the confined mode (small aliquot processing).[22] The method involved the use of a binary solvent system of toluene and water to afford rings of different morphologies that were stable and devoid of surfactants. It is noteworthy that scaling up using this confined mode approach is deemed problematic for large-scale applications. Since our earlier work, we have now further developed the use of the VFD for fabricating coiled SWCNT rings with scalability incorporated into the process, operating under continuous flow processing and systematically studied the magnetic responses of the rings using magnetic force microscopy (MFM).

The VFD is a relatively new and versatile thin film microfluidic platform with a number of applications in addition to forming SWCNT rings,[22] including slicing and controlling the lengths of CNTs while irradiating with a pulsed laser,[23,24]

Received: June 14, 2019
Accepted: July 19, 2019
Published: July 19, 2019

DOI: 10.1021/acsanm.9b01135
ACS Appl. Nano Mater. 2019, 2, 5282−5289

Supporting Information

High Yielding Fabrication of Magnetically Responsive Coiled Single Walled Carbon Nanotube Under Flow

Thaar M. D. Alharbi, [†, §] Yoshitaka Shingaya, [‡] Kasturi Vimalanathan, [†]
Tomonobu Nakayama [‡, *] and Colin L Raston [†, *]

[†] Flinders Institute for NanoScale Science and Technology, College of Science and Engineering, Flinders University, Adelaide SA 5001, Australia email: colin.raston@flinders.edu.au

[§] Physics Department, Faculty of Science, Taibah University, Almadinah Almunawarrah 42353, Saudi Arabia

[‡] International Center for Materials Nanoarchitectonics (WPI-MANA), National Institute for Materials Science (NIMS), Tsukuba, Ibaraki 305-0044, Japan

[*]Corresponding authors:

Tel: +61 8 82017958 E-mail address: colin.raston@flinders.edu.au (Colin Raston)

E-mail address: NAKAYAMA.Tomonobu@nims.go.jp (Tomonobu Nakayama)

Chapter Five

Shear stress mediated scrolling of graphene oxide

Thaar M. D. Alharbi[1, 2], David Harvey [1], Ibrahim K. Alsulami [1], Nazila Dehbari [1], Xiaofei Duan [3],
Robert N. Lamb [3], Warren D. Lawrance [1], Colin L Raston [2*]

[1] Flinders Centre for NanoScale Science & Technology, College of Science and Engineering, Flinders University, Adelaide SA 5001, Australia
[1]College of Science and Engineering, Flinders University, Adelaide SA 5001, Australia
[2] Physics Department, Faculty of Science, Taibah University, Almadinah Almunawarrah, Saudi Arabia
[3] School of Chemistry, TrACEES Platform, The University of Melbourne, Parkville, VIC 3010, Australia

This study was published in ***Carbon**,* Year 2018 137, 419-424. The first page of the publication and SI are attached.

Author contributions: **TA** performed all the VFD and most characterization experiments and data analysis, and wrote all the primary content. **DH** helped with the TGA measurements. **IA** helped on some VFD experiments. **ND** performed XPS measurements at Flinders University. **XD** and **RL** performed XPS measurements at The university of Melbourne. **WL** and **CR** supervised and coordinated the project and helped on the research directions and plan, and the final revision of the manuscript. All of the co-authors assisted with the revision of the manuscript before and during the publication process.

5.1. Abstract

Graphene oxide scrolls (GOS) are fabricated in high yield from a colloidal suspension of graphene oxide (GO) sheets under shear stress in a vortex fluidic device (VFD) while irradiated with a pulsed laser operating at 1064 nm and 250 mJ. This is in the absence of any other reagents with the structure of the GOS established using powder X-ray diffraction, thermogravimetric analysis, differential scanning calorimetry, X-ray photoelectron spectroscopy, Raman spectroscopy, transmission electron microscopy, atomic force microscopy and scanning electron microscopy.

Keywords

Graphene oxide scrolls; Shear stress; Laser irradiation; Vortex fluidics

Graphical Abstract

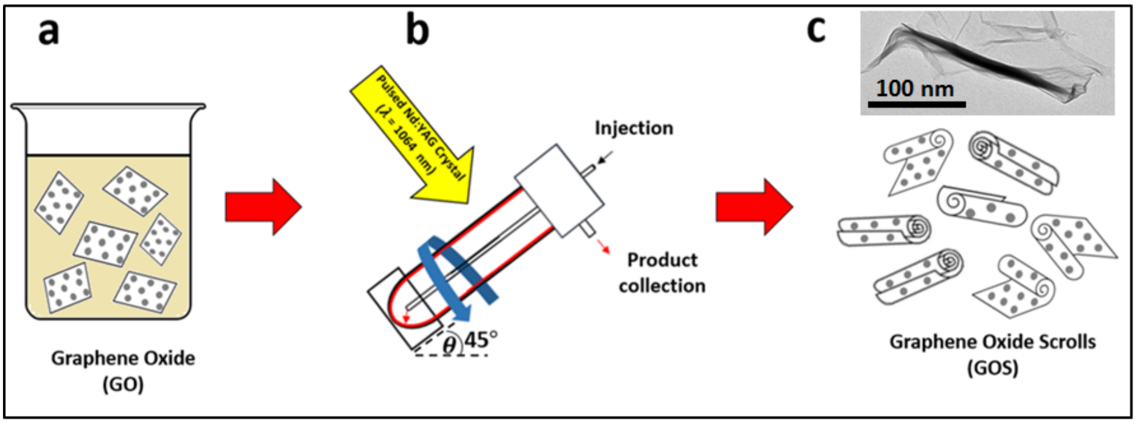

5.2. Introduction

In recent years, graphene scrolls have attracted attention as a novel one dimensional (1D) tubular topology materials derived from rolling up a 2D sheet of ubiquitous graphene. Graphene and graphene oxide (GO) scrolls have properties akin to other carbon nano-materials, including high thermal and electrical conductivities and excellent mechanical properties [1-2], with potential in a number of applications. These include hydrogen storage [3-4], supercapacitors [5-7], batteries [8-9], sensors [10] and electronic devices [11-12]. However, gaining access to graphene scrolls has proved challenging, not only for graphene, but also for graphene oxide and reduced graphene oxide.

Graphene scrolls are accessible directly from graphite using a spinning disc processor (SDP) [13], via sonication of graphite intercalation compounds [14] and from preformed graphene sheets in isopropyl alcohol [15]. Graphene oxide scrolls (GOS) have been prepared from graphene oxide using Lyophilization methods [16], microwave irradiation of graphene oxide [17] and a Langmuir–Blodgett approach, also from preformed graphite oxide [18]. Fabricating such scroll structures from graphene or graphene oxide usually suffers from limitations, including low yield, and using harsh chemicals and energy intensive high temperature and sonication processing, with long processing times. In the present research, we have developed a facile method for the synthesis of GOS from GO sheets in aqueous solution, under high shear stress in a vortex fluidic device (VFD) [19]. This dynamic thin film microfluidic platform has an angled tube rapidly rotating, with the angular dependence important in a number of applications. Within the thin film, typically below ca 500 μm thick, shear stress develops along with pressure waves which can mediate a number of biochemical, chemical and materials transformations [19]. The VFD can be operated in the so called confined mode which is suited for small scale processing, and under continuous flow mode. The latter is an attractive feature of the device for addressing scalability of any processing at the inception of the science. Here jet feeds deliver reagents into the inclined rapidly rotating tube, which is typically a 20 mm OD borosilicate glass or quartz tube.

The VFD is a versatile microfluidic platform with a number of applications, including slicing of single, double and multi-walled carbon nanotubes [20], protein folding [21], enhancing enzymatic reactions [22], protein immobilization [23], fabricating C_{60} tubules using water as an anti-solvent against toluene [24], exfoliation of graphite and boron nitride [25], growth of palladium and platinum nano-particles on carbon nano-onions [26], probing the structure of self-organized systems, and controlling chemical reactivity and selectivity [27].

In an earlier study we developed the use of a SPD, which by necessity operates under continuous flow, for preparing graphene scrolls directly from graphite, albeit in only 1% yield [13]. The mechanism of this simultaneous exfoliation and scroll formation is understood on a theoretical basis, with a graphene sheet lifting up and bending back under shear, then contacting the upper surface of this graphene sheet, as a stable transition state [13]. Further bending back then leads to spontaneous scroll formation [13]. We hypothesised that GO dispersed in solution has the potential to form scrolls under shear as a shape with the least resistance to shear stress. However, these scrolls will not be packed at the van der Waals limit between carbon atoms between successive turns of the scroll because of the high levels of defects and oxygenation. In contrast, graphene scrolls generated from graphite using a SDP have successive layers of carbon atoms at the van der Waals limit, at distances similar to the distances between layers in graphite itself. We also hypothesised that irradiation of GO under high shear using a pulsed NIR laser may facilitate scroll formation. This is based on the expected increased flexibility of the GO sheets with high induced vibrational energy. There is also potential for a reduction in site defects of the GO on absorption of laser light at 1064 nm, as has been established during slicing of carbon nanotubes in the VFD at the same wavelength [20].

In the present study, we systematically explored the different processing parameter space of the VFD for generating scrolls of GO dispersed in water, along with varying the laser power and the choice of solvent, including isopropyl alcohol (IPA) as a solvent that has been used in forming graphene scrolls [15], and which is environmentally friendly. Further optimization involved recycling the collected solution, but there was little change to the nature of the product (Figure S6. Supplementary Information).

5.3. Experimental

5.3.1. Chemicals and materials

Graphene oxide sheets (GO) (average sheet size: ~ 5 µm in cross section) was synthesized by a modified Hummer's method and purchased from Sigma Aldrich and Carbon Solution, with both product giving similar results.

5.3.2. Preparation of GOS

The as-received GO was dispersed in water at a number of different concentrations with each solution sonicated for 30 minutes to afford a black stable dispersion, noting that no scrolls were observed after sonication (Figure 5. 2a-c), prior to processing in the VFD under the described conditions, under a continuous flow rate of 0.45 mL/min in a rotating quartz glass tube 20 mm OD diameter and 18.5 cm long inclined at 45°. Optimal parameters for GOS formation were 4k rpm rotational speed, laser power 250 mJ and 0.2 mg/mL concentration of GO in water. The processing involved delivering a suspension of GO to the hemispherical base of the tube in the VFD with the resulting thin film irradiated by a 5 nanosecond pulsed Q-switch Nd: YAG laser operating at 1064 nm, with an 8 mm diameter laser beam and a repetition rate of 10 Hz.

5.3.3. Characterization

The GOS were characterized by scanning electron microscopy (SEM) performed using a FEI Quanta 450 High Resolution Field Emission SEM, with a voltage of 10 kV, and working distance of 10 mm, Atomic force microscopy (AFM) – (Nanoscope 8.10 tapping mode), Transmission electron microscopy (TEM) was conducted on a TECNAI 20 microscope operated at 120 and 200 kV. Raman measurements were recorded at an excitation wavelength of 532 nm (≤ 5mW) at room temperature. X-ray powder diffraction (XRD) data were collected using a Bruker Advanced D8 diffractometer (capillary stage) using Cu Kα radiation (λ= 1.5418 Å, 50 kW/40 mA, $2\theta = 5 – 80°$). Samples for SEM and Raman analysis were prepared on clean silicon wafers. The thermogravimetric analysis (TGA) and differential scanning calorimetry (DSC) measurements were recorded on a Perkin Elmerat operating at a heating rate of 3 C^o/min under a nitrogen gas flow. X-ray photoelectron spectroscopy (XPS) data was acquired using a Kratos Axis ULTRA X-ray Photoelectron Spectrometer incorporating a 165 mm hemispherical electron energy analyser. The incident radiation was monochromatic Al Kα X-rays (1486.6 eV) at 150 W (15 kV, 15 ma). Survey (wide) scans were taken at an analyser pass energy of 160 eV and multiplex (narrow) high resolution scans at 20eV. Scanned area is about 0.8 mm x 0.3 mm and the depth is less than 10 nm (volume is approx. 2400 □m^3). Survey scans were carried out over 1200-0 eV binding energy range with 1.0 eV steps and a dwell time of 100 ms. Narrow high-resolution scans were run with 0.05 ev steps and 250 ms dwell time. Base pressure in the analysis chamber was $1.0x10^{-9}$ torr and during sample analysis $1.0x10^{-8}$ torr.

5.4. Results and discussion

5.4.1. Optimisation of fabrication of GOS

Details of the processing for transforming 2D GO sheets into 1D tubular like GOS under shear stress within a VFD are summarised in Figure 5. 1 As received GO was readily dispersed in water as a stable uniform colloidal solution, which is made possible by the hydrophilic groups on the surface of the 2D sheets [6, 18]. Figure 5. 1a schematically shows flat sheets of GO, before processing in the VFD, with Figure 5. 1b showing the salient features of the VFD which houses a 20 mm OD diameter quartz tube, 18.5 cm in length, inclined at 45°, which is rapidly rotated with the solution irradiated with a pulsed laser operating at 1064 nm (see below discussions on optimisation studies). Figure 5. 1c schematically shows partially and fully scrolled GO after processing in the VFD, in accordance with the TEM images (see below).

Establishing the optimum conditions for forming GOS involved systematically exploring the parameter space of the VFD operating under continuous flow. This involved varying the rotational speed from 2k rpm to 8k rpm, followed by using different laser power, 250 mJ, 400 mJ and 600 mJ, at different flow rates of 0.1, 0.45, 1.0 and 1.5 mg/mL, and varying the concentration of GO, 0.1, 0.3 and 0.5 mg/mL. In addition, isopropyl alcohol (IPA), as an alternative solvent which is readily removed in vacuo post processing, was also tested for GOS formation, with GO at 0.2 mg/mL, for different rotational speeds (See Supplementary Information for details). A flow rate of 0.45 mL/min has been established as a good starting point for a number of applications of the VFD with the tube fixed at 45° tilt angle which is the optimal angle for all processing using the VFD [19]. The optimised parameters for the highest conversion to GOS were 4k rpm with the pulsed laser operating at 250 mJ, for an aqueous suspension of GO at 0.2 mg/mL. Under these conditions there is no evidence for residual 2D GO sheets and thus the conversion to GOS or partial GOS is essentially quantitative. Varying these parameters resulted in samples with significantly less GOS and partial GOS, as judged using a number of characterisation techniques (see below).

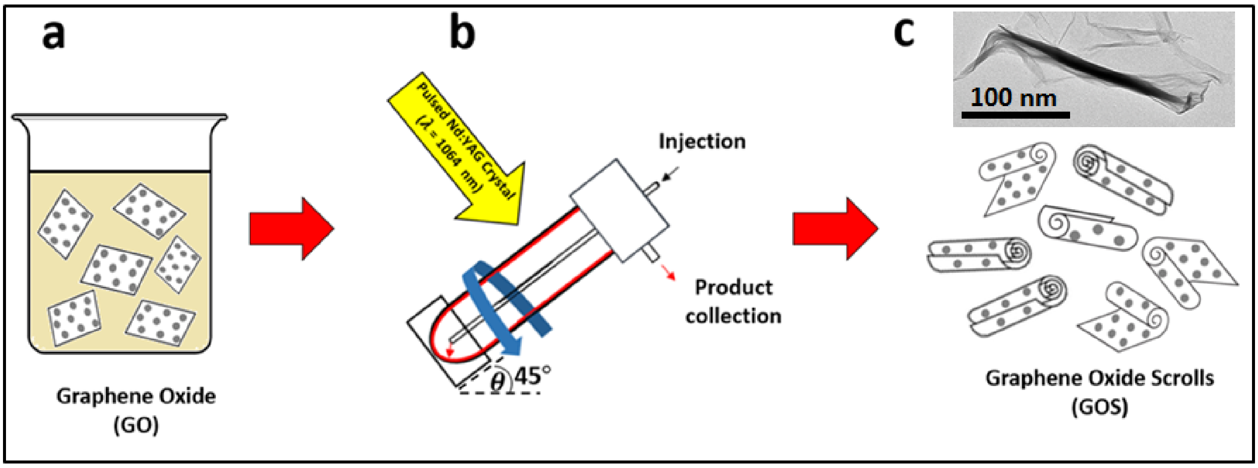

Figure 5. 1 Schematic illustration of the experimental procedure for fabricating GOS from GO sheets. (a) Solvated GO sheets before processing in the VFD. (b) Schematic of the experimental set up for the vortex fluidic device (VFD) and Nd:YAG pulsed laser irradiation (operating at 1064 nm with the optimised power at 250 mJ) and rotational speed at 4k rpm. (c) GOS after processing in the VFD, inset is TEM image for GOS.

5.4.2. Characterisation of the GOS

The structure of GOS was initially examined using transmission electron microscopy (TEM), atomic force microscopy (AFM) and scanning electron microscopy (SEM). Figure 5. 2 shows TEM and AFM images of GO before processing and after VFD processing, establishing the formation of GOS. TEM and AFM images in Figure 5. 2 a-c are for graphene GO before processing in the VFD, showing the presence of flat surfaces of GO of different sizes, which are one or more layers in thickness, according to the height profiles in Figure 5. 2d. In addition, TEM and AFM were used to establish the nature of individual scrolls, Figure 5. 2 e-k. Here the tubular structure of the GOS is revealed, with different diameters ranging from 500 nm to a few micrometres. While the shape of GOS are closely uniform, the differences in diameter presumably reflects the presence of different sizes of GO sheets in the as received material. TEM images establish that the GOS are composed of single scrolled GO sheets, or a relatively low number of graphene oxide layers, which is consistent with direct scrolling of the as received material.

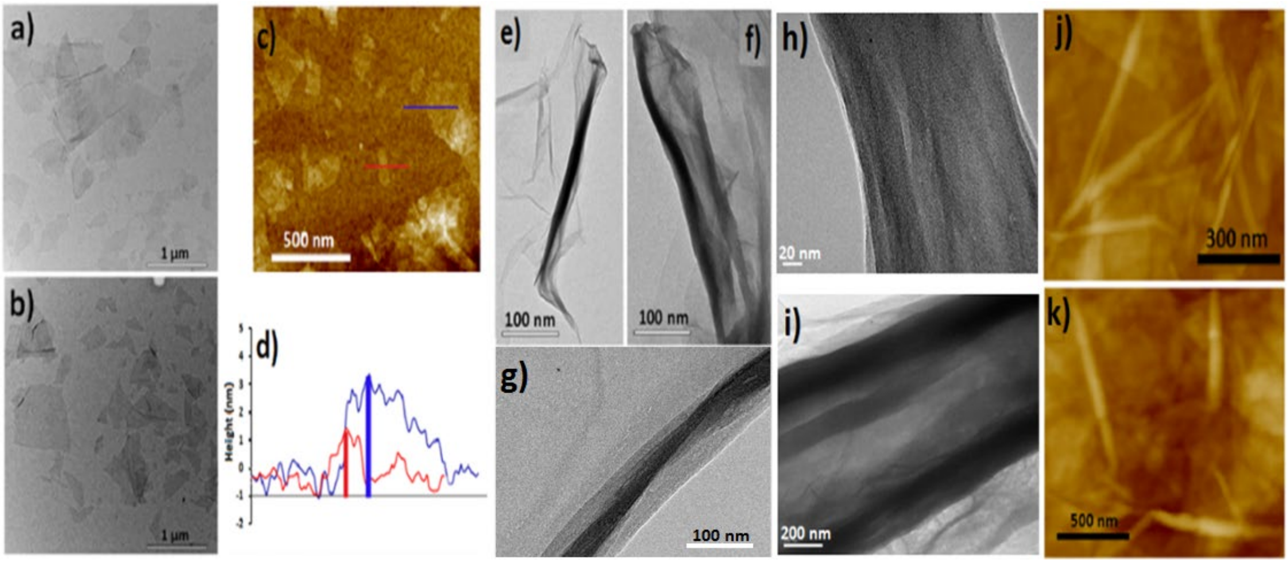

Figure 5. 2 (a-b) TEM images and (c) AFM images with height profiles in (d) of as-received GO (before processing). (e-i) TEM and (j-k) AFM images of GOS at different magnification after processing in the VFD at 4k rpm rotational speed, tilt angle 45° and a flow rate of 0.45 mL/min, coupled with laser irradiation at 250 mJ.

Further characterisation of the structure of these scrolls used SEM, at different magnification. SEM images of GOS at a low magnification are shown in Figure 5. 3 a-c, highlighting the uniformity of the GOS material, and thus high conversion of GO to the scrolls. For the optimised speed and concentration now in the absence of laser irradiation, as a control experiment, scroll formation is consistently minimal (Figure S2 e-f, Supplementary Information). Overall, the results show that GOS of uniform structure are fabricated using the VFD while irradiated with a pulsed laser, at the optimised parameters.

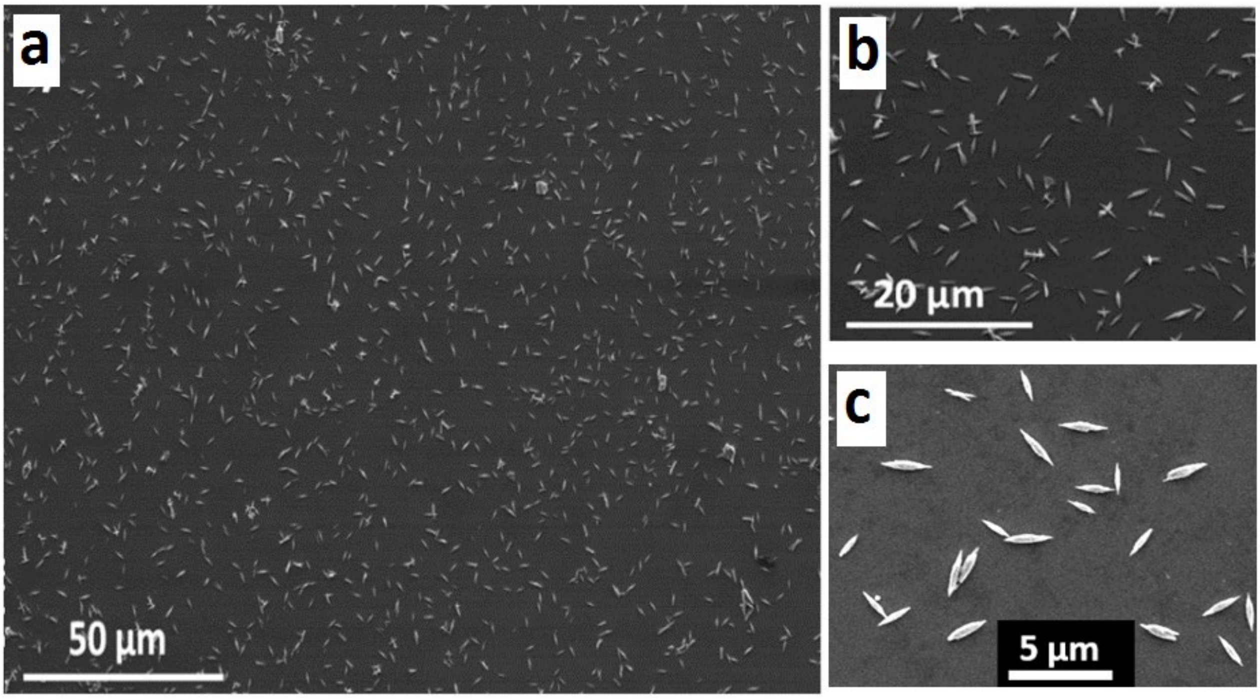

Figure 5. 3 SEM images of GOS at different magnifications after processing in the VFD at 4k rpm rotational speed, under continuous flow mode, tilt angle 45° and a flow rate of 0.45 mL/min, coupled with laser irradiation at 250 mJ.

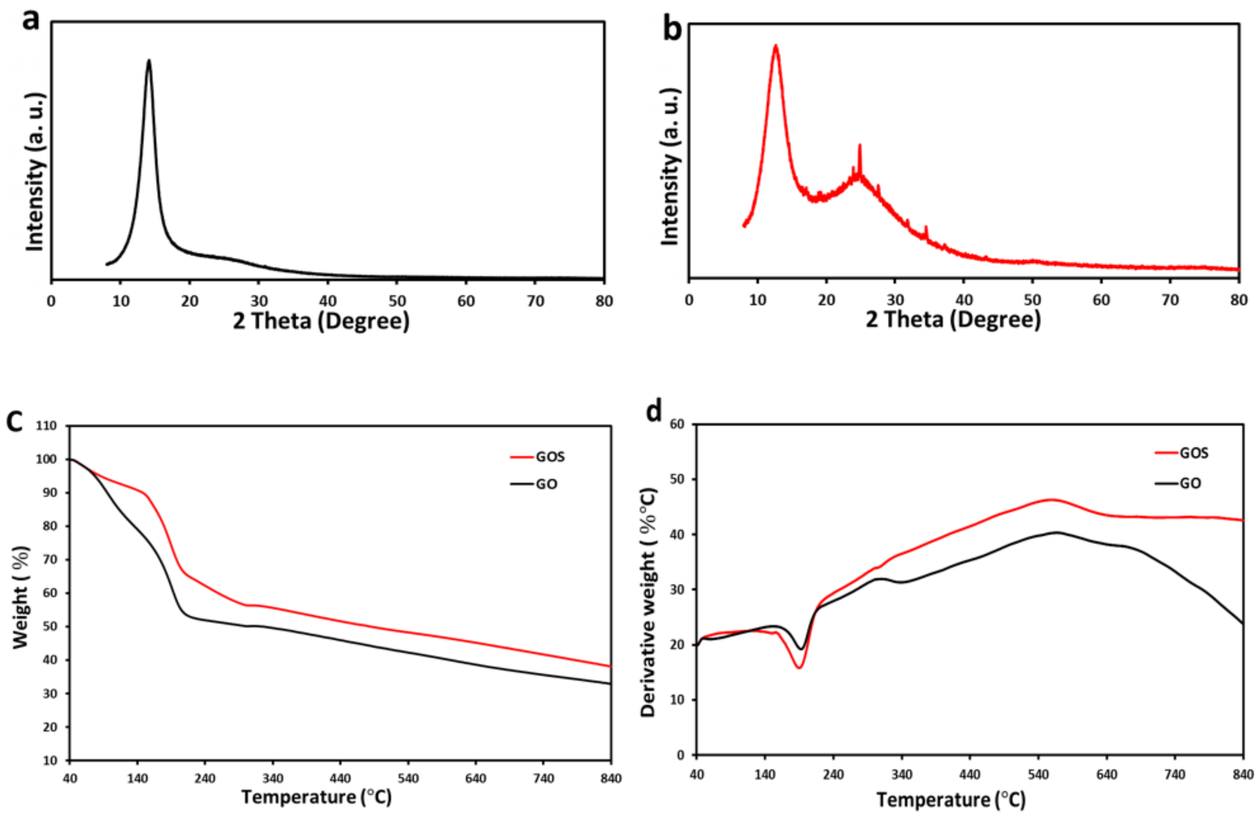

Figure 5. 4 XRD patterns of (a) as received GO and (b) GOS in the VFD at rotational speed at 4k rpm, under continuous flow mode, tilt angle 45°, with flow rate 0.45 mL/min, coupled with laser irradiation at 250 mJ. (c) TGA and (d) DSC curves of as received GO and GOS at scan rate of 10 °C per minute in a nitrogen atmosphere.

In order to further evaluate the quality of the GOS, x-ray powder diffraction (XRD), thermogravimetric analysis (TGA) and differential scanning calorimetry (DSC) were investigated. Figure 5. 4a displays XRD for as received GO which has a dominant diffraction peak corresponding to a d-spacing of 8.0818Å, attributed to the (001) plane of the material, as established elsewhere for GO [1, 16]. Figure 5. 4b reveals that GOS has two peaks, the peak present for as received GO, and another break peak at a d-spacing of 4.15302 Å which is characteristic of the (002) plane, and is consistent with some reduction of the GO in forming the GOS, as noted for laser irradiation of GO in the absence of VFD processing [28-29].

The TGA of GOS and as received GO, recorded under an atmosphere of nitrogen are shown in Figure 5. 4c. GO has around 30% mass loss up to150 ◦C and from 160 to 280 ◦C there is a 10% mass loss. This is due to loss of physisorbed water molecules as well as the removal of the oxygen-containing functional groups, as reported in the literature [30]. There is gradual mass loss beyond 250 ◦C, corresponding to further removal of the functional groups [30]. For GOS, there is a mass loss around 28% up to 300 ◦C, which is indicative of removal of some oxygen-containing groups during the VFD processing in the presence of the pulsed laser, and this is consistent with the XPS results (see below). Overall, the mass losses in GOS is lower than that of GO. This is consistent with removal of some of the functional groups during the VFD/laser processing. In this context, we note that processing of CNTs in the VFD while irradiated with a pulsed laser at 1064 nm results in a reduction in the defects along the tubes, presumably with a loss of oxygen functional groups [20]. Figure 5. 4d shows the DSC curves for GO and GOS, which revealed a narrow exothermic peak at about 196 ℃ for GO, whereas in GOS there is an exothermic peak at 190℃. The results are consistent with some oxygen-containing groups being removed during laser irradiation, analogous to that found in the literatures [30-32].

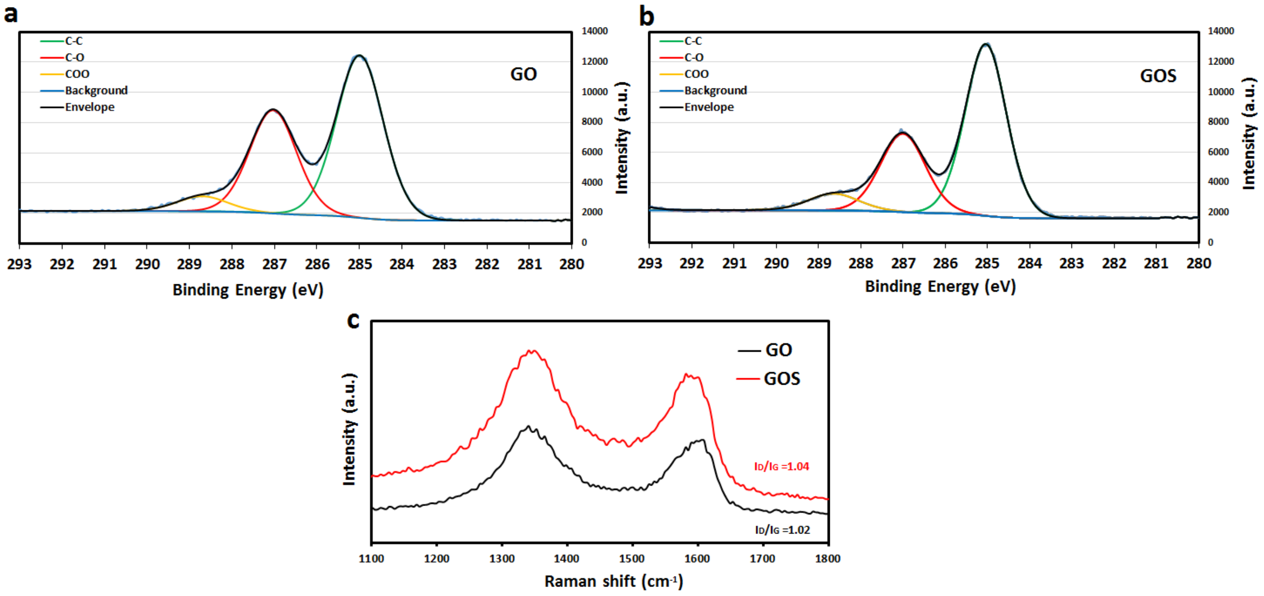

Figure 5. 5 (a) XPS C 1s spectra of as received GO before VFD processing and (b) GOS formed in the VFD at 4k rpm rotational speed, under continuous mode (flow rate 0.45 mL/min), tilt angle 45° while irradiated with a pulsed laser at 1064 nm and 250 mJ, and (c) Raman spectra of GO and GOS (prepared as for (b)).

In order to further analyse the structure of GOS, Raman spectroscopy and X-ray photoelectron spectroscopy (XPS) were recorded for as received GO and GOS, Figure 5. 5, along with processing GO in the VFD in the absence of laser irradiation (Figure S7, Supplementary Information). There is some change in the Raman spectra recorded using a 532 nm excitation laser, from GO to GOS formed in the VFD coupled with the pulsed laser irradiation, Figure 5. 4c. The D band is a defect-related mode and the G band is associated with the graphitic hexagon- pinch mode [33]. For GO, the G band is at 1600 cm^{-1} which corresponds to ordered *sp*^{2} bonded carbon, and the D band is at 1337 cm^{-1}, which is attributed to edge planes and disordered structures. For GOS, the Raman spectrum shows the presence of G and D bands at 1584 and 1337 cm^{-1}, respectively. It is noteworthy that the position of the G band for GOS is shifted by ≈10 cm^{-1} compared to the as received GO sheets, which is consistent with reduced disorder in the graphitic materials [34-35]. Analysis of the Raman spectra usually involves a comparison between the ratio of intensity of the G band and D bands. The D/G intensity ratio (ID/ IG) before (GO) and after scroll formation (GOS) are 1.02 and 1.04 respectively, whereas the ratio for processed material in the absence of laser was 1.06. While the difference is not dramatic, the results suggests that in forming GOS, some oxygen functional groups have been removed. This is likely to result in more $\pi-\pi$ interactions [29, 35-36].

X-ray photoelectron spectroscopy (XPS) was used to determine changes in the oxygen-containing carbonaceous functional groups (C–OH, C–O and COO) associated with VFD processing while irradiated with a pulsed laser. The high resolution XPS C*1s* spectra of GO and GOS are shown in Figure 5. 4a, b. The amount of C–C component in GO, estimated at ca 57.6 atomic percentage (at%), increased slightly to 60.5 at% in GOS. In addition, the amount of C–O component in GO, estimated at 36.6%, decreased to 30.3% in GOS. The C/O atomic ratio increased from 1.5 for GO to 2 for GOS. The results suggest that some of the oxygen-containing functional groups have been removed during scroll formation in the VFD in the presence of pulsed laser irradiation. More detailed data is presented in Table S1, 2. Supplementary Information. The XPS results are consistent with Raman spectroscopic data, with loss of some oxygen functional groups on forming GOS [29, 37]. XPS was also measured for processed GO in the absence of laser irradiation, with the C–C component estimated at 57.9% which is almost the same as the starting material, while the C–O component was estimated at 33.0 % which is less than that the 36.6% for as received GO (Table S1, 3. Supplementary Information).

The formation of GOS from GO sheets arises from the shear stress in the complex fluid dynamics in the thin film in the VFD [19]. At 45° tilt angle, the liquid is accelerated up the tube and pulled down by gravity, and there are rotational speed induced pressure waves [19-22]. Coupling shear and pressure waves with induced vibrational energy in the GO sheets upon laser irradiation presumably facilitates the formation of the scrolls. Moreover, it would account for no further improvement in the degree of scrolling for each GO sheet upon recycling the colloidal suspension of the GOS back through the VFD at the optimised processing parameters, at the same pressure waves present at 4k rpm. We note that in an earlier study the VFD was used to exfoliate graphite into single layer graphene sheets without the formation of any scrolls [19], in the absence of laser irradiation. Thus any loss of oxygen functionality at the edge of the GO sheets in the present study, under optimised VFD processing and laser irradiation is unlikely to facilitate scroll formation.

5.5. Conclusions

We have established an essentially quantitative formation of GOS directly from GO in water in a VFD microfluidic thin film processing platform while irradiated with a NIR pulsed laser, with the product devoid of 2D GO sheets. Importantly the processing is under continuous flow such that it can be scaled up, limited by the volume that can be delivered through a single VFD unit for a concentration of 0.2 mg/mL. Scale up beyond this is possible for a number of VFD units operating in parallel or in a single large VFD. The versatility of the VFD is further highlighted with this new application of the device, with the operating parameters readily systematically varied in arriving at the optimised settings, under continuous flow. The residence time of liquid entering the VFD and exiting at the top of the rotating tube is close to 11 minutes for a flow rate of 0.45 mL/min, such that the processing time for small volumes of water containing dispersions of GOS is short. This new strategy for generating GOS on demand, with the ability to scale up under continuous flow sets the scene for developing the applications of GOS, with synthetically useful quantities ca. 50 mg being readily prepared in a single VFD.

5.6. Acknowledgements

T.M.D.A. thanks Taibah University (Ministry of Education, Saudi Arabia) for funding his scholarship. The authors thank support of this work by the Australian Research Council, the Government of South Australia, and thanks the Australian Microscopy & Microanalysis Research Facility (AMMRF) and the Australian National Fabrication Facility (ANFF) for accessing microscopic facilities.

5.7. References

1. Yang, Y.; Zhang, X.; Wang, H.; Tang, H.; Xu, L.; Li, H.; Zhang, L., Preparation of Nanoscrolls by Rolling up Graphene Oxide–Polydopamine–Au Sheets using Lyophilization Method. *Chem. - Asian J.,* **2016,** *11*, 1821-1827.
2. Wang, X.; Yang, D.-P.; Huang, G.; Huang, P.; Shen, G.; Guo, S.; Mei, Y.; Cui, D., Rolling up graphene oxide sheets into micro/nanoscrolls by nanoparticle aggregation. *J. Mater. Chem.,* **2012,** *22*, 17441-17444.
3. Shi, X.; Pugno, N. M.; Gao, H., Mechanics of carbon nanoscrolls: a review. *Acta. Mech. Solida. Sin.,* **2010,** *23*, 484-497.
4. Mpourmpakis, G.; Tylianakis, E.; Froudakis, G. E., Carbon nanoscrolls: a promising material for hydrogen storage. *Nano lett.,* **2007,** *7*, 1893-1897.
5. Zeng, F.; Kuang, Y.; Liu, G.; Liu, R.; Huang, Z.; Fu, C.; Zhou, H., Supercapacitors based on high-quality graphene scrolls. *Nanoscale,* **2012,** *4*, 3997-4001.
6. Fan, T.; Zeng, W.; Niu, Q.; Tong, S.; Cai, K.; Liu, Y.; Huang, W.; Min, Y.; Epstein, A. J., Fabrication of high-quality graphene oxide nanoscrolls and application in supercapacitor. *Nanoscale Res. Lett.,* **2015,** *10*, 192.
7. Zhou, W.; Liu, J.; Chen, T.; Tan, K. S.; Jia, X.; Luo, Z.; Cong, C.; Yang, H.; Li, C. M.; Yu, T., Fabrication of Co 3 O 4-reduced graphene oxide scrolls for high-performance supercapacitor electrodes. *Phys. Chem. Chem. Phys.,* **2011,** *13*, 14462-14465.
8. Yan, M.; Wang, F.; Han, C.; Ma, X.; Xu, X.; An, Q.; Xu, L.; Niu, C.; Zhao, Y.; Tian, X., Nanowire templated semihollow bicontinuous graphene scrolls: designed construction, mechanism, and enhanced energy storage performance. *J. Am. Chem. Soc.,* **2013,** *135*, 18176-18182.
9. Li, X.; Zhang, Y.; Li, T.; Zhong, Q.; Li, H.; Huang, J., Graphene nanoscrolls encapsulated TiO 2 (B) nanowires for lithium storage. *J. Power Sources,* **2014,** *268*, 372-378.
10. Li, H.; Wu, J.; Qi, X.; He, Q.; Liusman, C.; Lu, G.; Zhou, X.; Zhang, H., Graphene oxide scrolls on hydrophobic substrates fabricated by molecular combing and their application in gas sensing. *Small,* **2013,** *9* , 382-386.
11. Sharifi, T.; Gracia-Espino, E.; Barzegar, H. R.; Jia, X.; Nitze, F.; Hu, G.; Nordblad, P.; Tai, C.-W.; Wågberg, T., Formation of nitrogen-doped graphene nanoscrolls by adsorption of magnetic γ-Fe2O3 nanoparticles. *Nature Commun.,* **2013,** *4*, 2319.
12. Feng, K.; Tang, B.; Wu, P., "Evaporating" graphene oxide sheets (GOSs) for rolled up GOSs and its applications in proton exchange membrane fuel cell. *ACS Appl. Mater. Interfaces,* **2013,** *5*, 1481-1488.
13. Chen, X.; Boulos, R. A.; Dobson, J. F.; Raston, C. L., Shear induced formation of carbon and boron nitride nano-scrolls. *Nanoscale,* **2013,** *5*, 498-502.
14. Savoskin, M. V.; Mochalin, V. N.; Yaroshenko, A. P.; Lazareva, N. I.; Konstantinova, T. E.; Barsukov, I. V.; Prokofiev, I. G., Carbon nanoscrolls produced from acceptor-type graphite intercalation compounds. *Carbon,* **2007,** *45*, 2797-2800.
15. Xie, X.; Ju, L.; Feng, X.; Sun, Y.; Zhou, R.; Liu, K.; Fan, S.; Li, Q.; Jiang, K., Controlled fabrication of high-quality carbon nanoscrolls from monolayer graphene. *Nano lett.,* **2009,** *9*, 2565-2570.
16. Xu, Z.; Zheng, B.; Chen, J.; Gao, C., Highly efficient synthesis of neat graphene nanoscrolls from graphene oxide by well-controlled lyophilization. *Chem. Mater.,* **2014,** *26*, 6811-6818.
17. Quintana, M.; Grzelczak, M.; Spyrou, K.; Calvaresi, M.; Bals, S.; Kooi, B.; Van Tendeloo, G.; Rudolf, P.; Zerbetto, F.; Prato, M., A simple road for the transformation of few-layer graphene into MWNTs. *J. Am. Chem. Soc.,* **2012,** *134*, 13310-13315.
18. Gao, Y.; Chen, X.; Xu, H.; Zou, Y.; Gu, R.; Xu, M.; Jen, A. K.-Y.; Chen, H., Highly-efficient fabrication of nanoscrolls from functionalized graphene oxide by Langmuir–Blodgett method. *Carbon,* **2010,** *48*, 4475-4482.

19. Britton, J.; Stubbs, K. A.; Weiss, G. A.; Raston, C. L., Vortex Fluidic Chemical Transformations. *Chem.- Eur. J.,* **2017**, 23, 13270–13278.
20. Vimalanathan, K.; Gascooke, J. R.; Suarez-Martinez, I.; Marks, N. A.; Kumari, H.; Garvey, C. J.; Atwood, J. L.; Lawrance, W. D.; Raston, C. L., Fluid dynamic lateral slicing of high tensile strength carbon nanotubes. *Sci. Rep.,* **2016,** *6*, 22865.
21. Yuan, T. Z.; Ormonde, C. F. G.; Kudlacek, S. T.; Kunche, S.; Smith, J. N.; Brown, W. A.; Pugliese, K. M.; Olsen, T. J.; Iftikhar, M.; Raston, C. L., Shear-Stress-Mediated Refolding of Proteins from Aggregates and Inclusion Bodies. *ChemBioChem,* **2015,** *16*, 393-396
22. Britton, J.; Meneghini, L. M.; Raston, C. L.; Weiss, G. A., Accelerating Enzymatic Catalysis Using Vortex Fluidics. *Angew. Chem.,* **2016,** *128*, 11559-11563.
23. Britton, J.; Raston, C. L.; Weiss, G. A., Rapid protein immobilization for thin film continuous flow biocatalysis. *Chem. Commun.,* **2016,** *52*, 10159-10162.
24. Vimalanathan, K.; Shrestha, R. G.; Zhang, Z.; Zou, J.; Nakayama, T.; Raston, C. L., Surfactant-free Fabrication of Fullerene C60 Nanotubules Under Shear. *Angew. Chem. Int. Ed.,* **2017,** *56*, 8398-8401.
25. Chen, X.; Dobson, J. F.; Raston, C. L., Vortex fluidic exfoliation of graphite and boron nitride. *Chem. Commun.,* **2012,** *48*, 3703-3705.
26. Yasin, F. M.; Boulos, R. A.; Hong, B. Y.; Cornejo, A.; Iyer, K. S.; Gao, L.; Chua, H. T.; Raston, C. L., Microfluidic size selective growth of palladium nano-particles on carbon nano-onions. *Chem. Commun.,* **2012,** *48*, 10102-10104.
27. Yasmin, L.; Chen, X.; Stubbs, K. A.; Raston, C. L., Optimising a vortex fluidic device for controlling chemical reactivity and selectivity. *Sci. Rep.,* **2013,** *3,* 2282.
28. Bo, Z.; Shuai, X.; Mao, S.; Yang, H.; Qian, J.; Chen, J.; Yan, J.; Cen, K., Green preparation of reduced graphene oxide for sensing and energy storage applications. *Sci. Rep.,* **2015,** *4*, 4684.
29. Huang, L.; Liu, Y.; Ji, L.-C.; Xie, Y.-Q.; Wang, T.; Shi, W.-Z., Pulsed laser assisted reduction of graphene oxide. *Carbon,* **2011,** *49*, 2431-2436.
30. Zhang, C.; Chen, M.; Xu, X.; Zhang, L.; Zhang, L.; Xia, F.; Li, X.; Liu, Y.; Hu, W.; Gao, J., Graphene oxide reduced and modified by environmentally friendly glycylglycine and its excellent catalytic performance. *Nanotechnology,* **2014,** *25*, 135707.
31. Li, H.; Zhu, G.; Liu, Z.-H.; Yang, Z.; Wang, Z., Fabrication of a hybrid graphene/layered double hydroxide material. *Carbon,* **2010,** *48*, 4391-4396.
32. Wu, J.; Shen, X.; Jiang, L.; Wang, K.; Chen, K., Solvothermal synthesis and characterization of sandwich-like graphene/ZnO nanocomposites. *Appl. Surf. Sci.,* **2010,** *256*, 2826-2830.
33. Dresselhaus, M. S.; Dresselhaus, G.; Saito, R.; Jorio, A., Raman spectroscopy of carbon nanotubes. *Phys. Rep.,* **2005,** *409*, 47-99.
34. Ferrari, A. C.; Robertson, J., Interpretation of Raman spectra of disordered and amorphous carbon. *Phys. Rev. B,* **2000,** *61*, 14095.
35. Amadei, C. A.; Stein, I. Y.; Silverberg, G. J.; Wardle, B. L.; Vecitis, C. D., Fabrication and morphology tuning of graphene oxide nanoscrolls. *Nanoscale,* **2016,** *8*, 6783-6791.
36. Suh, D. H., Formation of hexagonal boron nitride nanoscrolls induced by inclusion and exclusion of self-assembling molecules in solution process. *Nanoscale,* **2014,** *6*, 5686-5690.
37. Evlashin, S.; Dyakonov, P.; Khmelnitsky, R.; Dagesyan, S.; Klokov, A.; Sharkov, A.; Timashev, P.; Minaeva, S.; Maslakov, K.; Svyakhovskiy, S., Controllable Laser Reduction of Graphene Oxide Films for Photoelectronic Applications. *ACS Appl. Mater. Interfaces,* **2016,** *8*, 28880-28887.

Carbon 137 (2018) 419–424

Contents lists available at ScienceDirect

Carbon

journal homepage: www.elsevier.com/locate/carbon

Shear stress mediated scrolling of graphene oxide

Thaar M.D. Alharbi [a, b], David Harvey [a], Ibrahim K. Alsulami [a], Nazila Dehbari [a], Xiaofei Duan [c], Robert N. Lamb [c], Warren D. Lawrance [a], Colin L. Raston [a, *]

[a] *Flinders Institute for NanoScale Science & Technology, College of Science and Engineering, Flinders University, Adelaide, SA 5001, Australia*
[b] *Physics Department, Faculty of Science, Taibah University, Almadinah Almunawarrah, Saudi Arabia*
[c] *School of Chemistry, TrACEES Platform, The University of Melbourne, Parkville, VIC 3010, Australia*

ARTICLE INFO

Article history:
Received 5 March 2018
Received in revised form
16 April 2018
Accepted 20 May 2018
Available online 21 May 2018

Keywords:
Graphene oxide scrolls
Shear stress
Laser irradiation
Vortex fluidics

ABSTRACT

Graphene oxide scrolls (GOS) are fabricated in high yield from a colloidal suspension of graphene oxide (GO) sheets under shear stress in a vortex fluidic device (VFD) while irradiated with a pulsed laser operating at 1064 nm and 250 mJ. This is in the absence of any other reagents with the structure of the GOS established using powder X-ray diffraction, thermogravimetric analysis, differential scanning calorimetry, X-ray photoelectron spectroscopy, Raman spectroscopy, transmission electron microscopy, atomic force microscopy and scanning electron microscopy.

1. Introduction

In recent years, graphene scrolls have attracted attention as a novel one dimensional (1D) tubular topology materials derived from rolling up a 2D sheet of ubiquitous graphene. Graphene and graphene oxide (GO) scrolls have properties akin to other carbon nano-materials, including high thermal and electrical conductivities and excellent mechanical properties [1,2], with potential in a number of applications. These include hydrogen storage [3,4], supercapacitors [5–7], batteries [8,9], sensors [10] and electronic devices [11,12]. However, gaining access to graphene scrolls has proved challenging, not only for graphene, but also for graphene oxide and reduced graphene oxide.

Graphene scrolls are accessible directly from graphite using a spinning disc processor (SDP) [13], via sonication of graphite intercalation compounds [14] and from preformed graphene sheets in isopropyl alcohol [15]. Graphene oxide scrolls (GOS) have been prepared from graphene oxide using Lyophilization methods [16], microwave irradiation of graphene oxide [17] and a Langmuir–Blodgett approach, also from preformed graphite oxide [18]. Fabricating such scroll structures from graphene or graphene oxide usually suffers from limitations, including low yield, and using harsh chemicals and energy intensive high temperature and sonication processing, with long processing times. In the present research, we have developed a facile method for the synthesis of GOS from GO sheets in aqueous solution, under high shear stress in a vortex fluidic device (VFD) [19]. This dynamic thin film microfluidic platform has an angled tube rapidly rotating, with the angular dependence important in a number of applications. Within the thin film, typically below ca 500 μm thick, shear stress develops along with pressure waves which can mediate a number of biochemical, chemical and materials transformations [19]. The VFD can be operated in the so called confined mode which is suited for small scale processing, and under continuous flow mode. The latter is an attractive feature of the device for addressing scalability of any processing at the inception of the science. Here jet feeds deliver reagents into the inclined rapidly rotating tube, which is typically a 20 mm OD borosilicate glass or quartz tube.

The VFD is a versatile microfluidic platform with a number of applications, including slicing of single, double and multi-walled carbon nanotubes [20], protein folding [21], enhancing enzymatic reactions [22], protein immobilization [23], fabricating C_{60} tubules using water as an anti-solvent against toluene [24], exfoliation of graphite and boron nitride [25], growth of palladium and platinum nano-particles on carbon nano-onions [26], probing the structure of self-organized systems, and controlling chemical reactivity and selectivity [27].

---

* Corresponding author.
E-mail address: colin.raston@flinders.edu.au (C.L. Raston).

https://doi.org/10.1016/j.carbon.2018.05.040
0008-6223/

Supplementary Information for

Shear stress mediated scrolling of graphene oxide

Thaar M. D. Alharbi[1, 2], David Harvey [1], Ibrahim K. Alsulami [1], Nazila Dehbari [1], Xiaofei Duan [3], Robert N. Lamb [3], Warren D. Lawrance [1], Colin L Raston [1*]

[1] Flinders Centre for NanoScale Science & Technology, College of Science and Engineering, Flinders University, Adelaide SA 5001, Australia

[1]College of Science and Engineering, Flinders University, Adelaide SA 5001, Australia

[2] Physics Department, Faculty of Science, Taibah University, Almadinah Almunawarrah, Saudi Arabia

[3] School of Chemistry, TrACEES Platform, The University of Melbourne, Parkville, VIC 3010, Australia

---

[*] Corresponding author:

Tel: +61 8 82017958 E-mail address: colin.raston@flinders.edu.au (Colin Raston)

Chapter Six

Sub-micron moulding angled vortex fluid flow

Thaar M. D. Alharbi, [1,8] Matt Jellicoe, [1,8] Xuan Luo, [1,2,8] Kasturi Vimalanathan,[1] Ibrahim K. Alsulami,[1] Bediea AL Harbi,[1] Aghil Igder,[1,3] Xianjue Chen,[4] Keith A. Stubbs,[5] Justin M. Chalker,[1] Wei Zhang,[2] Ramiz A. Boulos,[1,6] Darryl B. Jones,[1] Jamie S. Quinton,[1] Stuart B. Dalzie[7] and Colin L. Raston[*1]

[1]Flinders Institute for Nanoscale Science and Technology, College of Science and Engineering, Flinders University, Bedford Park, S.A. 5042, Australia colin.raston@flinders.edu.au
[2]Centre for Marine Bioproducts Development, College of Medicine and Public Health, Flinders University, Adelaide, SA 5042, Australia.
[3]School of Engineering, Edith Cowan University, Joondalup, Perth, WA 6027, Australia.
[4]School of Chemistry, University of New South Wales, Sydney, NSW 2052, Australia.
[5]School of Chemistry and Biochemistry, The University of Western Australia, 35 Stirling Hwy, Crawley, W.A. 6009, Australia.
[6]BrightChem Consulting, Suite 16, 45 Delawney Street, Balcatta, WA 6021, Australia.
[7]Department of Applied Mathematics and Theoretical Physics, University of Cambridge, CB3 0WA, UK.
[8]Authors contributed equally to this work

In this chapter, the results of the study displayed and described below for the basis of a manuscript for submission for publication. Furthermore, as the research detailed here contains large Supplementary Information, and for reader convince, these have been placed in the Appendices of this thesis.

Author contributions; **T.M.D.A**. carried out graphene oxide experiments, **T.M.D.A.** and **I.K.A.** carried out the fullerene nano-cone experiments**, B.A.H.** and **T.M.D.A.** carried out the shear stress induced crystallisation of fullerene spicules and rods, **I.G.** carried out the polymer moulding experiments, **X.L.** carried out the BSA and MOF experiments, **M.J.** and **K.V.** carried out thermal imaging and mixing experiments, **M.J.** and **X.L.** determined film thickness, **X.C.** carried out the imaging experiments, **K.A.S., J.M.C., W.Z., S.B.D.** and **R.A.B.** contributed to the development of the experiments, **J.S.Q.** developed an understanding the dynamic equilibrium, **D.B.J.** developed an understanding of the forces in the thin films, and **C.L.R.** designed the VFD micofluidic platform, coordinated the research and developed the model for the fluid behaviour. All authors contributed to writing and editing the manuscript.

6.1. Abstract

Controlling organisation and forces in liquids under non-equilibrium conditions is fundamental for building complex systems and the function of living cells.[1] Shear stress in dynamic thin films, as in vortex fluidics, can be harnessed for generating non-equilibrium conditions, but the nature of the fluid flow is not understood. A rapidly rotating inclined tube in the vortex fluidic device (VFD) imparts shear stress (mechanical energy) into a thin film of liquid, depending on the physical characteristics of the liquid and rotational speed, ω, tilt angle, θ, and diameter of the tube.[2-7] Through understanding that the fluid exhibits resonance behaviour from the confining boundaries of the glass surface and the meniscus that determines the liquid film thickness, we have established that Coriolis forces and Faraday waves in the VFD result in specific topological fluid flow uniquely at a 45° tilt angle. These topologies have been established through materials processing, as circular flow normal to the surface of the tube, double helical flow across the thin film arising from the Faraday waves, and spicular flow, a transitional region where both effects contribute. The manifestation of flow patterns within the film have been observed by monitoring the mixing time, temperature profile, and film thickness against increasing ω. In addition, these flow patterns have unique signatures that enable the morphology of nanomaterials processed in the VFD to be predicted, for example in reversible scrolling, crumbling and unscrolling graphene oxide sheets. Shear stress induced crystallisation and polymerisation, at different rotational speeds, provide moulds of high-shear topologies, as 'positive' and 'negative' spicular flow behaviour. The grand sum of the different behaviours is a general fluid flow model that accounts for all processing in the VFD at an optimal tilt angle of 45°, and provides a new concept in fabricating nanomaterials and controlling the organisation of matter.

6.2. Introduction

Understanding fluid flow is important in microfluidics where processing has primarily focused on manipulating liquids through channels.[8] A less developed area of microfluidics involves films of liquid ≤ 500 μm thick which are centrifugally generated by passing liquids over rotating surfaces, as in spinning disc processors (reactors) ,[9,10] horizontally aligned rotating tube processors,[10,11] and in the vortex fluidic device (VFD),[2-7] Figure 6. 1(a-c). The latter is a variant of the rotating tube processor but where the orientation of the tube, θ, can be varied[2-7] and is distinctly different to Couette flows where liquids are periodically forced between two surfaces[12]. These processors are also distinctly different to conventional microfluidics and do not suffer from clogging. They are effective in controlling chemical reactions, probing the structure of self-organised systems, and in the top down and bottom up synthesis of nanomaterials.[2,9,10] The shear stress in the VFD itself is effective in a variety of applications, including in accelerating enzymatic reactions,[3] folding proteins,[4] slicing carbon nanotubes,[5] exfoliating graphene,[6] and wrapping bacteria in graphene oxide.[7] For the standard 20 mm diameter (internal dimeter 17.5 mm) quartz or glass tube in the VFD, changing of the fluid flow behaviour with the rotational speed (ω) over the range of 3k to 9 k rpm has revealed benefits of using the device specifically at a tilt angle θ = 45°.[2]

6.3. Results and discussion

Establishing the nature of the complex fluid dynamics within the VFD for utility in chemical processing proved challenging. For the range of accessible rotational speeds, and possible solvent substrates, Reynolds numbers (Re) in the range 500 to 10000 are readily achievable, such that flow will exhibit partial turbulence. Experimental attempts to observe the fluid flow in the VFD have been hampered by unavoidable distortions in the glass tube and wobble along its rotational axis, estimated to be collectively ≥ 100 μm. Direct measurement of fluid flow at the dimensionality of processing materials (ca 1 to 5 μm), for example, in scrolling graphene oxide (GO)[13] and generating cones of assembled fullerene C_{60}[14], is a longstanding issue. We hypothesised that manipulating self-assembly, crystallisation and polymerisation processes, and surface induced structural features can cast moulds of high shear regimes in the liquid, in determining the flow behaviour at the micron and submicron dimensions, Figure 6. 1(d). Following this led to establishing the fluid flow characteristics in the VFD at an inclination angle of $\theta = 45^{\circ}$, with rotational speed dependent Coriolis driven circular flow and double helical topological flow associated with Faraday waves, and the interplay of these as spicular flow, with the key outcomes of the findings presented in Figure 6. 1(d-g), and the experiments leading to these findings presented in Figure 6. 2 to 6. 4. Faraday waves are nonlinear standing waves that appear on liquids enclosed by a vibrating vessel,[17] and are characterised by pressure fluctuations that induce eddies, much like the pressure system and wind patterns exhibited in the Earth's atmosphere, but around the inside surface of a curved cylindrical surface, rather than the outside of a spherical one. Their presence and other fluid dynamic behaviour in the VFD will impact on the movement of the liquid (mixing), and consequently, the resultant heat and mass transfer. Variation in the relative strengths of these competing processes result in overall fluid behaviours that create regimes of unique processing conditions within the VFD, with each introducing a moulding or fabrication capability for their own unique nanostructures. Oscillating film thickness in the VFD at $\theta < 90^{\circ}$, Figure 6. 1(b), will drive the formation of Faraday waves in the VFD. These findings also prove that there are domains of fluid flow in the VFD where any outcome of processing is not limited by bulk diffusion control, but this is compounded by orientation effects associated with the different topological flows.

The confined mode of operation of the VFD is where a finite volume of liquid is spun in the tube, with the continuous flow mode having liquid constantly fed into the base of the tube or at positions along the tube, with the liquid centrifugally driven out of the top of the tube against gravity, Figure 6. 1(a)[2]. Continuous flow processing in the VFD addresses scalability of the experimental processing up front, and the effect is effectively the sum of the confined mode in between drops of liquid entering the tube[2]. This finding is understood herein by the reestablishment of the process specific fluid flow topologies, Figure 6. 1(e,f), between each drop. Importantly, for any processing in the VFD, the vortex has to be maintained to expose the base of the tube, otherwise the fluid behaviour is even more complex with partitioning of fluid flow, Figure 2(k) (Supplementary Information section 2, Movie S1.[15]

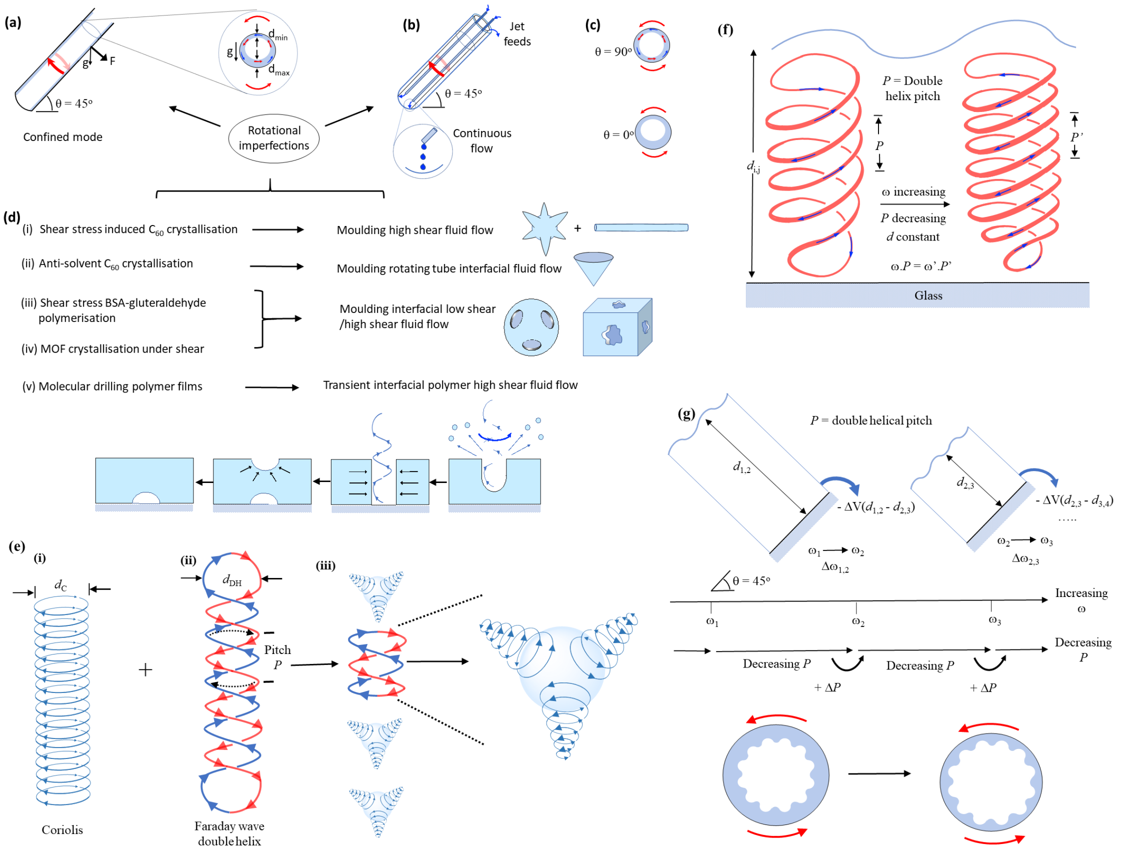

Figure 6. 1 Characteristics of the vortex fluidic device (VFD) and moulded fluid flow. (a) Confined mode of operation of the VFD with the expected oscillation in film thickness which also prevails in (b) the continuous flow mode where liquids are injected as droplets into the rapidly rotating tube. (c) Expected fluid flow and film thickness at 90° and 0° degree tilt angles (θ). (d) (i) Shear stress induced fullerene C_{60} crystallisation resulting in spicules or rods, (ii) anti-solvent crystallisation at the glass – liquid interface, leading to cones, (iii) BSA and glutaraldehyde polymerization in moulding high shear and low shear flow, (iv) as for (iii) for the nucleation and growth of a metal organic framework (MOF5), and (v) shear stress 'molecular drilling' of holes on polysulfone with their signature retained at the glass-polymer interface post positional shift of the double helical fluid flow. (e) Representation of the different fluid flows, and the collapse of circular Coriolis force flow and double helical flow from Faraday waves into spicular flow. (f) Double helical fluid flow with a reduction in helical pitch (*P*) for increasing rotational speed, ω, for the same thickness of the film, $d_{i,j}$, with preservation of ω.*P*. (g) Diagrammatic representation of change in film thickness in a type γ liquid which is dominated by double helical flow across the rotational landscape, and the reduction in film thickness and associated the Faraday waves driving the formation of linear arrays of double helical flows orientated parallel to the rotation axis of the tube.

Mixing experiments whereby the time taken for a drop of dye added to a finite volume of liquid in the tube to form a uniformly mixed solution half way up the film was measured across ω at θ = 45°, along with changes in temperature and film thickness at this atypical tilt angle. Collectively they provide a signature for the liquid, as depicted for initially water at *ca* 20 ºC in a 20 mm and 10 mm OD tube (17.5 mm and 8.5 mm ID respectively), Figure 6. 2(a,b), for use in predicting rotational speed processing outcomes. The temperature of the tube was also measured mid-way along its length using an IR thermal imaging camera, across ω and θ, for a 20 mm OD tube, revealing a significant rise in temperature at 4.5k rpm for water, approximately 2 ºC, only at a tilt angle of 45º, Figure 6. 2(c). The mixing profiles across different tilt angles for 20 mm and 10 mm diameter tubes have also been determined, Figure 6. 2(d) and Supplementary Information section 3, respectively. While mixing times vary dramatically, at $\theta = 45^o$, they provide insight into the fluid behaviour in the VFD.

Mixing time profiles, change in temperatures at $\theta = 45^o$ and change in film thickness vary for different liquids, for example, toluene, DMF, 3:1 ethanol/water, and 1:1 *o*-xylene/DMF, Figure 6. 2(e-h). This behaviour describes how the physical properties (such as viscosity, density, surface tension) of the liquid drive signature flow characteristics for the liquid within the VFD environment. For water, as the speed increases, the time for mixing dramatically drops at 3.0k rpm, where circular flow prevails (see below regarding scrolling of graphene oxide, GO), then increases above ca 3.8k rpm as spicular flow dominates (see below regarding shear stress induced crystallisation of fullerene C_{60}). This flow arises from the interplay of Faraday wave double helical flow and circular flow, Figure 6. 1(e). At speeds above 4.5k rpm, the circular component of flow diminishes and only the double helical flow remains. At 4.5k rpm there is a sharp rise in temperature, Figure 6. 2(a), which corresponds to transitioning from spicular flow to double helical flow (see below regarding shear stress induced crystallisation of C_{60} within the confines of the double helical flow), and is associated with a reduction in average film thickness. The large change in film thickness (determined from volume changes) at this speed (ca 50%) indicate that this is along the length of the film rather than being localised. We define this type of signature as corresponding to an α-liquid. Toluene behaves similarly with the onset of rapid mixing above 3k rpm, now with a rapid change in temperature at 6k rpm, Figure 6. 2(e), is likewise classified as an α-liquid, as is the classification of the fluid response for, Figure 6. 2(f). A mixture of ethanol and water (3:1) has distinctly different mixing and temperature profiles, Figure 6. 2(g), and is classified as a β-liquid, dominated by spicular for increasing ω, matching the moulding of high shear regimes in forming BSA-gluteraldehyde porous spheres (see below).

A sudden increase in temperature is associated with a transition from (i) spicular to double helical flow (ie. decoupling of circular and double helical flow) with a reduction in film thickness, or (ii) from double helical flow to a smaller pitch double helical flow (ie. collapse of opposing directional flow in the double helical flow), Figure 6. 1(f,g). These transitions will generate frictional heat from the double helical flow striking the surface of the tube (see below for 'drilling holes' in thin film of polymers attached to the inside of the tube), and amplified where the film thickness change is more dramatic and readily measurable. The 1:1 mixture of DMF and *o*-xylene has a distinct series of step increases in temperature, with double helical flow across the rotational landscape, Figure 6. 2(h), and this liquid is classified an γ liquid.

Any sudden increase in temperature (ΔT) with increasing ω, does not arise from vibrations induced from the motor or the two bearings at either end of the tube. This conclusion is based on the notion that different rotational speeds are needed for a sudden increase in temperature for a number of liquids, and for different diameters of the tube (20 versus 10 mm OD), along with the phenomenon being restricted to 45° tilt angle and that is independent of the choice of motor driving the rotation of the tube. If it were simply an artefact of the drive system, the behaviour would always appear for the correct liquid at a fixed rotational speed. Moreover, the position for rapid change in temperature of the liquid is independent of the volume of liquid in the tube, and with minimal change from one tube to another of the same diameter, Supplementary Information section 2, ruling out imperfections in the glass being responsible for generating the effect. Identifying positions of ΔT and change in volume/film thickness at θ 45° provides a powerful method to rapidly establish the rotational speed for transitioning from spicular like fluid flow to double helical flow, and for double helical flow of one diameter to a double helical flow of a smaller diameter tube, as in a 1:1 mixture of DMF and *o*-

xylene, for any liquid, without the need for prior knowledge of the properties of the liquid. High speed photography of water in a 10 mm OD tube reveals that as the speed increases, helical waves appear along the tube (distinctly different to the above double helical flow) (Supplementary Information section 4, Movie S2). However, they disappear at ca 5.6k rpm, where beyond this speed there is a plateau region of film thickness, Figure 6. 2(k). This approximates to ω for a sudden drop in liquid (and thickness of the film), Figure 6. 2(a) (and Supplementary Information section 5). A constant thickness for increasing rotational speed is consistent with double helical flow being maintained but with a reduction in pitch of the double helix as the rotational speed increases, Figure 6. 1(f), preserving $\omega.P$ (P = pitch of the double helix in the fluid flow). As the pitch decreases for increasing speed, a threshold will be reached where the distance between opposite flow up and down the helix cannot be maintained, resulting in disruption of the double helical flow, creating a dynamic equilibrium state. Increasing ω further results in a thinner film and double helical flow with a larger pitch, Figure 6. 1(g).

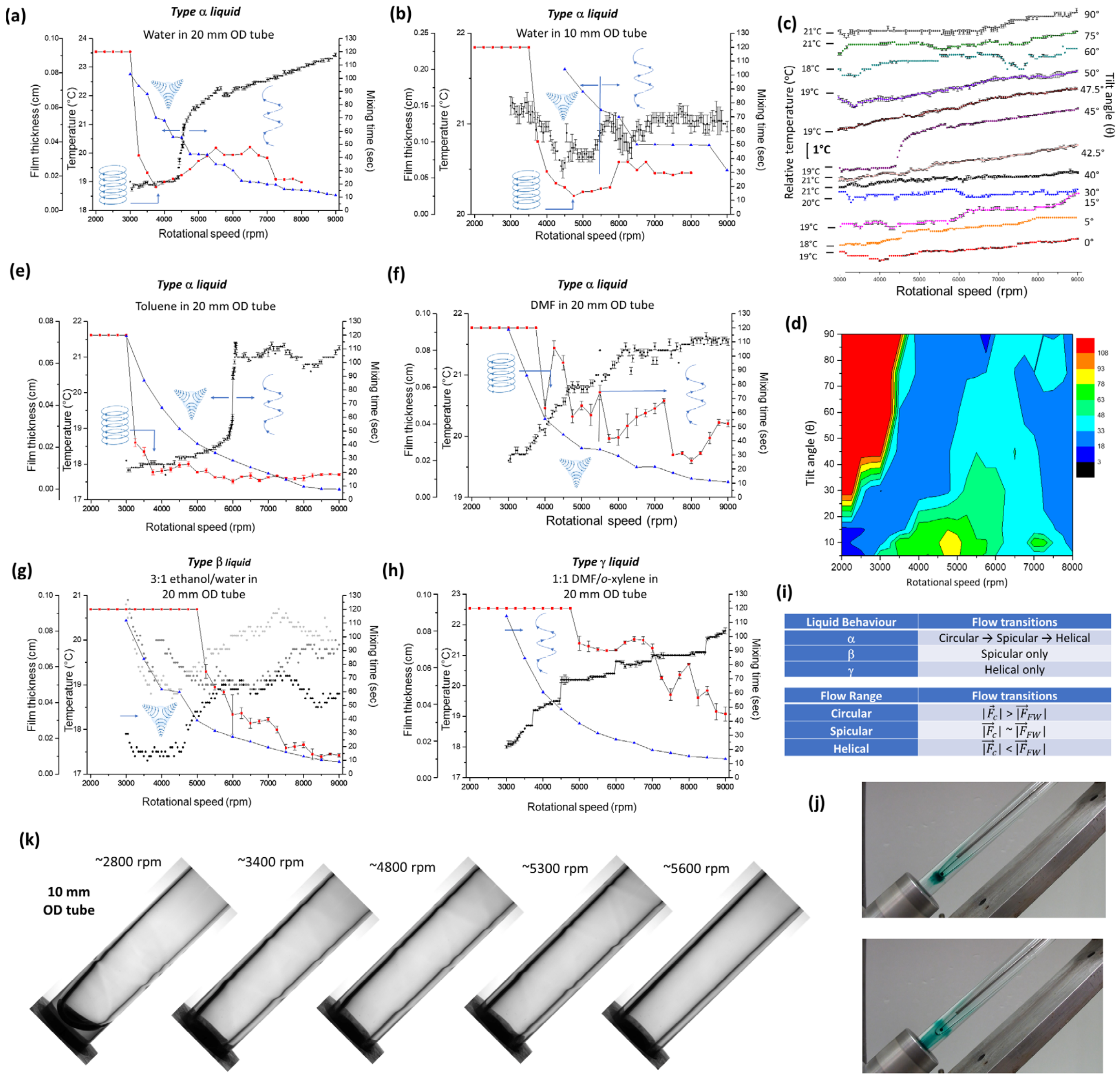

Liquid Behaviour	Flow transitions
α	Circular → Spicular → Helical
β	Spicular only
γ	Helical only

Flow Range	Flow transitions
Circular	$\lvert\vec{F}_c\rvert > \lvert\overrightarrow{F_{FW}}\rvert$
Spicular	$\lvert\overrightarrow{F_c}\rvert \sim \lvert\overrightarrow{F_{FW}}\rvert$
Helical	$\lvert\overrightarrow{F_c}\rvert < \lvert\overrightarrow{F_{FW}}\rvert$

Figure 6. 2 Mixing and thermal response, and film thickness. (a) and (b) Thermal response and mixing times, and change in average film thickness versus ω for water in a 20 mm OD quartz tube (17.5 mm ID) and 10 mm tube (8.5 mm ID) respectively. Mixing time (red) corresponds to the time taken for a drop of water containing a small amount of dye added at the bottom of the tube rotating at a specific speed to uniformly mix in half way up the preformed film generated from 2 mL of water. The temperature (black) was measured midway along the tube using an IR camera, for residual water present in the tube, being equivalent to the continuous flow mode of operation of the VFD (water along the complete length of the tube), with the average film thickness (blue) determined at θ = 45° for a specific speed from the mass of residual water also equivalent to the continuous flow mode of operation of the VFD, converted to a volume of liquid spread uniformly on the inner wall of the tube. (c) Thermal response for water in the tube, retaining the maximum amount of water at each speed, for varying tilt angles, θ, using a 20 mm OD tube. (d) Mixing response for 2 mL of liquid in the 20 mm OD tube for change in θ. (e) – (h) Thermal response, mixing times and film thickness versus ω for toluene, DMF, a 3:1 mixture of ethanol and water, and a 1:1 mixture of DMF and *o*-xylene in 20 mm OD tubes, respectively. Temperatures were recorded at the mid-point along the tube to minimise any heating from the bearings. Recording change in temperature starts at high ω relative to ω for recording mixing times, a consequence of requiring extra liquid in the tube when mimicking continuous flow processing, and this requires higher ω to generate a vortex to the bottom of the tube. (i) Summary of the different fluid flows, and flow regimes characterised by the relative strength of the Coriolis $(\overrightarrow{F_{FW}})$ and Faraday wave $(\vec{F}_{FW})$ forces, using computational fluid dynamics (CFD) simulations conducted using OpenFoam v1806, as detailed in the

Supplementary Information section 11. (j) Images of water in a 10 mm tube at different rotational speeds, captured from 5k frames/s (Movie S2). (k) Photographs of partitioned mixing of an aqueous dye in water into 2 mL of water in a 10 mm OD tube rotating at 2k rpm where the vortex is not developed to the bottom of the tube (Movie S1). Additional information is provided in the SI file).

To further understand the fluid dynamic response in the VFD, we subjected single graphene oxide (GO) sheets dispersed in DMF to different rotational speeds, Figure 6. 3(a) (and Supplementary Information section 7). At speeds aligned with a minimum mixing time in this solvent (4k rpm, Figure 6. 2(f)), GO is forced into scrolls, Figure 6. 3a(i), corresponding to circular flow, whereas at 5k rpm GO sheets collapse into globular shapes approximately 1-2 μm in diameter, Figure 6. 3a(ii), corresponding to spicular flow, and at 8k rpm (the shortest mixing times), the GO sheets are unaffected. However, at this speed, preformed GO scrolls become disrupted and unravelled, Figure 6. 3a(iii), and preformed globular GO become sheets. In the same way, preformed globular GO at 4k rpm become scrolls. These results clearly establish spherical like topological shear stress consistent with spicular fluid flow at 5 k rpm in DMF, and circular fluid flow at a Coriolis force dominated regime at 4k rpm. At 5k rpm, the rapid interconversion between specular and double helical flow results in shredding of the GO sheets into ca 80 nm particles, Figure 6. 3a(iv).

Unscrolling GO requires another force at play with smaller dimensionality than the diameter of the scrolls, and this we ascribe as coming from the resonant vibrational eddy currents associated with Faraday waves taking on a double helix arrangement, Figure 6. 1(e,f). We have previously established the ability to wrap bacteria with GO in water in a 10 mm diameter tube at 5k and 8k rpm[7], and this is now understood as coming from circular fluid flow. We found that recording changes in temperature in the smaller diameter tube are unreliable (Figure 6. 2(b)), presumably because of more rapid heat flow from a thinner film and thinner glass. The change in film thickness can be used instead to establish ω where different topological fluid flow prevails for increasing ω. The Coriolis forces arise from inertial forces, and therefore it will be more pronounced for the smaller diameter tubes, which is demonstrated herein, with ca 30% reduction in the dimensionality of the topological flow for a 10 mm dimeter tube relative to a 20 mm diameter tube (see below regarding the formation of C_{60} cones). Thus far the order of the type of fluid flow in the tube for increasing ω is circular flow followed by spicular flow, then double helical flow, for the 9k rpm rotational speed limit of the VFD housing a 20 mm (or 10 mm) OD tube, as an archetypal α-liquid.

Mixing a toluene solution of fullerene C_{60} with water in the VFD results in the crystallisation of tubules[17]. We have now established that subjecting a toluene solution of the fullerene (<< saturation level) to shear stress in the VFD, in the absence of water, results in the formation of self-assembled fullerene particles as a new form of crystallisation, adding to the limited number of ways of inducing crystallisation, namely sublimation, cooling, evaporating, and heating to strip away surfactants[18]. Fullerene C_{60} only slowly dissolves in toluene, so that any particles generated by the induced shear stress do not rapidly dissolve, with ample time for collecting by centrifugation and washing post VFD processing, before dissolution in reaching the thermodynamically controlled state. At ω < 6k rpm, spicules are generated with uniform size and number of spicules, Figure 6. 3(b(i)). These are made up of ca 6.5 nm particles of self-assembled C_{60} (Supplementary Information section 7) and these and the rods formed at > 6k rpm, Figure 6. 3(b(ii)), can only form at high shear in the liquid, otherwise they would re-dissolve under thermodynamic control. Thus, spicules are a mould of the fluid flow corresponding to a combination of circular and double helical flow, Figure 6. 1(e,f), with the edges of the spicules slightly curved, Figure 6. 3(b(i)). Close inspection of the rods revealed slightly curved surfaces, Figure 6. 3(c(ii)), and this is consistent with them being formed under shear within the double helical liquid flow, rather than the formation of well defined crystallographic controlled facets. Outside of this space they would re-dissolve, noting that circular flows from Coriolis force are negligible at high rotational speeds (>6000 rpm). In addition, the diameter of the rods (ca 0.5 μm) are consistent with the overall diameter of the double helix (see below). At the transitioning speed for toluene, 6k rpm (Figure 6. 2(e), a mixture of spicules and rods are formed, Figure 6. 3(b(iii)).

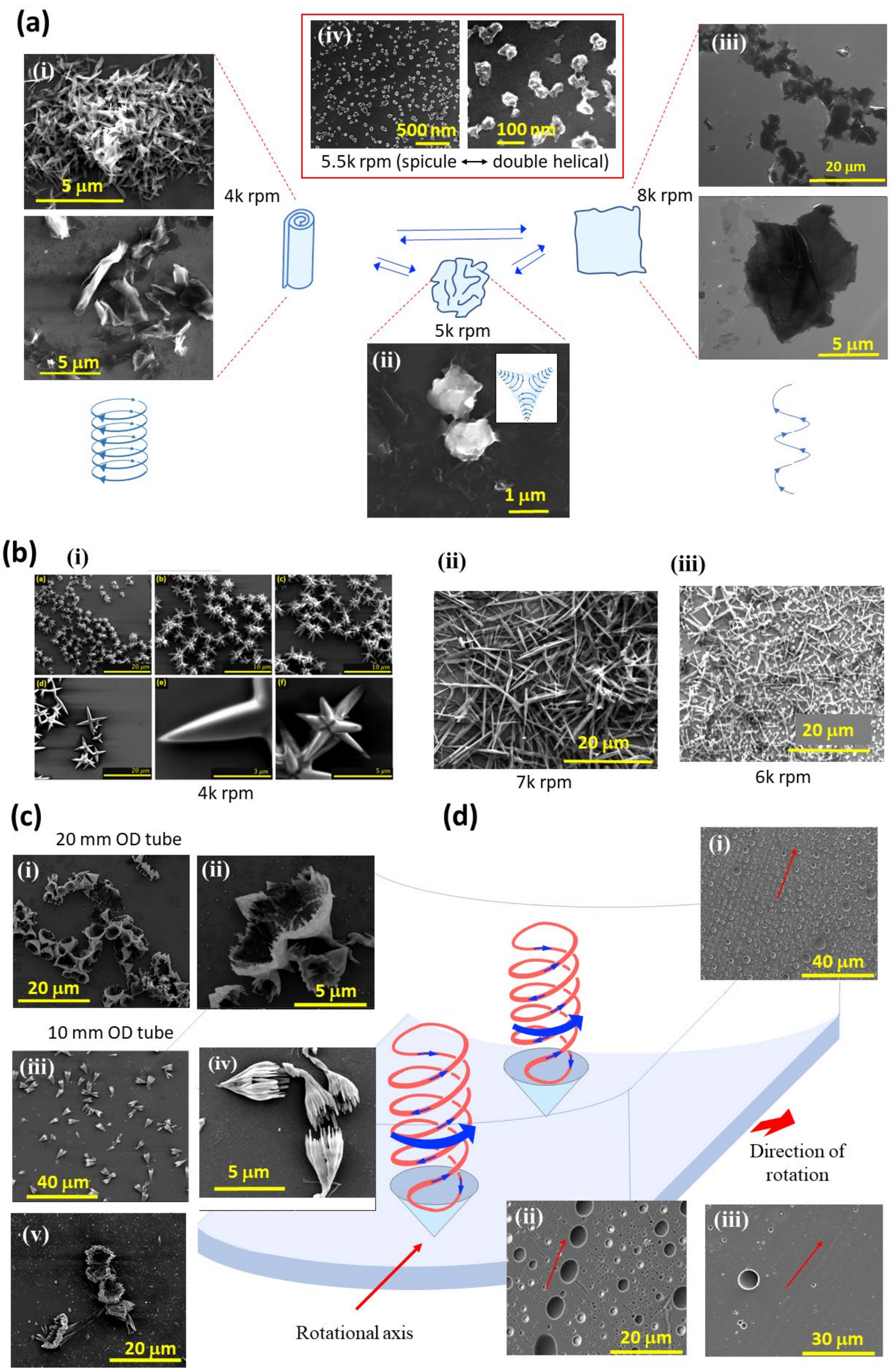

Figure 6. 3 Moulding nano-carbon and polymer material. (a) Processing GO in a 20 mm OD tube (17.5 cm ID) at θ 45°, 0.2 mg/mL in DMF, flow rate 0.45 mL/min, result in (i) scrolls at 4k rpm, (ii) crumbling into globular particles at 5k rpm, and (iii) no perturbation at 8k rpm, with the ability to cycle between the three forms of GO by changing the rotational speed akin to another form, with transformation of the GO into ca 100 nm spheroidal particles at 5.5k rpm (transition from spicular to double helical flow at the dynamic equilibrium). (b) Shear stress induced crystallisation and self-assembly of C_{60} in toluene (0.1 mg/mL, flow rate 0.1 mL/min, θ 45°), affording (i) spicules and mixtures of spicules and rods, and (iii) rods, at 4, 6, and 8k rpm, corresponding to spicular flow, transitioning from spicular to double helical flow and helical flow respectively. (c) Micromixing a 1:1 solution of *o*-xylene solution of C_{60} (0.1 mg/mL flow rate 0.1 mL/min) and DMF (0.1 mL/min) in a VFD, θ 45°, 20 mm OD tube, affording (i) regular and (ii) irregular cones in a 20 mm OD tube, and (iii) and (iv) sharper pitch cones with extended arms in a 10 mm OD tube. (v) Cones attached to the wall

of the glass tube in the VFD, post VFD processing in a 10 mm OD tube. (d) (i, ii) Signature of the pattern of the double helical flows formed at the interface of the glass tube and a thin film of polysulfone (ca 5 μm) formed in toluene at 20 ºC, θ = 45º, 7k rpm rotational speed, along the length of the tube, with the arrow representing the rotational direction of the axis of the tube. (iii) Snapshot of holes formed at the interface of the polymer with the liquid.

An alternative strategy for fluid flow moulding is the crystallisation of C_{60} using an anti-solvent approach. Injecting a solution of C_{60} in *o*-xylene into the base of the rotating tube in the VFD with another jet feed simultaneously injecting DMF in which the fullerene is only sparing soluble (as periodic drops), results in the formation of cones 0.5 - 2.5 mm in diameter which are comprised of ca 6.5 nm particles of *fcc* fullerene C_{60}, Figure 6. 3(c(i,ii))[15]. Cones formed in the 20 mm OD tube have small whiskers running parallel to the symmetry axis of the cones, and these are more pronounced for cones generated in the 10 mm OD tube, with the diameter of the cones reduced by ca 30% relative to those generated in the 20 mm OD tube, Figure 6. 3(c(iii,iv)). The formation of cones is consistent with the small first formed ca 6.5 nm nano-particles of C_{60} assembling at points of high shear on the surface of the tube, where the double helical flow strikes the surface of the tube. Thermal imaging reveals increasing temperatures for a 1:1 mixture of the two solvents as ω increases, Figure 6. 2(h), which correspond to ongoing fluctuations in pitch (decreasing then increasing), Figure 6. 1(e.g), and consequential change in film thickness, Figure 6. 2(h). In the absence of shear on mixing the two liquids (no VFD), the small nano-particles of the fullerene aggregate randomly[15], whereas in the VFD the ca 6.5 nm particles assemble only at the interface of high shear in the liquid and the surface of the tube, effectively 'writing' cones at the end of the double helix which itself is likely to be rotating along the axis of the helix, with all the cavities facing in the same direction. Given that the cones are formed under continuous flow whereby the product primarily exits the top of the VFD tube, any attachment to the tube through their apex must be weak and at the nm dimensions. Indeed, breaking a tube post-VFD processing revealed some cones attached to the surface of the tube at their apical positions, Figure 6. 3(c(v)) (and Supplementary Information section 7). Clearly the residence time of such structures near the surface of the tube is maximised, allowing them sufficient time to adhere.

Within the liquid, the combination of Faraday waves, Coriolis flow and resonant eddy currents, each of which tend to dominate in each of the operating regimes, could have transition points of 'dynamic equilibrium' within the liquid where they effectively cancel out each other as the operating conditions transition between the operating regimes. In such places mass transport of larger structures will be relatively slower than at other places within the liquid, and residence times for interaction with other smaller species will be longer.

Given the frailty of the point of attachment of the cones to the surface of the tube, the formation of cones doesn't provide information on the spatial arrangement of the associated double helical flow. For this we explored the possibility of double helical flow generating holes in a thin layer of polymer attached to the inner surface of the tube. The polymer of choice was polysulfone, and surprisingly the arrangement of double helices was determined from the surface of the polymer attached to the glass tube rather than the surface in contact with the liquid. Peeling the polymer from the glass surface revealed lines of holes several μm in diameter, Figure 6. 3(d) (and Supplementary Information section 8), which has the dimensionality of the moulding of the cones, although the solvent here was toluene with the tube rotating at 7k rpm where double helical flow prevails, Figure 6. 2(e). The holes are arranged in lines co-parallel to the rotational axis of the glass tube, and this arrangement explains the ability of double helical flow to exfoliate graphene from graphite,[6] and the above unscrolling of GO, Figure 6. 3(a), between rows of vertically arranged double helices. The original proposed mechanism involved exfoliation at the interface of the graphite flakes and the surface of the tube, and/or at the interface of the liquid and graphite held parallel to the surface of the tube.[6] The mechanism of formation of these holes, Figure 6. 1(d), has the double helical 'molecular drills' piercing the polymer film, and when they move to other locations, the centrifugal force results in collapse of the holes, trapping liquid at the base, with smoothing of the upper surface. The ability for the fluid flow to pierce the polymer layer is consistent with the friction associated with the double helical flow striking the surface of the tube thereby increasing the temperature of the liquid, and the melting the polymer which has an onset of glass > 120 ºC.[14] In addition, the pattern of holes is commensurate with the presence of arrays of Faraday waves on larger length scales.

Reaction of BSA with glutaraldehyde in the VFD in a 3:1 mixture of ethanol and water as PBS, a β liquid with specular flow, Figure 6. 2(g), results in the formation of porous polymeric spheres[19] Higher rates of polymerisation are expected at the highest shear stress,[2] ie. within the spicules, with the polymer then building up at the closest proximity with low shear, on the surface of a sphere with holes representing where the spicules protruded, Figure 6. 4(a,b). This material then represents a 'negative' mould of spicular flow, with the formation of the C_{60} spicules as the 'positive' mould. The size of the porous spheres is ca 10-38% smaller for the 10 mm tube relative to the 20 mm tube, Figure 6. 4(b) (and Supplementary Information section 9), as for the formation of C_{60} cones in the smaller tube. The number of holes in each sphere (= number of spicules of fluid flow) is not uniform for each sample preparation, as is the case for the formation of spicules of C_{60}, Figure 6. 2(b).

Terephthalate/Zn MOF5 formed using batch processing, as cuboid particles 200 to 500 nm in diameter,[20] is only sparing soluble in DMF, the solvent of choice for its synthesis. Confined mode synthesis in DMF in the VFD at 110ºC also produces cuboids of the same structure (Figure 6. 4 (c-f)) (and Supplementary Information section 10), except for processing below 5.5k rpm, where spicular flow prevails, Figure 6. 2(f), which generates cuboids with irregular shaped cavities on each face. The cavities are then the 'negative' moulds of high shear at the spicules, with any crystallisation in the cavities likely to lead to shear stress dissolution, and regrowth on the faces, away from the high shear. Thus, nucleation and growth of MOF5 provides a partial mould of spicular flow, with the position of spicule flow in DMF at 110ºC at ca 4krpm, which is 1.5k rpm lower than such flow at room temperature, Figure 6. 2(f).

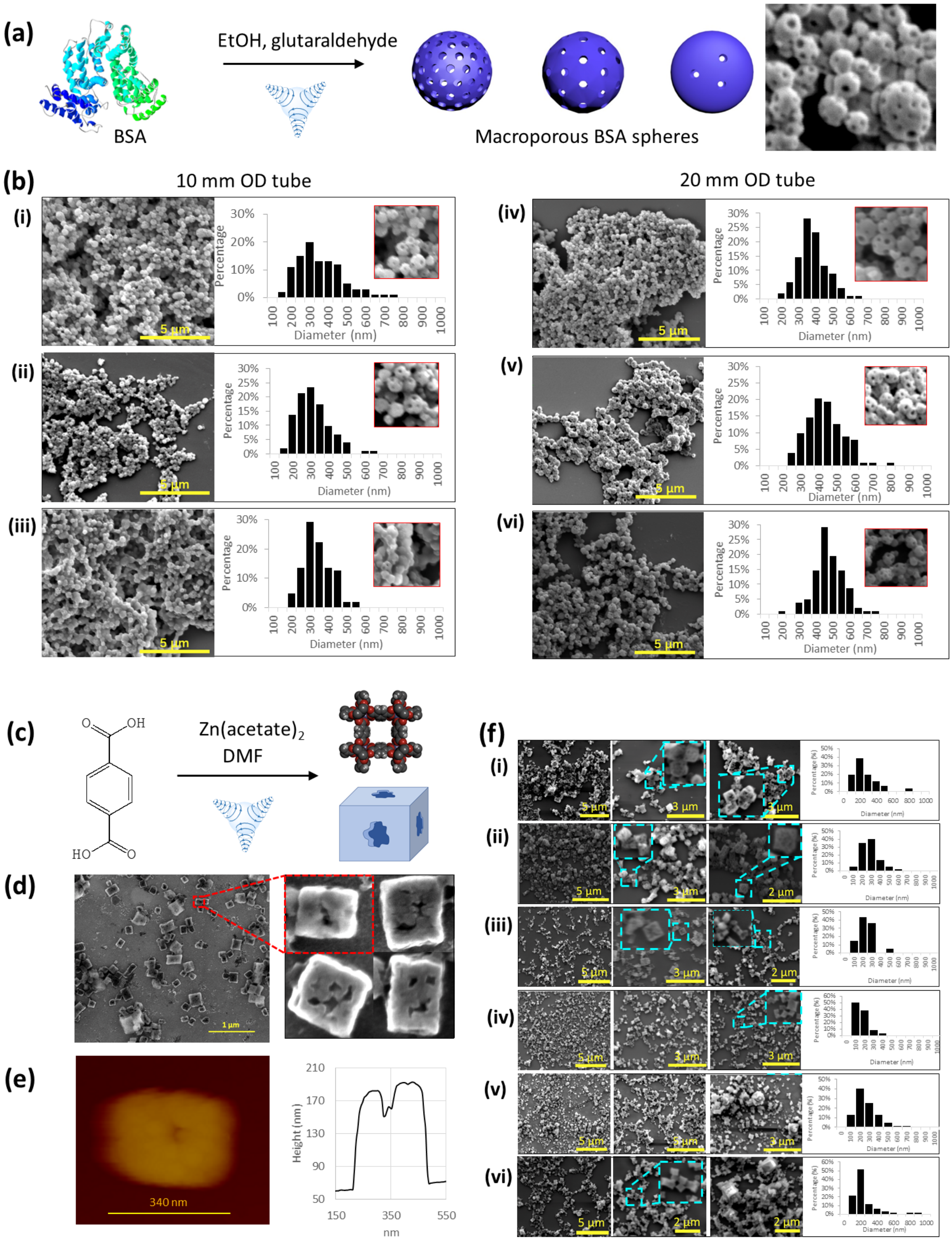

Figure 6. 4 Moulding polymer growth and metal organic frameworks. (a) Schematic of the formation of porous spheroidal particles of cross linked BSA with glutaraldehyde formed in the VFD under confined mode (BSA in aqueous 10 mM PBS of pH 7.4 (1 mg/mL) to ethanol ratio 1:3 (300:900 µL) and 15 µL of glutaraldehyde, using (b) 0.5 mL of combined solution in a 10 mm OD tube for 1 min at 3k, 5k and 7k rpm (i) – (iii) respectively, and 1 mL of combined solution for a 20 mm OD tube, for 1 min at 3k, 5k and 7k rpm (iv) – (vi) respectively, reporting SEM images and derived particle size distributions from 100 randomly chosen spheres. (c) Schematic of the synthesis of MOF5 where H_2BDC (63.3 mg) and triethylamine (106.3 µL) were dissolved in 4.9 mL of DMF and $Zn(OAc)_2 \cdot 2H_2O$ (169.9 mg) was dissolved in 5 mL of DMF. For a typical VFD experiment, 556 µL of zinc solution was added to 444 µL H_2BDC solution followed by 20 mm VFD processing for 30 min at 110ºC. (d) SEM and AFM images respectively for MOF5 formed at 110ºC for 30 min at 4k rpm.

(f) Variation in morphology of the particles formed under the same processing as a function of rotational speed (i) – (vi), 3k, 4k, 5k, 5.5k, 6k and 7k rpm, respectively, for the confined mode of operation of the VFD for 30 min, showing SEM images and particle size plots, determined by randomly counting 100 particles.

The above results provide a picture of fluid flow in the VFD. At the minimum mixing time the high shear circular flow, at most a few μm in diameter prevail. Beyond this speed Faraday waves combine with the circular flow, with the lines of high shear fluid flow on the surface of a spicule, and for higher speeds, as the mixing times peak, Faraday waves dominate, where the double helical eddies associated with them are normal to the thin film. For other liquids, double helical flow dominates across the rotational landscape. Eddies associated with Faraday waves are twisted into double helices by the circular flow, with flow up one strand of each helix, and down the other. Superimposing the associated vectors of flow with those of the circular flow necessarily creates a flow of liquid around a sphere, with a full turn of the double helix being the diameter of the double helical Faraday waves eddies, which corresponds to the diameter of the circular flow, Figure 6. 1(e). The spicular flow sphere of influence is approximately 1-2 μm for the 20 mm diameter tube, and ca 30% smaller for the 10 mm OD tube. For spicular flow, the diameter of the double helix is defined by the diameter of the fullerene C_{60} spicules, and thus the diameter of the associated double helix, d_{DH}, Figure 6. 1(e). For d_{DH} ca 2 μm, and assuming that for one rotation of the VFD tube, that eddies complete a full turn of the double helix, ca 5 μm, then at 6k rpm (100 Hz), the velocity of the molecules in the double helical flow is ca 0.5 mm/s. This is consistent with the shear stress in the VFD increasing the average velocity of the molecules, without external heating, and that the system has regimes which are not limited to diffusion control processes. Moreover, for increasing rotational speeds the path length of fluid flow induced by each rotation of the tube will decrease, and this explains why the enhancement effects of the VFD diminish above ca 8k rpm in a 20 mm OD tube.[2] Overall, the established fluid flow herein explains all the processing in the VFD, including protein folding and enzymatic rate enhancements, with double helical flow and associated pressure fluctuation from the Faraday waves themselves effective in accelerating enzymatic reactions.[3] It also accounts for the unique rotational dependence for an enzyme, which relates to their different sizes and shapes.[3]

6.4. Conclusions

We have established the topological features of high shear fluid flow in the vortex fluidic device (VFD) at sub-micron dimensions, at a tilt angle of 45°, which corresponds to the optimal angle for a myriad of applications of the device.[2-7] The rotational speeds for high shear circular, spicular and double helical flow can be determined by measuring changes in temperature and mixing times, and average film thickness as a unique signature for any liquid. Sudden increases in temperature of the liquid correspond to discontinuities in fluid flow, with a sudden reduction in film thickness for increasing rotational speed rather than continuously changing film thickness, as a new phenomenon in thin films. The present work also established that the VFD is effective in creating systems in non-equilibrium states, in establishing a new form of crystallization induced by shear stress, adding to the ubiquitous methods of sublimation, cooling and evaporating, and also stripping away surfactants[21]. Also of note is the ability to create novel spicule structures which map out the highest shear stress in a liquid, or the 'negative' of these structures where material formed in the spicular fluid flow under high shear assemble at the closest points of low shears, in between the spicules. With the VFD and an understanding of the operating regimes, structures are moulded with predictable shapes by the mechanical force of fluid flow and diffusion of species within the liquid. Fundamentally, the vast differences in the morphology of the resultant structures between the three topological fluid flow regimes must result from unique diffusion behaviour within the liquid. Thus, the VFD demonstrates the ability to mediate or control both the forces exerted by the liquid on nanostructures and the diffusion of species supplied to their surface. The findings also have implications on using shear stress driven boundary mediated control of fluid flow for controlling self-assembly and chemical reactions under non-equilibrium conditions, and manipulating cells under tuneable stress regimes, which are areas we are currently working on.

6.5. Acknowledgements

Support of this work by the Australian Research Council, the Australian Nuclear Science and technology Organisation, and the Government of South Australia is greatly acknowledged. The authors also acknowledge the expertise, equipment and support provided by the Australian Microscopy and Microanalysis Research Facility (AMMRF) and the Australian National Fabrication Facility (ANFF) at the South Australian nodes of the AMMRF and ANFF under the National Collaborative Research Infrastructure Strategy.

6.6. References

1. Ross, T. D.; Lee, H. J.; Qu, Z.; Banks, R. A.; Phillips, R.; Thomson, M., Controlling Organization and Forces in Active Matter Through Optically-Defined Boundaries. *Nature*, **2019**, 572, 224-229.
2. Britton, J.; Stubbs, K. A.; Weiss, G. A.; Raston, C. L., Vortex Fluidic Chemical Transformations. *Chem. Eur. J.,* **2017**, 23, 13270-13278.
3. Britton, J.; Meneghini, L. M.; Raston, C. L.; Weiss, G. A., Accelerating enzymatic catalysis using vortex fluidics. *Angew. Chem. Int Ed.,* **2016**, 55, 11387-11391.
4. Yuan, T. Z.; Ormonde, C. F.; Kudlacek, S. T.; Kunche, S.; Smith, J. N.; Brown, W. A.; Pugliese, K. M.; Olsen, T. J.; Iftikhar, M.; Raston, C. L., Shear-Stress-Mediated Refolding of Proteins from Aggregates and Inclusion Bodies. *ChemBioChem*, **2015**, 16, 393-396.
5. Alharbi, T. M.; Vimalanathan, K.; Lawrance, W. D.; Raston, C. L., Controlled slicing of single walled carbon nanotubes under continuous flow. *Carbon* **2018**, 140, 428-432.
6. Chen, X.; Dobson, J. F.; Raston, C. L., Vortex fluidic exfoliation of graphite and boron nitride. *Chemi. Commun.,* **2012,** *48*, 3703-3705.
7. HaniffáWahid, M. J. R. A., Microencapsulation of bacterial strains in graphene oxide nano-sheets using vortex fluidics. *RSC Advances*, **2015**, 5, 37424-37430.
8. Whitesides, G. M., The origins and the future of microfluidics. *Nature* **2006,** *442*, 368.
9. Brechtelsbauer, C.; Lewis, N.; Oxley, P.; Ricard, F.; Ramshaw, C., Evaluation of a spinning disc reactor for continuous processing1. *Org. Proc. Res. Dev.,* **2001,** *5*, 65-68.
10. Chen, X.; Smith, N. M.; Iyer, K. S.; Raston, C. L., Controlling nanomaterial synthesis, chemical reactions and self assembly in dynamic thin films. *Chem. Soc.Rev.,* **2014,** *43*, 1387-1399.
11. Lodha, H.; Jachuck, R.; Suppiah Singaram, S., Intensified biodiesel production using a rotating tube reactor. *Energy Fuels* **2012,** *26* , 7037-7040.

12. Sitepu, E. K.; Jones, D. B.; Tang, Y.; Leterme, S. C.; Heimann, K.; Zhang, W.; Raston, C. L., Continuous flow biodiesel production from wet microalgae using a hybrid thin film microfluidic platform. *Chemi. Commun.,* **2018,** *54*, 12085-12088.
13. Alharbi, T. M.; Harvey, D.; Alsulami, I. K.; Dehbari, N.; Duan, X.; Lamb, R. N.; Lawrance, W. D.; Raston, C. L., Shear stress mediated scrolling of graphene oxide. *Carbon,* **2018**. 137, 419-424
14. Alsulami, I.; Alharbi, T.; Harvey, D.; Gibson, C. T.; Raston, C. L., Controlling the growth of fullerene C60 cones under continuous flow. *Chem. Commun.* **2018**, 54, 7896-7899.
15. Périnet, N.; Gutiérrez, P.; Urra, H.; Mujica, N.; Gordillo, L., Streaming patterns in Faraday waves. *J. Fluid Mech.,* **2017,** *819*, 285-310.
16. Britton, J.; Dalziel, S. B.; Raston, C. L., The synthesis of di-carboxylate esters using continuous flow vortex fluidics. *Green Chem.,* **2016,** *18*, 2193-2200.
17. Vimalanathan, K.; Shrestha, R. G.; Zhang, Z.; Zou, J.; Nakayama, T.; Raston, C. L., Surfactant-free Fabrication of Fullerene C60 Nanotubules Under Shear. *Angew. Chem. Int. Ed.,* **2017,** *56*, 8398-8401.
18. Wu, L.; Willis, J. J.; McKay, I. S.; Diroll, B. T.; Qin, J.; Cargnello, M.; Tassone, C. J., High-temperature crystallization of nanocrystals into three-dimensional superlattices. *Nature,* **2017,** *548*, 197.
19. Malysheva, G.; Akhmetova, E. S.; Marycheva, A., Estimation of glass transition temperature of polysulfone-modified epoxy binders. *Glass Phys. Chem.,* **2014,** *40*, 543-548.
20. Luo, X.; Al-Antaki, A. H. M.; Harvey, D. P.; Ruan, Y.; He, S.; Zhang, W.; Raston, C. L., Vortex fluidic mediated synthesis of macroporous bovine serum albumin-based microspheres. *ACS Appl. Mater. Interfaces,* **2018,** *10*, 27224-27232.
21. Rosi, N. L.; Eckert, J.; Eddaoudi, M.; Vodak, D. T.; Kim, J.; O'Keeffe, M.; Yaghi, O. M., Hydrogen storage in microporous metal-organic frameworks. *Science,* **2003,** *300*, 1127-1129.

Chapter Seven

Continuous flow photolytic reduction of graphene oxide

Thaar M. D. Alharbi, [a, b] Amira R. M. Alghamdi, [a] Kasturi Vimalanathan, [a] and Colin L. Raston [a, *]

[a] Flinders Institute for Nanoscale Science and Technology, College of Science and Engineering, Flinders University, Adelaide SA 5001, Australia

[b] Physics Department, Faculty of Science, Taibah University, Almadinah Almunawarrah 42353, Saudi Arabia

This study was published in ***RSC Chemical Communication***, Year **2019**, 55, 11438-11441 The first page of the publication and SI are attached.

Author contributions: **TA** performed all the VFD and most characterization experiments and data analysis, and wrote all the primary content. **AA** helped with XPS measurements and fitting the data. **KV** helped with the revised the manuscript before submitting and also helped in addressing the reviewers' comments. **CR** supervised and coordinated the project and helped on the research directions and plan, and the final revision of the manuscript. All of the co-authors assisted with the revision of the manuscript before and during the publication process.

7.1. Abstract

Reduced graphene oxide (rGO) is generated from GO dispersed in water under continuous flow in the absence of harsh reducing agents, in a vortex fluidic device, such that the processing is scalable with uniformity of the product. This involves simultaneously UV irradiating (λ = 254 nm, 20 W) the dynamic thin film in the rapidly rotating glass tube in the microfluidic platform. The rGO is comparable to that formed using waste generating chemical based processing, with a film of the material having a resistance of $2.2\times 10^5\ \Omega$ and a remarkbaly high conductivity of 2×10^4 S/cm.

Graphical Abstract

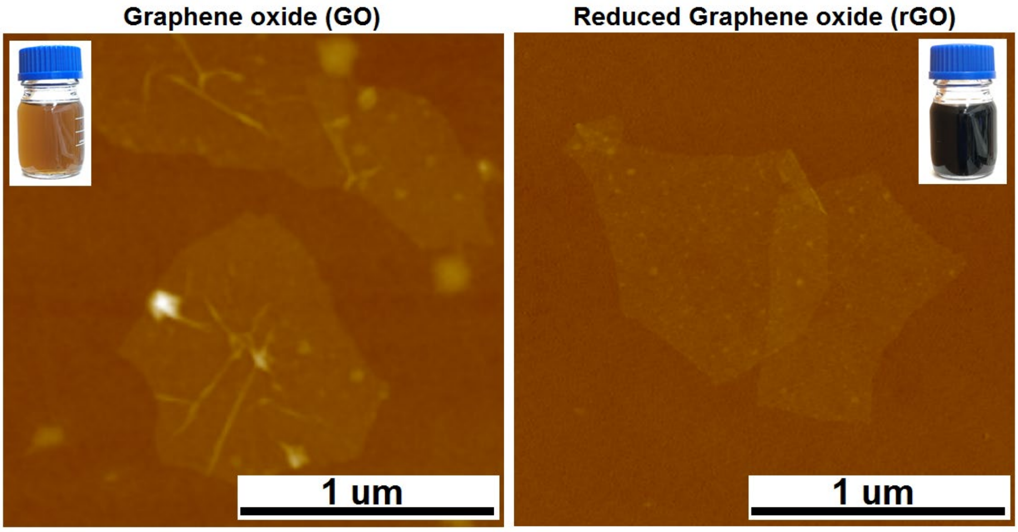

7.2. Introduction

Graphene and its derivatives such as graphene oxide (GO) and reduced graphene oxide (rGO) have unique structures and novel properties.[1-3] The surface functionalities and structural integrity of graphene materials significantly impact on their properties. Common methods for fabricating high quality graphene sheets include mechanical exfoliation[4] and chemical vapour deposition (CVD).[5] GO is prepared from graphite using the Brodie, Staudenmaier or Hummer methods[6] with the basal planes and edges of the graphene sheets heavily decorated with oxygen functionalities which render them hydrophilic and soluble in water. However, graphene oxide is electrically insulating due to the loss of electronic conjugations associated with surface functionalisation. There have been a number of efforts to restore the conjugated network and electrical properties using thermal and chemical reduction methods.[6, 7] Formation of this reduced graphene oxide (rGO) typically requires the use of hydrazine, urea, acids, hydroquinone, vitamin C, tea, hydrogen gas and $NaBH_4$, laser irradiation, and more.[8-17]

Herein we report a facile method for fabricating water-soluble rGO from GO under continuous flow conditions in a high shear generating thin film vortex fluidic device (VFD). The method involves UV irradiation of an aqueous dispersion of GO within the dynamic thin films in an angled glass tube in the VFD, at room temperature. The colloidally stable rGO is uniquely different compared to other methods in that the processing is (1) under flow, thereby facilitating scaling up of the process, as a feature of VFD processing in general, (2) environmentally friendly, using water as a benign solvent, and avoiding the use of harsh chemicals and reducing agents while minimising the generation of hazardous waste, and (3) simple, avoiding the need for complex operations. The VFD is an innovative processing technology which has been used for a diversity of applications, including in fabricating other carbon nanomaterials, as in slicing of SWCNTs with control over their length [18], exfoliating graphene from graphite and similarly hexagonal boron nitride,[19] scrolling GO,[20] the top down synthesis of carbon dots,[21] and assembling C_{60} into tubules.[22] The VFD allows the introduction of field effects into the processing, as exemplified in the present work, and with a thin film of liquid there is more uniform exposure to the field and thus the likelihood of more uniform product. This is important in irradiating a thin film of a dispersion of CNT with a pulsed Nd:YAG laser operating at 1064 nm, for slicing single, double and multi walled CNTs,[23] and similarly generating carbon dots from multi walled CNTs dispersed in aqueous hydrogen peroxide. Other applications of the VFD include controlling chemical reactivity and selectivity including photoredox reactions, protein folding and enhancing enzymatic reactions.[24, 25] The dynamic thin film in a VFD has the expected Stewartson/Ekman layers, and Faraday pressure waves, with the liquid moving up the rapidly rotating tube against gravity and exiting at the top.[24] The continuous flow mode of operation of the VFD has the attractive feature of addressing scalability of a process, with jet feeds delivering reagents into the inclined rapidly rotating 20 mm OD glass or quartz tube.

7.3. Results and discussion

GO suspended in water was processed in the VFD, systematically exploring the parameter space of the device, Figure 7. 1, initially in the so-called confined mode, for then translating to continuous flow where the GO solution is continually introduced into the rotating tube through a jet. This strategy has proven effect for optimizing a variety of processing in the VFD.[24, 25] The confined mode is where a finite amount of liquid is added to the VFD tube with the resulting shear stress at high rotation speeds effective, for example, in exfoliating graphene directly from graphite.[19] The rotational speed, concentration of the GO in water, and the flow rate were varied, with the tilt angle at 45°, as the optimized angle for a large number of processes in the VFD.[18-21] Both confined and continuous flow modes of VFD operation were effective in the reduction of the GO. As an additional control experiment, there was no evidence for reduction of GO in the VFD in the absence of the UV-light irradiation, as for a solution of GO in the absence of the UV-light without using VFD processing (SI Figure S4).

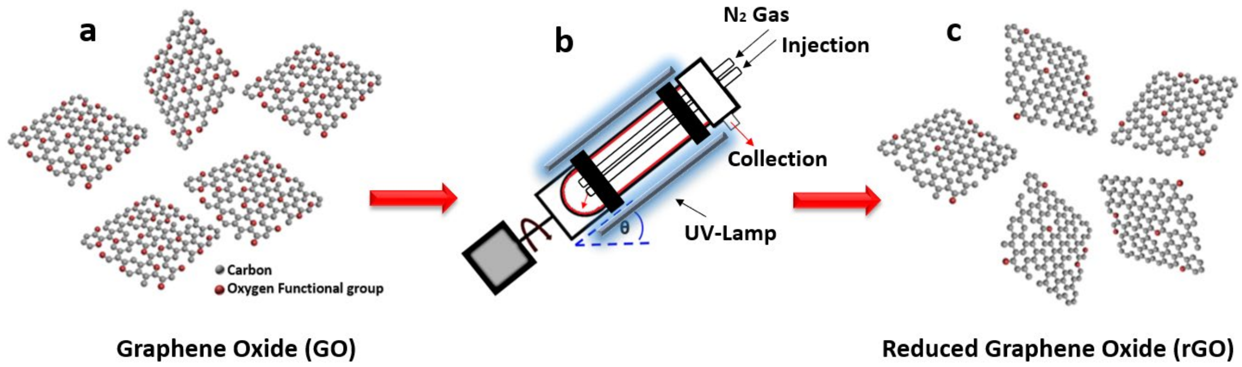

Figure 7. 1 Schematic of the set up for the reduction of GO in water in a VFD where a quartz tube (20 mm OD) tilted at 45° is irradiated with UV under nitrogen atmosphere, and the rotational speed systematically varied, along with concentration of the GO in water.

For the confined mode studies, 2 mL of aqueous solution of GO was added to the 20 mm O.D. (17.5 mm I.D.) quartz tube while simultaneously UV irradiated at λ= 254 nm, at 20 W, for 30 min under a nitrogen atmosphere. The rotational speed of the VFD was then set at 4, 5, 6, and 8k rpm, Figure S3. At 4k rpm, the colour of the GO solution turned dark brown, Figure 7. 2a, as an indicator of reduction of the GO.[16] The reaction time was then subsequently optimised, with 60 min resulting in a dark black liquid, the colour change being consistent with converting GO to rGO, where there is some restoration of electronic conjugation.[15, 26] Prolonging the processing time to 120 min gave the same visible result. The low effective rotational speed in the VFD, 4k rpm, is consistent with a higher residence time (longer reaction time) of liquid passing through the device relative to higher rotational speeds, although fluid flow differences and thus different shear stresses may also be at play.

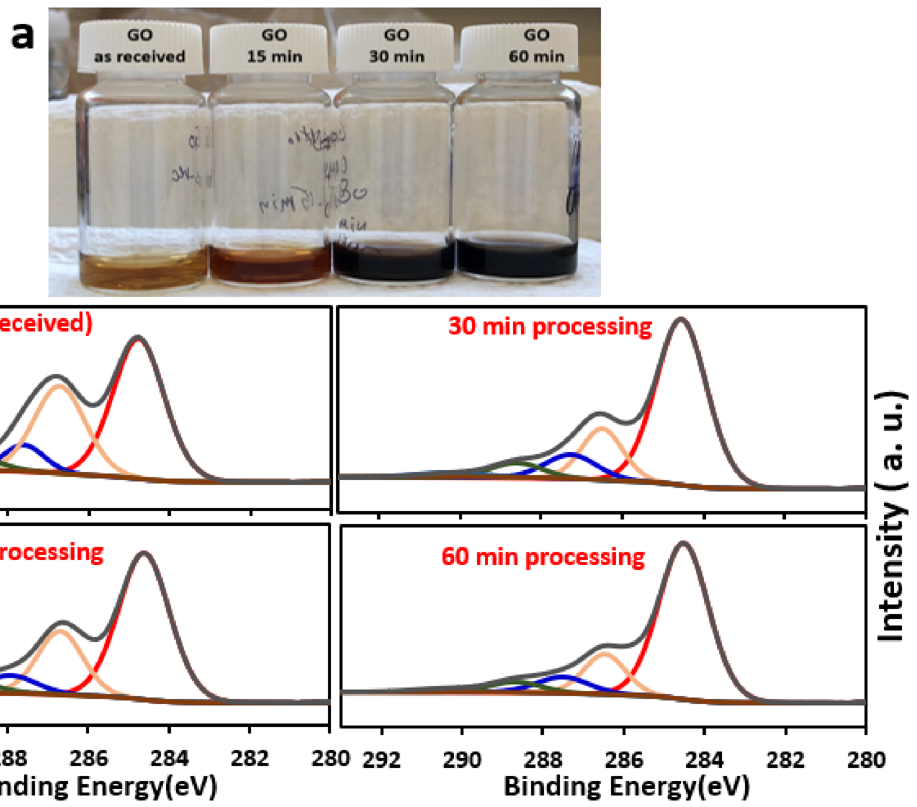

Figure 7. 2 (a) rGO solutions processed at different reaction times in the VFD, 15, 30 and 60 min; (b) High-resolution C1s XPS core-level spectra of the as received GO and after processing at different reaction times, 15, 30 and 60 min.

X-ray photoelectron spectroscopy (XPS) was used to ascertain the level of reduction, notably the reduction in oxygen content. Figure 7. 2b shows high-resolution C1s spectra of GO and the processed rGO at different reaction times, 15, 30 and 60 min respectively. The peak area of the C 1s peak of the processed samples were deconvoluted giving assignable peaks at ~ 284.0 eV, 285.0 eV, 288.0 eV, and 289.0 eV, which can be attributed to C=C/C−C, C−O, C=O, and HO−C=O, respectively. For as-received GO, the C–O (epoxy and alkoxy) and C=O peaks account for 23.8% and 5.3% of the oxygen present, [26] whereas this percentage dropped after the reduction process in the VFD, down to 13.1 % and 5% respectively, for 30 min processing. Thus, there is a significant amount of C=O groups remaining during the processing, with more detailed data presented in Table S1, ESI†.

Next, for scaling purposes, we translated the processing in the VFD to continuous flow, firstly varying the flow rate, selecting 0.20, 0.45, and 1.00 mL/min, using the 4k rpm optimal rotational speed for confined mode, at 45° tilt angle. The lowest, 0.2 mL/min was found to be optimal, with the aqueous suspension of GO delivered to the bottom of the rotating quartz tube through a stainless steel jet feed. To further increase the reduction of the GO, two sequential cycles of the UV-VFD processing were carried out, labelled as rGO (cycle 1) and rGO (cycle 2). The optimised parameters for continuous flow processing were the same as those in the confined mode, as the established norm for translating any process to continuous flow.[24] This is consistent with the flow rate being limited to 0.2 mL/min and that the effect of continuous flow is primarily the sum of the fluid dynamic response between drops entering the tube, with steady state achieved when liquid is exiting the tube, as in the present study.

Figure 7. 3a and b show the change in colour of the GO solution from light yellow to dark brown after the first cycle and then to a black solution when cycled through for the second time. The significant colour change is consistent with reduction of the GO and partial restoration of the π-π network [27, 28]. The rGO produced in the VFD was further studied using UV–visible spectroscopy, Figure 7. 4b. There is an increase in the absorption spectrum of rGO compared to the GO as received, which is consistent with GO being significantly reduced under UV irradiation. As the number of cycles increases, the reduction of the oxygen functional groups is increased. Overall, the UV-visible spectra are in good agreement with the literature for rGO prepared using other methods.[15, 16]

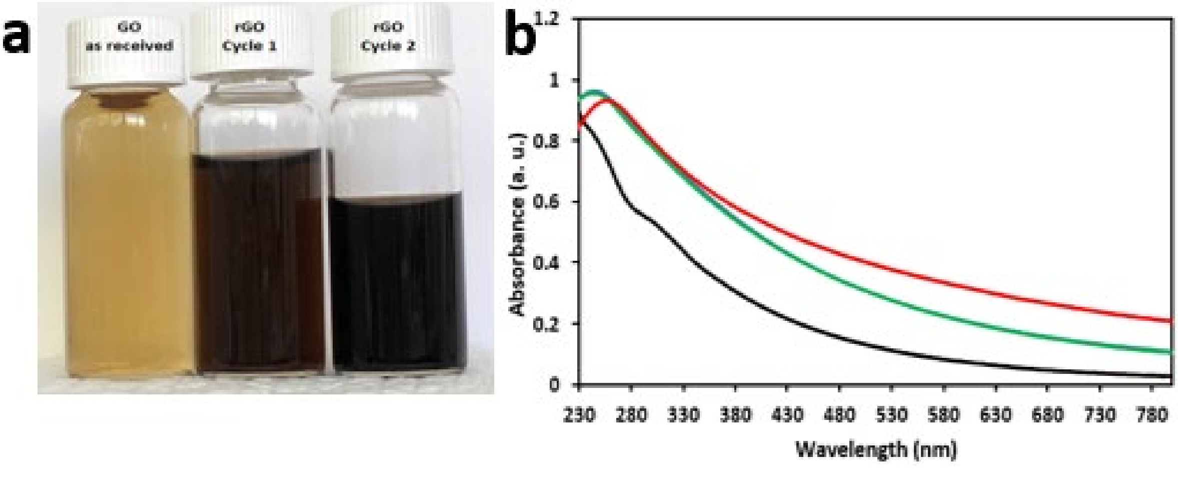

Figure 7. 3 (a) Change in colour of GO before and after VFD processing with UV irradiation, under nitrogen. (b) Absorption spectra of GO as received before processing, and rGO (Cycle 1) and rGO (Cycle 1) after processing at 4k rpm, tilt angle 45° and under continuous flow (0.2 mL/min), while UV irradiated.

Scanning electron microscopy (SEM) was used to investigate the morphology of GO and rGO, Figure(7. 4a-b). As received GO has wrinkled surfaces, folded edges and some aggregation whereas for rGO prepared herein, SEM images Figure (7. 4c-d) show smooth surfaces, devoid of wrinkles. In addition, atomic force microscopy (AFM) was also used to investigate the morphology as well as the height profiles of GO and rGO. Figure 7. 4e shows as received GO is wrinkled with folded edges, with a height of 1.1 nm, Figure 7. 4f, whereas rGO, Figure 7. 4g, has smooth surfaces, with a of 0.9 nm, Figure 7. 4h, which is consistent with removal of some oxygen functional groups.[29]

High-resolution C 1s XPS spectra for all three samples were fitted with multipeak as shown in Figure 7. 5a. For all, the main peak at ~284.6 eV corresponds to the C−C. Other peaks correspond to different oxygen functional groups; C−O at ~285.6 eV, C=O at ~287.5 eV and O=C−O at ~288.8 eV. After UV irradiation in the VFD, the dominated peak at 284.6 eV increased, whereas other peaks that relate to the oxygen functional groups dramatically decreased, with the results consistent with removal of oxygen functional groups. The survey scans, Figure S5, show that the oxygen content associated with functional groups decreases on recycling. Two sequential continuous VFD-UV irradiation cycles of the same sample (θ 45°, 4k rpm rotational speed, 20 W UV light power) further reduced the oxygen content. The atomic ratios of C1s/O1s, which represent the degree of reduction, are 1.5, 2.1 and 2.5 for GO as received, rGO (cycle 1) and rGO (cycle 2), respectively, clearly establishing a reduction in the amount of oxygen functional groups.

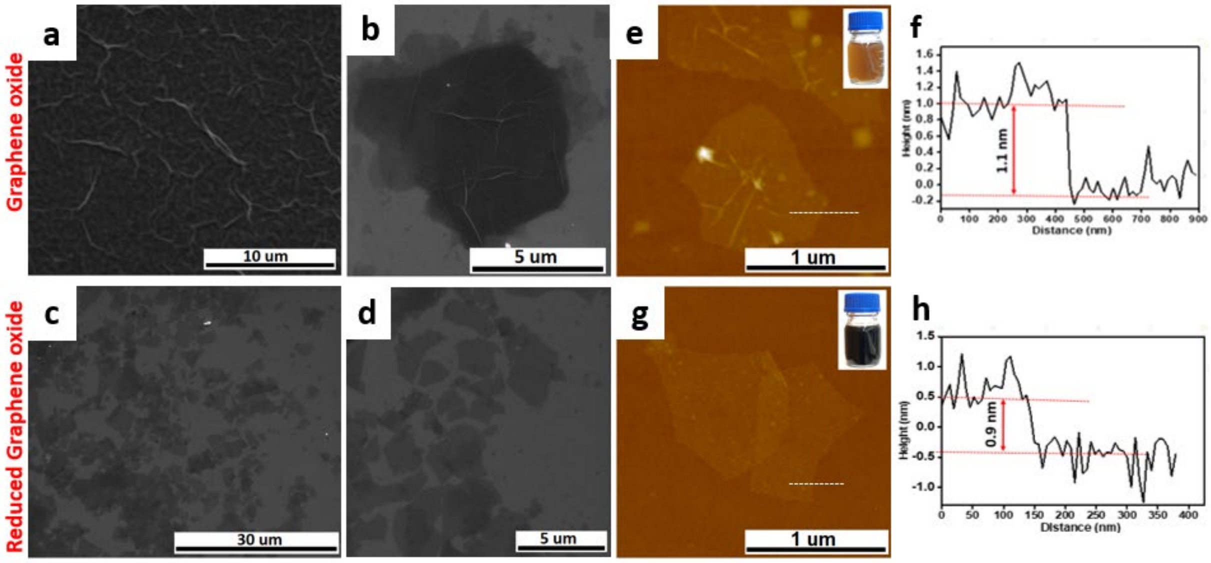

Figure 7. 4 (a-b) SEM and (e) AFM images of as received GO sheets before processing in the VFD, with the corresponding height profile in (f). (c-d) SEM and (g) AFM images images of rGO (cycle 2), with the corresponding height profile in (h). Inserted are optical images for GO solutions (0.2 mg/mL) before and after processing in the VFD at 4k rpm, tilt angle 45° and flow rate 0.2 mL/min, with UV irradiation, λ = 254 nm at 20 W, under nitrogen atmosphere.

Reduction of GO was also confirmed using Raman spectroscopy, Figure 7. 5b for GO, rGO(cycle 1) and rGO (cycle 2). The Raman spectra show two main features, a typical D-band at 1345 cm^{-1} and G-band at 1590 cm^{-1} for GO; these two peaks represent the structural disorders (sp^3) and tangential vibration of carbon atoms (sp^2), respectively.[30] The intensity ratio of D and G band (I_D/I_G) represents the disorder level of graphitic material. In the present study, the I_D/I_G value was determined as 1.02, 1.08 and 1.10 for GO, rGO (cycle 1) and rGO (cycle 2), respectively. The gradual increase of I_D/I_G from GO to rGO (cycle 2) is consistent with a decrease in oxygen content after processing, and thus an increase in conjugation in the sp^2 carbon graphene network.[26, 29] These results are in accordance with UV–visible absorption studies, as well as with XPS results (both confined and continuous flow modes), further supporting reduction of the GO dispersed in water during the VFD-UV irradiation processing. Table S2, ESI† show high-resolution XPS C1s spectra of GO (as received) and rGO from the two cycles of continuous flow processing in the VFD. After successive cycles, the C-C bond content increases from 50.50% (GO) to 64.21% for rGO (cycle 1) then to 68.14% for rGO (cycle 2), with the percentage of C-O bond content decreasing from 45.28% (GO) to 16.24% for rGO (cycle 1) then further to 14.89% for rGO (cycle 2). The above results establish that the oxyen functional group content in rGO is dramatically reduced using the VFD-UV mediated processing.

X-ray powder diffraction (XRD) patterns of as received GO and rGO are presented in Figure 7. 6a. That of as received GO shows the main characteristic peak at ~2θ 11.5°, corresponding to a d-spacing of 8.0818 Å, being attributed to the (001) plane of the material, with a small peak at 2θ ~26.60° attributed to the (001) plane.[31] After processing in the VFD under UV irradiation, a broad peak is present around 25°, which has a d-spacing of 4.15302 Å, being characteristic of the (002) plane. This is also consistent with the removal of oxygen containing groups of GO, forming rGO.[32]

TGA was used to further characterize the GO and rGO and to evaluate their thermal degradation, Figure 7. 6b, under an atmosphere of nitrogen with a heating rate of 5 ºC/min. The as received GO shows a sharp mass loss (~ 50 %) up to 250 ºC, due to the loss of physisorbed water as well as the removal of much of the oxygen-containing functional groups, as reported in the literature.[32] There is gradual mass loss beyond 250 ºC, corresponding to further removal of the functional groups.[32] In contrast, rGO has a ~27 % mass loss up to 500 ºC, much lower than that of as received GO, which supports removal of some oxygen-containing groups during reduction in the VFD-UV processing. rGO shows a sharp mass loss (52 %) between 500 to 640 ºC,[32] in accordance with XPS and Raman results, and potentially reflects the different structure of rGO formed under high shear relative to other forms of rGO.[33]

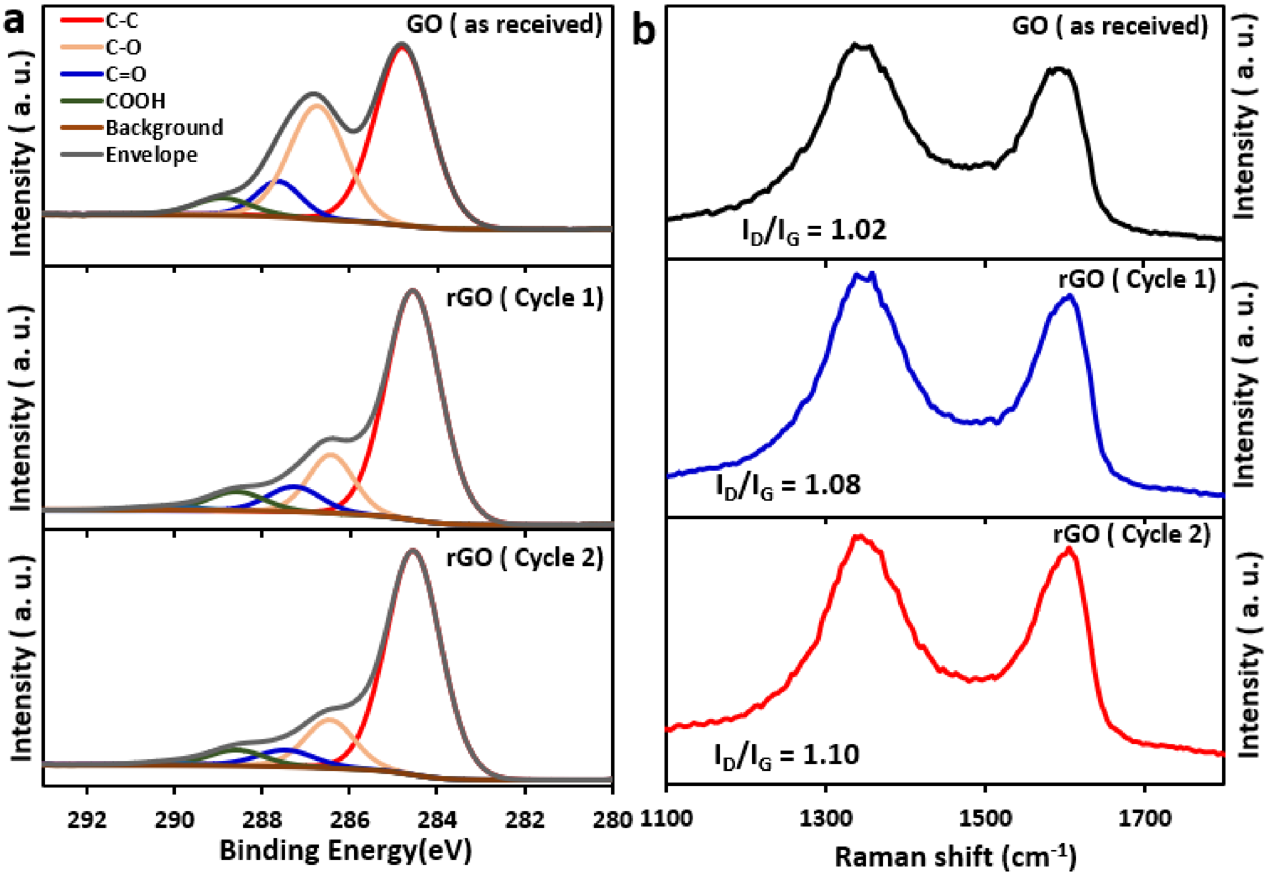

Figure 7. 5 (a) High-resolution C 1s XPS core-level spectra and (b) Raman spectrum of the as received GO, rGO (Cycle 1) and rGO (Cycle 1) after processing in the VFD at 4k rpm, under continuous flow, flow rate 0.2 mL/min, tilt angle 45°, while irradiated with UV at λ = 254 nm, 20 W, under nitrogen atmosphere.

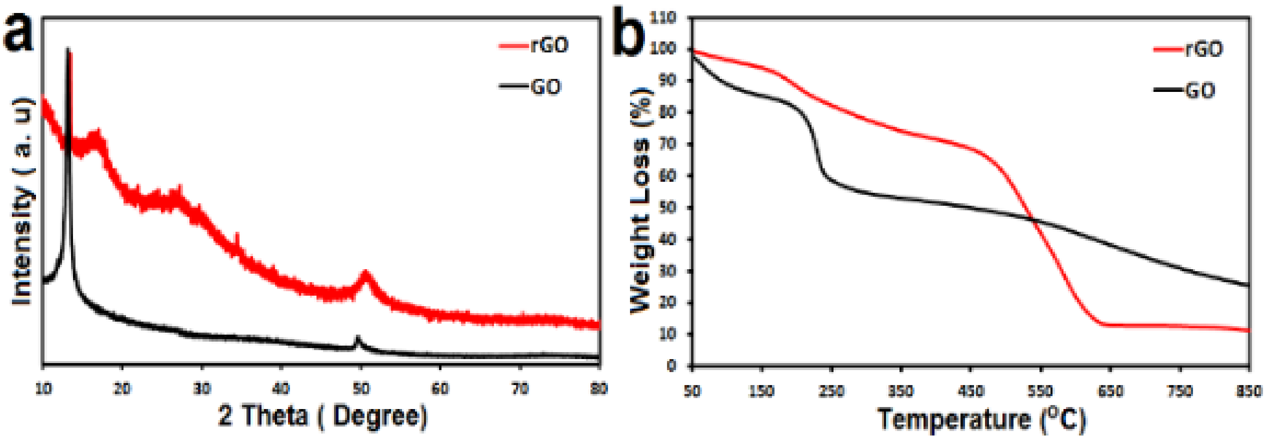

Figure 7. 6 (a) XRD and (b) TGA curves of GO as received (black line) and (b) rGO (cycle 2) (red line) after processing in the VFD at 4k rpm rotational speed, tilt angle 45°, under continuous flow (0.2 mL/min) while UV irradiated λ = 254 nm, 20 W.

The conductivity and resistance measurements of the GO and rGO was then carried out to further verify the degree of reduction. For comparison, a uniform film of the GO, rGO (cycle 1) and rGO (cycle 2) suspensions from the same concentrations, approximately 690 nm thick were prepared. Conductivity and resistance measurements were carried out using a four point probe. As shown in Figure 7. 7d, the GO film showed a high resistance of 3.8× 10^5**Ω**. The resistance of the rGO decreased to 3.3× 10^5 **Ω** and 2.2× 10^5**Ω** after Cycle 1 and 2 respectively. The decrease in the resistance further confirms reduction of the GO using the UV-VFD process. Figure 7. 7 shows the conductivity of GO (as received), which was 4.83×10^2 S/cm increasing to 3.5 × 10^3 S/cm for rGO (cycle 1) and 2× 10^4 S/cm in rGO (cycle 2). The difference in electrical conductivity is in accord with re-installing some π-conjugated network in the graphitic lattice.[26] Pei et al.[26] reduced GO using high temperatures, and showed that at 1100 °C the electrical conductivity of the rGO film obtained was 550 S/cm, while for the current room temperature generated rGO conductivity was 2× 10^4 S/cm, and indeed is the highest thus far reported.

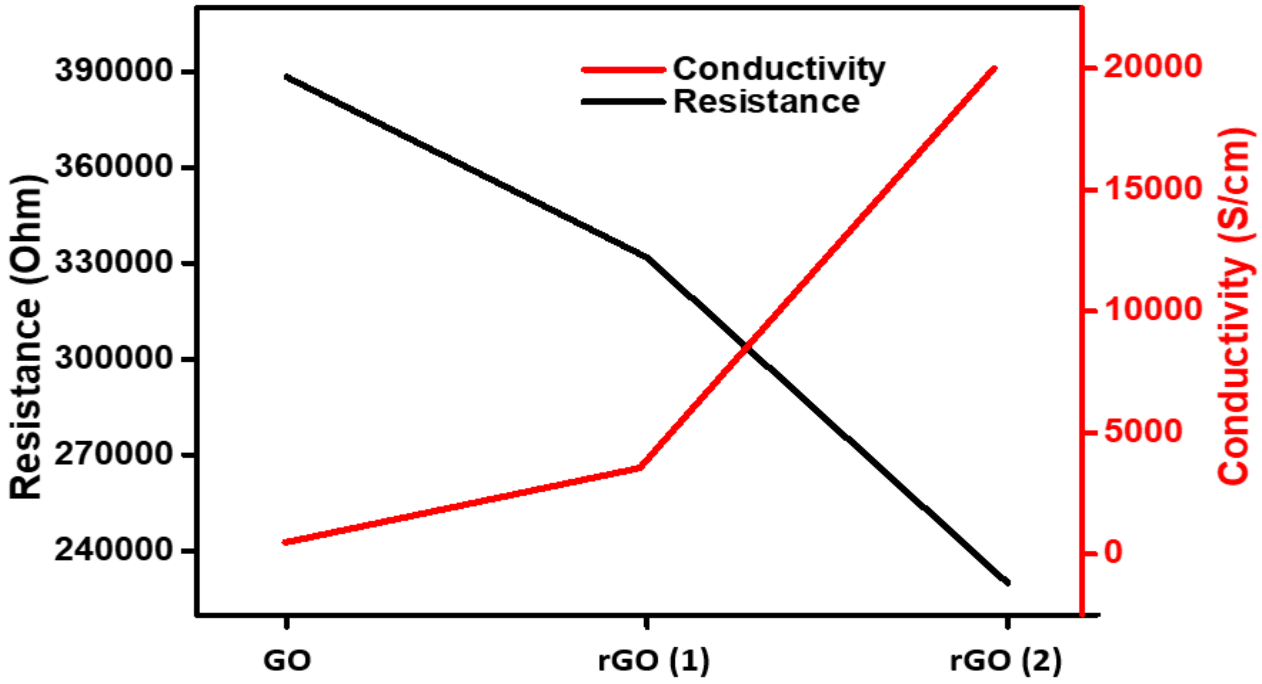

Figure 7. 7 The sheet resistance (black) and the conductivity (red) of as received GO and after VFD processing, cycle 1 and cycle 2.

7.4. Conclusions

We have established a facile method for reducing GO under continuous flow in the versatile vortex fluidic device where the dynamic thin film of liquid is uniformly UV irradiated. The properties of the rGO are comparable to those prepared using other methods while avoiding the generation of a waste stream. Moreover, these other methods are based on batch processing, which can suffer from batch-to-batch variation of product.

7.5. Acknowledgements

T. M. D. A thanks Taibah University (Ministry of Education, Saudi Arabia) for funding his scholarship. The authors also thank the Australian Research Council, The Government of South Australia, and AMMRF for support of this work.

Conflicts of interest

There are no conflicts to declare.

7.6. References

1. Li, Z.; Liu, Z.; Sun, H.; Gao, C., Superstructured assembly of nanocarbons: fullerenes, nanotubes, and graphene. *Chem. Rev.,* **2015,** *115*, 7046-7117.
2. Georgakilas, V.; Perman, J. A.; Tucek, J.; Zboril, R., Broad family of carbon nanoallotropes: classification, chemistry, and applications of fullerenes, carbon dots, nanotubes, graphene, nanodiamonds, and combined superstructures. *Chem. Rev.,* **2015,** *115*, 4744-4822.
3. Yang, Z.; Ren, J.; Zhang, Z.; Chen, X.; Guan, G.; Qiu, L.; Zhang, Y.; Peng, H., Recent advancement of nanostructured carbon for energy applications. *Chem. Rev.,* **2015,** *115* (11), 5159-5223.
4. Hernandez, Y.; Nicolosi, V.; Lotya, M.; Blighe, F. M.; Sun, Z.; De, S.; McGovern, I.; Holland, B.; Byrne, M.; Gun'Ko, Y. K., High-yield production of graphene by liquid-phase exfoliation of graphite. *Nat. Nanotechnol.,* **2008,** *3*, 563-568.
5. Li, X.; Magnuson, C. W.; Venugopal, A.; An, J.; Suk, J. W.; Han, B.; Borysiak, M.; Cai, W.; Velamakanni, A.; Zhu, Y., Graphene films with large domain size by a two-step chemical vapor deposition process. *Nano Lett.,* **2010,** *10*, 4328-4334.
6. Singh, R. K.; Kumar, R.; Singh, D. P., Graphene oxide: strategies for synthesis, reduction and frontier applications. *RSC Adv.,* **2016,** *6*, 64993-65011.
7. Stankovich, S.; Dikin, D. A.; Piner, R. D.; Kohlhaas, K. A.; Kleinhammes, A.; Jia, Y.; Wu, Y.; Nguyen, S. T.; Ruoff, R. S., Synthesis of graphene-based nanosheets via chemical reduction of exfoliated graphite oxide. *Carbon,* **2007,** *45*, 1558-1565.
8. Park, S.; An, J.; Potts, J. R.; Velamakanni, A.; Murali, S.; Ruoff, R. S., Hydrazine-reduction of graphite-and graphene oxide. *Carbon,* **2011,** *49*, 3019-3023.
9. Gao, W.; Alemany, L. B.; Ci, L.; Ajayan, P. M., New insights into the structure and reduction of graphite oxide. *Nat. Chem.,* **2009,** *1*, 403.
10. Shin, H. J.; Kim, K. K.; Benayad, A.; Yoon, S. M.; Park, H. K.; Jung, I. S.; Jin, M. H.; Jeong, H. K.; Kim, J. M.; Choi, J. Y., Efficient reduction of graphite oxide by sodium borohydride and its effect on electrical conductance. *Adv. Funct. Mater.,* **2009,** *19*, 1987-1992.
11. Wang, G.; Yang, J.; Park, J.; Gou, X.; Wang, B.; Liu, H.; Yao, J. J. T., Facile synthesis and characterization of graphene nanosheets. *J. Phys. Chem. C*, **2008,** *112*, 8192-8195.
12. Chen, W.; Yan, L.; Bangal, P. R., Preparation of graphene by the rapid and mild thermal reduction of graphene oxide induced by microwaves. *Carbon,* **2010,** *48*, 1146-1152.
13. Wakeland, S.; Martinez, R.; Grey, J. K.; Luhrs, C. C., Production of graphene from graphite oxide using urea as expansion–reduction agent. *Carbon,* **2010,** *48*, 3463-3470.
14. Chen, J.; Shepherd, R. L.; Razal, J. M.; Huang, X.; Zhang, W.; Zhao, J.; Harris, A. T.; Wang, S.; Minett, A. I.; Zhang, H., Scalable solid-template reduction for designed reduced graphene oxide architectures. A*CS Appl. Mater. Interfaces,* **2013,** *5*, 7676-7681.
15. Wang, Y.; Shi, Z.; Yin, J., Facile synthesis of soluble graphene via a green reduction of graphene oxide in tea solution and its biocomposites. *ACS Appl. Mater. Interfaces,* **2011,** *3*, 1127-1133.
16. Huang, L.; Liu, Y.; Ji, L.-C.; Xie, Y.-Q.; Wang, T.; Shi, W.-Z., Pulsed laser assisted reduction of graphene oxide. *Carbon,* **2011,** *49*, 2431-2436.
17. Trusovas, R.; Ratautas, K.; Račiukaitis, G.; Barkauskas, J.; Stankevičienė, I.; Niaura, G.; Mažeikienė, R., Reduction of graphite oxide to graphene with laser irradiation. *Carbon,* **2013,** *52*, 574-582.
18. Alharbi, T. M.; Vimalanathan, K.; Lawrance, W. D.; Raston, C. L., Controlled slicing of single walled carbon nanotubes under continuous flow. *Carbon* **2018**, 140, 428-432.
19. Chen, X.; Dobson, J. F.; Raston, C. L., Vortex fluidic exfoliation of graphite and boron nitride. *Chem. Commun.,* **2012,** *48*, 3703-3705.
20. Alharbi, T. M.; Harvey, D.; Alsulami, I. K.; Dehbari, N.; Duan, X.; Lamb, R. N.; Lawrance, W. D.; Raston, C. L., Shear stress mediated scrolling of graphene oxide. *Carbon,* **2018**, 137, 419-424.

21. Luo, X.; Al-Antaki, A. H. M.; Vimalanathan, K.; Moffatt, J.; Zheng, K.; Zou, Y.-C.; Zou, J.; Duan, X.; Lamb, R.; Wang, S., Laser irradiated vortex fluidic mediated synthesis of luminescent carbon nanodots under continuous flow. *React. Chem. Eng.,* **2018**, 3, 164-170.
22. Vimalanathan, K.; Shrestha, R. G.; Zhang, Z.; Zou, J.; Nakayama, T.; Raston, C. L., Surfactant-free Fabrication of Fullerene C60 Nanotubules Under Shear. *Angew.Chem, Int, Ed.,* **2017**, 56, 8398-8401.
23. Vimalanathan, K.; Gascooke, J. R.; Suarez-Martinez, I.; Marks, N. A.; Kumari, H.; Garvey, C. J.; Atwood, J. L.; Lawrance, W. D.; Raston, C. L., Fluid dynamic lateral slicing of high tensile strength carbon nanotubes. *Sci. Rep.,* **2016,** *6*, 22865.
24. Britton, J.; Stubbs, K. A.; Weiss, G. A.; Raston, C. L., Vortex Fluidic Chemical Transformations. *Chem.- Eur. J.,* **2017**, 23, 13270-13278.
25. Vimalanathan, K.; Raston, C. L., Dynamic Thin Films in Controlling the Fabrication of Nanocarbon and Its Composites. *Adv. Mater. Technol.,* **2017**, 2, 1600298.
26. Pei, S.; Cheng, H.-M., The reduction of graphene oxide. *Carbon,* **2012,** *50*, 3210-3228.
27. Becerril, H. A.; Mao, J.; Liu, Z.; Stoltenberg, R. M.; Bao, Z.; Chen, Y., Evaluation of solution-processed reduced graphene oxide films as transparent conductors. *ACS Nano,* **2008,** *2*, 463-470.
28. Williams, G.; Seger, B.; Kamat, P. V., TiO2-graphene nanocomposites. UV-assisted photocatalytic reduction of graphene oxide. *ACS Nano,* **2008,** *2*, 1487-1491.
29. Huang, L.; Liu, Y.; Ji, L.-C.; Xie, Y.-Q.; Wang, T.; Shi, W.-Z., Pulsed laser assisted reduction of graphene oxide. *Carbon,* **2011,** *49*, 2431-2436.
30. Amadei, C. A.; Stein, I. Y.; Silverberg, G. J.; Wardle, B. L.; Vecitis, C. D., Fabrication and morphology tuning of graphene oxide nanoscrolls. *Nanoscale* **2016,** *8*, 6783-6791.
31. Yang, Y.; Zhang, X.; Wang, H.; Tang, H.; Xu, L.; Li, H.; Zhang, L., Preparation of Nanoscrolls by Rolling up Graphene Oxide–Polydopamine–Au Sheets using Lyophilization Method. *Chem. –Asian J.,* **2016,** *11*, 1821-1827.
32. Alotaibi, F.; Tung, T. T.; Nine, M. J.; Kabiri, S.; Moussa, M.; Tran, D. N.; Losic, D., Scanning atmospheric plasma for ultrafast reduction of graphene oxide and fabrication of highly conductive graphene films and patterns. *Carbon,* **2018,** *127*, 113-121.
33. Li, L.; Yin, J; Liu. Y.; and Zhao, X., Graphene oxide vs. reduced graphene oxide as core substrate for core/shell-structured dielectric nanoplates with different electro-responsive characteristics. *J. Mater. Chem. C*, 2015, 3, 5098–5108.

ChemComm

COMMUNICATION

View Article Online
View Journal | View Issue

Check for updates

Cite this: Chem. Commun., 2019, 55, 11438

Received 8th July 2019, Accepted 27th August 2019

DOI: 10.1039/c9cc05217h

rsc.li/chemcomm

Continuous flow photolytic reduction of graphene oxide†

Thaar M. D. Alharbi,[ab] Amira R. M. Alghamdi,[a] Kasturi Vimalanathan[a] and Colin L. Raston *[a]

Reduced graphene oxide (rGO) is generated from GO dispersed in water under continuous flow in the absence of harsh reducing agents, in a vortex fluidic device, such that the processing is scalable with uniformity of the product. This involves simultaneously UV irradiating (λ = 254 nm, 20 W) the dynamic thin film in the rapidly rotating glass tube in the microfluidic platform. The rGO is comparable to that formed using waste generating chemical based processing, with a film of the material having a resistance of $2.2 \times 10^5\ \Omega$ and a remarkably high conductivity of 2×10^4 S cm^{-1}.

Graphene and its derivatives such as graphene oxide (GO) and reduced graphene oxide (rGO) have unique structures and novel properties.[1–3] The surface functionalities and structural integrity of graphene materials significantly impact on their properties. Common methods for fabricating high quality graphene sheets include mechanical exfoliation[4] and chemical vapour deposition (CVD).[5] GO is prepared from graphite using the Brodie, Staudenmaier or Hummer methods[6] with the basal planes and edges of the graphene sheets heavily decorated with oxygen functionalities which render them hydrophilic and soluble in water. However, graphene oxide is electrically insulating due to the loss of electronic conjugations associated with surface functionalisation. There have been a number of efforts to restore the conjugated network and electrical properties using thermal and chemical reduction methods.[6,7] Formation of this reduced graphene oxide (rGO) typically requires the use of hydrazine, urea, acids, hydroquinone, vitamin C, tea, hydrogen gas and NaBH$_4$, laser irradiation, and more.[8–17]

Herein we report a facile method for fabricating water-soluble rGO from GO under continuous flow conditions in a high shear generating thin film vortex fluidic device (VFD). The method involves UV irradiation of an aqueous dispersion of GO within the dynamic thin films in an angled glass tube in the VFD, at room temperature. The colloidally stable rGO is uniquely different compared to other methods in that the processing is (1) under flow, thereby facilitating scaling up of the process, as a feature of VFD processing in general, (2) environmentally friendly, using water as a benign solvent, and avoiding the use of harsh chemicals and reducing agents while minimising the generation of hazardous waste, and (3) simple, avoiding the need for complex operations. The VFD is an innovative processing technology which has been used for a diversity of applications, including in fabricating other carbon nanomaterials, as in slicing of SWCNTs with control over their length,[18] exfoliating graphene from graphite and similarly hexagonal boron nitride,[19] scrolling GO,[20] the top down synthesis of carbon dots,[21] and assembling C$_{60}$ into tubules.[22] The VFD allows the introduction of field effects into the processing, as exemplified in the present work, and with a thin film of liquid there is more uniform exposure to the field and thus the likelihood of more uniform product. This is important in irradiating a thin film of a dispersion of CNT with a pulsed Nd:YAG laser operating at 1064 nm, for slicing single, double and multi walled CNTs,[23] and similarly generating carbon dots from multi walled CNTs dispersed in aqueous hydrogen peroxide. Other applications of the VFD include controlling chemical reactivity and selectivity including photoredox reactions, protein folding and enhancing enzymatic reactions.[24,25] The dynamic thin film in a VFD has the expected Stewartson/Ekman layers, and Faraday pressure waves, with the liquid moving up the rapidly rotating tube against gravity and exiting at the top.[24] The continuous flow mode of operation of the VFD has the attractive feature of addressing scalability of a process, with jet feeds delivering reagents into the inclined rapidly rotating 20 mm OD glass or quartz tube.

GO suspended in water was processed in the VFD, systematically exploring the parameter space of the device, Fig. 1, initially in the so-called confined mode, for then translating to continuous flow where the GO solution is continually introduced into the rotating tube through a jet. This strategy has proven effect for optimizing a

---

[a] *Flinders Institute for Nanoscale Science and Technology, College of Science and Engineering, Flinders University, Adelaide, SA 5001, Australia. E-mail: colin.raston@flinders.edu.au*

[b] *Physics Department, Faculty of Science, Taibah University, Almadinah Almunawarrah, Saudi Arabia*

† Electronic supplementary information (ESI) available. See DOI: 10.1039/c9cc05217h

Electronic Supplementary Material (ESI) for ChemComm.

Supplementary Information for

Continuous flow photolytic reduction of graphene oxide

Thaar M. D. Alharbi, [a,b] Amira R. M. Alghamdi, [a] Kasturi Vimalanathan, [a] and Colin L. Raston *[a]

[a] Flinders Institute for NanoScale Science and Technology, College of Science and Engineering, Flinders University, Adelaide SA 5001, Australia email: colin.raston@flinders.edu.au

[b] Physics Department, Faculty of Science, Taibah University, Almadinah Almunawarrah, Saudi Arabia

*Corresponding authors:

Tel: +61 8 82017958 E-mail address: Colin.raston@Flinders.edu.au (Colin Raston)

Chapter Eight

High Yielding Continuous Flow Synthesis of Spheroidal C_{60}@Graphene – Composites as Supercapacitor

Ibrahim K. Alsulam,[†,‖] Thaar M. D. Alharbi,[†, §,‖] Mahmoud Moussa,[‡,⊥] and Colin L. Raston [†, *]

[†] Flinders Institute for Nanoscale Science and Technology, College of Science and Engineering, Flinders University, Adelaide SA 5001, Australia

[§] Physics Department, Faculty of Science, Taibah University, Almadinah Almunawarrah 42353, Saudi Arabia

[‡] School of Chemical Engineering, The University of Adelaide, Adelaide SA 5001,

[⊥] Department of Chemistry, Faculty of Science, Beni-Suef University, Beni-Suef 62111, Egypt

[‖] These authors contributed equally to this work.

This study was published in ***ACS Omega,*** Year **2019**, 21, 19279-19286. The first page of the publication and SI are attached.

Author contributions: **IA** preformed the original work and carried out the SEM and XRD measurements. **TA** performed most of the VFD and most characterization experiments and data analysis, and wrote the primary content. **MM** performed the electrochemical measurements. **CR** supervised and coordinated the project and helped on the research directions and plan, and the final revision of the manuscript. All of the co-authors assisted with the revision of the manuscript before and during the publication process.

8.1. Abstract

Graphene spheres confining fullerene C_{60} are quantitatively formed under high shear and continuous flow processing using a vortex fluidic device (VFD). This involves intense micromixing a colloidal suspension of graphite in DMF and an *o*-xylene solution of C_{60} at room temperature in the absence of surfactants and other auxiliary substances. The diameters of the composite spheres, C_{60}@graphene, can be controlled with size distributions ranging from 1.5 to 3.5 µm, depending on the VFD operating parameters, including rotational speed, flow rate, relative ratio of C_{60} to graphite and the concentration of the fullerene. An electrode of the composite material has high cycle stability, with a high areal capacitance of 103.4 mF cm^{-2}, maintaining its capacitances to 24.7 F g^{-1} and 86.4 mF cm^{-2} (83.5%) at a high scan rate of 100 mV s^{-1}.

KEYWORDS: Graphene • fullerene C_{60} • Spheres • Composites • Vortex fluidic device • Scalability

Graphical Abstract

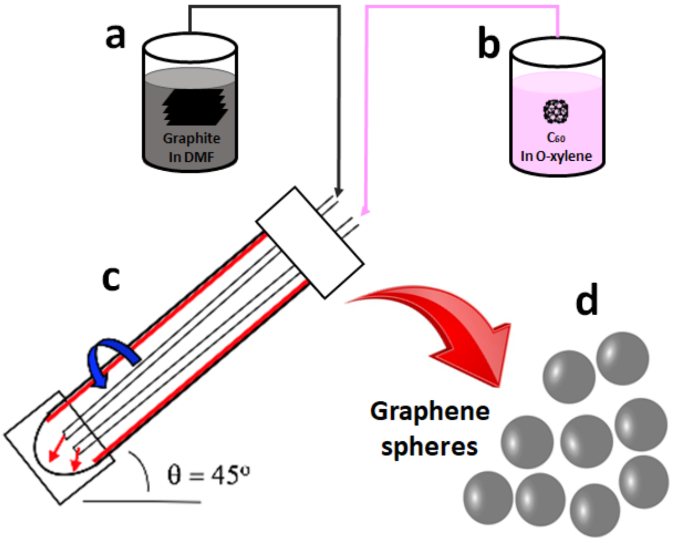

8.2. Introduction

Carbon nanomaterials have emerged as key materials for future technology, for developing complex functional structures devoid of potentially toxic metals and metals which are likely to have supply chain issues in the near future.[1] Graphene, as a single 2D planar sheet of graphite arranged in a hexagonal lattice,[2] is one of the newest forms of such nanomaterials. It has remarkable chemical, physical, and electrical properties, with high conductivity in the absence of defects and wrinkles, large specific surface area and excellent mechanical flexibility,[1, 3] and features in a growing number of applications. These include in batteries, super-capacitors, catalyst support, drug-delivery, electrode materials for energy storage devices, membranes, biomedical devices, and coatings, and these relate to its multifarious and interdisciplinary properties.[1, 3-7]

Graphene can be transformed into other structures including 0D nanoparticles (carbon dots), 1D nanofibers (carbon nanofibers and nanotubes), 2D nanosheets (graphene oxide) and 3D nanostructure (hollow carbon nanospheres) and fullerenes, and composites of these.[8-11] Among these different carbon nano-materials, graphene spheres have promise in a wide range of applications covering energy storage including lithium ion batteries, separation systems, oxygen-reduction, catalyst supports, nanoreactors and adsorption.[12-21]

The synthesis of graphene spheres with smooth surfaces and uniform size use soft template processing,[22] hard templating (silicon template),[23] solvothermal techniques,[24] sol pyrolysis,[25] microemulsion polymerization[26] and hydrothermal reduction[27, 28] and gelation.[29] Related to this is extended oxidation strategies to alter the morphology and surface topography of graphene oxide (GO) nanosheets, as a potential route to build up 3D graphene architectures.[30, 31] However, the synthetic strategies for gaining access to such architectures are limited by the high cost of production, the use of harsh chemicals or surfactants, high temperature processing as a high-energy penalty, and limited scope for scaling up the process.[5] A challenge is to develop a scalable, low-cost method high in green chemistry or sustainability metrics, for gaining access to 3D graphene-based materials, including graphene spheres and composites thereof.

To this end we have explored the use of continuous flow processing to prepare graphene spheres and graphene-fullerene composite spheres directly from graphite and fullerene C_{60}, at room temperature, avoiding the use of auxiliary reagents. This involved the use of the in-house developed continuous flow vortex fluidic device (VFD) which was developed early this decade.[4] It is a versatile microfluidic platform containing a dynamic thin film, in contrast to traditional channel based microfluidics which can suffer from clogging. Mechanoenergy is delivered into the liquid in the VFD in a controlled way.[4] Under continuous flow VFD processing, jet feeds deliver solution into an inclined rapidly rotating tube, opened at one end and usually housing a glass or quartz tube 20 mm outside diameter (OD) and 16.000 ± 0.013 mm internal diameter (ID), Figure 8. 1,[32] with the liquid whirling up and out of the tube. In the confined mode of operation of the VFD, a finite volume of liquid is processed in the tube, and this is effective in processing small volumes of liquid as well as a proven method for exploring the operating parameter space of the VFD for a particular process prior to extending the process into continuous flow.[33]

The versatile VFD has a number of remarkable applications, encompassing probing the structure of self-organised systems, material processing, controlling chemical reactivity and selectivity, including enhancing enzymatic reactions, and more.[34] The first publication reporting the VFD was in 2012, describing the exfoliation of graphite along with hexagonal boron nitride, using the confined mode of operation of the device.[35] Since then other forms of carbon have been fabricated in the device, including toroidal structures of self-assembled single walled carbon nanotubes,[36] laser aided slicing of single and multi-walled carbon nano-tube[37] the formation of carbon dots (from multi-walled carbon nanotubes),[33] controlling the self-assembly of fullerene C_{60} molecules into nanotubules using water as an 'anti-solvent'[32] and the fabrication of fullerene C_{60} cones in a 1:1 mixture of *o*-xylene and DMF.[38] The VFD is also effective in controlling the nucleation and growth of palladium nanoparticles on graphene,[39] the decoration of palladium nanoparticle on carbon nano-onions,[40] and transforming graphene oxide into graphene oxide scrolls.[41]

We report a facile room temperature one-step synthesis of graphene spheres confining fullerene C_{60}, directly from graphite dispersed in DMF and an *o*-xylene solution of the fullerene. Remarkably, the composite material, C_{60}@graphene, is formed quantitatively with respect to graphite, with the ability to tune the size of the spheres, while avoiding using auxiliary substances such as surfactants which can affect surface properties of the resulting nanomaterials. To demonstrate an application of C_{60}@graphene, its supercapacitor performance was evaluated using the spheres as electrodes, which delivered a gravimetric capacitance of 29.5 F g^{-1} at a scan rate of 5 mV s^{-1}. While other types of graphene can reach such capacitance up to 250 F g^{-1},[42-45] the C_{60}@graphene electrode has an areal capacitance of 103.4 mF cm^{-2} which is higher than values for other carbon derivatives, for example in (GF-CNT@Fe_2O_3) (53.56 mF/cm^2 at 10 mA/cm^2).[46] Moreover, the device reported herein can maintain its capacitances to 24.7 F g^{-1} and 86.4 mF cm^{-2} (83.5%) at a high scan rate of 100 mV s^{-1}, establishing a high rate capability of graphene spheres electrode and potential of the material in the next-generation energy storage devices.

8.3. Experimental section

8.3.1. Materials and chemicals

Graphite flakes of 99% purity were suspended in 99.5% Dimethyformamide (DMF), and fullerene C_{60} (99.5% purity) was dissolved in *o*-xylene, with both materials and solvents purchased from Sigma Aldrich.

8.3.2. Sample preparation and materials synthesis

Suspensions of graphite in DMF were prepared at different concentrations, namely 1, 1.5, 2 and 2.5 mg/mL, and then sonicated for 15 min, followed by centrifuged for 30 min to remove undispersed graphite. Solutions of fullerene C_{60} were prepared in *o*-xylene at different concentrations, namely 0.5, 1, 1.5 and 2 mg/mL. Initially, as received fullerene was added to *o*-xylene and the mixture allowed to stand at room temperature for 24 hours, whereupon it was filtered (60 μm filter paper) to remove undissolved particles, before mixing with graphite dispersed in DMF in the VFD using different jet feeds, Figure 8. 1 Operating parameter space for the VFD was systematically explored, in particular the rotational speed of the rapidly rotating glass tube, concentration of graphite and fullerenes, flow rate and ratio of the two solvents. After VFD processing, the resulting carbon material was collected via centrifugation at g=1.751 rfc for 20 min.

8.3.3. Characterization

Samples of C_{60}@graphene on silicon wafers were prepared by drop casting, followed by evaporation under ambient conditions. The morphology, size and shape of the particles and their properties were studied using a number of complementary techniques including scanning electron microscope (SEM) with an accelerating voltage of 5 kV, and operating at 10 mm working distance, transmission electron microscopy (TEM) conducted on a TECNAI 20 microscope operated at 120 and 200 kV, X-ray diffraction (XRD) with the data collected using a Bruker ADVANCE D8 ECO, Co- Kα, at an operating wavelength of 1.7988 Å with 2θ varied from 10^o to 80^o. Samples of as prepared material were formed by drying them in nitrogen at 55 C^o for three days. They were then stored and kept at room temperature for 48 hours. Raman spectroscopy was used to confirm structure integrity of the as prepared carbon materials, with the spectra recorded using a Horiba XploRA apparatus at fixed wavelength of 532 nm.

8.3.4. Electrochemical characterization and Supercapacitor fabrication

To fabricate the supercapacitors, the active material was mixed with carbon black and polyvinylidene difluoride (PVDF) in a mass ratio of 80:10:10. The resulting paste was pressed and attached to platinum foils as the current collectors, between which a piece of filter paper was sandwiched as a separator and 1.0 M H_2SO_4 was used as electrolyte. All electrochemical tests including cyclic voltammetry (CV), galvanostatic charge/discharge (CD) and electrochemical impedance spectroscopy (EIS) were carried out using a two-electrode cell configuration by a CHI 760C electrochemical workstation.

8.4. Results and discussion

8.4.1. Fabrication of C_{60}@graphene spheres

Conventional methods for fabricating graphene/carbon spheres require complex multistep procedures which are typically non-scalable. We find that a graphene- fullerene C_{60} composite is readily prepared in the VFD in the absence of other reagents, and importantly in essentially quantitative yield relative to graphite with the processing illustrated in Figure 8. 1a. Under continuous flow mode of operation in the VFD, one jet feed delivered an *o*-xylene solution of C_{60}, with another jet feed delivering a suspension of graphite in DMF, both to the hemispherical base of the rapidly rotating glass tube. The operating parameters of the VFD were systematically varied to form the optimal product, as the most uniform in terms of morphology, size and shape distributions of the spheres, and highest yield. For this the rotational speed was 4k rpm, tilt angle of the glass tube θ= 45°, concentration of C_{60} in *o*-xylene at 0.5 mg/mL, concentration of graphite in DMF at 1 mg/mL, with a 1:1 ratio of the two solvents, and the flow rate for both liquids at 0.5 mL /min. The tilt angle of the tube in the VFD was fixed at 45°, where there is unique complex fluid dynamics, and is the optimized angle for a plethora of processing applications of the device.[4]

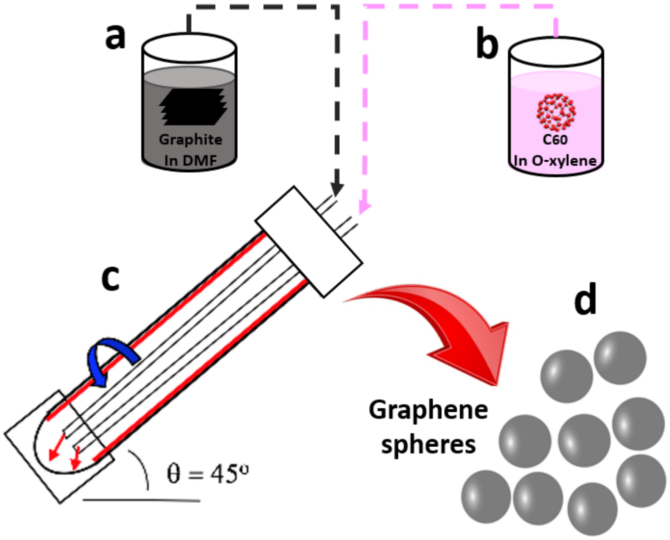

Figure 8. 1 Schematic illustration of the overall method for fabricating the composite spheres under shear stress in a vortex fluidic device (VFD), using a 1:1 mixture of an o-xylene solution of C_{60} and a suspension of graphite in DMF, with the optimized conditions at a rotational speed (ω) = 4k rpm, flow rate ($\acute{v}$)= 0.5 mL/min, θ = 45°, concentration of graphite in DMF 1 mg/mL, and concentration of C_{60} in o-xylene 0.5 mg/mL.

8.4.2. The mechanism of formation of the composite spheres

Intense micromixing DMF with *o*-xylene in a 1:1 ratio in the absence of graphite results in the formation of cones comprised of ca 0.5 to 2.5 µm diameter self assembled particles of C_{60}, also under continuous flow conditions and with the optimal rotational speed also at 4k rpm. [38] As in the present study the DMF acts as an anti-solvent, resulting in the formation of nanoparticles of the fullerene which are likely to adhere to the surface of the graphite flakes, Figure 8. 2a, facilitating exfoliation by leveraging the graphene layers which then wrap up the fullerene particles under high shear, Figure 8. 2b. Then the process starts again on the resulting exposed graphene surface once a certain threshold of fullerene particles adheres to the surface, and so on. This accounts for the fullerene particles being primarily confined within an outer layer of graphene sheets Figure 8. 2c. Processing in the absence of C_{60} (for a 1:1 mixture of *o*-xylene and DMF), affords exfoliated graphene, whereas the same processing for C_{60} in the absence of graphite results in the formation of particles of the fullerene < 100 nm, Figure S1, which importantly are similar to the size of the fullerene particles present within the spheres. These were determined by sonicating the isolated spheres in DMF for 30 min, Figure 8. 2d, with the resulting ruptured spheres containing particles of C_{60} in the range 5 to 100 nm. These findings give credence to the proposed mechanism of the formation of particles of C_{60} adhering to the exposed graphene surface of graphite, presumably favored by π-π interactions between the two components. These are then transformed into spheres comprising of at most a few layers of graphene, with the number of sheets of stacked graphene limited by the mechanical energy imparted in dynamic thin film in the device.

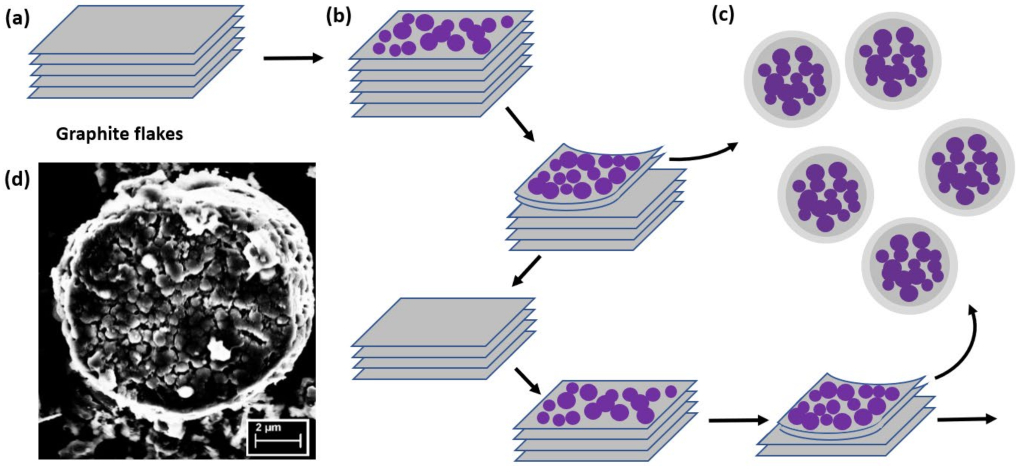

Figure 8. 2 Proposed mechanism of the VFD synthesis of graphene spheres confining particles of self assembled C_{60}, along with an SEM image of a fragmented sphere formed during sonication post VFD processing, scale bar 2 μm.

8.4.3. Morphology of the C_{60}@graphene spheres

SEM images of different magnification of graphene sphere composites, formed under the above optimized conditions, are shown in Figure 8. 3, along with a size distribution inset, centered at 3.5 μm. The particles are regular spheres with smooth surfaces and are not highly aggregated. The spheres were also examined using TEM, Figure 8. 4(a, b), which revealed small particles of C_{60} ca 10 to 50 nm in diameter attached to the surface of the composite materials, and other nanoparticles of comparable size unattached, and with C_{60} particles on the inside. The presence of C_{60} particles on the surface of the spheres, and inside the spheres, is in accordance with the observation of SEM, Figure. 3. The high-resolution TEM image (Figure 8. 4(c, d)) reveals that the graphene spheres have some C_{60} particles on the surface of the spheres as well as inside them.

We found that the morphology, size and shape of the spheres varied on changing the rotational speed, flow rate of both liquids and changing the concentration of graphite and fullerene, as established using SEM. The optimized speed for generating smooth spheres was 4k rpm, Figure 8. 3 a-e. At much higher speed, 7.5k rpm, with the other parameters unchanged, the surfaces of the spheres are textured, but remarkably the spheres now have a hole connecting the outer surface and inner surface of the tube, Figure S5. At 6k and 9k rpm, with the other parameters unchanged, the surfaces of the spheres are also textured and non-uniform, Figure S4 & S6. The ratio of the two solutions delivered to the VFD tube was initially set at 1:1, which was based on the success of this ratio in forming the fullerene cones [38] of comparable diameter to the spheres in the present study, the only difference being the absence of graphite. The initial flow rate of both solutions was fixed at 0.5 mL /min, which was subsequently found to be optimal. Increasing the flow rate of both solutions shut down the formation of spheres, Figure S3. Increasing the flow rate of DMF containing graphite up to 2.5 mL /min and the flow rate of the fullerene *o*-xylene solution to 2 mL /min produced dissimilar structures, with irregular spheroidal structures, Figure S2.

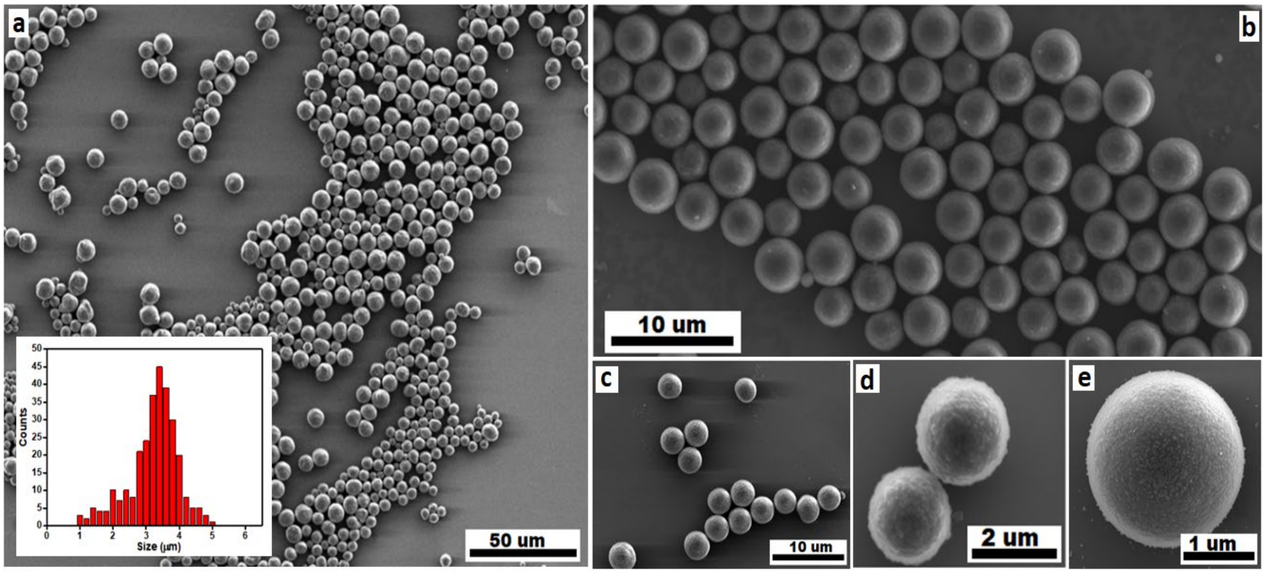

Figure 8. 3 SEM images of C$_{60}$@graphene, with a size distribution inset, formed in o-xylene and DMF, under continues flow mode 1:1 ratio (ω =7.5k rpm, concentration of C$_{60}$ in o-xylene 0.5 mg/mL, concentration of graphite in DMF 1 mg/mL, flow rate $\dot{v}$ = 0.5 mL/min for both liquids entering the rotating tube in the VFD, and θ = 45°).

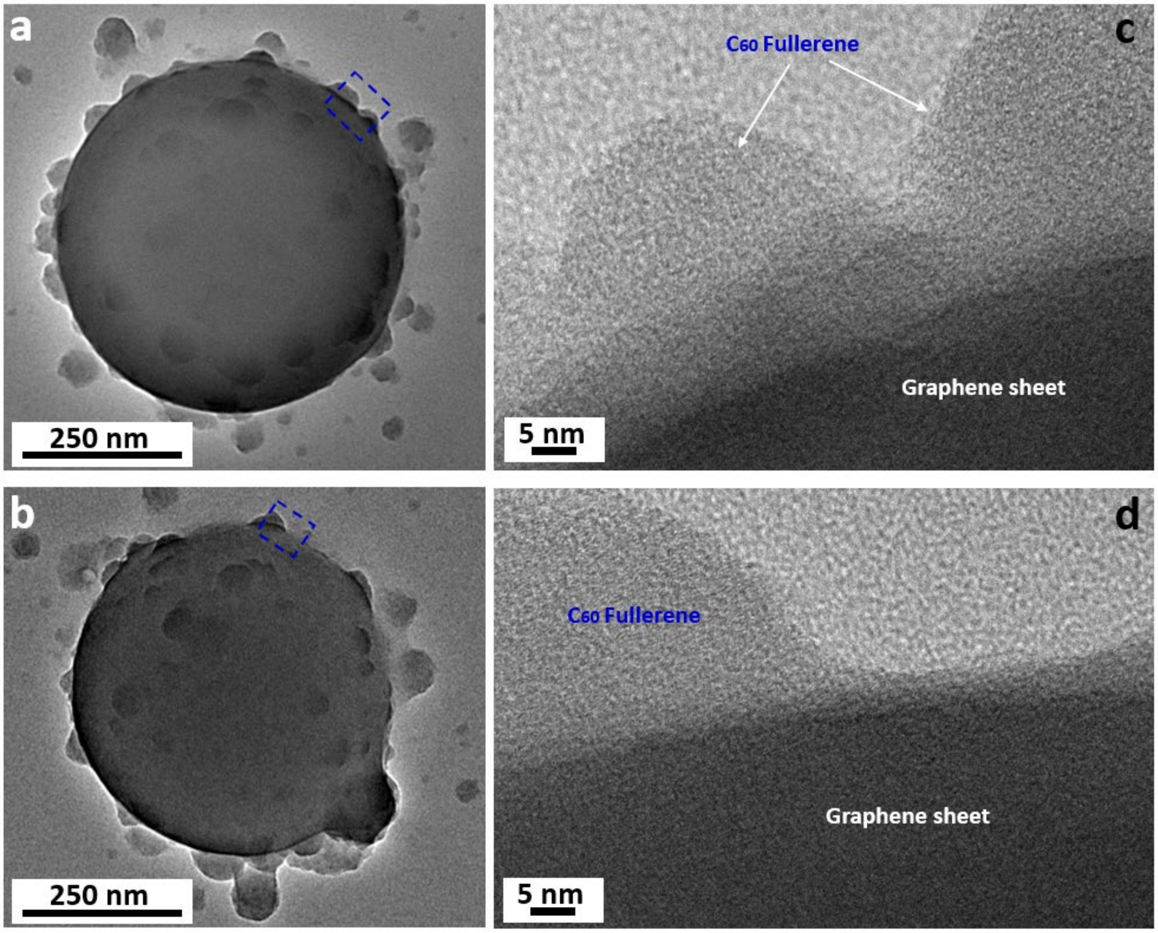

Figure 8. 4 (a,b) TEM images of graphene spheres, (b,c) HRTEM images of graphene spheres formed in o-xylene and DMF, under continues flow mode 1:1 ratio at 4 k rpm, concentration of fullerenes C$_{60}$ in o-xylene 0.5 mg/mL, concentration of graphite in DMF 1 mg/mL, flow rate 0.5 mL/min for both liquids entering the rotating tube in the VFD, and θ = 45°.

XRD patterns of the spheres are consistent with the material being comprised of graphite/graphene and fullerene $C_{60,}$[32] Figure 8. 5a-c. The spheres were collected immediately after VFD processing by centrifugation for 30 min, and washing twice with hexane and dried at 55°C for three days. The major peaks of *fcc* fullerene C_{60} are at 2θ 10.8°, 17.7°, and 20.8°, corresponding to the (111), (220), and (311), with the major peaks at 30.2°, 10.8°, 60.8° corresponding to the (002) and (004) planes of graphite. Clearly the XRD data establishes the formation of a hybrid composite material comprised of *fcc* C_{60} and graphene. From the Scherrer equation, the crystal domains of fullerenes C_{60} were estimated as 6.5 nm in diameter. The presence of graphene as one or a limited number of stacked sheets is consistent with shifts in the graphite diffraction pattern, [47] as well as consideration of the energetics of bending a finite number of sheets, as discussed above. Moreover, the absence of some graphite peaks can be attributed to assembled fullerene C_{60} on the surface of graphene.[47] Raman spectra (532 nm excitation) for the spheres prepared at the optimized conditions and for comparison as received graphite and fullerene C_{60} before processing, Figure 8. 5d-f, were recorded. Graphite itself has three main peaks, the D band, G band and 2D band at 1349 cm^{-1}, 1579 cm^{-1} and 2717 cm^{-1} respectively,[48, 49] and pristine C_{60} has the pentagonal pinch mode [Ag(2)] at 1469 cm^{-1} and additional Hg modes at 1420 and 1570 cm^{-1}. [50, 51] In contrast, the spheres have two Raman peaks at 1364 and 1600 cm^{-1}, which can be attributed to the D band and G band respectively of graphene, in agreement with the literature.[50, 52, 53]

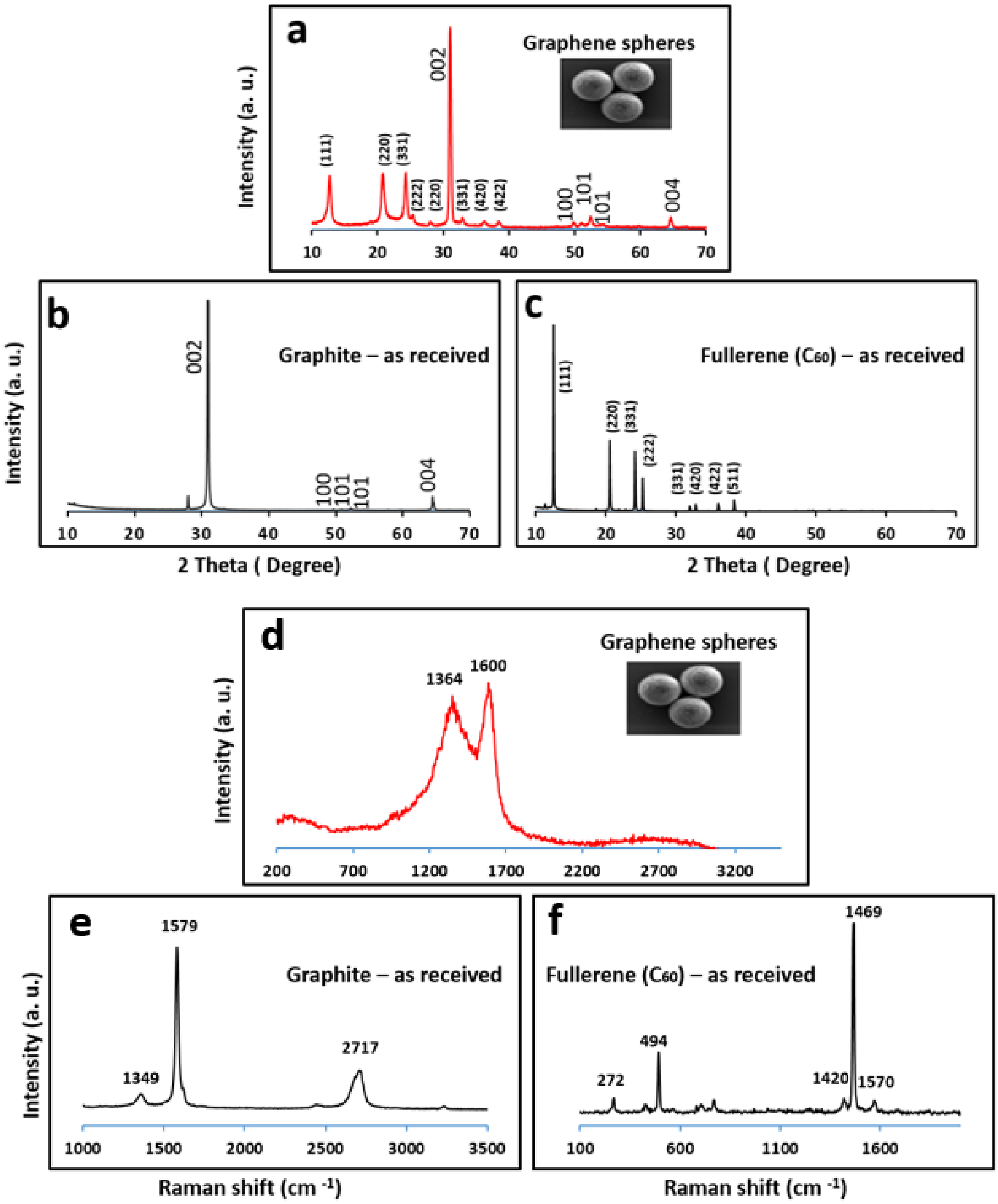

Figure 8. 5 XRD pattern of (a) spheres prepared in the VFD, (b) graphite as received, (c) fullerene C_{60} as received and Raman spectra of (d) spheres, prepared in the VFD, under continuous flow at a 1:1 ratio, 4k rpm rotational speed, concentration of fullerene 0.5 mg/mL, graphite concentration 1 mg/mL, flow rate 0.5 mL/min for both liquids and tilt angle 45°, (e) as received graphite, and (f) as received C_{60}.

8.4.4. Electrochemical performance

The electrochemical performance of the composite material as symmetrical supercapacitor is summarised in Figure 8. 6. A C_{60}@graphene electrode shows a cyclic voltammetry (CV) with a nearly rectangular shape (Figure 8. 6a), indicating an ideal capacitive behaviour similar to commercial electrochemical capacitors. Figure 6a and b illustrate the CV curves at different scan rates (5 to 1000 mV/s), revealing the stability and ability of the electrode to maintain the ideal rectangular CV shapes during operation over a wide range of scan rates. The response anodic and cathodic currents (recorded from the CV curves at 0.5 V) showed a linear relationship at different scan rates (Figure 8. 6c) with R^2 values of 0.9975 and 0.9979 for the charge and discharge curves, respectively.

The galvanostatic charge/discharge (CD) curves at different current densities, Figure 8. 6d, show nearly triangular shapes of the CD curves due to the efficient EDLC nature of graphene spheres electrode and fast kinetic of the electrolyte ions transportation through the porous carbon electrode structure. Additionally, the low equivalent series resistance (ESR) of the fabricated device can be predicted from a small voltage drop (IR) of 0.0075 V at the start of the discharge curve measured at current density of 1 A g^{-1}. Figure 8. 6e displays the calculated gravimetric and areal capacitances for graphene spheres electrode at different scan rates, delivering gravimetric capacitance of 29.5 F g^{-1} at scan rate of 5 mV s^{-1}, compared to different types of graphene spheres. [54] This value is lower due to the absence of residual oxygen-containing functional groups compared to reduced graphene oxide.[55, 56] However, the graphene spheres electrode has an areal capacitance of 103.4 mF cm^{-2}, which is much higher than reported values for other carbon derivatives.[46, 57] Moreover, this device can maintain its capacitances to 24.7 F g^{-1} and 86.4 mF cm^{-2} (83.5%) at high scan rate of 100 mV s^{-1}, confirming the high rate capability of graphene spheres electrode.

A Nyquist plot of graphene spheres electrode, Figure 8. 6f, shows a vertical curve at lower frequencies and no observed a semicircle higher-frequency region, indicating a nearly ideal capacitive behaviour of the cell. The device shows also a lower equivalent series resistance (ESR) of 0.5 Ω owing to the low internal resistance of the designed electrode material. Impedance phase angle versus frequency for graphene spheres electrode is illustrated in Figure 8. 7a. The device provides a phase angle of -83.8° (close to −90°) at low frequencies, showing an ideal capacitive behavior. Furthermore, the time constant τ_0 at a phase angle of −45° is found to be 0.16 s; this fast frequency response of the graphene spheres is directly related to significant ion transport rate of the large accessible surface area of the material. The cyclic stability of the composite electrode was examined by cyclic voltammetry at a scan rate of 100 mV s^{-1} for

5000 cycles (Figure 8. 7b), showing a capacity retention of 97.5%. The nearly identical CV curves for first and last cycles (Figure 8. 7b, inset) confirms the good stability and high reversibility of the C_{60}@graphene electrode.

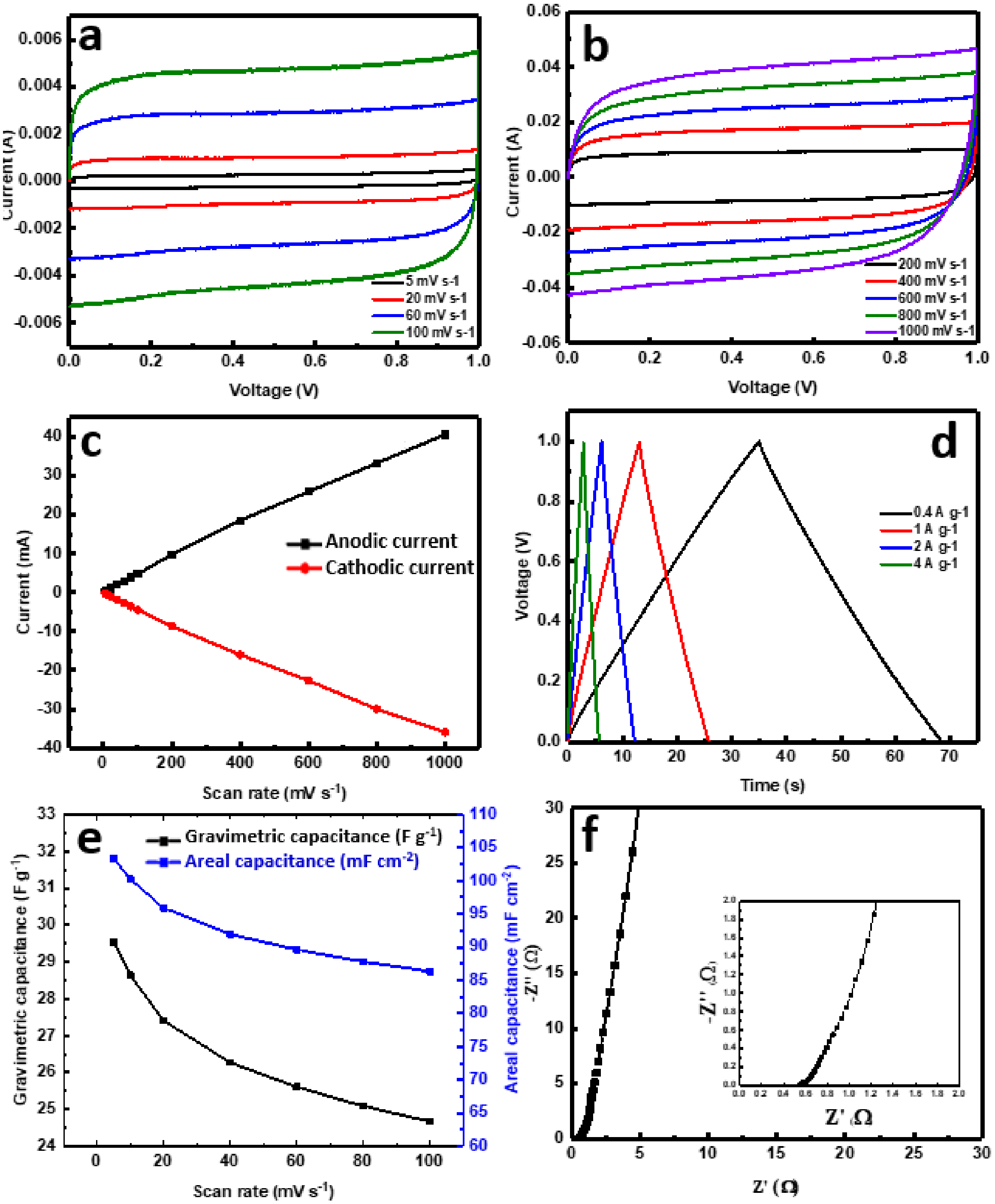

Figure 8. 6 (a) Cyclic Voltammogram (CV) curves of graphene sphere composites formed using the VFD, under continuous flow at a 1:1 ratio, 4k rpm rotational speed, concentration of fullerene 0.5 mg/mL, graphite concentration 1 mg/mL, flow rate 0.5 mL/min for both liquids and tilt angle 45°, at different scan rates from 5 to 100 mV s^{-1}, (b) at different scan rates from 200 to 1000 mV s^{-1}, (c) The response anodic and cathodic currents, (d) charge–discharge curves of graphene sphere composites at different current densities, (d) Gravimetric capacitance

and areal capacitance values versus scanning rate calculated from the CV curves of the graphene sphere composites and (f) Nyquist plot of graphene sphere composites.

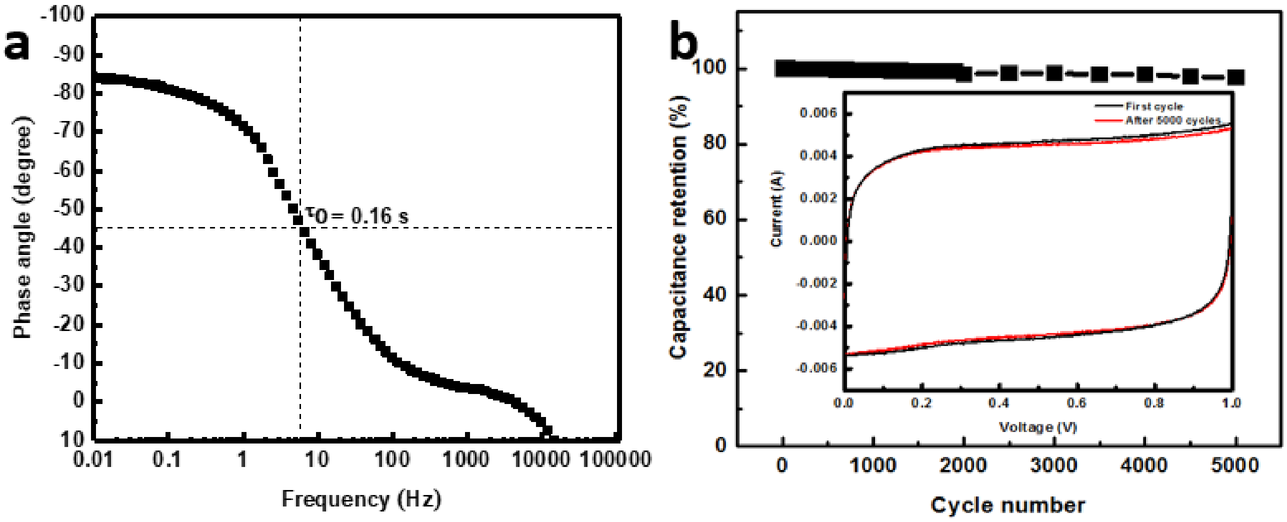

Figure 8. 7 (a) Impedance phase angle versus frequency for a C_{60}@Graphene sphere electrode, with the material formed using the VFD, under continuous flow at a 1:1 ratio of liquids, 4k rpm rotational speed, concentration of fullerene 0.5 mg/mL, graphite concentration 1 mg/mL, flow rate 0.5 mL/min for both liquids and tilt angle 45°. (b) Cyclic stability of the composite electrode at a scan rate of 100 mV s^{-1}; inserted is the nearly identical CV curves for first and last cycles of the electrode.

8.5. Conclusions

A simple and effective method to fabricate all carbon spheres built of fullerene C_{60} and graphene, under continuous flow mode of operation of the VFD microfluidic platform, has been developed. The structure and the morphology of the spheres were evaluated by SEM, TEM, HR-TEM, XRD and Raman spectroscopy. The spheres are rather uniform in size and shape, and importantly the yield of graphene spheres is high, and the processing is scalable. The method has potential for the synthesis of spheroidal composite material of fullerenes with other 2D materials. In addition, the use of the composite material of assembled spheres in an electrochemical device and in supercapacitance, with high capacitance maintained at a high scan rate, has potential in developing all carbon energy storage materials.

ASSOCIATED CONTENT

Supporting Information. Additional information on control experiments and optimizing conditions for fabricating the composite spheres. This material is available free of charge via the Internet at http://pubs.acs.org.

AUTHOR INFORMATION

Corresponding Author

* E-mail address: colin.raston@flinders.edu.au (Colin Raston)

Author Contributions

These authors contributed equally to this work, the manuscript was written through contributions of all authors. All authors have given approval to the final version of the manuscript.

Notes

The authors declare no competing financial interest.

8.6. Acknowledgements

The authors gratefully acknowledge support of this work by the Australian Research Council and the Government of South Australia, and the Australian Microscopy & Microanalysis Research Facility (AMMRF) at the Flinders Institute for Nanoscale Science and Technology, Flinders University and Adelaide Microscopy. T.M.A would like to thank Taibah University for funding his scholarship.

8.7. References

1. Song, L.; Xin, S.; Xu, D. W.; Li, H. Q.; Cong, H. P.; Yu, S. H., Graphene-Wrapped Graphitic Carbon Hollow Spheres: Bioinspired Synthesis and Applications in Batteries and Supercapacitors. *ChemNanoMat,* **2016,** *2*, 540-546.
2. Xiang, Z.; Chen, Y.; Li, J.; Xia, X.; He, Y.; Liu, H., Submicro-sized porous SiO2/C and SiO2/C/graphene spheres for lithium ion batteries. *Solid State Electrochem.,* **2017,** *21*, 2425-2432.
3. Wu, Z.; Wang, W.; Wang, Y.; Chen, C.; Li, K.; Zhao, G.; Sun, C.; Chen, W.; Ni, L.; Diao, G., Three-dimensional graphene hollow spheres with high sulfur loading for high-performance lithium-sulfur batteries. *Electrochim. Acta,* **2017,** *224*, 527-533.
4. Britton, J.; Stubbs, K. A.; Weiss, G. A.; Raston, C. L., Vortex Fluidic Chemical Transformations. *Chem.- Eur. J.,* **2017**, *23*, 13270–13278.
5. Chen, X.; Eggers, P. K.; Slattery, A. D.; Ogden, S. G.; Raston, C. L., Template-free assembly of three-dimensional networks of graphene hollow spheres at the water/toluene interface. *J. Colloid Interface Sci.,* **2014,** *430*, 174-177.
6. Wang, Q.; Zhang, Y.; Jiang, H.; Hu, T.; Meng, C., In situ generated $Ni_3Si_2O_5$ $(OH)_4$ on mesoporous heteroatom-enriched carbon derived from natural bamboo leaves for high-performance supercapacitors. *ACS Appl. Energy Mater.,* **2018,** *1*, 3396-3409.
7. Wang, Q.; Zhang, Y.; Jiang, H.; Meng, C., In-situ grown manganese silicate from biomass-derived heteroatom-doped porous carbon for supercapacitors with high performance. *J. Colloid Interface Sci.,* **2019,** *534*, 142-155.
8. Georgakilas, V.; Perman, J. A.; Tucek, J.; Zboril, R., Broad family of carbon nanoallotropes: classification, chemistry, and applications of fullerenes, carbon dots, nanotubes, graphene, nanodiamonds, and combined superstructures. *Chem. Rev.,* **2015,** *115*, 4744-4822.
9. Li, Z.; Liu, Z.; Sun, H.; Gao, C., Superstructured assembly of nanocarbons: fullerenes, nanotubes, and graphene. *Chem. Rev.,* **2015,** *115*, 7046-7117.
10. Yang, Z.; Ren, J.; Zhang, Z.; Chen, X.; Guan, G.; Qiu, L.; Zhang, Y.; Peng, H., Recent advancement of nanostructured carbon for energy applications. *Chem. Rev.,* **2015,** *115*, 5159-5223.
11. Cheng, Y.; Zhang, Y.; Meng, C., Template Fabrication of Amorphous Co_2SiO_4 Nanobelts/Graphene Oxide Composites with Enhanced Electrochemical Performances for Hybrid Supercapacitors. *ACS Appl. Energy Mater.,* **2019**, *2*, 3830–3839**.**
12. Tang, J.; Liu, J.; Torad, N. L.; Kimura, T.; Yamauchi, Y., Tailored design of functional nanoporous carbon materials toward fuel cell applications. *Nano Today,* **2014,** *9*, 305-323.
13. Meng, Y.; Gu, D.; Zhang, F.; Shi, Y.; Yang, H.; Li, Z.; Yu, C.; Tu, B.; Zhao, D., Ordered mesoporous polymers and homologous carbon frameworks: amphiphilic surfactant templating and direct transformation. *Angew. Chem., Int. Ed.,* **2005,** *44*, 7053-7059.
14. Zhang, C.; Wu, H. B.; Yuan, C.; Guo, Z.; Lou, X. W., Confining sulfur in double-shelled hollow carbon spheres for lithium–sulfur batteries. *Angew. Chem., Int. Ed.,* **2012,** *51*, 9592-9595.
15. Benzigar, M. R.; Joseph, S.; Baskar, A. V.; Park, D. H.; Chandra, G.; Umapathy, S.; Talapaneni, S. N.; Vinu, A., Ordered Mesoporous C70 with Highly Crystalline Pore Walls for Energy Applications. *Adv. Funct. Mater.,* **2018,** *28*, 1803701.
16. Paul, R.; Zhu, L.; Chen, H.; Qu, J.; Dai, L., Recent Advances in Carbon-Based Metal-Free Electrocatalysts. *Adv. Mater.,* **2019**, *31,* 1806403.
17. Liu, J.; Zhu, D.; Zheng, Y.; Vasileff, A.; Qiao, S.-Z., Self-supported earth-abundant nanoarrays as efficient and robust electrocatalysts for energy-related reactions. *ACS Catal.,* **2018,** *8*, 6707-6732.
18. Vasileff, A.; Zheng, Y.; Qiao, S. Z., Carbon Solving Carbon's Problems: Recent Progress of Nanostructured Carbon-Based Catalysts for the Electrochemical Reduction of CO_2. *Adv. Energy Mater.,* **2017,** *7*, 1700759.

19. Tan, H.; Li, Y.; Jiang, X.; Tang, J.; Wang, Z.; Qian, H.; Mei, P.; Malgras, V.; Bando, Y.; Yamauchi, Y., Perfectly ordered mesoporous iron-nitrogen doped carbon as highly efficient catalyst for oxygen reduction reaction in both alkaline and acidic electrolytes. *Nano Energy*, **2017,** *36*, 286-294.
20. Tan, H.; Li, Y.; Kim, J.; Takei, T.; Wang, Z.; Xu, X.; Wang, J.; Bando, Y.; Kang, Y. M.; Tang, Sub-50 nm Iron–Nitrogen-Doped Hollow Carbon Sphere-Encapsulated Iron Carbide Nanoparticles as Efficient Oxygen Reduction Catalysts. *Adv. Sci.,* **2018,** *5*, 1800120.
21. Zheng, J.; Zhang, Y.; Wang, Q.; Jiang, H.; Liu, Y.; Lv, T.; Meng, C., Hydrothermal encapsulation of VO 2 (A) nanorods in amorphous carbon by carbonization of glucose for energy storage devices. *Dalton Trans.,* **2018,** *47*, 452-464.
22. Caruso, F., Hollow capsule processing through colloidal templating and self-assembly. *Chem. Eur. J.,* **2000,** *6*, 413-419.
23. Wang, Y.; Su, F.; Lee, J. Y.; Zhao, X., Crystalline carbon hollow spheres, crystalline carbon−SnO2 hollow spheres, and crystalline SnO2 hollow spheres: synthesis and performance in reversible li-ion storage. *Chem. Mater.,* **2006,** *18*, 1347-1353.
24. Zou, G.; Yu, D.; Lu, J.; Wang, D.; Jiang, C.; Qian, Y., A self-generated template route to hollow carbon nanospheres in a short time. *Solid State Commun.,* **2004,** *131*, 749-752.
25. Han, S.; Yun, Y.; Park, K. W.; Sung, Y. E.; Hyeon, T., Simple Solid-Phase Synthesis of Hollow Graphitic Nanoparticles and their Application to Direct Methanol Fuel Cell Electrodes. *Adv. Mater.,* **2003,** *15*, 1922-1925.
26. Jang, J.; Li, X. L.; Oh, J. H., Facile fabrication of polymer and carbon nanocapsules using polypyrrole core/shell nanomaterials. *Chem. Commun.,* **2004,** 794-795.
27. Tang, Z.; Shen, S.; Zhuang, J.; Wang, X., Noble-metal-promoted three-dimensional macroassembly of single-layered graphene oxide. *Angew. Chem., Int. Ed.,* **2010,** *122*, 4707-4711.
28. Wang, Q.; Zhang, Y.; Jiang, H.; Li, X.; Cheng, Y.; Meng, C., Designed mesoporous hollow sphere architecture metal (Mn, Co, Ni) silicate: A potential electrode material for flexible all solid-state asymmetric supercapacitor. *Chem. Eng. J.,* **2019,** *362*, 818-829.
29. Compton, O. C.; An, Z.; Putz, K. W.; Hong, B. J.; Hauser, B. G.; Brinson, L. C.; Nguyen, S. T., Additive-free hydrogelation of graphene oxide by ultrasonication. *Carbon,* **2012,** *50*, 3399-3406.
30. Bonaccorso, F.; Lombardo, A.; Hasan, T.; Sun, Z.; Colombo, L.; Ferrari, A. C., Production and processing of graphene and 2d crystals. *Mater. Today,* **2012,** *15*, 564-589.
31. Zhang, Y.; Wang, C.; Jiang, H.; Wang, Q.; Zheng, J.; Meng, C., Cobalt-Nickel Silicate Hydroxide on Amorphous Carbon Derived from Bamboo Leaves for Hybrid Supercapacitors. *Chem. Eng. J.,* **2019**, *375,* 121938.
32. Vimalanathan, K.; Shrestha, R. G.; Zhang, Z.; Zou, J.; Nakayama, T.; Raston, C. L., Surfactant-free Fabrication of Fullerene C_{60} Nanotubules Under Shear. *Angew. Chem., Int. Ed.*, **2017,** *56*, 8398-8401.
33. Luo, X.; Al-Antaki, A. H. M.; Vimalanathan, K.; Moffatt, J.; Zheng, K.; Zou, Y.-C.; Zou, J.; Duan, X.; Lamb, R.; Wang, S., Laser irradiated vortex fluidic mediated synthesis of luminescent carbon nanodots under continuous flow. *React. Chem. Eng.*, **2018**, *3,* 164-170.
34. Yasmin, L.; Chen, X.; Stubbs, K. A.; Raston, C. L., Optimising a vortex fluidic device for controlling chemical reactivity and selectivity. *Sci. Rep.,* **2013,** *3*, 2282.
35. Chen, X.; Dobson, J. F.; Raston, C. L., Vortex fluidic exfoliation of graphite and boron nitride. *Chem. Commun.*, **2012,** *48*, 3703-3705.
36. Vimalanathan, K.; Chen, X.; Raston, C. L., Shear induced fabrication of intertwined single walled carbon nanotube rings. *Chem. Commun.*, **2014,** *50*, 11295-11298.
37. Vimalanathan, K.; Gascooke, J. R.; Suarez-Martinez, I.; Marks, N. A.; Kumari, H.; Garvey, C. J.; Atwood, J. L.; Lawrance, W. D.; Raston, C. L., Fluid dynamic lateral slicing of high tensile strength carbon nanotubes. *Sci. Rep.,* **2016,** *6*, 22865.

38. Alsulami, I.; Alharbi, T.; Harvey, D.; Gibson, C. T.; Raston, C. L., Controlling the growth of fullerene C_{60} cones under continuous flow. *Chem. Commun.*, **2018**, *54,* 7896-7899.

39. Goh, Y. A.; Chen, X.; Yasin, F. M.; Eggers, P. K.; Boulos, R. A.; Wang, X.; Chua, H. T.; Raston, C. L., Shear flow assisted decoration of carbon nano-onions with platinum nanoparticles. *Chem. Commun.*, **2013,** *49*, 5171-5173.

40. Yasin, F. M.; Boulos, R. A.; Hong, B. Y.; Cornejo, A.; Iyer, K. S.; Gao, L.; Chua, H. T.; Raston, C. L., Microfluidic size selective growth of palladium nano-particles on carbon nano-onions. *Chem. Commun.*, **2012,** *48*, 10102-10104.

41. Alharbi, T. M.; Harvey, D.; Alsulami, I. K.; Dehbari, N.; Duan, X.; Lamb, R. N.; Lawrance, W. D.; Raston, C. L., Shear stress mediated scrolling of graphene oxide. *Carbon,* **2018**, *137,* 419-424.

42. Ma, X.; Gan, L.; Liu, M.; Tripathi, P. K.; Zhao, Y.; Xu, Z.; Zhu, D.; Chen, L., Mesoporous size controllable carbon microspheres and their electrochemical performances for supercapacitor electrodes. *J. Mater. Chem. A,* **2014,** *2*, 8407-8415.

43. Liu, M.; Qian, J.; Zhao, Y.; Zhu, D.; Gan, L.; Chen, L. J., Core–shell ultramicroporous@ microporous carbon nanospheres as advanced supercapacitor electrodes. *J. Mater. Chem. A,* **2015,** *3*, 11517-11526.

44. Zhu, D.; Wang, Y.; Gan, L.; Liu, M.; Cheng, K.; Zhao, Y.; Deng, X.; Sun, D., Nitrogen-containing carbon microspheres for supercapacitor electrodes. *Electrochim. Acta*, **2015,** *158*, 166-174.

45. Zhou, J.; Lian, J.; Hou, L.; Zhang, J.; Gou, H.; Xia, M.; Zhao, Y.; Strobel, T. A.; Tao, L.; Gao, F., Ultrahigh volumetric capacitance and cyclic stability of fluorine and nitrogen co-doped carbon microspheres. *Nat. Commun.,* **2015,** *6*, 8503.

46. Zhang, X.; Lai, Y.; Ge, M.; Zheng, Y.; Zhang, K.-Q.; Lin, Z. J., Fibrous and flexible supercapacitors comprising hierarchical nanostructures with carbon spheres and graphene oxide nanosheets. *J. Mater. Chem. A,* **2015,** *3*, 12761-12768.

47. Zhang, K.; Zhang, Y.; Wang, S., Enhancing thermoelectric properties of organic composites through hierarchical nanostructures. *Sci. Rep.*, **2013,** *3*, 3448.

48. Kudin, K. N.; Ozbas, B.; Schniepp, H. C.; Prud'Homme, R. K.; Aksay, I. A.; Car, R., Raman spectra of graphite oxide and functionalized graphene sheets. *Nano Lett.,* **2008,** *8*, 36-41.

49. Park, J.; Reina, A.; Saito, R.; Kong, J.; Dresselhaus, G.; Dresselhaus, M., G′ band Raman spectra of single, double and triple layer graphene. *Carbon,* **2009,** *47*, 1303-1310.

50. Qu, S.; Li, M.; Xie, L.; Huang, X.; Yang, J.; Wang, N.; Yang, S., Noncovalent functionalization of graphene attaching [6, 6]-phenyl-C61-butyric acid methyl ester (PCBM) and application as electron extraction layer of polymer solar cells. *ACS Nano,* **2013,** *7*, 4070-4081.

51. Bethune, D. S.; Meijer, G.; Tang, W. C.; Rosen, H. J., The vibrational Raman spectra of purified solid films of C_{60} and C_{70}. *Chem. Phys. Lett.,* **1990,** *174*, 219-222.

52. Yu, D.; Park, K.; Durstock, M.; Dai, L., Fullerene-grafted graphene for efficient bulk heterojunction polymer photovoltaic devices. *J. Phys. Chem. Lett.*, **2011,** *2*, 1113-1118.

53. Yu, X.; Dong, Z.; Yang, J. K.; Wang, Q. J., Room-temperature mid-infrared photodetector in all-carbon graphene nanoribbon-C 60 hybrid nanostructure. *Optica* **2016,** *3*, 979-984.

54. Wang, H.; Shi, L.; Yan, T.; Zhang, J.; Zhong, Q.; Zhang, D. J., Design of graphene-coated hollow mesoporous carbon spheres as high performance electrodes for capacitive deionization. *J. Mater. Chem. A*, **2014,** *2*, 4739-4750.

55. Moussa, M.; Zhao, Z.; El-Kady, M. F.; Liu, H.; Michelmore, A.; Kawashima, N.; Majewski, P.; Ma, J., Free-standing composite hydrogel films for superior volumetric capacitance. *J. Mater. Chem. A*, **2015,** *3*, 15668-15674.

56. Moussa, M.; El-Kady, M. F.; Abdel-Azeim, S.; Kaner, R. B.; Majewski, P.; Ma, J., Technology, Compact, flexible conducting polymer/graphene nanocomposites for supercapacitors of high volumetric energy density. *Compos. Sci. Technol.,* **2018,** *160*, 50-59.

57. Sheberla, D.; Bachman, J. C.; Elias, J. S.; Sun, C.-J.; Shao-Horn, Y.; Dincă, M., Conductive MOF electrodes for stable supercapacitors with high areal capacitance. *Nat. Mater.,* **2017,** *16*, 220.

ACS OMEGA

Article

Cite This: ACS Omega XXXX, XXX, XXX−XXX

http://pubs.acs.org/journal/acsodf

High-Yield Continuous-Flow Synthesis of Spheroidal C_{60}@Graphene Composites as Supercapacitors

Ibrahim K. Alsulam,[†,∥] Thaar M. D. Alharbi,[†,§,∥] Mahmoud Moussa,[‡,⊥] and Colin L. Raston*[,†]

[†]Flinders Institute for Nanoscale Science and Technology, College of Science and Engineering, Flinders University, Adelaide SA 5001, Australia

[§]Physics Department, Faculty of Science, Taibah University, Al Madinah Al Munawwarah 42353, Saudi Arabia

[‡]School of Chemical Engineering, The University of Adelaide, Adelaide SA 5001, Australia

[⊥]Department of Chemistry, Faculty of Science, Beni-Suef University, Beni-Suef 62111, Egypt

Supporting Information

ABSTRACT: Graphene spheres confining fullerene C_{60} are quantitatively formed under high-shear and continuous-flow processing using a vortex fluidic device (VFD). This involves intense micromixing a colloidal suspension of graphite in DMF and an *o*-xylene solution of C_{60} at room temperature in the absence of surfactants and other auxiliary substances. The diameters of the composite spheres, C_{60}@graphene, can be controlled with size distributions ranging from 1.5 to 3.5 μm, depending on the VFD operating parameters, including rotational speed, flow rate, relative ratio of C_{60} to graphite, and the concentration of fullerene. An electrode of the composite material has high cycle stability, with a high areal capacitance of 103.4 mF cm^{-2}, maintaining its capacitances to 24.7 F g^{-1} and 86.4 mF cm^{-2} (83.5%) at a high scan rate of 100 mV s^{-1}.

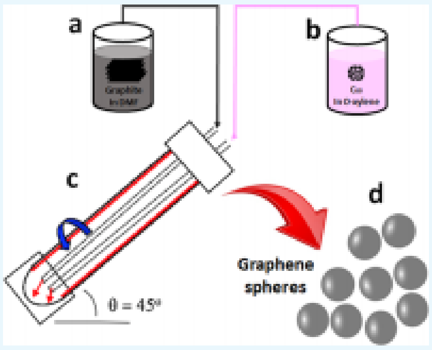

INTRODUCTION

Carbon nanomaterials have emerged as key materials for future technology, for developing complex functional structures devoid of potentially toxic metals and metals, which are likely to have supply chain issues in the near future.[1] Graphene, as a single 2D planar sheet of graphite arranged in a hexagonal lattice,[2] is one of the newest forms of such nanomaterials. It has remarkable chemical, physical, and electrical properties, with high conductivity in the absence of defects and wrinkles, large specific surface area, and excellent mechanical flexibility,[1,3] and features in a growing number of applications. These include batteries, supercapacitors, catalyst supports, drug delivery, electrode materials for energy storage devices, membranes, biomedical devices, and coatings, and these relate to its multifarious and interdisciplinary properties.[1,3−7]

Graphene can be transformed into other structures including 0D nanoparticles (carbon dots), 1D nanofibers (carbon nanofibers and nanotubes), 2D nanosheets (graphene oxide), 3D nanostructures (hollow carbon nanospheres), fullerenes, and composites of these.[8−11] Among these different carbon nanomaterials, graphene spheres show promise in a wide range of applications covering energy storage including lithium ion batteries, separation systems, oxygen-reduction, catalyst supports, nanoreactors, and adsorption.[12−21]

The synthesis of graphene spheres with smooth surfaces and uniform sizes uses soft template processing,[22] hard templating (silicon template),[23] solvothermal techniques,[24] sol pyrolysis,[25] microemulsion polymerization,[26] hydrothermal reduction,[27,28] and gelation.[29] Related to this are extended oxidation strategies to alter the morphology and surface topography of graphene oxide (GO) nanosheets, as a potential route to build up 3D graphene architectures.[30,31] However, the synthetic strategies for gaining access to such architectures are limited by the high cost of production, the use of harsh chemicals or surfactants, high temperature processing as a high-energy penalty, and limited scope for scaling up the process.[5] A challenge is to develop a scalable, low-cost method that is high in green chemistry or sustainability metrics, for gaining access to 3D graphene-based materials, including graphene spheres and composites thereof.

To this end, we have explored the use of continuous-flow processing to prepare graphene spheres and graphene-fullerene composite spheres directly from graphite and fullerene C_{60}, at room temperature, avoiding the use of auxiliary reagents. This involved the use of the in-house developed continuous-flow vortex fluidic device (VFD), which was developed early this decade.[4] It is a versatile microfluidic platform containing a dynamic thin film, in contrast to traditional channel based microfluidics, which can suffer from clogging. Mechanoenergy is delivered into the liquid in the VFD in a controlled way.[4] Under continuous-flow VFD processing, jet feeds deliver solution into an inclined rapidly rotating tube, opened at one

Received: August 18, 2019
Accepted: October 25, 2019

DOI: 10.1021/acsomega.9b02656
ACS Omega XXXX, XXX, XXX−XXX

High Yielding Continuous Flow Synthesis of Spheroidal C_{60}@Graphene – Composites as Supercapacitor

Ibrahim K. Alsulam,[†,‖] Thaar M. D. Alharbi,[†, §,‖] Mahmoud Moussa,[‡,⊥] and Colin L. Raston [†, *]

[†] *Flinders Institute for Nanoscale Science and Technology, College of Science and Engineering, Flinders University, Adelaide SA 5001, Australia*

[§] *Physics Department, Faculty of Science, Taibah University, Almadinah Almunawarrah 42353, Saudi Arabia*

[‡] *School of Chemical Engineering, The University of Adelaide, Adelaide SA 5001,*

[⊥] *Department of Chemistry, Faculty of Science, Beni-Suef University, Beni-Suef 62111, Egypt*

[‖] *These authors contributed equally to this work.*

Chapter Nine

Three-step-in-one synthesis of supercapacitor MWCNT superparamagnetic magnetite composite material under flow

Thaar M. D. Alharbi [†, §], Ahmed H. M. Al-Antaki[†], Mahmoud Moussa[‡], Wayne D. Hutchison[⊥] and Colin L Raston [†, *]

[†] Flinders Institute for NanoScale Science and Technology, College of Science and Engineering, Flinders University, Adelaide SA 5001, Australia email: colin.raston@flinders.edu.au
[§] Physics Department, Faculty of Science, Taibah University, Almadinah Almunawarrah, Saudi Arabia
[‡] School of Chemical Engineering, The University of Adelaide, Adelaide SA 5001, Australia
[⊥] School of Science, University of New South Wales, ADFA campus, Canberra BC, Australian Capital Territory 2610, Australia

This study was published in ***Nanoscale Adv.,*** Year **2019**, 1, 3761-3770. The first page of the publication and SI are attached.

Author contributions: **TA** performed all the VFD and most characterization experiments and data analysis, and wrote all the primary content. **AA** preformed XRD and helped with some VFD experiments. **MM** performed the electrochemical measurements. **WH** helped with the magnetization measurements. **CR** supervised and coordinated the project and helped on the research directions and plan, and the final revision of the manuscript. All of the co-authors assisted with the revision of the manuscript before and during the publication process.

9.1. Abstract

Composites of multi-walled carbon nanotubes (MWCNTs) and superparamagnetic magnetite nanoparticles, Fe_3O_4@MWCNT, were synthesized in DMF in a vortex fluidic device (VFD). This involved *in situ* generation of the iron oxide nanoparticles by laser ablation of bulk iron metal at 1064 nm using a pulsed laser, over the dynamic thin film in the microfluidic platform. The overall processing is a three-step in one operation: (i) slicing MWCNTs, (ii) generating the superparamagnetic nanoparticles and (iii) decorating them on the surface of the MWCNTs. The Fe_3O_4@MWCNT composites were characterized by transmission electron microscopy, scanning transmission electron microscope, TG analysis, X-ray diffraction and X-ray photoelectron spectroscopy. They were used as an active electrode for supercapacitor measurements, establishing high gravimetric and areal capacitances of 834 F g^{-1} and 1317.7 mF cm^{-2} at a scan rate of 10 mV s^{-1}, respectively, which are higher values than those reported using similar materials. In addition, the designer material has a significantly higher specific energy of 115.84 Wh kg^{-1} at a specific power of 2085 W kg^{-1}, thereby showing promise for the material in next-generation energy storage devices.

Keywords: Multi-walled carbon nanotubes, magnetite nanoparticles, superparamagnetic, vortex fluidic device, supercapacitance.

Graphical Abstract

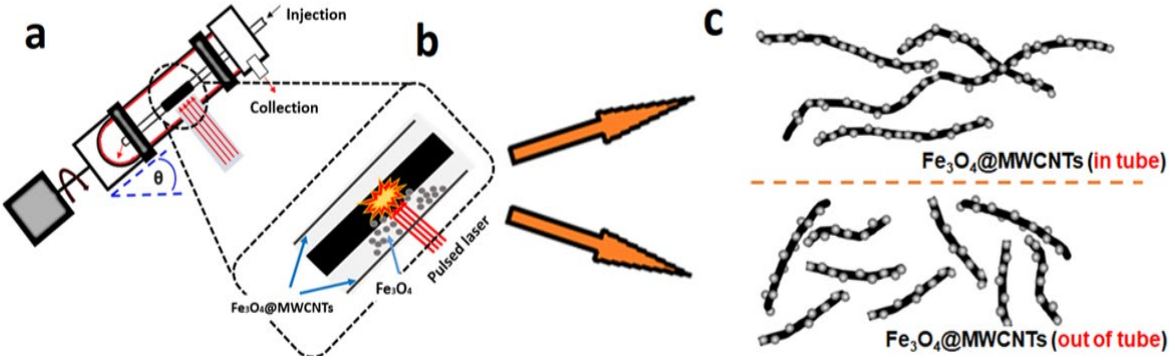

9.2. Introduction

In recent years the drive for safe, efficient and high-performance energy storage devices, has resulted in major research efforts in supercapacitors. This has been driven by their potential for high power density, outstanding safety, fast charge/discharge rates, excellent reliability, and long cycling life.[1-3] Several nanostructured materials have shown to be effective as electrodes for supercapacitors. These include carbon nanotubes,[1, 4] graphene,[5, 6] a number of other types of structured nanoparticles,[7, 8] nanowires,[9, 10] porous nanoflakes,[11, 12] and nanospheres,[13, 14] Composites of metal oxides and carbon based materials, especially carbon nanotubes, have been used as electrode materials, establishing that the electrochemical performance is enhanced.[15, 16]

Decorating carbon nanotubes with inorganic nanoparticles has received considerable attention both in fundamental research and the industrial arena.[17] This relates to the unique physical and chemical properties of the composite materials. Indeed, MWCNTs decorated with iron oxide particles in general are promising composite materials for a variety of applications such as hydrogen storage,[18] imaging and therapy,[17, 19] gas sensors,[20] catalysis,[17, 21] CNT-based magnetic materials,[22] CNT field emitters,[17, 23] and CNT-based electronic devices.[17, 24, 25] Various routes have been developed in gaining access to such material, including solvothermal,[26] hydrothermal,[27] microwave,[28] laser ablation [29] and ultra-sonication processing, [30] high-temperature decomposition,[31] laser pyrolysis [32] and chemical vapour deposition.[33] Freedman et al. [34] and Singhal et al. [35] have demonstrated that a magnetic carbon nanotube pipette is effective for transferring liquid into and within a single cell. In addition, Syljuki et al. [36] have shown that the electrochemical activity of carbon nanotubes for the reduction of H_2O_2 can arise from iron oxide nanoparticles decorated on CNT. Also noteworthy is that carbon nanotubes decorated with iron(III) oxide (Fe_2O_3) nanoparticle embedded in a co-polymer (derived from pyrrole and 3-carboxylated pyrrole) are highly sensitive for detecting H_2S, as reported by Kim et al. [37] Thus CNT-iron oxide nanoparticle composites have a diverse range of applications, and accordingly we sort to develop a robust synthesis of such material, ideally under continuous flow, as a potentially scalable process.

Previously we reported on the synthesis of superparamagnetic magnetite (Fe_3O_4) nanoparticles, spheroidal and hexagonal shaped, with an average size of ca. 15 nm, using a vortex fluidic device (VFD).[38] Here the magnetite nanoparticles are generated by pulsed laser ablation of an iron rod (high purity, >99.998%) at 1064 nm, with the rod positioned over the dynamic thin film in the VFD, Figure 9.1a, under at atmosphere of air. This is a single-step continuous flow process, and the operation of the VFD is effectively using it as a metal vapour synthesiser. In an analogous way, the VFD has been used for decorating hexagonal boron nitride (*h*-BN) with similar sized magnetite nano-particles, now as a one step process for making composite materials.[39] Inspired by the aforementioned findings, we were motivated to translate this knowhow into developing a facile continuous flow VFD mediated process for decorating MWCNTs with magnetite nanoparticles, Fe_3O_4@MWCNT, in using the shear stress in the VFD to disentangle the MWCNTs which while irradiated with a the pulsed laser are sliced into more processible lengths.[40] Thus it is a novel three in one continuous flow process, and we establish that the resulting composite material, Fe_3O_4@MWCNTs, is an active electrode for supercapacitance, achieving a high gravimetric (834 F g^{-1}) and areal (1317.7 mF cm^{-2}) capacitances, which are enhanced compared with those previously reported for iron oxide/carbon anodes.[41] We note that the decoration of SWCNTs with magnetite nanoparticles has been established using the related spinning disc processor (SDP), also under continuous flow, but the process requires the use of harsh chemicals and pre-treatment (oxidation and binding of Fe^{2+} and Fe^{3+}) of the SWCNTs,[42] and thus where the integrity of the carbon nanotubes is lost.

The VFD is a versatile microfluidic platform with a diversity of applications, including in processing carbon nanomaterials, as in slicing of SWCNTs, especially in controlling their length,[43] exfoliation of graphite and boron nitride,[44] transforming graphene oxide sheets into scrolls,[45] decorating carbon nano-onions with Pt [46] and Pd [47] nanoparticles, the synthesis of carbon dots,[48] and the fabrication of C_{60} tubules using water as an 'anti-solvent'.[49] Other applications of the VFD include controlling chemical reactivity and selectivity,[50] protein folding, [51] enhancing enzymatic reactions [52] and protein immobilization.[53] The dynamic thin film in a VFD has Stewartson/Ekman layers and Faraday pressure waves, with the liquid moving up the rapidly rotating tube under gravitational force and exiting at the top,. [54] The continuous flow mode of operation of the VFD has the attractive feature of addressing scalability of a process at the inception of the research. Here jet feeds deliver reagents into an inclined rapidly rotating tube, typically a 20 mm O.D. glass or quartz tube.[55]

9.3. Experimental section

9.3.1. Materials

MWCNTs used in the present work have an average outside diameter (O.D.) × inside diameter (I.D.) × length equivalent dimensions 10 nm ± 1 nm × 4.5 nm ± 0.5 nm, and 3 to 6 μm respectively. They were purchased from Sigma-Aldrich, as chemical vapour deposition prepared material with an as received purity ≥ 98%, and were used as received. N, N-dimethylformamide (DMF) was purchased from Sigma-Aldrich and used as received. High purity Fe (>99.998%) 8361 h iron rod, 5 mm in diameter (Koch- Light Laboratories) was used as the laser target and source of metal.

9.3.2. Fabrication of Fe_3O_4@MWCNT

The preparation of Fe_3O_4@MWCNT nanocomposites is shown in Figure 9.1a. MWCNTs were dispersed in N, N-dimethylformamide (DMF) at a concentration of 0.08 mg/mL and the mixture ultrasonicated for 15 minutes prior to VFD processing. The experimental setup mainly followed the previously published work for the VFD mediated slicing of CNTs and the synthesis of superparamagnetic nanoparticles,[38, 40, 43] in merging two different applications of the VFD. The experiments were carried out using the continuous flow mode of operation of the device at a flow rate of 0.45 mL min^{-1}. Stainless steel jet feed was used to deliver MWCNTs dispersed in DMF solution to the bottom of the rapidly rotating quartz tube (O.D. 20 mm, I.D. 17.5 mm). The tilt angle (θ) of the device was 45°, which is the optimal angle for a number of VFD processes,[43-45, 48] relative to the horizontal position. For fabricating Fe_3O_4@MWCNTs, the iron rod was immobilized on a stainless steel jet feed and irradiated in the VFD tube at a wavelength of 1064 nm using a Q-switched Nd:

YAG laser (Spectra Physics GCR170) operating at a pulse repetition rate of 10 Hz. The power of the laser was optimized first by conducting the experiment under continuous flow conditions at different laser powers, 250 mJ, 400 mJ and 600 mJ, as shown in Figure S5 (supporting information). For high laser powers, 400 and 600 mJ, the MWCNTs were unzipped and fragmented, whereas at the optimum laser power (250mJ), Fe_3O_4 nanoparticles were generated and decorated on the surface of MWCNTs. Initially the MWCNTs were dispersed in DMF at a concentration of 0.08 mg/mL and were injected into the base of the quartz tube through a jet feed using a 50 mL glass syringe, at a flow rate of 0.45 mL/min while the iron rod was irradiated with the pulsed laser. After the 50 mL of the solutions was delivered, the experiment was stopped, affording two products, one exiting the VFD tube during the processing (collected), which accounted for 42% of the isolated material, with 58% of the material generated remaining in the tube (retained). Both products contained MWCNTs decorated with Fe_3O_4 nanoparticles in a high yield, based on the amount of MWCNTs consumed and the overall weight of the combined product taking into account the ratio of magnetite to MWCNTs.

9.3.3. Electrochemistry

A specific amount of active material (10 mg) was sonicated for 1 h in 20 ml of ethanol. Next, the resulting suspension was vacuum filtered through a PTFE membrane to make a free–standing film. The composite film was cut into electrodes of footprint area of 1 cm^2, and platinum foils were used as current collectors and 1 M Na_2SO_4 as electrolyte. Cyclic voltammetry (CV) and galvanostatic charge/discharge (CD) were carried out by a two-electrode configuration using a CHI 660E electrochemical workstation. All measurements were performed at room temperature. The gravimetric capacitance and areal capacitance were calculated from CV curves

9.3.4. Characterization

X-ray powder diffraction (XRD) data were collected using a Bruker Advanced D8 diffractometer (capillary stage) using Co-Kα (λ= 1.7889 Å, 35 kW/28 mA, 2θ = 10 – 90°). Thermogravimetric analysis (TGA) was recorded on a Perkin Elmer STA8000 operating at a heating rate of 10ºC/min under an air gas flow. Atomic force microscopy (AFM) using a Nanoscope 8.10 in tapping mode and

Transmission electron microscopy (TEM) was conducted on a TECNAI 20 microscope operated at 120 and 200 kV. STEM investigation and compositional mapping were conducted using an aberration-corrected FEI Titan Themis TEM operating at 200 kV equipped with an energy dispersive x-ray spectroscopy (EDX) detector. Magnetization measurements used a Quantum Design PPMS with ACMS option at room temperature (295 K) in applied magnetic fields up to 2.50 T.

9.4. Results and discussion

9.4.1. Fabrication of Fe_3O_4@MWCNT

We have developed a high yielding method for preparing a composite material based on MWCNTs decorated with superparamagnetic magnetite (Fe_3O_4) nanoparticles, Fe_3O_4@MWCNT, as a three in one process - slicing, laser ablation and growth of nanoparticles, and decoration. The solvent of choice was DMF, with the processing devoid of other reagents, and the processing is therefore limiting the generation of a waste stream for any downstream applications. Salient features for preparing Fe_3O_4@MWCNT are schematically illustrated in Figure 9.1 The Fe_3O_4 nanoparticles (NPs) are generated *in situ* in the VFD by irradiating a high purity (>99.998%) iron rod (5 mm diameter) with a pulsed laser (Q-switched Nd:YAG) operating at 1064 nm wavelength, Figure 9.1(b). MWCNTs dispersed in DMF were delivered to the bottom of the rapidly rotating quartz VFD tube through a jet feed with an iron rod attached. As the liquid passes through the laser beam the MWCNTs are sliced into shorter tubes and simultaneously decorated with Fe_3O_4 NPs, Figure 9.1(c). The length distribution of Fe_3O_4@MWCNT exiting the tube is centred at 500 nm (inset Figure 9.3a). MWCNTs which were retained in the VFD during the processing were similarly decorated with Fe_3O_4 NPs, Figure 9.1(c), but they are significantly longer at *ca* 2 μm. The reason for the longer lengths of MWCNTs in the composite material being retained in the tube presumably relates to the build-up, on both sides of the laser beam, of magnetite being faster than untangling and slicing of the MWCNTs. Such build up is likely to result in magnetite particles bridging different tube which are then locked into place, with the shear stress in the fluid dynamics unable to separate them. MWCNTs sliced prior to a substantial build-up of magnetite particles on their surface, can then be decorated and move under the fluid flow. See below for further discussion on the size of the magnetite NPs and associated mass differences, and potential effect on the processing.

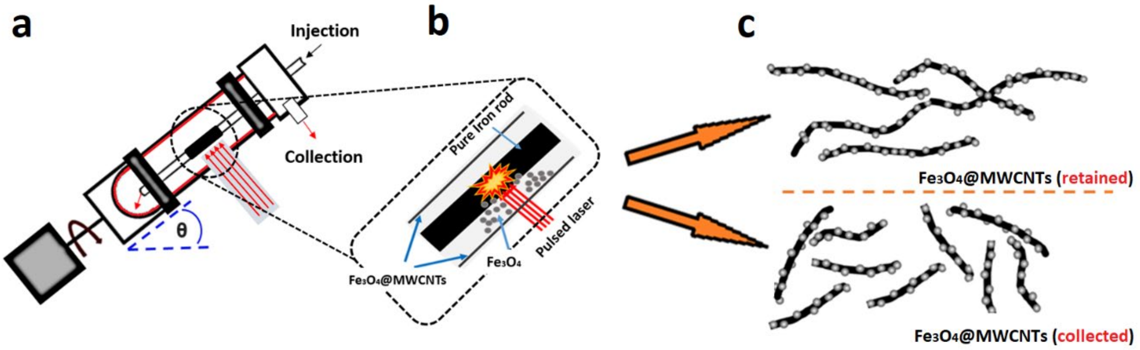

Figure 9. 1 Schematic illustration of the experimental procedure for the preparation for Fe_3O_4@MWCNT. (a) The vortex fluidic device (VFD) and laser Nd:YAG processing at 1064 nm. (b) Zoomed in schematic for generating Fe_3O_4 NPs under laser irradiation of an iron rod (power at 250 mJ). (c) Fe_3O_4@MWCNT exiting the tube under continuous flow (collected) and retained in the tube.

9.4.2. Characterisation

The nature of the Fe_3O_4@MWCNT nanocomposite was investigated using AFM, TEM, HRTEM and STEM. Figure 9.2a, d show AFM and low magnification TEM images for the material retained in the tube during processing revealing bundles of strands mixed with a high density of Fe_3O_4 nanoparticles, seen as black areas. These modified MWCNTs appear unaltered in length relative to the as received material. Figure 9.2b, c show TEM and HRTEM images of the same material, revealing MWCNTs decorated with Fe_3O_4 NPs. Corresponding images for Fe_3O_4@MWCNT flowing out of the tube (collected) are shown in Figure 9.3a, d, clearly establishing that the MWCNTs have been sliced down to 500 nm in length (inset Figure. 9.3a) as well as being decorated with Fe_3O_4 nanoparticles. Figure 9.3b, c show TEM and HRTEM images of the collected Fe_3O_4@MWCNT, which are also decorated with Fe_3O_4 NPs. We note that Fe_3O_4@MWCNTs (retained) has MWCNTs decorated with Fe_3O_4 nanoparticles with an average diameter of 15.1 ± 2.4 nm, as determined using HRTEM, Figure 9.2c, whereas they are smaller in diameter, 10 ± 1.2 nm, for the material exiting the VFD tube under flow, Figure 9.3c.

High-resolution STEM was used to gain further insight into the nature of the Fe_3O_4@MWCNT nanocomposite. Figure 9.4a displays BF and HAADF-STEM images of collected Fe_3O_4@MWCNT along with the elemental mapping. Interestingly, while most Fe_3O_4 NPs decorate the surface of the MWCNTs, Figure 9.3a-b, there are some that are encapsulated inside the MWCNTs, Figure 9.4 a, as highlighted by elemental mapping of Fe and O. BF and HAADF-STEM images, and the corresponding elemental mapping, for the collected material are shown in Figure 9.4b, with the mapping consistent with coating of MWCNTs with Fe_3O_4 NPs. BF and HAADF, and STEM images, Figure 9.4a, b also establish that the size of Fe_3O_4 nanoparticles for the collected material are smaller than those of the retained material. In addition, VFD processing in the absence of MWCNTs, generated Fe_3O_4 nanoparticles which were also smaller for the collected material, average diameter *ca.* 10 nm, compared to the material retained in the VFD, average diameter *ca.* 15, as determined using AFM (supporting information Figure S8). This is in good agreement with HRTEM results for the NPs formed in the presence of MWCNTs, Figure 9.2c and Figure 9.3c. The results suggest that the larger particles, which have higher mass, determine whether the MWCNTs are decorated and sliced and free to leave the tube, or decorated without slicing and retained in the tube, ie. if the build-up of NPs on the surface of MWCNTs is too fast relative to slicing the MWCNTs, then they will be retained in the quartz tube in the VFD. Additional STEM images are provided in the supporting information, Figure S3 and S4.

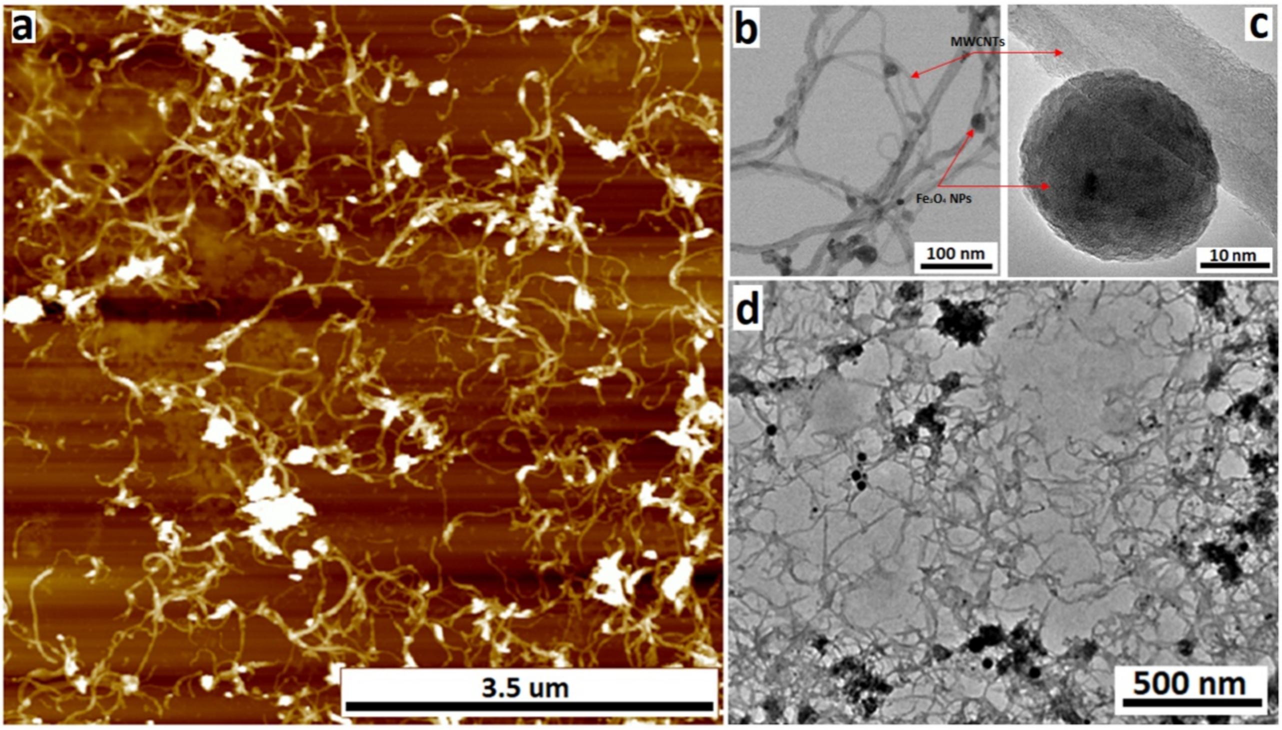

Figure 9. 2 (a) AFM image, (b) STEM image, (c) HRTEM image and (d) TEM of Fe_3O_4@MWCNT (retained), formed in the VFD (optimised parameters) operating at 8.5k rpm rotational speed, under continuous flow, with the concentration of the as received MWCNTs at 0.08 mg/mL (DMF)), tilt angle 45°, flow rate 0.45 mL/min, and laser power 250 mJ, with the MWCNTs ca 2 μm in length.

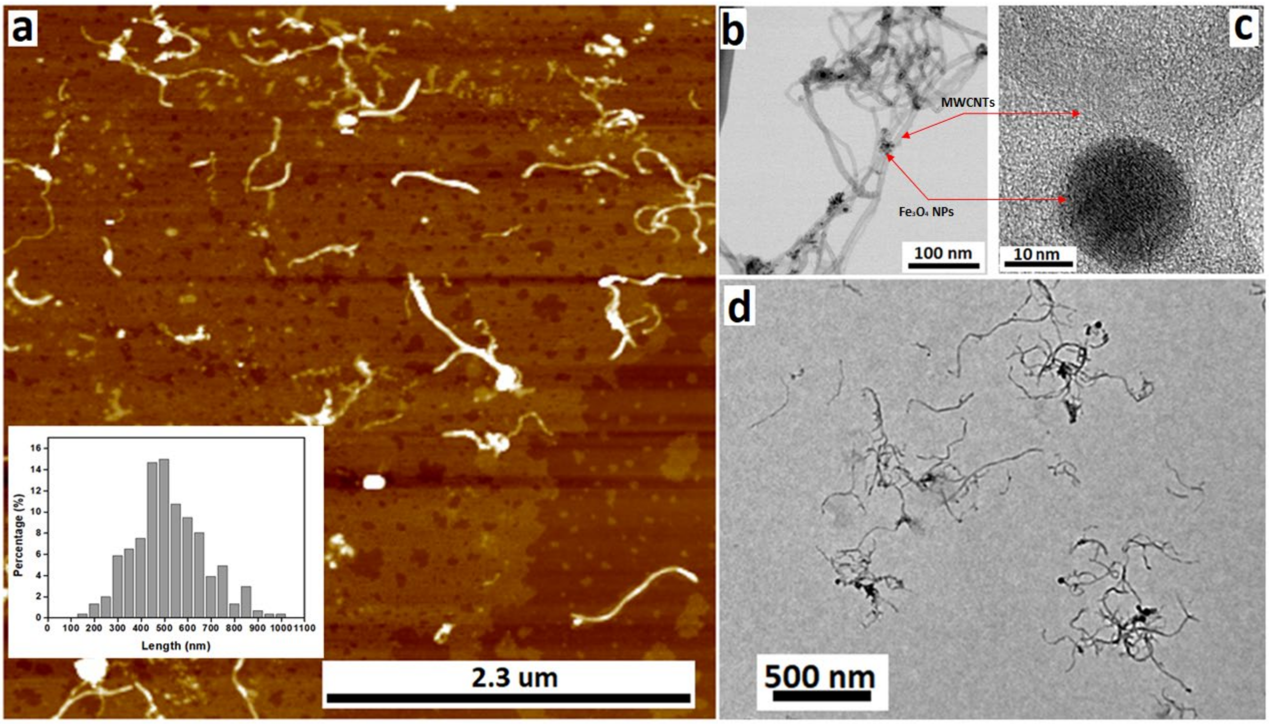

Figure 9. 3 (a) AFM image, (b) STEM image, (c) HRTEM image and (d) TEM image of Fe_3O_4@MWCNT exiting the tube under continuous flow (collected), processed in the VFD (optimised parameters) operating at 8.5k rpm rotational speed, with the concentration of the as received MWCNTs at 0.08 mg/mL (DMF)), tilt angle 45°, flow rate 0.45 mL/min, and laser power 250 mJ. The inset in (a) is the length distribution of the carbon nanotubes in Fe_3O_4@MWCNTs (collected).

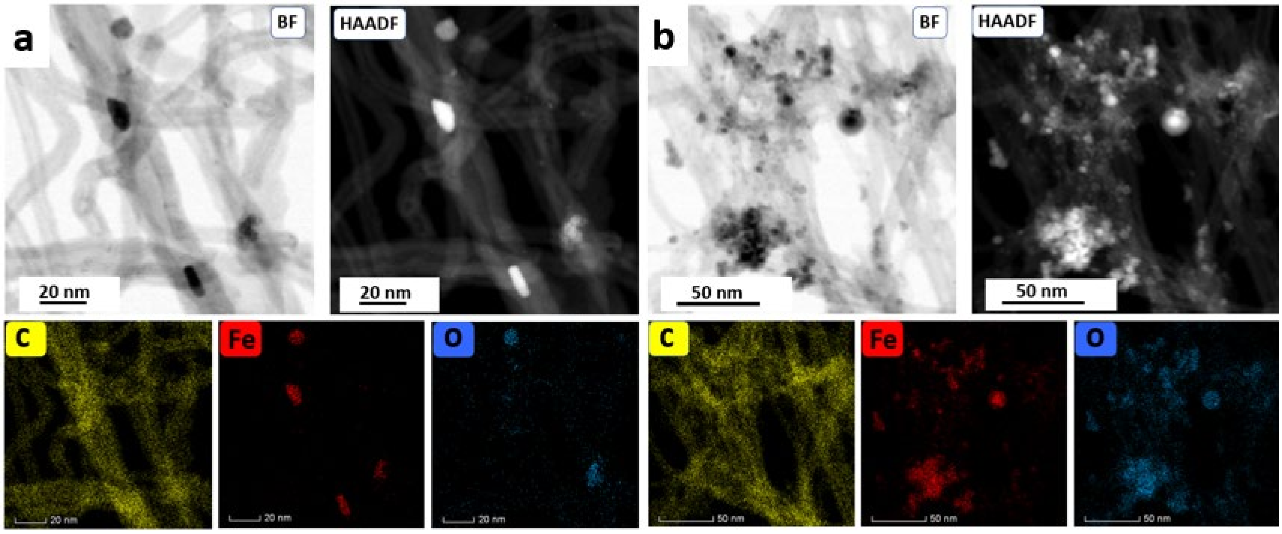

Figure 9. 4 (a) BF and HAADF - STEM images of Fe_3O_4@MWCNT (collected) with the corresponding STEM element mapping. (b) BF and HAADF - STEM image of Fe_3O_4@MWCNT (retained) with the corresponding STEM element mapping.

The X-ray diffraction (XRD) patterns of MWCNTs before processing (as received), Fe_3O_4@MWCNT (collected and retained) samples are shown in Figure 9.5a. MWCNTs (as received) have diffraction peaks at 29.7° and 51.2°, which are assigned to the (002) and (110) planes of MWCNTs (supporting information Figure S6),[15,27] whereas for Fe_3O_4 nanoparticles only, there are seven characteristic peaks (21.5°, 37.3°, 44.6°, 54.9°, 62°, 69.1°, and 74.1°) which correspond to the (111), (220), (311), (400), (422), (511), and (440) reflections of magnetite (Fe_3O_4) (supporting information Figure S6).[26-27,31,38] XRD pattern for the nanocomposite material is shown in Figure 9.5a, establishing the formation of magnetic NPs, with all of the peaks corresponding to magnetite and MWCNTs, consistent with the formation of Fe_3O_4@MWCNT.

Thermogravimetric analysis (TGA) was carried out under air, for MWCNTs (as received), (supporting information Figure S7), and both Fe_3O_4@MWCNT nanocomposite materials (retained and collected), Figure 9.5b. For as-received MWCNTs the material is stable when the temperature is < 550 °C, with then a significant weight loss > 600°C corresponding to the decomposition of MWCNTs.[56] The weight loss of retained Fe_3O_4@MWCNT nanocomposite was about 29.6 wt%

between temperature 350 – 650°C, whereas, the collected nanocomposite shows greater weight loss for increasing temperatures. Here there are two regions of weight loss, 40 and 25 wt.% between 50 – 400 °C and 400 – 650 °C, respectively. The differences in the weight loss between two nanocomposite material (retained and collected) is ascribed to the uptake of DMF in solution when the MWCNTs are sliced. If the material retained in the VFD quartz tube is unsliced or has very little slicing, the end caps of the MWCNTs will limit the amount of solvent that can be taken up inside the nanotubes.[57, 58] Specific surface area from BET for MWCNTs (as received), Fe_3O_4@MWCNT (collected) and Fe_3O_4@MWCNT (retained) are 127.0396 m^2/g, 83.8937 m^2/g and 55.1279 m^2/g, respectively, Figure S9. The lower surface area for Fe_3O_4@MWCNT (collected) and Fe_3O_4@MWCNT (retained) compared to as received MWCNTs presumably relates to the build up of magnetite material, lowering the relative surface area. The higher surface area for the material exiting the tube relates to the now availability of the internal surface of the sliced MWCNTs.[59]

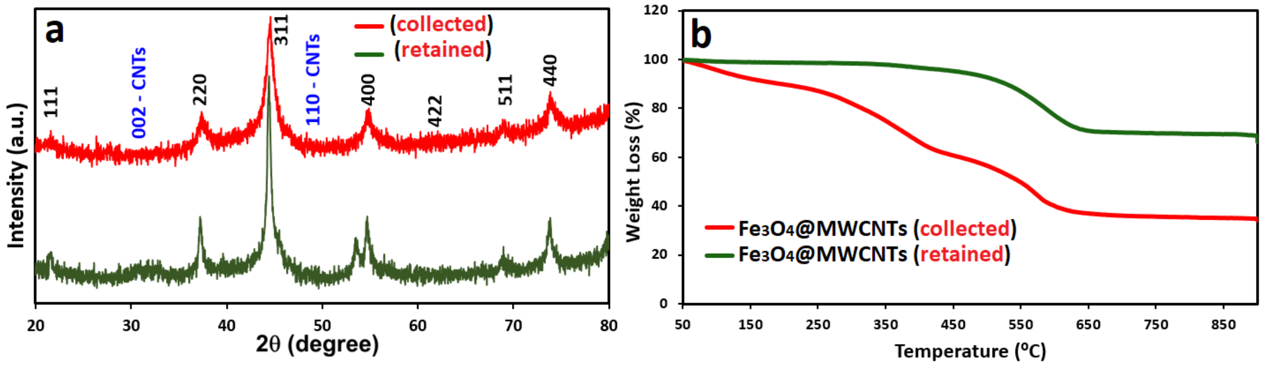

Figure 9. 5 (a) XRD patterns and (b) TGA curves for Fe_3O_4@MWCNT exiting (red) and retained (green) in the quartz tube, processed in the VFD (optimised parameters) operating at 8.5k rpm rotational speed, with the concentration of the as received MWCNTs at 0.08 mg/mL (DMF)), tilt angle 45°, flow rate 0.45 mL/min, and laser power 250 mJ.

X-ray photoelectron spectroscopy (XPS) was used to investigate the elemental composition and chemical state of Fe_3O_4@MWCNT, with the results shown in Figure 9.6. The XPS C1s spectrum for Fe_3O_4@MWCNT (retained and collected) is shown in Figure 9.6a and 9.6c respectively, with three peaks, at 285.1 eV, 286.8 eV and 289.1 eV, corresponding to C-C, C-O and C=O groups,[60, 61] respectively. Figure 9.6b and 6d show the XPS Fe 2p spectra for retained and collected material, with two peaks at 711.5 and 724.7 eV, which are assigned to the Fe $2p_{3/2}$ and Fe $2p_{1/2}$ binding energies,[37, 62] respectively.

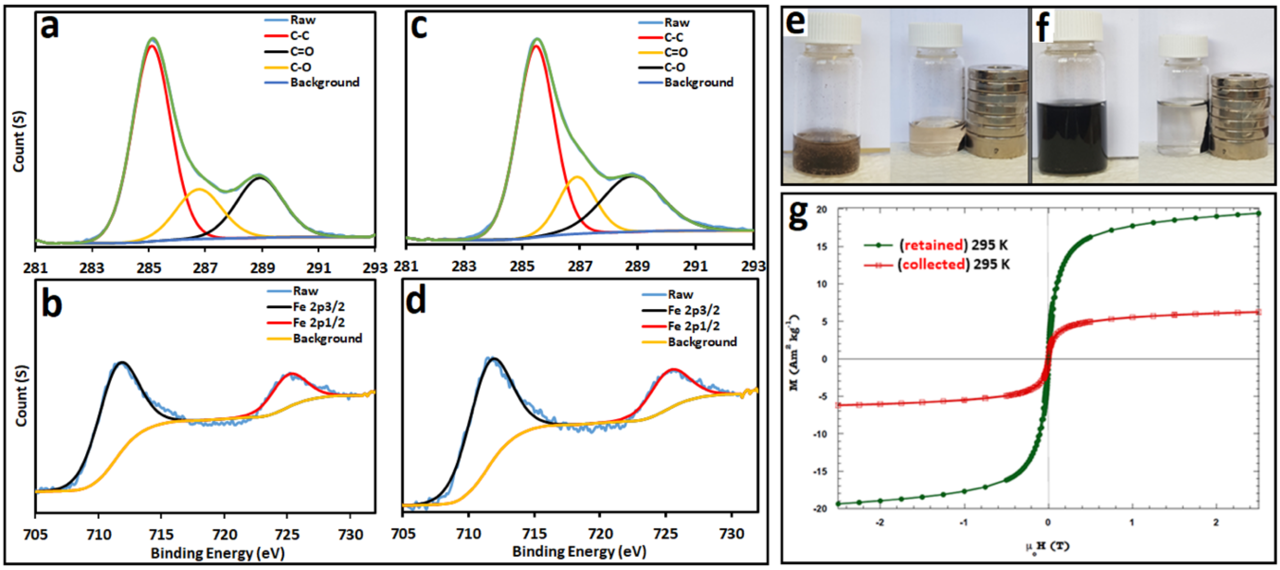

Figure 9. 6 High-resolution XPS spectra for Fe_3O_4@MWCNT: (a) C 1s and (b) Fe 2p (collected), and (c) C 1s and (d) Fe 2p (retained). (e) Photographs of Fe_3O_4@MWCNT, collected and retained when placed next to a magnet, and (g) magnetic hysteresis loops for Fe_3O_4@MWCNTs (collected out of the tube, red line, and retained in the tube, green line), processed in the VFD (at optimised condition) operating at 8.5k rpm rotational speed, under continuous flow, with the concentration of the as received MWCNTs at 0.08 mg/mL (DMF)), tilt angle 45°, flow rate 0.45 mL/min, and laser power 250 mJ.

The magnetic behaviour of Fe_3O_4@MWCNT composites was investigated by placing a suspension of the composite materials Fe_3O_4@MWCNTs in water, separately retained and collected, close to an external magnet, Figure 9.6e, f. Both show a dramatic response with accumulation of the material towards the magnet. In addition, their response to magnetic fields between ±2.5 T where studied, with the results presented in Figure 9.6g. Both composite materials (retained and collected) have similar shaped hysteresis loops. The saturation magnetization (Ms) of Fe_3O_4@MWCNT (retained) is 19.3 Am^2kg^{-1} establishing high magnetism and exhibiting typical ferromagnetic behaviour, being consistent with the results in literature values for superparamagnetic nanoparticles of magnetite.[57] In contrast, Fe_3O_4@MWCNT collected under continuous flow has weak magnetic properties, with Ms of 6.2 Am^2kg^{-1}. This is consistent with smaller sized magnetite particles decorating the MWCNTs (collected).[63-65]

9.4.3. Electrochemical Response

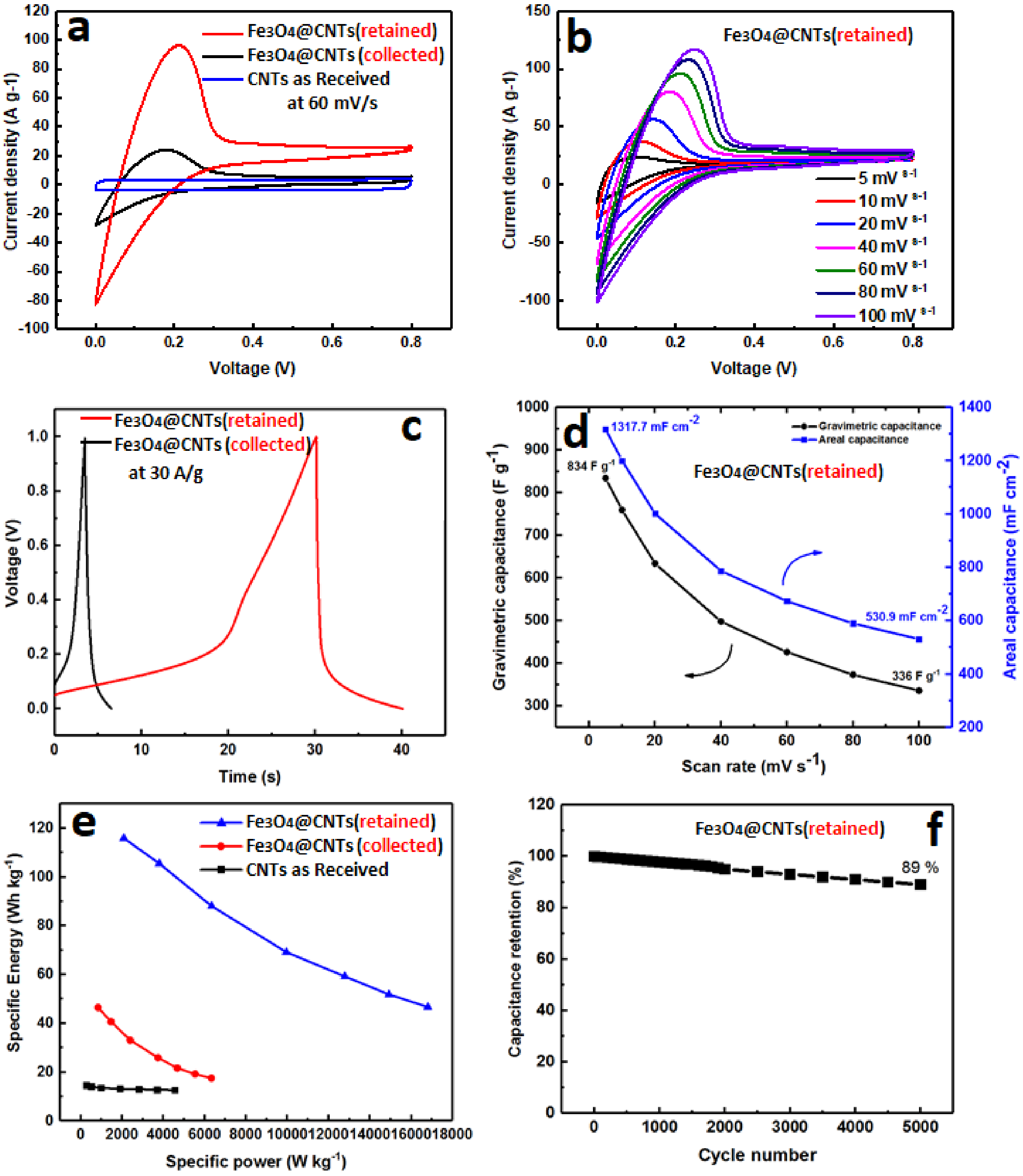

Figure 9. 7 (a) Cyclic Voltammogram (CV) curves of MWCNTs (as received), Fe_3O_4@MWCNT (retained) and Fe_3O_4@MWCNTs (collected) at 60 mV/s, (b) CV curves of Fe_3O_4@MWCNT (collected) at different scan rates from 5 to 100 mV s−1 and (c) charge–discharge curves of Fe_3O_4@MWCNT (retained and collected), (d) gravimetric capacitance and areal capacitance values versus scanning rate calculated from the CV curves of the Fe_3O_4@MWCNT (retained). (e) Specific energy vs specific power of Fe_3O_4@MWCNT (retained). (f) Cycle performance of the Fe_3O_4@MWCNT (retained).

Finally, in order to demonstrate a practical application of Fe_3O_4@MWCNT composites, they were used as electrodes for assembly of a supercapacitor with the performance presented for selected results in Figure 9.7**.** The electrochemical behaviour of MWCNTs (as received), and Fe_3O_4@MWCNTs (retained and collected) were tested using cyclic voltammetry (CV) and galvanostatic charge/discharge (CD) in a two-electrode cell configuration with 1.0 M Na_2SO_4 as an electrolyte by a CHI 760E electrochemical workstation. Figure 9.7a shows the CV curves of electrodes of these materials at a scan rate of 60 mVs^{-1}. MWCNTs (as received) displayed CV curves with typical rectangular shape due to the clear EDLC behaviour. After adding Fe_3O_4 as pseudocapacitive material, Fe_3O_4@MWCNT (retained) and Fe_3O_4@MWCNTs (collected) had deformed CV curves with larger integrated area than MWCNTs (as received), thereby confirming the role of Fe_3O_4 in the composites for improving the electrochemical performance. However, the Fe_3O_4@MWCNT (retained) electrode exhibited much higher current densities than those of the collected Fe_3O_4@MWCNT electrode, and the enclosed area of Fe_3O_4@MWCNTs (retained) is also much larger than that of Fe_3O_4@MWCNTs (collected), showing that the capacitance is significantly increased after adding more Fe_3O_4 decoration owing to the significant synergistic effect between the Fe_3O_4 and MWCNTs in the composite. The CV curves of Fe_3O_4@MWCNTs (retained) at different scan rates, ranging from 5 to 100 mV/s, are shown in Figure 9.7b, displaying typical pseudocapacitive behaviour at different scan rates, indicating good charge propagation at the electrode surface. The current response in the CV curves increases proportionally with increasing scan rates, suggesting that the rates of electronic and ionic transport are not limiting at scan rates as high as 100 mV/s.

The charge/discharge (CD) curves of both Fe_3O_4@MWCNT (retained and collected) are shown in Figure 9.7c, confirming the same behaviour as displayed in CV measurements, and that Fe_3O_4@MWCNT (retained) has a longer charge and discharge time than Fe_3O_4@MWCNTs (collected) with noticeable deviation from linearity. Figure 9.7d shows the areal and gravimetric (C_{wt}) capacitances of the Fe_3O_4@MWCNTs (retained) at different scan rates, ranging from 10 to 100 mV s−1, which were calculated from the CV curves of Equations S1 and S2 in the supplementary information. The Fe_3O_4@MWCNTs (retained) electrode delivers gravimetric of 834 F g^{-1} and areal capacitance of 1317.7 mF cm^{-2} at a scan rate of 10 mV s^{-1}. The exceptionally high value of the areal capacitance of the Fe_3O_4@MWCNTs (retained) electrode (1317.7 mF cm^{-2}), highlights potential advantages of these composite materials and the method which was used to prepare them. The areal capacitance achieved in the present study is considerably higher or comparable than the recently reported values when using composite carbon materials for supercapacitor, such as (GF-CNT@Fe_2O_3) (659.5 mF/cm^2 at 5 mA/cm^2) [41], (Ni/GF/Fe_2O_3)(572 mF cm^{-2} at 1 mA cm^{-2}),[66] (rGO-PEDOT/PSS films) (448 mF cm^{-2} at 10 mV s^{-1}),[67] (H_2SO_4-PVA this electrolyte, find materials) (402mF/cm^2),[68] (FeOOH-MWCNT)(0.58 F cm^{-2} at 100 mV s^{-1}),[69] (MN_3O_4-MWCNTs)(2.8 F cm^{-2} at 2 mV s^1),[70] (CNT hydrogel film with PANI) (680 mF cm^{-2} at 1 mA cm^{-2}),[71] and (V_2O_3-MWCNT)(4.4 F cm^{-2} at 2 mV s^{-1}).[72] Figure 9.7e features the Ragon plot of the calculated specific energy and specific power based on the total mass of electroactive materials in the two electrodes. The Fe_3O_4@MWCNT (retained) electrode delivers a significant high specific energy of 115.84 Wh kg^{-1} at specific power of 2085 W kg^{-1}. However, it can only provide a specific energy of 46.68 Wh kg^{-1} at a specific power of 16803.33 W kg^{-1}. More interestingly, the cyclic durability of the Fe_3O_4@MWCNTs (retained), shown in Figure 9.7f, establishes excellent cycling ability. The Fe_3O_4@MWCNT (retained) electrode was tested for 5000 charge−discharge cycles at a current density of 30 A/g, retaining 89% of the initial capacitance, and thus establishing good cycling performance.

9.5. Conclusions

We report a simple and effective method for decorating MWCNTs with superparamagnetic magnetite (Fe_3O_4) NPs using the VFD thin film microfluidic platform. The main advantages of the processing include that it is a focused three in one process, involving slicing the MWCNTs, generating the magnetite nanoparticles *in situ*, and the decoration of the MWCNTs. Both the slicing and the generation of the magnetite nanoparticles features the use of a pulsed laser operating at 1064 nm. This dual field effect application of the VFD adds to the versatility of the device, extending its field effect capabilities, with others including plasma processing and continuous light sources.[73, 74]

The generation of Fe_3O_4@MWCNT directly from pristine MWCNTs avoids the use of harsh chemicals while dramatically reducing the processing time, all of which are important in developing any applications. To this end, we have demonstrated the utility of the composite material retained in the VFD tube, in a high performing supercapacitor. The nanocomposite material (retained), resulted in a high areal capacitance (1317.7 mF cm-2) which is much larger than reported for other Fe_3O_4@CNTs electrodes.

9.6. Acknowledgements

T. M. D. A would like to thank Taibah University (Ministry of Education, Saudi Arabia) for funding his scholarship. The authors also thank the Australian Research Council, The Government of South Australia, Adelaide Microscopy and AMMRF for support of this work.

Associated content

Supporting Information. Additional information on controlling experiments and optimizing conditions for fabricating composites of multi-walled carbon nanotubes (MWCNTs) and superparamagnetic magnetite nanoparticles. This material is available free of charge via the Internet at http://pubs.acs.org.

Author information

Corresponding Author

* E-mail address: colin.raston@flinders.edu.au (Colin Raston)

Author Contributions

All authors have given approval to the final version of the manuscript.

Notes

The authors declare no competing financial interest.

9.7. References

1. Jiang, H.; Lee, P. S.; Li, C., 3D carbon based nanostructures for advanced supercapacitors. *Energy Environ. Sci.,* **2013,** *6*, 41-53.
2. Ran, F.; Yang, X.; Shao, L., Materials, H., Recent progress in carbon-based nanoarchitectures for advanced supercapacitors. *Adv. Compos. Hybrid. Mater.,* **2018,** *1*, 32-55.
3. Yang, Z.; Ren, J.; Zhang, Z.; Chen, X.; Guan, G.; Qiu, L.; Zhang, Y.; Peng, H., Recent advancement of nanostructured carbon for energy applications. *Chem. Rev.,* **2015,** *115*, 5159-5223.
4. Zhang, L. L.; Zhao, X., Carbon-based materials as supercapacitor electrodes. *Chem. Soc. Rev.,* **2009,** *38*, 2520-2531.
5. Zhang, L. L.; Zhou, R.; Zhao, X. S., Graphene-based materials as supercapacitor electrodes. *J. Mater. Chem.,* **2010,** *20*, 5983-5992.
6. Huang, Y.; Liang, J.; Chen, Y., An overview of the applications of graphene-based materials in supercapacitors. *Small,* **2012,** *8*, 1805-1834.
7. Liao, Q.; Li, N.; Jin, S.; Yang, G.; Wang, C., All-solid-state symmetric supercapacitor based on Co3O4 nanoparticles on vertically aligned graphene. *ACS Nano,* **2015,** *9*, 5310-5317.
8. Yuan, L.; Lu, X.-H.; Xiao, X.; Zhai, T.; Dai, J.; Zhang, F.; Hu, B.; Wang, X.; Gong, L.; Chen, J., Flexible solid-state supercapacitors based on carbon nanoparticles/MnO2 nanorods hybrid structure. *ACS Nano,* **2011,** *6*, 656-661.
9. Chen, Z.; Augustyn, V.; Wen, J.; Zhang, Y.; Shen, M.; Dunn, B.; Lu, Y., High-performance supercapacitors based on intertwined CNT/V2O5 nanowire nanocomposites. *Adv. Mater.,* **2011,** *23*, 791-795.
10. Chen, P.-C.; Shen, G.; Shi, Y.; Chen, H.; Zhou, C., Preparation and characterization of flexible asymmetric supercapacitors based on transition-metal-oxide nanowire/single-walled carbon nanotube hybrid thin-film electrodes. *ACS Nano,* **2010,** *4*, 4403-4411.
11. Zhao, Y.; Ran, W.; He, J.; Huang, Y.; Liu, Z.; Liu, W.; Tang, Y.; Zhang, L.; Gao, D.; Gao, F., High-performance asymmetric supercapacitors based on multilayer MnO2/graphene oxide nanoflakes and hierarchical porous carbon with enhanced cycling stability. *Small,* **2015,** *11*, 1310-1319.
12. Mohamed, S. G.; Chen, C.-J.; Chen, C. K.; Hu, S.-F.; Liu, R.-S., High-performance lithium-ion battery and symmetric supercapacitors based on FeCo2O4 nanoflakes electrodes. *ACS appl. Mater. Interfaces,* **2014,** *6*, 22701-22708.
13. Chang, J.; Jin, M.; Yao, F.; Kim, T. H.; Le, V. T.; Yue, H.; Gunes, F.; Li, B.; Ghosh, A.; Xie, S., Asymmetric supercapacitors based on graphene/MnO2 nanospheres and graphene/MoO3 nanosheets with high energy density. *Adv. Funct. Mater.,* **2013,** *23*, 5074-5083.
14. Guo, C. X.; Li, C. M., A self-assembled hierarchical nanostructure comprising carbon spheres and graphene nanosheets for enhanced supercapacitor performance. *Energy Environ. Sci.,* **2011,** *4*, 4504-4507.
15. Reddy, A. L. M.; Ramaprabhu, S. J. T., Nanocrystalline metal oxides dispersed multiwalled carbon nanotubes as supercapacitor electrodes. *J. Phys. Chem. C,* **2007,** *111*, 7727-7734.
16. Zhi, M.; Xiang, C.; Li, J.; Li, M.; Wu, N., Nanostructured carbon–metal oxide composite electrodes for supercapacitors: a review. *Nanoscale,* **2013,** *5*, 72-88.
17. Tucek, J.; Kemp, K. C.; Kim, K. S.; Zboril, R., Iron-oxide-supported nanocarbon in lithium-ion batteries, medical, catalytic, and environmental applications. *ACS Nano,* **2014,** *8*, 7571-7612.
18. Kim, H.-S.; Lee, H.; Han, K.-S.; Kim, J.-H.; Song, M.-S.; Park, M.-S.; Lee, J.-Y.; Kang, J.-K., Hydrogen storage in Ni nanoparticle-dispersed multiwalled carbon nanotubes. *J. Phys. Chem. B,* **2005,** *109*, 8983-8986.

19. Liu, X.; Marangon, I.; Melinte, G.; Wilhelm, C.; Ménard-Moyon, C. c.; Pichon, B. P.; Ersen, O.; Aubertin, K.; Baaziz, W.; Pham-Huu, C., Design of covalently functionalized carbon nanotubes filled with metal oxide nanoparticles for imaging, therapy, and magnetic manipulation. *ACS Nano,* **2014,** *8*, 11290-11304.
20. Star, A.; Joshi, V.; Skarupo, S.; Thomas, D.; Gabriel, J.-C. P., Gas sensor array based on metal-decorated carbon nanotubes. *J. Phys. Chem. B,* **2006,** *110*, 21014-21020.
21. Yang, G.-W.; Gao, G.-Y.; Wang, C.; Xu, C.-L.; Li, H.-L., Controllable deposition of Ag nanoparticles on carbon nanotubes as a catalyst for hydrazine oxidation. *Carbon,* **2008,** *46*, 747-752.
22. Liu, Q.; Ren, W.; Chen, Z.-G.; Liu, B.; Yu, B.; Li, F.; Cong, H.; Cheng, H.-M., Direct synthesis of carbon nanotubes decorated with size-controllable Fe nanoparticles encapsulated by graphitic layers. *Carbon,* **2008,** *46*, 1417-1423.
23. Lee, S. Y.; Choi, W. C.; Jeon, C.; Park, C.-Y.; Yang, J. H.; Kwon, M. H., Field emitter density control effect on emission current density by Ag–Cu alloy coating on carbon nanotubes. *Appl. Phys. Lett.,* **2008,** *93*, 103101.
24. Liebau, M.; Unger, E.; Duesberg, G.; Graham, A.; Seidel, R.; Kreupl, F.; Hoenlein, W., Contact improvement of carbon nanotubes via electroless nickel deposition. *Appl. Phys. A,* **2003,** *77*, 731-734.
25. Ma, P. C.; Tang, B. Z.; Kim, J.-K., Effect of CNT decoration with silver nanoparticles on electrical conductivity of CNT-polymer composites. *Carbon,* **2008,** *46*, 1497-1505.
26. Deng, J.; Wen, X.; Wang, Q., Solvothermal in situ synthesis of Fe3O4-multi-walled carbon nanotubes with enhanced heterogeneous Fenton-like activity. *Mater. Res. Bull.,* **2012,** *47*, 3369-3376.
27. Guan, D.; Gao, Z.; Yang, W.; Wang, J.; Yuan, Y.; Wang, B.; Zhang, M.; Liu, L., Hydrothermal synthesis of carbon nanotube/cubic Fe3O4 nanocomposite for enhanced performance supercapacitor electrode material. *Mater. Sci. Eng., B,* **2013,** *178*, 736-743.
28. Chen, Y.; Gu, H., Microwave assisted fast fabrication of Fe3O4-MWCNTs nanocomposites and their application as MRI contrast agents. *Mater. Lett.,* **2012,** *67*, 49-51.
29. Henley, S. J.; Mollah, S.; Giusca, C. E.; Silva, S. R. P., Laser-induced self-assembly of iron oxide nanostructures with controllable dimensionality. *J. Appl. Phys.,* **2009,** *106*, 064309.
30. Sun, Z.; Li, Z.; Huang, C.; Zhao, Y.; Zhang, H.; Tao, R.; Liu, Z., Ultrasonication-assisted uniform decoration of carbon nanotubes by various particles with controlled size and loading. *Carbon,* **2011,** *49*, 4376-4384.
31. Zhou, H.; Zhang, C.; Li, H.; Du, Z., Decoration of Fe3O4 nanoparticles on the surface of poly (acrylic acid) functionalized multi-walled carbon nanotubes by covalent bonding. *J. Polym. Sci., Part A: Polym. Chem.,* **2010,** *48*, 4697-4703.
32. Morales, M.; Bomati-Miguel, O.; De Alejo, R. P.; Ruiz-Cabello, J.; Veintemillas-Verdaguer, S.; O'Grady, K., Contrast agents for MRI based on iron oxide nanoparticles prepared by laser pyrolysis. *J. Magn. Magn. Mater.,* **2003,** *266*, 102-109.
33. Tristao, J. C.; Oliveira, A. A.; Ardisson, J. D.; Dias, A.; Lago, R. M., Facile preparation of carbon coated magnetic Fe3O4 particles by a combined reduction/CVD process. *Mater. Res. Bull.,* **2011,** *46*, 748-754.
34. Freedman, J.; Mattia, D.; Korneva, G.; Gogotsi, Y.; Friedman, G.; Fontecchio, A. K., Magnetically assembled carbon nanotube tipped pipettes. *Appl. Phys. Lett.,* **2007,** *90*, 103108.
35. Singhal, R.; Orynbayeva, Z.; Sundaram, R. V. K.; Niu, J. J.; Bhattacharyya, S.; Vitol, E. A.; Schrlau, M. G.; Papazoglou, E. S.; Friedman, G.; Gogotsi, Y., Multifunctional carbon-nanotube cellular endoscopes. *Nat. nanotechnol.,* **2011,** *6*, 57.
36. Šljukić, B.; Banks, C. E.; Compton, R. G., Iron oxide particles are the active sites for hydrogen peroxide sensing at multiwalled carbon nanotube modified electrodes. *Nano lett.,* **2006,** *6*, 1556-1558.

37. Kim, W.; Lee, J. S.; Jang, J., Facile synthesis of size-controlled Fe 2 O 3 nanoparticle-decorated carbon nanotubes for highly sensitive H 2 S detection. *RSC Adv.,* **2018,** *8*, 31874-31880.
38. Luo, X.; Al-Antaki, A. H.; Alharbi, T. M.; Hutchison, W. D.; Zou, Y.-c.; Zou, J.; Sheehan, A.; Zhang, W.; Raston, C. L., Laser-Ablated Vortex Fluidic-Mediated Synthesis of Superparamagnetic Magnetite Nanoparticles in Water Under Flow. *ACS Omega,* **2018,** *3*, 11172-11178.
39. Al-antaki, A. H. M.; Luo, X.; Duan, A.; Lamb, R. N.; Eroglu, E.; Hutchison, W.; Zou, Y.-C.; Zou, J.; Raston, C. L., Continuous flow synthesis of phosphate binding h-BN@ magnetite hybrid material. *RSC Adv.,* **2018,** *8*, 40829-40835.
40. Vimalanathan, K.; Gascooke, J. R.; Suarez-Martinez, I.; Marks, N. A.; Kumari, H.; Garvey, C. J.; Atwood, J. L.; Lawrance, W. D.; Raston, C. L., Fluid dynamic lateral slicing of high tensile strength carbon nanotubes. *Sci. Rep.,* **2016,** *6*, 22865.
41. Guan, C.; Liu, J.; Wang, Y.; Mao, L.; Fan, Z.; Shen, Z.; Zhang, H.; Wang, J., Iron oxide-decorated carbon for supercapacitor anodes with ultrahigh energy density and outstanding cycling stability. *ACS Nano,* **2015, *9***, 5198-5207.
42. Chin, S. F.; Iyer, K. S.; Raston, C. L., Fabrication of carbon nano-tubes decorated with ultra fine superparamagnetic nano-particles under continuous flow conditions. *Lab Chip,* **2008,** *8*, 439-442.
43. Alharbi, T. M.; Vimalanathan, K.; Lawrance, W. D.; Raston, C. L., Controlled slicing of single walled carbon nanotubes under continuous flow. *Carbon,* **2018**, 140, 428-432.
44. Chen, X.; Dobson, J. F.; Raston, C. L., Vortex fluidic exfoliation of graphite and boron nitride. *Chem. Commun.,* **2012,** *48*, 3703-3705.
45. Alharbi, T. M.; Harvey, D.; Alsulami, I. K.; Dehbari, N.; Duan, X.; Lamb, R. N.; Lawrance, W. D.; Raston, C. L., Shear stress mediated scrolling of graphene oxide. *Carbon,* **2018**, 137, 419-424.
46. Goh, Y. A.; Chen, X.; Yasin, F. M.; Eggers, P. K.; Boulos, R. A.; Wang, X.; Chua, H. T.; Raston, C. L., Shear flow assisted decoration of carbon nano-onions with platinum nanoparticles. *Chem. Commun.,* **2013,** *49*, 5171-5173.
47. MdáYasin, F.; YongáHong, B.; SwaminathanáIyer, K.; TongáChua, H., Microfluidic size selective growth of palladium nano-particles on carbon nano-onions. *Chem. Commun.,* **2012,** *48*, 10102-10104.
48. Luo, X.; Al-Antaki, A. H. M.; Vimalanathan, K.; Moffatt, J.; Zheng, K.; Zou, Y.-C.; Zou, J.; Duan, X.; Lamb, R.; Wang, S., Laser irradiated vortex fluidic mediated synthesis of luminescent carbon nanodots under continuous flow. *React. Chem. Eng.,* **2018**, 3, 164-170.
49. Vimalanathan, K.; Shrestha, R. G.; Zhang, Z.; Zou, J.; Nakayama, T.; Raston, C. L., Surfactant-free Fabrication of Fullerene C60 Nanotubules Under Shear. *Angew. Chem. Int. Ed.,* **2017,** *56*, 8398-8401.
50. Yasmin, L.; Chen, X.; Stubbs, K. A.; Raston, C. L., Optimising a vortex fluidic device for controlling chemical reactivity and selectivity. *Sci. Rep.,* **2013,** *3*, 2282.
51. Yuan, T. Z.; Ormonde, C. F. G.; Kudlacek, S. T.; Kunche, S.; Smith, J. N.; Brown, W. A.; Pugliese, K. M.; Olsen, T. J.; Iftikhar, M.; Raston, C. L., Shear-Stress-Mediated Refolding of Proteins from Aggregates and Inclusion Bodies. *ChemBioChem,* **2015,** *16*, 393-396
52. Britton, J.; Meneghini, L. M.; Raston, C. L.; Weiss, G. A., Accelerating Enzymatic Catalysis Using Vortex Fluidics. *Angew. Chem.,* **2016,** *128*, 11559-11563.
53. Britton, J.; Raston, C. L.; Weiss, G. A., Rapid protein immobilization for thin film continuous flow biocatalysis. *Chem.Commun.,* **2016,** *52*, 10159-10162.
54. Britton, J.; Stubbs, K. A.; Weiss, G. A.; Raston, C. L., Vortex Fluidic Chemical Transformations. *Chem. - Eur. J.,* **2017**, , 23, 13270-13278.
55. Vimalanathan, K.; Raston, C. L., Dynamic Thin Films in Controlling the Fabrication of Nanocarbon and Its Composites. *Adv.Mater. Technol.,* **2017**, 2, 1600298.

56. Muruganathan, M.; Mizuta, H.; Sundara, R., Enhanced Sodium Ion Storage in Interlayer Expanded Multiwall Carbon Nanotubes. *Nano lett.,* **2018**, 18, 5688-5696.
57. Jia, X.; Li, W.; Xu, X.; Li, W.; Cai, Q.; Yang, X., Numerical characterization of magnetically aligned multiwalled carbon nanotube–Fe3O4 nanoparticle complex. *ACS Appl. Mater. Interfaces,* **2015,** *7*, 3170-3179.
58. Hao, M.; Tang, M.; Wang, W.; Tian, M.; Zhang, L.; Lu, Y., Silver-nanoparticle-decorated multiwalled carbon nanotubes prepared by poly (dopamine) functionalization and ultraviolet irradiation. *Composites, Part B,* **2016,** *95*, 395-403.
59. Marques Neto, J. O.; Bellato, C. R.; de Souza, C. H.; Silva, R. C. d.; Rocha, P. A., Synthesis, characterization and enhanced photocatalytic activity of iron oxide/carbon nanotube/Ag-doped TiO2 nanocomposites. *J. Braz. Chem. Soc.,* **2017,** *28*, 2301-2312.
60. Chen, H.; Zhang, Z.; Wang, X.; Chen, J.; Xu, C.; Liu, Y.; Yu, Z.; Wang, X., Fabrication of Magnetic Fe/Zn Layered Double Oxide@ Carbon Nanotube Composites and Their Application for U (VI) and 241Am (III) Removal. *ACS Appl. Nano Mater.,* **2018,** *1*, 2386-2396.
61. Okpalugo, T.; Papakonstantinou, P.; Murphy, H.; McLaughlin, J.; Brown, N., High resolution XPS characterization of chemical functionalised MWCNTs and SWCNTs. *Carbon,* **2005,** *43*, 153-161.
62. Liu, L.; Lang, J.; Zhang, P.; Hu, B.; Yan, X., Facile synthesis of Fe_2O_3 nano-dots@ nitrogen-doped graphene for supercapacitor electrode with ultralong cycle life in KOH electrolyte. *ACS Appl. Mater. Interfaces,* **2016,** *8*, 9335-9344.
63. Wu, J.; Kong, L., High microwave permittivity of multiwalled carbon nanotube composites. *Appl. Phy. lett.,* **2004,** *84*, 4956-4958.
64. Huiqun, C.; Meifang, Z.; Yaogang, L., Decoration of carbon nanotubes with iron oxide. *J.Solid State Chem.,* **2006,** *179*, 1208-1213.
65. Zhao, W.; Zhu, L.; Lu, Y.; Zhang, L.; Schuster, R. H.; Wang, W., Magnetic nanoparticles decorated multi-walled carbon nanotubes by bio-inspired poly (dopamine) surface functionalization. *Synth. Met.,* **2013,** *169*, 59-63.
66. Chi, K.; Zhang, Z.; Lv, Q.; Xie, C.; Xiao, J.; Xiao, F.; Wang, S., Well-ordered oxygen-deficient CoMoO4 and Fe2O3 nanoplate arrays on 3D graphene foam: toward flexible asymmetric supercapacitors with enhanced capacitive properties. *ACS Appl. Mater. Interfaces,* **2017,** *9*, 6044-6053.
67. Liu, Y.; Weng, B.; Razal, J. M.; Xu, Q.; Zhao, C.; Hou, Y.; Seyedin, S.; Jalili, R.; Wallace, G. G.; Chen, J., High-performance flexible all-solid-state supercapacitor from large free-standing graphene-PEDOT/PSS films. *Sci. Rep.,* **2015,** *5*, 17045.
68. Xu, Y.; Lin, Z.; Huang, X.; Liu, Y.; Huang, Y.; Duan, X., Flexible solid-state supercapacitors based on three-dimensional graphene hydrogel films. *ACS Nano,* **2013,** *7*, 4042-4049.
69. Chen, R.; Puri, I. K.; Zhitomirsky, I., High areal capacitance of FeOOH-carbon nanotube negative electrodes for asymmetric supercapacitors. *Ceram. Int.,* **2018,** *44*, 18007-18015.
70. Ata, M.; Milne, J.; Zhitomirsky, I. J., Fabrication of Mn3O4–carbon nanotube composites with high areal capacitance using cationic and anionic dispersants. *J Colloid Interface Sci.,* **2018,** *512*, 758-766.
71. Zeng, S.; Chen, H.; Cai, F.; Kang, Y.; Chen, M.; Li, Q. J., Electrochemical fabrication of carbon nanotube/polyaniline hydrogel film for all-solid-state flexible supercapacitor with high areal capacitance. *J. Mater. Chem. A,* **2015,** *3*, 23864-23870.
72. Wallar, C.; Poon, R.; Zhitomirsky, I., High Areal Capacitance of V2O3–Carbon Nanotube Electrodes. *J. Electrochem. Soc.,* **2017,** *164*, A3620-A3627.
73. Jones, D. B.; Chen, X.; Sibley, A.; Quinton, J. S.; Shearer, C. J.; Gibson, C. T.; Raston, C. L., Plasma enhanced vortex fluidic device manipulation of graphene oxide. *Chem. Commun.,* **2016,** *52*, 10755-10758.

74. Ho, L. A.; Raston, C. L.; Stubbs, K. A., Angled Vortex Fluidic Mediated Multicomponent Photocatalytic and Transition Metal-Catalyzed Reactions. *Chem.– Eur. J.,* **2018**, 24, 8869-8874.

Nanoscale Advances

ROYAL SOCIETY OF CHEMISTRY

PAPER

View Article Online
View Journal | View Issue

Check for updates

Cite this: *Nanoscale Adv.*, 2019, 1, 3761

Three-step-in-one synthesis of supercapacitor MWCNT superparamagnetic magnetite composite material under flow†

Thaar M. D. Alharbi,[ab] Ahmed H. M. Al-Antaki,[a] Mahmoud Moussa,[c]
Wayne D. Hutchison[d] and Colin L. Raston*[a]

Composites of multi-walled carbon nanotubes (MWCNTs) and superparamagnetic magnetite nanoparticles, Fe_3O_4@MWCNT, were synthesized in DMF in a vortex fluidic device (VFD). This involved *in situ* generation of the iron oxide nanoparticles by laser ablation of bulk iron metal at 1064 nm using a pulsed laser, over the dynamic thin film in the microfluidic platform. The overall processing is a three-step in one operation: (i) slicing MWCNTs, (ii) generating the superparamagnetic nanoparticles and (iii) decorating them on the surface of the MWCNTs. The Fe_3O_4@MWCNT composites were characterized by transmission electron microscopy, scanning transmission electron microscope, TG analysis, X-ray diffraction and X-ray photoelectron spectroscopy. They were used as an active electrode for supercapacitor measurements, establishing high gravimetric and areal capacitances of 834 F g^{-1} and 1317.7 mF cm^{-2} at a scan rate of 10 mV s^{-1}, respectively, which are higher values than those reported using similar materials. In addition, the designer material has a significantly higher specific energy of 115.84 W h kg^{-1} at a specific power of 2085 W kg^{-1}, thereby showing promise for the material in next-generation energy storage devices.

Received 2nd June 2019
Accepted 16th August 2019

DOI: 10.1039/c9na00346k

rsc.li/nanoscale-advances

1. Introduction

In recent years the drive for safe, efficient and high-performance energy storage devices, has resulted in major research efforts in supercapacitors. This has been driven by their potential for high power density, outstanding safety, fast charge/discharge rates, excellent reliability, and long cycling life.[1-3] Several nano-structured materials have shown to be effective as electrodes for supercapacitors. These include carbon nanotubes,[1,4] graphene,[5,6] a number of other types of structured nanoparticles,[7,8] nanowires,[9,10] porous nanoflakes,[11,12] and nanospheres.[13,14] Composites of metal oxides and carbon based materials, especially carbon nanotubes, have been used as electrode materials, establishing that the electrochemical performance is enhanced.[15,16]

Decorating carbon nanotubes with inorganic nanoparticles has received considerable attention both in fundamental research and the industrial arena.[17] This relates to the unique physical and chemical properties of the composite materials. Indeed, MWCNTs decorated with iron oxide particles in general are promising composite materials for a variety of applications such as hydrogen storage,[18] imaging and therapy,[17,19] gas sensors,[20] catalysis,[17,21] CNT-based magnetic materials,[22] CNT field emitters,[17,23] and CNT-based electronic devices.[17,24,25] Various routes have been developed in gaining access to such material, including solvothermal,[26] hydrothermal,[27] microwave,[28] laser ablation[29] and ultra-sonication processing,[30] high-temperature decomposition,[31] laser pyrolysis[32] and chemical vapour deposition.[33] Freedman *et al.*[34] and Singhal *et al.*[35] have demonstrated that a magnetic carbon nanotube pipette is effective for transferring liquid into and within a single cell. In addition, Šljukić *et al.*[36] have shown that the electrochemical activity of carbon nanotubes for the reduction of H_2O_2 can arise from iron oxide nanoparticles decorated on CNT. Also noteworthy is that carbon nanotubes decorated with iron(III) oxide (Fe_2O_3) nanoparticle embedded in a co-polymer (derived from pyrrole and 3-carboxylated pyrrole) are highly sensitive for detecting H_2S, as reported by Kim *et al.*[37] Thus CNT–iron oxide nanoparticle composites have a diverse range of applications, and accordingly we sort to develop a robust synthesis of such

---

[a] *Flinders Institute for Nanoscale Science and Technology, College of Science and Engineering, Flinders University, Adelaide, SA 5001, Australia. E-mail: colin.raston@flinders.edu.au*

[b] *Physics Department, Faculty of Science, Taibah University, Almadinah Almunawarah, Saudi Arabia*

[c] *School of Chemical Engineering and Advanced Materials, The University of Adelaide, Adelaide, SA 5001, Australia*

[d] *School of Science, University of New South Wales, ADFA campus, Canberra BC, Australian Capital Territory 2610, Australia*

† Electronic supplementary information (ESI) available: Additional information on controlling experiments and optimizing conditions for fabricating composites of multi-walled carbon nanotubes (MWCNTs) and superparamagnetic magnetite nanoparticles. See DOI: 10.1039/c9na00346k

Electronic Supplementary Material (ESI) for Nanoscale Advances.

Supporting Information

Three-step-in-one synthesis of supercapacitor MWCNT superparamagnetic magnetite composite material under flow

Thaar M. D. Alharbi [†, §], Ahmed H. M. Al-Antaki[†], Mahmoud Moussa[‡], Wayne D. Hutchison[⊥] and Colin L Raston [†, *]

[†] Flinders Institute for Nanoscale Science and Technology, College of Science and Engineering, Flinders University, Adelaide SA 5001, Australia email: colin.raston@flinders.edu.au

[§] Physics Department, Faculty of Science, Taibah University, Almadinah Almunawarrah, Saudi Arabia

[‡] School of Chemical Engineering, The University of Adelaide, Adelaide SA 5001, Australia

[⊥] School of Science, University of New South Wales, ADFA campus, Canberra BC, Australian Capital Territory 2610, Australia

CONTENTS

Chapter Ten

Conclusions and Future Directions

10.1. Conclusions

This dissertation focused on the use of the VFD thin film microfluidic platform, as part of a paradigm shift in materials processing, in gaining access to material in a more practical way, and indeed in some cases in ways that are not possible using conventional batch processing. Novel methods have been developed in using the VFD to fabricate carbon nanomaterials and composites thereof involving both ‘top down’ and ‘bottom up’ strategies. The primary focus of the research was to develop continuous flow methods that are environmentally and economically sustainable while addressing the issue of scalability, such that the research processor, the VFD, can become the production processor, depending on the processing volume requirements. Overall, the findings further highlight the potential of the VFD in materials processing relative to conventional batch processing, in some cases with exquisite control of size and morphology of nanomaterials.

Chapters 2 and 3 report significant advances in slicing carbon nanotubes (CNTs) with results forming the basis of two publications, one in *Carbon* , the other in *Nanoscale*.[1, 2] They describe a method of debundling and slicing SWCNTs and MWCNTs with controllable length distributions, with minimal surface defects, that would benefit uptake by industry for a number of applications where a specific length of pristine material is required. This includes electronic devices, solar cell technology and biomedical sciences. Importantly the processing is simple, using shear stress in the VFD to bend and slice the tubes while irradiated with a NIR pulsed laser. Moreover, the processing avoids the need for using any other reagents, is scalable under continuous flow conditions, and does not introduce defects into the side walls of the CNTs.

The ability to vertically self assemble short MWCNTs on a silicon substrate with control of the surface density coverage using a simple dipping and rinsing method, as detailed in Chapter 2 and the above mentioned publication in *Nanoscale*,[2] is without precent. There have been extensive studies on vertically aligning CNTs on substrates, and the most common methods are either direct growth of the CNTs, as in chemical vapour deposition (CVD), onto substrates, or the immobilization of shortened CNTs on substrates via engineered covalent attachment.[3-5] However, these methods have limited economic and environmental sustainability metrics, due to their complex processing and the use of toxic reagents. Thus, the thin film processing in the VFD not only allows controlling the length of the MWCNTs, it also provides material with functionality that allows them to self-assemble of surfaces.

Chapter 3 is a detailed study on fabricating coiled SWCNTs under continuous flow in the VFD, using an immiscible solvent system of toluene and water. This is a significant advance in the field, as is the magnetic properties of the rings, as established using magnetic force microscopy (MFM). Different structures of coiled SWCNTs rings impacts on their properties, differently to straight SWCNTs, but the ability to prepare such rings prior to the findings herein has been challenging. The shear stress within the dynamic thin film in the VFD was effective is forming coiled SWCNT rings, under ambient conditions, and in high yield, ~80%, and importantly it is in the absence of any surfactants or any auxiliary reagents such that the final product is not coated in any way. The average diameter of these rings was ca. 300 nm with a wall thicknesses varying between 3 and 70 nm. Also important is that MFM was shown to be a viable technique for examining the magnetic response of the coils, which strongly depends on the thickness of the coiled SWCNT rings. This work is the basis of a publication in *ACS Appl. Nano Mater.*[6]

Another significant advance was establishing a high yielding VFD mediated method to transform colloidally stable sheets of graphene oxide into graphene oxide scrolls (GOS) using water as the solvent, as detailed in Chapter 5. The shear stress in the VFD coupled with irradiation of the GO with a pulsed laser operating at 1064 nm and 250 mJ, results in the formation of scrolls, and this controlled manipulation of GO is important in understanding the nature of the fluid dynamics in the device. The now availability of 1D GOS, the synthesis of which can be readily scaled under continuous flow in the VFD, offers scope for developing applications of the material, for example in supercapacitors and for hydrogen storage. This work is the basis of a publication in *Carbon*.[7]

Chapter 6 focused on further manipulation of GO in the VFD as part of a major research effort to understand the fluid dynamics in the device, with a process established to be able scroll GO at low speeds and unscroll the material at high speeds, using a single solvent (DMF), depending on the rotational speed of the rapidly rotating tube in the VFD and the nature of the liquid, defined as the signature of a liquid. Establishing the so-called signature of a specific liquid is important in being able to predict the outcome of any processing in the VFD. Prior to this discovery, the level of predictability of processing in the VFD was limited. Also included in this chapter are related findings on predicting the outcome of processing in the VFD. They focus on controlling the nucleation and growth of sell-assembled C_{60} nano-structures, which depend on the processing parameters of the VFD, and more.

A facile, simple and environmentally friendly method has been developed for converting water-soluble GO to water-soluble reduced graphene oxide, rGO, under continuous flow conditions in the VFD, as detailed in Chapter 7. The process involves UV irradiation of an aqueous dispersion of GO within the VFD, at room temperature with the rGO uniquely different yet comparable to that formed using other methods such as waste generating chemical based processing. The properties of the rGO film of the material having a resistance of 2.2×10^5 Ω and a remarkably high conductivity of 2×10^4 S cm^{-1}. This work is the basis of a publication in *Chem. Commun.*[8]

Chapter 8 and 9 report novel pathways for fabricating carbon-based composite materials using the VFD with the materials showing promise as active electrodes in supercapacitors, with the results featuring in two publications, one in *ACS Omega*, the other in *Nanoscale Adv*ances.[9, 10] A remarkable fining is the ability to form spheres of few layered graphene directly from graphite, shrouding self-assembled fullerene C_{60}. They are formed in high yield and under scalable continuous flow conditions, as detailed in chapter 8. This material is formed in a one-step process, where a colloidal suspension of graphite in DMF is mixed with an o-xylene solution of C_{60} at room temperature in a VFD, in the absence of surfactants and other auxiliary substances. The diameters of the composite spheres are controllable, in the range from 1.5 to 3.5 μm, and the findings represent a significant advance in fabricating all carbon composite material. The C_{60}@graphene spheres can be incorporated into an electrode with high cycle stability, high areal capacitance of 103.4 mF cm^{-2}, while maintaining capacitance to 24.7 F g^{-1} and 86.4 mF cm^{-2} (83.5%) at a high scan rate of 100 mV s^{-1}. This work is the basis of a publication in *ACS Omega.*[9]

Chapter 9 reports on a novel three in one VFD mediated process for fabricating a composite comprised of superparamagnetic magnetite (Fe_3O_4) nanoparticles shrouding MWCNTs, Fe_3O_4@MWCNT. The processing using DMF as the solvent incorporates slicing of the MWCNTs while generating the magnetite nanoparticles *in situ*, which spontaneously decorate the MWCNTs. The Fe_3O_4 nanoparticles are generated by laser ablation of pure iron metal at 1064 nm using a pulsed laser, over the dynamic thin film in the microfluidic platform. The magnetic MWCNTs were used as an active electrode for supercapacitor, establishing high gravimetric and areal capacitances of 834 F g^{-1} and 1317.7 mF cm^{-2} at a scan rate of 10 mV s^{-1}, respectively, which are higher values than those reported using similar materials. This work is the basis of a publication in *Nanoscale Advances*.[10]

10.2. Future directions

10.2.1. Slicing CNTs without the need for NIR laser irradiation

One of the major challenges for harnessing the full potential of carbon nanotubes (CNTs) is controlling their length. As prepared CNTs are long, up to mm in length, and are tangling, both of which need to be overcome for many applications requiring specific lengths, for example, in medicine and electronics. Intensified research efforts have been conducted for slicing and shortening CNTs. Controlled slicing/shortening of SWCNTs and MWCNTs occurs in the VFD while NIR irradiated by a pulsed laser, under continuous flow conditions, with the results featured in Chapters 2 and 3 respectively.

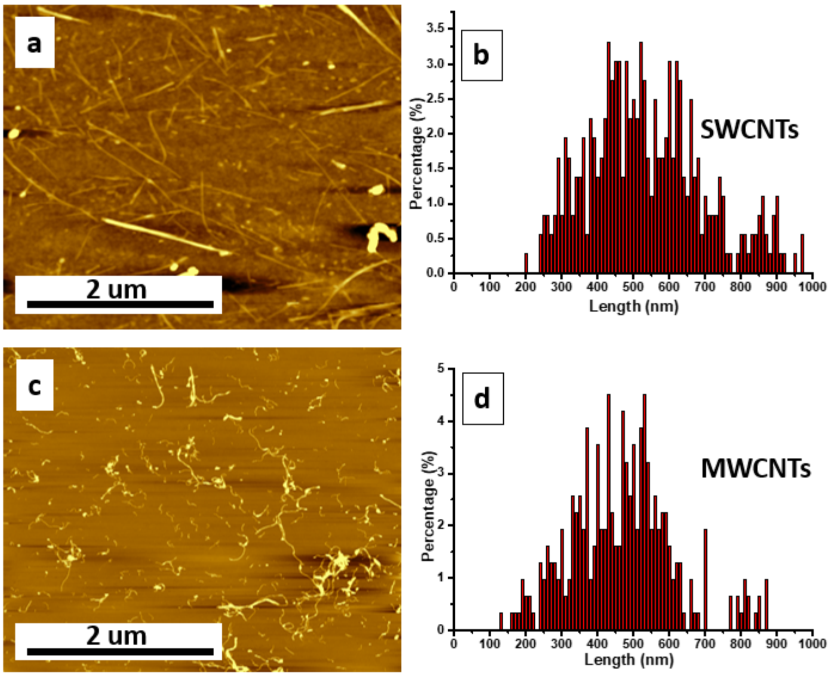

Figure 10. 1 VFD mediated slicing of SWCNTs and MWCNTs using a 1:1 mixture of o-xylene and water, under continuous flow (rotational speed 7500 rpm, concentration 0.16 mg. mL^{-1}, flow rate 0.45 m. min^{-1}, and θ= 45°). (a) AFM image of sliced SWCNTs with the derived length distribution in (b), and (c) AFM image of sliced MWCNTs with the derived length distribution in (d).

Shear stress in the dynamic thin film is important for the above slicing, primarily in that it bends the SWCNTs and MWCNTs. But is the shear stress alone able to slice CNTs. If so, this would dispense with the need for irradiation from a pulsed laser, and thus would reduce the cost of the slicing process, as well is improving the green chemistry metrics. To this end, feasibility studies have been undertaken to develop such a process, as summarised in Figure 10. 1 A number of different solvents and solvents mixtures were explored, with a mixture of water and *o*-xylene being the most effective, using a 20 mm OD (17.5 mm ID, and 20 cm long) tube, inclined at 45° relative to the horizontal position, 7500 rpm rotational speed, and flow rate 0.45 mL.min^{-1}. This was effective for slicing both SWCNTs and MWCNTs, as established using AFM, Figure 10. 1a and c. Length distributions for both SWCNTs and MWCNTs are shown in Figure 10. 1b and d, from counting 300 individual tubes, which are at 490 nm and 500 nm respectively. Clearly more research is required to be able to vary the length, which may be possible by changing the diameter of the tube, as predicted now that the full fluid dynamics on the VFD is understood (Chapter 6). In addition, the integrity of the chirality of the SWCNTs post-VFD processing, conducting versus semiconducting, needs to be investigated. The use of a pulsed laser to facilitate slicing of SWCNTs is likely to alter their chirality, which is an area that need to be explored systematically, which realistically is a major research project in its own right.

10.2.2. Fabricating toroidal SWCNTs

Carbon nanorings are a unique member of carbon nanomaterials family. They have attracted a great deal of interest as they are predicted to have extraordinary electronic and magnetic properties.[11, 12] The same also applies to composites containing carbon nanorings, especially with polymers. Carbon nanorings were first synthesized by Liu et al,[13] in 1997 using the laser growth method. When the rings have a number of coils of SWCNTs, they are usually named as "dounts" or bundles of SWCNTs. There are a number of methods for fabricating such structure, including using ultrasonication,[14] organic reactions,[15] chemical vapor deposition (CVD),[16] and VFD processing. [6, 17] Feasibility studies have been undertaken on preparing single coiled SWCNT where the ends of the tube are fused, as a continuous toroidal SWCNT. This involved slicing SWCNTs to around 700 nm in length using the VFD,[1] then treating them dispersed in a mixture of toluene and water (ratio 1:1) to shear stress in VFD, while being irradiated with a pulsed laser at low energy, 100 mJ, much lower than for slicing,[1] Figure 10.2. The rings are symmetrical and are 1 SWCNT thick, and ca 120 nm in diameter, Figure 10. 2 a-d. Interestingly, this is the diameter that has been predicted to have special ring current effect but their synthesis until now has remained ellusive.[18, 19] But much needs to be done, in fully characterising this new form of molecular carbon, which has no terminal/dangling bonds. This includes SEM, TEM and HRTEM, Raman spectroscopy, photoluminescence, and ring current and magnetic interactions using CFM and MFM respectively.

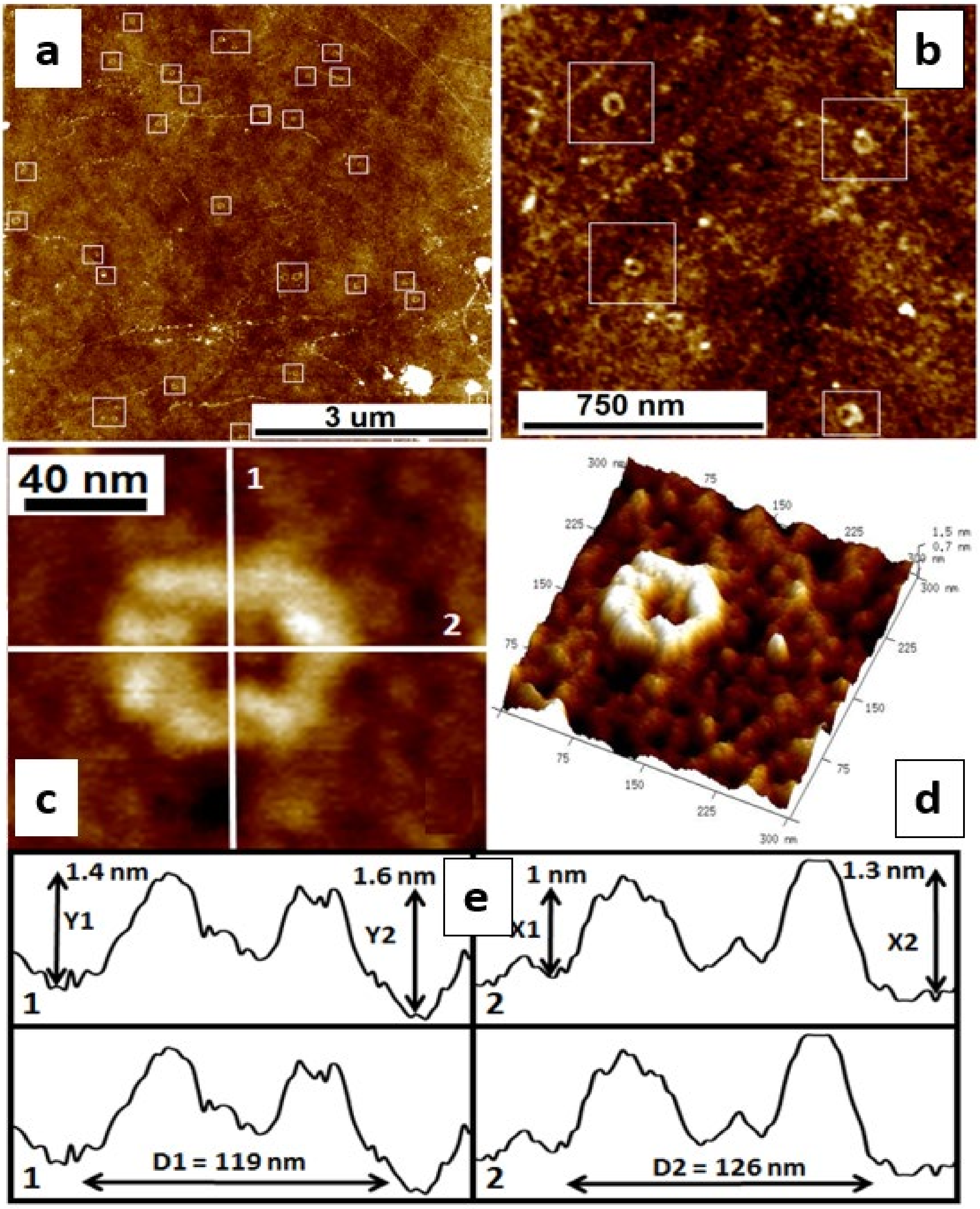

Figure 10. 2 Fused "single" SWCNTs toroidal rings generated in a VFD, using a 1:1 mixture of toluene and water while irradiated by a 1064 nm pulsed laser operating at 100 mJ, under confined mode of operation of the device (rotational speed 7500 rpm, CNTs concentration 0.16 mg. mL^{-1} and θ = 45˚) and (a-b) AFM images of fused toroidal rings of SWCNT, highlighted by while boxes. (c) AFM image for SWCNT rings - zoomed and 3D plot of this ring is shown in (d) and (e) height profile of SWCNT ring, showing heights ca 1.3 nm, and diameter ca 120 nm.

10.2.3. Graphene Oxide Polymer Composites

Graphene composites have become a hot research area, incorporating the extraordinary physical and chemical properties of the nanomaterial with the properties of polymers. This applies also to graphene oxide (GO), with the composite materials having applications in thermal resistance, lower coefficients of thermal expansion, and improved mechanical properties. [20-23] Indeed, there are a number of reports on preparing composites of GO and polymers, including polyacrylate ester, epoxy resin, polycarbonate, high-impact polystyrene, with the later having enhance flame resistant and higher thermal stability compared to the polymers itself.[24-27] A feasibility study was undertaken on using the VFD under continuous flow conditions to prepare GO polymer composites. This was motivated by the intense micromixing in the device, and the results establish that nanoparticles of polystyrene can be decorated on the surface of GO, Figure 10.3 a-b. Changing the polymer to polyurethanes, results in a change in structure and morphology of the composite material, now forming scrolls, Figure 10.3 c-d. Full characterisation of these materials is required, as well as optimising the processing in targeting the different morphologies, then appraisal in applications, including in pollutant separation, energy storage and flame retardants.[28-32]

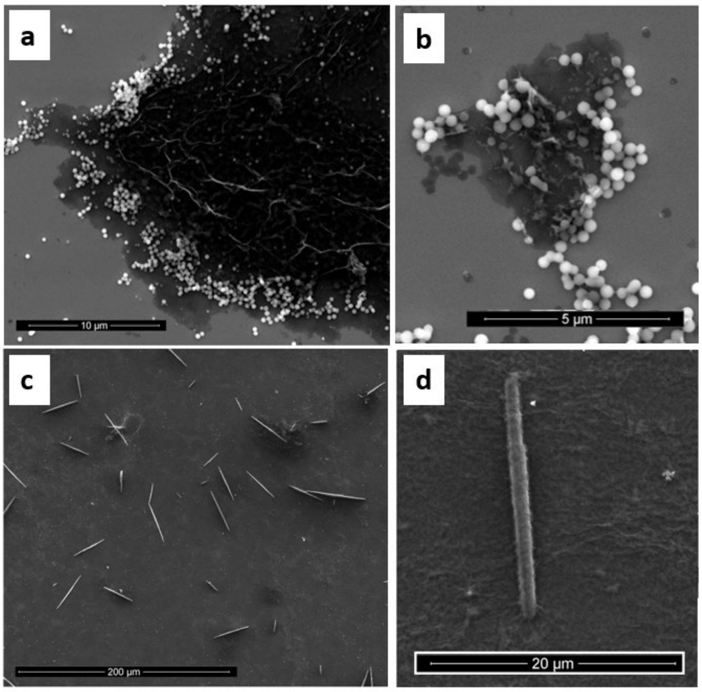

Figure 10. 3 SEM images of (a-b) polystyrene decorated on the surface of GO. (c-d) Scroll structures of polyurethanes fabricated in a VFD operating under continuous flow conditions (rotational speed 8000 rpm, flow rate 0.45 mL.min-1, and $\theta = 45^\circ$). The concentration of the polymer in DMF was 20 mg. mL^{-1}, which was delivered in one jet feed to the VFD tube, with another jet feed delivering a colloidal suspension of GO at 0.2 mg. mL^{-1}.

10.2.4. Scrolling and exfoliating of molybdenum disulfide (MoS_2) and other 2D nanomaterials

2D Transition metal chalcogenides have attracted considerable research interest in recent years because of their unique properties,[33-37] with molybdenum disulfide (MoS_2) the most investigated member of the family. Different approaches have been reported for scrolling and exfoliating MoS_2, including liquid phase exfoliation, [38, 39] mechanical exfoliation,[40] direct chemical vapour deposition (CVD), [41, 42] and chemical routes.[43] Of these, liquid exfoliation involving sonication,[19,23] is the most common. As to scroll formation of the 2D material, this features the use of sonication, evaporation, induced by metal nanoparticles and CVD.[44-46] Developing a scalable process for exfoliating and scrolling MoS_2 is a challenge, especially while incorporating green chemistry metrics, and given the utility of the VFD in exfoliating other 2D material, feasibility studies were undertaken in using the VFD to generate nanomaterials of the 2D material, at room temperature, under continuous flow conditions, as summarized in Figure 10.4c-d. The findings are the start of the journey in developing a versatile method for preparing 2D-sheets and scrolls of MoS_2, and much needs to be dome on optimising the conditions, and fully characterising the materials. This is part of a more challenging project, in developing a universal method of exfoliating and scrolling 2D materials in the VFD.

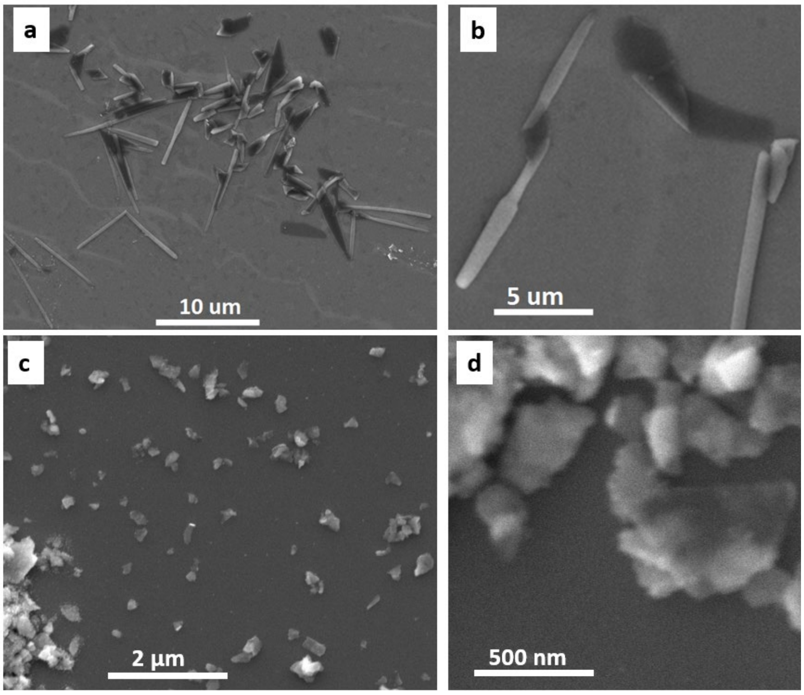

Figure 10. 4 SEM images of MoS2 scrolls (a-b) formed in the VFD at 4000 rpm, under continuous flow (concentration 0.2 mg. mL^{-1} in a 1: 1 mixture of ethanol and water, flow rate 0.45 $mL.min^{-1}$, and $\theta = 45^{\circ}$. (c-d) Exfoliated MoS2 a few layers thick, formed at 8000 rpm, with all the other conditions unchanged.

10.3. References

1. Alharbi, T. M.; Vimalanathan, K.; Lawrance, W. D.; Raston, C. L., Controlled slicing of single walled carbon nanotubes under continuous flow. *Carbon,* **2018**, 140, 428-432.
2. Alharbi, T.; Vimalanathan, K.; Alsulami, I.; Raston, C. L. J. N., Vertically Aligned Laser Sliced MWCNTs. *Nanoscale*, **2019**, 11, 21394-21403.
3. In, J. B.; Grigoropoulos, C. P.; Chernov, A. A.; Noy, A., Growth kinetics of vertically aligned carbon nanotube arrays in clean oxygen-free conditions. *ACS Nano,* **2011,** *5*, 9602-9610.
4. Yu, J.; Shapter, J. G.; Quinton, J. S.; Johnston, M. R.; Beattie, D. A., Direct attachment of well-aligned single-walled carbon nanotube architectures to silicon (100) surfaces: a simple approach for device assembly. *Phys. Chem. Chem. Phys.,* **2007,** *9*, 510-520.
5. Macdonald, T.; Gibson, C. T.; Constantopoulos, K.; Shapter, J. G.; Ellis, A. V., Functionalization of vertically aligned carbon nanotubes with polystyrene via surface initiated reversible addition fragmentation chain transfer polymerization. *Appl. Surf. Sci.,* **2012,** *258*, 2836-2843.
6. Alharbi, T. M.; Shingaya, Y.; Vimalanathan, K.; Nakayama, T.; Raston, C. L., High Yielding Fabrication of Magnetically Responsive Coiled Single Walled Carbon Nanotube Under Flow. *ACS Appl. Nano Mater.,* **2019**, 2 , 5282-5289
7. Alharbi, T. M.; Harvey, D.; Alsulami, I. K.; Dehbari, N.; Duan, X.; Lamb, R. N.; Lawrance, W. D.; Raston, C. L., Shear stress mediated scrolling of graphene oxide. *Carbon,* **2018**, 137, 419-424.
8. Alharbi, T.; Alghamdi, A. R.; Vimalanathan, K.; Raston, C. L., Continuous flow photolytic reduction of graphene oxide. *Chem. Commun.,* **2019**, 55, 11438-11441.
9. Alsulam, I. K.; Alharbi, T. M.; Moussa, M.; Raston, C. L., High-Yield Continuous-Flow Synthesis of Spheroidal C60@ Graphene Composites as Supercapacitors. *ACS Omega,* **2019**, 4, 19279-19286.
10. Alharbi, T.; Al-Antaki, A. H. M.; Moussa, M.; Hutchison, W.; Raston, C. L., Three-step-in-one synthesis of supercapacitor MWCNT superparamagnetic magnetite composite material under flow. *Nanoscale Adv.,* **2019**, 1 , 3761-3770.
11. Liu, L.; Zhang, L.; Gao, H.; Zhao, J., Structure, energetics, and heteroatom doping of armchair carbon nanotori. *Carbon,* **2011,** *49*, 4518-4523.
12. Sun, J.; Liu, H.; Chen, X.; Evans, D. G.; Yang, W.; Duan, X., Carbon nanorings and their enhanced lithium storage properties. *Adv. Mater.,* **2013,** *25*, 1125-1130.
13. Liu, J.; Dai, H.; Hafner, J.; Colbert, D.; Smalley, R., Fullerene 'Crop Circles'. *Nature,* **1997,** *385*, 780-781.
14. Komatsu, N., Ultrasonic isolation of toroidal aggregates of single-walled carbon nano tubes. *Carbon* **2006,** *44*, 2091-2093.
15. Geng, J.; Ko, Y. K.; Youn, S. C.; Kim, Y.-H.; Kim, S. A.; Jung, D.-H.; Jung, H.-T., Synthesis of SWNT rings by noncovalent hybridization of porphyrins and single-walled carbon nanotubes. *J. Phys.Chem. C* **2008,** *112*, 12264-12271.
16. Song, L.; Ci, L.; Sun, L.; Jin, C.; Liu, L.; Ma, W.; Liu, D.; Zhao, X.; Luo, S.; Zhang, Z., Large-Scale Synthesis of Rings of Bundled Single-Walled Carbon Nanotubes by Floating Chemical Vapor Deposition. *Adv. Mater.,* **2006,** *18*, 1817-1821.
17. Vimalanathan, K.; Chen, X.; Raston, C. L., Shear induced fabrication of intertwined single walled carbon nanotube rings. *Chem. Commun.,* **2014,** *50*, 11295-11298.
18. Garapati, K. V.; Salhi, M.; Kouchekian, S.; Siopsis, G.; Passian, A., Poloidal and toroidal plasmons and fields of multilayer nanorings. *Phys. Rev. B,* **2017,** *95*, 165422.
19. Garapati, K. V.; Bagherian, M.; Passian, A.; Kouchekian, S., Plasmon dispersion in a multilayer solid torus in terms of three-term vector recurrence relations and matrix continued fractions. *J. Phys. Commun*., **2018,** *2*, 015031.
20. Kim, H.; Abdala, A. A.; Macosko, C. W., Graphene/polymer nanocomposites. *Macromolecules,* **2010,** *43*, 6515-6530.

21. Zhu, X.; Zhou, Y.; Hao, J.; Bao, B.; Bian, X.; Jiang, X.; Pang, J.; Zhang, H.; Jiang, Z.; Jiang, L., A charge-density-tunable three/two-dimensional polymer/graphene oxide heterogeneous nanoporous membrane for ion transport. *ACS Nano,* **2017,** *11*, 10816-10824.
22. Wu, N.; She, X.; Yang, D.; Wu, X.; Su, F.; Chen, Y., Synthesis of network reduced graphene oxide in polystyrene matrix by a two-step reduction method for superior conductivity of the composite. *J. Mater. Chem.,* **2012,** *22*, 17254-17261.
23. Weir, M. P.; Johnson, D. W.; Boothroyd, S. C.; Savage, R. C.; Thompson, R. L.; Parnell, S. R.; Parnell, A. J.; King, S. M.; Rogers, S. E.; Coleman, K. S.; Clarke, N., Extrinsic wrinkling and single exfoliated sheets of graphene oxide in polymer composites. *Chem. Mater.,* **2016,** *28*, 1698-1704.
24. Chen, X.; Yi, Z.; Lei, J.; Yi, H.; Yao, W.; Zhu, W.; Duan, T., Preparation and Perfomance of an Aging-Resistant Nanocomposite Film of Binary Natural Polymer–Graphene Oxide. *ACS Omega,* **2016,** *1*, 1173-1181.
25. Yu, L.; Yu, H., Light-powered tumbler movement of graphene oxide/polymer nanocomposites. *ACS Appl. Mater. Interfaces,* **2015,** *7*, 3834-3839.
26. Cui, Y.; Kundalwal, S.; Kumar, S., Gas barrier performance of graphene/polymer nanocomposites. *Carbon,* **2016,** *98*, 313-333.
27. Cai, D.; Song, M., Recent advance in functionalized graphene/polymer nanocomposites. *J. Mater. Chem.,* **2010,** *20*, 7906-7915.
28. Han, Y.; Wu, Y.; Shen, M.; Huang, X.; Zhu, J.; Zhang, X., Preparation and properties of polystyrene nanocomposites with graphite oxide and graphene as flame retardants. *J. Mater. Sci.* **2013,** *48*, 4214-4222.
29. Zheng, Z.; Zheng, X.; Wang, H.; Du, Q., Macroporous graphene oxide–polymer composite prepared through Pickering high internal phase emulsions. *ACS Appl. Mater. Interfaces,* **2013,** *5*, 7974-7982.
30. Li, D.; Gao, D.; Qi, J.; Chai, R.; Zhan, Y.; Xing, C., Conjugated Polymer/Graphene Oxide Complexes for Photothermal Activation of DNA Unzipping and Binding to Protein. *ACS Appl. Bio Mater.,* **2018,** *1*, 146-152.
31. Jin, L.; Wu, D.; Kuddannaya, S.; Zhang, Y.; Wang, Z., Fabrication, characterization, and biocompatibility of polymer cored reduced graphene oxide nanofibers. *ACS Appl. Mater. Interfaces,* **2016,** *8*, 5170-5177.
32. Liu, Y.; Ma, J.; Wu, T.; Wang, X.; Huang, G.; Liu, Y.; Qiu, H.; Li, Y.; Wang, W.; Gao, J., Cost-effective reduced graphene oxide-coated polyurethane sponge as a highly efficient and reusable oil-absorbent. *ACS Appl. Mater. Interfaces,* **2013,** *5*, 10018-10026.
33. Tan, C.; Cao, X.; Wu, X.-J.; He, Q.; Yang, J.; Zhang, X.; Chen, J.; Zhao, W.; Han, S.; Nam, G.-H.; Sindoro, N., Recent advances in ultrathin two-dimensional nanomaterials. *Chem. Rev.* **2017,** *117*, 6225-6331.
34. Zhang, H., Ultrathin two-dimensional nanomaterials. *ACS Nano,* **2015,** *9*, 9451-9469.
35. He, R.; Hua, J.; Zhang, A.; Wang, C.; Peng, J.; Chen, W.; Zeng, J., Molybdenum disulfide–black phosphorus hybrid nanosheets as a superior catalyst for electrochemical hydrogen evolution. *Nano Lett.,* **2017,** *17*, 4311-4316.
36. Dai, C.; Zhou, Z.; Tian, C.; Li, Y.; Yang, C.; Gao, X.; Tian, X., Large-scale synthesis of graphene-like MoSe2 nanosheets for efficient hydrogen evolution reaction. *J. Phys. Chem. C,* **2017,** *121*, 1974-1981.
37. Sheng, Y.; Chen, T.; Lu, Y.; Chang, R.-J.; Sinha, S.; Warner, J. H., High-Performance WS2 Monolayer Light-Emitting Tunneling Devices Using 2D Materials Grown by Chemical Vapor Deposition. *ACS Nano,* **2019,** *13*, 4530-4537.
38. Cunningham, G.; Lotya, M.; Cucinotta, C. S.; Sanvito, S.; Bergin, S. D.; Menzel, R.; Shaffer, M. S.; Coleman, J. N., Solvent exfoliation of transition metal dichalcogenides: dispersibility of exfoliated nanosheets varies only weakly between compounds. *ACS Nano,* **2012,** *6*, 3468-3480.

39. Coleman, J. N.; Lotya, M.; O'Neill, A.; Bergin, S. D.; King, P. J.; Khan, U.; Young, K.; Gaucher, A.; De, S.; Smith, R. J. *et al.,* et al. Two-dimensional nanosheets produced by liquid exfoliation of layered materials. *Science,* **2011,** *331*, 568-571.
40. Yin, Z.; Li, H.; Li, H.; Jiang, L.; Shi, Y.; Sun, Y.; Lu, G.; Zhang, Q.; Chen, X.; Zhang, H., Single-layer MoS2 phototransistors. *ACS Nano,* **2011,** *6*, 74-80.
41. Lee, Y. -H.; Zhang, X. -Q.; Zhang, W.; Chang, M. -T.; Lin, C. -T.; Chang, K. -D.; Yu, Y. -C.; Wang, J. T. -W.; Chang, C. -S.; Li, L.-J; Lin, T.-W, Synthesis of large-area MoS2 atomic layers with chemical vapor deposition. *Adv. Mater.,* **2012,** *24*, 2320-2325.
42. Najmaei, S.; Liu, Z.; Zhou, W.; Zou, X.; Shi, G.; Lei, S.; Yakobson, B. I.; Idrobo, J.-C.; Ajayan, P. M.; Lou, J., Vapour phase growth and grain boundary structure of molybdenum disulphide atomic layers. *Nat. Mater.,* **2013,** *12*, 754-759.
43. Zeng, Z.; Sun, T.; Zhu, J.; Huang, X.; Yin, Z.; Lu, G.; Fan, Z.; Yan, Q.; Hng, H. H.; Zhang, H., An effective method for the fabrication of few-layer-thick inorganic nanosheets. *Chem., Int. Ed.,* **2012,** *51*, 9052-9056.
44. Hao, S.; Yang, B.; Gao, Y. J., Fracture-induced nanoscrolls from CVD-grown monolayer molybdenum disulfide. *Phys. Status Solidi RRL,* **2016,** *10*, 549-553.
45. Choi, K. H.; Park, J. E.; Suh, D. H., Highly efficient hydrogen evolution reaction by strain and phase engineering in composites of Pt and MoS 2 nano-scrolls. *Phys. Chem. Chem. Phys.,* **2017,** *19*, 18356-18365.
46. Fang, X.; Wei, P.; Wang, L.; Wang, X.; Chen, B.; He, Q.; Yue, Q.; Zhang, J.; Zhao, W.; Wang, J.; Lu, G.; Zhang, H.; Huang, W.; Huang, X.; Li, H., Transforming Monolayer Transition-Metal Dichalcogenide Nanosheets into One-Dimensional Nanoscrolls with High Photosensitivity. *ACS Appl. Mater. Interfaces, 2***018,** *10*, 13011-13018.

Appendices

SUPPLEMENTARY INFORMATION FOR

Sub-micron moulding angled vortex fluid flow

1. General materials and methods

All chemicals were used as received unless otherwise stated. High molecular weight polymer beads of polysulfone (PSF) was purchased from Sigma Aldrich. Dichloromethane (DCM) (99.8%), Toluene (99.5%) and Hexane fraction were purchased from Chem-Supply. Bovine serum albumin (BSA), ethanol, PBS and glutaraldehyde were obtained from Sigma-Aldrich as analytical grades. PBS was prepared at 10 mM of pH 7.4 at room temperature using MilliQ water. Zinc acetate dihydrate ($Zn(OAc)_2 \cdot 2H_2O$), terephthalic acid (H_2BDC), dimethylformamide (DMF) and trimethylamine (TEA) were obtained from Sigma-Aldrich as analytical grades. All materials were used without further purification.

Graphene oxide materials, fullerenes materials, macroporous BSA microspheres and MOFs were characterized by scanning electron microscopy (SEM) performed using a FEI Quanta 450, atomic force microscopy using the Nanoscope 8.10 in tapping mode, High Resolution Field Emission SEM, with a voltage of 5 kV and working distance of 10 mm, and transmission electron microscopy and high-resolution transmission electron microscopy (TEM and HRTEM), and X-ray diffraction data were recorded using a Bruker D8 ADVANCE ECO system (Co- Kα, λ=1.7889 Å). Samples for TEM were prepared by drop-casting the material onto standard carbon coated copper grids prior to characterization. TEM, HR-TEM and selected area electron diffraction (SAED) were taken on a JEM- 2100F (200 kV) equipped with an EDS module. Real-time SANS experiments were done at the Australian Nuclear Science and Technology Organisation (ANSTO), using the Quokka instrument.

2. Temperature change in the VFD for different solvents at different rotational speeds (ω) and inclination angle (θ)

A FTIR camera was used to record temperature variation of different liquids at rotational speeds between 2k to 9k rpm for the confined mode of operation of the VFD, and 3k to 9k rpm for mimicking the continuous flow mode of operation at an inclination angle θ = 45°. The settings of the FTIR camera included emissivity 0.95, object distance 30.48 cm, relative humidity 50%, and the use of the rainbow colour pallet. All experiments were conducted in triplicate using the same quartz tube for consistency of measurements within a temperature-controlled environment (average temperature 19 °C). There were two modes of operation of the VFD: Confined mode where 1 mL of liquid (unless otherwise stated) was added to the rapidly rotating tube or mimicking continuous flow where the rotational speed corresponds to a thin film of liquid extending to the lip at the top of the tube.

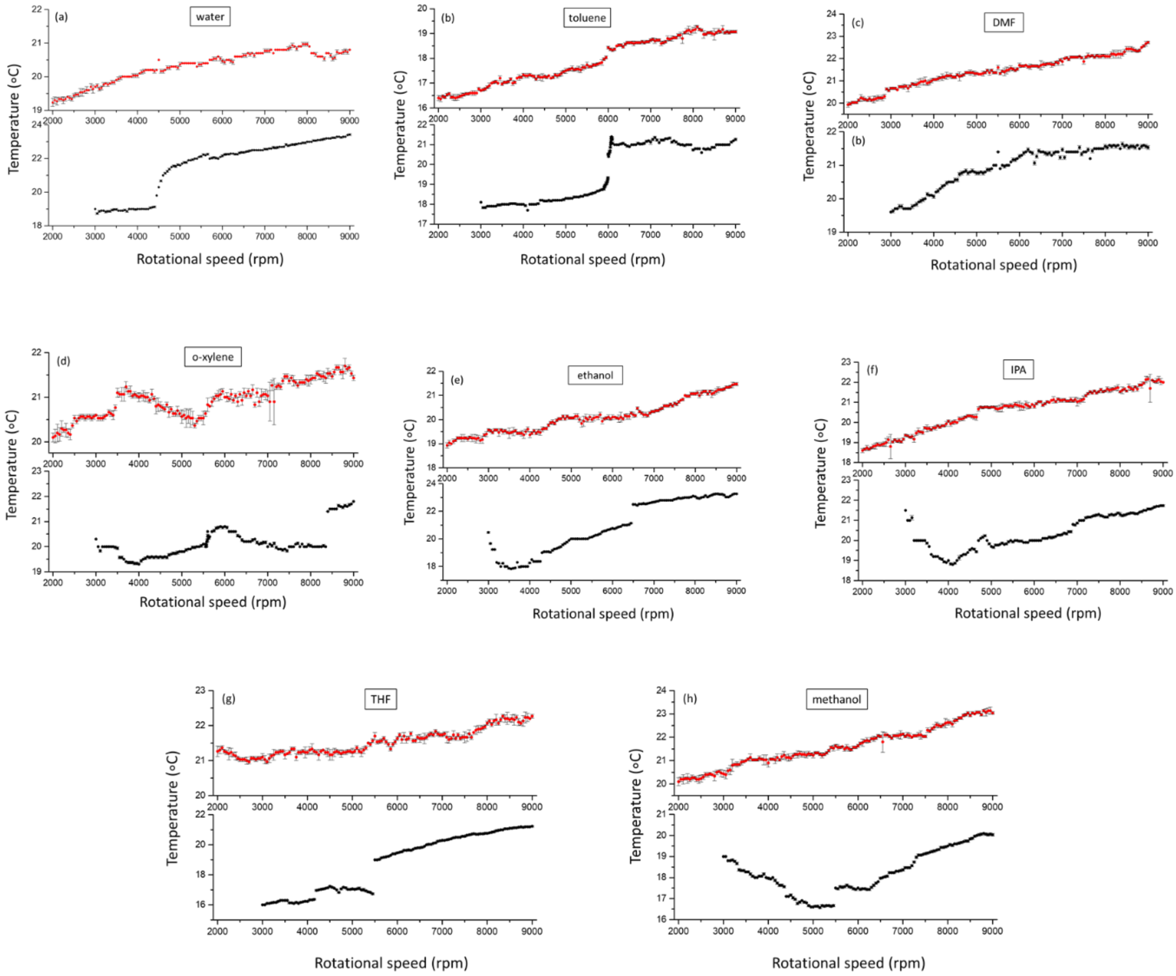

Figure S2a: Temperature change of solvents as a function of rotations speed at θ = 45°, ω = 2k to 9k rpm for the confined mode (1mL of liquid (—)) and ω = 3k to 9k rpm for mimicking continuous flow (thin film extended to the lip of the tube, (—)), noting that for the latter, for ω < 3k rpm the vortex does not extend and expose the bottom of the tube (20 mm OD, 17.5 mm ID).

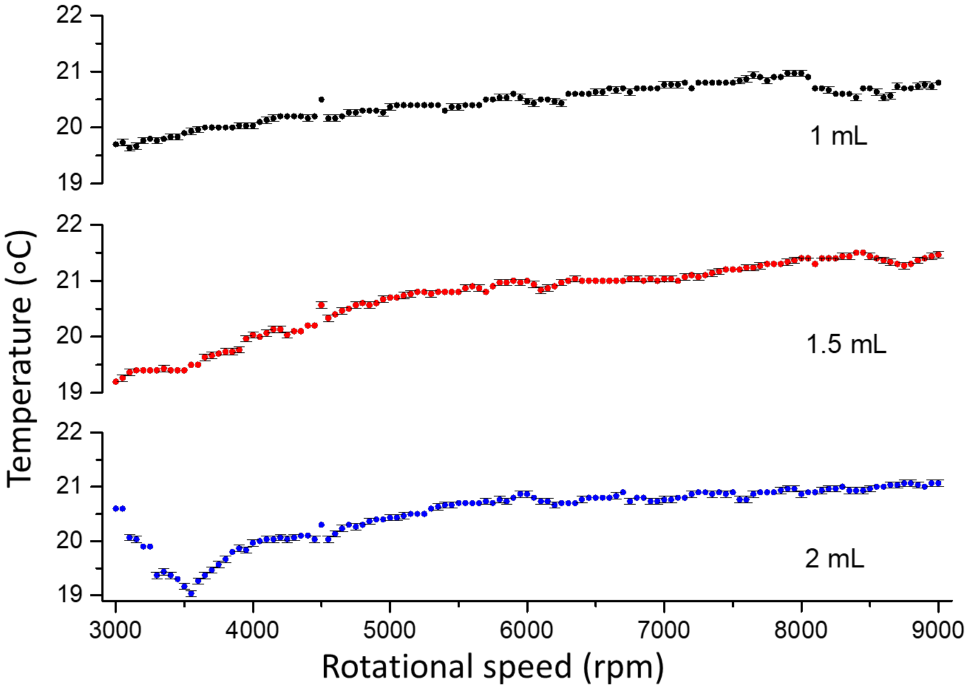

Figure S2b: Temperature change as a function of volume of water in a 20 mm OD (17.5 mm ID) rotating tube for the confined mode of operation in the VFD, with $\theta = 45^o$.

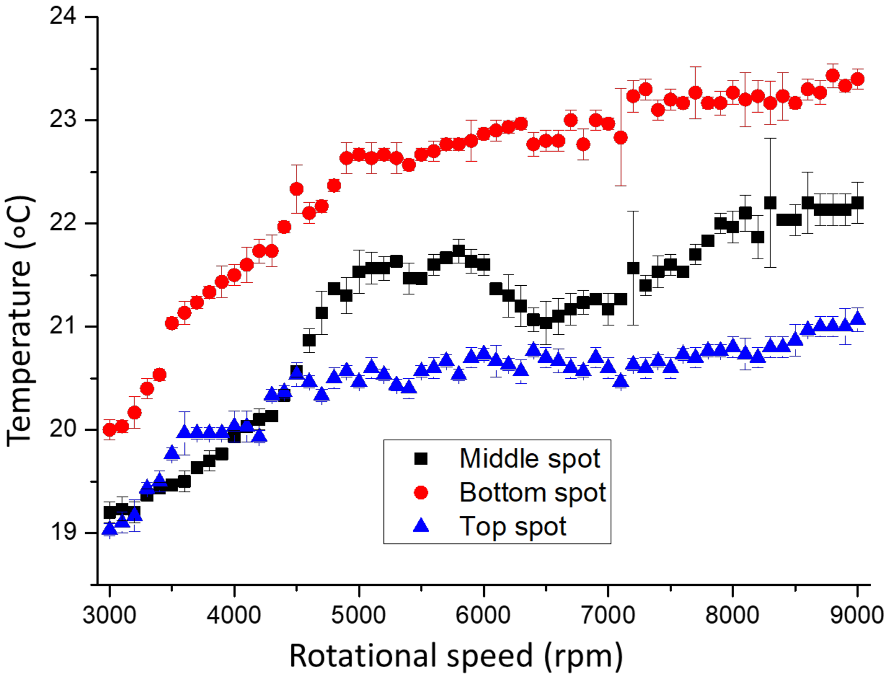

Figure S2c: Temperature change measurements for water in a 20 mm OD (17.5 mm ID) tube, θ = 45°, at 3 different spots on the rotating tube; mid-way along the tube, and 2 cm away from the upper and lower bearings (top and bottom).

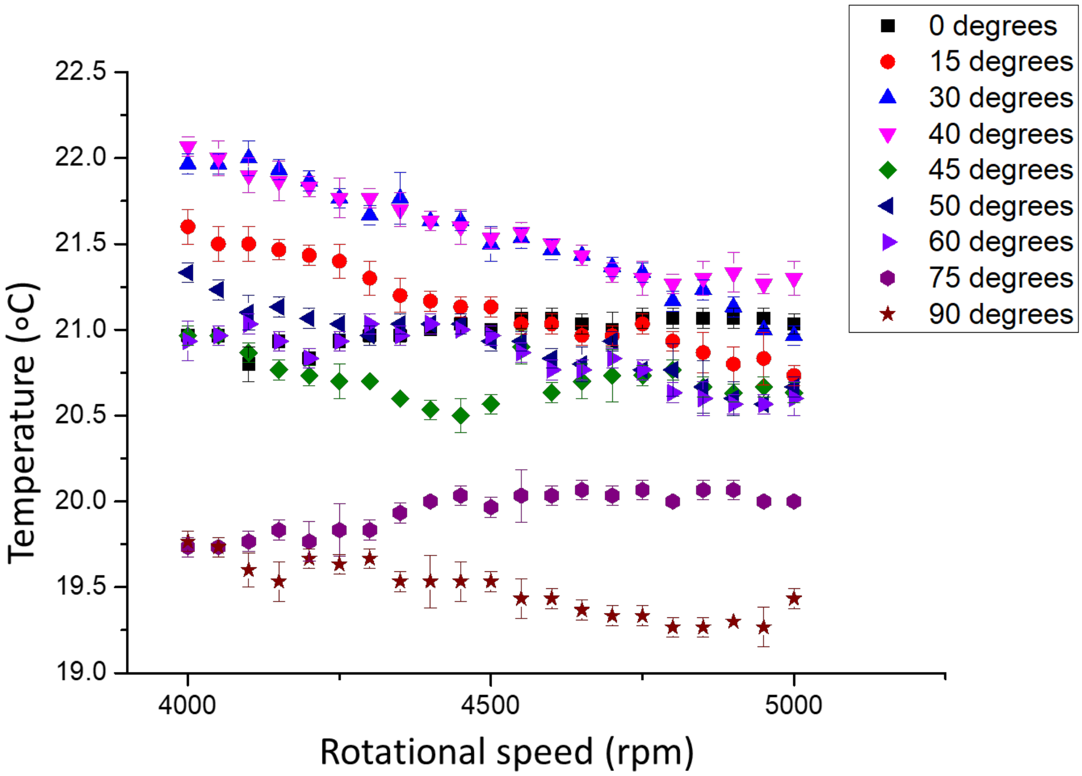

Figure S2d: Temperature change measurements for water (mimicking continuous flow) in a 10 mm OD (8.5 mm ID) tube, as a function of change in inclination angle for rotational speeds between 4k and 5k rpm.

3. Mixing times of water at different rotational speeds and inclination angle in a 10 mm OD tube.

Mixing time corresponds to the time taken for a drop of water containing a small amount of dye added at the bottom of the tube rotating at a specific speed to uniformly mix in half way up the preformed film generated from 1 mL of water (measured in triplicates).

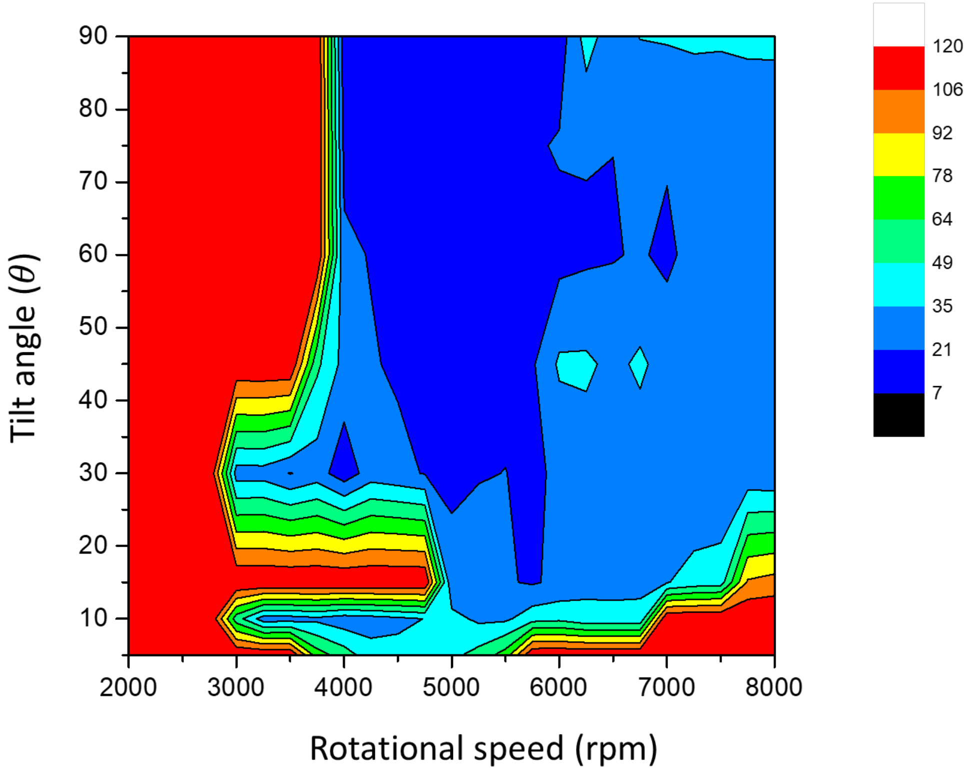

Figure S3: Mixing times (colour pallet in seconds) as a function of ω and θ in a 10 mm OD (8.5 mm ID) tube.

4. Captured images from high speed photography of a thin film in a 10 mm OD VFD glass tube, θ = 45º.

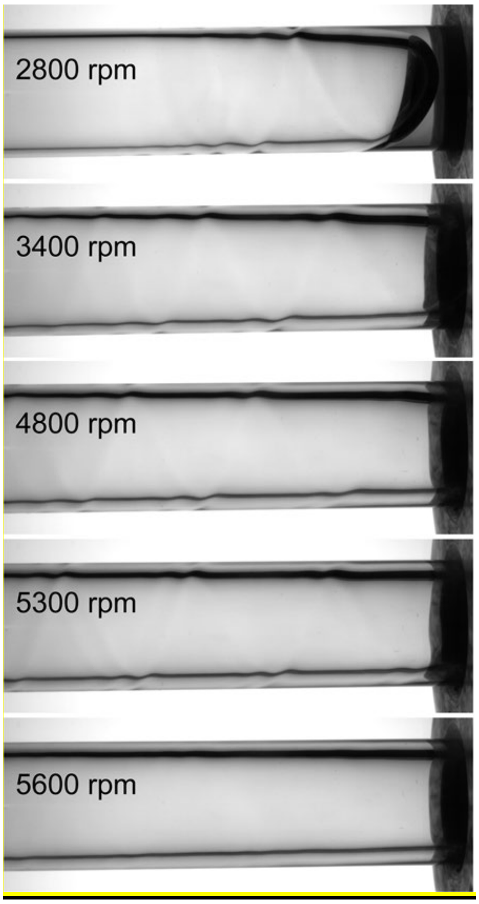

Figure S4: Snapshots were adapted from Video S1 attached. They illustrate the statuses of the liquid (dye water) spun in a 10 mm OD tube (8.5 mm ID) at θ = 45°. The high-speed camera (FASTCAM SA1.1 model 675K-M1) was also positioned at θ = 45°, with a record rate (fps) of 1000. The spinning rates were calculated by studying the motion of the tube in each frame with the fps of the video. We noted that circular flow was generated as the tube rotated. The average liquid film thickness decreases with the increase of the spinning rate. There was a sudden transition of the flow (the disappearance of the "wavy" flow) at a rotational rate of ~5.6k rpm, which is close to the value (~6k rpm) recorded in the sudden change in average thickness for a 10 mm tube at θ = 45°, which correspond closely to transitioning from spicule flow to double helical flow.

5. Average film thickness as a function of ω, at θ = 45°.

Excess liquid was added to a weighed quart tube (20 mm OD, 17.5 mm ID) and spun at 3k for 1 minute, such that excess liquid was ejected at the top of the tube. After 1 minute the tube was weighed to determine the volume of liquid left post VFD processing. Experiments were repeated for increasing rotational speeds from 3k to 9k rpm at 250 rpm increments, and were all done in triplicates. Water, toluene, DMF, *o*-xylene, DMF/*o*-xylene (1:1 volume ratio) were studied in this way. In addition, water was similarly studied in a 10 mm OD glass tube (8. 5 mm ID). The average film thickness for each liquid was determined according to:

$$d = r - \sqrt{r^2 - \left(\frac{V}{\pi h}\right)}$$

Where *d* = film thickness (cm) *r* = radius of tube (cm), *V* = volume of liquid (mL), and *h* = height of tube, 18.5 cm.

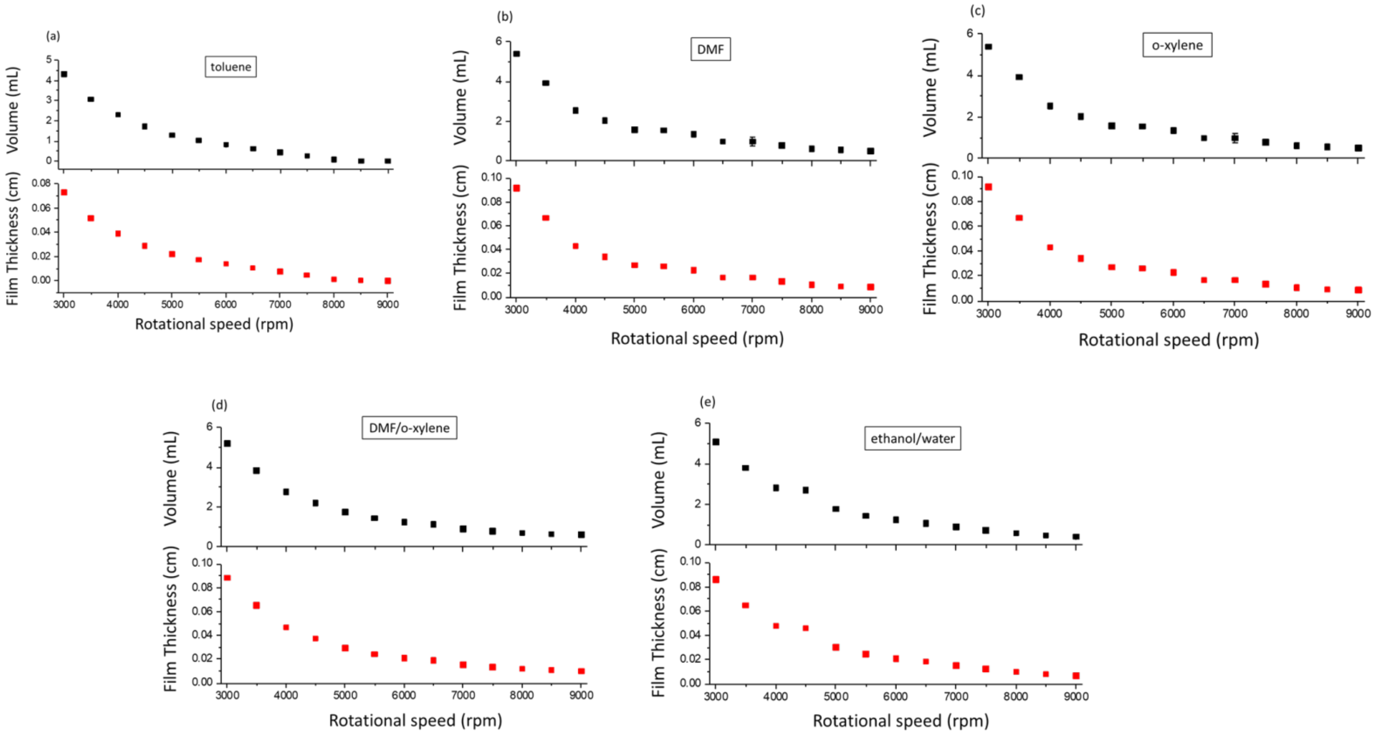

Figure S5a: Average film thickness and volume of liquid left in a quartz tube (20 mm OD, 17.5 mm ID) as a function of ω at θ = 45°, for (a) toluene, (b) DMF, (c) *o*-xylene, (d) DMF/*o*-xylene (1:1 volume ratio) and (e) ethanol/water (1:1 volume ratio).

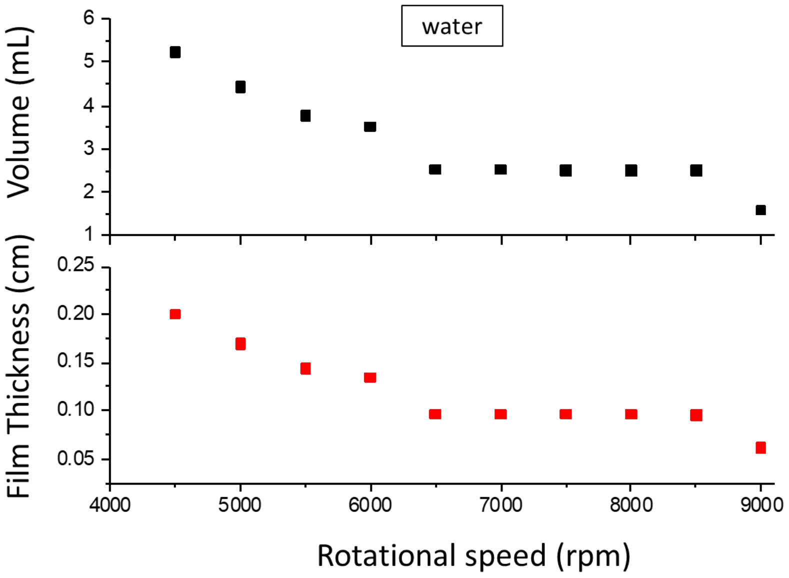

Figure S5b: Average film thickness and volume of water left in a quartz tube (10 mm OD, 8.5 mm ID) as a function of ω at θ = 45°.

6. Manipulating graphene oxide in DMF in the VFD

Outcome of processing of graphene oxide at specific rotational speeds in the VFD, at θ = 45°.

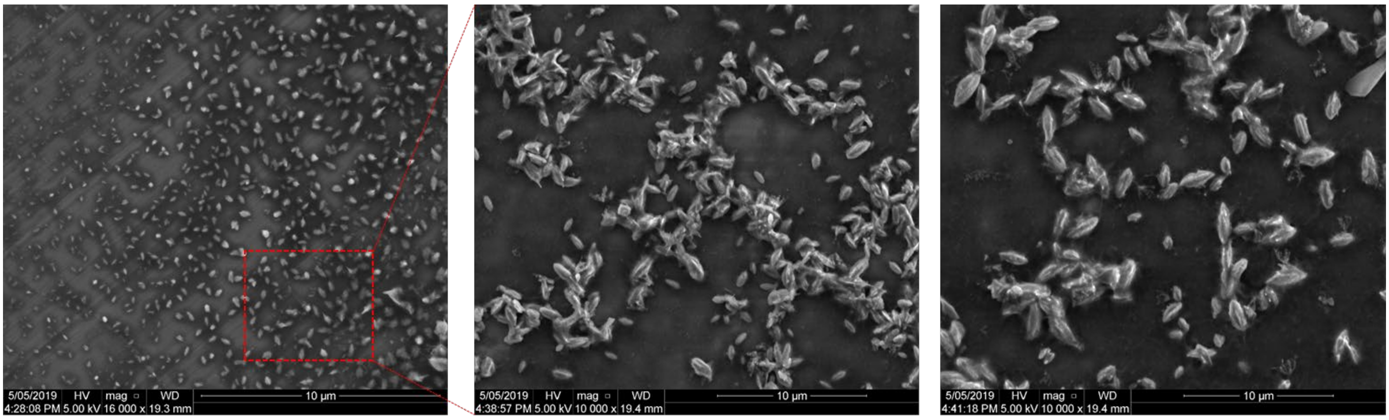

Figure S6a: SEM images of graphene oxide scrolls formed in DMF in a VFD (20 mm OD, 17.5 mm ID) glass tube) at the optimised conditions; concentration of graphene oxide 0.2 mg/mL, rotational speed 4k rpm and flow rate 0.45 mL/min, at room temperature.

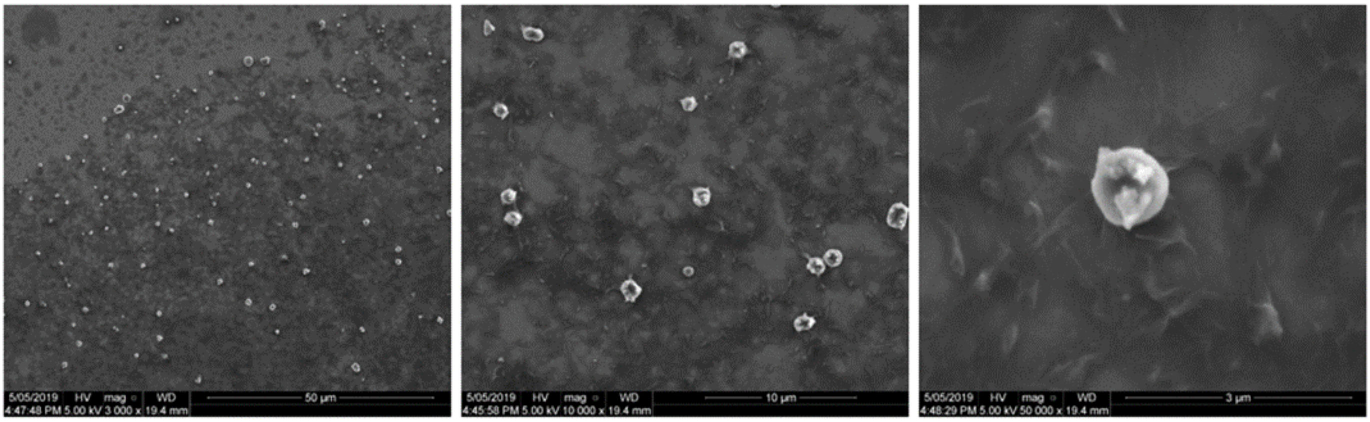

Figure S6b: SEM images of crumbled graphene oxide sheets, formed in DMF in a VFD (20 mm OD, 17.5 mm ID) glass tube; concentration of graphene oxide 0.2 mg/mL, rotational speed 5k rpm (only change relative to Figure S5a) and flow rate 0.45 mL/min, at room temperature.

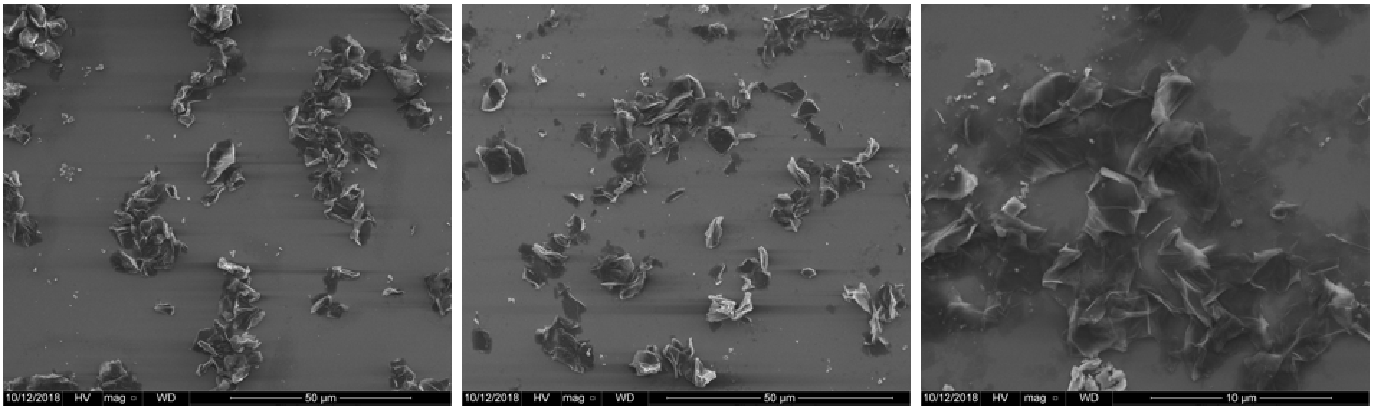

Figure S6c: SEM images of crumbled graphene oxide sheets, formed in DMF in a VFD (20 mm OD, 17.5 mm ID) glass tube; concentration of graphene oxide 0.2 mg/mL, rotational speed 6k rpm (only change relative to Figure S5a and Figure S5b) and flow rate 0.45 mL/min, at room temperature.

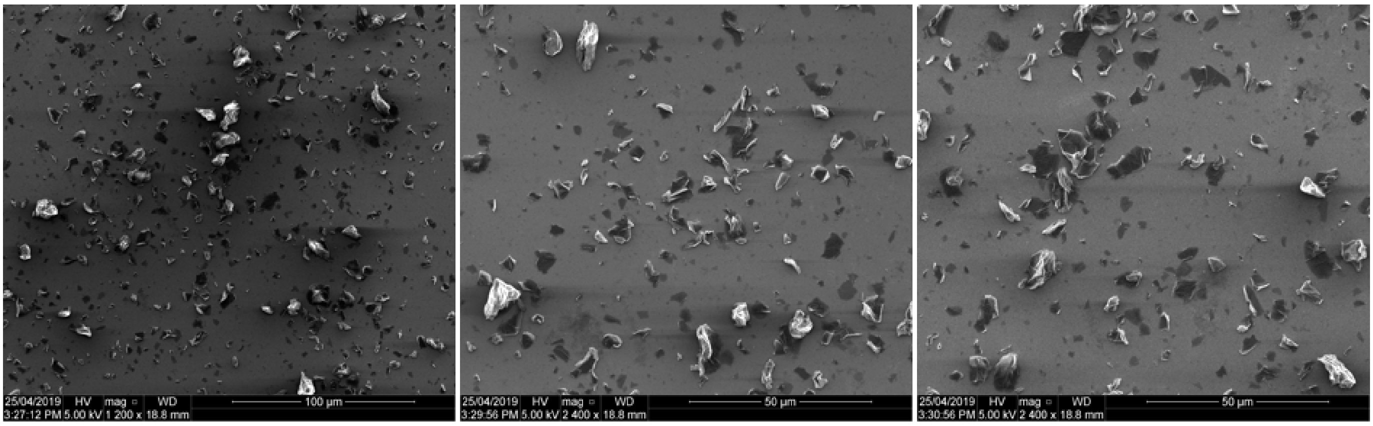

Figure S6d: SEM images of crumbled graphene oxide sheets, formed in DMF in a VFD (20 mm OD, 17.5 ID glass tube); concentration of graphene oxide 0.2 mg/mL, rotational speed 7k rpm (only change relative to

Fig. S5a-c) and flow rate 0.45 mL/min, at room temperature.

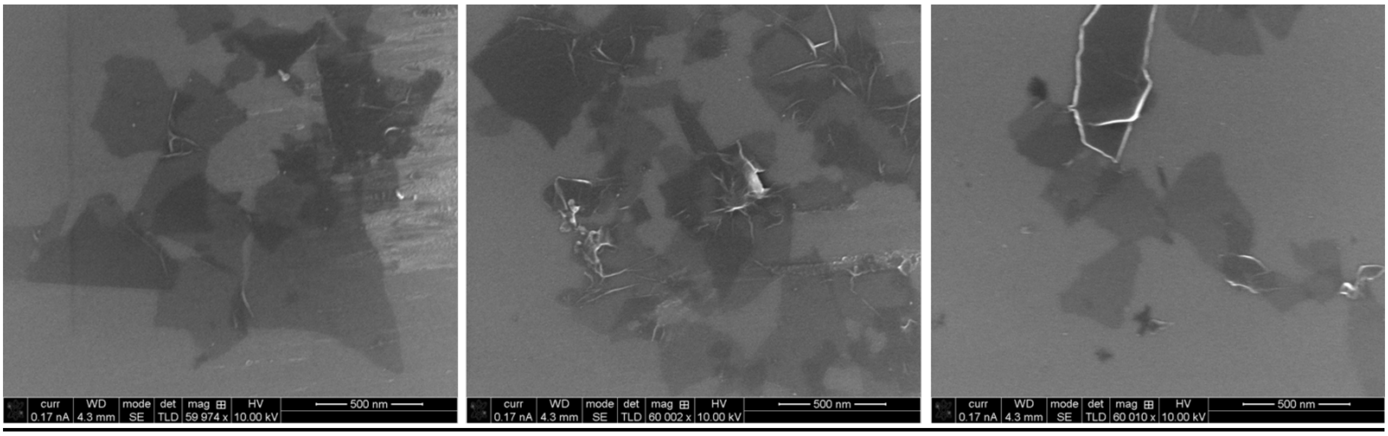

Figure S6e: SEM images of crumbled graphene oxide sheets, formed in DMF in a VFD (20 mm OD, 17.5 mm ID) glass tube; concentration of graphene oxide 0.2 mg/mL, rotational speed 8k rpm (only change relative to Figure S5a-d) and flow rate 0.45 mL/min, at room temperature.

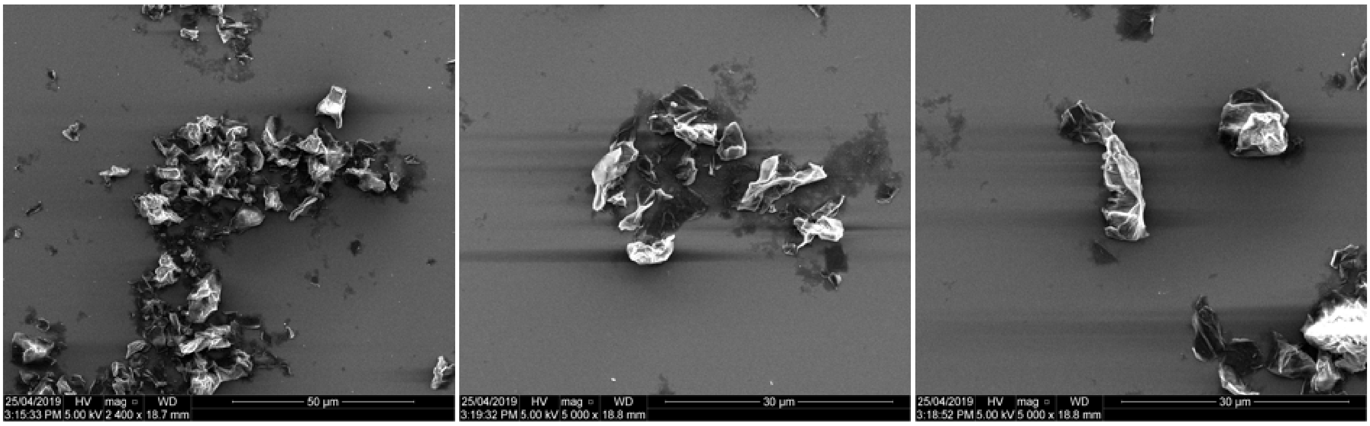

Figure S6f: SEM images of crumbled graphene oxide sheets, formed in DMF in a VFD (20 mm OD, 17.5 mm ID) glass tube; concentration of graphene oxide 0.2 mg/mL, rotational speed 9k rpm (only change relative to Figure S5a-e) and flow rate 0.45 mL/min, at room temperature.

7. Controlling the assembly of fullerene C_{60}

Shear stress induced crystallisation of fullerene C_{60}

Fullerene C_{60} (purities of 99.5 % and 99+ %) were purchased from Sigma Aldrich and Bucky US, respectively. Toluene ≥99.9% was purchased from Sigma Aldrich. Solutions of C_{60} were prepared in toluene at different concentrations, namely 0.05, 0.1 0.2, 0.5 and 1 mg/mL. This involved adding solid material to the solvent, with the mixture left for 24 hours at room temperature. The samples were then filtered to remove undissolved particles and the supernatant was used immediately processing in the VFD.

VFD confined mode and continuous flow processing were explored in established the shear stress induced crystallisation of fullerene C_{60}. For the confined mode, 1 mL of C_{60} in toluene (0.05 mg/mL, 1.0 mg/mL) was added to a VFD (20 mm OD), $\theta = 45^{o}$, and spun at different speeds for 30 min, and thereafter the liquid was collected and processed. This involved centrifugation at 1811 g, and the solid collected on a filter paper. The solid material redissolves in toluene over several hours such that there is sufficient time to collect the material with minimal re-dissolution post VFD processing. The optimal conditions were found at 5k rpm, 0.05 mg/mL, and 7.5k rpm, 1.0 mg/mL for spicules and rod like structures, respectively, Figure S7a. The concentration of C_{60} in toluene at 0.05 mg/mL, flow rate of 0.5 mL/min of the toluene solution were then used in continuous flow mode of operation of the VFD, at $\theta = 45^{o}$. At $\omega = 5$k rpm, spicules also formed, Figure S7d-a , albeit in low yield, but the yield increases on lowering the rotational speed to 4k rpm, with a further increase on increasing the concentration of C_{60} in toluene to 0.1 mg/mL, affording more specular particles, Figure S7b and Figure 7d-f. Optimal rotational speed for the formation of the rod like structures under continuous flow was also less than for confined mode, at 7k rpm, for a flow rate of 1.0 mL/min, Figure S7c. Results for changing the concentration of the fullerene in toluene, different flow rates, different tilt angles, and different rotational speeds and flow rates, are detailed in Figure S7d, Figure S7e and Figure S7f, respectively.

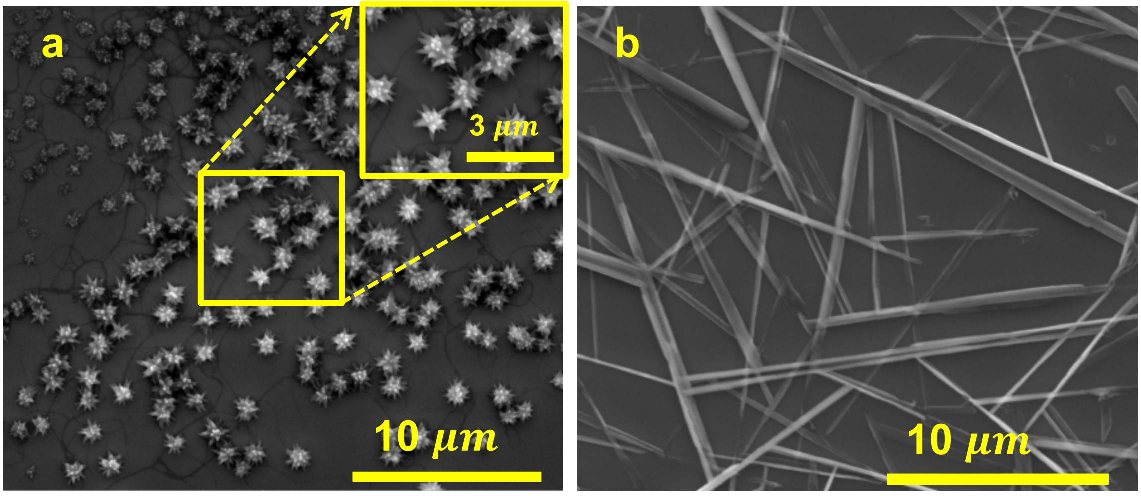

Figure S7a: SEM images of C_{60} particles formed in toluene using a 20 mm OD (177.5 mm ID) VFD operating in the confined mode at (a) 4k rpm, (0.05 mg/mL) and (b) 7.5k rpm, (1.0 mg/mL), $\theta = 45^{o}$.

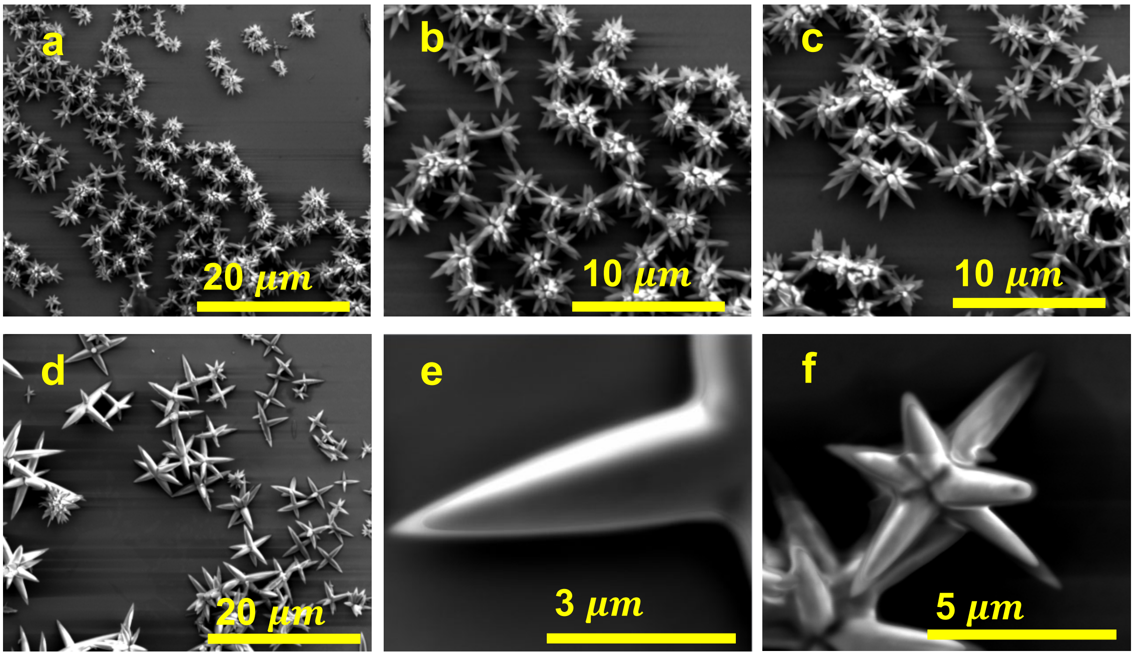

Figure S7b: (a-f) SEM images of specular particles of C_{60} formed in the VFD (20 mm OD, 17.5 mm ID tube), concentration of fullerene 0.1 mg/mL, at the optimal conditions under continuous flow, 4k rpm, flow rate 0.5 mL/min, θ = 45°.

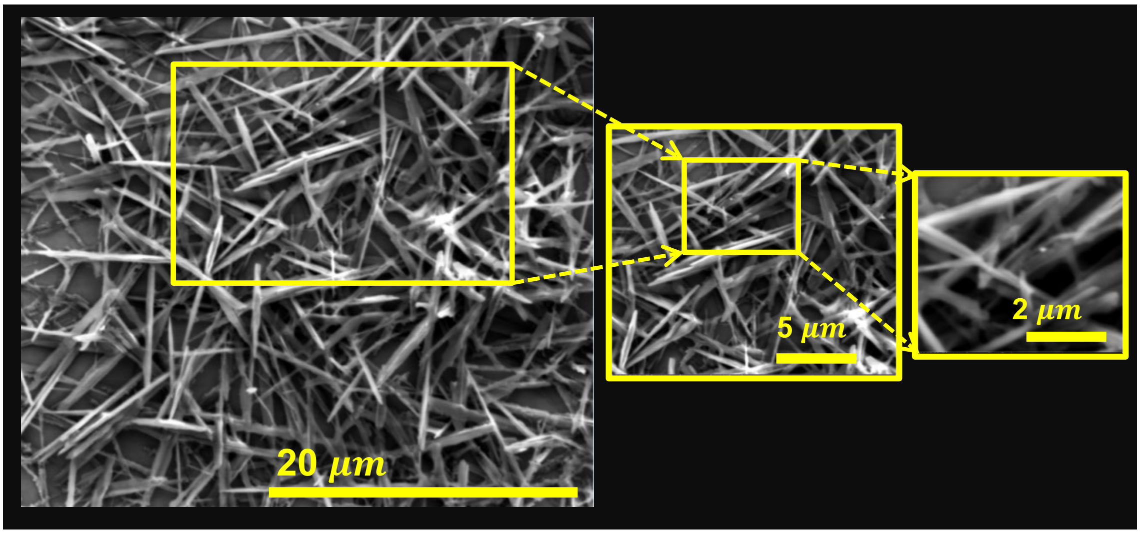

Figure S7c: SEM images of shear stress induced C_{60} rod like structures, obtained from a toluene solution of C_{60} solution with the VFD tube (20 mm OD, 17.5 mm ID) rotating at 7k rpm, concentration 0.1 mg/mL, flow rate 1 mL/min and θ = 45°.

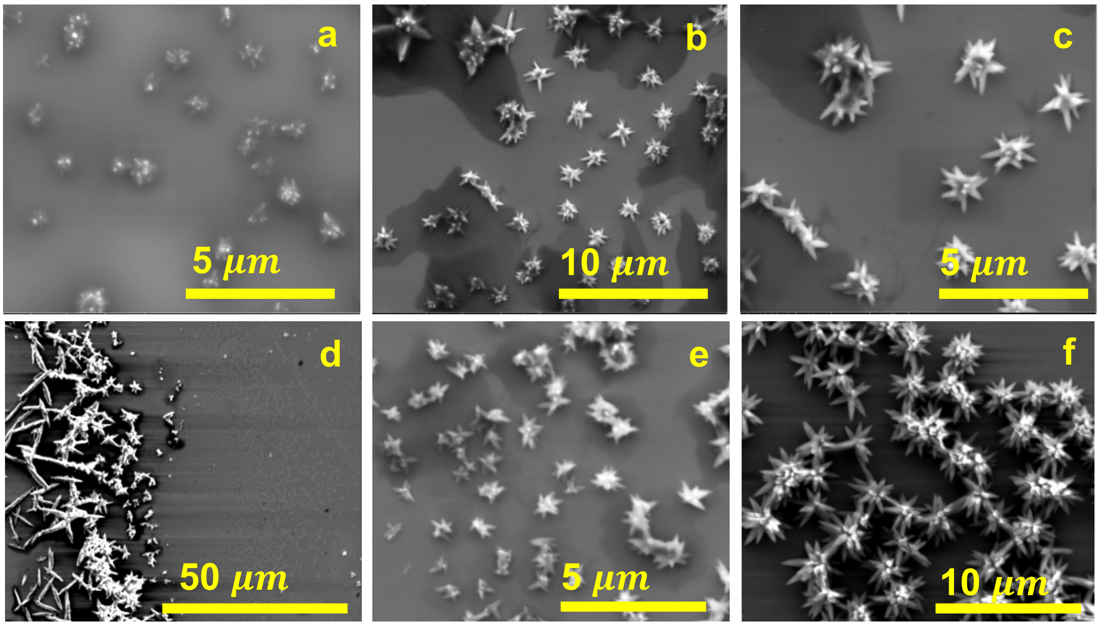

Figure S7d: SEM images of spicules of fullerene C_{60} formed in the VFD (20 mm OD, 17.5 mm ID tube) in a solution of the fullerene in toluene, (a) ω = 5k rpm, θ = 45°, 0.05 mg/mL, 0.5 mL/min, (b,c) ω = 4k rpm, 0.05 mg/mL, 0.5 mL/min , (d) ω = 3k rpm, 0.1 mg/mL, 1.0 mL/min (e) ω = 4k rpm, 0.05 mg/mL, 0.1 mL/min, and (f) ω = 4k rpm, 0.1 mg/mL, 0.1 mL/min.

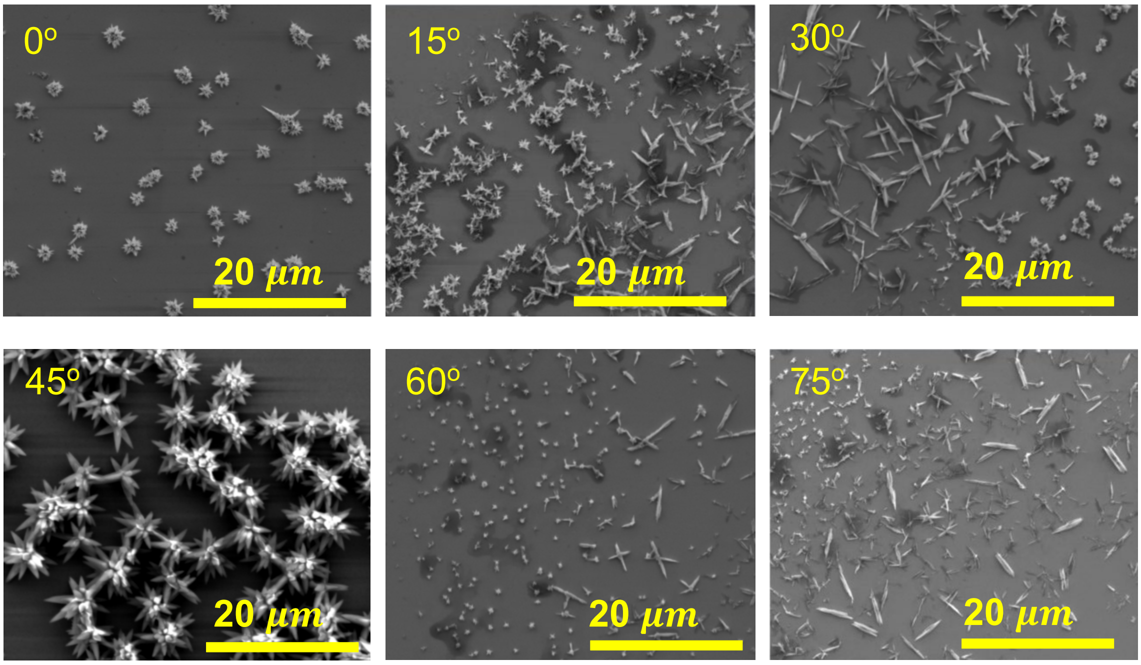

Figure S7e: SEM images of material formed under shear stress in the VFD (20 mm OD) in C_{60} solutions of toluene, 0.1 mg/mL, ω = 4k rpm, at different tilt angles, θ, as specified.

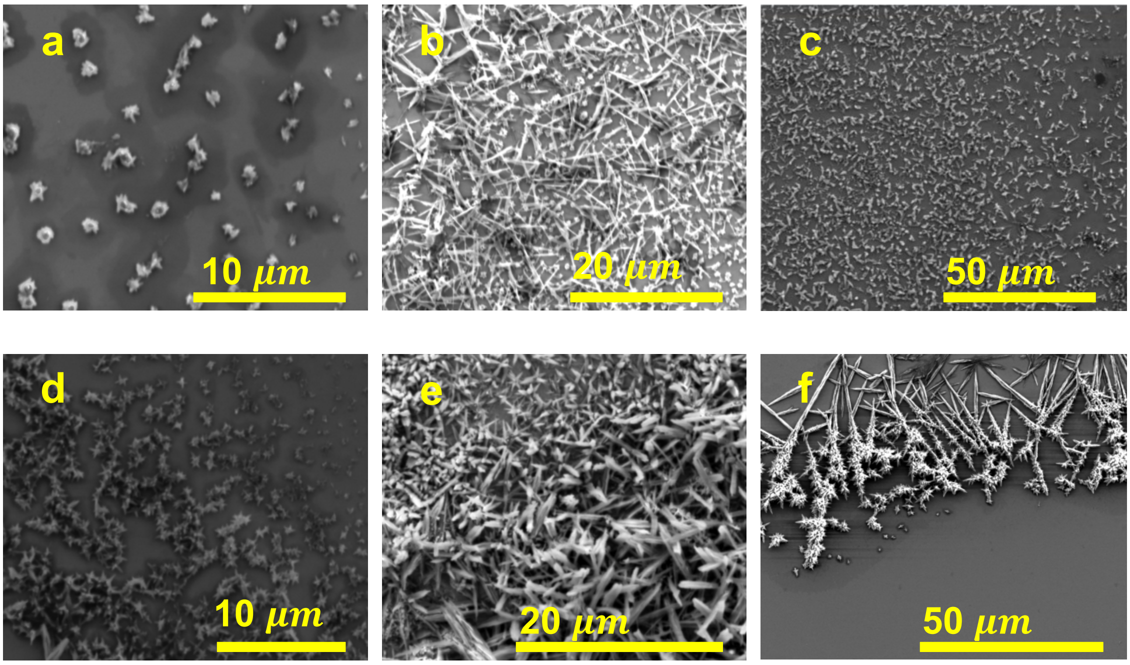

Figure S7f: (a-f) SEM images shear stress induced nanoparticles of C_{60} from a solution of the fullerene in toluene, 0.1 mg/mL, at different speeds and flow rates (a) 3k rpm, 0.5 mL/min, (b) 6k rpm, 0.5 mL/min, (c) 9k rpm, 1 mL/min, (d) 3k, 0.1 mL/min, (e) 6k rpm, 0.1 mL/min, (f) 3k rpm, 1.0 mL/min.

Visible spectroscopy studies on toluene solutions of fullerene C_{60} immediately post-VFD processing under continuous flow.

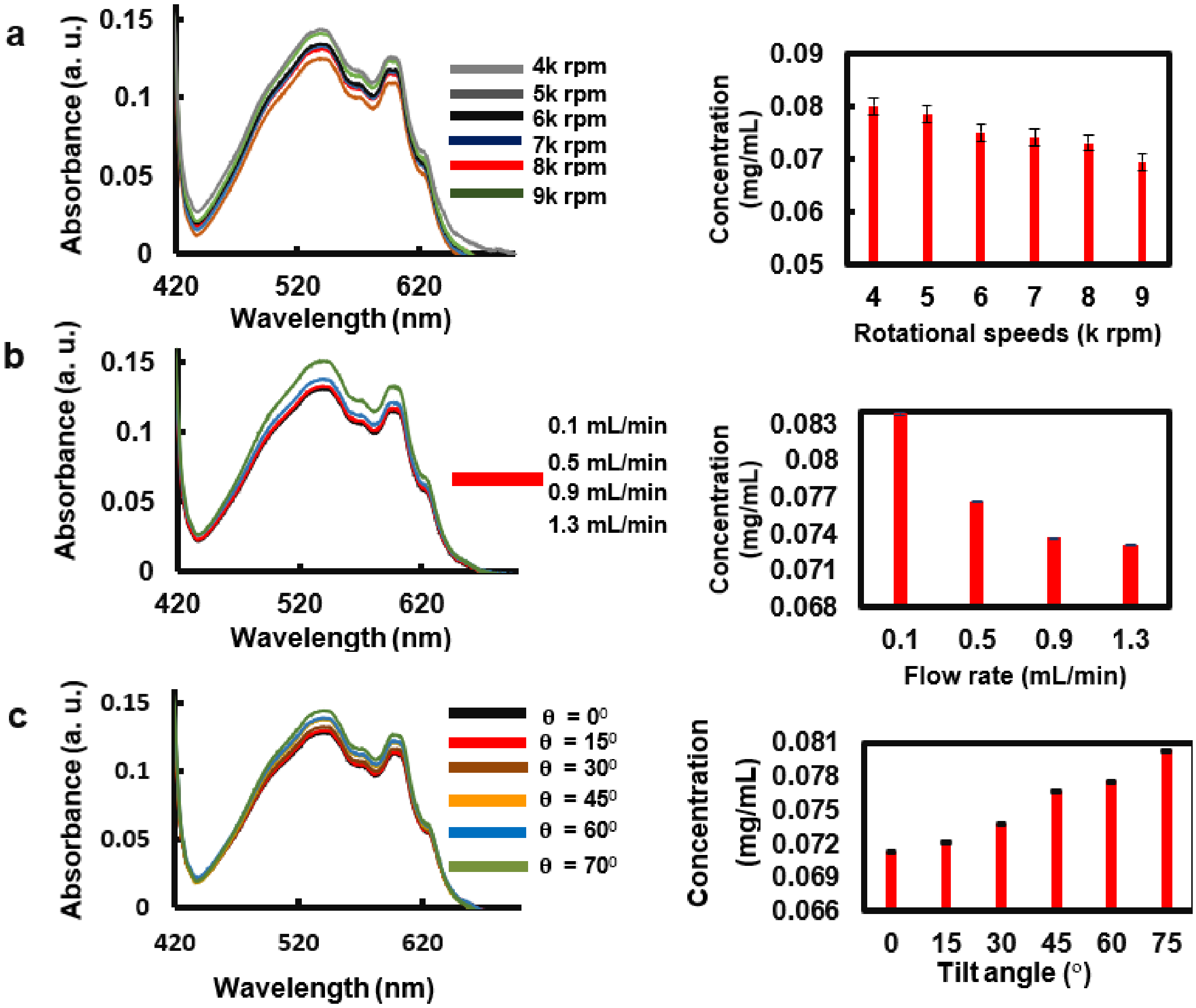

Figure S7g: Visible spectra and residual concentrations of toluene solutions of C_{60} immediately post-processing in the VFD (20 mm OD, 17.5 mm ID), as a function of (a) different rotational speeds, concentration 0.1 mg/mL, θ = 45°, flow rate 0.1 mL/min, (b) different flow rates, concentration 0.1 mg/mL, θ = 45°, ω = 4k rpm, and (c) different tilt angles, concentration 0.1 mg/mL flow rate 0.1 mL/min, ω = 4k rpm (Left). (Right) the distributions concentration of Rotational speeds, flow rate and tilt angle were determined using Beer's Law, $A = \varepsilon l\ c$ (ε molar absorptivity, l, path length and c concentration), knowing the molar absorptivity,ε, for fullerene C_{60} in toluene at 540 nm is 933.

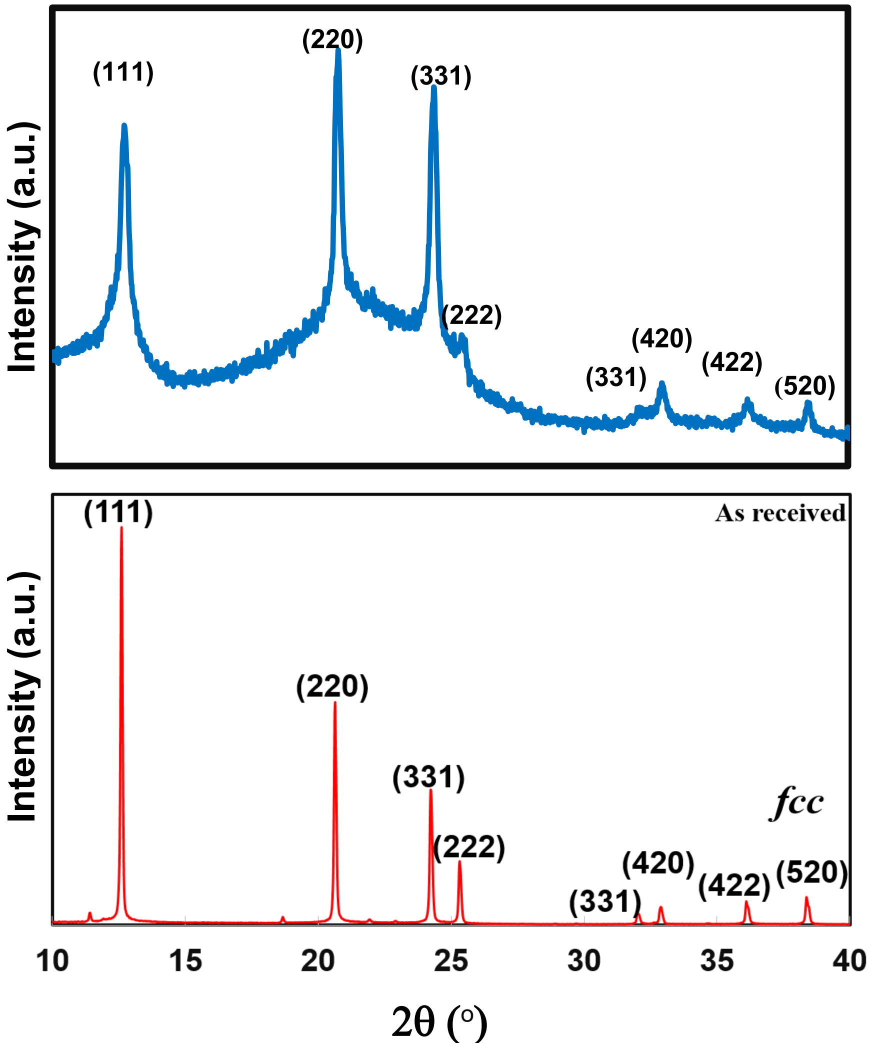

Figure S7h: X-ray diffraction pattern for the spicules formed at the optimal conditions, 0.1 mg/mL of C_{60} in toluene, ω = 4k rpm, flow rate 0.5 mL/min, θ = 45° (top) versus as received C_{60} (bottom).

Fullerene C_{60} cones

The synthesis of fullerene C_{60} cones follows the published procedure[1] using a 20 mm OD tube, herein adapted for a 10 mm OD (8.5 mm ID) glass tube operating under continuous flow conditions, using 2 jets feeds delivering equal amounts of liquid to the base of the tube, with one jet delivering an *o*-xylene solution of C_{60} and the other DMF as the anti-solvent.

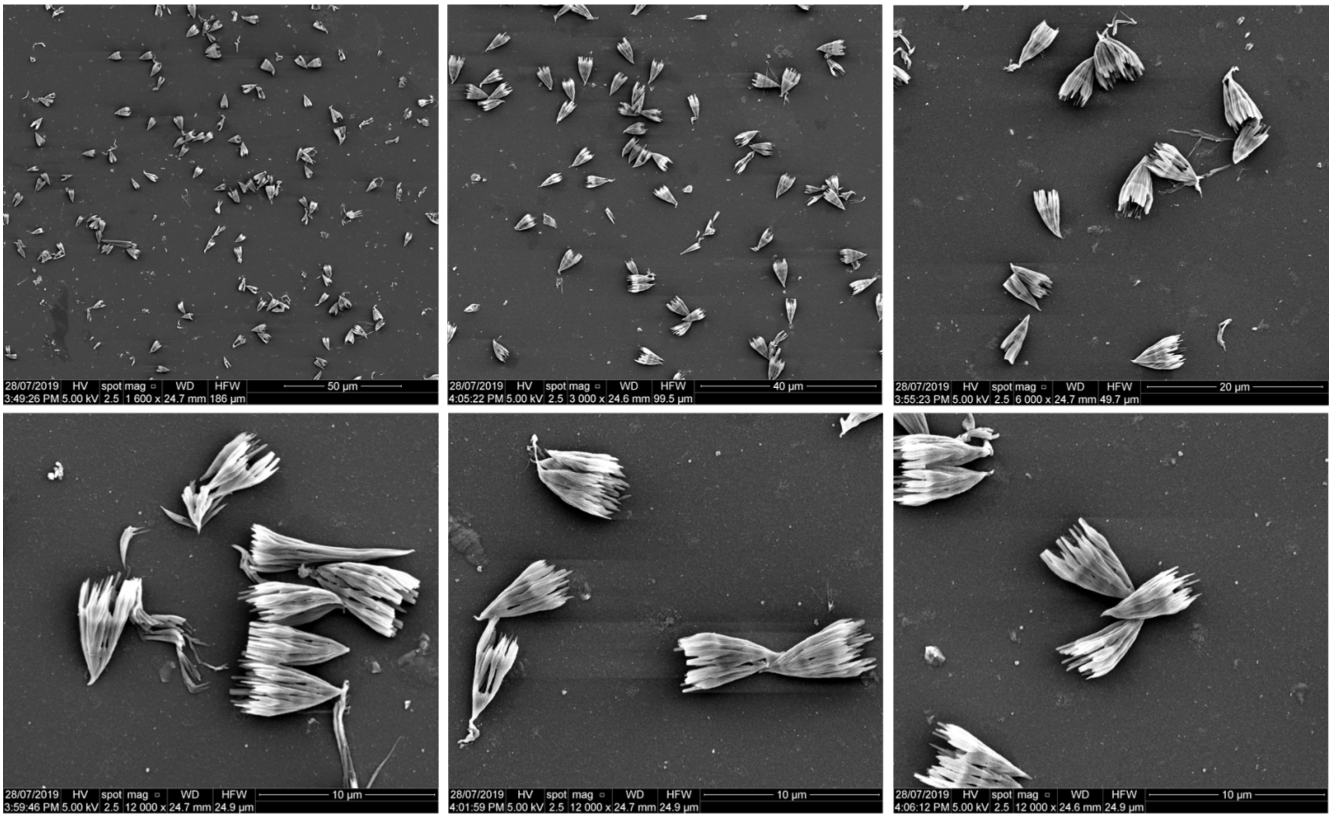

Figure S7a: SEM images of C_{60} cones formed on micromixing a 1:1 solution of *o*-xylene solution of C_{60} (0.1 mg/mL, flow rate 0.1 mL/min) and DMF (0.1 mL/min)□in a 10 mm OD VFD tube, ω = 4k rpm, θ 45°, the product being collected by centrifugation at $1180 \times g$ and washed with hexane, then air dried.

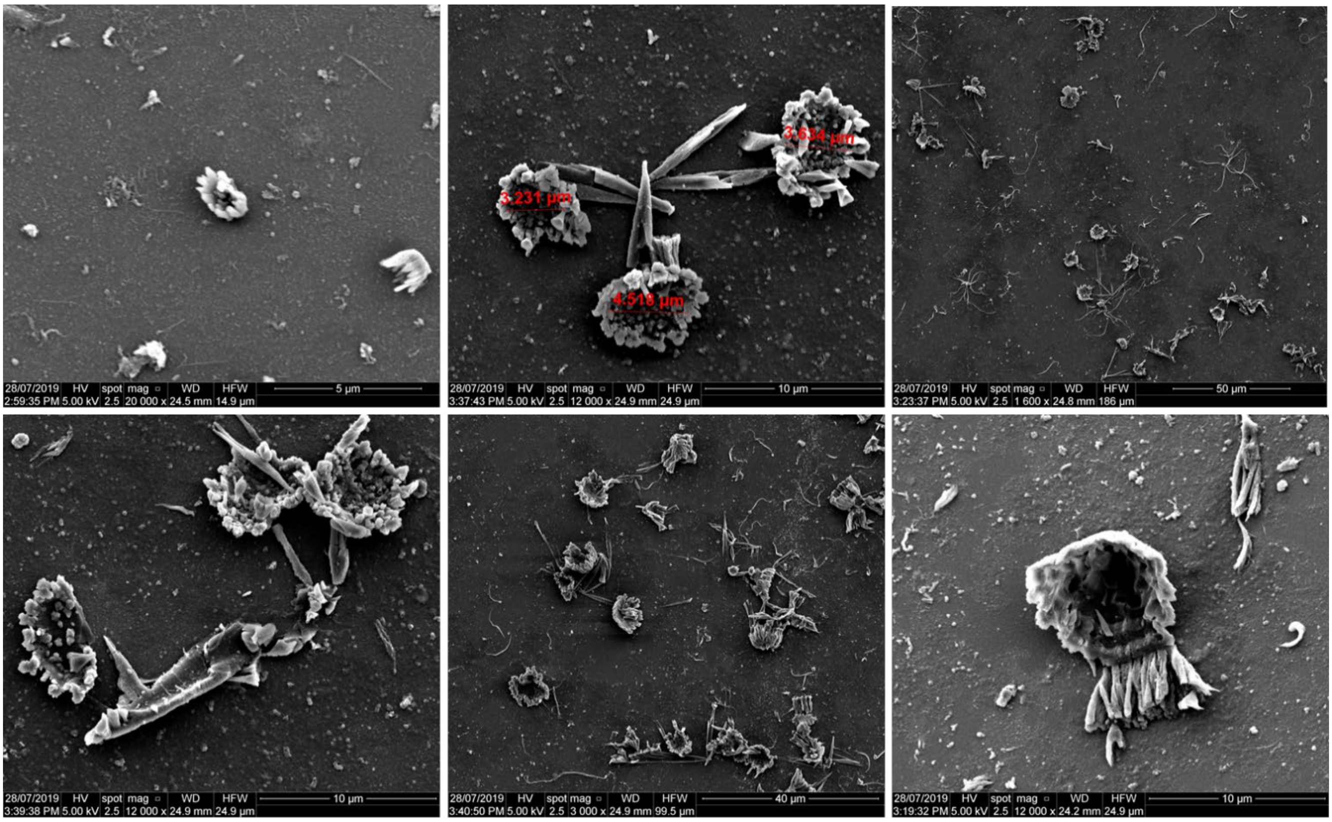

Figure S7b: SEM images of C_{60} cones and other material located on the inner surface of the 10 mm OD glass tube following the processing in Figure S7a (micromixing a 1:1 solution of *o*-xylene solution of C_{60} (0.1 mg/mL, flow rate 0.1 mL/min) and DMF (0.1 mL/min□□in a 10 mm OD VFD tube, ω = 4k rpm, θ 45^{o}).

8. Moulding of polysulfone (PSF) in the VFD

Different concentrations of a PSF solutions were explored to generate a uniform thin-film adhering to the inner surface of the tube. Ultimately this led to using 1 mL of 50 mg/ml of PSF dissolved in dichloromethane (DCM) to generate such a film, Figure S8a. This involved adding a solution of the polymer to a VFD tube (20 mm OD, 17.5 mm ID) tilted at 5° which was then spun at 6k rpm for ~15 min. Evaporation was facilitated by high mass and heat transfer in the tube which was left open to the atmosphere. The film was washed several times with hexane and then dried under a flow of dry nitrogen. Sections of the film was then peeled from the surface of the tube at three different locations, Figure S8b. Figure S8c shows that the thin film created in the VFD is relatively uniform with occasional deformations on the upper surface (air contact) whereas the lower surface (glass contact) is smooth - devoid of any structure variation.

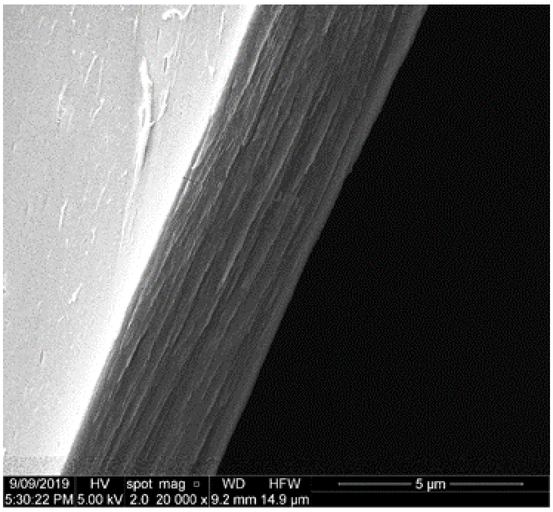

Figure S8a: SEM image of the thin-film of PSF created in the VFD tube (20 mm OD, 17.5 mm ID) at 6k rpm rotational speed, θ = 5° and room temperature during 15 min, after adding 1 mL of 50 mg/ml of PSF dissolved in DCM.

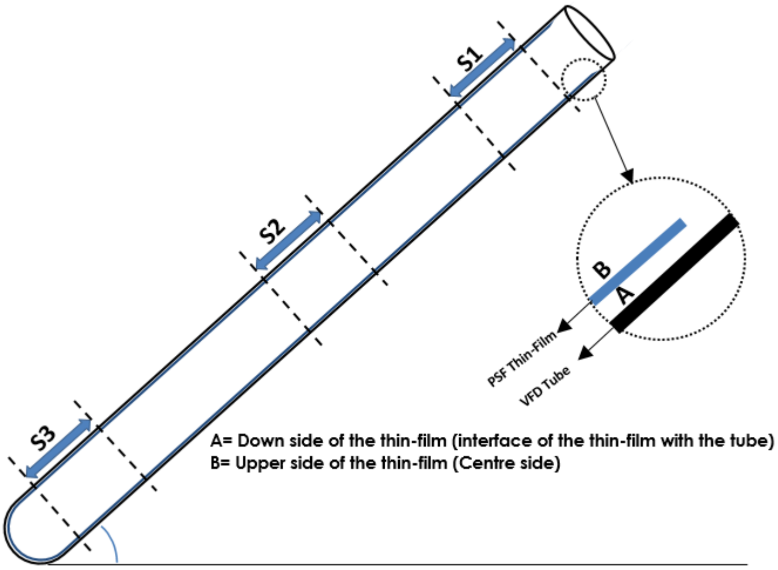

Figure S8b: Locations of samples S1, S2 and S3 taken from the PSF thin-film formed in the VFD; sample S1A and S1B refer to the interface of film with the tube and air from the bottom of the tube respectively, and similarly S2A and S2B, and S3A and S3B, from the middle and top of the tube

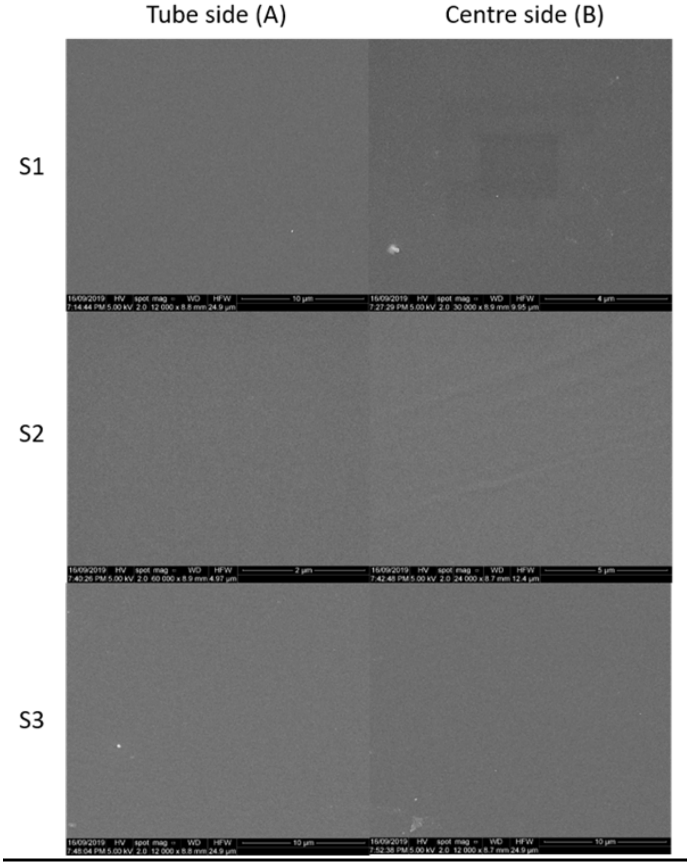

Figure S8c: SEM images of S1, S2, and S3 from both sides (left: bottom of the thin film, right; upper side of the thin-film) of a thin-film created in the VFD (20 mm OD tube) at 6k rpm, θ = 5°, at room temperature during 15 min of processing.

Toluene and water (0.5 mL) were independently added to a VFD tube coated with a thin film of PSF, in which the polymer is only sparingly soluble, and the tube was rotated at 7k rpm at θ = 45°, at room temperature, for one hour. After processing, the liquid was drained, and the film washed with hexane several times and purged with nitrogen gas for drying purposes, for 2h. A section of the film was removed from the middle of each tube and studied using SEM, Figure S8d and S8e, for toluene and water respectively, with the red arrow essentially parallel to the rotation axis of the tube when θ = 45°, and in the direction of the upper lip. This revealed arrays of indentations and some holes on the side A of the polymer film processed in toluene, with a limited number of such structures for water. SEM imaging the other side of the PSF film (side B) post-VFD processing using the same conditions revealed smooth surface, for both toluene or water (Figure S8f). Given the structures revealed on surface SA for toluene, all subsequent processing was done in toluene followed by washing with hexane, and as a control processing in toluene and not washing with hexane afford the same morphology, Figure S8i. The change in morphology of the surface of the PSF film that was in contact with the glass during VFD in toluene provides information on the fluid behaviour, as shown diagrammatically in Figure 1.

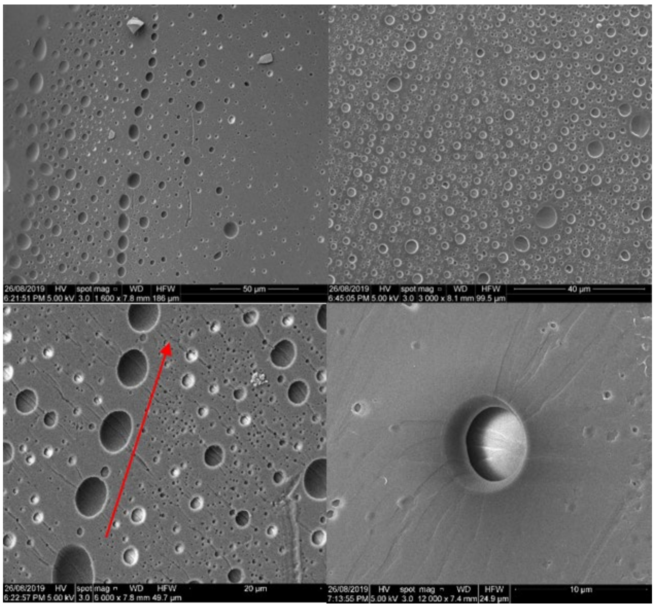

Figure S8d: SEM images of the central inner surface of the film (S2A) after VFD processing (20 mm OD, 17.5 mm ID tube) in toluene, at room temperature ω = 7k rpm, θ = 45° for ~1h, after washing with hexane.

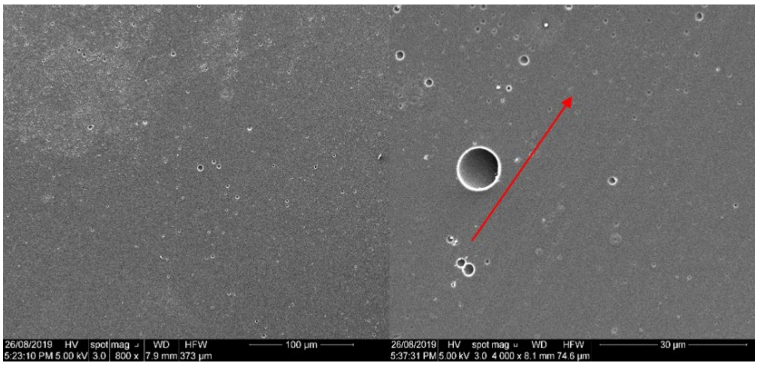

Figure S8e: SEM images of the central inner surface of the film (S2A) after VFD processing (20 mm OD tube) in water, at room temperature, ω = 7k rpm, θ = 45°, for ~1h, after washing with hexane.

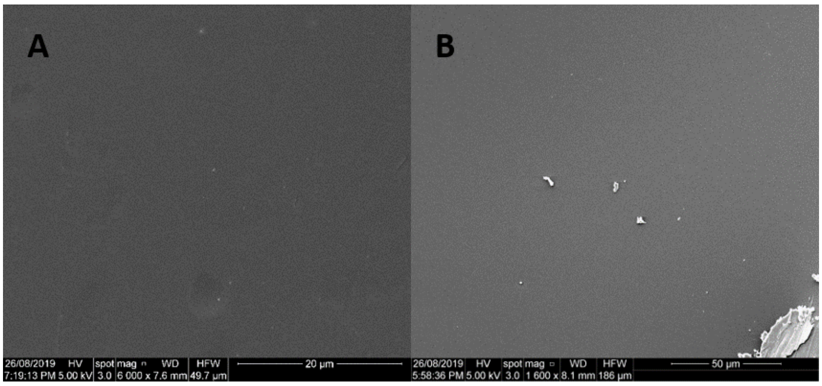

Figure S8f: SEM images of the central upper surface (S2B) after VFD processing (20 mm OD tube) in water, at room temperature ω = 7k rpm, θ = 45° for ~1h, in (A) toluene and (B) water, after washing with hexane and drying with nitrogen gas for 2h

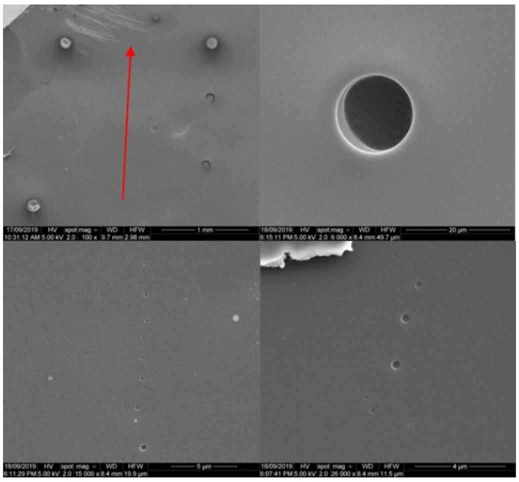

Figure S8i: SEM images of the central inner surface of the film (S2A) after VFD processing (20 mm OD tube) in toluene, at room temperature ω = 7k rpm, θ = 45° for ~1h, and drying with nitrogen gas for 2h, without washing with hexane prior to SEM imaging.

Molecular drilling control experiment

Table S8: Control experiments for determining the 'molecular drilling' on a PSF thin film in the VFD tube, in high shear fluid flow at room temperature.

Sample	**Rotational Speed (k rpm)**	**θ (°)**	**Volume of Toluene (mL)**	**Time (min)**
Thin-film	6k	5	**----**	15
1	7k	45	0.85	30
2	5k	45	1.9	30
3	3.5	45	5	30
4	7	30	0.75	30
5	5	30	1.7	30
6	3.5	30	4.7	30
7	7	60	1	30
8	5	60	2.1	30

9	3.5	60	5.4	30

Notes:

(i) The first entry is for creating the PSF thin-film in a VFD tube (20 mm OD, 17.5 mm ID) from a solution of the polymer in dichloromethane at 6k rpm, with θ = 5° to ensure the film is formed close to the full length of the tube during the evaporation of the solvent, ca 15 min.

(ii) The volume of polymer solution for each sample corresponds to that required to create a film across the entire length of the tube at θ = 5°, with the then 'molecular drilling' experiments carried out at θ = 30, 45, and 60°.

(iii) The films of PSF in the VFD were washed with hexane and purged with nitrogen gas prior to peeling off the glass tube.

(iv) Three sections of the films (S1, S2 and S3, Figure S8b) were taken from every sample, with both sides (A and B) studied using SEM, affording six images for each sample, designated S1A, S2A, S3A, S1B, S2B and S3B, as elaborated below.

Thin-film

Rotational speed : 6k rpm
Tilt angle, q θ : 5°
Solvent : CH_2Cl_2
Time : 15 min

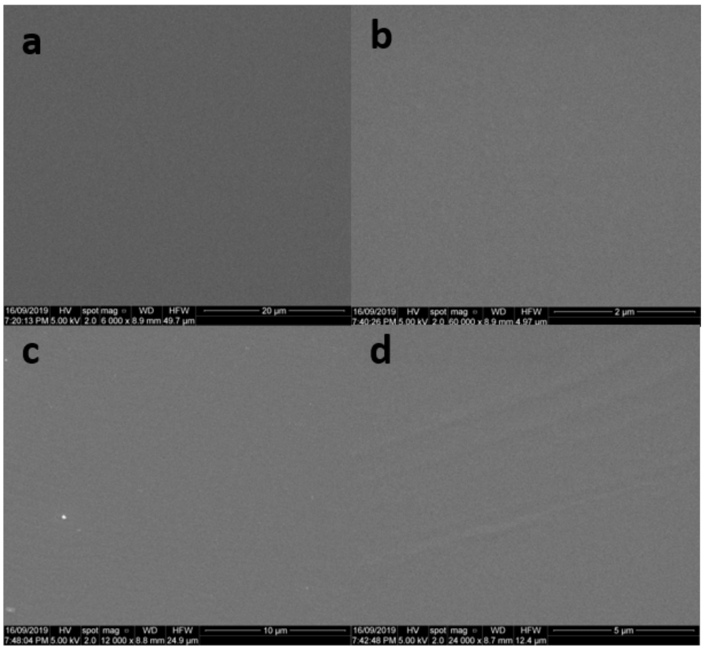

Figure S8j: SEM images of PSF thin-film created in the VFD tube (20 mm OD) at 6k rpm, θ = 5° at room temperature during 15 min of evaporation of DCM: (a) S1A, (b) S2A, (c) S3A and (d) S2B, revealing smooth surfaces present, prior to processing in toluene.

Sample 1:

Rotational speed : 7k rpm
Tilt angle, θ : 45°
Solvent : Toluene
Time : 30 min

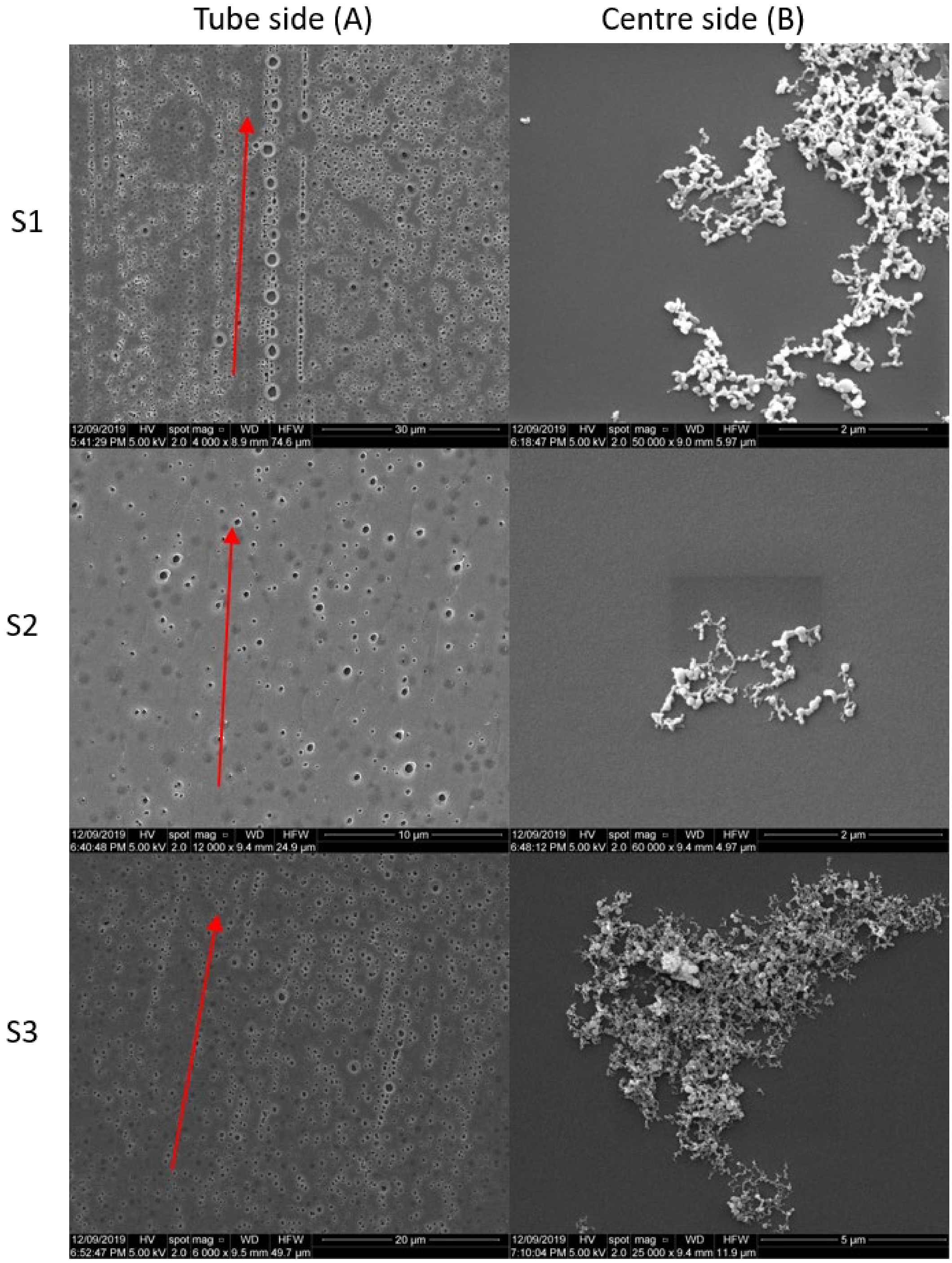

Figure S8k: SEM images of S1, S2, and S3 from both sides (left: bottom of the thin film (A), right; upper side of the thin-film (B) of the thin-film processed in toluene at 7k rpm, θ = 45°, room temperature, and 30 min processing, then washed with hexane, and dried under nitrogen gas. The red arrows define the direction of rotation of the axis of the tube, directed out of the tube.

Sample 2:

Rotational speed	: 5k rpm
Tilt angle, θ	: 45°
Solvent	: Toluene
Time	: 30 min

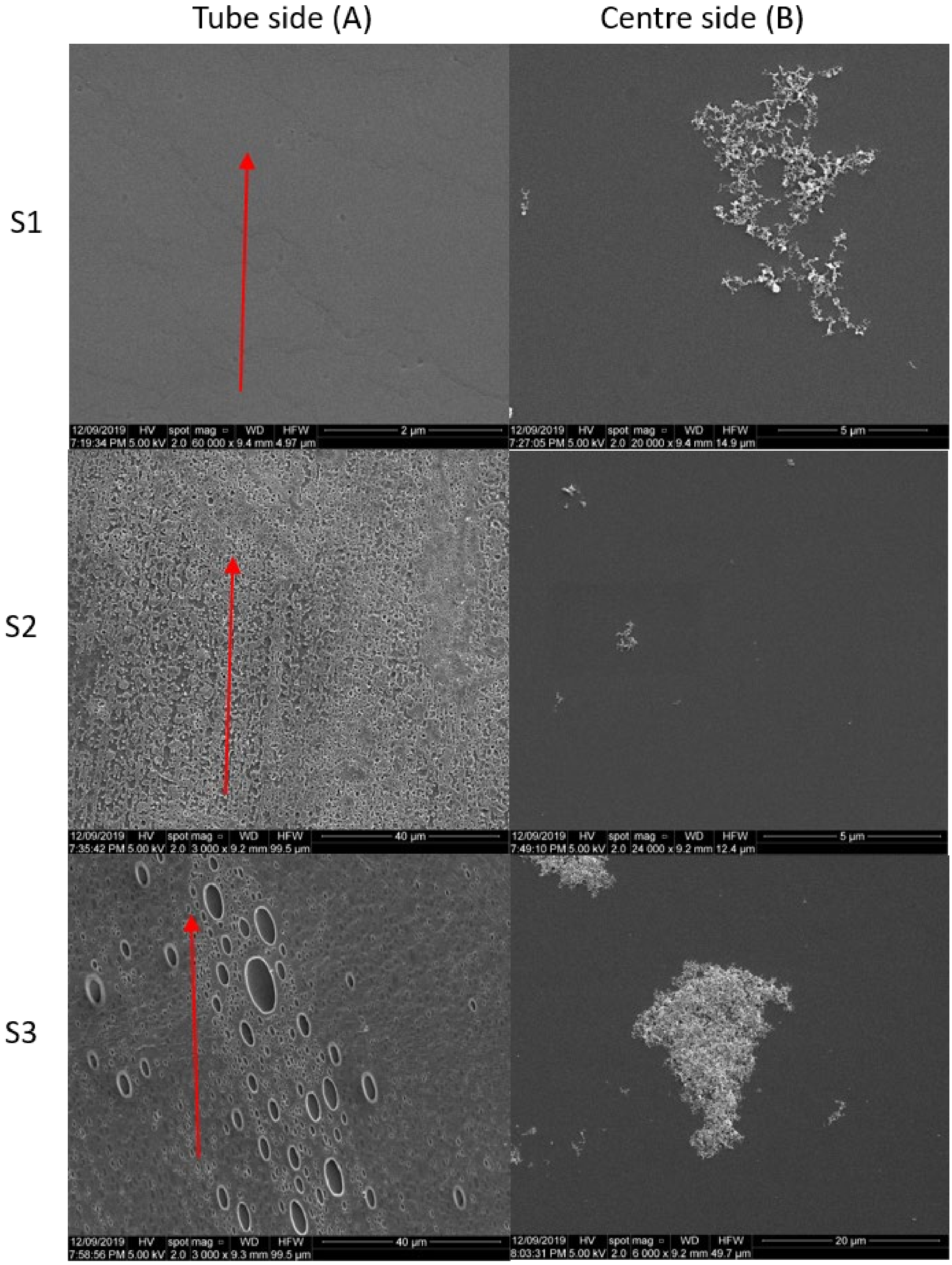

Figure S8l: SEM images of S1, S2, and S3 from both sides (left: bottom of the thin film (A), right; upper side of the thin-film (B) of the thin-film processed in toluene at 5k rpm, θ = 45°, room temperature, and 30 min processing, then washed with hexane, and dried under nitrogen gas. The red arrows define the direction of rotation of the axis of the tube, directed out of the tube.

Sample 3:

Rotational speed : 3.5k rpm
Tilt angle, θ : 45°
Solvent : Toluene
Time : 30 min

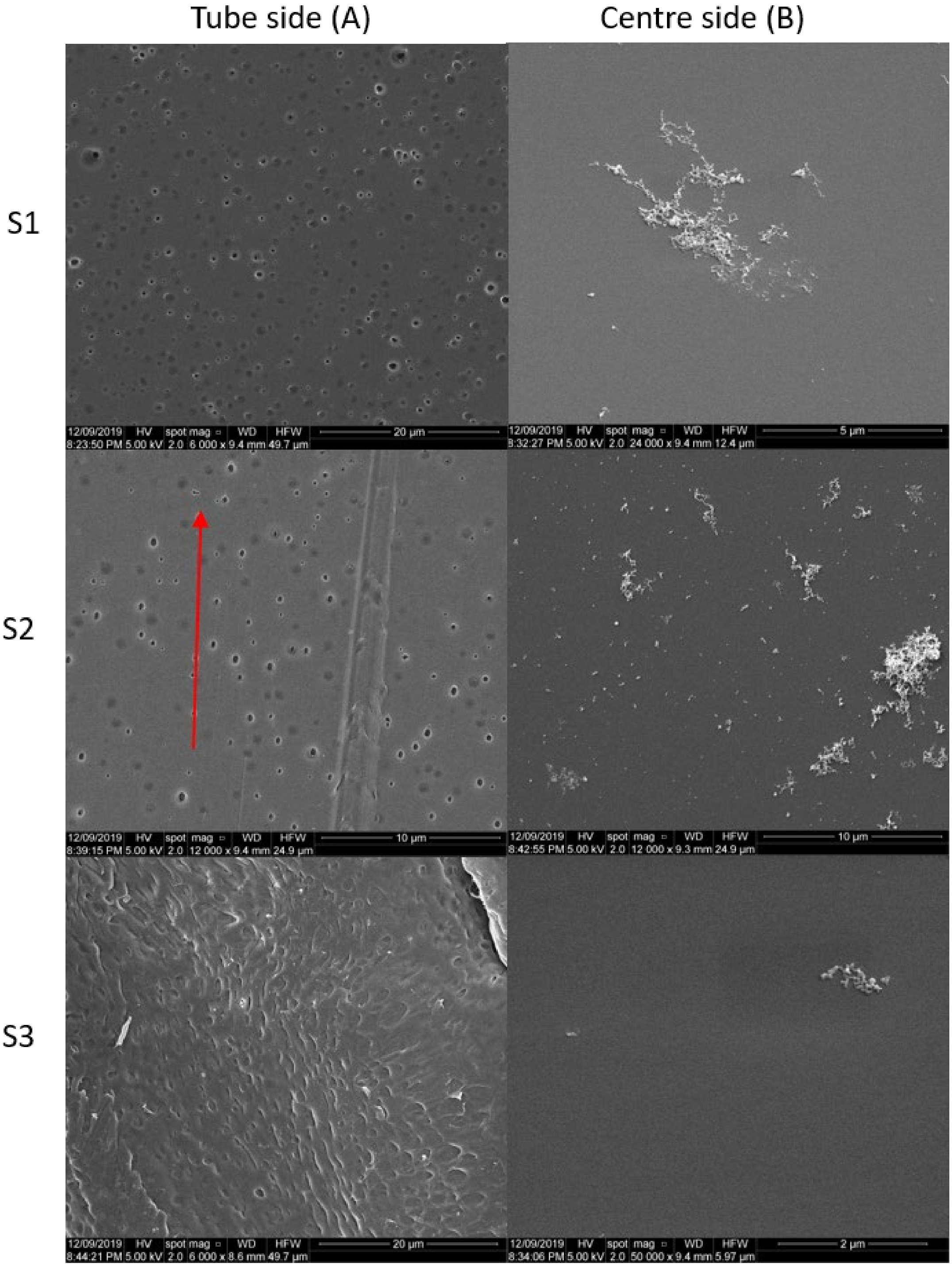

Figure S8m: SEM images of S1, S2, and S3 from both sides (left: bottom of the thin film (A), right; upper side of the thin-film (B) of the thin-film processed in toluene at 3.5k rpm, θ = 45°, room temperature, and 30 min processing, then washed with hexane, and dried under nitrogen gas. The red arrow defines the direction of rotation of the axis of the tube, directed out of the tube.

Sample 4:

Rotational speed	: 7k rpm
Tilt angle, θ	: 30°
Solvent	: Toluene
Time	: 30 min

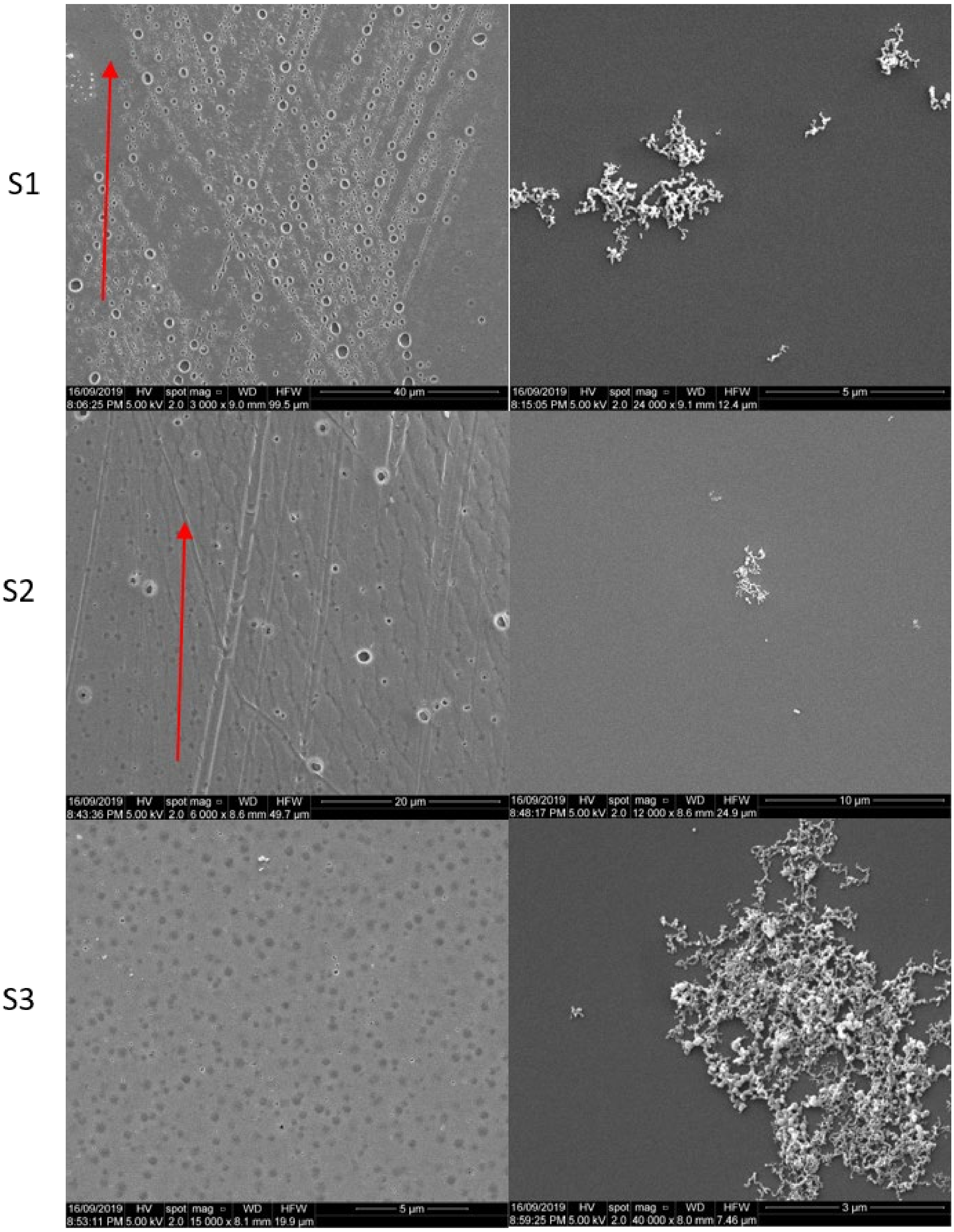

Figure S8n: SEM images of S1, S2, and S3 from both sides (left: bottom of the thin film (A), right; upper side of the thin-film (B) of the thin-film processed in toluene at 7k rpm, θ = 30°, room temperature, and 30 min processing, then washed with hexane, and dried under nitrogen gas. The red arrows define the direction of rotation of the axis of the tube, directed out of the tube.

Sample 5:

Rotational speed : 5k rpm
Tilt angle, θ : 30°
Solvent : Toluene
Time : 30 min

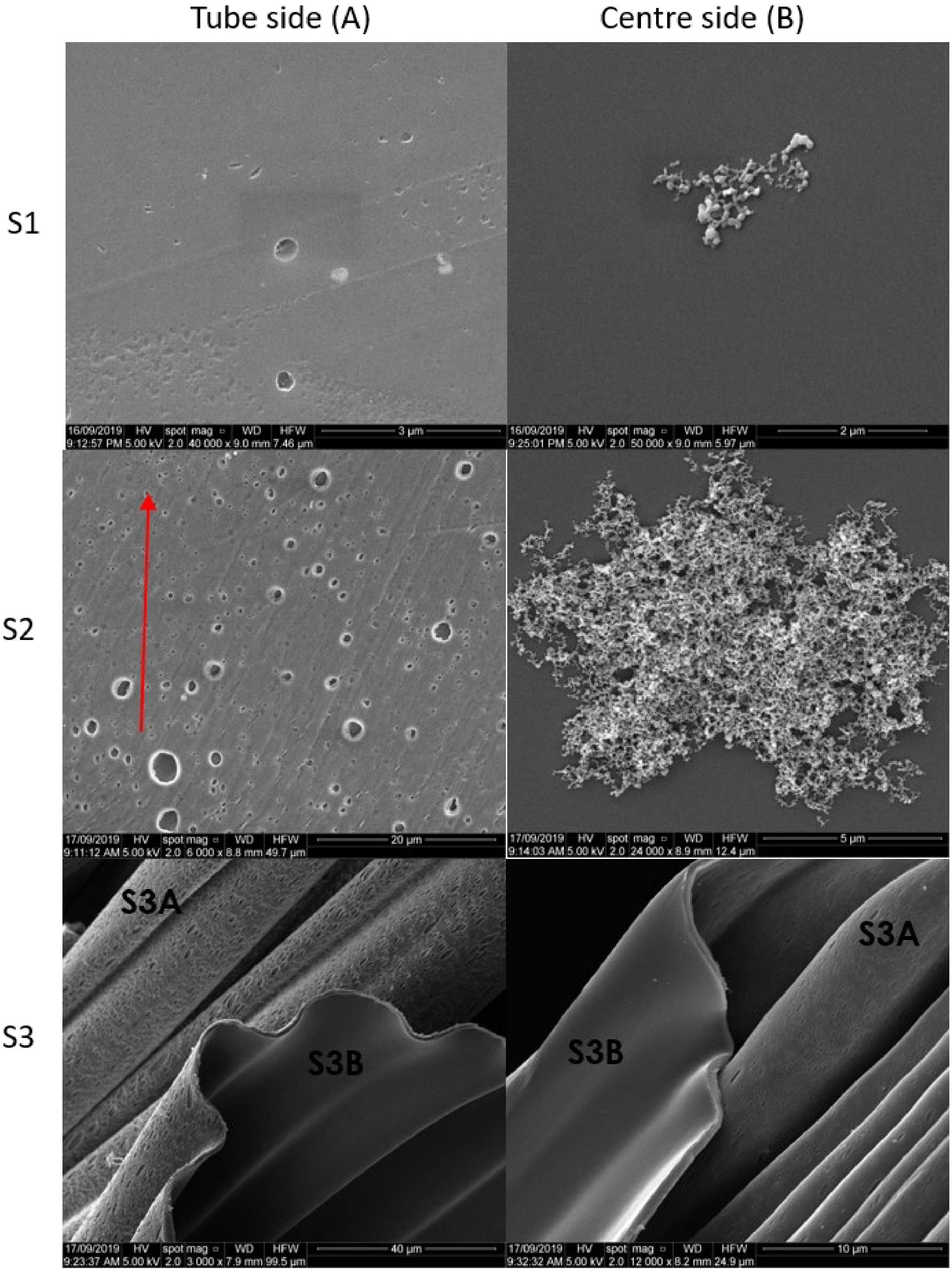

Figure S8o: SEM images of S1, S2, and S3 from both sides (left: bottom of the thin film (A), right; upper side of the thin-film (B) of the thin-film processed in toluene at 5k rpm, θ = 30°, room temperature, and 30 min processing, then washed with hexane, and dried under nitrogen gas. The red arrow defines the direction of rotation of the axis of the tube, directed out of the tube.

Sample 6:

Rotational speed : 3.5k rpm
Tilt angle, θ : 30°
Solvent : Toluene
Time : 30 min

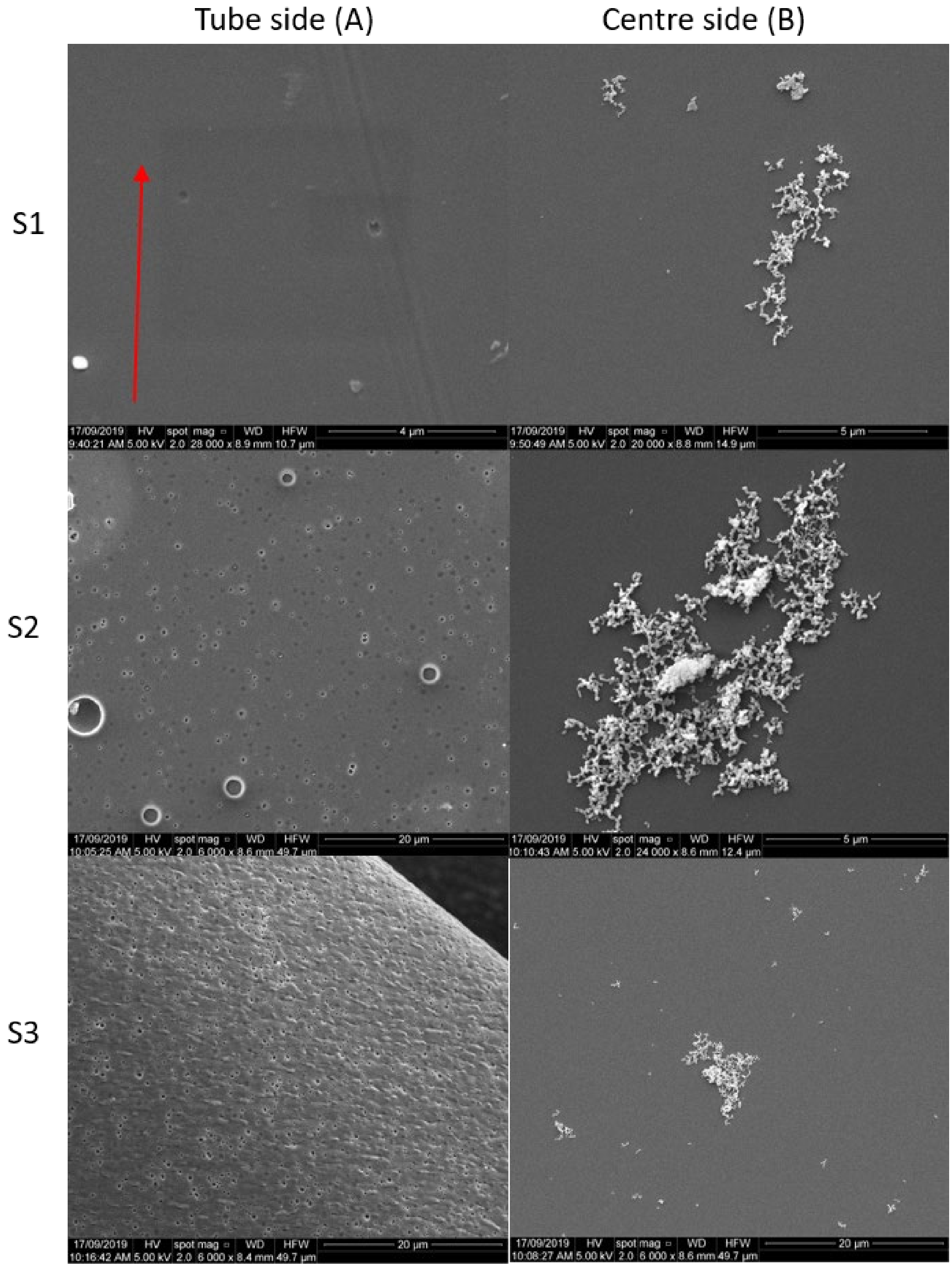

Figure S8p: SEM images of S1, S2, and S3 from both sides (left: bottom of the thin film (A), right; upper side of the thin-film (B) of the thin-film processed in toluene at 3.5k rpm, θ = 30°, room temperature, and 30 min processing, then washed with hexane, and dried under nitrogen gas. The red arrow defines the direction of rotation of the axis of the tube, directed out of the tube.

Sample 7:

Rotational speed : 7k rpm
Tilt angle, θ : 60°
Solvent : Toluene
Time : 30 min

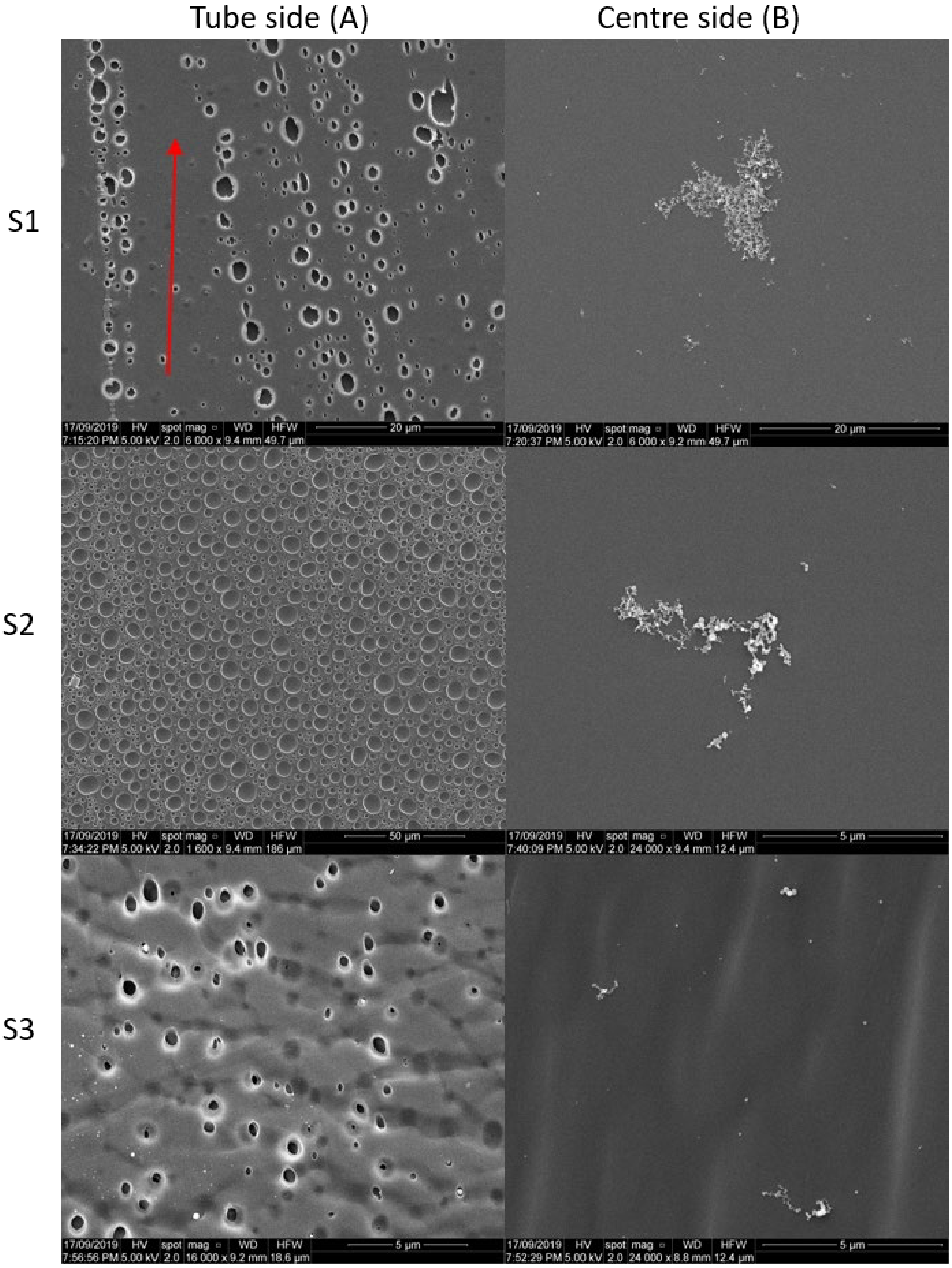

Figure S8q: SEM images of S1, S2, and S3 from both sides (left: bottom of the thin film (A), right; upper side of the thin-film (B) of the thin-film processed in toluene at 7k rpm, $\theta = 60°$, room temperature, and 30 min processing, then washed with hexane, and dried under nitrogen gas. The red arrow defines the direction of rotation of the axis of the tube, directed out of the tube.

Sample 8:

Rotational speed : 5k rpm
Tilt angle, θ : 60°
Solvent : Toluene
Time : 30 min

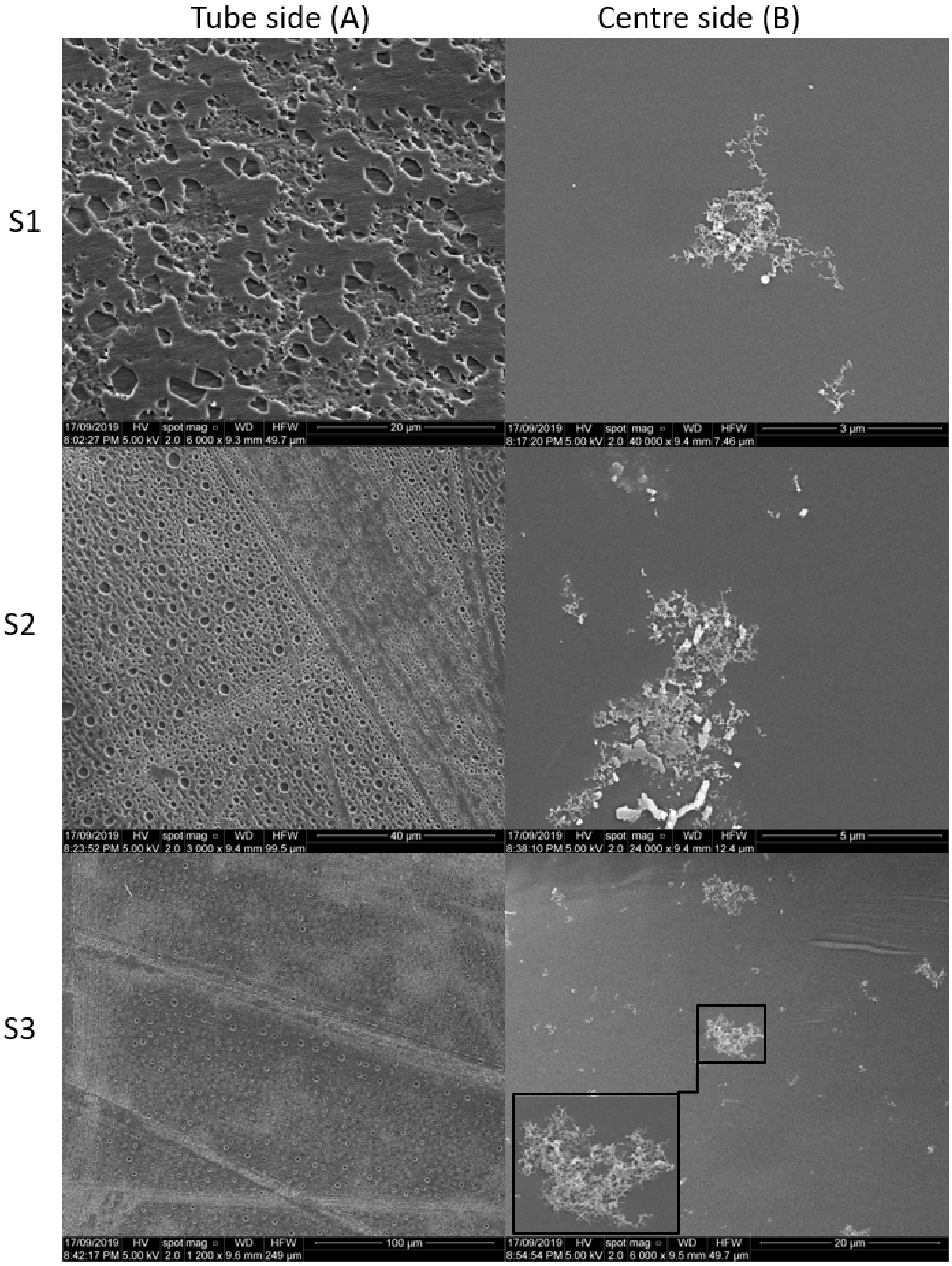

Figure S8r: SEM images of S1, S2, and S3 from both sides (left: bottom of the thin film (A), right; upper side of the thin-film (B) of the thin-film processed in toluene at 5k rpm, θ = 60°, room temperature, and 30 min processing, then washed with hexane, and dried under nitrogen gas.

Sample 9:

Rotational speed : 3.5k rpm
Tilt angle, θ : 60°
Solvent : Toluene
Time : 30 min

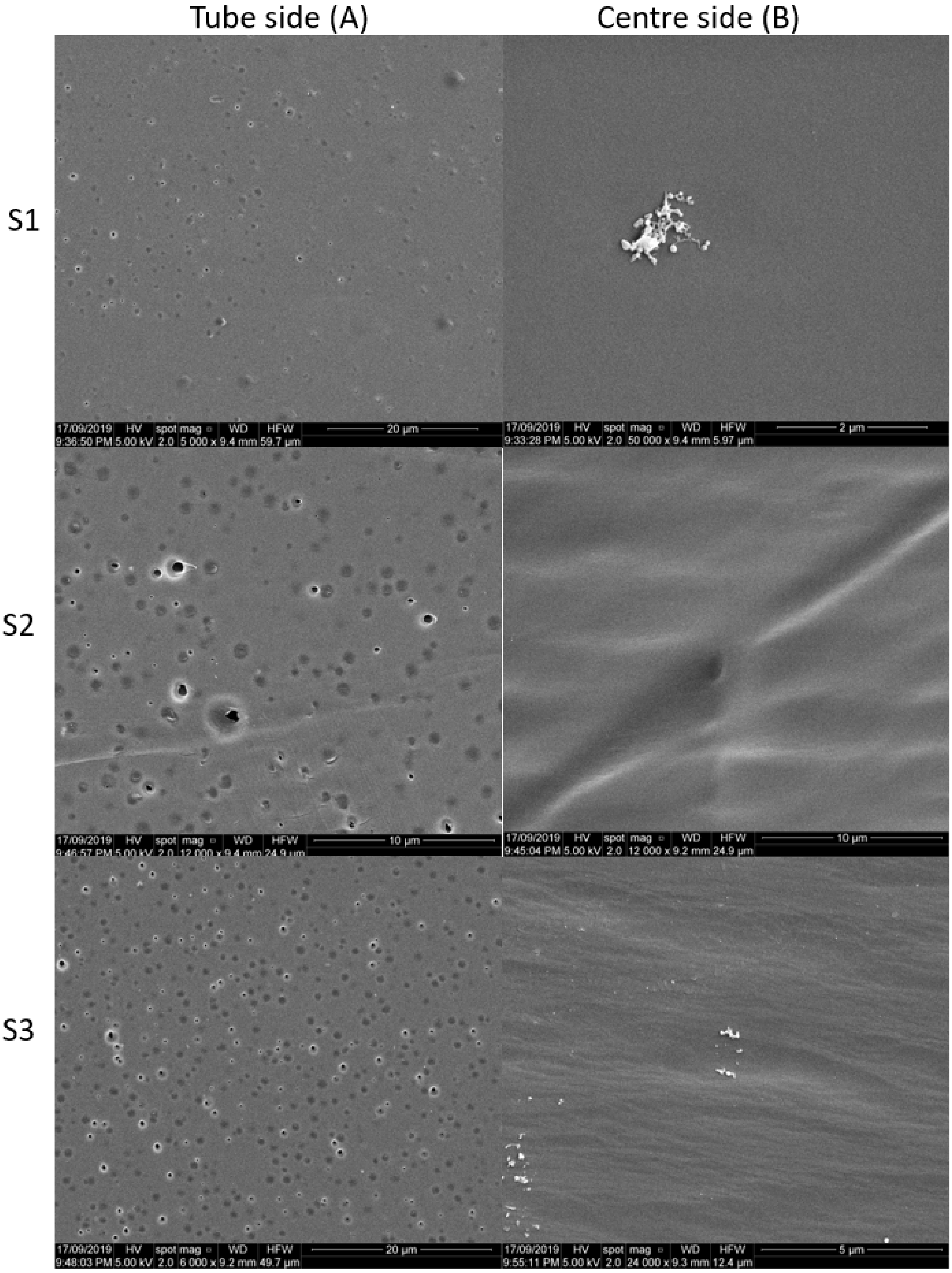

Figure S8s: SEM images of S1, S2, and S3 from both sides (left: bottom of the thin film (A), right; upper side of the thin-film (B) of the thin-film processed in toluene at 3.5k rpm, θ = 60°, room temperature, and 30 min processing, then washed with hexane, and dried under nitrogen gas.

Fig. S8j-S8s show that thin-films of PSF formed in the VFD (20 mm OD, 17.5 mm ID tube) involving evaporation of a DCM solution of the polymer, have smooth surfaces, both on the surface in contact with the glass, and the surface exposed to air. Processing then with toluene in the tube reveals indentations/holes on the surface attached to the glass, with periodic regularity and alignment with the direction of rotation of the tube, for θ = 45°, for rotational speeds ≥ 5k rpm, with the indentations/holes smaller and more uniform compared with those created at 5k rpm, and for ω= 3.5k rpm the films have fewer holes, with no evidence of them being ordered. This finding for toluene is in accord with the signature for toluene, where double helical flow prevails > 6k rpm, Figure 2. Processing of toluene solutions at θ = 30 and 60° also show 'molecular drilling', but these angles are not optimal for any applications of the VFD. While the upper surfaces (SB) of the films are almost devoid of holes, regions of agglomerated particles of the polymer are evident, ca 100 nm in diameter, for example in Figure S8k. These particles are likely formed during the 'molecular drilling' process, when the double helical flow strikes the surface of the tube, Figure 1, but attempts to measure them using DLS were unsuccessful, and we then turned to using small angle neutron scattering (SANS) for further characterisation, with the findings reported below.

Real time VFD processing small angle neutron scattering (SANS)

Understanding the effect of the fluid flow in the VFD (confined mode) was explored using real time SANS. This was to determine any change in morphology of the surface of the polymer film and identify any nanoparticles of the polymer extruded from the polymer film during 'molecular drilling' (double helical flow) into the dynamic thin film of toluene.

A 20 mm OD (17.5 mm ID) VFD quartz tube containing 2 mL of toluene-d8 was rotated at 5k rpm and the scattered neutrons were counted for 2 hours in both high and low Q-range, at 1.3 and 14-meter camera length respectively. Combining both Q-range data resulted in flat curves shown in Figure S8t. The internal surface of quartz VFD tubes were then coated with a PSF thin-film at θ = 5 °, ω = 6k rpm, at room temperature during 15 min (as discussed above). 5, 2 and 1 mL of toluene-d8 was then added to these tubes and individually studied using real-time SANS, for □ = 3.5k, 5k and 7k rpm, respectively, using both 1.3 and 14-meter camera lengths. Scattering for the whole Q-ranges of PSF films in the presence of toluene-d8 at these rotational speeds are plotted in Figure S8u.

The recorded scattering curves for toluene-d8 (no PSF film in the tube) are similar to scattering curves for toluene-d8 and PSF film, taking into account thinner films of toluene for high rotational speeds. The thickness of the PSF thin-film was ~ 4 μm which is out of range of SANS capabilities, as is the case for pores of the size commensurate with the morphology of the films post VFD processing, established using SEM. Importantly there was no scattering associated with nanoparticles of polymer present in solution during the processing. The presence of such particles was expected given the presence of small amounts of aggregates of them post VFD processing, albeit only on the upper surface of the PSF film (SB), ca 100 nm in dimeter. Thus, such particles present during processing are in low concentration, beyond the level of perturbing the scattering curve for the *in situ* SANS experiments. This finding is consistent with such generated particles being constantly taken up in the polymer film, driven by the associated centrifugal force in the VFD, with the only particles present representing a snapshot of nanoparticles in equilibrium with the polymer film. Moreover, this is also consistent with the smoothing out of holes generated by the 'molecular drilling', with their presence inferred from the pocket of liquid trapped on the surface of the PSF film in contact with the surface.

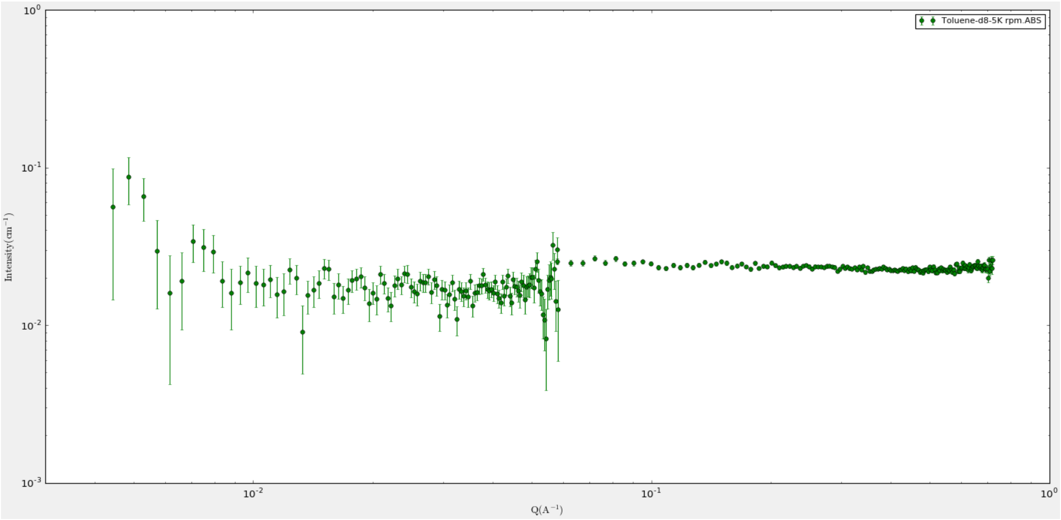

Figure S8t: Real time SANS scattering in the VFD for 2 mL of toluene-d8 in a 20 mm OD quartz tube (no PSF coating) rotated at 5k rpm for 2 hours, at room temperature, θ = 45°.

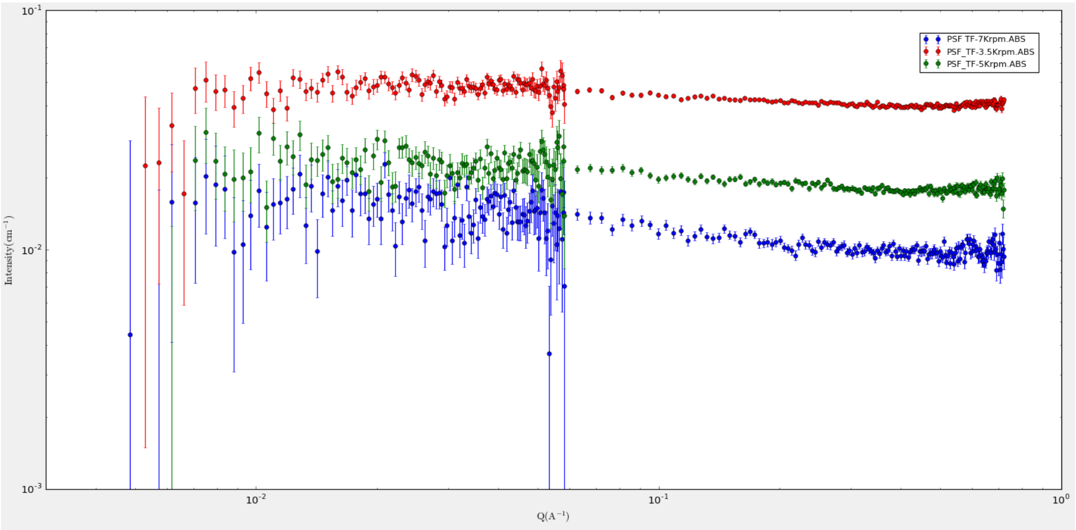

Figure S8u: Real time SANS scattering in the VFD for toluene-d8 in a PSF coated 20 mm OD quartz rotated at 3.5k, 5k and 7k rpm (using 5, 2 and 1 mL of toluene-d8, respectively), for 2 hours at room temperature, θ = 45°.

9. BSA polymerisation with glutaraldehyde

The process for fabricating macroporous spheroidal particles using the VFD involved adding specific volumes of ethanol solution to a specified volume of BSA using the de-solvation method at 1 mg/mL at room temperature as a slightly modified published process.[2] As shown in Figure S9a, in a 'standard' VFD (20 mm OD, 17.5 mm ID, length 18.9 cm), volume combinations for BSA (1 mg/mL in 10 mM PBS), ethanol, and glutaraldehyde were 300, 900, and 15 µL, respectively. Then, 1 mL of a combined solution was quickly transferred to the VFD and the glass tube was spun at 3k, 5k, 6k, 7k or 9k rpm for 1 min. For the VFD housing a 'small' VFD tube (10 mm OD, 8.5 mm ID, length 19.9 cm), volume combinations for BSA (1 mg/mL in 10 mM PBS), ethanol, and glutaraldehyde were the same as for 20 mm OD VFD tube. Then, 0.5 mL of the combined solutions was quickly transferred to the 10 mm tube which was spun at 3k, 5k, 6k, 7k or 9k rpm for 1 min. Post VFD processing, samples were recovered by centrifugation at 11800 g for 15 min and washed with the same volume of MilliQ water three times to remove excess reactants.

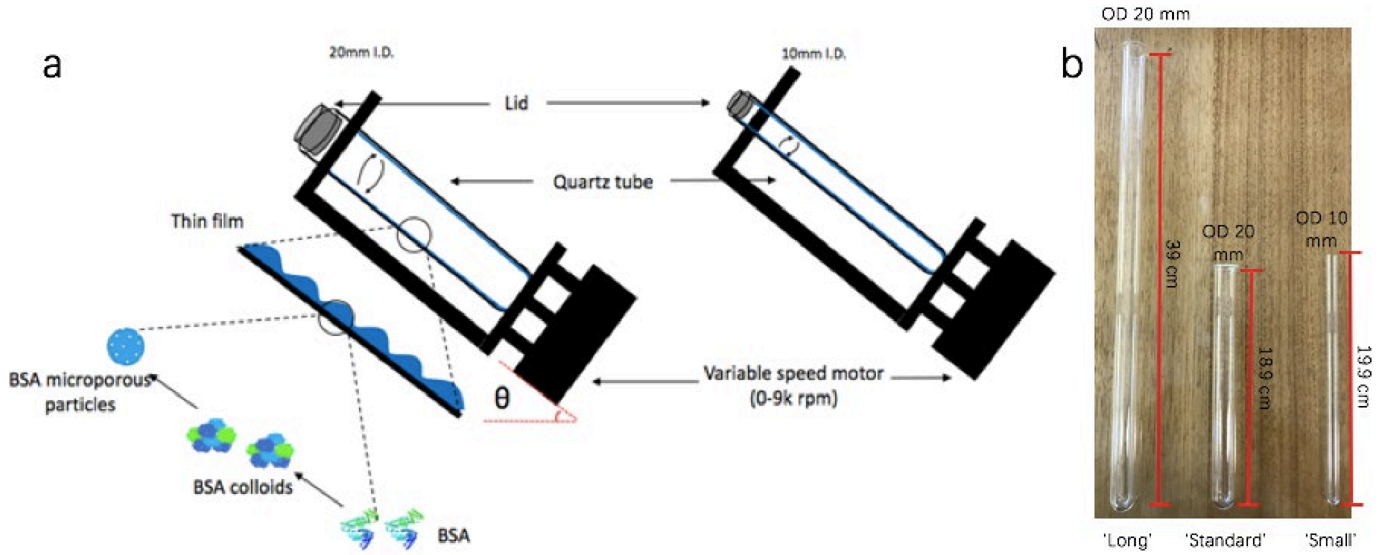

Figure S9a: (a) Schematic of the preparation of BSA nanoparticles in a standard VFD (20 mm OD, 17.5 mm ID) and a VFD (10 mm OD, 8.5 mm ID) operated under confined mode of operation, at θ = 45°. (b) Photo of the VFD tubes in three different dimensions labelled as 'Long' for a long VFD tube (20 mm OD, 17.1 mm ID, 39 cm length), 'standard' for a standard length VFD tube (20 mm OD, 17.5 mm ID, 18.9 cm length) and 'Small' for a small diameter VFD tube (10 mm OD, 8.5 mm ID, 19.9 cm length).

Reaction of BSA with glutaraldehyde in the VFD in a 3:1 mixture of ethanol and PBS (10 mM dissolved in MilliQ water) results in polymeric spheres with inbuilt porosity.[2] Synthesis of homogeneous spheroidal BSA nanoparticles applies to both 10 mm and 20 mm VFD for all the explored rotational speeds, 3k, 5k, 6k, 7k and 9k (Figure 4 and Figure S9b). The average size of the spheres fluctuates slightly from 3k to 9k in both 10 mm and 20 mm OD VFD tubes (Figure S9b). The size of the porous spheres is *ca*. 10-30% less for the 10 mm OD tube relative to the 20 mm tube, except at 3k rpm (Figure S9c(a)). Particle size [dynamic light scattering (DLS)] was determined using a Malvern particle size analyzer (Malvern Zetasizer). The results for material prepared in a 'standard' 20 mm OD and 'small' 10 mm OD VFD tube are compared with results obtained previously using a 'long' VFD tube[2] (diameter *ca.* 358 to 600 nm), with the particles prepared in the 'standard' and 'short' tubes less monodispersed in solution (Figure S9c(b)) compared to those prepared in the long VFD tube.[2] Agglomeration was observed when samples were dispersed in MilliQ water. On the other hand, VFD generated macroporous BSA nanoparticles are always more uniform in size relative to using conventional benchtop vortex mixing (0.5 mL or 1 mL) (Figure S9c(b,c)), affording spheres with less inbuilt porosities, no inbuilt porosities and irregular microsized structures (Figure S9d(a,b)). The results are consistent with the DLS (Figure S9c(c)) and previously published result.[2]

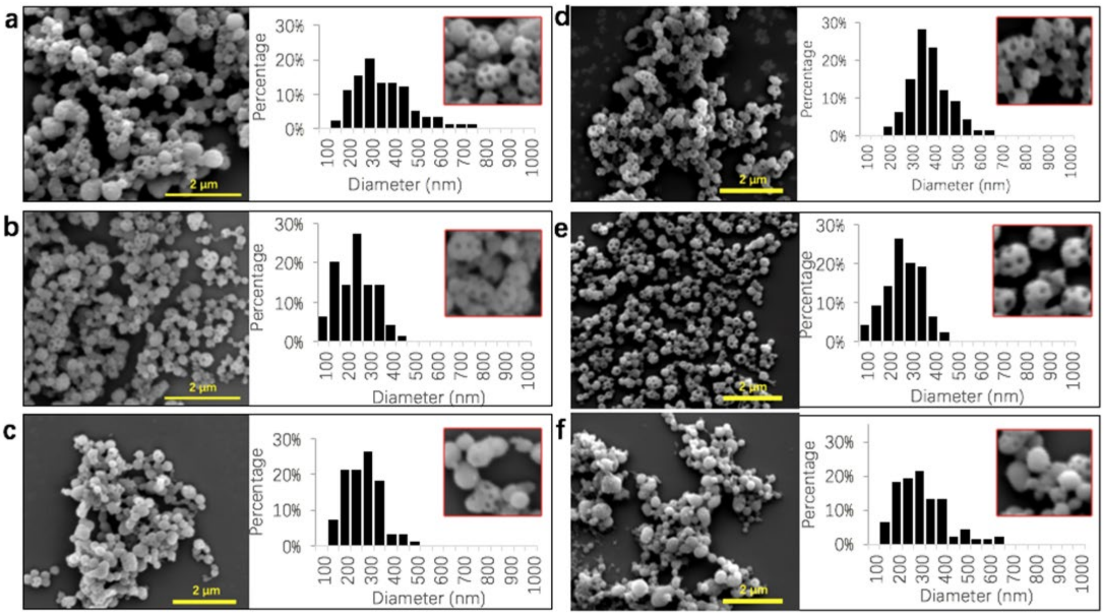

Figure S9b: SEM images of BSA nanoparticles fabricated in the VFD for 1 min with BSA (1 mg/mLin 10 mM PBS), ethanol and glutaraldehyde of 300 μL, 900 μL and 15 μL, respectively. 0.5 mL of combined solution in a 10 mm OD tube at 3k, 5k and 7k rpm (a) – (c) respectively, and 1 mL of combined solution for a 20 mm OD tube, at 3k, 5k and 7k rpm (d) – (f) respectively, reporting SEM images and derived particle size distributions from 100 randomly chosen spheres.

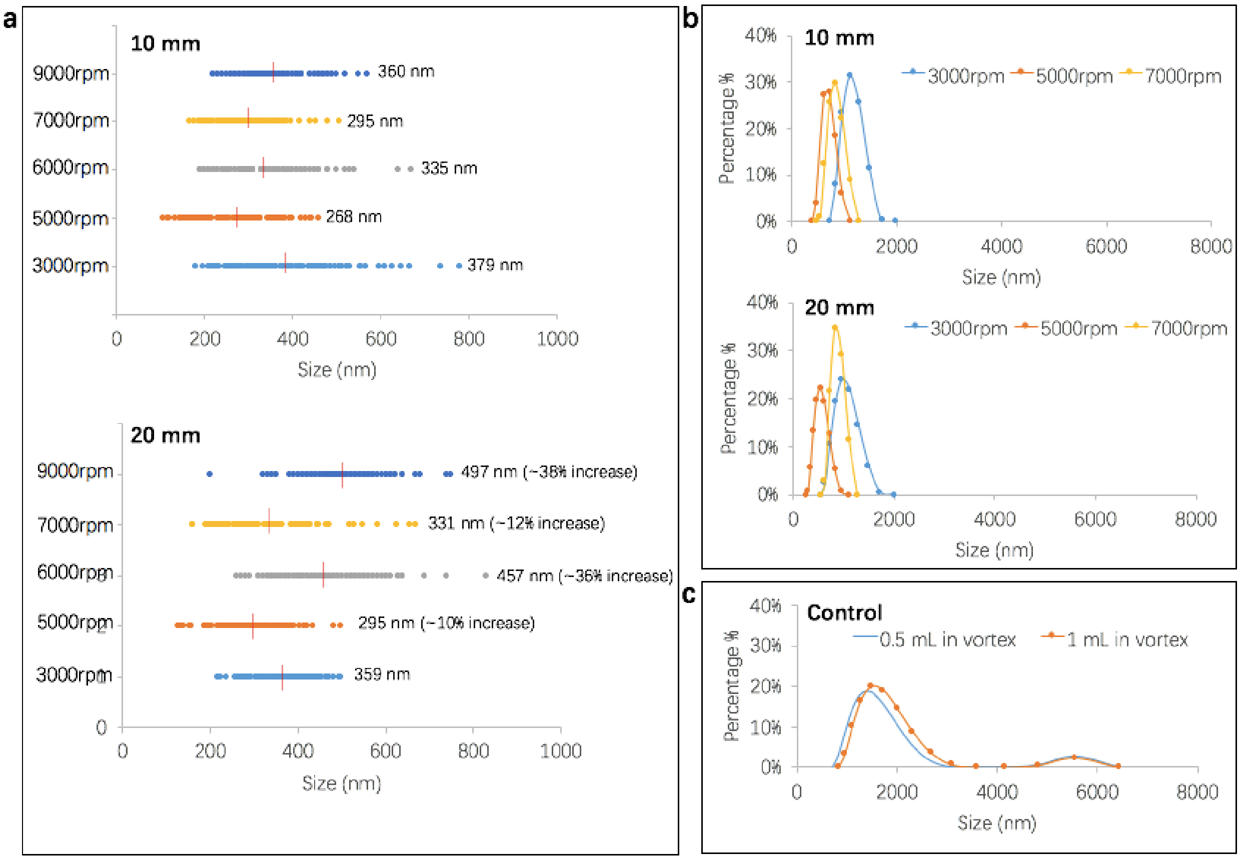

Figure S9c: (a) Size distribution of BSA nanoparticles (based on SEM) prepared in 10 and 20 mm OD VFD tubes rotating at 3k, 5k, 6k, 7k or 9k rpm, respectively. The average sizes of the particles are shown behind each condition, with the percentage of size increment for a 20 mm OD VFD tube shown in brackets relative to those prepared in a 10 mm OD VFD tube, and highlighted as red dash lines. (b) DLS of BSA nanoparticles prepared in 10 and 20 mm OD VFD tubes (c) DLS of BSA nanoparticles prepared using bench-top vortex. Controls were prepared in two volume combinations, in either 0.5 mL or 1.0 mL, which is equivalent to VFD processing.

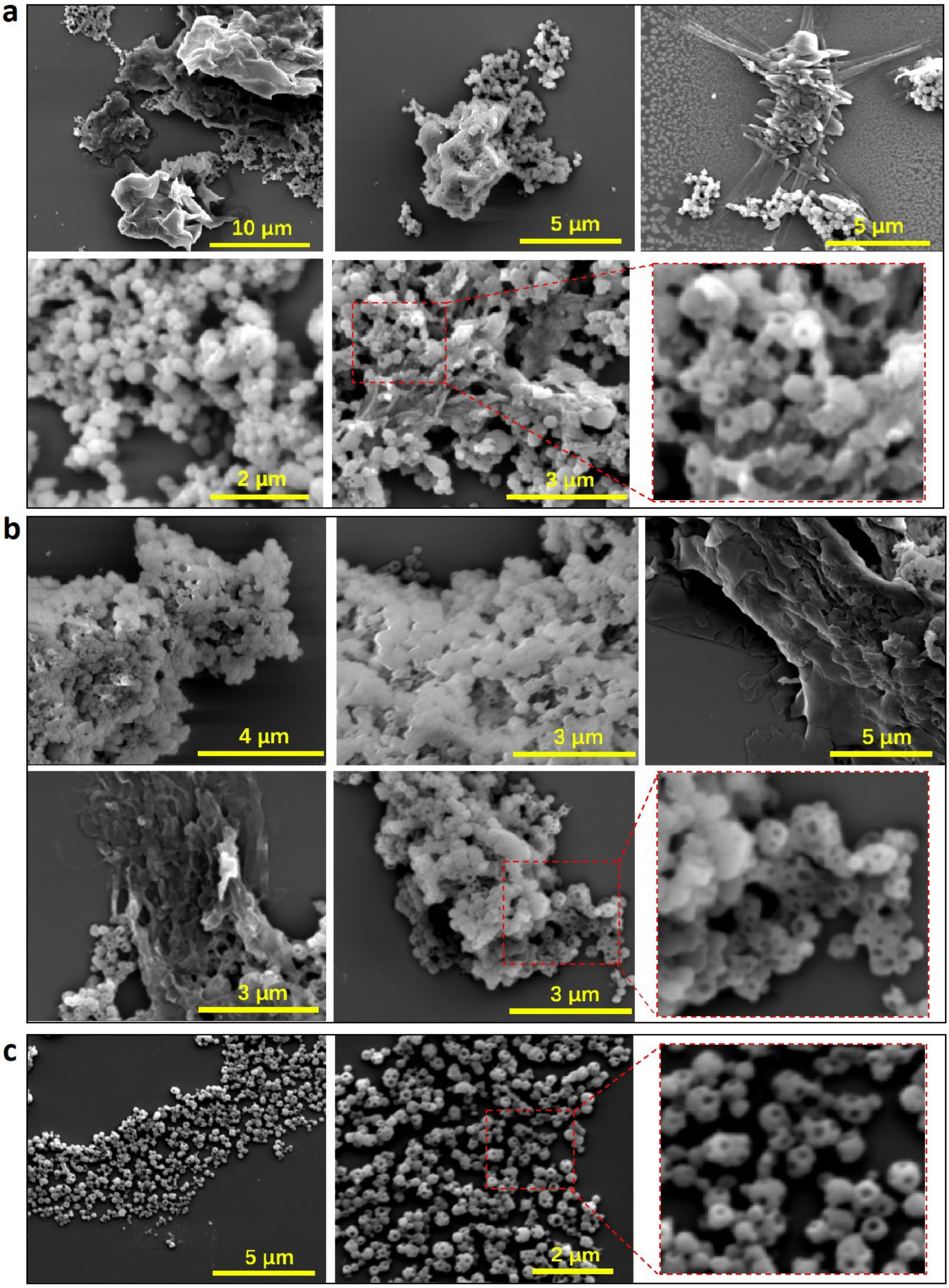

Figure S9d: SEM images of the BSA nanoparticles fabricated for 1 min from BSA (1 mg/mL in 10 mM PBS), ethanol and glutaraldehyde, for 300, 900 and 15 µL, respectively (a) and (b) SEM of material formed in 0.5

mL or 1 mL respectively, of combined solution using a bench-top vortex, compared to (c) using 1 mL of combined solution in a 20 mm OD VFD tube rotating at 5k rpm.

10. MOF-5 fabrication

Conventional nano-molding technology (NMT) or injection moulding is a method of producing polymeric products of all shapes and sizes with nanoscale dimensions.[3] Different from conventional NMT, the fluid flow in the VFD is used to fabricate micron/sub-micron particle, as new concept in nano-moulding. To mould the liquid of flow, several material systems were utilized. Porous metal organic frameworks (MOFs) feature in the VFD moulding experiments, focusing on MOF-5 or $Zn_4O(BDC)_3$ which normally forms crystals with cubic morphology.[4]

The fabrication of MOF-5 using VFD was conducted as previously published method with modifications.[5] A solution of $Zn(OAc)_2 \cdot 2H_2O$ (85.2 mM), H_2BDC (33.56 mM) and TEA (67.13 mM) in 1 mL DMF was prepared and allowed to react in the VFD. Briefly, H_2BDC (63.3 mg) and TEA (106.3 µL) were dissolved in 4.894 mL of DMF. $Zn(OAc)_2 \cdot 2H_2O$ (169.9 mg) was dissolved in 5 mL of DMF. For a typical VFD experiment, 556 µL of zinc solution was added to 444 µL H_2BDC followed by 20 mm VFD processing for 30 min at a temperature as indicated. The synthesis of MOF-5 involving VFD processing is based on the observation of phase purity and crystal morphology, using XRD and SEM. Post-VFD processing at 110ºC there was some material adhering to the surface of the tube ($MOF_{surface}$) with the rest falling to the bottom of the tube (MOF_{tube}) (Figure S10a). In this case, the two samples were separately collected and mounted on silicon wafer for SEM imaging. To minimise exposure to humid air, silicon wafers with mounted samples were quickly dried in oven at 110ºC, followed immediately by SEM imaging.

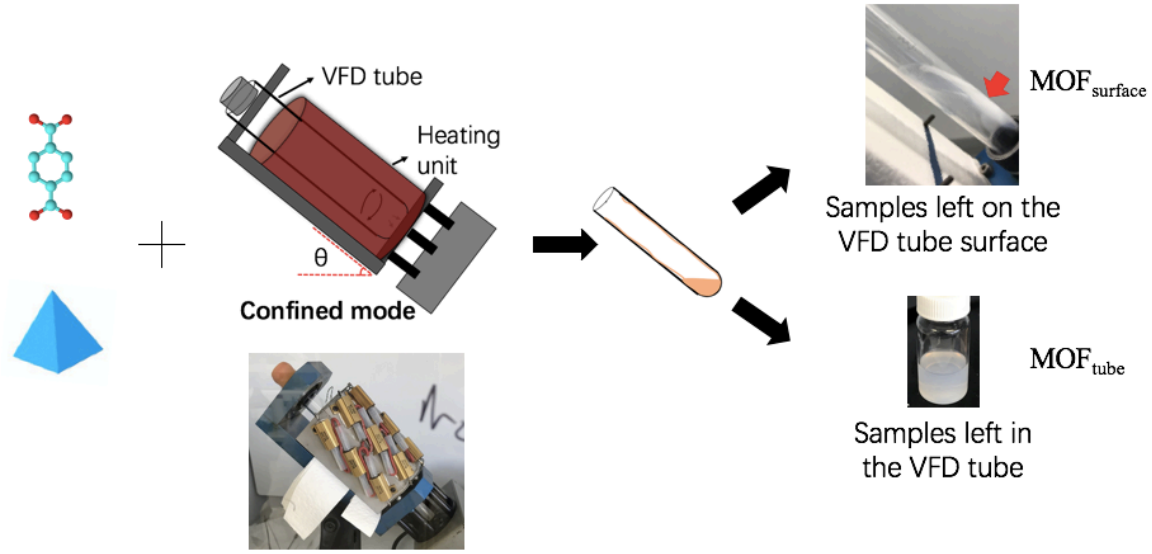

Figure S10a: Schematic of the synthesis of MOF5. H_2BDC (63.3 mg) and triethylamine (106.3 µL) were dissolved in 4.894 mL of DMF. $Zn(OAc)_2 \cdot 2H_2O$ (169.9 mg) was dissolved in 5 mL of DMF. For a typical VFD experiment, 556 µL of zinc solution was added to 444 µL H_2BDC followed by VFD processing in a 20 mm OD tube for 30 min at 110ºC. Post-VFD processing, MOF$_{surface}$ material was separated from MOF$_{tube}$ material collected at the bottom of the tube.

MOF-5 is commonly prepared using solvothermal method by heating a mixture of H_2BDC and zinc nitrate.[6] However, this involves long processing times, hours to weeks.[5] Tranchemontagne *et al.* reported a method of preparing MOF-5 at ambient temperature over 2.5 h using zinc acetate.[5] Subsequent addition of triethylamine resulted in deprotonation of the H_2BDC and precipitation of MOF-5. This result led to adapting the reaction for the growth of MOF-5 crystals using VFD processing.

To minimise errors associated with exposure to air, sample preparation was first optimised for characterisation using SEM, noting that the morphology of MOF-5 is affected by exposing to water or humid air (Figure S10b(a,b)), in agreement with previous findings.[7] In addition, any residual solvent needs to be rapidly removed post processing, for reproducible purposes (Figure S10b(c)). Therefore, samples were centrifuged at 2350 g for 15 min post VFD processing to separate from the solvent, with the material then mounted on a silicon wafer and carefully dried at the same temperature as that used in VFD processing. VFD processing at 22ºC induces the formation of nanoscale MOF seeds with spherical shape, for all speeds from 3k to 7k rpm, after a reaction time of 30 min (Figure S10c), which showed no significant difference relative to the control experiment conducted without VFD. Increasing the temperature to 60 and 110ºC resulted in cubic crystals, which was barely observed for the control (Figure S10d and S10e). XRD of the material formed in the VFD established that they are MOF-5 by comparing with the pattern simulation from the EVA database (Figure S10f). Operating the processing in the VFD at either 60 or 110ºC had no effect on the phase composition after 30 min of processing, all in a 20 mm OD tube, with θ at 45º.

It was noted that at 110ºC, white materials appeared along the VFD tube surface (named as MOF$_{surface}$) and these were automatically separated from the samples collected from the bottom of the tube (named as MOF_{tube}) after stopping the VFD (Figure S10a). $\text{MOF}_{\text{surface}}$ samples were dominated by porous surfaces, especially at 3, 4 and 5k rpm. Above 5k rpm, the particles have flat surfaces (Figure 4f). Time dependent study for 15, 30 and 60 min VFD processing at 4k rpm, 110ºC all revealed porous crystal surfaces (Figure S10g).

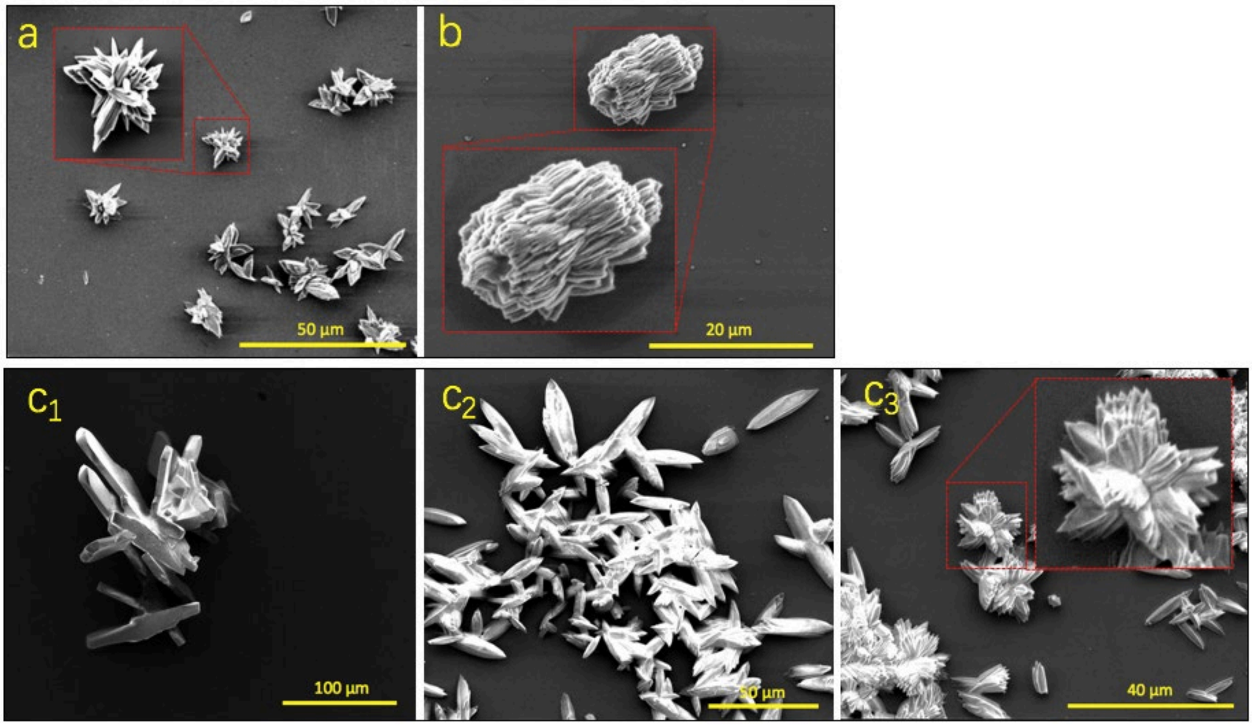

Figure S10b: SEM images of MOF-5, prepared in the VFD at 4k rpm for 30 min. (a) Post VFD processed material, where the sample for SEM was prepared by quickly diluting the solution *ca* 200 times in water, then drop cast on a clean silicon wafer and air dried. (b) As for (a) but with the dilution in DMF, (c) Post VFD processed material, where samples were directly drop cast on a clean silicon wafer without centrifugation and air dried; C_1-C_3 show SEM images from three independent experiments.

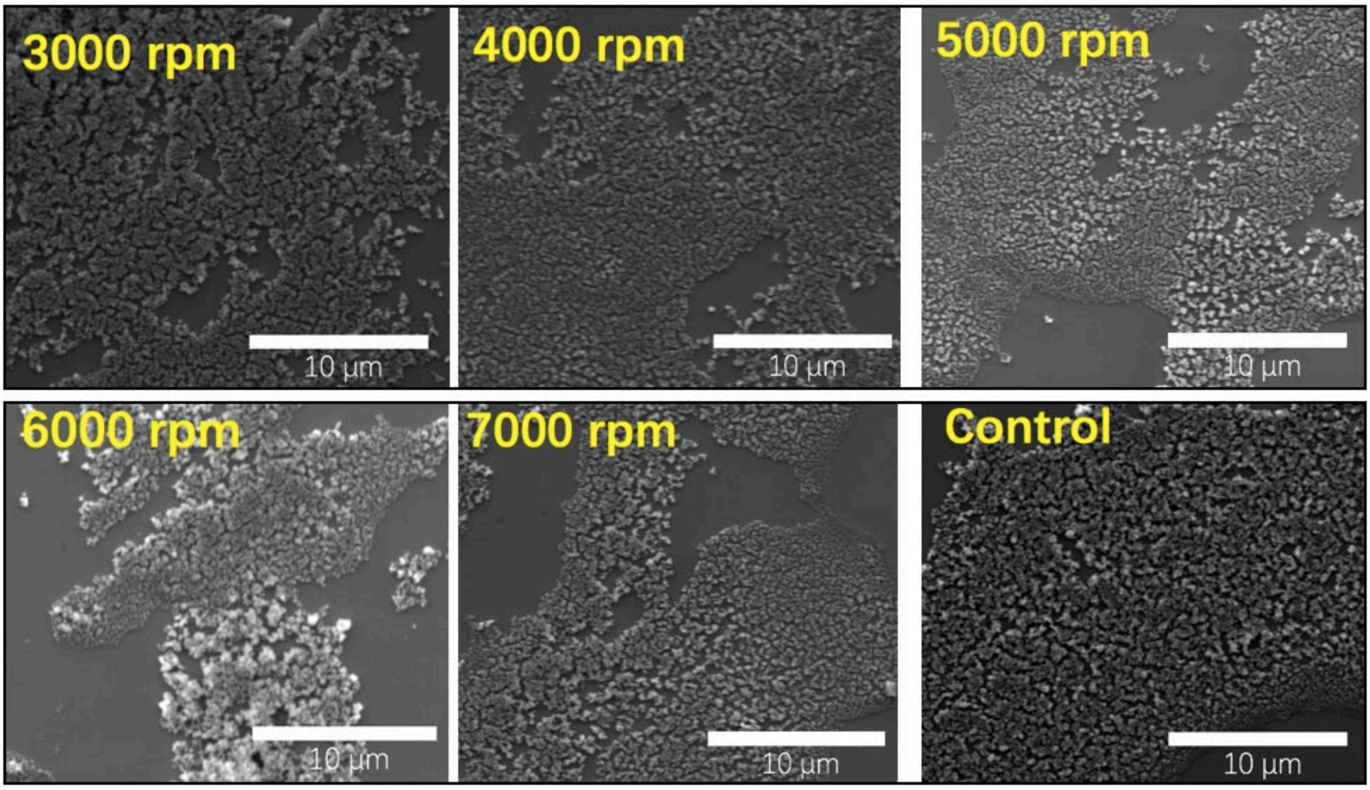

Figure S10c: SEM images of material formed in 1 mL DMF solution of $Zn(OAc)_2 \cdot 2H_2O$ (85.2 mM), H_2BDC (33.56 mM) and TEA (67.13 mM). VFD processing at 22ºC for 30 min, 20 mm OD tube, θ = 45º, for different rotational speeds relative to the control experiment carried out at the same temperature, no VFD. Post processing, MOF_{tube} samples (as specified in Figure S10a) were centrifuged at 2350 g for 15 min with some of the collected pellet drop cast on a silicon wafer and dried at 22ºC prior to SEM characterisation.

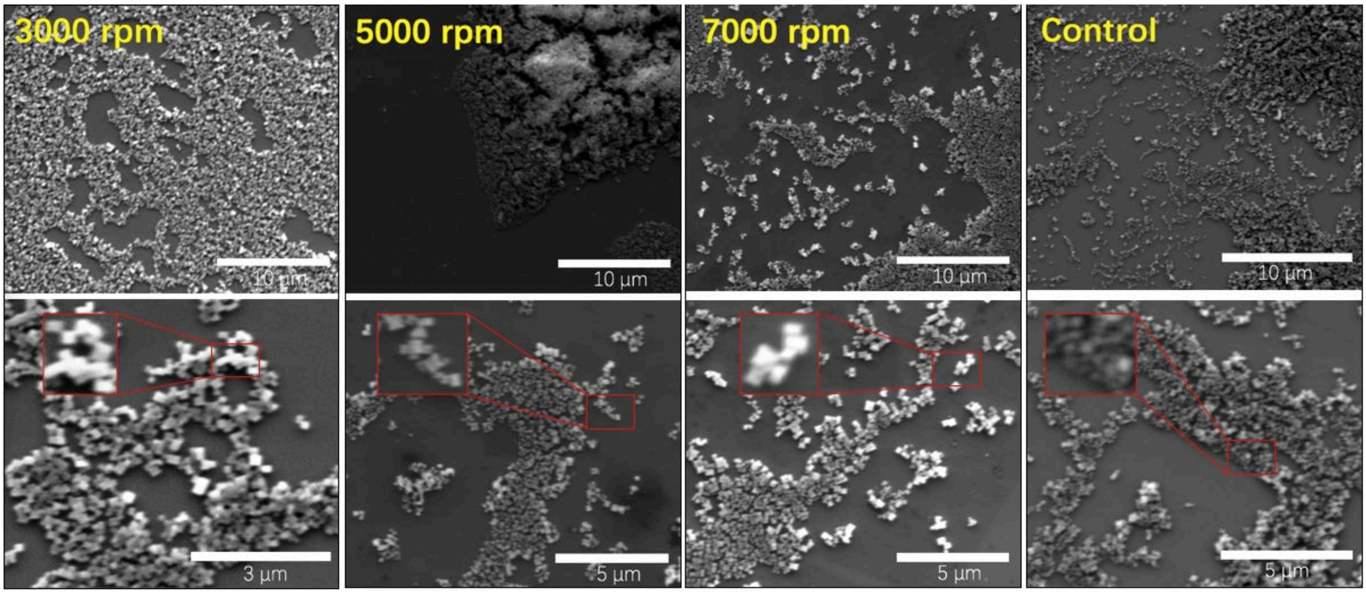

Figure S10d: SEM images of material prepared in a 1mL DMF solution of $Zn(OAc)_2 \cdot 2H_2O$ (85.2 mM), H_2BDC (33.56 mM) and TEA (67.13 mM). VFD processing at 60ºC for 30 min, 20 mm OD tube, θ = 45º, for different rotational speeds relative to the control experiment carried out at the same temperature, no VFD. Post processing, MOF_{tube} samples (as specified in Figure S10) were centrifuged at 2350 g for 15 min, with some of the collected pellet drop cast on a silicon wafer and dried at 60ºC prior to SEM characterisation.

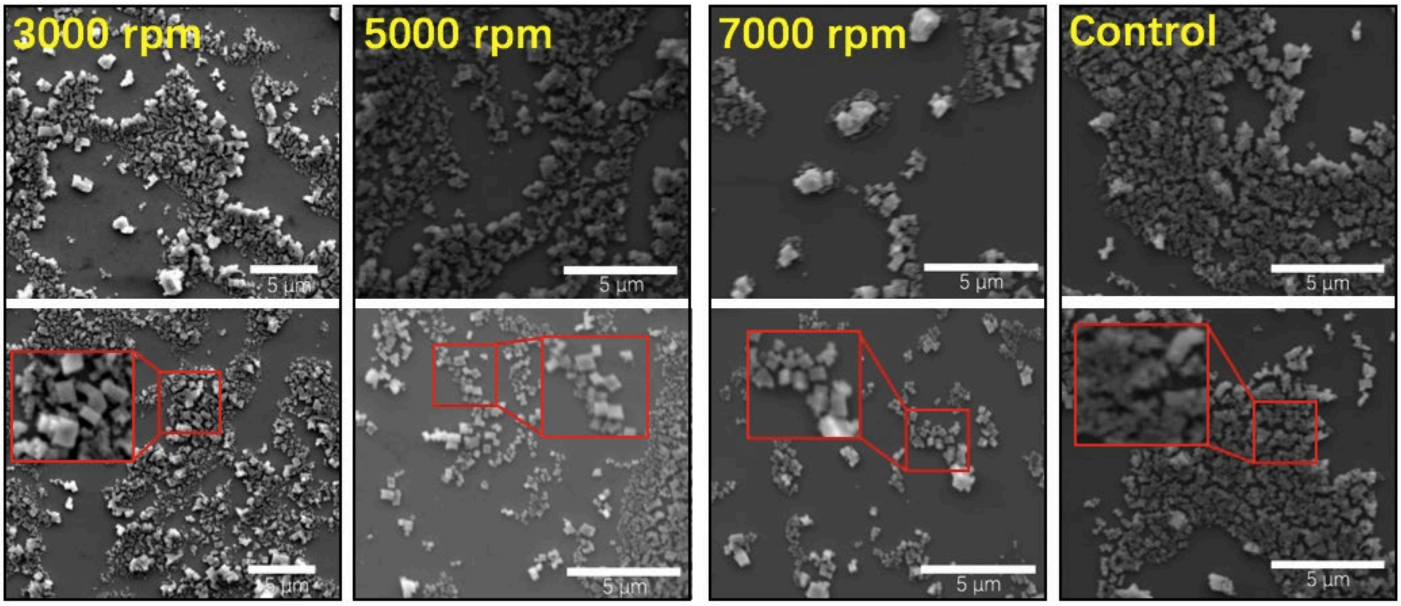

Figure S10e: SEM image of material prepared in a 1 mL DMF solution of $Zn(OAc)_2 \cdot 2H_2O$ (85.2 mM), H_2BDC (33.56 mM) and TEA (67.13 mM). VFD processing at 110ºC for 30 min, 20 mm OD tube, θ = 45º, for different rotational speeds relative to the control experiment carried out at the same temperature, no VFD. Post processing, MOF_{tube} samples (as specified in Figure S10) were centrifuged at 2350 g for 15 min, with some of the collected pellet drop cast on a silicon wafer and dried at 110ºC before SEM characterisation.

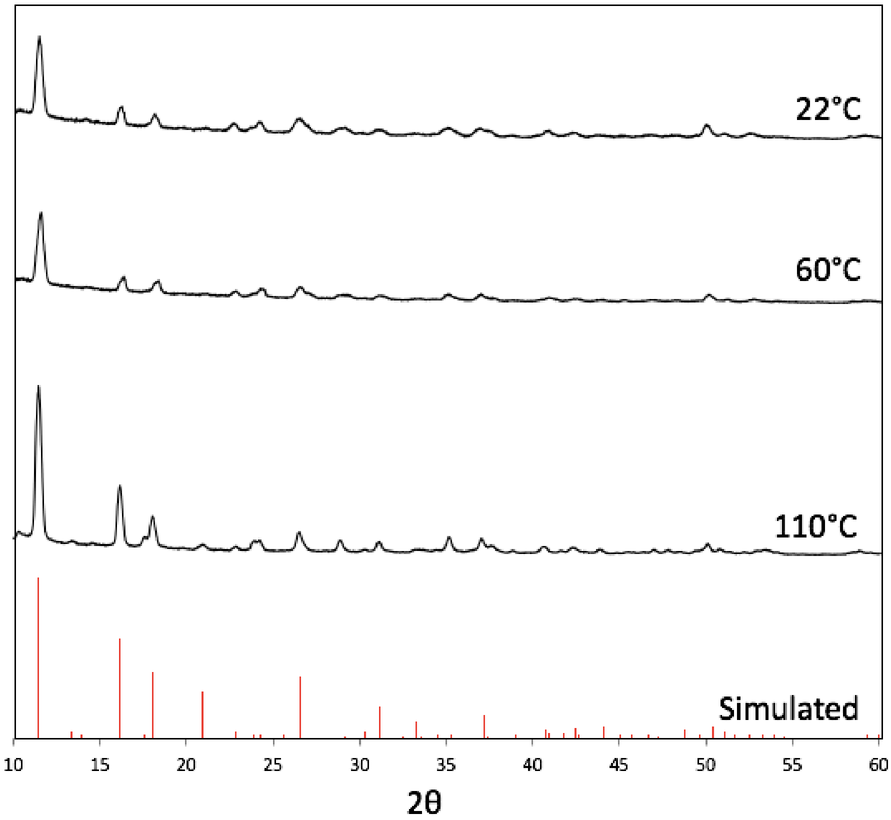

Figure S10f: XRD pattern of MOF-5 prepared using VFD (MOF_{tube}), formed at ω = 5k rpm for 30 min at 22, 60 or 110ºC, respectively, θ = 45º, for a 20 mm OD tube, along with the simulated pattern for the MOF derived from the EVA database.

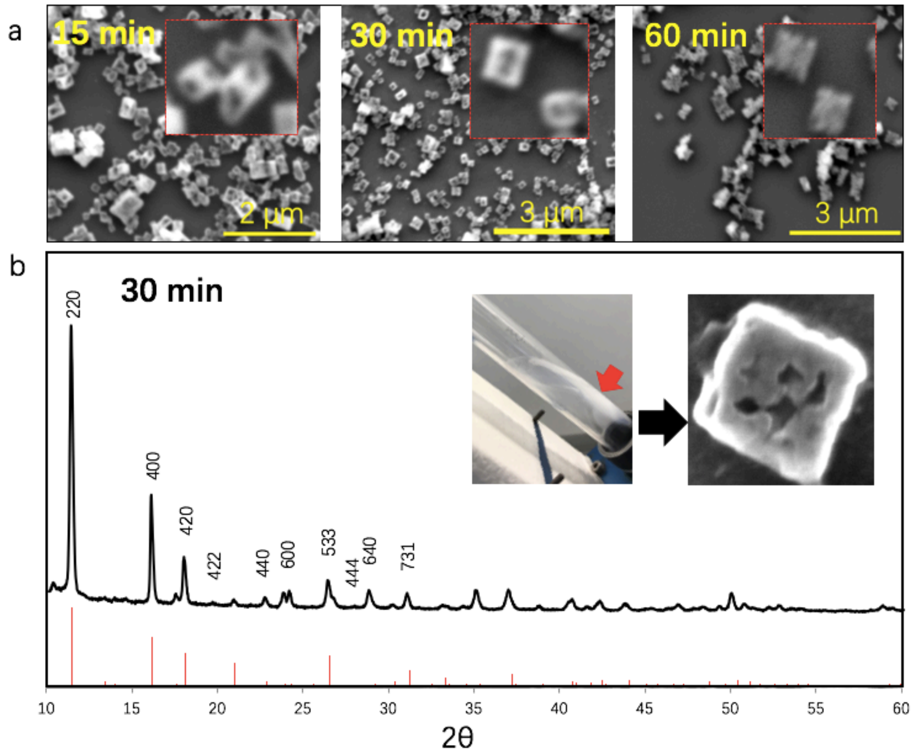

Figure S10g: (a) A solution of $Zn(OAc)_2{\cdot}2H_2O$ (85.2 mM), H_2BDC (33.56 mM) and TEA (67.13 mM) in 1 mL DMF was prepared and processed in the VFD (confined mode, 20 mm OD tube) at 110ºC for 15 min, 30 min and 1 h, ω = 4k rpm, θ = 45°, with the resulting $\mathrm{MOF}_{\mathrm{surface}}$ sample characterised using SEM. (b) XRD pattern of MOF-5 ($\mathrm{MOF}_{\mathrm{surface}}$) formed after 30 min at 110ºC and the simulated structure derived from the EVA database.

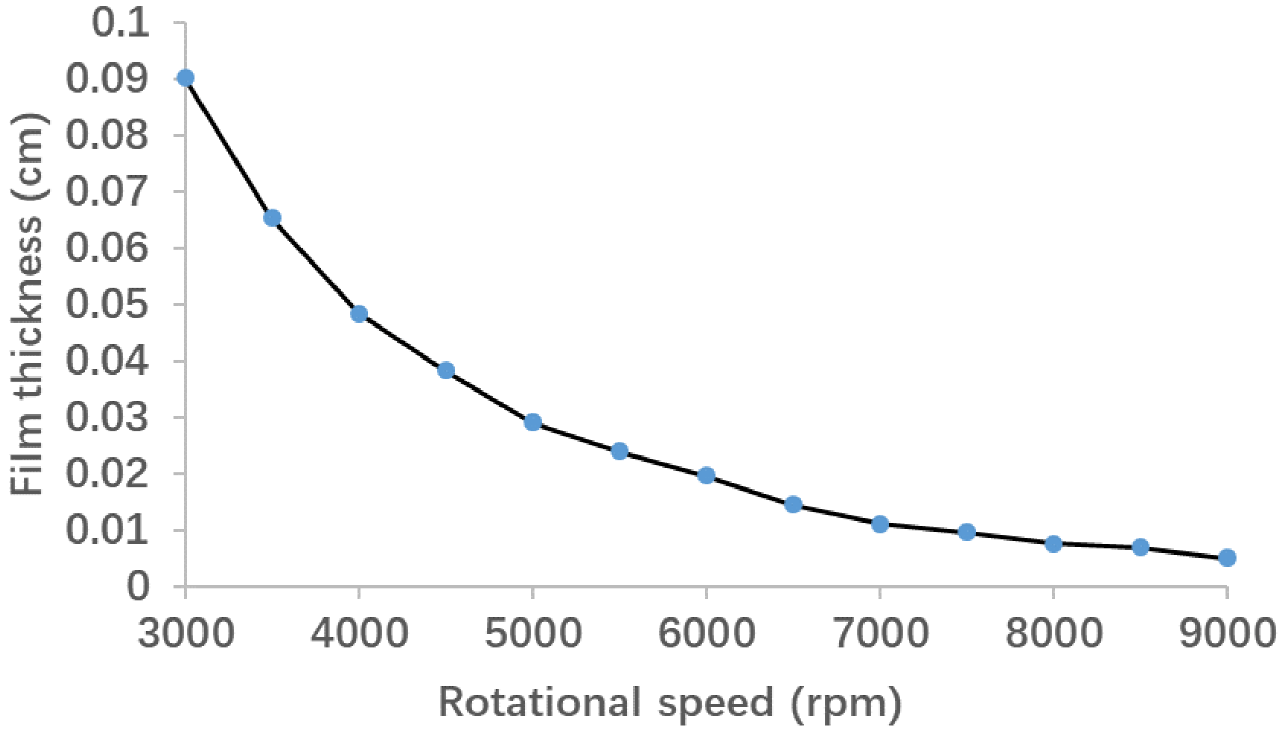

Figure S10h: The change in film thickness, *d*, for DMF as a function of rotational speed, ω, at 110ºC in a 20 mm OD tubes, at θ = 45°. This is derived from measuring the volume of the liquid in the tube at each speed, where the liquid is to the top of the tube while being spun at a particular ω, with each data point repeated in triplicates. The experimental set up with a heating block over the rotating glass tube, circumvented determining the other signature characteristics of DMF at 110ºC, namely any increasing in temperature and effects on mixing as ω increases.

11. Fluid Dynamics within the Vortex Fluidic Device

In order to further explain the fluid dynamics within the VFD, computational fluid dynamics (CFD) simulations have been conducted using the OpenFoam v1806[8]. In order to build a practical simulation to investigate the fluid dynamics within the VFD, a thin-cross section of the VFD tube perpendicular to the axis of rotation was modelled. The CFD simulation was reduced into 2D by considering a thin slab, *d*=100 nm (1 cell thickness). This meshing of the cylindrical slab in the *xy*-plane was divided in two regions (see Figure S11a). Here we have a high resolution mesh region (Region 1, 100 x 100 cells) and a low resolution mesh region (Region 2, 100 x 100 Cells). Region 2 describes the internal volume of the cylinder, with radius 8.3 mm, while region 2 describes the volume outside of Region 1 to the internal test tube wall, r = 8.75 mm. The high resolution mesh at the outermost radii was required in order to describe the thin liquid film located on the test tube wall. The outside wall of Region 1 provided a rotational wall boundary condition about the VFDs axis of rotation (*z*-axis). Here the rotational wall velocity, ω, corresponds to the rotational speed of the VFD tube. The interFoam solver was select to perform the simulations. This solver implements a volume of fluid (VOF) phase-fraction based approach to solve the continuity, phase-fraction transport, and momentum equations. Here the alpha phase fraction, proportions a cell between the liquid (water or toluene, α=1) and gas (air, α=0) phase fractions.

The simulation was run using a fixed volume of fluid method, initiated by filling the outermost cylindrical section with fluid (α = 1) for radii, r >8.55 mm (giving a uniform thickness liquid layer of 200 µm). The calculation was implemented using α = 1 and constant pressure boundary conditions on the inner tube wall.

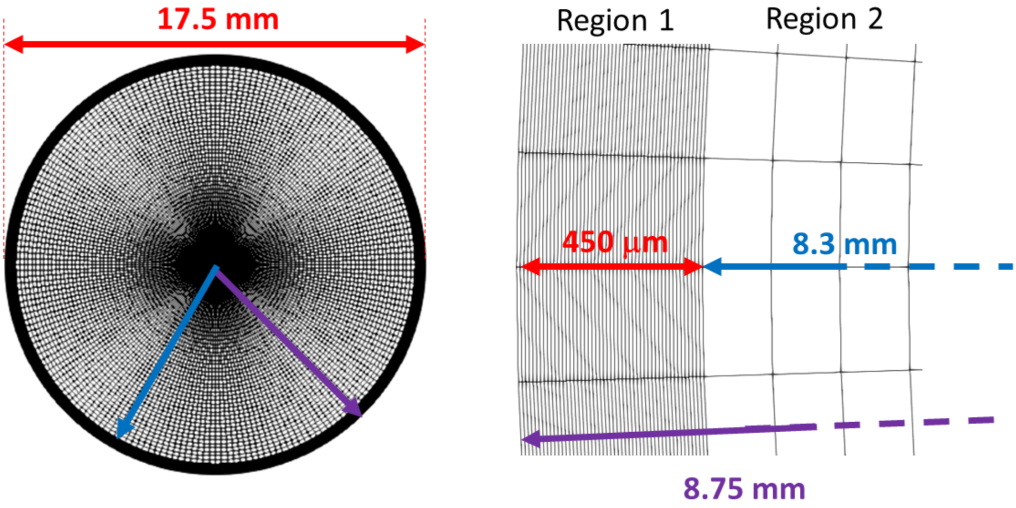

Figure S11a: The mesh of the VFD tube used for the CFD simulations.

In analysing the results, the relative flow velocity ($\boldsymbol{u_r}$) (in the rotating frame of reference) is first considered;

$$\boldsymbol{u_r} = \boldsymbol{u} - \boldsymbol{\omega} \times \boldsymbol{r}$$

Here $\boldsymbol{u}$ is the calculated fluid velocity (m/s) in the inertial reference frame, $\boldsymbol{\omega}$ is the angular velocity vector (rad/s) and $\boldsymbol{r}$ is the radial vector from the axis of rotation (m). Note that the relative velocity is important, as it is responsible for the introduction of Coriolis effects through the creation of the Coriolis force per unit mass in the rotating frame, where

$$\boldsymbol{F_{Cor}} = -\boldsymbol{2\omega} \times \boldsymbol{u_r}$$

Results from the CFD simulations are presented in Fig. S11b-d and Fig. S11e-g for water and toluene at 3000, 6000 and 9000 rpm, respectively.

At low rotational speed (3000 rpm), the relative velocity, $\boldsymbol{u_r}$, oscillates between being parallel and antiparallel to the rotational direction. Here the orientation is parallel (anti-parallel) at the bottom (top) of tube with reference to the gravitational projection. This is likely to induce the Coriolis-driven circular flows, with the strength of the relative velocity component increasing in going from the tube wall towards the fluid-air interface. Note that as the viscosity of the fluid increases, the relative velocity will decrease in magnitude, lessening the importance of the Coriolis forces (as in a 3:1 ethanol/water mixture), and hence circular flows.

As the rotational speed increases to 6000 rpm, these effects remain, but the magnitude of the relative velocity is decreasing. This will manifest as a reduced influence of the Coriolis force on the fluid flow, which is consistent with the dominance of double helical flow at high ω. Note further that as the rotational period of the fluid decreases, the time/lengths scales over which the Coriolis forces are able to act decreases.

As the rotational speed is increased to 9000 rpm, the relative velocity, $\boldsymbol{u_r}$, is always anti-parallel to the rotational direction. In this case, the Coriolis force is always directed radially outwards. As such we expect that there is a fluid movement along the tube axis.

The Reynolds number of the fluid flow[9],

$$Re = \frac{uD}{\nu}$$

Where $D = \frac{4A}{p}$ is the hydraulic diameter with A being the cross sectional area of the flow, and *p* being the wetted perimeter. In our case, this characteristic length (D) becomes four times the film thickness, *t*. Note that the film thickness depends on the fluid volume in the tube, and the rotational speed. The film thickness also varies along the tube axis. For the purpose of the analysis, the average film thickness is set at 200 µm, to be consistent with our simulations. The calculated Reynolds number for both water and toluene are contained in Table S11a. Here we observe that at the lowest rotational speeds, the flow should be laminar. With the increasing rotational speed, a transitional flow region (*Re* > 2000) prevails, although as Re <10000 it is not expected that the axial flow can develop into a fully turbulent flow regime.

Table S11a: Summary of rotational parameters in the VFD. The Reynolds numbers (Re) are calculated using the Wall velocity, the film thickness of 200 μm and the transport properties detailed in Table S11b.

Rotational Speed (rpm)	ω (rad/s)	*f* (s^{-1})	Period, T (ms)	Wall Velocity, |*U*| (m/s)	*Re* (Water)	*Re* (Tol.)
1000	104.72	16.7	60.00	0.916	733	1078
2000	209.44	33.3	30.00	1.833	1466	2156
3000	314.16	50.0	20.00	2.749	2199	3234
4000	418.88	66.7	15.00	3.665	2932	4312
5000	523.60	83.3	12.00	4.582	3665	5390
6000	628.32	100.0	10.00	5.498	4398	6468
7000	733.04	116.7	8.57	6.414	5131	7546
8000	837.76	133.3	7.50	7.330	5864	8624
9000	942.48	150.0	6.67	8.247	6597	9702

Table S11b: Transport properties used in the simulations.

Phase	kinematic viscosity (ν) (m^2/s)	Density (*ρ*) (kg/m^3)	Surface tension to the air-phase. (*σ*) (N/m)
air	1.48E-5	1	-
water	1E-6	1000	.07
toluene	6.8E-7	867	.03
DMF	8.5E-7	945	.037

Water/Ethanol (1:3)	2.5E-6	855	.025
DMF/*o*-xylene	9.2E-7	909	

Table S11c: Fluid Flow Types.

Liquid Behaviour	Flow transitions
α	Circular → Spicular → Helical
β	Spicular only
γ	Helical only

Table S11c: Flow regimes characterised by the relative strength of the Coriolis $\overrightarrow{(F_{FW})}$ and Faraday wave ($\vec{F}_{FW}$) forces.

Flow Range	Flow transitions
Circular	$\vec{F}_c > \vec{F}_{FW}$
Spicular	$\vec{F}_c \sim \vec{F}_{FW}$
Double helical	$\vec{F}_c < \vec{F}_{FW}$

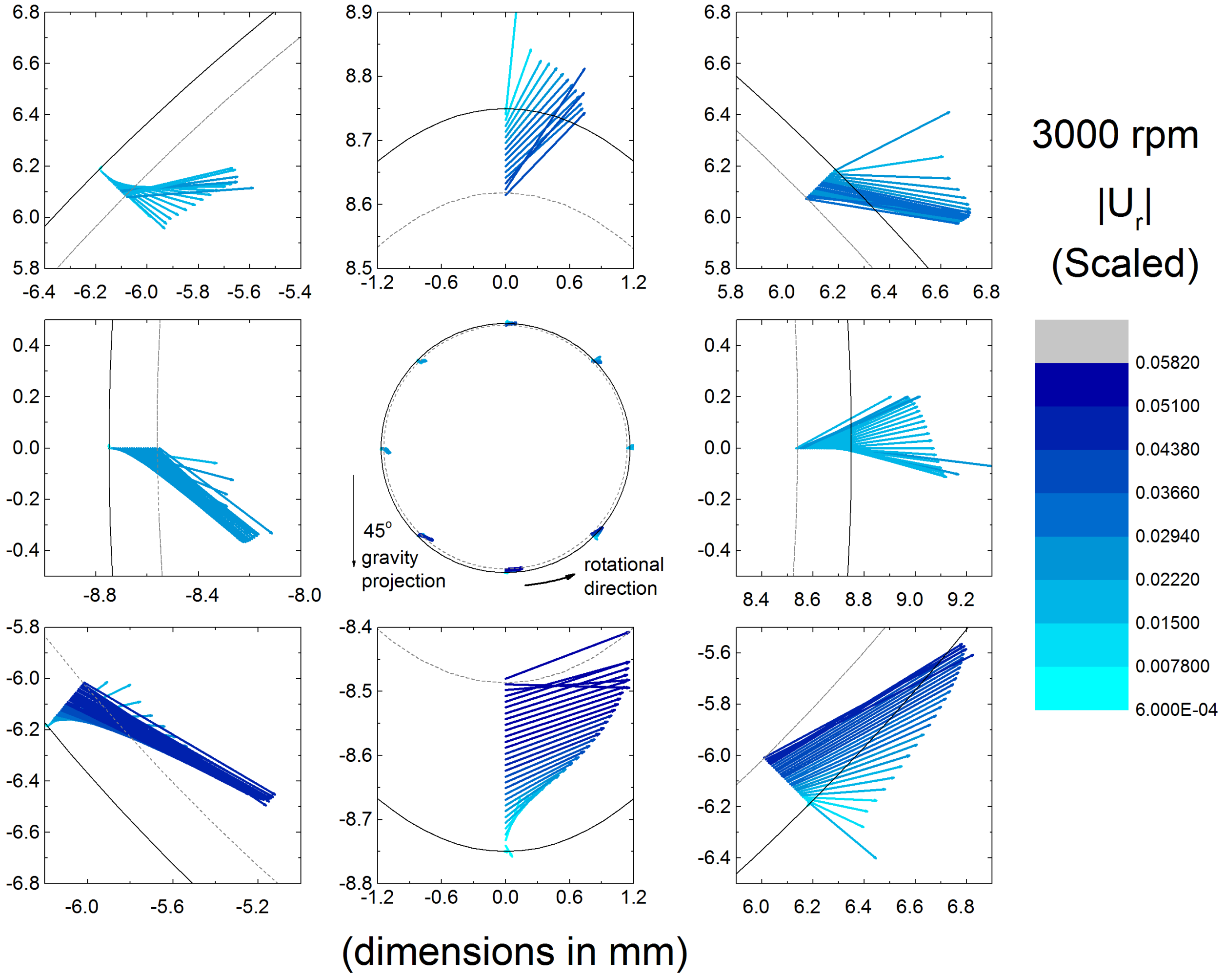

Figure S11b: Relative velocity of water across the film thickness at various angular position about the rotational axis of the VFD at a rotational speed of 3000 rpm and a 45° tilt angle. A scale factor of 0.02 has been applied to the relative velocity vector. Solid line- tube wall, grey dashed line – film profile.

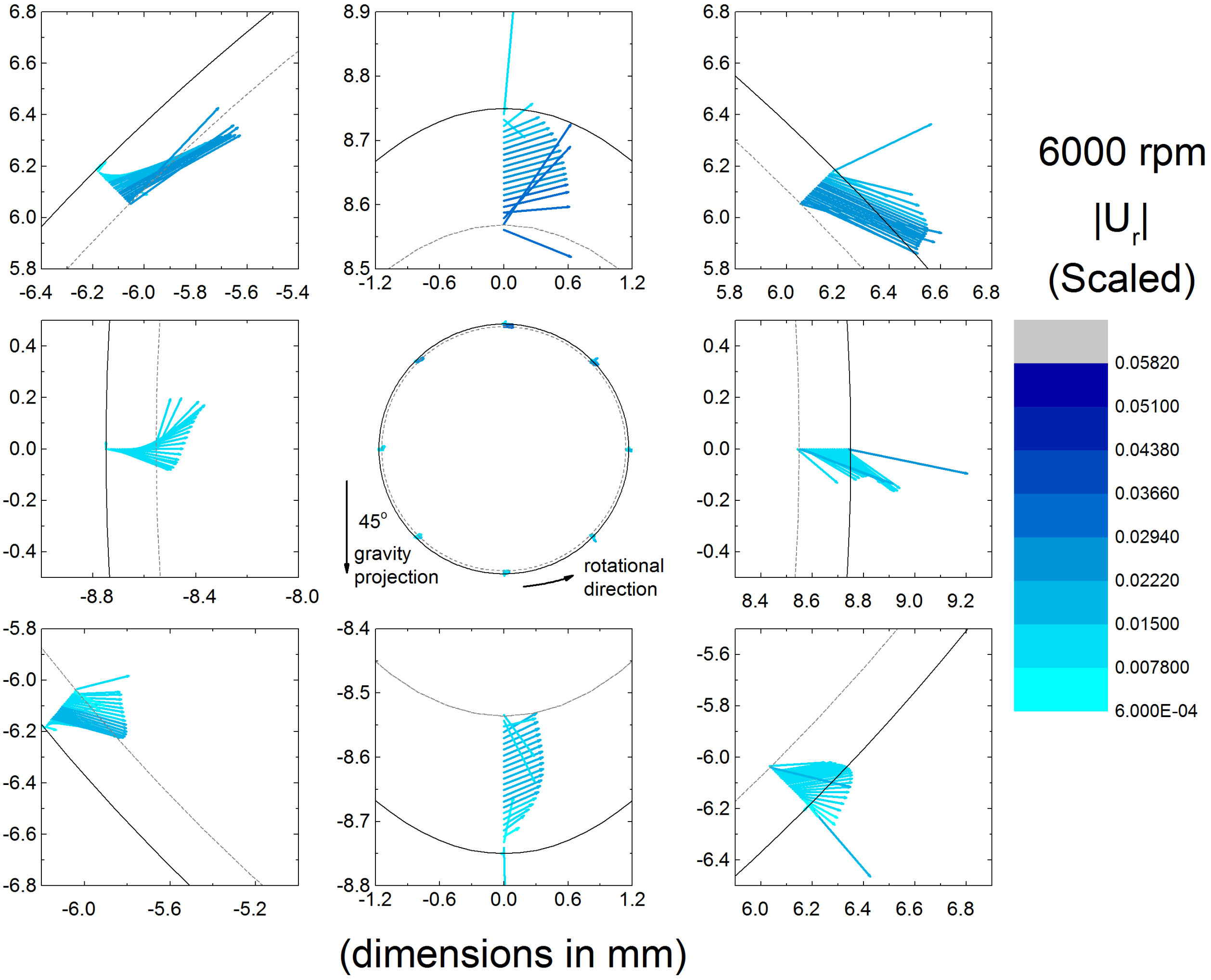

Figure S11c: Relative velocity of water across the film thickness at various angular position about the rotational axis of the VFD at a rotational speed of 6000 rpm and a 45° tilt angle. A scale factor of 0.02 has been applied to the relative velocity vector. Solid line- tube wall, grey dashed line – film profile.

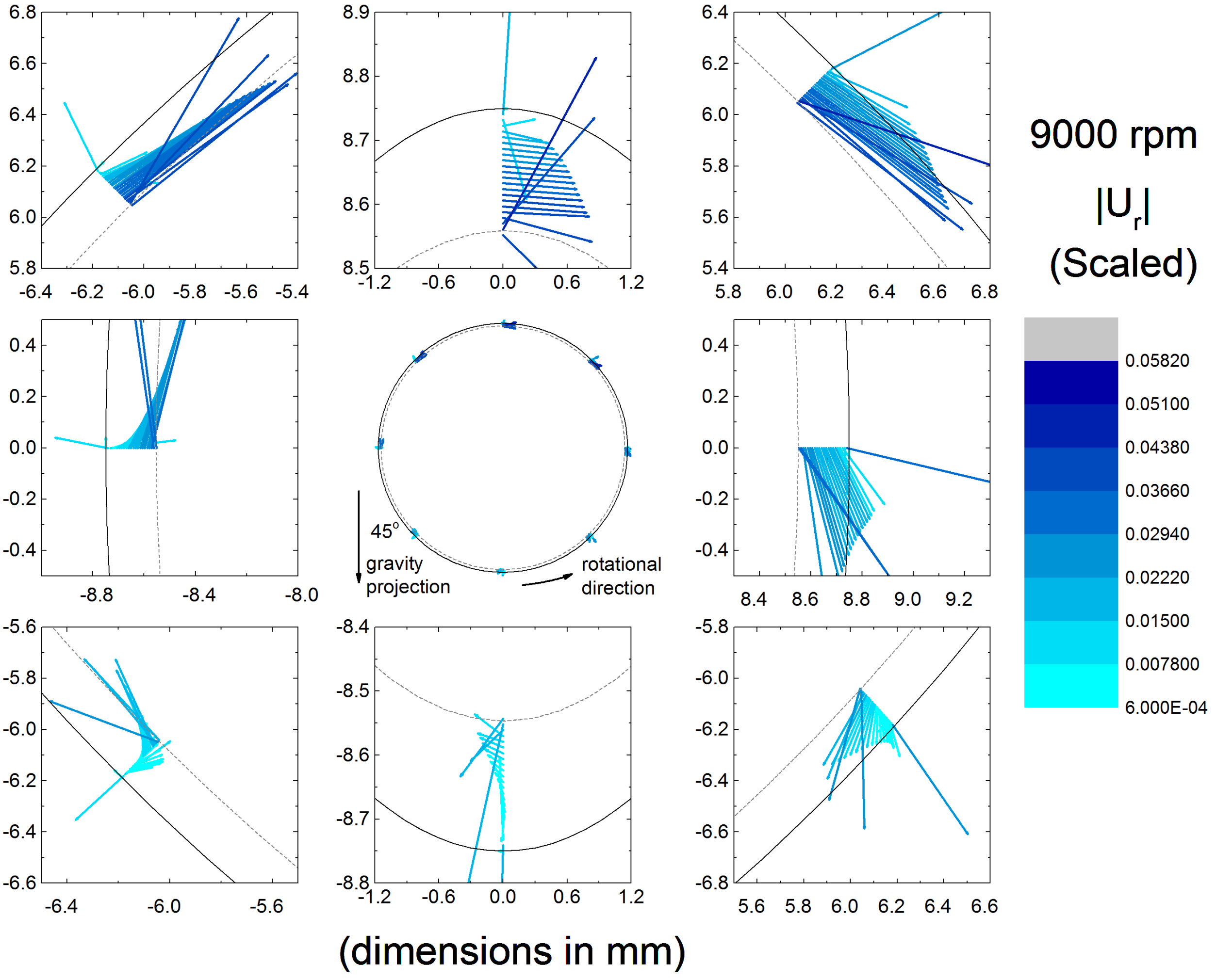

Figure S11d: Relative velocity of water across the film thickness at various angular position about the rotational axis of the VFD at a rotational speed of 9000 rpm and a 45° tilt angle. A scale factor of 0.02 has been applied to the relative velocity vector. Solid line- tube wall, grey dashed line – film profile.

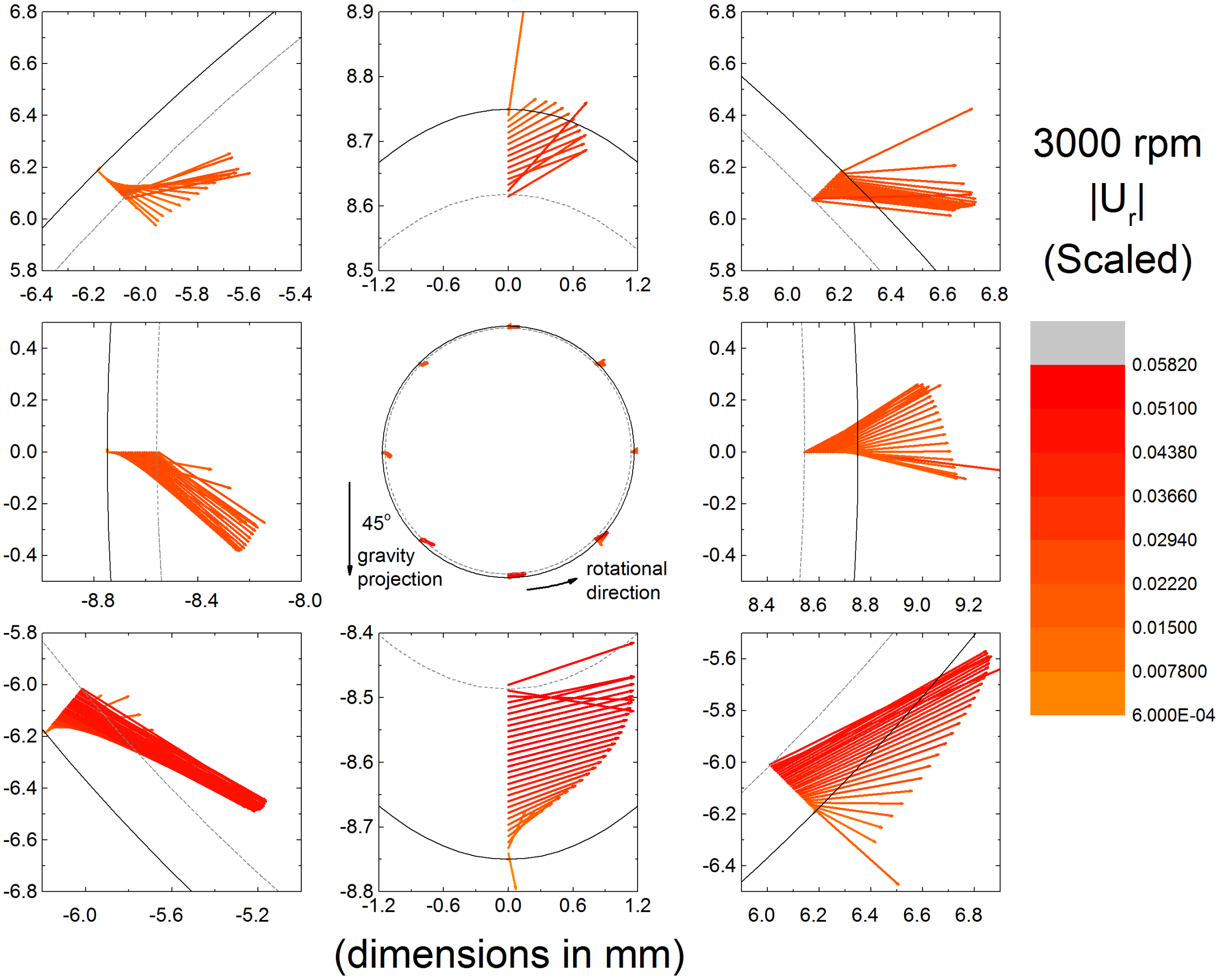

Figure S11e: Relative velocity of toluene across the film thickness at various angular position about the rotational axis of the VFD at a rotational speed of 3000 rpm and a 45° tilt angle. A scale factor of 0.02 has been applied to the relative velocity vector. Solid line- tube wall, grey dashed line – film profile.

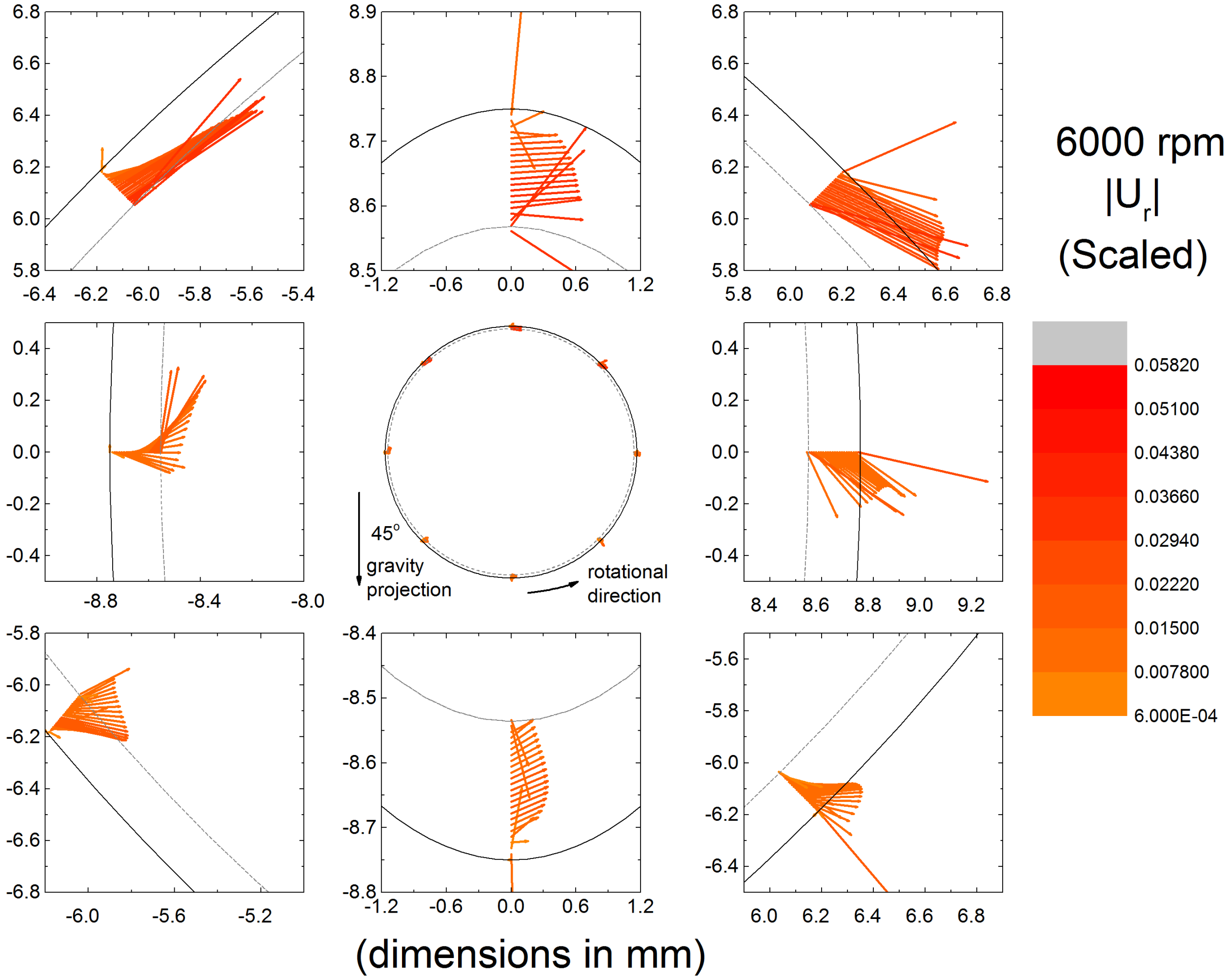

Figure S11f: Relative velocity of toluene across the film thickness at various angular position about the rotational axis of the VFD at a rotational speed of 6000 rpm and a 45° tilt angle. A scale factor of 0.02 has been applied to the relative velocity vector. Solid line- tube wall, grey dashed line – film profile.

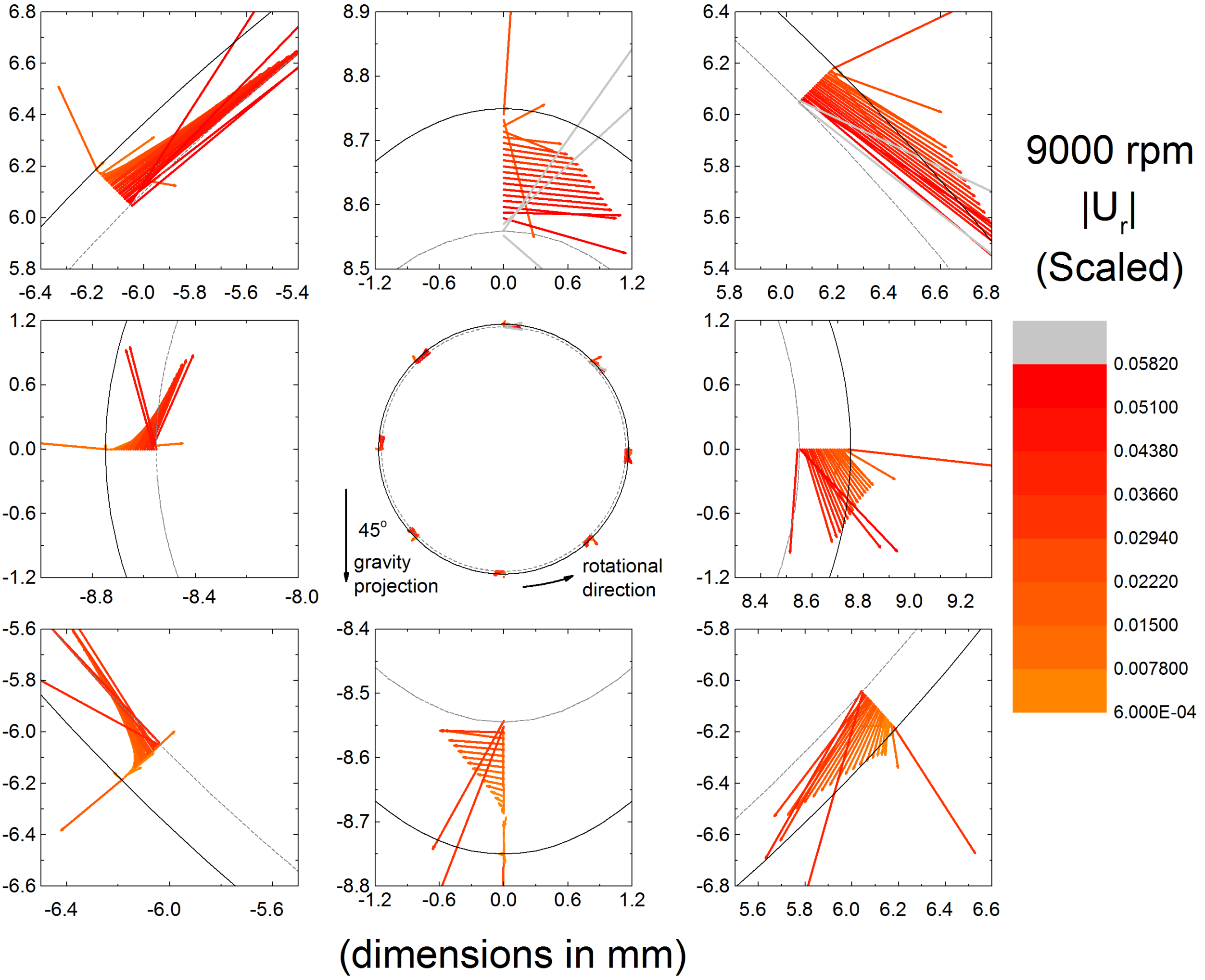

Figure S11g: Relative velocity of toluene across the film thickness at various angular position about the rotational axis of the VFD at a rotational speed of 9000 rpm and a 45° tilt angle. Here a scale factor of 0.02 has been applied to the relative velocity vector. Solid line- tube wall, grey dashed line – film profile.

References

1. Alsulami, I.; Alharbi, T.; Harvey, D.; Gibson, C. T.; Raston, C. L., Controlling the growth of fullerene C60 cones under continuous flow. *Chem. Commun.,* **2018**, 54, 7896-7899.
2. Luo, X.; Al-Antaki, A. H. M.; Harvey, D. P.; Ruan, Y.; He, S.; Zhang, W.; Raston, C. L., Vortex fluidic mediated synthesis of macroporous bovine serum albumin-based microspheres. *ACS Appl. Mater. Interfaces,* **2018,** *10*, 27224-27232.
3. Stormonth-Darling, J. M.; Pedersen, R. H.; How, C.; Gadegaard, N., Injection moulding of ultra high aspect ratio nanostructures using coated polymer tooling. *J. Micromech Microeng.,* **2014,** *24*, 075019.
4. Zheng, C.; Greer, H. F.; Chiang, C.-Y.; Zhou, W., Microstructural study of the formation mechanism of metal–organic framework MOF-5. *CrystEngComm,* **2014,** *16*, 1064-1070.
5. Tranchemontagne, D. J.; Hunt, J. R.; Yaghi, O. M., Room temperature synthesis of metal-organic frameworks: MOF-5, MOF-74, MOF-177, MOF-199, and IRMOF-0. *Tetrahedron* **2008,** *64*, 8553-8557.
6. Millward, A. R.; Yaghi, O. M., Metal− organic frameworks with exceptionally high capacity for storage of carbon dioxide at room temperature. *J. Am. Chem. Soc.,* **2005,** *127*, 17998-17999.
7. Greathouse, J. A.; Allendorf, M. D., The interaction of water with MOF-5 simulated by molecular dynamics. *J. Am. Chem. Soc.,* **2006,** *128*, 10678-10679.